AES 2022 Marrakesh - Morocco

The 8th International Conference on Antennas and Electromagnetic Systems

Proceedings

ISSN 2491-2417

aesconference.org

AES 2022 Marrakesh - Morocco

The 8th International Conference on Antennas and Electromagnetic Systems

Share your comments, photos & videos !

https ://www.facebook.com/aesconferences

@aes_conference

Edited by

Said Zouhdi | Paris-Saclay University, France

CONTENTS

ABOUT AES 3
AES 2022 ORGANIZATION 4
PLENARY SPEAKERS 5
KEYNOTE SPEAKERS 12
CONFERENCE TUTORIALS 14
AES 2022 VENUE 16
GUIDELINES FOR ORAL PRESENTERS 18
GUIDELINES FOR POSTER PRESENTERS 19
TABLE OF CONTENTS 20

ABOUT AES

The International Conference on Antennas and Electromagnetic Systems (AES) serves as an international multidisciplinary forum for deliberations on recent advances and developments in all aspects of Antennas, Electromagnetics, Propagation, and Measurements. Of special interest are : :

- Antenna theory and design ;
- Active, adaptive and reconfigurable antennas ;
- Array antennas ;
- Broadband and multi-band antennas ;
- Antennas for wireless power transmission and harvesting ;
- Millimeter/Terahertz and nano-optical antennas ;
- MIMO, antenna diversity, smart and signal processing antennas ;
- Electromagnetic theory ;
- Computational and numerical techniques ;
- Optimization techniques ;
- Nonlinear electromagnetics ;
- Metamaterials, metasurfaces, FSS and EBG ;
- Photonics and plasmonics ;
- Quantum optics ;
- Propagation theory ;
- 5G propagation ;
- Propagation and remote sensing in complex and random media ;
- Millimeter/terahertz and UWB propagation ;
- Propagation in biological tissues ;
- Antenna and propagation measurement techniques ;
- Material characterization and non-destructive testing ;
- EMI/EMC/PIM chambers, instrumentation, and measurements.

Additionally, through its unique from-Conference-to-Journal-Publication concept, AES offers a rare opportunity for authors to submit papers to Advanced Electromagnetic (AEM) journal and then be considered for publication.

The conference program typically features an excursion program and a banquet.

Following a now well-established tradition AES takes place in unique locations around the world.

Year	Organizers	Venue
2019	Antonio Topa, Said Zouhdi	Lisbon, Portugal
2018	Said Zouhdi	Western Mediteranean Cruise
2017	Junsuk Rho, Said Zouhdi	Incheon, Korea
2016	Enrique Márquez Segura, Eva Rajo-Iglesias, Said Zouhdi	Torremolinos (Malaga), Spain
2014	Lingling Sun, Ke Wu, Said Zouhdi	Hangzhou, China
2013	Hamid M. K. Al-Naimiy, Said Zouhdi	Sharjah-Dubai, United Arab Emirates
2012	Xavier Begaud, Said Zouhdi	Paris, France

AES 2022 ORGANIZATION

Said Zouhdi, General Chair
Paris–Saclay University, France

Local Organizing Committee

Abdelhakim Moutaouakil (Chair), Morocco
Nada Aghad, Morocco
Abderrahim Bakak, Morocco
Omaima Benkhadda, Morocco
Halima Charkaoui, Morocco

Scientific Advisory Committee

Yahia Antar, Canada
Christos Christopoulos, UK
Tie Jun Cui, China
Peter de Maagt, Netherlands
Apostolos Georgiadis, Spain
D. V. Giri, USA
Xun Gong, USA
Lixin Guo, China
Yang Hao, UK
Nathan Ida, USA
Koichi Ito, Japan
Ahmed Kishk, Canada
Kwai Man Luk, Hong Kong
Andrea Massa, Italy
Alain Sibille, France
Ari Sihvola, Finland
Paul Smith, Australia
J(Yiannis) C. Vardaxoglou, UK
Junhong Wang, China

TECHNICAL PROGRAM COMMITTEE

Christos Argyropoulos, USA
Silvio Ernesto Barbin, Brazil
Xavier Begaud, France
Yangjian Cai, China
Pai-Yen Chen, USA
Christophe Craeye, Belgium
Tian Sen Jason Horng, Taiwan
Zhirun Hu, UK
Ruey-Bing Hwang, Taiwan
Sungtek Kahng, Korea
Ali Khenchaf, France
Sebastien Lallechere, France
Allen M. Larar, USA
Howard Lee, USA
Jensen Li, Hong Kong
Jean-Marc Lopez, France
Ozlem Ozgun, Turkey
Oscar Quevedo-Teruel, Sweden
Eva Rajo-Iglesias, Spain
Blaise Ravelo, China
Junsuk Rho, Korea
Josaphat T. Sri Sumantyo, Japan
Van Yem Vu, Viet Nam
Amir I. Zaghloul, USA
Kuang Zhang, China
Qi-Jun Zhang, Canada
Linjie Zhou, China
Arkady Zhukov, Spain

SPECIAL SESSIONS ORGANIZERS

Kofi Edee, Institut Pascal, France
Bratin Ghosh, Indian Institute of Technology - Kharagpur, India

PLENARY SPEAKERS

Goutam Chattopadhyay

NASA-Jet Propulsion Laboratory, USA

Microwave Antennas and Systems for Space Applications

Biography : Goutam Chattopadhyay is a Senior Scientist at the NASA's Jet Propulsion Laboratory, California Institute of Technology, a Visiting Professor at the Division of Physics, Mathematics, and Astronomy at the California Institute of Technology, Pasadena, USA. He received the Ph.D. degree in electrical engineering from the California Institute of Technology (Caltech), Pasadena, in 2000. He is a Fellow of IEEE (USA) and IETE (India) and an IEEE Distinguished Lecturer.

His research interests include microwave, millimeter-wave, and terahertz receiver systems and radars, and development of space instruments for the search for life beyond Earth.

He has more than 350 publications in international journals and conferences and holds more than twenty patents. He also received more than 35 NASA technical achievement and new technology invention awards. He received the IEEE Region-6 Engineer of the Year Award in 2018, Distinguished Alumni Award from the Indian Institute of Engineering Science and Technology (IIEST), India in 2017. He was the recipient of the best journal paper award in 2020 and 2013 by IEEE Transactions on Terahertz Science and Technology, best paper award for antenna design and applications at the European Antennas and Propagation conference (EuCAP) in 2017, and IETE Prof. S. N. Mitra Memorial Award in 2014.

Are We Alone? NASA Technologies to Find Life Beyond Earth and Answers to Other Science Questions

Fundamental science questions drives the selection of NASA missions. We develop instruments to make measurements that can answer those science questions. In this presentation, we will present an overview of the state of the art instruments that we are currently developing and layout the details of the science questions they will try to answer.

Ahmed A. Kishk

Concordia University, Canada

Gap Waveguide Technology Helps Design Efficient Antennas Arrays for mmWave Applications

Biography : Ahmed A. Kishk received a BSc degree in Electronics and Communication Engineering from Cairo University, Cairo, Egypt, in 1977, and BSc. in Applied Mathematics from Ain-Shams University, Cairo, Egypt 1980. In 1981, he joined the Department of Electrical Engineering, University of Manitoba, Winnipeg, Canada, where he obtained his M. Eng. and Ph.D. degrees in 1983 and 1986. From 1977 to 1981, he was a research assistant and an instructor at the Faculty of Engineering, Cairo University. From 1981 to 1985, he was a research assistant at the Department of Electrical Engineering, University of Manitoba. In 1986, he joined the Department of Electrical Engineering, University of Mississippi, as an Assistant Professor. He was on sabbatical leave at the Chalmers University of Technology, Sweden, during the 1994-1995 and 2009-2010 academic years. He was a Professor at the University of Mississippi (1995-2011). He was the Center for Applied Electromagnetic System Research (CAESR) director during 2010-2011. Currently, he is a Professor at Concordia University, Montréal, Québec, Canada (since 2011) as Tier 1 Canada Research Chair in Advanced Antenna Systems. He was an Associate Editor of Antennas and Propagation Society Newsletters from 1990 to 1993. He was a distinguished lecturer for the Antennas and Propagation Society (2013-2015). He was an Editor of Antennas and Propagation Magazine (1993-2014). He was a Co-editor of the special issue, "Advances in the Application of the Method of Moments to Electromagnetic Scattering Problems," in the ACES Journal. He was also an editor of the ACES Journal during 1997. He was an Editor-in-Chief of the ACES Journal from 1998 to 2001. He was the chair of the Physics and Engineering Division of the Mississippi Academy of Science (2001-2002). He was a Guest Editor of the special issue on artificial magnetic conductors, soft/hard surfaces, and other complex surfaces, in the IEEE Transactions on Antennas and Propagation, January 2005. He was a co-guest Editor in IEEE Antennas and Propagation and Wireless Letter on the special cluster on "5G/6G enabling antenna systems and associated testing technologies." He was a technical program committee member for several international conferences. He was a member of the AP-S AdCom (2013-2015). He was the 2017 AP-S president.

Prof. Kishk and his students received several awards. He won the 1995 and 2006 outstanding paper awards for papers published in the Applied Computational Electromagnetic Society Journal. He received the 1997 Outstanding Engineering Educator Award from the Memphis section of the IEEE. He received the Outstanding Engineering Faculty Member of the Year in 1998 and 2009, Faculty research award for outstanding research performance in 2001 and 2005. He received the Award of Distinguished Technical Communication for IEEE Antennas and Propagation Magazine's entry, 2001. He also received The Valued Contribution Award for outstanding Invited Presentation, "EM Modeling of Surfaces with STOP or GO Characteristics – Artificial Magnetic Conductors and Soft and Hard Surfaces" from the Applied Computational Electromagnetic Society. He received the Microwave Theory and Techniques Society, Microwave Prize 2004. He received the 2013 Chen-To Tai Distinguished Educator Award of the IEEE Antennas and Propagation Society. In recognition, "For contributions and continuous improvements to teaching and research to prepare students for future careers in antennas and microwave circuits, Kishk is a Fellow of IEEE since 1998, Fellow of Electromagnetic Academy, and a Fellow of the Applied Computational Electromagnetics Society (ACES). He is a member of the Antennas and Propagation Society, Microwave Theory and Techniques, Sigma Xi Society, Senior member of International Union of Radio Science, Commission B, Phi Kappa Phi, Electromagnetic Compatibility, and Applied Computational Electromagnetics Society.

Gap Waveguide Technology Helps Design Efficient Antennas Arrays for mmWave Applications
Gap waveguide (GWG) technology will be introduced in this talk, which is a highly efficient guiding structure at millimeter-wave bands. It is self-packaged with no radiation losses. Based on this technology, several highly efficient antenna arrays will be presented. In addition, examples of added functions to the arrays will be presented, such as Diplexers separating transmit and receive bands and monopulse array with compact comparable based on the gap waveguide technology, and leaky-wave antenna array for frequency scanning properties.

Stefano Maci

University of Siena, Italy

From the second to the third generation of metasurface antennas

Biography : Stefano Maci received the Laurea Degree cum Laude at University of Florence in 87 and from '97 is a Professor at the University of Siena. His research interest includes high-frequency and beam representation methods, computational electromagnetics, large phased arrays, planar antennas, reflector antennas and feeds, metamaterials and metasurfaces. Since 2000 he was member the Technical Advisory Board of 12 international conferences, member of the Review Board of 6 International Journals. He organized 25 special sessions in international conferences, and he held 10 short courses in the IEEE Antennas and Propagation Society (AP-S) Symposia about metamaterials, antennas and computational electromagnetics. In 2004-2007 he was WP leader of the Antenna Center of Excellence (ACE, FP6-EU) and in 2007-2010 he was International Coordinator of a 24-institution consortium of a Marie Curie Action (FP6). He has been Principal Investigator from 2010 of 6 cooperative projects financed by European Space Agency. In 2004 he was the founder of the European School of Antennas (ESoA), a post graduate school that presently comprises 34 courses on Antennas, Propagation, Electromagnetic Theory, and Computational Electromagnetics and 150 teachers coming from 15 countries. Since 2004 is the Director of ESoA.

Professor Maci is IEEE Fellow since 2004, he has been a former member of the AdCom of IEEE Antennas and Propagation Society (AP-S), associate editor of AP-Transaction, Chair of the Award Committee of IEEE AP-S, and member of the Board of Directors of the European Association on Antennas and Propagation (EurAAP). From 2008 to 2015 he has been Director of the PhD program in Information Engineering and Mathematics of University of Siena, and from 2013 to 2015 he was member of the National Italian Committee for Qualification to Professor. He has been former member of the Antennas and Propagation Executive Board of the Institution of Engineering and Technology (IET, UK). He is presently the director of the consortium FORESEEN, presently involving 48 European Institutions, and principal investigator of the Future Emerging Technology project "Nanoarchitectronics" of the 8th EU Framework program. He was co-founder of 2 Spin-off Company. He is a Distinguished Lecturer of the IEEE Antennas and Propagation Society (AP-S), and recipient of the EurAAP Award in 2014, of the IEEE Shelkunoff Transaction Prize 2015, and of the Chen-To Tai Distinguished Educator award 2016. In 2020 will be TPC Chair of the METAMATERIAL conference. In the last ten years he has been invited 25 times as key-note speaker in international conferences. The research activity of Professor Maci is documented in 150 papers published in international journals, (among which 100 on IEEE journals), 10 book chapters, and about 400 papers in proceedings of international. These papers have received around 6800 citations with h index 41.

Manipulating Circularly Polarized Optical Radiation with Functional Metasurfaces
Metasurfaces have the potential to emerge as essential components for classical and nonclassical optical fields. In this talk, I will first present two examples on how to use metasurfaces to design quarter-wave plates that can not only allow broadband circular-to-linear polarization conversion but also generate vector vortex beams or function as a versatile beam splitter. After that, I will talk about a conceptually new approach to the room-temperature generation of circularly polarized, well-collimated single photons.

Marta Martínez-Vázquez

Renesas Electronics Europe, Germany

The challenge of simulation in modern antenna design

Biography : Marta Martínez-Vázquez was born in Santiago de Compostela, Spain, in 1973. She obtained her MSc. and PhD. degrees in Telecommunication Engineering from the Universidad Politécnica de Valencia, Spain, in 1997 and 2003, respectively. In 2000 she joined the Antennas and EM Modelling department of IMST GmbH in Germany. She is now with Renesas Electronics (Germany). Her research interests include the design and applications of antennas for mobile devices, array antennas , sensors, and RF systems.

Dr. Martínez-Vázquez is currently a member of the IEEE AP-S Education Committee and the IEEE AP-S Distinguished Lecturers Committee. She is a former vice-chair of the European Association of Antennas and Propagation (EurAAP) and a former member of the Administrative Committee of the IEEE Antennas & Propagation Society. She has served as a Distinguished Lecturer for the IEEE AP-S. She has been the chair of the COST IC1102 Action “Versatile, Integrated and Signal-aware Technologies for Antennas (VISTA) and the vice-chair of the COST IC0603 Action “Antenna Sensors and Systems for Information Society Technologies.” Previously, she was a member of the Executive Board of the ACE (Antennas Centre of Excellence) Network of Excellence and the leader of its small antennas activity.

She is currently a feature Editors of the IEEE Antennas & Propagation Magazine and an Associate Editor of the IET Microwaves, Antennas & Propagation Journal. She has over 90 publications, including books, book chapters, journal and conference papers and patents. Dr. Martínez-Vázquez has been awarded the 2004 Best Ph.D. award of the Universidad Politécnica de Valencia and the 2013 IEEE AP-S Lot Shafai Mid-Career Distinguished Achievement Award.

The challenge of EM simulation for the design of automotive radar frontends
This presentation analyses the trends for automotive radar systems, including high-definition imaging and new sensor architectures. The focus will be on RF performance and its impacts on the frontend design. Design bottlenecks like the interface between the MMIC and the radar board, electromagnetic interference or the effect of the casing and the fascia will be discussed.

Yahya Rahmat-Samii

University of California - Los Angeles, USA

From EBG's to Meta-Surfaces and Beyond : Recent Developments and Novel Engineering Applications

Biography : Yahya Rahmat-Samii is a Distinguished Professor, a holder of the Northrop-Grumman Chair in electromagnetics, a member of the U.S. National Academy of Engineering (NAE), a Foreign Member of the Chinese Academy of Engineering (CAE) and the Royal Flemish Academy of Belgium for Science and the Arts, the winner of the 2011 IEEE Electromagnetics Field Award, and the Former Chairman of the Electrical Engineering Department, University of California at Los Angeles (UCLA), Los Angeles, CA, USA. He was a Senior Research Scientist with the Caltech/NASA's Jet Propulsion Laboratory. He has authored or coauthored more than 1100 technical journal and conference papers and has written over 36 book chapters and six books and is the holder many patents. He has more than 20 cover-page IEEE publication articles.

Prof. Rahmat-Samii is a fellow of IEEE, AMTA, ACES, EMA, and URSI. He was a recipient of the Henry Booker Award from URSI, in 1984, which is given triennially to the most outstanding young radio scientist in North America, the Best Application Paper Prize Award (Wheeler Award) of the IEEE Transactions on Antennas and Propagation in 1992 and 1995, the University of Illinois ECE Distinguished Alumni Award in 1999, the IEEE Third Millennium Medal and the AMTA Distinguished Achievement Award in 2000. In 2001, he received an Honorary Doctorate Causa from the University of Santiago de Compostela, Spain. He received the 2002 Technical Excellence Award from JPL, the 2005 URSI Booker Gold Medal presented at the URSI General Assembly, the 2007 IEEE Chen- To Tai Distinguished Educator Award, the 2009 Distinguished Achievement Award of the IEEE Antennas and Propagation Society, the 2010 UCLA School of Engineering Lockheed Martin Excellence in Teaching Award, and the 2011 campus-wide UCLA Distinguished Teaching Award. He was also a recipient of the Distinguished Engineering Educator Award from The Engineers Council in 2015, the John Kraus Antenna Award of the IEEE Antennas and Propagation Society and the NASA Group Achievement Award in 2016, the ACES Computational Electromagnetics Award and the IEEE Antennas and Propagation S. A. Schelkunoff Best Transactions Prize Paper Award in 2017. Rahmat-Samii was the recipient of the prestigious Ellis Island Medal of Honor in 2019. The medals are awarded annually to a group of distinguished U.S. citizens who exemplify a life dedicated to community service. These are individuals who preserve and celebrate the history, traditions, and values of their ancestry while exemplifying the values of the American way of life and are dedicated to creating a better world. Among the receipts of this honor are seven US presidents to name the few. He is listed in Who's Who in America, Who's Who in Frontiers of Science and Technology and Who's Who in Engineering. He has been a plenary and millennium session speaker at numerous national and international symposia.

He has had pioneering research contributions in diverse areas of electromagnetics, antennas, measurements and diagnostics techniques, numerical and asymptotic methods, satellite and personal communications, human/antenna interactions, RFID and implanted antennas in medical applications, frequency-selective surfaces, electromagnetic band-gap and meta-material structures, applications of the genetic algorithms and particle swarm optimizations. He is the designer of the IEEE Antennas and Propagation Society logo which is displayed on all IEEE AP-S publications. He was the 1995 President of the IEEE Antennas and Propagation Society and 2009–2011 President of the United States National Committee (USNC) of the International Union of Radio Science (URSI). He has also served as an IEEE Distinguished Lecturer presenting lectures internationally.

From EBG's to Meta-Surfaces and Beyond : Recent Developments and Novel Engineering Applications

This plenary talk will review the development of various electromagnetic meta-structures, as well as the state-of-the-art concepts, designs and manufacturing techniques including Fused Deposition Modeling (FDM), Stereolithography (SLA), Direct Metal Laser Sintering (DMLS), Inkjet printing and Charge-Programmed Multi-material 3D Printing. Furthermore, a wealth of practical examples will be presented to illustrate promising applications of these intriguing concepts.

David R. Smith

Duke University, USA

Large Aperture Metasurface Antennas to Enable Rapid-Revisit, Satellite-Based Synthetic Aperture Radar

Biography : David R. Smith is the James B. Duke Distinguished Professor of the Electrical and Computer Engineering Department at Duke University, where he also serves as Director for the Center for Metamaterial and Integrated Plasmonics. Dr. Smith is also the Founding Director of the Metamaterials Commercialization Center at Intellectual Ventures in Bellevue, Washington. Dr. Smith received his Ph.D. in 1994 in Physics from UCSD. Dr. Smith's research interests include the theory, simulation and characterization of unique electromagnetic structures, including photonic crystals, metamaterials and plasmonic nanostructures. Smith and his colleagues demonstrated the first left-handed (or negative index) metamaterial at microwave frequencies in 2000, and also demonstrated a metamaterial "invisibility cloak" in 2006. In 2005, Dr. Smith was part of a five-member team that received the Descartes Research Prize, awarded by the European Union, for their contributions to metamaterials and other novel electromagnetic materials. In 2006, Dr. Smith was selected as one of the "Scientific American 50." Since 2009, Dr. Smith has continually been named a "Citation Laureate" by ISI Web of Knowledge for having among the most number of highly cited papers in the field of Physics. Dr. Smith is a co-recipient of the McGroddy Prize for New Materials, awarded by the American Physical Society, for "the discovery of metamaterials" (2013). In 2016, Dr. Smith was elected to the National Academy of Inventors. Dr. Smith has recently been active in transitioning metamaterial concepts for commercialization, being a co-founder of Evolv Technology, Echodyne Corporation, Pivotal Commware, and advisor to Kymeta Corporation—all companies devoted to developing metamaterial products.

Large Aperture Metasurface Antennas to Enable Rapid-Revisit, Satellite-Based Synthetic Aperture Radar

We present the case for waveguide-fed, metasurface apertures as spaceborne antennas for synthetic aperture radar (SAR) imaging. Remote surveillance of earth has gained increasing relevance, both for military as well as commercial purposes. Low- and mid-frequency microwaves have the advantage of penetrating clouds and possibly other obstructions, enabling the capability to persistently monitor terrestrial targets. However, widescale coverage over large portions of the earth requires a significantly large constellation of satellites, each equipped with an appropriate SAR system operating in either a monostatic mode or cooperating with other satellites in a multstatic mode. The SAR antenna must have a suitably large aperture to produce a reasonable beam profile ; must have minimal DC power requirements ; must be efficient, preferably without active heat management ; should be able to steer over a wide angular range electronically ; should be low-cost ; and should have minimal weight and profile. These and many other similar requirements motivate the use of metasurface apertures, which can be designed to satisfy all of these requirements due to their simplified architecture. With recent advances in launch capabilities rapidly driving down the costs and complexity of satellite deployment, a high-performance, low-profile, and low-cost SAR antenna is the key component to enable an appropriately sized constellation for earth observation. Such a constellation could achieve rapid revisit times, allowing the same target to be imaged at radio frequencies over intervals of tens of minutes or fewer. Given the cost per square meter and relative performance of the metasurface aperture, we believe metasurface apertures will play a pivotal role in future satellite-based SAR systems.

Nikolay Zheludev

University of Southampton (UK) and Nanyang Technological University (Singapore)

Metamaterials, anapoles and flying donuts

Biography : Nikolay Zheludev is fellow of the Royal Society and member of the United States National Academy of Engineering. He graduated and was awarded PhD and DSc from Moscow State University. After working as a group leader at the Nonlinear Optics Laboratory at Moscow State University he was appointed a lecturer at the University of Southampton in 1991. He became Chair Professor of Physics and Astronomy in 2000 and Deputy Director (Physics) of Southampton Optoelectronics Research Centre in 2006. Since 2019 he is deputy director of Zepler Institute at Southampton University. From 2012 he became the Founding Director of the Centre for Disruptive Photonic Technologies (CDPT) at Nanyang Technological University (NTU), Singapore. In 2014 he became founding co-Director of the Photonics Institute at NTU.

Professor Nikolay Zheludev is duly regarded by his peers as a pioneer and world leader in the fields of nanophotonics and metamaterials that will make light a major enabling technology of the 21st century. In particular he made seminal contributions to paradigm of metamaterials with “Optical Properties on Demand”, he developed metamaterials with controlled dispersion, boundary conditions and polarization properties, pioneered a new generation of nonlinear, gain, switchable, nano-mechanical and memory metamaterials, introduced the ground-breaking concept of nanophotonics of structural transformations, introduced and developed the “active plasmonics” paradigm, provided the first experimental studies of optical super-oscillations and discovered several new phenomena of nonlinear polarization optics. They are laying the foundation for the development of the new generation of nanotechnology enabled solutions operating across the entire electromagnetic spectrum such as high-bandwidth low-intensity optical switching solution, wavefront management dispersion and polarization control devices, data processing, optical tagging and optical data storage devices, super-resolution imaging devices, detectors and nanolasers and many others. Professor Zheludev is the Web of Science Highly Cited Researcher.

Professor Zheludev has been recognized by the academic community and stakeholders as one of the most influential researchers : he was appointed to Leverhulme Trust Senior Research Professor awarded to “outstanding researchers” (2000), as an EPSRC Senior Research Professor awarded to “outstanding academic scientists and engineers of international repute” by the of the Engineering and Physical Sciences Research Council (2002) and was awarded the Royal Society Wolfson Research Professor (Merit Award) to “respected scientists of outstanding achievement and potential” (2009). He is Fellow of the Institute of Physics (London), Optical Society of America, American Physical Society and European Physical Society that only has less than 100 fellows. In 2015 he received the Thomas Young Medal. (IOP) for “global leadership and pioneering, seminal work in optical metamaterials and nanophotonics”. In 2018 he received The Nanyang Research Award.

Metamaterials, anapoles and flying donuts
In this talk we overview recent progress in toroidal electrodynamics including discoveries of toroidal moments, anapoles and the generation and detection of toroidal pulses. We will report on the unique super-toroidal pulses, propagating skyrmionic formations of electromagnetic fields that can be non-diffracting and exhibit superoscillatory behaviour.

KEYNOTE SPEAKERS

Federico Capasso

Harvard University, USA

Structured light and dark

Wenshan Cai

Georgia Institute of Technology, USA

Field- and Carrier-Enabled Nonlinear Nanophotonics

Debashis Chanda

University of Central Florida, USA

Building Uncooled Infrared Camera based on One Atom Thick Graphene

Christophe Couteau

University of Technology of Troyes (UTT), France

Quantum photonics using nanodiamonds and integrated optics

Christophe Craeye

Université catholique de Louvain, Belgium

Integral equations for metasurface design

Juan Sebastian Gomez Diaz

University of California, Davis, USA

Non-reciprocal phased-array antenna systems

Mona Jarrahi

University of California Los Angeles, USA

Plasmonic heterodyne terahertz receivers with quantum-level sensitivity at room temperature

Panagiotis Kosmas

Kings' College London, UK & Meta Materials Europe SA, Athens, Greece

Microwave Imaging for Medical Diagnostics

Masaya Notomi

NTT Basic Research Labs., Japan

Generating topological states with non-Hermitcity and symmetry breaking

Eva Rajo-Iglesias

University Carlos III of Madrid, Spain

Gap Waveguide Technology using Periodic Structures with Higher Symmetries

Junsuk Rho

Pohang University of Science and Technology (POSTECH), Korea

Intelligent inverse design in nanophotonics using deep-learning

Kaushik Sengupta

Princeton University, USA

Terahertz Chip-Scale Systems

CONFERENCE TUTORIALS

AES 2022 will initiate a series of technical tutorials instructed by world-leading experts on various topics of interest to the AES community. Tutorials are intended to provide a high quality learning experience to conference attendees.

Tutorials & Instructors

Prof. Qammer H. Abbasi

University of Glasgow, UK

Tuesday 24th May
15:00 - 16:00 — Auditorium I

Machine learning enabled wearables for plants and humans at nano scale

Advancement in nanotechnology has made it possible to manufacture sensors, circuits and devices measuring only nano-meters in size. This development is creating an extraordinary opportunity to observe, interact, and optimize physical systems from the very bottom. Wireless communication and networking at nanoscale, however, faces new challenges not encountered in conventional sensor networks. For example, nanoscale antenna calls for wireless communication in the Terahertz band, which encounters new path loss d noise phenomena posing significant challenges for many target applications of such networking. Nanoscale computing and communication is a new and rapidly growing field of research promoting collaboration between wireless networking, nanotechnology, and other fundamental disciplines. However, the research is in its early stages to realize communication and networking at the nanoscale. Currently, there is no definitive standard that provides guidelines and regulation for nanoscale communication and networking. This motivates this proposal to shed light on and promote this area of research and foster.

The objective of this tutorial is to present the opportunities, challenges, and recent advancements of this new and growing inter-disciplinary field explicitly in healthcare and agricultural technology domains using terahertz frequencies.

Prof. Stefano Maci

University of Siena, Italy

Thursday 26th July
15:00 - 16:00 — Auditorium I

Guidance and Radiation of Metasurface-Waves

Metasurfaces constitute a class of thin metamaterials, which can be used from microwave to optical frequencies to create new electromagnetic engineering devices. At microwave frequencies, they are obtained by a dense periodic texture of small elements printed on a grounded slab. Changing the dimension of the elements, being the sub-wavelength 2D-periodicity equal, gives the visual effect of a pixelated image and the electromagnetic effect of a modulation of the equivalent local reactance. The modulated metasurface reactance (MMR) so obtained is able to transform surface or guided waves into different wavefield configurations with required properties. The MMR allows a local modification of the dispersion equation and, at constant operating frequency, of the local wavevector. Therefore, a metasurface modulation permits addressing the propagation path of a surface wave, according with a generalized Fermat principle, as happen in ray-field propagation in inhomogeneous solid medium. This may serve for designing lenses or point-source driven beam-forming networks. When the MMR exhibits a periodic modulation along the SW wavevector, the wave propagation is accompanied by leakage ; i.e., a surface wave is transformed into a leaky-wave, and the structure itself becomes an extremely flat antenna. In every case, introducing asymmetry in the pixel allows for a polarization control. In this tutorial, the basic wave mechanisms will be reviewed showing several antenna applications.

AES 2022 VENUE

AES 20122 is held at

Kenzi Rose Garden Hotel
Avenue President Kennedy
Marrakesh, Morocco

CONGRESS CENTER FLOOR PLANS

Conference Center - Kenzi Rose Garden Farah Marrakech

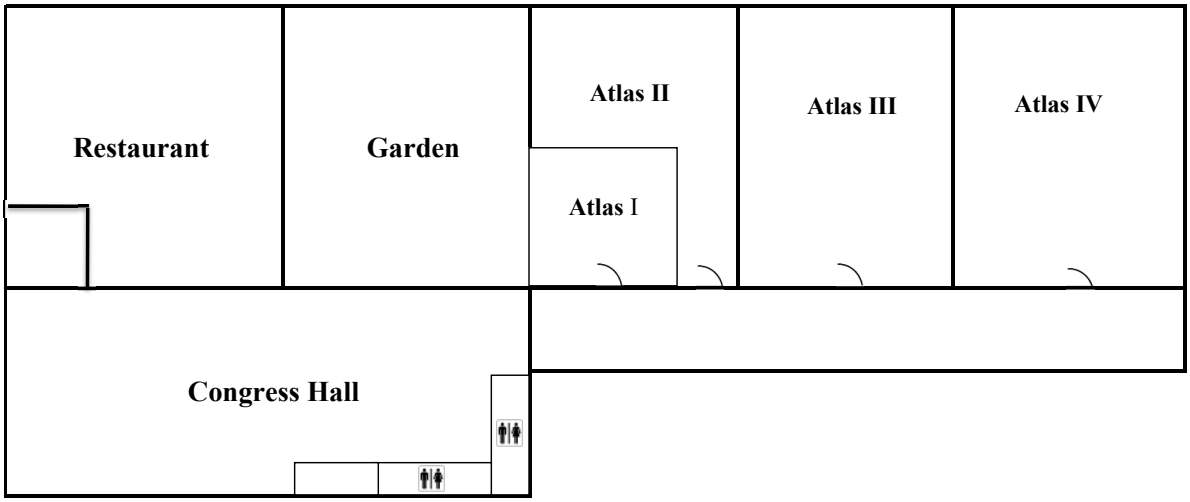

GENERAL INFORMATION

Registration

Registered participants may pick up their conference material at the registration desk which will be located at the Conference Center of the Kenzi Rose Garden Hotel :

• Monday, May 23 (15 :00 - 18 :00)
• Tuesday, May 24 (8 :00 - 17 :30)

Conference Dinner and Horse (Fantasia) Show

Venue : Chez Ali Restaurant
Price : €50 (first come, first served basis)
Schedule : Thursday, May 26 at 20 :00.

Free Shuttle bus service will be provided between the Conference Hotel and Chez Ali Restaurant.

Pick-up time : 19 :30 at Kenzi Rose Garden Hotel.

GUIDELINES FOR ORAL PRESENTERS

IN-PERSON ORAL PRESENTATIONS

Each session room is equipped with a stationary computer connected to a LCD projector. Presenters must load their presentation files in advance onto the session computer. Technician personnel will be available to assist you.

Scheduled time slots for oral presentations are 15 mn for regular, 20 mn for invited presentations, 30 mn for keynote talks and 35 mn for plenary talks, including questions and discussions. Presenters are required to report to their session room and to their session Chair at least 15 minutes prior to the start of their session.

The session chair must be present in the session room at least 15 minutes before the start of the session and must strictly observe the starting time and time limit of each paper :
https://aesconference.org/index.php/AES22/index/pages/view/inperson_oral

ON-LINE ORAL PRESENTATIONS

On-line oral presenters at AES 2022 will be required to submit a pre-recorded presentation (regular : 15-minutes duration, invited : 12-minutes, keynote : 30-minutes and plenary : 35-minutes) which will be made available to view by the participants up to four weeks after the conference.

All speakers have the possibility to give their talk **live** in the allotted time specified in the technical program. At the time of the presentation, the session chairperson will allow the speaker to share their computer screen with the audience (the pre-recording will be used as a backup in case of a no-show or technical difficulty). Speakers also have the option to have their **pre-recorded** presentation played during the live session. **However, all authors, no matter what format they select (live or on replay) should submit a pre-recorded presentation by the deadline of April 25th**.

For both live or on-demand presentations, a 5-minute Question and Answer (Q&A) session will follow each presentation. At least one of the paper's authors must be online to answer questions after the talk.

Detailed instructions available on the conference website :
https://aesconference.org/index.php/AES22/index/pages/view/online_oral

GUIDELINES FOR POSTER PRESENTERS

IN-PERSON POSTER PRESENTATIONS

Presenters are requested to stand by their posters during their session. One poster board, A0 size (118.9 x 84.1 cm), in portrait orientation, will be available for each poster. Pins or thumbtacks are provided to mount your posters on the board. All presenters are required to mount their papers 30mn before the session and remove them at the end of their sessions. Posters must prepared using the standard AES poster template (available on the conference website) :
https://aesconference.org/index.php/AES22/index/pages/view/inperson_poster

ON-LINE POSTER PRESENTATIONS

Poster presenters will be required to submit a poster in **digital format**. Questions can be posted at any time via special chat channels. During the conference, there will be poster sessions scheduled over different time zones where poster presenters will discuss their posters with the attendees via video conferencing. Additional information on the on-line poster presentations are available on the conference website :
https://aesconference.org/index.php/AES22/index/pages/view/online_poster

TABLE OF CONTENTS

Plenary presentations

Are We Alone? NASA Technologies to Find Life Beyond Earth and Answers to Other Science Questions (pp. 35)
Goutam Chattopadhyay,

The challenge of EM simulation for the design of automotive radar frontends (pp. 36)
Marta Martinez-Vazquez,

The Next Generation of Metasurface Antennas (pp. 37)
Stefano Maci,

Gap Waveguide Technology Helps Design Efficient Antennas Arrays for mmWave Applications (pp. 38)
Ahmed A. Kishk,

Electromagnetic Skyrmions of Free Space (pp. 39)
Nikitas Papsimakis, Yijie Shen, Nikolay i. Zheludev,

From EBG's to Meta-Surfaces and Beyond: Recent Developments and Novel Engineering Applications (pp. 40)
Yahya Rahmat-Samii,

Large Aperture Metasurface Antennas to Enable Rapid-Revisit, Satellite-Based Synthetic Aperture Radar (pp. 41)
David R. Smith, Michael Boyarsky, Milton Perque, Tom Driscoll, Russell Hannigan,

Keynote presentations

Nonreciprocal Phased-Array Antenna Systems (pp. 43)
J. Sebastian Gomez,

Terahertz Chip-Scale Systems (pp. 45)
Kaushik Sengupta,

Gap Waveguide Technology using Periodic Structures with Higher Symmetries (pp. 46)
Eva Rajo-iglesias,

Microwave imaging for Medical Diagnostics (pp. 47)
Panagiotis Kosmas,

integral equations for metasurface design (pp. 48)
Christophe Craeye, Modeste Bodehou, Jean Cavillot, Denis Tihon,

Plasmonic Heterodyne Terahertz Receivers with Quantum-Level, Sensitivity at Room Temperature (pp. 49)
Mona Jarrahi,

Metaoptics for Active Photonics (pp. 50)
Federico Capasso,

Field- and Carrier-Enabled Nonlinear Nanophotonics (pp. 51)
Wenshan Cai,

Quantum photonics using nanodiamonds and integrated optics (pp. 52)
Christophe Couteau,

Building Uncooled infrared Camera based on One Atom Thick Graphene (pp. 53)

Debashis Chanda,

Generating topological states with non-Hermiticity and symmetry breaking (pp. 54)
Masaya Notomi,

Conference Tutorials

Machine learning enabled wearables for plants and humans at nano scale (pp. 56)
Qammer H. Abbasi,

Guidance and Radiation of Metasurface-Waves (pp. 57)
Stefano Maci,

Antenna theory and design

A Single-Layer, Near-to-Zero index Metasurface Superstrate for Gain-Enhanced, Circularly Polarized Antenna Designs (pp. 59)
Fatima Khoutar, Mariem Aznabet, Hung Luyen, Otman E. Mrabet, Nader Behdad,

A slotted partial ground plane microstrip patch antenna for ultrawide-band applications (pp. 61)
Saida ibnyaich, Samira Chabaa, Layla Wakrim, Abdessalam El Yassini, Moha M'rabet Hassani, Abdelouheb Zeroual,

Koch Curve Polar Coordinate Transform for UWB Antenna Applications (pp. 62)
Mac Cartier, Rahul Sreekumar, Elisa Pantoja, Mircea R. Stan,

Polarization Reconfigurable Patch Antenna with Ground Slots for Sub-6GHz Applications (pp. 66)
Manpreet Kaur, Hari Shankar Singh, Mayank Agarwal,

Advances in the theory of Characteristic Modes (pp. 69)
Miguel Ferrando-Bataller, Marta Cabedo-Fabres, Eva Antonino-Daviu,

Antennas for wireless power transmission and harvesting

PiFA Multi-layers for smart watch application in the 2.4 GHz for the Bluetooth Low Energy BLE (pp. 72)
Abdelhakim Adli, Marta Cabedo-Fabres, Miguel Ferrando Bataller,

Array antennas, active, adaptive and reconfigurable antennas

Microstrip Antenna Array design for UAV Detection (pp. 76)
Pedro Mendes Ruiz, Xavier Begaud, Francois Magne, Etienne Leder,

10 to 40 GHz ultra-wideband magneto-electric phased array (pp. 84)
Senglee Foo,

Characteristic Modes for the design of compact radiators on complex platforms (pp. 86)
Simone Genovesi, Francesco Alessio Dicandia,

Recent Advances in Conformal Transmitarrays (pp. 88)
Peiyuan Qin, Y. Jay Guo,

Reconfigurable intelligent Surfaces for Future Wireless Communication (pp. 89)
Qammer H. Abbasi,

Decentralized Wireless Coordination for Distributed Antenna Arrays (pp. 90)
Jeffrey Nanzer,

Broadband and multi-band antennas

Wideband Printed Planar Monopole Antenna Element for Wearable Application (pp. 92)
Pedro Falcao, Custodio Peixeiro,

Design and Characterization of Compact Aspen Shape Multi-Element Antenna with isolation improvement for SWB Applications (pp. 94)
N. Suguna, S. Revathi, Ch. Murali Krishna,

A New Microstrip Sierpinski Carpet Antenna Using a Circular Pattern With improved Performance (pp. 101)
Abdelhakim Moutaouakil, Younes Jabrane, Abdelati Reha, Abdelaziz Koumina,

Engineering Highly Directive Optical Waveguide Antennas (pp. 103)
Henna Farheen, Lok-Yee Yan, Till Leuteritz, Siqi Qiao, Florian Spreyer, Christian Schlickriede, Viktor Quiring, Christof Eigner, Thomas Zentgraf, Stefan Linden, Jens Forstner, Viktor Myroshnychenko,

Wideband Design and Optimization of Reflectarray Antennas (pp. 105)
Manuel Arrebola, Daniel R. Prado, Marcos R. Pino,

Dielectric resonator antennas, lens antennas and radomes

Design and Fabrication of ceramic-based antennas (pp. 108)
Wenzhong Lu, Xiao Chuan Wang, Yi Hui Lou,

Millimeter/Terahertz and nano-optical antennas

60 GHz Planar Antenna Array on Glass Substrate for WiGig Communications (pp. 111)
Jacqueline Damas, Niels Neumann, Klaus Wolf, Dirk Plettemeier,

Planar Terahertz Goubau-line Antenna with Endfire Radiation Based on Substrate Mode (pp. 113)
Qing Le Zhang, Bao Jie Chen, Kam Man Shum, Chi Hou Chan,

Graphene loaded 1 x 3 MiMO Terahertz Wideband Antenna with High isolation for Medical and Short indoor Applications (pp. 115)
Ch. Murali Krishna, N. Suguna, S. Revathi,

Base Station and User Equipment Antennas for 60-GHz-Band Near-Field Wireless Communication System: GATE (pp. 121)
Takashi Tomura, Jiro Hirokawa,

Generation of high-quality tunable terahertz vortices based on difference frequency generation (pp. 123)
Katsuhiko Miyamoto, Takashige Omatsu,

The physics of optical patch antennas (pp. 125)
Antoine Moreau,

Phase control of THz-wave in multi-port waveguide structure coupled with bull's-eye antenna (pp. 127)
Seigo Ohno,

Non Conventional Reflectarray and Transmitarray Configurations for Next Generation Applications (pp. 129)

Paola Pirinolo,

THz transmission for fixed wireless services under severe weather conditions (pp. 131)
Tetsuya Kawanishi,

Status and progress of millimeter-wave GaN transistors for next generation high-power radar systems (pp. 132)
Kathia Harrouche, Sri Saran Vankatachalam, Elodie Carneiro, Francois Grandpierron, Farid Medjdoub,

Gain and Efficiency Enhancement of mm-Wave On-Chip Antennas Through Artificial Magnetic Conductors (pp. 133)
Atif Shamim,

Conformal leaky-wave antennas for terahertz wireless links (pp. 134)
Hichem Guerboukha, Rabi Shrestha, Joshua Neronha, Zhaoji Fang, Daniel Mittleman,

Novel resonant-tunneling-diode terahertz oscillators and applications (pp. 135)
Safumi Suzuki,

RFiD antennas/sensors and systems

Statistical Analysis of Matching Properties of Randomly Distributed Thin and Thick Dipoles (pp. 137)
imad Adjali, Benoit Poussot, Shermila Mostarshedi, Jean-Marc Laheurte,

RFiD-UHF Tag Antenna for e-Healthcare Applications (pp. 139)
Mohamed El Khamlichi, Alejandro Alvarez Melcon, Mohamed-Ali Ennasar, Otman EL Mrabet, Juan Hinojosa,

Radar Cross Section estimation of a set of randomly distributed dipoles as an application to RFiD in a high density context (pp. 141)
Aiman Mughal, Jithin Mudakkarappilli Sudersanan, Shermila Mostarshedi, Benoit Poussot, Jean-Marc Laheurte,

Analytical, Computational and numerical techniques

A fast hybrid approach to model roughness effects for 2D the tropospheric maritime long-range propagation (pp. 146)
Thomas Bonnafont, Othmane Benhmammouch, Ali Khenchaf,

A TLM Algorithm forWave Propagation in Human Fat and Muscle TissuesWith a Cole-Cole Dispersion Model (pp. 149)
Mohammed Kanjaa, Otman El Mrabet, Mohsine Khalladdi,

First-order perturbation theory for electromagnetic eigenmodes (pp. 151)
Zoltan Sztranyovszky, Wolfgang Langbein, Egor A. Muljarov,

Accurate and Efficient Analysis of the Electromagnetic Scattering from a thin disk (pp. 153)
Mario Lucido,

Full-vectorial polynomial modal method for circular waveguides. Application to reflection and diffraction at the end of radially inhomogeous cylinders. (pp. 157)
Gerard Granet,

Fundamental limits to electromagnetic response across geometric, frequency, and configuration degrees of freedom (pp. 159)
Owen Miller,

Biophotonics, Biomedical Optics, and imaging

3D printed microrobots controlled by light - Towards environmental and biomedical applications (pp. 161)
Ada-ioana Bunea, Einstom Engay, Alexandre Emmanuel Wetzel, Rafael Taboryski,

Electromagnetic interaction and coupling

The Numerical Results of the Magnetic Behavior of the Thin-layers SFCL (pp. 164)
Salah Belkhiri, Fethi Ben Mebarek, Mohamed Lotfi Khene,

Electromagnetic modelling of Leaf Water Potential under Ultra-Wide Band Microwaves Sensing (pp. 170)
Youness Zaarour, Fatima Zahrae El Arroud, Rafiq El Alami, Hafid Griguer, M'Hamed Drissi,

Enhancement of Light Emission Using ZnO Grating Nanowires: An Experimental and Numerical Study (pp. 174)
Fatima Omeis, Rafik Smaali, Aubry Marin, Audrey Potdevin, Francois Reveret, Emmanuel Centeno, Elena Silaeva, Yves Jourlin, Genevieve Chadeyron, Michel Langlet,

Coupling Between Surface Acoustic Waves and Localized Plasmons in Pillared Phononic Crystals (pp. 176)
Bahram Djafari Rouhani, Adnane Noual, Rock Akiki, Yan Pennec, El Houssaine El Boudouti,

Electromagnetic theory

Symmetry protected and accidental bound states in the continuum in photonic-crystal structures, studied by the resonant-state expansion (pp. 183)
Sam Neale, Egor Muljarov,

Reflection and transmission coefficients at plane interfaces between transformation-optics media (pp. 185)
Mircea Giloan,

GSTC formulation for Maxwell's equations (pp. 186)
Agnes Maurel, Nicolas Lebbe, Kim Pham,

imaging, inverse scattering and remote sensing

Cylindrical Microwave imaging System with Extended Gap Ridge Horn Probes (pp. 189)
Youness Akazzim, Lluis Jofre Roca, Otman EL Mrabet,

Electromagnetic and Geophysical models to estimate wind speed from Sentinel 1 radar images - C band (pp. 191)
Ali Khenchaf,

A New Measurement Configuration for the Microwave Breast Cancer imaging (pp. 193)
ibrahim Akduman, Aleksandar Janjic,

Laser, Laser Source and Application

Hybrid Photonic Crystal lasers for Refractive index Sensing (pp. 195)
Liam O'Faolain,

Metamaterials, metasurfaces, FSS and EBG

On the propagation of surface plasmon polaritons at the interface of low-dimensional acoustic metamaterials (pp. 197)
Tatjana Gric, Edik Rafailov,

Single-shot quantitative phase imaging facilitated by a bifunctional metasurface (pp. 199)
Einstom Llego Engay, Dewang Huo, Radu Malureanu, Ada-ioana Bunea, Andrei Lavrinenko,

THz Range Perforated Metasurface-integrated Multiband Fabry-Perot Microstrip Patch Antenna (pp. 201)
Garima Joshi, R. Vijaya,

All-optical terahertz modulation with an epsilon near-zero material (pp. 203)
Eduardo Alvear-CabezoÌ•n, Emmanuel Centeno, Rafik Smaali, Fernando Gonzalez-Posada, Stephane Blin, Thierry Taliercio,

Synthesis of Ultra-Wide Bandgaps for 2-D Photonic Crystals of Finite Thickness (pp. 205)
Yuriy Sirenko, Kostyantyn Sirenko, Nataliya Yashina, Gerard Granet,

Effective model of propagation across a metasurface with resonant Mie inclusions (pp. 207)
Kim Pham, Agnes Maurel,

Spectral tuning of SPP reflection by quasi-symmetric metal nano-block arrays (pp. 209)
Naoki ichiji, Atsusi Kubo,

Mutual coupling Reduction in antenna arrays using Metasurface (pp. 211)
Safia Jaouad, Mariam Aznabet, Otman EL Mrabet, Mohsine Khalladi,

Design and optimization of holographic nonlinear metasurfaces (pp. 212)
David Hohnel, Jens Forstner, Viktor Myroshnychenko,

Novel Sensing Technique for Non-destructive Composites Monitoring (pp. 214)
Valentina Zhukova, Paula Corte-Leon, Alexandra Allue, Koldo Gondra, Mihail ipatov, Juan Maria Blanco, Julian Gonzalez, Julian Gonzalez, Arkady Zhukov,

Modeling of Spatially Dispersive Quadrupolar Metasurfaces (pp. 216)
Karim Achouri, Ville Tiukuvaara, Olivier J. F. Martin,

Tunable infrared Metasurface based on VO2 for Anti-Counterfeiting and Adaptive Radiative Cooling (pp. 218)
Junichi Takahara,

Conformable metasurface patches for mm-waves holographic applications (pp. 220)
Jianling Xiao, Simon Horsley, Robert i. Hunter, Sebastian A. Schulz, Graham Smith, Duncan A. Robertson, Andrea Di Falco,

Development of Three-Dimensional Fabrication Technologies Using Laser Processing and 3D Printing for Terahertz Optics Production (pp. 222)
Kuniaki Konishi,

Bismuth-based Metamaterials: Fundamentals and Applications (pp. 224)
Johann Toudert, Rosalia Serna,

Manipulating the Polarization of Electromagnetic Waves via Metastructures (pp. 225)
Ruwen Peng, Mu Wang,

Tunable Carbon-Based Nanomaterials for THz Applications (pp. 226)
Aleksandra Przewloka, Nikolaos Xenidis, Serguei Smirnov, Aleksandra Krajewska, Piotr Drozdz, Dmitri Lioubtchenko,

Plasmonic and metamaterial devices based on highly doped semiconductors for infrared applications (pp. 228)
Emmanuel Centeno, Rafik Smaali, Fernando Gonzalez Posada Flores, Laurent Cerutti, Antoine Moreau, Fatima Omeis, Thierry Taliercio,

Breaking the limit of emission suppression in low contrast 3D media (pp. 229)
Meraj E. Mustafa, Lukas Maiwald, Soumyadeep Saha, Mikhail S. Sidorenko, Ruslan R. Yafyasov, Mikhail V. Rybin, Manfred Eich,

Alexander Y. Petrov,

Fast Scattering Matrix Computation for Complex Media and Metasurfaces (pp. 231)
Ho-Chun Lin, Zeyu Wang, Chia Wei Hsu,

Multiphysics simulations for phase change material based nanophotonics (pp. 233)
Dmitry Chigrin,

Radiation control with exceptional points in non-Hermitian plasmonic systems (pp. 234)
Yuto Moritake,

Simultaneously photonic and phononic metamaterials (pp. 236)
Oliver B. Wright, Motonobu Tomoda, Osamu Matsuda, Ting Zhang, Tetsuya Ueda,

Nonlinear Nanomechanical Photonic Metamaterials (pp. 238)
Kevin F. MacDonald, Jinxiang Li, Dimitrios Papas, Jun-Yu Ou, Eric Plum, Nikolay i. Zheludev,

Software-defined reconfigurable metasurfaces for programmable wireless environments (pp. 239)
Maria Kafesaki, O. Tsilipakos, Ch. Liaskos,

Water-based metamaterials for advanced microwave control and sensing (pp. 240)
Rasmus E. Jacobsen, Alex Krasnok, Andrea Alu, Samel Arslanagic, Andrei V. Lavrinenko,

Optomechanics of ultra thin photonic metasurfaces (pp. 241)
Ognjen ilic,

Exact, Feasible and Practical Cloaks for Static and Quasistatic Magnetic Fields (pp. 242)
Alvar Sanchez,

Generation of tunable order Bessel beams with cascaded metasurfaces (pp. 243)
Yan Zhang, Guocui Wang, Bin Hu, Xinke Wang,

Manipulating Circularly Polarized Optical Radiation with Functional Metasurfaces (pp. 245)
Fei Ding,

Non-Hermitian THz metasurfaces based ultra-sensitive sensing (pp. 246)
Teun-Teun Kim, Soojeong Beak, Hosub Lim, Sang Hyun Park, Bumki Min,

Dragging and amplifying light with space-time metamaterials (pp. 247)
P. A. Huidobro, M. G. Silveirinha, E. Galiffi, J. B. Pendry,

Recent progress in the frequency selective metasurfaces in mid infrared wavelength (pp. 249)
Yoshiaki Nishijima, Naoki To,

Subwavelength waveguide arrays for spatial phase manipulation of microwaves (pp. 250)
Dominic Palm, Marco Rahm,

Forward and inverse Design of Electromagnetic Metasurfaces (pp. 251)
Willie John Padilla, Simiao Ren, Jordan M. Malof,

Wideband metamaterial absorber: from concept to naval applications (pp. 252)
Xavier Begaud, Anne Claire Lepage, Michel Soiron, Andre Barka, Sarah Laybros,

Meta-waveguides: a marriage between metasurface and integrated photonics enabling subwavelength control of guided waves (pp. 253)
Xingjie Ni,

Nanophotonics, plasmonics and quantum optics

interplay between nonlinear effects at the nanoscale in engineered optical nanoantennas (pp. 255)
Attilio Zilli, Andrea Locatelli, Davide Rocco, Luca Carletti, Paolo Biagioni, Lamberto Duo, Xiaofei Wu, Swen Grossmann, Carlo Gigli, Giuseppe Marino, Giuseppe Leo, Costantino De Angelis, Bert Hecht, Michele Celebrano, Marco Finazzi,

Analytical and numerical study of T-shaped plasmonic demultiplexer based on Fano and induced transparency resonances (pp. 257)
Madiha Amrani, Soufyane Khattou, Adnane Noual, Abdelkader Mouadili, El Houssaine El Boudouti, Bahram Djafari-Rouhani,

Near-field spectroscopy of a phonon polariton infrared metasurface (pp. 259)
Andrea Mancini, Christopher R. Gubbin, Rodrigo Berte, Alberto Politi, Yi Li, Simone De Liberato, Stefan A. Maier,

Large-area self-assembly of anisotropic Palladium nanostructures for SERS applications (pp. 261)
Mohammad Navvabpour, Pierre Michel Adam, Safi Jradi, Suzanna Akil,

Excitation and Modulation of Surface Plasmon Polaritons at PN++ Junctions (pp. 263)
Dentcho Angelov Genov, Rajkumar Vinnakota, Zuoming Dong, Andrew Briggs, Leland Nordin, Seth Bank, Daniel Wasserman,

inverse Design of Plasmonic Nano-Antenna (pp. 265)
Zhou Zeng, Prabhukumar Venuthurumilli, Xianfan Xu,

Surface Enhanced Visible Absorption of Dye Molecules in the Near-Field of Gold Nano-Antennas (pp. 267)
Zouheir Sekkat,

Emergent PT symmetry and quantum fluctuations in a double-quantum-dot circuit QED set-up (pp. 268)
Archak Purkayastha, Manas Kulkarni, Yogesh Joglekar,

integrated single photons sources based on tapered optical nanofibers (pp. 270)
Alberto Bramati,

Plasmonic nanoantennas and their applications (pp. 271)
Pierre Berini,

Large scale metasurfaces: from plasmonics to photon harvesting in 2D semiconductor layers (pp. 273)
Maria Caterina Giordano, Matteo Gardella, Matteo Barelli, Giorgio Zambito, Giulio Ferrando, Pham Duy Long, Nguyen Si Hieu, Francesco Buatier de Mongeot,

Towards efficient detection and spectroscopy of photons emitted by Er3+ ions in silicon (pp. 275)
Attilio Zilli, Michele Castriotta, Michele Celebrano, Giorgio Ferrari, Lamberto Duo, Marco Finazzi, Enrico Prati,

Magnetoplasmonic nanocavities for the enhanced magnetic control of light polarization via hybridization with dark plasmons (pp. 277)
Paolo Vavassori, Andrey Chuvilin, Alberto Lopez-Ortega, NicolÃ³ Maccaferri, Mario Zapata-Herrera, Matteo Pancaldi,

Controlling the PT Symmetry of Non-Hermitian Graphene Dirac Plasmons and its Application to Terahertz Lasers (pp. 278)
Taiichi Otsuji,

Scalable quantum dot single-photon sources (pp. 279)
Leonardo Midolo,

Light induced exotic chiral surface reliefs in azo-polymers (pp. 280)
Takashige Omatsu,

Dipole-Dipole Coupling Mediated by Lattice Resonances (pp. 282)
Alejandro Manjavacas,

Scalable and efficient photonic designs using disordered metamaterial nanounits (pp. 283)
Ekmel Ozbay,

Universal light encoders: artificial intelligence hardware for light processing components and integrated systems (pp. 284)
A. B. Lopez, F. Getman, M. Makarenko, Q. Wang, A. Fratalocchi,

Temporal dynamic of strongly coupled epsilon-near-zero media (pp. 285)
Mehdi H. Ebrahim, Andrea Marini, Nathaniel Kinsey, Jacob B. Khurgin, Lucia Caspani, Marcello Ferrera, Vladimir M. Shalaev, Alexandra Boltasseva, Daniele Faccio, Matteo Clerici,

Dynamically Tuneable Conducting Polymer Nanooptics (pp. 286)
Magnus Jonsson,

Quantum dynamics in structured photonic fields (pp. 287)
Jonas Wotzel, Jamal Berakdar,

Tunable Mie resonances in silicon nanostructures probed with electron energy-loss spectroscopy (pp. 288)
SÃ¸ren Raza,

Riesz-projection based simulation and analysis of resonant photonic devices and machine-learning based parameter optimization (pp. 289)
Fridtjof Betz, Felix Binkowski, Matthias Plock, Lilli Kuen, Phillip Manley, Philipp-immanuel Schneider, Martin Hammerschmidt, Lin Zschiedrich, Sven Burger,

Optoinduced magnetization from the spin and orbital angular momenta of light (pp. 290)
Vage Karakhanyan, Clement Eustache, Yannick Lefier, Thierry Grosjean,

ENSEMBLE3 - Novel materials for photonics - possibilities provided by crystal growth (pp. 292)
Dorota A. Pawlak,

Strong Light-Matter interaction in nanohybrid architectures (pp. 293)
Andrea Toma,

Optics and Photonics

Laser scanners with rotational Risley prisms: A graphical method to determine and study exact scan patterns (pp. 295)
Virgil-Florin Duma, Alexandru-Lucian Dimb,

High-Speed Fiber-Wireless-Fiber Bridge System for Fixed Wireless Link in Millimeter-Wave Band Using Photonic Technology (pp. 297)
Dat Pham,

Giant Pockels Effect in Thin Film Barium Titanate for Reconfigurable Photonics (pp. 299)
Aaron Danner,

Shapeshifting diffractive optical elements (pp. 300)
Antonio Ambrosio,

integrated microresonator frequency comb source for massive-parallel optical communication (pp. 301)
Takasumi Tanabe, Soma Kogure, Shun Fujii,

Photothermal effects in nanostructures: from ultrafast optical symmetry breaking to extreme heat dissipation (pp. 303)
Alessandro Alabastri,

Optoelectronics, Photonic Materials and Devices

Electronic and optoelectronic properties of black phosphorous (pp. 305)
Vivek Chaudhary, Petr Neugebauer, Omar Mounkachi, Salma Lahbabi, Abdelouahed Elfatimy,

Towards far-field multipole retrieval with a reconfigurable photonic integrated circuit (pp. 306)
Johannes Butow, Jorg Eismann, Varun Sharma, Dorian Braandmuler, Peter Banzer,

Towards Robust Optical Data Processing with Photonic integrated Circuits (pp. 308)
Jian Wang,

Long Wavelength infrared Detection by Combining Nano-Thermoelectrics and Sub-Wavelength Absorbers (pp. 309)
Aapo Varpula, Anton Murros, Kuura Sovanto, Jonna Tiira, Kirsi Tappura, Mika Prunnila,

Scattering and diffraction

Effective Scattering Control of Graphene Micro-disks Utilizing the Fundamental Plasmon Resonances (pp. 311)
Stamatios Amanatiadis, Vasileios Salonikios, Michalis Nitas, Theodoros Zygiridis, Nikolaos Kantartzis, Traianos Yioultsis,

Scattering by a dielectric cylinder with arbitrary cross section using Pseudo-spectral Modal Method (pp. 313)
Tsirinantenaina A. Rafalimanana, Gerard Granet, Karyl Danielson Raniriharinosy,

Limits on Electromagnetic Scattering (pp. 315)
Pengning Chao, Benjamin Strekha, Rodrick K. Defo, Sean Molesky, Alejandro W. Rodriguez,

5G propagation

Design of Multiband-Filters for Mobile Radio Applications (pp. 317)
Mohamed Karim Laoufi, Slimane Mekaoui, Mohamed Lamine Tounsi,

Body-centric propagation

A Biomedical implantable Patch Antenna with X shaped slot for Wireless Communication Networks (pp. 320)
Sarosh Ahmad, Shuvra Barua, Ayesha Akram, Bilal Manzoor,

Millimeter/terahertz and UWB propagation

A Terahertz Polarization Splitter Using a Hybrid Plasmonic Waveguide (pp. 327)
Jun Shibayama, Arata Yamamoto, Junji Yamauchi, Hisamatsu Nakano,

Non-linear THz studies at the TeraFERMi beamline (pp. 329)
Andrea Perucchi,

Propagation for vehicular communications

A Stochastic Ray-Based Model for UAV-to-Ground Radio Channels in Built-Up Environments (pp. 331)
Claude Oestges,

Propagation theory

Critical distances for near-ground propagation: application to dipole antennas (pp. 334)
Hocine Anis Belaid, Shermila Mostarshedi, Benoit Poussot, Jean-Marc Laheurte,

Radar systems, target detection, localization, and tracking

Target DOA Estimation using GLRT and Crosstalk Reduction for MiMO Radar (pp. 339)
Oscar Gomez, Florence Nadal, Benoit Poussot, Pascale Jardin, Genevieve Baudoin,

Object reconstruction via radar detection behind walls (pp. 343)
Aihua Wood, Ryan Wood, Matthew Charnley,

Small target detection from a drone-based phased-array radar (pp. 345)
Zaynab Guerraou, Ali Khenchaf, Fabrice Comblet, Phillipe Morgand, Phillipe Pouliguen, Florent Jangal,

Antenna and propagation measurement techniques

THz Corrugated Horn Antennas as TEM Mode-Convertor for Power Measurement and Material Characterization in Free-Space (pp. 348)
Alireza Kazemipour, Johannes Hoffmann, Michael Wollensack, Daniel Stalder, Juerg Ruefenacht, Markus Zeier,

EMi/EMC/PiM chambers, instrumentation, and measurements

Assessment of Electromagnetic Field Threats to a Military Airport (pp. 351)
D. V. Giri, F. M. Tesche,

Material Characterization and non-destructive testing

High Sensitivity SSR Based Sensor Used for Permittivity Measurement (pp. 354)
Youness Zaarour, Mohammed Ali Ennasar, Otman El Mrabet, Hafid Griguer, M'Hamed Drissi,

Giant Magnetoimpedance Microwires for Sensor Applications (pp. 357)
Arkady Zhukov, Paula Corte-Leon, Lorena Gonzalez-Legarreta, Mihail ipatov, Juan Maria Blanco, Valentina Zhukova,

Real-time measurement system using multi-wavelength THz-wave parametric generation and detection (pp. 359)
Kosuke Murate, Kodo Kawase,

Backward Terahertz-wave parametric oscillator and its application in nondestructive testing (pp. 361)
Hiroaki Minamide,

Mm-wave, THz, and quasi-optical antenna measurements

Ultrabroadband terahertz pulses from a Ge:Au photoconductive emitter (pp. 364)
Abhishek Singh, Alexej Pashkin, Stephan Winnerl, Malte Welsch, Cornelius Beckh, Philipp Sulzer, Alfred Leitenstorfer, Manfred Helm, Harald Schneider,

Advanced numerical and theoretical tools as applied to domains ranging from modern nanophotonics

An Asynchronous Co-Simulation Method for Time-Dependent Simulations: Application to a Transmission Line Network (pp. 367)
imane Massaoudi, Pierre Bonnet,

Efficient computation of EM scattering from a dielectric cylinder covered with graphene strips (pp. 369)
Brahim Guizal, Youssef Jeyar, Mauro Antezza,

The polariton laser ridge: an exception to the rule (pp. 371)
Christelle Brimont, Hassen Souissi, M. Gromovyi, T. Gueye, L. Doyennette, D. D. Solnyshkov, G. Malpuech, E. Cambril, S. Bouchoule, B. Alloing, S. Rennesson, F. Semond, J. Zuniga-Perez, T. Guillet,

Casimir interaction on gratings (pp. 373)
Brahim Guizal, Mauro Antezza,

Graphene surface magneto-plasmons excited through a magnetostatic biased graphene-strip grating : Semi analytical Approach (pp. 374)
Maha Ben Rhouma, Kofi Edee, Brahim Guizal,

A direct and an inverse domain decomposition method applied to Fourier modal method: simulation of large scale device response (pp. 376)
Kofi Edee, Gerard Granet, Francoise Paladian, Pierre Bonnet,

Other EM topics

Separated Microstrip Antenna for Satellite Simulators (pp. 379)
Shahin Salarian, Dariush Mirshekar,

MMV 60 GHz Tunable Periodic Filter (pp. 387)
Abdolreza Divsalar, Shahin Salarian, Dariush Mirshekar-Syahkal,

Plenary presentations

© 2022 California Institute of Technology. Govt. sponsorship acknowledged.

Are We Alone? NASA Technologies to Find Life Beyond Earth and Answers to Other Science Questions

Goutam Chattopadhyay
NASA-Jet Propulsion Laboratory, California Institute of Technology
4800 Oak Grove Drive, Pasadena, CA 91109, USA.

NASA's Jet Propulsion Laboratory, which completed eighty years of its existence in 2016, builds instruments for NASA missions. Exploring the universe and our own planet Earth from space has been the mission of NASA. Robotics missions such as Voyager, which continues to go beyond our solar system, missions to Mars and other planets, exploring the stars and galaxies for astrophysics missions, exploring and answering the question, "*are we alone in this universe*?" has been the driving force for NASA scientists for more than six decades.

Fundamental science questions drives the selection of NASA missions. We develop instruments to make measurements that can answer those science questions. In this presentation, we will present an overview of the state of the art instruments that we are currently developing and layout the details of the science questions they will try to answer. Rapid progress on multiple fronts, such as commercial software for component and device modeling, low-loss circuits and interconnect technologies, cell phone technologies, and submicron scale lithographic techniques are making it possible for us to design and develop smart, low-power yet very powerful instruments that can even fit in a SmallSat or CubeSat. We will also discuss the challenges of the future generation instruments in addressing the needs for critical scientific applications.

The research described herein was carried out at the Jet Propulsion Laboratory, California Institute of Technology, Pasadena, California, USA, under contract with National Aeronautics and Space Administration.

The challenge of EM simulation for the design of automotive radar frontends

Marta Martínez-Vázquez

Automotive Analog & Power Product Marketing Division, Automotive Solution Business Unit, Renesas Electronics Europe GmbH, Düsseldorf, Germany
marta.martinez.wh@renesas

Abstract

RADAR has proved its reliability and performance in ADAS applications like adaptive cruise control, and it is expected that its use will be extended. This presentation analyses the trends for automotive radar systems, including high-definition imaging and new sensor architectures. The focus will be on RF performance and its impacts on the frontend design. Design bottlenecks like the interface between the MMIC and the radar board, electromagnetic interference or the effect of the casing and the fascia will be discussed.

The Next Generation of Metasurface Antennas

Stefano Maci

[1]Department of Information Engineering and Mathematics, University of Siena, Siena, Italy
E-mail: macis@dii.unisi.it

Abstract

"Metasurface" (MTS) denotes a surface constituted at microwave frequency by PCB or 3D printed elements small in terms of wavelengths that collectively exhibits equivalent homogeneous boundary conditions to any interacting electromagnetic fields. MTSs have had and are having a strong impact in Antenna applications. In the years 2000-2010 MTS for antennas were essentially uniform in space and realized by periodic printed elements. This was the first generation of MTS. In the second generation (2010-2020), MTS for antennas was constructed in such a way to change boundary conditions in space and control the scattered field. Today we are facing a transition to the third generation of MTS antennas, where MTSs change boundary conditions in space and time, opening new perspectives in 5G communications and beyond. In this presentation, the evolution of MTS antennas is described, with new ideas and examples on future communication scenarios. Fig. 1 presents a roadmap and some pictures of prototypes presented in the talk.

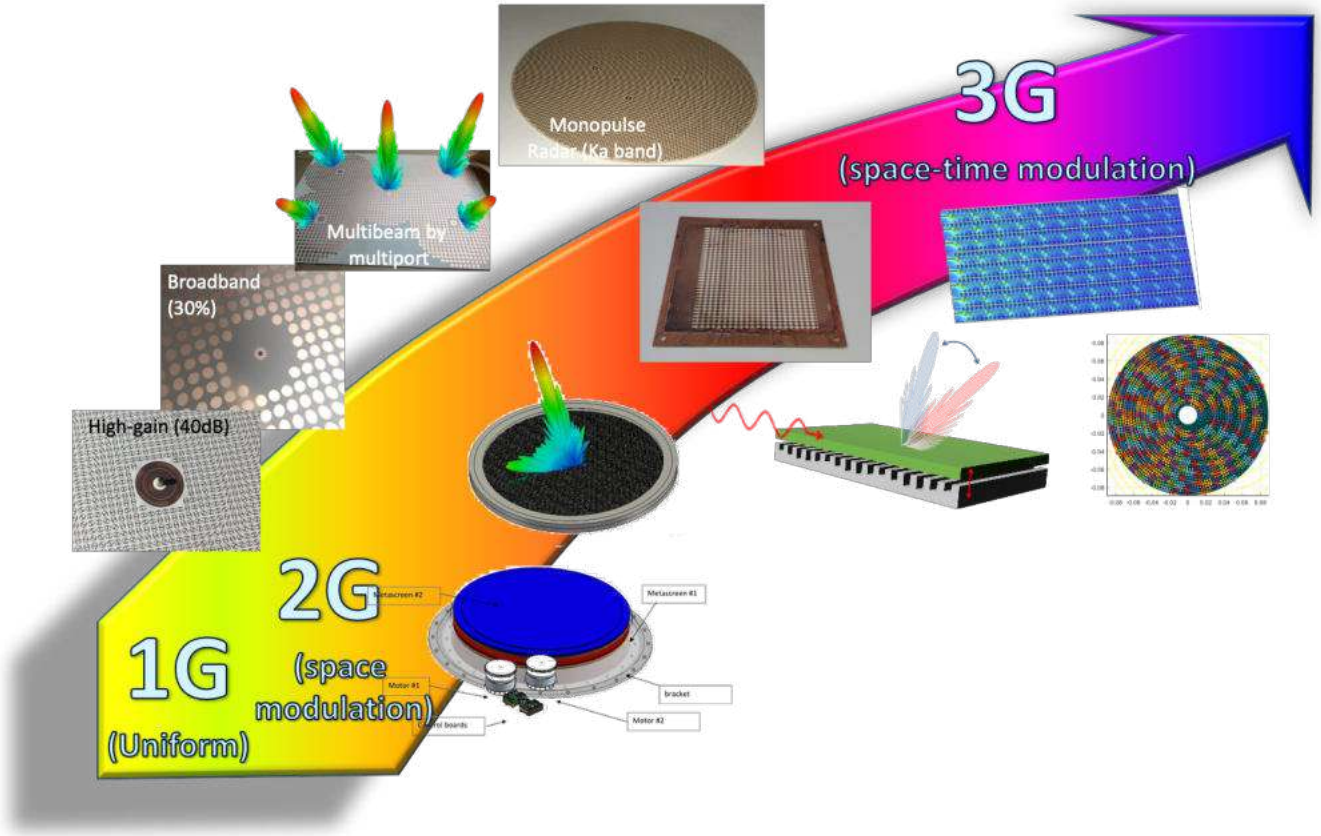

Fig. 1 Roadmap of metasurface antennas and some of the prototypes discussed in the talk.

Gap Waveguide Technology Helps Design Efficient Antennas Arrays for mmWave Applications

Ahmed A Kishk

Department of Electrical and Computer Engineering, Concordia University
Montreal, Canada
*corresponding author, E-mail: ahmed.kishk@concordia.ca

Abstract

Gap waveguide (GWG) technology will be introduced in this talk, which is a highly efficient guiding structure at millimeter-wave bands. It is self-packaged with no radiation losses. Based on this technology, several highly efficient antenna arrays will be presented. In addition, examples of added functions to the arrays will be presented, such as Diplexers separating transmit and receive bands and monopulse array with compact comparable based on the gap waveguide technology, and leaky-wave antenna array for frequency scanning properties.

The fifth-generation (5G) and beyond for the wireless network was the driving force in increasing the demand for millimeter-wave frequency systems to cover the high demand for faster data and reliable service in mobile communication. At these frequencies, the propagation path loss and material losses increase reducing the system efficiency. Therefore, there is a need for efficient millimeter-wave guiding structures that overcome such limitations. Gap waveguide (GWG) technology is found to overcome such limitations at millimeter-wave bands. The advantages of this structure are in its suitability for millimeter-wave applications as it is self-packaged with no radiation losses. Such a guiding structure is based on the bandwidth of the electromagnetic bandgap (EBG) of a periodic structure within which the guiding structure is operating. A minimum of 1:2 bandwidth is achievable with the possibility of increasing it under some conditions. The GWG can be realized using several technologies. Using such highly efficient guiding structures, highly efficient antenna arrays are realized. In this talk, several highly efficient antenna arrays will be presented. In addition, examples of added functions to the arrays will be presented such as Diplexers separating transmit and receive bands and monopulse array with compact comparable based on the gap waveguide technology, and leaky wave antenna array for frequency scanning properties.

Electromagnetic Skyrmions of Free Space

Nikitas Papsimakis[1], Yijie Shen[1], Nikolay I. Zheludev[1,2]

[1]University of Southampton, UK and [2]Nanyang Technological University, Singapore

E-mail: zheludev@souton.ac.uk

Abstract

The transverse electromagnetic waves generated by oscillating Hertzian dipole emitters are major information and energy carriers. In 1996, Hellwarth and Nouchi theoretically identified a radically new, non-transfer type of propagating electromagnetic pulses of toroidal topology that are propagating counterparts of the localized toroidal dipoles. In this talk we overview recent progress in toroidal electrodynamics including generation and detection of toroidal pulses, the study of their space-time "entanglement" and isodiffraction behaviour and light-matter interactions involving anapoles. We will report on the unique supertoroidal pulses, propagating skyrmionic formations of electromagnetic fields that can be non-diffracting and exhibit superoscillatory behavior.

From EBG's to Meta-Surfaces and Beyond: Recent Developments and Novel Engineering Applications

Yahya Rahmat-Samii

University of California Los Angeles, ECE Department Los Angeles, CA 90095-1594, USA

E-mail: rahmat@ee.ucla.edu

Abstract

It has been over a quarter of a century that modern engineered materials have found their ways in manipulating electromagnetic waves. Advanced prototyping approaches and sound theoretical developments attracted many researchers worldwide to contribute and suggest novel devices with out-of-the-box characteristics. There exist now many applications in diverse areas of electromagentics engineering and antenna designs that researchers and engineers are excited to utilize the so-called "meta-materials" as part of their design tool kits. From frequency selective surfaces (FSS) to electromagnetic band-gap (EBG) ground planes, from impedance boundaries to Huygens metasurfaces, novel electromagnetic structures have been emerging in both microwaves and optics. Many intriguing phenomena occur within and on the surfaces of these structures with profound utilizations in practical applications such as low profile antennas, reflectarrays, transmitarrays, bending lights, orbital angular momentum beams, etc. This plenary talk will review the development of various electromagnetic meta-structures, as well as the state-of-the-art concepts, designs and manufacturing techniques including Fused Deposition Modeling (FDM), Stereolithography (SLA), Direct Metal Laser Sintering (DMLS), Inkjet printing and Charge-Programmed Multi-material 3D Printing. Furthermore, a wealth of practical examples will be presented to illustrate promising applications of these intriguing concepts. Representative materials will also be presented from two recent books, "*Surface Electromagnetics: With Applications in Antenna, Microwave and Optical Engineering", Eds. F. Yang and Y. Rahmat-Samii, Cambridge University Press, 2019*, and "*Electromagnetic Band Gap Structures in Antenna Engineering", F. Yang and Y. Rahmat-Samii, Cambridge University Press, 2009*.

Large Aperture Metasurface Antennas to Enable Rapid-Revisit, Satellite-Based Synthetic Aperture Radar

David R. Smith[1,2*], Michael Boyarsky[1], Milton Perque[2], Tom Driscoll[3], and Russell Hannigan[4]

[1]Department of Electrical and Computer Engineering, Duke University, Durham, North Carolina, USA
[2]Metacept Corporation, Durham, North Carolina, USA
[3]Echodyne Corporation, Redmond, Washington, USA
[4]Xplore Corporation, Redmond, Washington, USA
*corresponding author, E-mail: drsmith@duke.edu

Abstract

We present the case for waveguide-fed, metasurface apertures as spaceborne antennas for synthetic aperture radar (SAR) imaging. Remote surveillance of earth has gained increasing relevance, both for military as well as commercial purposes. Low- and mid-frequency microwaves have the advantage of penetrating clouds and possibly other obstructions, enabling the capability to persistently monitor terrestrial targets. However, widescale coverage over large portions of the earth requires a significantly large constellation of satellites, each equipped with an appropriate SAR system operating in either a monostatic mode or cooperating with other satellites in a multstatic mode. The SAR antenna must have a suitably large aperture to produce a reasonable beam profile; must have minimal DC power requirements; must be efficient, preferably without active heat management; should be able to steer over a wide angular range electronically; should be low-cost; and should have minimal weight and profile. These and many other similar requirements motivate the use of metasurface apertures, which can be designed to satisfy all of these requirements due to their simplified architecture. With recent advances in launch capabilities rapidly driving down the costs and complexity of satellite deployment, a high-performance, low-profile, and low-cost SAR antenna is the key component to enable an appropriately sized constellation for earth observation. Such a constellation could achieve rapid revisit times, allowing the same target to be imaged at radio frequencies over intervals of tens of minutes or fewer. Given the cost per square meter and relative performance of the metasurface aperture, we believe metasurface apertures will play a pivotal role in future satellite-based SAR systems.

Keynote presentations

Nonreciprocal Phased-Array Antenna Systems

J. Sebastian Gomez-Diaz

Electrical and Computer Engineering Department, University of California, Davis, USA
E-mail: jsgomez@ucdavis.edu

Abstract

This talk describes the concept and experimental demonstration of nonreciprocal phased-array antennas able to exhibit (i) an independent control of their transmission and reception patterns at the same operation frequency; and (ii) nonreciprocity at the polarization level, i.e., the antennas transmit with one polarization but receive with the opposite handedness. The proposed approach can be applied to develop efficient nonreciprocal phased-array antennas across the electromagnetic spectrum and find broad applications in wireless communication and polarimetric radar and sensing systems.

1. Summary

Magnetless nonreciprocity [1] has recently attracted significant attention to realize a wide variety of CMOS-compatible devices such as isolators [2], circulators [3], and filters [4,5] operating from radiofrequencies to the infrared and telecom wavelengths [6,7]. However, these techniques have mostly been applied to develop *nonreciprocal guided components* whereas little attention has so far been devoted to *nonreciprocal antennas*. Such devices have the potential to significantly impact wireless communication, radar, and sensing systems by enabling an independent manipulation of their transmission and reception patterns, including polarization, at the same operation frequency. The prospective applications of such devices are enormous: from enhanced channel capacity in MIMO radio links and radar systems able to effectively handle jamming signals and strong interferences to polarimetric sensors with boosted performance that do not interfere the environment that they are monitoring.

Very recent efforts in the field of nonreciprocal antennas have been focused on spatio-temporally modulated leaky-wave structures [8-10] that exploit space-time transition to provide isolation between transmission and reception in specific directions in space. Unfortunately, it is challenging to manipulate the radiation pattern and polarization of leaky-wave antennas at a fixed frequency, and these devices are usually bulky and with little use in practice. Other option could be to connect a standard antenna, like a planar Yagi-Uda, with a nonreciprocal band-pass filter based on spatio-temporal modulation [11]. Even though this approach provides over 20dB of isolation between transmission and reception that can be reversed at will, it lacks reconfiguration schemes to favor specific directions in space. In this context, it should be mentioned that several types of time-modulated metasurfaces have recently been put forward [12-15] to manipulate plane waves propagating in free-space, including frequency translation and nonreciprocal reflection/refraction at fixed spatial directions.

In this invited talk, we will discuss a new type of nonreciprocal component recently developed in our group: *phased-array antennas able to independently manipulate their transmission and reception patterns at the same operation frequency [16]*. Our approach is based on merging time-modulated resonators with high-Q structures –such a patch antennas– to achieve very efficiency conversion between only two frequencies (one related to waves in free-space and other to guided signals) and then taking advantage of the photonic Aharonov-Bohm effect [17] to control in a nonreciprocal manner the relative phases of the fields radiated/received by the elements of the array. We will demonstrate isolation over 40dB at desired, tunable directions in space using a simple 2 element phased-array system at 2.4 GHz, with important implications in the next generation of radar and wireless communication systems.

Furthermore, *we will theoretically and experimentally demonstrate that a single antenna element can exhibit nonreciprocity at the polarization level* – i.e., transmit waves with one polarization but receive waves with opposite handedness [18]. Nonreciprocal polarization control has critical implications in sensing systems. For instance, let us consider an antenna radiating right-handed circularly polarized (RHCP) waves. Upon a simple reflection on a metallic screen, such waves acquire a left-handed circular polarization (LHCP) and thus cannot be effectively received by the same antenna. Antennas with nonreciprocal polarization handedness are perfectly suited to receive circularly polarized waves reflected on metallic surfaces and, more broadly, to test the polarization response of unknown objects. Our efforts constitute a significant step forward in the state of the art of polarimetric systems, which usually require independent transmit and receive antennas prone to misalignments, and find exciting applications in sensors and weather radars among many others.

Acknowledgements

This work was supported by the National Science Foundation with CAREER Grant No. ECCS-1749177. Author wish to warmly thank everyone involved in the development of non-reciprocal components and antennas at the University of California, Davis, including Prof. Alvarez-Melcon (during

his sabbatcal at Davis), Dr. J. Zang, Dr. J. Do, Dr. X. Wu, and Prof. X. Liu.

References

[1] D. L. Sounas and A. Alù, "Non-reciprocal photonics based on time modulation", Nat. Photonics, 11, 774, 2017.

[2] S. Taravati, "Self-biased broadband magnet-free linear isolator based on one-way space-time coherency," Phys. Rev. B., 96, 35150, 2017.

[3] A. Kord, D. L. Sounas, and A. Alu, "Magnet-less circulators based on spatiotemporal modulation of bandstop filters in a delta topology," IEEE Trans. Microw. Theory Techn., 66, 911-926, 2018.

[4] X. Wu, X. Liu, M. D. Hickle, D. Peroulis, J. S. Gomez-Diaz, and A. A. Melcon, "Isolating bandpass filters using time-modulated resonators," IEEE Trans. Microw. Theory Techn., 67, 2331-2345, 2019.

[5] A. Alvarez-Melcon, X. Wu, J. Zang, X. Liu, and J. S. Gomez-Diaz, "Coupling matrix representation of nonreciprocal filters based on time modulated resonators," IEEE Trans. on Microw. Theory and Techn. 67, 4751-4763, 2019.

[6] D. Correas-Serrano and J. S. Gomez-Diaz, "Nonreciprocal and collimated surface plasmons in drift-biased graphene metasurfaces", Physical Review B, 100, 081410, 2019.

[7] D. Correas-Serrano, A Alù, J.S. Gomez-Diaz," Magnetic-free nonreciprocal photonic platform based on time-modulated graphene capacitors", Physical Review B, 98, 165428, 2018.

[8] Y. Hadad, J. C. Soric, and A. Alù, "Breaking temporal symmetries for emission and absorption", Proc. Natl. Acad. Sci. U.S.A. 113, 3471, 2016.

[9] D. Correas-Serrano, J. S. Gomez-Diaz, D. L. Sounas, Y. Hadad, A. Alvarez-Melcon, and A. Alù, "Nonreciprocal graphene devices and antennas based on spatiotemporal modulation", IEEE Antennas Wireless. Propag. Lett. 15, 1529, 2016.

[10] S. Taravati and C. Caloz, "Mixer-duplexer-antenna leaky-wave system based on periodic space-time modulation", IEEE Trans. Antennas Propag. 65, 442, 2017.

[11] J. Zang, X.T. Wang, A. Alvarez Melcon, and J. S. Gomez-Diaz, "Nonreciprocal Yagi-Uda Filtering Antennas", IEEE Antennas Wireless Propag. Lett., 18, 2661-2665, 2019.

[12] M. Liu, D. A. Powell, Y. Zarate, and I. V. Shadrivov, "Huygens' metadevices for parametric waves", Phys. Rev. X 8, 031077, 2018.

[13] L. Zhang, X. Q. Chen, S. Liu, Q. Zhang, J. Zhao, J. Y. Dai, G. D. Bai, X. Wan, Q. Cheng, G. Castaldi, V. Galdi, and T. J. Cui, "Space-time-coding digital metasurfaces", Nat. Commun. 9, 4334 2018.

[14] Z. Wu and A. Grbic, "Serrodyne frequency translation using time-modulated metasurfaces", IEEE Transactions on Antennas and Propagation, vol. 68, 1599-1606, 2020.

[15] J. Zang, D. Correas-Serrano, J. T. S. Do, X. Liu, A. Alvarez-Melcon, and J. S. Gomez-Diaz, "Nonreciprocal wavefront engineering with time-modulated gradient metasurfaces", Phys. Rev. Appl. 11, 05405, 2019.

[16] J. Zang, A. Alvarez-Melcon, and J. S. Gomez-Diaz, "Nonreciprocal Phased Array Antennas", Phys. Rev. Appl. 12, 054008, 2019.

[17] K. Fang, Z. Yu, and S. Fan, "Experimental demonstration of a photonic Aharonov-Bohm effect at radio frequencies", Phys. Rev. B 87, 060301, 2013.

[18] M. A. Bourkov, J. Do, X. Liu, A. Alvarez-Melcon, and J. S. Gomez-Diaz, "Time-modulated Patch Antennas with Nonreciprocal Polarization Handedness", IEEE Antennas and Propagation Symposium, 2020.

Terahertz Chip-Scale Systems

Kaushik Sengupta

IMRL Lab., Princeton University, Princeton, NJ, USA
*corresponding author, E-mail: kaushiks@princeton.edu

Abstract

Terahertz spectrum, through its ability to foster ultra-high speed dense networks and high resolution sensing applications, can address a new class of emerging and exciting applications in autonomous systems, robotics, cyber-physical systems and industrial quality control for 6G and beyond. While the last decade has seen tremendous advances in the field, enabling scalable and chip-scale THz technology is still a major challenge. In this talk, we will discuss how new design approaches crosscutting circuits/EM/systems partitions, to open new possibilities in enabling programmability and adaptability in these THz chip technologies including programmable chip-scale THz sensors, THz metasurfaces and spatio-temporal control of THz fields for physical layer security, and how these can enable new applications in sensing, imaging, security and localization.

Gap Waveguide Technology using Periodic Structures with Higher Symmetries

Eva Rajo-Iglesias[1,*]

[1]Dpt. Signal Theory and Communications, University Carlos III of Madrid, Spain
* E-mail: eva.rajo@uc3m.es

Abstract

Gap waveguide technology was first proposed ten years ago. Most of the existing designs are based on the use of the bed of nails as periodic structure to create the required parallel plate stop band. In this work, the use of holes instead of pins for the implementation of the groove version is presented. The periodic structure based on the use of holes requires the glide symmetrical disposition of the unit cell to provide a complete and wide stopband for the parallel plate modes. Design guidelines for this version will be detailed and the advantages in terms of manufacturing will be discussed together with the limitations when compared to the use of pins. Some examples of designed antennas and components in the millimeter wave band using this approach will be presented in the talk.

Microwave Imaging for Medical Diagnostics

Panagiotis Kosmas[1,2]

[1]Department of Engineering, King's College London, London, United Kingdom
[2]Meta Materials Europe SA, Athens, Greece
E-mail: panagiotis.kosmas@kcl.ac.uk; panagiotis.kosmas@metamaterial.com

Abstract

The talk will briefly introduce the principles of medical microwave imaging (MWI) and then review recent progress from Dr Kosmas' team on the development and validation of this technique for brain imaging. This will include a study on the impact of using a metasurface to enhance signal penetration as well as a comparison of two-dimensional and three-dimensional tomographic approaches. Results from complex numerical and experimental phantoms will examine the impact of critical MWI aspects such as prior information.

Integral equations for metasurface design

Christophe Craeye*[1], Modeste Bodehou[1], Jean Cavillot[1], Denis Tihon[1]

[1]ICTEAM Institute, Université catholique de Louvain,,Louvain-la-Neuve, Belgium
*corresponding author, E-mail: Christophe.craeye@uclouvain.be

Abstract

Among the different ways to solve Maxwell's equations, integral-equation approaches are probably offering the most physical insight. They allow the prediction of surface waves and their transformation into leaky waves. We will explain how integral equations can be turned into a direct design tool, beyond traditional field analysis. This allows the design of metasurfaces with prescribed radiation patterns, as well as the creation of multi-beam metasurfaces. Such a perspective on numerical methods may also serve other fields of engineering.

Plasmonic Heterodyne Terahertz Receivers with Quantum-Level, Sensitivity at Room Temperature

Mona Jarrahi*
UCLA, USA
*corresponding author, E-mail: mjarrahi@ucla.edu

Abstract

We introduce a terahertz receiver that uses plasmonic photomixing for frequency downconversion to offer quantum-level sensitivities at room temperature for the first time. Frequency downconversion is achieved by mixing terahertz radiation and a heterodyning optical beam with a terahertz beat frequency in a plasmonics-enhanced semiconductor active region. With a versatile design capable of broadband spectrometry, over a 0.1-5 THz bandwidth, we demonstrate receiver sensitivities down to 3 times the quantum-limit at room temperature.

Metaoptics for Active Photonics

Federico Capasso[1]

[1]John A. Paulson School of Engineering and Applied Sciences, Harvard University, Cambridge, USA
E-mail: capasso@seas.harvard.edu

Abstract

Metaoptics offer unique opportunities for light control through dispersion engineering and optical nonlinearities. Here we demonstrate ultrashort pulse shaping with metasurfaces and new schemes for spatial light modulation and Gigahertz speed transmission modulation based on Mie resonances and on organic layers with giant electrooptic coefficient.

Transparent materials do not absorb light but have profound influence on the phase evolution of transmitted radiation. One consequence is chromatic dispersion causing ultrashort laser pulses to elongate in time while propagating. We experimentally demonstrated ultrathin nanostructured coatings that resolve this challenge: we tailored the dispersion of silicon nanopillar arrays such that they temporally reshape pulses upon transmission using slow light effects and act as ultrashort laser pulse compressors.[1] The coatings induce anomalous group delay dispersion in the visible to near-infrared spectral region around 800 nm wavelength over an 80 nm bandwidth. We characterized the arrays' performance in the spectral domain via white light interferometry and directly demonstrate the temporal compression of femtosecond laser pulses. Applying these coatings to conventional optics renders them ultrashort pulse compatible and suitable for a wide range of applications.

Tailored nanostructures also provide at-will control over the properties of light using nonlinear optics, with applications in imaging and spectroscopy. Nanomaterials with $\chi(2)$ nonlinearities achieve highest switching speeds. Current demonstrations typically require a trade-off: they either rely on traditional $\chi(2)$ materials, which have low non-linearities, or on quantum well heterostructures that exhibit a high $\chi(2)$ in a narrow band. We have shown that a thin film of organic electro-optic molecules JRD1 in polymethylmethacrylate combined with nanograting provides excellent performance for free-space optics: broadband record-high nonlinearity (10-100 times higher than traditional materials at wavelengths 1100-1600 nm), a custom-tailored nonlinear tensor at the nanoscale, and engineered optical and electronic responses.[2] We demonstrated a tuning of optical resonances by $\Delta\lambda = 11$ nm at DC voltages and a modulation of the transmitted intensity up to 40%. We realize 2×2 single- and 1×5 multi-color spatial light modulators and demonstrated their potential for imaging and remote sensing.[2] The compatibility with compact laser diodes, the achieved millimeter size and the low power consumption are further key features for laser ranging or reconfigurable optics emitters.

We have also employed a metasurface from sub-wavelength Mie resonators that support quasi bound states in the continuum (BIC) as a key mechanism to demonstrate electro-optic modulation of 34 free-space light with high efficiency at GHz speeds. Our geometry relies on hybrid silicon-organic 35 nanostructures that feature low loss (Q = 550 at λ=1594 nm) while being integrated with GHz compatible coplanar waveguides. We maximize the electro-optic response by using high-performance electro-optic molecules (whose electro-optic tensor we engineer in-device to exploit r_{33} = 100 pm/V) 38 and by nanoscale optimization of the optical modes. We demonstrate both DC tuning and high -speed modulation up to 5 GHz .

1. M. Ossiander, Y.-W. Huang, W. T. Chen, Z Wang, X Yin, YA Ibrahim, M Schultze, and F. Capasso. Nature Communications, 12, 6518 (2021)
2. Ileana-Cristina Benea-Chelmus, M. L Meretska, D. L Elder, M. Tamagnone, L. R Dalton, and F. Capasso. Nature Communications, 12, 5928 (2021)

Field- and Carrier-Enabled Nonlinear Nanophotonics

Wenshan Cai[1,2]

[1] School of Electrical & Computer Engineering, Georgia Institute of Technology, Atlanta, Georgia 30332-0250, United States
[2] School of Materials Science & Engineering, Georgia Institute of Technology, Atlanta, Georgia 30332-0245, United States
E-mail: wcai@gatech.edu

Abstract

The active manipulation of optical properties via external stimuli and the nonlinear wave-mixing of light with controlled means are among compelling research directions in nanophotonics. In this talk, we explore active and nonlinear plasmonic metamaterials by leveraging the field-induced disruption of the inversion symmetry for second-order optical processes, and exploiting the hot-carrier-induced perturbation in structured optical media for ultrafast all-optical modulation and nonlinear signal generation.

Quantum photonics using nanodiamonds and integrated optics

Christophe Couteau[1]

[1]Laboratory Light, nanomaterials & nanotechnologies – L2n
University of Technology of Troyes UTT and CNRS EMR 7004
12 rue Marie Curie, 10000 Troyes, France

Abstract

We will present our recent work on integrated quantum photonics based on a hybrid system made of colour centres in nanodiamonds and single photons within a common optical bus. This platform is a first step towards scalability for quantum communications. Ultimately, we aim to achieve entanglement via the interaction between two nodes thanks to a common photonics waveguide. We will present how we plan to control the positioning of nanodiamonds as well as the quantum optics properties of such emitters.

Building Uncooled Infrared Camera based on One Atom Thick Graphene

Debashis Chanda

NanoScience Technology Center,
Dept. of Physics,
CREOL, College of Optics and Photonics,
University of Central Florida, Florida, USA
Debashis.Chanda@ucf.edu
http://www.nanoscience.ucf.edu/chanda

Abstract

The talk will outline a novel strategy for uncooled, tunable, multispectral infrared detection. Due to the low photon energy, detection of infrared photons is challenging at room temperature. One atom thick graphene offers an alternative mechanism bypassing material bandgap restriction. Further, the ability of carrier concentration modulation on graphene via external voltage offers dynamic spectral selectivity for "color" night vision/sensing. The performance of preliminary demonstration compares favorably even with present cryogenically cooled detection schemes paving the path for commercial development.

Generating topological states with non-Hermiticity and symmetry breaking

Masaya Notomi[1,2]

[1]Department of Physics, School of Science, Tokyo Institute of Technology, Tokyo, Japan
[2]NTT Basic Research Laboratories, Nippon Telegraph and Telephone Corp., Atsugi, Japan
*corresponding author, E-mail: notomi@phys.titech.ac.jp

Abstract

We present our recent theoretical and experimental works regarding ways to generate photonic topological states in photonic crystals, by breaking the crystal symmetry, with adding phase-change materials / non-Hermitian periodic modulation. We also show various interplays of polarization singular points and exceptional points in non-Hermitian photonic crystals, leading to interesting chiral properties.

Conference Tutorials

Machine learning enabled wearables for plants and humans at nano scale

Qammer H. Abbasi

University of Glasgow, UK

Abstract

Advancement in nanotechnology has made it possible to manufacture sensors, circuits and devices measuring only nano-meters in size. This development is creating an extraordinary opportunity to observe, interact, and optimize physical systems from the very bottom. Wireless communication and networking at nanoscale, however, faces new challenges not encountered in conventional sensor networks. For example, nanoscale antenna calls for wireless communication in the Terahertz band, which encounters new path loss d noise phenomena posing significant challenges for many target applications of such networking. Nanoscale computing and communication is a new and rapidly growing field of research promoting collaboration between wireless networking, nanotechnology, and other fundamental disciplines. However, the research is in its early stages to realize communication and networking at the nanoscale. Currently, there is no definitive standard that provides guidelines and regulation for nanoscale communication and networking. This motivates this proposal to shed light on and promote this area of research and foster.

Guidance and Radiation of Metasurface-Waves

Stefano Maci

University of Siena, Italy

Abstract

Metasurfaces constitute a class of thin metamaterials, which can be used from microwave to optical frequencies to create new electromagnetic engineering devices. At microwave frequencies, they are obtained by a dense periodic texture of small elements printed on a grounded slab. Changing the dimension of the elements, being the sub-wavelength 2D-periodicity equal, gives the visual effect of a pixelated image and the electromagnetic effect of a modulation of the equivalent local reactance. The modulated metasurface reactance (MMR) so obtained is able to transform surface or guided waves into different wavefield configurations with required properties. The MMR allows a local modification of the dispersion equation and, at constant operating frequency, of the local wavevector. Therefore, a metasurface modulation permits addressing the propagation path of a surface wave, according with a generalized Fermat principle, as happen in ray-field propagation in inhomogeneous solid medium. This may serve for designing lenses or point-source driven beam-forming networks. When the MMR exhibits a periodic modulation along the SW wavevector, the wave propagation is accompanied by leakage; i.e., a surface wave is transformed into a leaky-wave, and the structure itself becomes an extremely flat antenna. In every case, introducing asymmetry in the pixel allows for a polarization control. In this tutorial, the basic wave mechanisms will be reviewed showing several antenna applications.

Antenna theory and design

A Single-Layer, Near-to-Zero Index Metasurface Superstrate for Gain-Enhanced, Circularly Polarized Antenna Designs

Fatima Khoutar[1], Mariem Aznabet[1], Hung Luyen[2], Otman EL Mrabet[1], and Nader Behdad[2]

[1]System of Information and Telecommunications Laboratory (LaSIT), Faculty of Science, Abdelmalek Essaadi University, Tétouan 93000, Morocco
[2]Department of Electrical and Computer Engineering, University of Wisconsin-Madison, Madison, WI, 53706, USA
*Otman EL Mrabet, E-mail: o.elmrabet@uae.ac.ma

Abstract

This paper presents a single-metallic-layer, near-to-zero-index metasurface (NZIM) as a superstrate for an antenna to achieve gain enhancement and circular polarization. The proposed metasurface comprises an array of split ring resonators (SRRs) rotated and aligned diagonally to provide linear-to-circular polarization conversion when placed above a linearly polarized patch antenna. Simulated and measured results show that the proposed antenna system has a 3-dB axial ratio bandwidth of 200 MHz, exhibits a right-hand circular polarization (RHCP) with a good cross polarization level, and achieves a 6-dB gain enhancement thanks to the use of the NZIM superstrate.

1. Introduction

Metasurfaces with zero or near-to-zero refractive index, permittivity, or permeability are among emerging techniques to enhance performance of antennas [1-2]. While most studies in the literature have been focusing on integrating these metasurfaces with antennas to provide radiation patterns with enhanced gains and linear polariziations, very little attention has been given to circular polarization applications. Circularly polarized (CP) antennas with high gain, however, have being widely used in satellite, radar, and space wireless communication systems [3-5]. More recently, reference [6] introduces a linear-to-circular polarization convertor using a zero-index metasurface, which is implemented by two metallic layers sandwiching a dielectric substrate. The circular polarization is obtained by tuning two parameters, which are the two slits on the two square rings of the unit cell. In this work, we propose an NZIM with a similar function as the one presented in [6] but having only one metallic layer, allowing for potentially reduced implementation cost and simpler design procedure. The proposed NZIM is used as a superstrate of a linearly polarized patch antenna to achieve gain enhancement and circularly polarized radiation. The circular polarization is achieved by rotating the SRRs, which can generate two orthogonal modes with a 90º phase difference. In what follow, the design and numerical and experimental characterization of the proposed high-gain, circularly polarized antenna are presented.

2. Proposed Superstrate-Loaded Antenna Design

Fig. 1 shows the configuration of the proposed design. It consists of a rectangular patch antenna placed below an NZIM superstrate. The patch has dimensions of 16.29 × 21.5 mm^2 and is printed on a grounded substrate of Rogers RT/Duroid 5880 with a permittivity of 2.2, loss tangent of 0.002 and thickness of 0.787 mm. The patch antenna is fed by a 50-Ω coaxial probe and was optimized in full-wave simulations using CST Microwave Studio to provide a low reflection coefficient as well as a linear polarization around the center frequency of 5.8 GHz. The NZIM superstrate is placed at a distance of 30 mm (about λ/2 at 5.8 GHz) above the patch antenna to convert the linear polarized wave radiated by the patch into a circularly polarized one. The metasurface is a 2-D array of 9 × 9 elements and has the same aperture area of 67.4 x 67.4 mm^2 as the radiating patch's substrate. Each element of the metasurface consisted of a smaller split-ring resonator (SSR) nested inside another bigger SSR. The two SSRs have opposite slot orientations: one ring has the slot at φ=135º while another ring has the slot at φ=315º (refer to Fig. 1(b)). The outer ring has a radius of 3.3 mm, the widths of the rings are 0.8 mm, the gap between inner and outer rings is 0.8 mm, and the widths of the splits are 0.4 mm. These parameters were selected to place the quasi-static resonance of the unit SRRs within the C-band of the microwave spectrum according to the theory developed in [7]. The most attractive feature of this element is its ability to exhibit a quasi-static resonant frequency at wavelengths that are much larger than its own size.

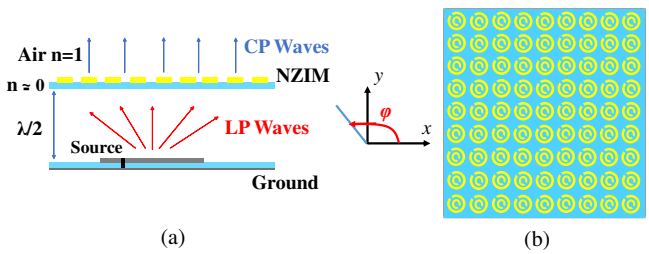

Figure 1: Proposed circular polarization High-Gain antenna with NZIM polarizer. (a) Front view (b) NZIM metasurface polarizer

3. Simulation and Measurement Results

We designed, fabricated, and measured a prototype of the proposed high-gain CP antenna. The measured and simulated reflection coefficients are presented in Figure 2(a). It can be seen that placing the NZIM above the patch antenna slightly improves the impedance matching without shifting the resonant frequency of the patch. Figure 2(b) shows the simulated and measured axial ratios (ARs) of the superstrate-loaded antenna prototype, demonstrating the effectiveness of the NZIM metasurface in providing linear-to-circular polarization conversion. The 3-dB axial-ratio bandwidths observed from the simulation and measurement are from 5.72 to 5.91 GHz (3.27 %) and from 5.83 to 6.11GHz (4.82%), respectively.

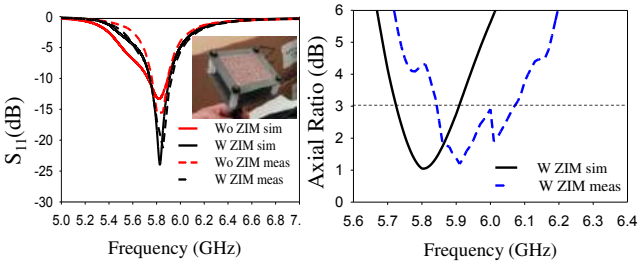

(a) (b)

Figure 2: (a) Simulation and measurement results for the (a) reflection coefficient and (b) axial ratio of the high gain CP antenna.

The measured and simulated realized gains of the patch antenna without and with the NZIM metasurface around the resonant frequency are depicted in Fig. 3. The measurement and simulation results show good agreement. The measured peak gain of 11.8 dBic is observed for the superstrate-loaded antenna at the central operating frequency of 5.8 GHz, which is about 6 dB higher than that of the patch antenna without the superstrate. As expected, the antenna gain can be enhanced significantly in the whole operating bandwidth (5.72-5.92 GHz) when the patch antenna is loaded with the NZIM. The increase in gain can be explained by the fact that the NZIM superstrate exhibits a near-zero refractive index around the resonant frequency of the patch antenna as discussed above. According to the Snell–Descartes laws, when an incident wave radiated from the patch antenna goes from a positive medium (air) to a near-to-zero refractive index medium (the NZIM) with a grazing angle, the transmitted wave will propagates normal to the interface, producing a collimated beam, and hence the gain enhancement.

There are slight frequency shifts observed between the simulation and measurement results for the AR/realized gain of the antenna with the NZIM superstrate (as seen in Figs. 2-3). These small frequency shifts can be mainly attributed to fabrication tolerances of the NZIM substrate and uncertainties in positioning of the superstrate with respect to the patch antenna. The fact that there is no discernible frequency shift between the simulation and measurement results for the patch antenna alone (shown in Fig. 3) further supports this hypothesis.

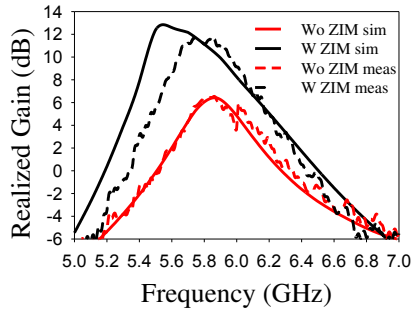

Figure 3: Simulated and measured realized gains of the antenna with and without ZIM polarizer superstrate.

4. Conclusions

A low profile, high-gain, circularly polarized antenna using a NZIM metasurface is presented. The measurement results agree well with full-wave simulations results, demonstrating the effectiveness of the NZIM in enhancing the antenna's gain and converting a liner polarization to a circular one. Future research on achieving larger AR bandwidths is being conducted by the authors.

[1] D. Li, Z. Szabo, X. Qing, E. Li and Z. N. Chen, "A High Gain Antenna With an Optimized Metamaterial Inspired Superstrate," in IEEE Transactions on Antennas and Propagation, vol. 60, no. 12, pp. 6018-6023, Dec. 2012.

[2] A. K. Singh, M. P. Abegaonkar and S. K. Koul, "High-Gain and High-Aperture-Efficiency Cavity Resonator Antenna Using Metamaterial Superstrate," in IEEE Antennas and Wireless Propagation Letters, vol. 16, pp. 2388-2391, 2017.

[3] S. Chen, D. K. Karmokar, Z. Li, P. Qin, R. W. Ziolkowski and Y. J. Guo, "Circular-Polarized Substrate-Integrated-Waveguide Leaky-Wave Antenna With Wide-Angle and Consistent-Gain Continuous Beam Scanning," in IEEE Transactions on Antennas and Propagation, vol. 67, no. 7, pp. 4418-4428, July 2019.

[4] S. J. Chen, C. Fumeaux, Y. Monnai and W. Withayachumnankul, "Dual Circularly Polarized Series-Fed Microstrip Patch Array with Coplanar Proximity Coupling," in IEEE Antennas and Wireless Propagation Letters, vol. 16, pp. 1500-1503, 2017.

[5] W. A. Imbriale, S. Gao, and L. Boccia, Space Antenna Handbook. New York, NY, USA: Wiley, 2012.

[6] Puneeth Kumar Tharehalli Rajanna , Karthik Rudramuni, and Krishnamoorthy Kandasamy, A High-Gain Circularly Polarized Antenna Using Zero-Index Metamaterial,'' IEEE Antennas Wireless Propag. Lett., vol. 18, pp. 1129-1132, 2019.

[7] Marqués R, Martín F, Sorolla M. Metamaterials with negative parameters: theory, design, and microwave application. New York (NY): John Wiley; 2008.

A slotted partial ground plane microstrip patch antenna for ultrawide-band applications

S.Ibnyaich[1], S. Chabaa[1,2], L.Wakrim[1], A.El yassini[1], M.M. Hassani[1], A.Zeroual[1]

[1]Department of physics, Cadi Ayyad University Faculty of Sciences, Semlalia Marrakesh, Morocco
[2]Industrial Engineering Department, National School of Applied Sciences, Ibn Zohr University, Agadir, Morocco

Abstract:

A New, compact, slotted partial ground plane, microstrip patch antenna developed for use in Ultrawide-band application is studied in this paper.

To obtain the final and optimal UWB antenna design, a parametric analysis of the defected ground plane structure was carried out to ensure that the antenna has a stable performance and an improved bandwidth, The size of the defected ground plane was studied and investigated. This investigation and optimization study was generated with help of the computer simulation technology CST simulator.

The antenna has an electrical small dimensions with a good gain, a notable efficiency and a wide impedance bandwidth. Which make this antenna a good candidate for ultawide-band wireless communication, microwave imaging and radar applications as well.

Key words:

Mictrostrip antenna, Ultrawide-band, defected ground plane, slotted ground plane, partial ground plane.

Koch Curve Polar Coordinate Transform for UWB Antenna Applications

Mac Cartier, Rahul Sreekumar, Elisa Pantoja, Mircea R. Stan

Department of Electrical and Computer Engineering,
University of Virginia, Charlottesville, USA
E-mail: mc3vc,rs2xd,rep9cy,mrs8n@virginia.edu

Abstract

Fractal antennas allow for the design of Ultrawide-band (UWB) antennas with a reduced footprint; we present a novel technique for generating antenna geometries which extend the Koch snowflake to angles other than 60 degrees. This is achieved by generating a Koch curve of an arbitrary indentation angle and then circumscribing the curve about the origin. Using our method, we achieve a 36 percent footprint area reduction compared to a traditional Koch snowflake antenna with a center frequency of 4.1 GHz.

1. Introduction

The self-similar characteristics of fractal antennas allow unique multi-band characteristics that are of importance in UWB applications [1]. As fractal iterations increase, the area of the antenna approaches a finite limit while the perimeter of the fractal theoretically diverges to infinity; this yields the *space-filling property* of fractals [2]. The space-filling property allows a fractal antenna to have a large *electrical length* within a compact form factor [3].

The Koch curve is one of the most commonly-used fractal antenna geometries because it demonstrates excellent efficiency at sizes approaching the theoretical limit for small antennas [2].

The frequency characteristics of Koch curve antennas are significantly affected by the fractal dimension of the geometry, which is in turn affected by several factors: the iteration, the indentation angle, and the scale. The fractal iteration is an effective design parameter for the Koch curve antenna; as the iteration increases, the first resonant frequency decreases and the harmonics shift nearer to the resonant frequency. Similarly, the indentation angle can be modulated to achieve desired frequency characteristics [4].

A Koch curve is created by iteratively transforming a line segment into 4 equal line segments, each $\frac{1}{4}$ the size of the initial segment, which are arranged such that an equilateral triangle is added to the center of the line. A conventional Koch snowflake is created by performing the aforementioned iteration process on the sides of an equilateral triangle. Because the initiator shape for a Koch snowflake is an equilateral triangle instead of a simple line as in the Koch curve, the indentation angle can not be modulated in a Koch snowflake as it can be in a Koch curve.

This work provides an analytical framework for the angular transformation of an arbitrary linear Koch curve into a closed snowflake geometry that allows designers more control over frequency and bandwidth without compromising the overall footprint. For our work we use inkjet printing as it decreases fabrication time, and allows direct modification of the design since the antenna can go from simulation to fabrication in a few steps. The Koch snowflake antennas are made of a conductive ink printed directly on a polyimide-based dielectric substrate. Printed antennas have become low cost to manufacture, compact form factor, and high-frequency characteristics [5]. Examples of the use for this type of inkjet-printed antennas on light and flexible substrates are mobile devices that require lightweight antenna elements that will not easily break if bent [6]. Other applications are low-cost IoT devices, and wearable RF devices that can be flexed, bent, and manipulated without damage or plastic deformation [7].

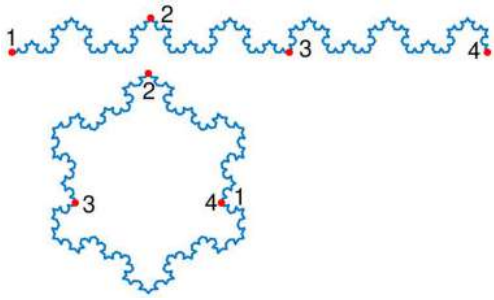

Figure 1: Visualization of transformation procedure of Koch curve to polar Koch snowflake.

2. Polar Transformation of Koch Curve

2.1. Theoretical Modeling

The circumscription process begins with a Koch curve in Cartesian coordinates generated from an initiating line segment of length L. The Koch curve iteration process is performed on this line segment with a given indentation angle until the desired curve is reached.

Let K_n be the set of all points in the nth iteration Koch curve. We propose a transformation $T : \mathbb{R}^2 \mapsto \mathbb{R}^2$ on $K_n \subset$

$\mathbb{R}^2$, defined as follows.

$$\forall p = (a, b) \in K_n$$
$$T(p) = (b + R)\left(\cos\left(\frac{2\pi}{L}a\right), \sin\left(\frac{2\pi}{L}a\right)\right)$$

This can be intuitively understood as the x-axis wrapping around the unit circle in a counter-clockwise direction so that the first and last points of the curve meet, thus forming a closed geometry and can be visualized in Figure 1. The resultant polar functions, $r = r(\hat{y})$ and $\theta = \theta(\hat{x})$, are then mapped to Cartesian coordinates for simplicity of plotting and manufacturing with the transformation $C : \mathbb{R}^2 \mapsto \mathbb{R}^2$ given as;

$$x = r\cos\theta \tag{1}$$
$$y = r\sin\theta \tag{2}$$

The composite transforms $x(\hat{x}, \hat{y})$ and $y(\hat{x}, \hat{y})$, are given below.

$$x = (\hat{y} + R)\cos\left(\frac{2\pi}{L}\hat{x}\right) \tag{3}$$
$$y = (\hat{y} + R)\sin\left(\frac{2\pi}{L}\hat{x}\right) \tag{4}$$

Figure 2 shows that the return loss of the circumscribed 3rd iteration 60° Koch curve is very similar to that of a Koch snowflake with the same height, angle, and iteration. For the base case, a 60° snowflake, the polar transformation method generates a snowflake with almost identical perimeter and area characteristics as a conventional Koch snowflake. This suggests that the polar transformation method is a valid extension of the traditional Koch snowflake.Furthermore, as can be seen in Figure 3, the area and perimeter characteristics are similar for both a standard Koch snowflake and the transformation described in this work.

2.2. Design & Simulation

There are several new parameters made available to the designer by the polar transformation method which were not previously available using a simple Koch snowflake, the most significant being the indentation angle. The indentation angle strongly determines the fractal dimension of the radiating patch geometry, which in turn inversely affects the frequency response [4]. As the indentation angle decreases, the center frequency also decreases and the additional resonant frequencies shift closer to one another. Conversely, decreasing the angle has the opposite effect, moving the resonant frequencies further apart and higher.

Increasing the fractal iteration of a conventional Koch snowflake antenna decreases the resonant frequency, increases the quality factor, and increases the radiation resistance, but with diminishing returns [8]. The same trend is reflected in simulations of the polar Koch geometries. The

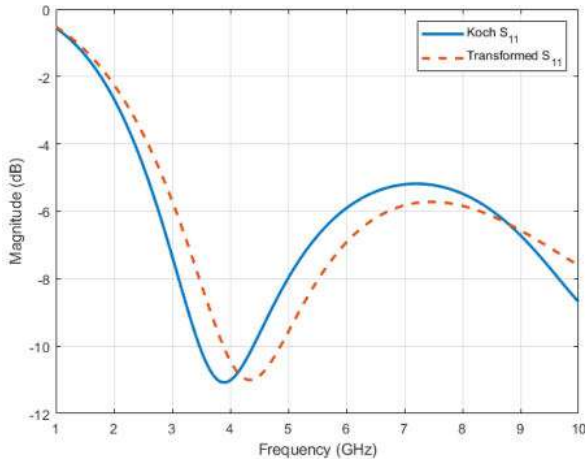

Figure 2: S_{11} characteristics of Koch snowflake vs. wrapped Koch snowflake for 60° indentation.

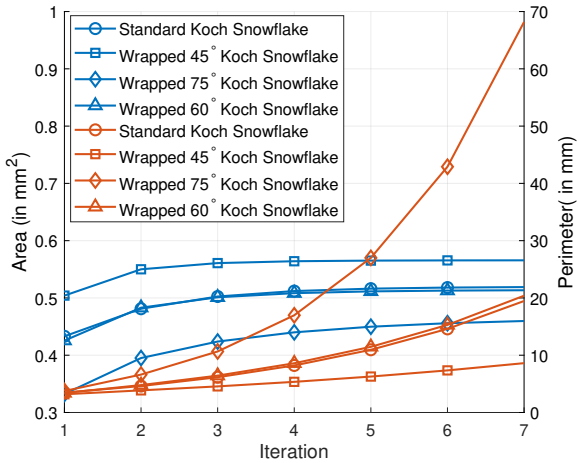

Figure 3: Area plot(blue lines) and Perimeter(orange lines) plots of a various wrapped Koch snowflakes in comparison to a standard Koch snowflake.

radius of the polar circumscription affects the scale of the patch geometry which in turn has an inverse relationship with resonant frequency.

We designed antennas using the proposed method which were printed with silver ink on Kapton polyimide film as shown in Figure 7 and measured using an Agilent PNA N5230A Vector Network Analyzer. The ground patch was made small so that the effect of the radiating patch geometries could be isolated from ground plane interactions.Inkjet printing simplifies the antenna fabrication process keeping it low-cost. The desired pattern is written directly onto the substrate followed by a rapid curing thermal treatment. For the inkjet-printing of the antenna area we used a conductive ink based on silver salt particles. After curing at 140 °C for 10 minutes the ink forms a conductive layer of the printed pattern. The printer used for this work is a BotFactory SV2 PCB printer.

The measured results in Figure 5 show that the indenta-

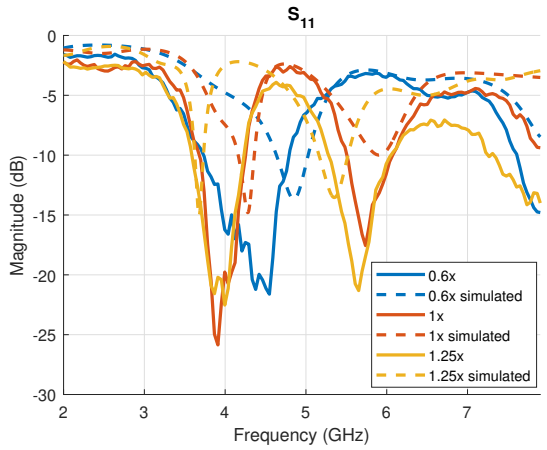

Figure 4: Measured S_{11} parameters of proposed geometry for various scales

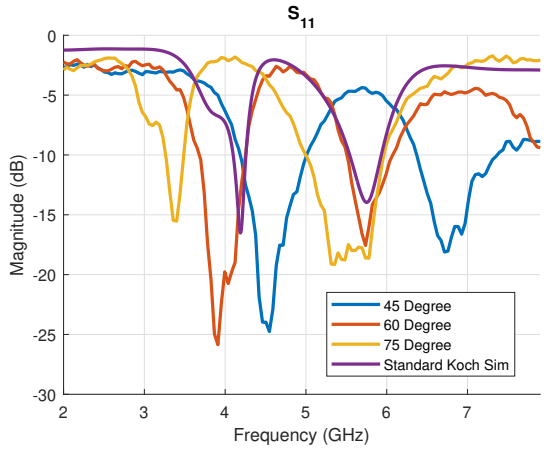

Figure 5: Measured S_{11} parameters of proposed geometry for various indentation angles & simulated S_{11} for traditional Koch snowflake

tion angle effectively sets the multi-band characteristics and resonant frequencies as expected. The measured frequency characteristics for the 60° polar Koch geometry are similar to the simulated characteristics for the standard Koch snowflake. Additionally, the 60° transformed and standard snowflakes have very similar areas and perimeters through various iterations, suggesting that the polar transformation method is a valid extension of the standard Koch snowflake, maintaining the same radiative and geometric features. Figure 4 shows that the measured results for different scales of 60° polar snowflakes have the same pattern as in simulation.

Simulations of standard Koch snowflake antennas and polar Koch antennas with an angle of 75° which are designed to have the same primary resonant frequency demonstrate the area-saving capabilities of the method laid out in this work. The extent of these savings can be seen in Figure 6. The area savings in this instance appear to diminish as the resonant frequency increases because as the radiating patch becomes smaller, the feed lines become dominant. In order to maintain a fair comparison, the feed lines were not modified between resonant frequencies.

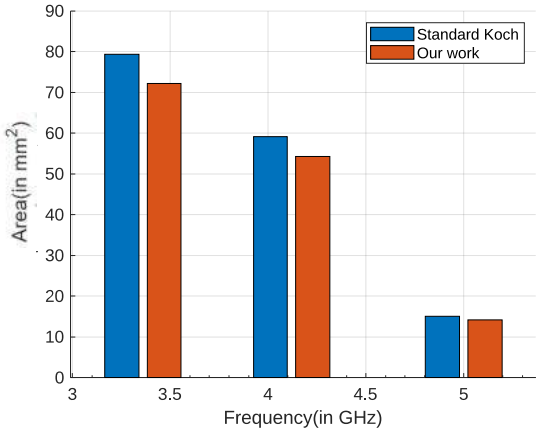

Figure 6: Overall area savings achieved for different antenna designs as a function of center frequency.

Figure 7: Design of three transformed Koch snowflakes for 45°, 60°, and 75°

3. Conclusions

This work introduces a method for expanding the design space of Koch snowflake UWB antennas through an additional design knob (indentation angle) with a procedure for transforming a Koch curve into a polar Koch snowflake. This allows designers to manipulate the indentation angle to alter the frequency characteristics without increasing the antenna footprint. Our measured results have validated the technique and prove that indentation angle is an effective additional design parameter for UWB antennas.

References

[1] B. Manimegalai, S. Raju, and V. Abhaikumar, "A multifractal cantor antenna for multiband wireless applications," *IEEE Antennas and Wireless Propagation Letters*, vol. 8, pp. 359–362, 2009.

[2] C. Puente, J. Romeu, and A. Cardama, "The koch monopole: A small fractal antenna," *IEEE Transactions on Antennas and Propagation*, vol. 48, no. 1, pp. 1773–1781, Nov. 2000.

[3] V. R. Gupta and N. Gupta, "Analysis of a fractal microstrip patch antenna," *International Journal of Microwave and Optical Technologies*, vol. 2, no. 2, pp. 124–129, Apr. 2007.

[4] K. J. Vinoy, "Fractal shaped antenna elements for wide- and multi-band wireless applications," Ph.D. dissertation, Pennsylvania State University, Aug. 2002.

[5] S. Bhatt, P. Mankodi, A. Desai, and R. Patel, "Analysis of ultra wideband fractal antenna designs and their applications for wireless communication: A survey," in *2017 International Conference on Inventive Systems and Control (ICISC)*, 2017, pp. 1–6.

[6] S. J. Chen, T. Kaufmann, R. Shepherd, B. Chivers, B. Weng, A. Vassallo, A. Minett, and C. Fumeaux, "A compact, highly efficient and flexible polymer ultra-wideband antenna," *IEEE Antennas and Wireless Propagation Letters*, vol. 14, pp. 1207–1210, 2015.

[7] A. Arif, M. Zubair, M. Ali, M. U. Khan, and M. Q. Mehmood, "A compact, low-profile fractal antenna for wearable on-body wban applications," *IEEE Antennas and Wireless Propagation Letters*, vol. 18, no. 5, pp. 981–985, 2019.

[8] Z. Yu, J. Yu, C. Zhu, and Z. Yang, "An improved koch snowflake fractal broadband antenna for wireless applications," in *2017 IEEE 5th International Symposium on Electromagnetic Compatibility*. IEEE, 2017, pp. 1–5.

Polarization Reconfigurable Patch Antenna with Ground Slots for Sub-6GHz Applications

Manpreet Kaur[1], Hari Shankar Singh[1,2], and Mayank Agarwal[1,2]

[1]Department of Electronics and Communication Engineering
Thapar Institute of Engineering and Technology
Patiala-147 004, Punjab, India
[2]HAMA IoT Solutions Private Limited, Sonbhadra
231216, UP, India
*corresponding author, E-mail: harishankar1990@gmail.com

Abstract

A polarization reconfigurable patch antenna truncated at the corners has been presented in this paper. The proposed antenna is covering the sub-6GHz band (4.8-5GHz). In order to achieve reconfigurability, D-shaped slots have been cut in the ground plane and two PIN diodes are inserted in each slot. The antenna is capable of switching between two polarization states i.e. linear polarization and circular polarization. Moreover, 3D radiation pattern of the design is also shown in order to check the pattern stability.

1. Introduction

In recent years, reconfigurable antennas have gained extreme popularity due to their dynamic characteristics. According to their functionality, they can be classified into various types like polarization reconfigurable, pattern reconfigurable, and frequency reconfigurable antennas [1]. Nowadays, circularly polarized antennas are in high demand in the sub-6GHz band for 5G applications [2]. To fulfill such requirement, many antennas have been developed with dynamically switched polarization states. Polarization reconfigurable antennas mainly uses PIN diodes [3], micro electromechanical systems (MEMS) [4], or varactor diodes [5] for switching.

Various single-fed [6-10] antennas have been developed in the last few decades. Some of them showed the alteration in the symmetry of the patch [6-8] while others shown the alteration in the ground plane [9-10] in order to switch the polarization states (linear to circular or LHCP to RHCP and vice versa). Additionally, multi-fed polarization reconfigurable antennas have also been developed in the past few years. In [11], a square patch antenna is fed by two ports at adjacent sides. Perturbations are added at the opposite corners of the patch to achieve circular polarization (CP). Ref. 12 presents a polarization diversity patch antenna using reconfigurable feeding network. This polarization reconfigurable design is able to provide dual linear and dual circular polarizations. Furthermore, some designs use metasurface to achieve the reconfigurability [13-15]. The metasurface is placed on top of the substrate and is able to switch the antenna between linear polarization (LP), left-hand circular polarization (LHCP) and right-hand circular polarization (RHCP).

In this paper, a polarization reconfigurable patch antenna which is truncated at the corners has been proposed. The design is able to cover the sub-6GHz band from 4.8GHz to 5GHz. Two slots are cut in the ground plane and pin diodes are inserted in each slot to achieve reconfigurability. The paper is structured as follows: Section 2 describes the design of the proposed antenna, Section 3 shows the results and finally, the conclusion is drawn in Section 4.

2. Design of the patch antenna with polarization reconfigurability

The proposed reconfigurable antenna is composed of three layers namely patch, dielectric substrate, and ground. The patch and ground are made of metal (copper) having thickness 0.035mm and conductivity σ=5.96×10^7 S/m. The antenna is designed on a low-cost FR-4 substrate having dielectric constant 4.4 and loss tangent tanδ=0.025. The thickness of a dielectric substrate is 0.8mm. The design configuration with detailed dimensions of the proposed reconfigurable antenna is shown in Fig. 1. The top layer consists of a metallic patch truncated at the corners while two D-shaped slots are cut from the bottom layer (ground plane). Further, two diodes are inserted in each slot, thus, in total four diodes are incorporated in the proposed antenna design to achieve polarization reconfigurability. The proposed design is excited by 50Ω coaxial cable.

3. Results and Discussions

All the simulations of the proposed design are carried out using CST MWS [16]. Fig. 2 shows the S-parameter at three different diode cases; case 1-when all the four diodes are on; case 2-when D1 (element 1), D2 (element 2) are on and D3 (element 3), D4 (element 4) are off; case 3- when D1, D2 are off and D3, D4 are on. It is observed that the simulated S-parameter bandwidth of the proposed design is more than 300MHz (4.73GHz-5.06GHz), covering the sub-

6GHz band (4.8GHz-5GHz). Moreover, it is also noted that the resonance frequency remains same in all the cases.

In order to check the polarization reconfigurability of the proposed antenna, axial ratio plot for the three mentioned cases are shown in Fig. 3. It is observed that in case-1, linear polarization is obtained as the axial ratio is more than 3dB for the entire frequency band whereas in case-2 and case-3, circular polarization is obtained (axial ratio ≤ 3dB) with an axial ratio bandwidth of 80MHz. Fig. 4 shows the 3D radiation pattern in three different cases. It is observed that the pattern at the resonating frequency is same in all the cases. Thus, it can be concluded that the proposed design is polarization reconfigurable in the sub-6GHz band, without affecting the frequency and pattern of the design.

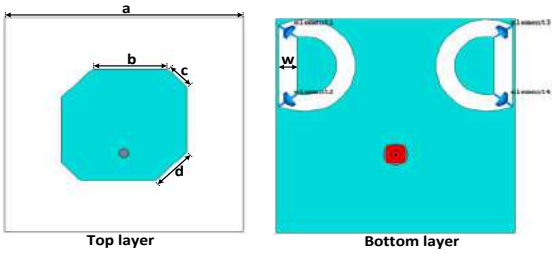

Figure 1: Detailed dimensions of the proposed reconfigurable antenna. a=30.00mm, b=9.28mm, c=3.51mm, d=5.69mm, and w=2.35mm.

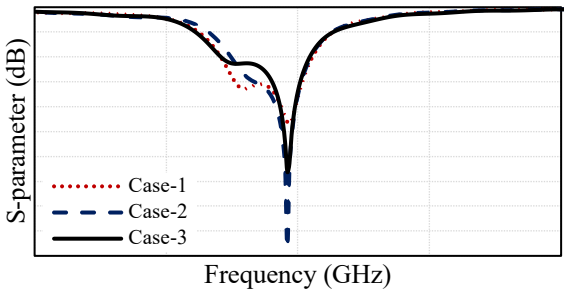

Figure 2: S-parameter of the proposed reconfigurable antenna.

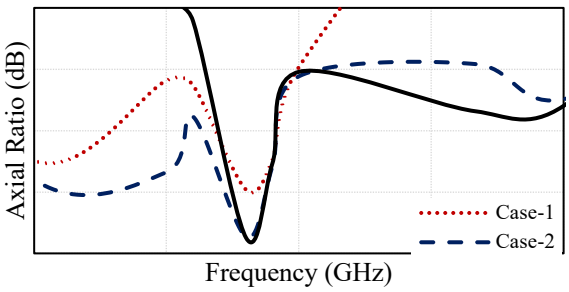

Figure 3: Axial ratio plot of the proposed reconfigurable antenna.

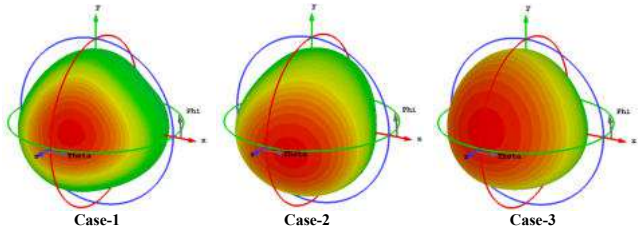

Figure 4: 3D radiation pattern of the proposed antenna at 4.8GHz in three different cases.

4. Conclusion

The paper describes the patch antenna, truncated at the corners with D-shaped slots in the ground plane for polarization reconfigurability. The proposed antenna is able to cover the sub-6GHz band i.e. 4.8GHz-5GHz. PIN diodes are incorporated in slots to switch the antenna between two polarization states i.e. linear polarization and circular polarization.

Acknowledgement

Authors would like to thank the Thapar Institute of Engineering and Technology, Patiala, for providing financial assistance under seed money grant to carry out this research.

References

[1] G.P. Jin, C.H. Deng, J. Yang, Y.C. Xu, S.W. Liao, A new differentially-fed frequency reconfigurable antenna for WLAN and Sub-6GHz 5G applications, *IEEE Access* 7: 56539-56546, 2019.

[2] Q. Wu, J. Hirokawa, J. Yin, C. Yu, H. Wang, W. Hong, Millimeter-wave multibeam endfire dual-circularly polarized antenna array for 5G wireless applications, *IEEE Transactions on Antennas and Propagation* 66: 4930-4935, 2018.

[3] Y.J. Sung, T.U. Jang, Y.S. Kim, A reconfigurable microstrip antenna for switchable polarization, *IEEE Microwave and Wireless Components Letters* 14: 534-536, 2004.

[4] J.M. Kovitz, H. Rajagopalan, Y. Rahmat-Samii, Design and implementation of broadband MEMS RHCP/LHCP reconfigurable arrays using rotated E-shaped patch elements, *IEEE Trans. Antennas Propag.* 63: 2497-2507, 2015.

[5] T. Korosec, P. Ritos, M. Vidmar, Varactor-tuned microstrip-patch antenna with frequency and polarisation agility, *Electron. Lett.* 42: 1015-1016, 2006.

[6] A. Khidre, K.F. Lee, F. Yang, A.Z. Elsherbeni, Circular polarization reconfigurable wideband E-shaped patch antenna for wireless applications, *IEEE Transactions on Antennas and Propagation* 61: 960-964, 2013.

[7] Y.I.A.A. Yasir, A.S. Abdullah, N.O. Parchin, R.A.A. Alhameed, J.M. Noras, A new polarization-reconfigurable antenna for 5G applications, *Electronics* 7: 293 (1-9), 2018.

[8] A. Bharathi, L. Merugu, Polarization Reconfigurable Square Slot Ring Antenna with CPW -to-Slotline Transition, *IEEE Region 10 Conference (TENCON), Singapore*, 22-25 Nov. 2016.

[9] X.X. Yang, B.C. Shao, F. Yang, A.Z. Elsherbeni, B. Gong, A polarization reconfigurable patch antenna with loop slots on the ground plane, *IEEE Antennas and Wireless Propagation Letters* 11: 69-72, 2012.

[10] Z.X. Yang, H.C. Yang, J.S. Hong, Y. Li, Bandwidth enhancement of a polarization reconfigurable patch antenna with stair-slots on the ground, *IEEE Antennas and Wireless Propagation Letters* 13: 579-582, 2014.

[11] X.X. Yang, B. Gong, G. Tan, Z. Lu, Reconfigurable patch antennas with fourpolarization states agility using dual feed ports, *Progress In Electromagnetics Research B* 54: 285-301, 2013.

[12] J.S. Row, M.J. Hou, Design of polarization diversity patch antenna based on a compact reconfigurable feeding network, *IEEE Transactions on Antennas and Propagation* 62: 5349-5352, 2014.

[13] H.L. Zhu, S.W. Cheung, K.L. Chung, T.I. Yuk, Linear-to-circular polarization conversion using metasurface, *IEEE Transactions on Antennas and Propagation* 61: 4615-4623, 2013.

[14] C. Ni, M.S. Chen, Z.X. Zhan, Design of frequency and polarization reconfigurable antenna based on the polarization conversion metasurface, *IEEE Antennas and Wireless Propagation Letters* 17: 78-81, 2018.

[15] K. Krishnamoorthy, B. Majumder, J. Mukherjee, K.P. Ray, Low RCS and polarization reconfigurable antenna using cross slot based metasurface, *IEEE Antennas and Wireless Propagation Letters* 14: 1638-1641, 2015.

[16] CST Microwave Studio available, www.cst.com.

Advances in the theory of Characteristic Modes

Miguel Ferrando-Bataller*, Marta Cabedo-Fabrés, Eva Antonino-Daviu

Universitat Politècnica de València, Spain
*Corresponding author, E-mail: mferrand@dcom.upv.es

Abstract

The Characteristic Mode Theory was developed by Professor Roger F. Harrington and his collaborators, relating currents in the radiating structure to the associated modal fields. It has been extensively developed following the paper published by the authors of this communication, revisiting the theory and applying it to the analysis of planar antennas. The latest advances in cubesat, planar lens structures, antennas for MIMO applications for 5G applications and metamaterials are presented.

Characteristic Mode Theory

The theory of characteristic modes can be applied to 3D structures to achieve different types of antennas. As an example, the currents and radiation patterns of the first modes of a cube are shown in Fig. 1 and 2.

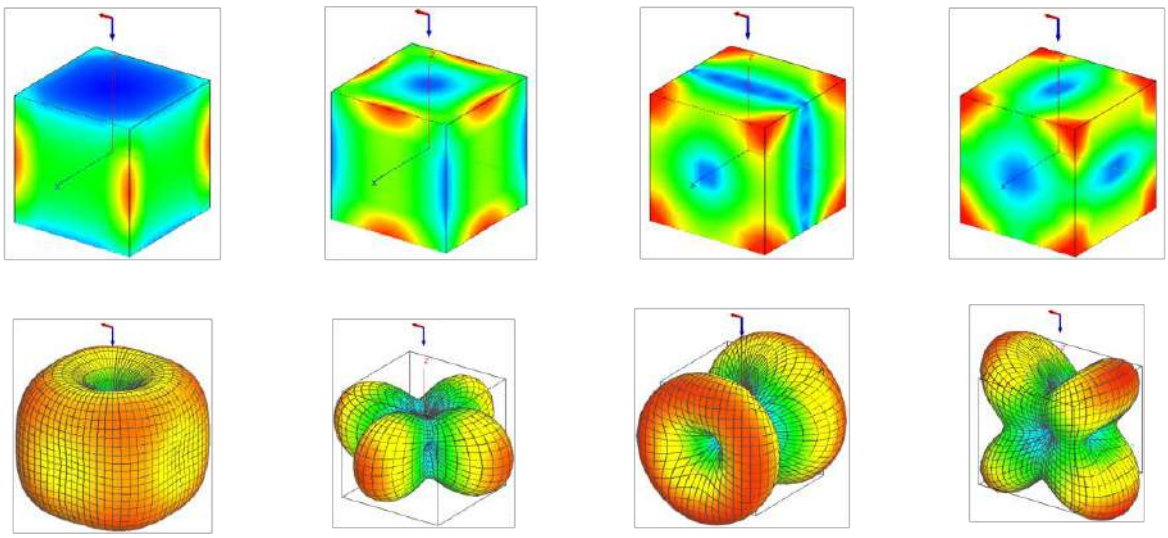

Fig. 1. Current density and radiation pattern of the Electric Characteristic Modes of the cube at first resonance

The presentation will show some applications of lenses, metamaterials and MIMO applications.

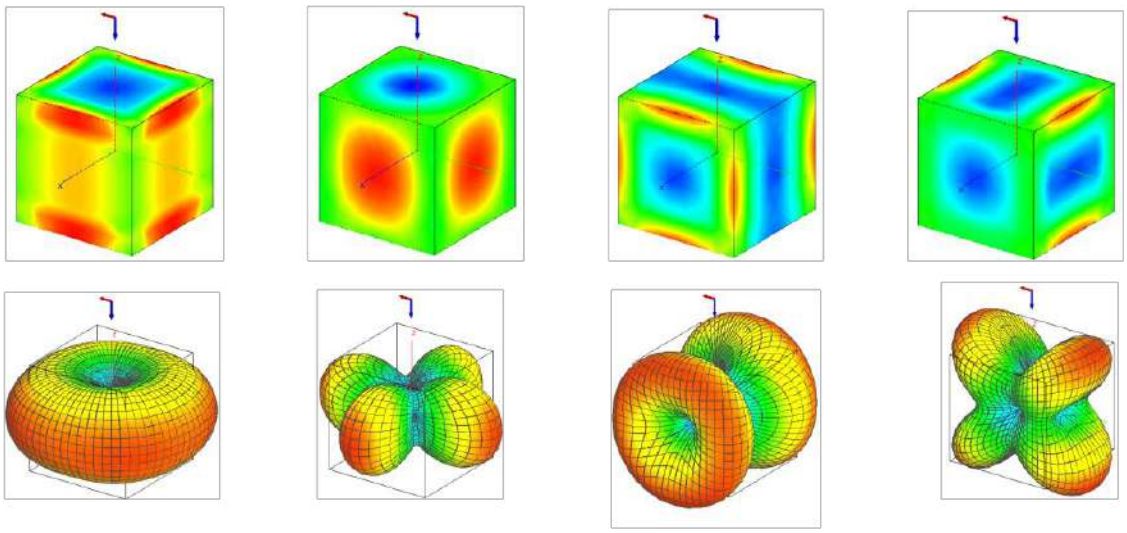

Fig. 2. Current density and radiation pattern of the Magnetic Characteristic Modes of the cube at first resonance

References

[1] R. Harrington and J. Mautz, "Theory of characteristic modes for conducting bodies," in IEEE Transactions on Antennas and Propagation, vol. 19, no. 5, pp. 622-628, September 1971, doi: 10.1109/TAP.1971.1139999.

[2] R. Harrington and J. Mautz, "Computation of characteristic modes for conducting bodies," in IEEE Transactions on Antennas and Propagation, vol. 19, no. 5, pp. 629-639, September 1971, doi: 10.1109/TAP.1971.1139990.

[3] M. Cabedo-Fabres, E. Antonio-Daviu, M. Ferrando-Bataller and A. Valero-Nogueira, "On the use of characteristic modes to describe patch antenna performance," IEEE Antennas and Propagation Society International Symposium. Digest. Held in conjunction with: USNC/CNC/URSI North American Radio Sci. Meeting (Cat. No.03CH37450), 2003, pp. 712-715 vol.2, doi: 10.1109/APS.2003.1219335.

[4] M. Cabedo-Fabres, E. Antonino-Daviu, A. Valero-Nogueira and M. F. Bataller, "The Theory of Characteristic Modes Revisited: A Contribution to the Design of Antennas for Modern Applications," in IEEE Antennas and Propagation Magazine, vol. 49, no. 5, pp. 52-68, Oct. 2007, doi: 10.1109/MAP.2007.4395295.

[5] Systematic design of antennas using the theory of characteristic modes. Phd Thesis. Cabedo Fabrés, M. (2007). Systematic design of antennas using the theory of characteristic modes. Universitat Politècnica de València. https://doi.org/10.4995/Thesis/10251/1883

[6] Analysis and design of antennas for wireless communications using modal methods. PhD Thesis. Antonino Daviu, E. (2008). Analysis and design of antennas for wireless communications using modal methods. Universitat Politècnica de València. https://doi.org/10.4995/Thesis/10251/2188

[7] E. Antonino-Daviu, M. Fabres, M. Ferrando-Bataller and V. M. R. Penarrocha, "Modal Analysis and Design of Band-Notched UWB Planar Monopole Antennas," in IEEE Transactions on Antennas and Propagation, vol. 58, no. 5, pp. 1457-1467, May 2010, doi: 10.1109/TAP.2010.2044323.

[8] N. Mohamed Mohamed-Hicho, E. Antonino-Daviu, M. Cabedo-Fabrés and M. Ferrando-Bataller, "Designing Slot Antennas in Finite Platforms Using Characteristic Modes," in IEEE Access, vol. 6, pp. 41346-41355, 2018, doi: 10.1109/ACCESS.2018.2847726.

[9] E. Antonino-Daviu, M. Cabedo-Fabrés, M. Sonkki, N. Mohamed Mohamed-Hicho and M. Ferrando-Bataller, "Design Guidelines for the Excitation of Characteristic Modes in Slotted Planar Structures," in IEEE Transactions on Antennas and Propagation, vol. 64, no. 12, pp. 5020-5029, Dec. 2016, doi: 10.1109/TAP.2016.2618478.

[10] D. Sánchez-Escuderos, H. C. Moy-Li, E. Antonino-Daviu, M. Cabedo-Fabrés and M. Ferrando-Bataller, "Microwave Planar Lens Antenna Designed With a Three-Layer Frequency-Selective Surface," in IEEE Antennas and Wireless Propagation Letters, vol. 16, pp. 904-907, 2017, doi: 10.1109/LAWP.2016.2614342.

[11] H. C. Moy-Li, D. Sánchez-Escuderos, E. Antonino-Daviu and M. Ferrando-Bataller, "Low-Profile Radially Corrugated Horn Antenna," in IEEE Antennas and Wireless Propagation Letters, vol. 16, pp. 3180-3183, 2017, doi: 10.1109/LAWP.2017.2767182.

Antennas for wireless power transmission and harvesting

PIFA Multi-layers for smart watch application in the 2.4 GHz for the Bluetooth Low Energy BLE

Adli Abdelhakim, Marta Cabedo-Fabrés and Miguel Ferrando Bataller
ITEAM, Universitat Politècnica de València, València, Spain
E-mail: adab1@doctor.upv.es

Abstract

This paper presents a Planar Inverted-F Antenna (PIFA) design for a smartwatch application, optimized to operate on the 2.4 GHz Bluetooth frequency band, on the proximity of the human forearm. The PIFA antenna is mounted on the watchstrap that is used as the antenna substrate. The antenna is fed in a singular way, since a coplanar wave-guide (CPW) transmission line is used to excite the antenna. The antenna is integrated in the watchstrap, curved over the phantom forearm and simulated along with the watchcase. By a multi-layer substrate, half air half rubber we obtain a return loss of –20 dB is obtained at 2.4 GHz, and an efficiency of -5 dB, which represents a good efficiency taking into account the effect of the human forearm.

***Keywords*—PIFA antenna, on-body application, smartwatch, BLE.**

1. Introduction

In recent years, research into wearable antenna applications has gained a growing attention due to its potential applications in areas such as E-health systems, home care, security, and entertainment.

The antenna is to be lightweight, low cost, and maintenance-free, to meet the requirements of the application and the market. Considering the miniaturization and stable performance close to the human body, the planar inverted-F antenna (PIFA) can be considered a good candidate [1].

The structure proposed is a conventional PIFA optimized to operate at 2.4 GHz, conformed on the watchstrap, along with a CPW transmission line, that connects the antenna with the watchcase. The watchstrap is made of a flexible material, which will constitute the substrate on where the antenna is mounted.

The simulation take into account the curving effect of the antenna, the substrate used as the watchstrap, the watchcase, the feeding technic, and the human body effect, to have a more closer view to the behavior of the antenna in a real case user.

Finally, the antenna reflection coefficient, efficiency and the pattern radiation are evaluated with CST 2020, taking into account the whole watch structure in the presence of the human forearm phantom. A comparative table between the proposed antenna and other existing antenna will be presented as well.

2. Geometry of the antenna

The proposed structure is a Planar Inverted-F antenna, optimized to operate at 2.4 GHz band. The main advantage of using a PIFA is its reduced electric length and folded structure. Moreover, the impedance matching of the PIFA can be obtained by optimizing the space between feed and shorting pins. The main idea designing a PIFA is not to use any extra lumped components for matching network, and thus avoid any losses due to those elements [2]-[3].

Fig. 1 shows the geometry of the antenna. The dimensions of the antenna are summarized in Table I. Using two shorting pins instead of a shorting wall facilitates the connection of the feeding CPW transmission line, besides having an easy fabrication. A 50 Ω CPW line transmits the power from the watchcase to the antenna. Six shorting pins are placed on both sides of the CPW line to connect the ground plane of the CPW line with the antenna ground plane, as shown in Fig 1(a). The CPW has the dimensions Wcpw, and g. The CPW feeds the radiating plate at a distance fx from the shorted edge of the antenna. The substrate used is half rubber half air. The antenna element and CPW transmission line are made of cupper of thickness 0.35 µm. Fig.2 shows an overall view of the curved PIFA antenna fed by a CPW line.

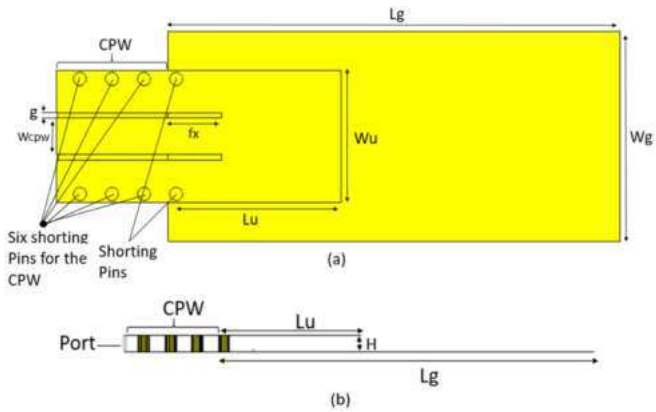

Figure 1: Geometry of the proposed PIFA antenna fed by a CPW transmission line (a) Top view and (b) Side view.

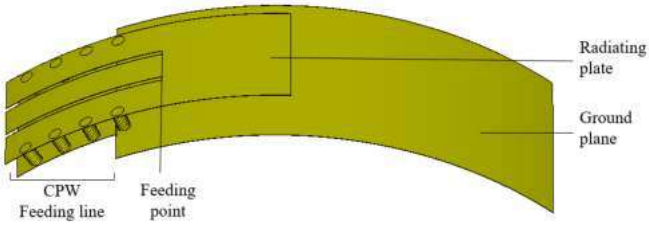

Figure 2: Geometry of the proposed PIFA antenna fed by a CPW transmission.

Table 1: Dimensions of the antenna and CPW (units in mm)

Lg	Wg	H	Lu	Wu	Wcpw	g	fx
45.3	18.97	1.84	16.2	11.97	3.3	0.5	4.85

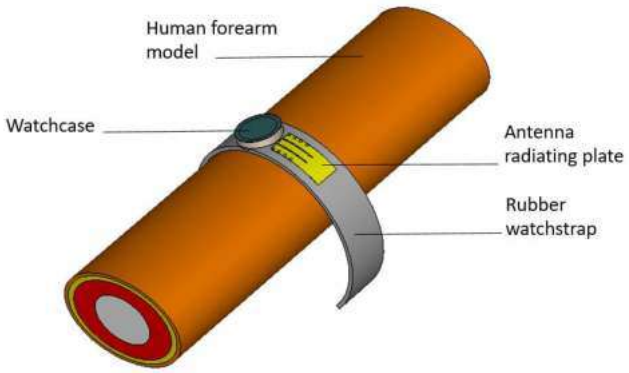

Figure 3: Human forearm phantom, with the PIFA antenna mounted on the rubber substrate of the watchcase.

Fig.3 shows the antenna mounted on the watch strap, modelled with a flexible substrate. The watch strap has standard dimensions: Ls=200 mm, Ws=20 mm and thickness Hs=1.84 mm. The substrate, which is the watchstrap, is made of rubber, with a dielectric constant of 3 and loss tangent 0.001. The watchcase is modelled by three elements: an external case made of polycarbonate dielectric constant of 2.9 and a loss tangent of 0.1, a battery made of PEC and a top cover made of glass. Fig.3 present the human forearm model used for this simulation, and table.2 the component. the human forearm phantom has four layers [4]: The skin, fat, muscle and bone.

3. Discussion

In this section, the proposed antenna, mounted on the watchstrap, along with the watchcase and the human forearm phantom, is simulated and evaluated.

3.1. Reflection coefficient

The antenna's reflection coefficient (S_{11}) simulated from 1 GHz to 4 GHz is depicted in Fig. 4. The reflection coefficient is -20.6 dB at the 2.4 GHz. The matching bandwidth for a -10 dB reference goes from 2.38 GHz to 2.43 GHz.

3.2. Radiation efficiency and total efficiency

The total efficiency (green curve) and radiation efficiency (red curve) are shown in Fig. 5. As observed, at 2.4 GHz, the total efficiency is -5.17 dB, and the radiation efficiency is -5 dB.

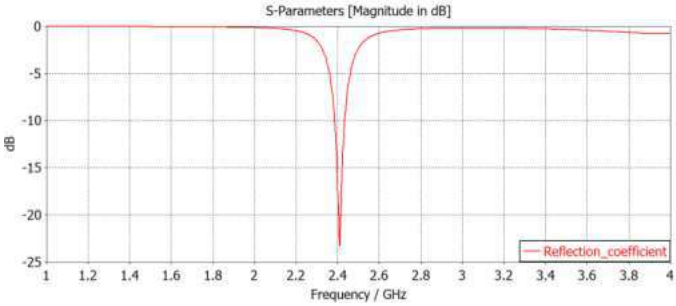

Figure 4: Simulated reflection coefficient of the proposed antenna integrated in the watch strap in the presence of the human forearm model.

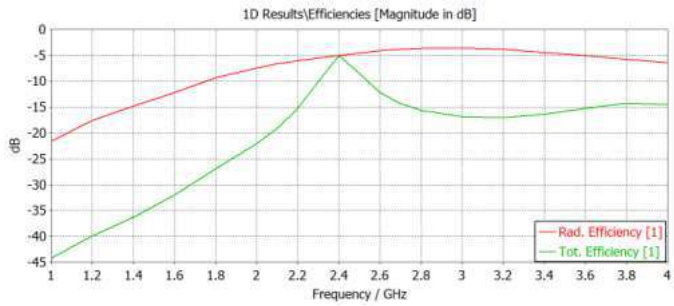

Figure 5: Simulated total efficiency (green curve) and radiation efficiency (red curve) of the proposed antenna considering the human forearm and the complete watch.

4. Conclusions

A compact PIFA antenna designed for smartwatch application, on the Bluetooth frequency band has been presented. The antenna is mounted on a rubber watchstrap to increase the available space inside the watch case. The effect of the human body has been taking into account and a realistic technique to feed the antenna using a CPW transmission line has been proposed. The simulated results confirm that the antenna is a good candidate for the smartwatch application. A prototype of the antenna will be fabricated to validate the simulated results and the Specific Absorption Rate (SAR) will be calculated.

Acknowledgements

This work has been supported by the Spanish Ministry of Science and Innovation (Ministerio Ciencia e Innovación) under project PID2019-107885GB-C32

References

[1] G. Gao, C. Yang, B. Hu, R. Zhang and S. Wang, "A Wide-Bandwidth Wearable All-Textile PIFA With Dual Resonance Modes for 5 GHz WLAN Applications," in IEEE Transactions on Antennas and

Propagation, vol. 67, no. 6, pp. 4206-4211, June 2019, doi: 10.1109/TAP.2019.2905976.

[2] Wong Kin Lu. Planar antennas for wireless communication, John Wiley & Sons, New York, 2003.

[3] *David M. Pozar, Microwave Engineering. Hoboken, NJ :Wiley, 2012.*

[4] H. A. Damis, R. Mirzavand, H. Chung and P. Mousavi, "Flexible printed square loop antennas for wearable applications," *2016 17th International Symposium on Antenna Technology and Applied Electromagnetics (ANTEM)*, 2016, pp. 1-2, doi: 10.1109/ANTEM.2016.7550212.

[5] R S. Lin, Y. Lin, J. Peng and Y. Tuan, "Microstrip antennas for smart watch," *2016 IEEE 5th Asia-Pacific Conference on Antennas and Propagation (APCAP)*, 2016, pp. 109-110, doi: 10.1109/APCAP.2016.7843122.

[6] K. Zhao, Z. Ying and S. He, "Antenna designs of smart watch for cellular communications by using metal belt," *2015 9th European Conference on Antennas and Propagation (EuCAP)*, 2015, pp. 1-5.

A. Shafqat, F. A. Tahir and H. M. Cheema, "A Compact Uniplanar Tri-band Antenna for Wearable Smart Watches," *2018 18th International Symposium on Antenna Technology and Applied Electromagnetics (ANTEM)*, 2018, pp. 1-3, doi: 10.1109/ANTEM.2018.8

Array antennas, active, adaptive and reconfigurable antennas

Microstrip Antenna Array Design for UAV Detection

Pedro Mendes Ruiz[1*], Xavier Begaud[2], François Magne[3], Etienne Leder[1]

[1]Bowen ERTE-ETSA, Les Ulis, France

[2]LTCI, Télécom Paris, Institut Polytechnique de Paris, Palaiseau, France

[3]When-AB, Paris, France

*corresponding author, E-mail: pedro.mendes@bowenfr.com

Abstract

This work presents the design and realization of four linear arrays of microstrip rectangular patch antennas. This linear array is one of the elements of a passive radar using signals from 4G base stations for UAV detection. The arrays have been validated and operate from 2.62 GHz to 2.69 GHz, with a HPBW of 82° in H-plane and a maximal gain going from 11.1 dB to 12.2 dB in the required bandwidth, with a cosecant squared pattern in the E-plane.

1. Introduction

The threat of easy-to-deploy low-cost drones requires an advanced detection for the protection of sensible sites (e.g. airport runways, stadiums, industrial sites). The goal of the DIOD project (Detection & Identification Of Drones) is to develop a passive radar that uses 4G base stations to detect small targets. This work presents the design of the receiving antenna developed in the framework of the FUI (Fond Unique Interministériel) DIOD project.

Many solutions exist to detect the presence of drones with mechanical, optical, or antenna array based solutions [1]. Passive detection of UAV can be obtained by using multiple antennas and DOA estimation [2],[3]. Another solution presented in this article is to use an antenna composed of several linear arrays that will cover an angular sector by beam steering. Each linear array is designed to produce a cosecant squared beam [4] in a plane (E-plane for this work) to receive a power independent of the radar range for a constant height target. It is also required to have a rapid decrease of the radiation pattern just before the cosecant squared shape in order to not radiate toward the ground. In the orthogonal plane (H-plane), the beam is required to be large to have a nice field of view. Each linear array must operate from 2.62 GHz to 2.69 GHz.

In section 2, we present the design of the patch antenna. In section 3, we detail the design of the feeding network. In section 4, we present simulations of the full linear array, as well as simulations using periodic boundaries to characterize the coupling of the 2D array and simulations of the 4-column array. Finally, in section 5 we present the prototype and its measurements.

2. Patch Antenna Design

The first step in our design is to optimize the patch antenna. This optimization includes the rectangular patch with an inset feed [5], the microstrip line arriving at the patch, a mitered bend and a couple of quarter wavelength transformers. The design with the optimized values is presented in Fig. 1.

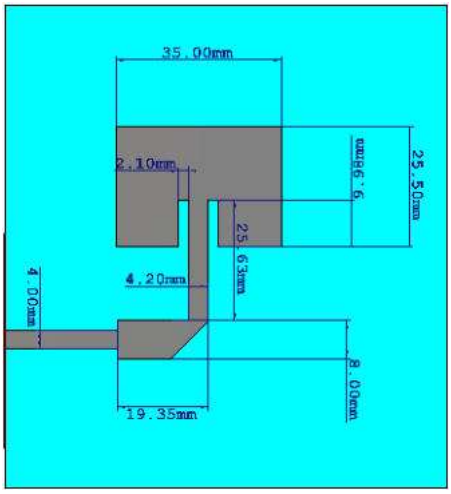

Figure 1: Front view of the optimized rectangular patch antenna with an inset feed, the feeding line arriving at the patch, a mitered bend and two quarter wavelength transformers.

Those elements were optimized using CST Studio Suite to maximize the bandwidth of the element around 2.655 GHz, the central frequency of our targeted bandwidth [6].

The substrate used for this design is AD430 from Rogers Corp., with a permittivity equal to 4.3 and a thickness of 3.175 mm. This substrate allows the rectangular patch to have good matching properties over the desired bandwidth

[5]. Moreover, using this substrate allows for an element spacing of approximately 0.56 free space wavelength when using the feeding network architecture presented in the next section.

In Fig. 2, we present the reflection coefficient of the designed patch antenna, which is below -10 dB from 2.61 GHz to 2.69 GHz. The patch antenna presented a gain of 6.5 dB and an efficiency of 80% inside the 2.62 GHz– 2.69 GHz bandwidth.

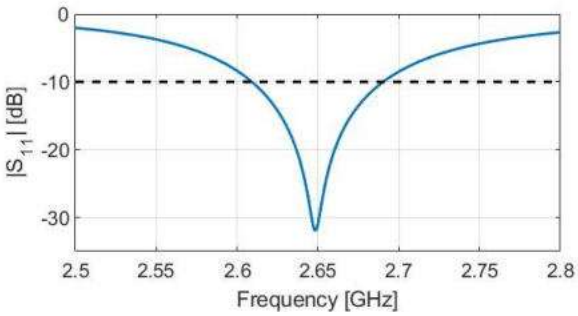

Figure 2: Reflection coefficient of the microstrip antenna presented on Fig. 1.

3. Feeding Network Design

In this section, we will first present the feeding network architecture used for this antenna array. We will then present the method used to synthesize the parameters of this feeding network, which includes:

- A multi objective genetic algorithm to obtain the currents magnitudes and phases of the array that generate the desired cosecant squared pattern;
- A transmission line model to calculate the lengths and widths of the microstrip lines to obtain those currents magnitudes and phases with the feeding network;
- An iterative procedure using CST Microwave Studio to correct the radiating pattern accounting for the different couplings and model imperfections.

3.1. Proposed Architecture

The proposed feeding network architecture consists of two series of quarter wavelength transformers with T-junctions in between them to feed each of the patch elements and with a bend at the last quarter wavelength transformer to feed the last patch antenna [7].

In between these branches, we have two microstrip lines of unequal electrical lengths, to enforce a phase difference between the two branches, and impedances, to balance the power sent to each of the branches [7].

Both of those microstrip lines arrive at a T-junction that leads to a coaxial feed.

The full architecture with the patch antennas included can be observed in Fig. 3.

3.2. Multi Objective Genetic Algorithm

In order to obtain the desired cosecant squared we used a multi objective genetic algorithm optimization [8]. For this optimization, we considered the set of four consecutive quarter wavelength transformers as equivalent to an amplitude ponderation of the currents on the ith patch in comparison to the $(i-1)^{th}$ patch, with the first patch of each branch normalized to one. As a first approach we consider that the amplitudes on the patches are decreasing the farther we go from the center feed and the maximal reduction is bounded to a third.

Table 1: Feeding Network Optimization Parameters

Left Branch			Right Branch			Phase
$\frac{I_{1left}}{I_{2left}}$	$\frac{I_{2left}}{I_{3left}}$	$\frac{I_{3left}}{I_{4left}}$	$\frac{I_{1right}}{I_{2right}}$	$\frac{I_{2right}}{I_{3right}}$	$\frac{I_{3right}}{I_{4right}}$	$X_{left} - X_{right}$
1.82	1.74	1.09	1.94	1.93	1.09	60°

Moreover, the lines with unequal electrical length on the central feed are equivalent to a phase difference between the currents on left patches and the right patches. Those parameters are summed up in Table I. The indexes of the current magnitudes go from one for the patches closer to the center to four for the outer patches.

The design variables are then optimized to minimize three cost functions:

- one to optimize the formed radiation pattern (Eq. 1);

$$cost_1 = \max\{20*\log_{10}[E_{model}(\theta)/\csc^2\theta]\}, \quad (1)$$

$$0° < \theta < 40°$$

- one for the sidelobe level (Eq. 2);

$$cost_2 = \max\{20*\log_{10}[E_{model}(\theta)/\max(E_{model}(\theta))]\}, \quad (2)$$

$$\theta < 0° \ \& \ \theta > 40°$$

- one for the decrease rate of the main beam of the radiation pattern towards the ground (Eq. 3).

$$cost_3 = \theta_{AFpeak} - \theta_{null}, \quad (3)$$

with θ_{AFpeak} corresponding to the maximum of the array factor for θ between 0° and 40° and $\theta_{null} < \theta_{AFpeak}$ the closest angle to θ_{AFpeak} which satisfies Eq. 4.

$$20*\log_{10}(E_{model}(\theta_{AFpeak}) / E_{model}(\theta_{null})) = 17dB, \quad (4)$$

The radiation pattern of the array was modeled as an Array Factor multiplied by a $\cos\theta^q$ model of the element pattern (Eq. 5) for the calculation of the cost functions [9].

$$E_{model}(\theta) = AF(\theta) \cos^q\theta, \ q=3.5, \quad (5)$$

with the value of q chosen to approximate the element pattern of the patch from Section 2.

We used the Matlab multi objective genetic algorithms from the Global Optimization Toolbox [10] to optimize this

design. The multi objective genetic algorithm gives us 70 dominant solutions for the optimization problem. We restricted these solutions by selection only those which respect the inequalities in Eq. 6.

$$\text{cost1} < 3\text{dB}, \text{cost2} < -10\text{dB}, \text{cost 3} < 15°, \quad (6)$$

We manually selected a solution with a good trade-off between the three cost functions from this reduced set of dominant solutions and the design currents obtained from this solution are presented in Table 1.

3.3. Feeding Network Parameters

Once we calculated the design currents, we moved on to calculating the physical dimensions of the feeding network capable of realizing them. First, we will calculate the impedances of the quarter wavelength transformers needed for this design. Then we will use LineCalc, a Keysight ADS microstrip design tool [11], in order to calculate the physical widths and lengths of each microstrip quarter wavelength transformer.

In order to calculate the impedances we will use (1), which gives the magnitude of the current on the ith element in function of the magnitude of the currents on the $(i-1)^{th}$ element and the impedances of four consecutive quarter wavelength transformers [7].

$$\frac{I_{i-1}}{I_i} = \frac{Z_{c1}Z_{c3}}{Z_{c2}Z_{c4}}, \quad (7)$$

The indexes of the quarter wavelength transformers in each group of four goes from 1 for the transformers closer to the center of the array to 4 for the ones farther from the center.

We have chosen the impedances of the first and fourth transformer in each group of four quarter wavelength transformers to be equal to, respectively, 70 Ω and 50 Ω. The other two transformers are then calculated to obtain the desired current magnitudes. The impedances of the quarter wavelength transformers are summed up in Table 2.

Concerning the center feed lines we calculated their electrical length in order to realize the phase difference between the patches to the left and to the right of the coaxial feed. As for their impedance, we simulated the full feeding network using ADS and tuned the values in order to balance the power sent to the patches to the left and to the right of the coaxial feed [11].

Table 2: Quarter Wavelength Transformer Impedances

Left Branch 1st		Left Branch 2nd		Left Branch 3rd	
Zc2_1L	Zc3_1L	Zc2_2L	Zc3_2L	Zc2_3L	Zc3_3L
50 Ω	65 Ω	52 Ω	65 Ω	65 Ω	51 Ω
Right Branch 1st		Right Branch 2nd		Right Branch 3rd	
Zc2_1R	Zc3_1R	Zc2_2R	Zc3_2R	Zc2_3R	Zc3_3R
50 Ω	69 Ω	50 Ω	69 Ω	65 Ω	51 Ω

3.4. Iterative Correction

Using the patch antenna from Fig. 1 and the feeding network parameters calculated as in the last section we simulated the full array using CST Microwave Studio [6].

However, because of coupling effects not taken into account during the design, the amplitude of the currents arriving at the patches does not follow the designed values.

Moreover, the phase difference between the patches to the left and to the right of the coaxial feed is more dependent on frequency then expected from the ADS simulations.

Finally, the resonance frequency of the reflection coefficient is no longer placed at the center of the target bandwidth.

Table 3: Feeding Network Physical Dimensions

All values in mm	Zc2		Zc3	
	Length	Width	Length	Width
Transformer 1 Left	14.81	11.90	16.44	0.92
Transformer 2 Left	16.03	2.26	15.12	8.09
Transformer 3 Left	15.34	6.11	15.92	2.71
Transformer 1 Right	14.99	9.47	15.98	2.48
Transformer 2 Right	15.67	3.96	15.82	3.16

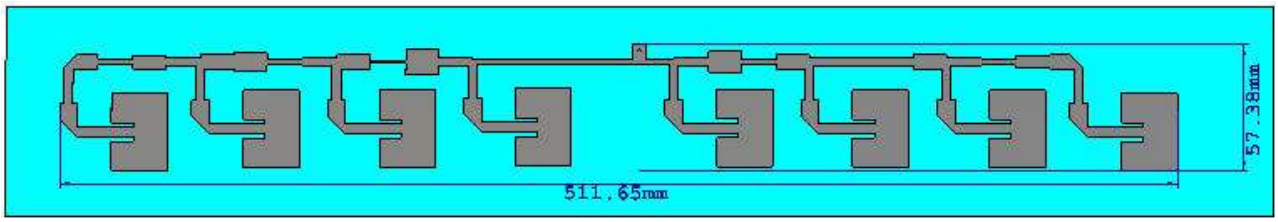

Figure 3: Front view of the optimized linear array of microstrip rectangular patches with inset feeds (Fig. 1). The array is fed from the center via a coaxial cable. Two microstrip lines of different lengths realize the phase difference between the four patches to the left and the four patches to the right.

Transformer 3 Right	15.88	2.88	15.51	4.94
	Zc1		Zc4	
	Length	Width	Length	Width
All Transformers	15.80	3.36	15.34	6.25
	Left of coaxial feed		Right of coaxial feed	
	Length	Width	Length	Width
Center feed	76.25	1.80	15.88	2.91

In order to correct the resonance frequency, it is sufficient to slightly change the length of the patches, while proportionally changing the length of the inset feed.

As for the feeding currents, we followed an iterative correction based on the observation of surface currents obtained from the CST simulation:

- We simulate the array using CST with a surface current monitor at the lower, upper and central frequencies (2.62GHz, 2.655GHz and 2.69GHz);
- If the S11 resonance is not centered we fine tune the length of the patches (keeping the inset feed length at the same proportional length);
- We check the radiating pattern at the lower, upper and central frequencies (2.62GHz, 2.655GHz and 2.69GHz). If they are as designed, we stop.
- When look at the surface current RMS value at each of the patches radiating edges at the side further from the feeding network (which is less disturbed by it). We calculate the ratios from one patch to the next and, if the value is different from the prescribed value from Table 1 we change the transformer impedances to compensate this variation. We also check if both central patches have the same RMS current, and if not we change the impedance of one of the lines in the center of the array to compensate.
- We check the phases of the surface currents at the patches radiating edges to assure the phase difference is as prescribed. If it is not the case, we compensate by varying the length of the transmission lines at the center of the array.

The parameters of the optimized design are shown in Table 3, and the array front view is presented in Fig. 3.

4. Antenna Array Simulations

In this section we will present the simulation results of the antenna array design following the procedure described in Section 3 (Table 3, Fig. 3). We will first present the results for one isolated column. Then we will include the coupling effects when using several columns side by side in a 2D array by means of periodic boundaries conditions.

4.1. Single Column Simulation

In Fig. 4, we show, for the array in Fig. 3, the reflection coefficient and the realized gain in E and H-planes at 2.62 GHz, 2.65 GHz and 2.69 GHz.

As we can see on the E-plane plane, the array presents a slow decrease rate in the realized gain inside of the formed zone, while presenting lobes at least 10 dB than the main beam. The array presents a HPBW of 76° in the H-plane cut. The array has a reflection coefficient bandwidth going from 2.62 GHz to 2.70 GHz. The maximal realized gain of the array goes from 12.3 dB to 13.2 dB in the design bandwidth.

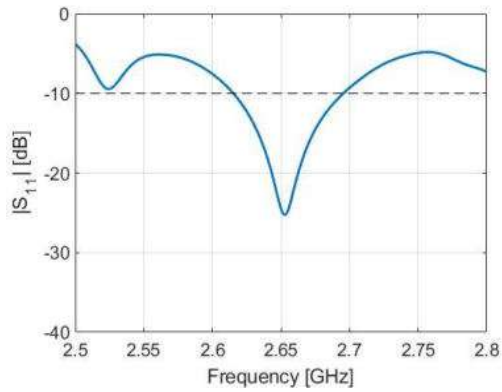

(a)

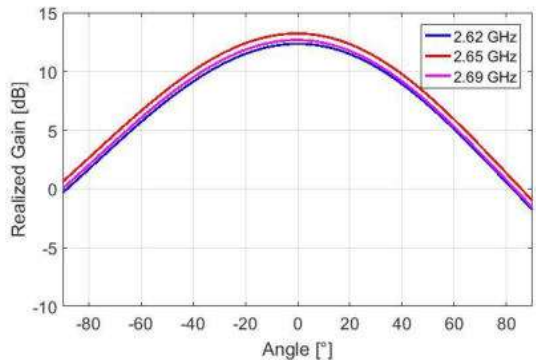

(b)

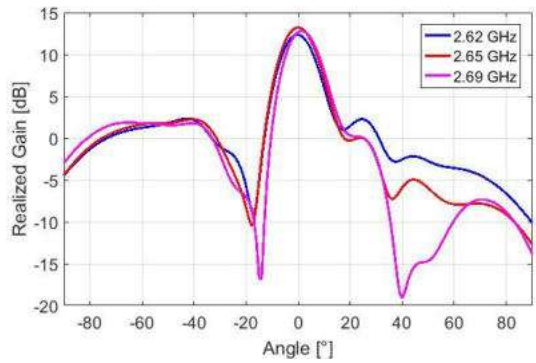

(c)

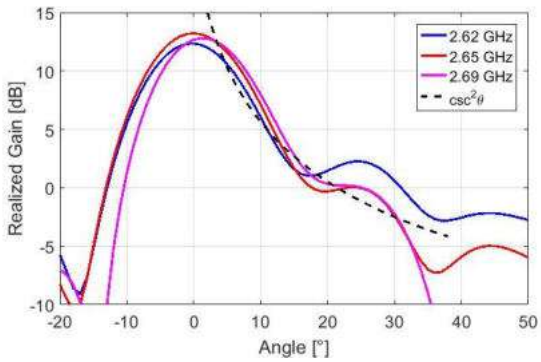

(d)

Figure 4: Results from the simulation of the array in Fig. 3. In (a) we have the reflection coefficient, in (b) the realized gain in the H-plane, in (c) the realized gain in the E-plane and in (d) a zoom on Fig. 4 (c) with the $csc^2\theta$ pattern superposed for reference.

4.2. Coupling effects

In Fig. 5, we show, for the array in Fig. 3 calculated with periodic boundaries conditions to obtain an infinite array with a spacing of 65 mm, the reflection coefficient and the realized gain in E and H planes at 2.62 GHz, 2.65 GHz and 2.69 GHz.

As we can see on the E-plane, the array presents a slow decrease rate in the realized gain inside of the formed zone as expected from the results in Fig.4. However, at 2.69 GHz the coupling between the arrays causes a 1.7 dB rise of the sidelobe level.

The array presents a HPBW of 90° in the H-plane cut, 14° larger than the isolated array. The main beam direction is however skewed by 20°.

The array presents a reflection coefficient bandwidth going from 2.62 GHz to 2.71 GHz, slightly larger than that of the isolated array. There is a small drop in the realized gain, which goes from 11.1 dB to 12 dB in the design bandwidth. The coupling between arrays causes this drop.

The performances of the array are not substantially degraded by the presence of neighboring linear arrays, thus this linear array is suitable for use in a 2D array.

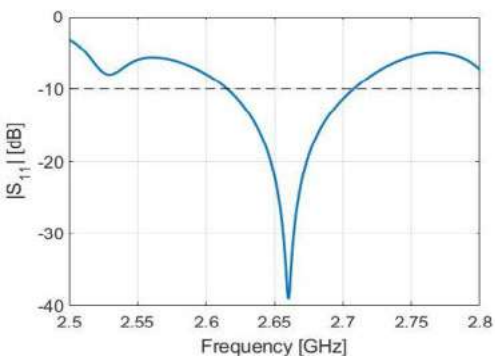

(a)

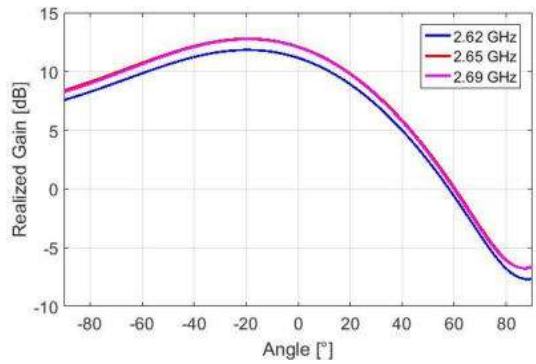

(b)

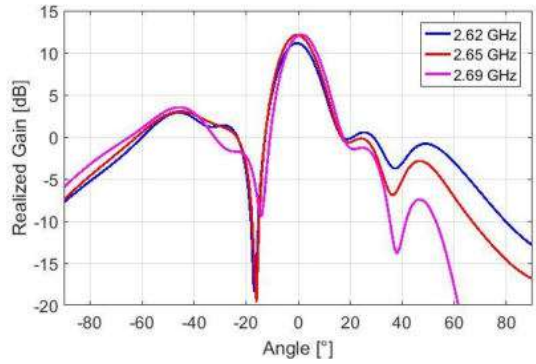

(c)

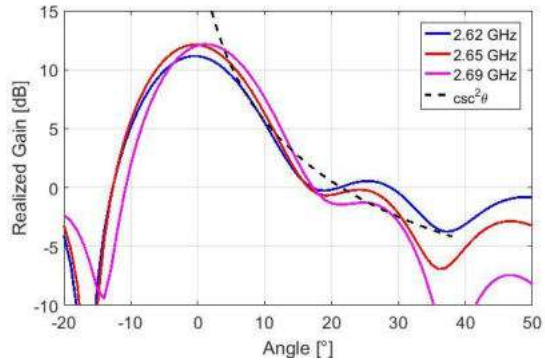

(d)

Figure 5: Results from the simulation of the array in Fig. 3 with periodic boundaries (spacing between columns equal to 65 mm). In (a) we have the reflection coefficient, in (b) the realized gain in the H-plane, in (c) the realized gain in the E-plane and in (d) a zoom on Fig. 5 (c) with the $csc^2\theta$ pattern superposed for reference.

4.3. Four Column Simulation

In Fig. 6, we show the four columns finite array, consisting of four copies of the array in Fig. 3 spaced by 65mm. In Fig. 7, we present the reflection coefficient and the realized gain in E and H planes at 2.62 GHz, 2.65 GHz and 2.69 GHz for this array.

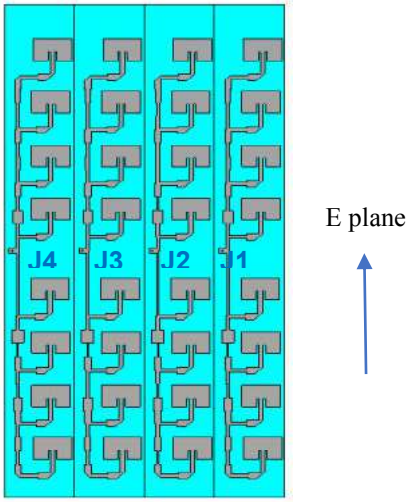

Figure 6: Front view of the 4-column array of microstrip rectangular patches with inset feeds. The array is fed from the center of each column via coaxial cables.

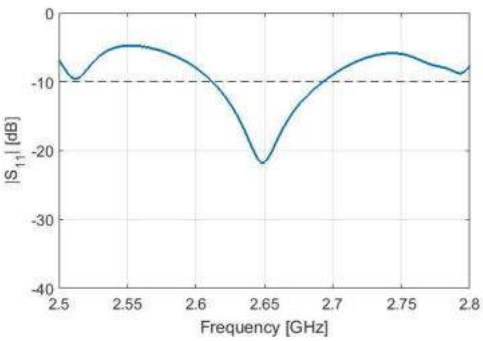

(a)

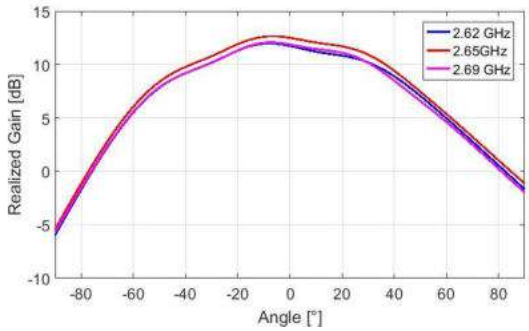

(b)

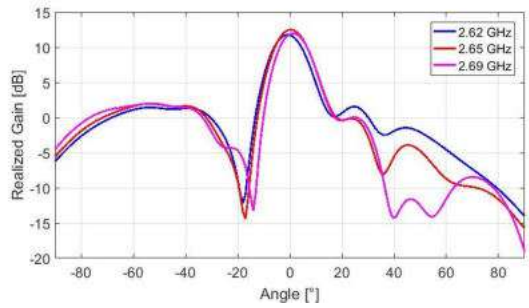

(c)

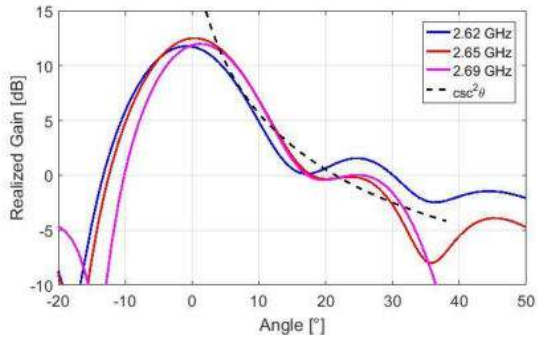

(d)

Figure 7: Results from the simulation of the array in Fig. 6 (4 times the array in Fig. 3 with spacing between columns equal to 65 mm). In (a) we have the reflection coefficient, in (b) the realized gain in the H-plane, in (c) the realized gain in the E-plane and in (d) a zoom on Fig. 5 (c) with the $csc^2\theta$ pattern superposed for reference.

As we can see on the E-plane, the array presents a slow decrease rate in the realized gain inside of the formed zone as expected from the results in Fig.4 and Fig. 5.The worst case sidelobe level is below -10 dB.

The array presents a HPBW of 78° in the H-plane cut, closer to that predicted by the isolated array. The main beam direction is however skewed by 8°, less than predicted by the infinite array simulation.

The array presents a reflection coefficient bandwidth going from 2.61 GHz to 2.69 GHz. The realized gain goes from 11.6 dB to 12.5 dB in the design bandwidth, in between the values for the single column and the infinite array.

5. Antenna Array Prototype

The array was designed originally using the AD430 substrate. However, the material became obsolete so we choose to build it using the Kappa438 substrate, which has very similar characteristics to the AD430. The datasheet value for the relative permittivity for this material is 4.38 and the thickness for our prototype is 3.048mm

As the thickness used for our antenna is not a standard value for this substrate, we built a first prototype of the single column array so that we could obtain the material properties by retrofitting simulations. By closely analyzing the Kappa438 properties, we noticed that it presents a certain level of anisotropy [12]. For our retrofit simulations (Fig. 8), we considered this anisotropy and converged at the value:

$$(\varepsilon_{rx}, \varepsilon_{ry}, \varepsilon_{rz}) = (4.55, 4.55, 4.16), \qquad (8)$$

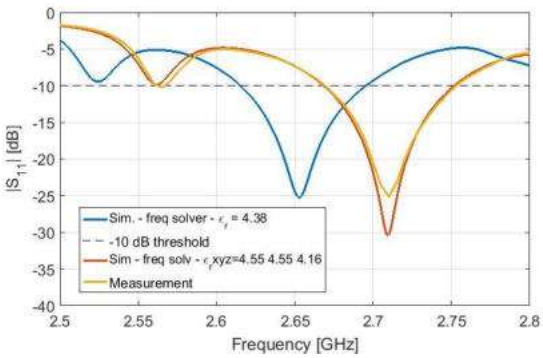

Figure 8: Reflection coefficient of the array in Fig. 3 simulated with CST using a $\varepsilon_r = 4.38$ substrate in blue, using a (ε_{rx}, ε_{ry}, ε_{rz}) = (4.55, 4.55, 4.16) substrate in red and the measured prototype first run in yellow.

The first prototype had the bandwidth slightly shifted up from the desired bandwidth and, to correct that, we scaled the entire array by 1.02 (verifying that it did bring the bandwidth to the desired range, 2.62GHz - 2.69GHz, by simulating the array using the retrofitted values of the Kappa438).

The antenna compose with four linear arrays was realized and measured in an anechoic chamber. The measurement of the reflection coefficient is given in Fig. 9. Each linear array is measured when 50 Ohms load the others.

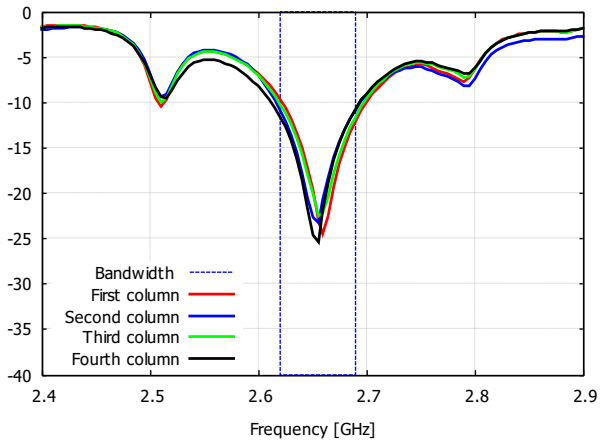

Figure 9: Reflection coefficient of one linear array among the three others.

The levels are below -10 dB in the required bandwidth between 2.62 GHz and 2.69 GHz. We can also note a good similarity between the four measurements. The coupling terms were also measured and are less than -20 dB throughout the bandwidth.

The measured radiation pattern in the E plane is plotted in Fig. 10 and compared to the simulations. Only the J3 array is fed (the other arrays being loaded by 50 Ohms).

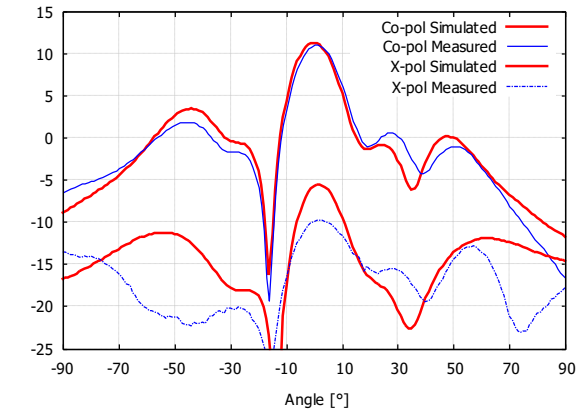

a)

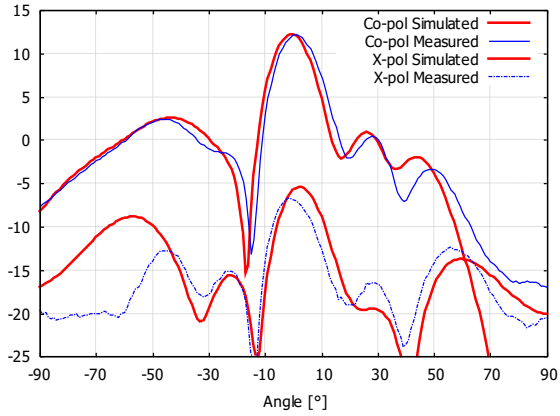

b)

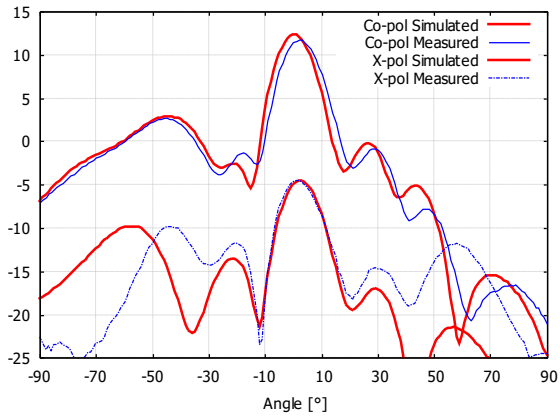

c)

Figure 10: Comparison between the measured and simulated E-plane radiation patterns when the J3 array is fed at 2.62 GHz (a), 2.655GHz (b) and 2.69 GHz (c).

The measured radiation pattern in the H plane is plotted in Fig. 11 and compared to the simulations. Only the J3 array is fed (the other arrays being loaded by 50 Ohms).

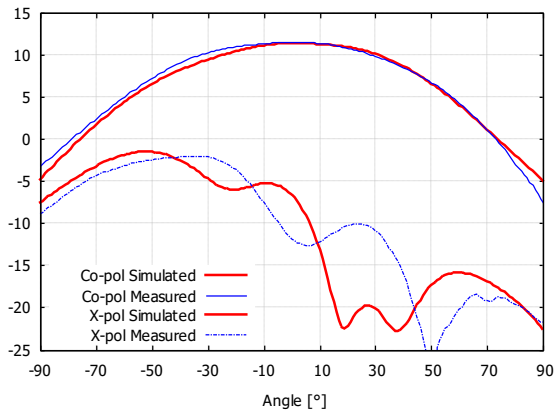

a)

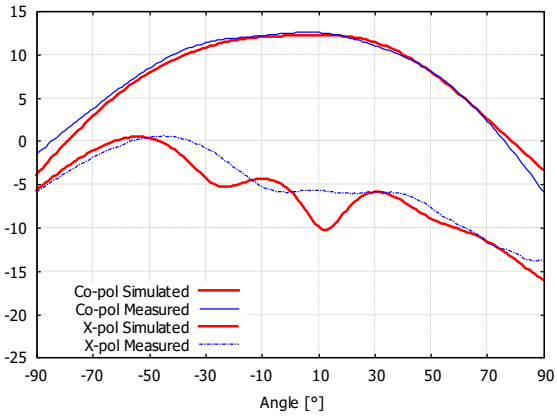

b)

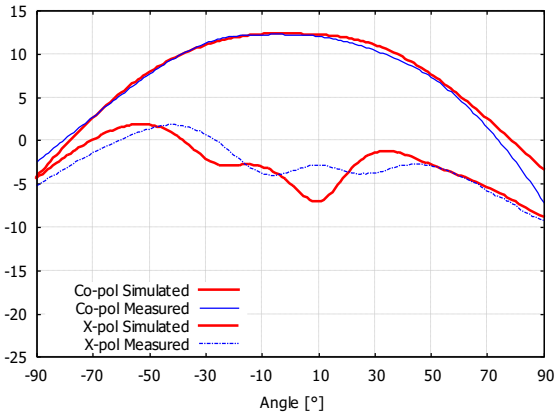

c)

Figure 11: Comparison between the measured and simulated H-plane radiation patterns when the J3 array is fed at 2.62 GHz (a), 2.655GHz (b) and 2.69 GHz (c).

For all the measurements, there is good agreement with the simulated results. In E-plane, the shape of the radiation pattern follows the cosecant squared law (towards the sky, positive angles) and the decrease of the radiation pattern is obtained around 15° (towards the ground, negative angles). In H-plane, the radiation patterns have HPBW equal to 84° at 2.62 GHz, 88° at 2.655 GHz and 82° at 2.69 GHz. The gain levels vary between 11 dB and 12.9 dB. The cross polarization components remains 17 dB below the main component on-axis.

6. Conclusions

Four linear arrays of microstrip rectangular patches has been developed and simulated using different simulators. Each linear array has been designed to have a cosecant squared radiation pattern in the E-plane and to presents a 90° HPBW in the H-plane. The design steps procedure has been detailed and a first realization made it possible to take into account the deviations of the materials used. Then four linear arrays has been realized and measured. Each array bandwidth goes from 2.62 GHz to 2.69 GHz with a reflection coefficient below -10 dB and the realized gain that goes from 11.1 dB to 12.2 dB in the required bandwidth. These measurement results, in agreement with the simulation, demonstrate that the arrays have the required specifications in terms of matching and shape of radiation patterns. All of these results validate the design of the four linear arrays.

Acknowledgements

This project has received funding from the Banque Publique d'Investissement and the Conseil Régional d'Ile-de-France (Paris Region) in the framework of the FUI program DIOD.

References

[1] S. Park, H. T. Kim, S. Lee, H. Joo and H. Kim, Survey on Anti-Drone Systems: Components, Designs, and Challenges, *IEEE Access*, vol. 9, pp. 42635-42659, 2021.

[2] R. K. Miranda, D. A. Ando, J. P. da Costa, and M. T. de Oliveira, Enhanced direction of arrival estimation via received signal strength of directional antennas, *Proceedings of the 2018 IEEE International Symposium on Signal Processing and Information Technology (ISSPIT)*, pp. 162–167, 2018.

[3] D. A. Ando, R. K. Miranda, J. P. da Costa, and M. T. de Oliveira, A novel direction of arrival estimation algorithm via received signal strength of directional antennas, *Proceedings of the 2018 Workshop on Communication Networks and Power Systems (WCNPS)*, pp. 1–5, 2018.

[4] R. C. Hansen, Array pattern control and synthesis, *Proc. IEEE*, vol. 80, pp. 141-151, Jan. 1992.

[5] J. L. Volakis, *Antenna Engineering Handbook*, 4th Edition, McGraw-Hill Education, 2014.

[6] CST Studio Suite 2016.

[7] D. M. Pozar, *Microwave Engineering*, 4th Edition, John Wiley & Sons, 2012.

[8] R. L. Haupt, D. H. Werner, *Genetic Algorithms in Electromagnetics*, John Wiley & Sons, 2006.

[9] R. L. Haupt, *Antenna Arrays, a Computational Approach,* John Wiley & Sons, 2010.

[10] Matlab 2018 Global Optimization Toolbox.

[11] ADS 2018 Keysight.

[12] MWI Microwave Impedance Calculator, Rogers Corporation, 2019.

10 to 40 GHz ultra-wideband magneto-electric phased array

Senglee Foo

Huawei Technologies Canada, R&D, Ottawa, Ontario, Canada
E-mail: senglee.Foo@huawei.com

Abstract

In the past decade, current sheet antenna (CSA) or tightly-coupled dipole arrays (TCDA) have been developed based on current-sheet periodic structure to achieve ultra-broadband impedance performance with wide scanning capability. This paper presents an alternative ultra-broadband periodic array using continuous magneto-electric (ME) currents, which can be implemented using radiating slots and horizontal monopoles. The proposed ME array is scalable from sub-6GHz to millimeter-wave and has the advantage of much simpler feed structure and does not require extremely small capacitive gap between radiating elements.

1. Introduction

Various forms of ultra-broadband phased arrays have been developed in the past based on the principle of current-sheet antenna (CSA), such as the tightly-coupled dipole arrays (TCDA) [1]-[2] and travelling-wave antennas [3]. These types of arrays apply broadband impedance matching/balun techniques to an array of closely-coupled, electrically small dipole elements with very small capacitive gaps between radiating elements. They have shown to exhibit well-behaved impedance and radiation patterns with very wide scanning angles over multi-octave of frequency bandwidth. For a grating-lobe free array, the maximum element spacing is limited to 0.5λ. As a result, a broadband active phased array is typically designed to operate between 0.5λ to 0.1λ, which results in real impedance of dipole elements between 100 to a few hundred ohms. Consequently, these types of arrays require design of a relatively complex feed/balun circuit and a means of achieving the narrow capacitive gaps.

The magneto-electric (ME) phased array was first proposed as a composite-right-left-handed (CRLH) array structure [4] to achieve the ultra-broadband performance with capability of surface-wave suppression in a finite array. Instead of the continuous electric current sheet model in the TCDA, the proposed ME array is based on continuously alternating electric and magnetic currents. This concept results in lower real-part impedance (50Ω at 0.5λ element spacing) and does not requires small capacitive gaps between elements. The ME array concept is scalable from sub-6GHz to millimeter-wave frequencies. This paper presents an implementation of the ME array for ultra-wideband (4:1) millimeter-wave applications (10 GHz to 40 GHz).

2. Magneto-electric phased array

Unlike TCDA, the proposed ME phased array is based on alternating magnetic and electric currents, which is implemented using a periodic cascade of monopoles and slots.

Fig.1 shows a detailed dual-cell model of the proposed ME phased array. Each monopole is connected directly to an unbalanced coaxial line from below a ground plane, which induces displacement current across a series-capacitor gap (slot) formed between ground plates. This periodic structure of monopole and slot forms a continuous line of alternating electric and magnetic current along the array axis.

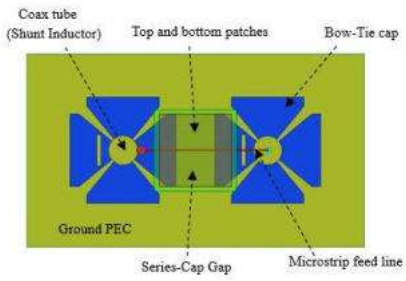

(a) Top view

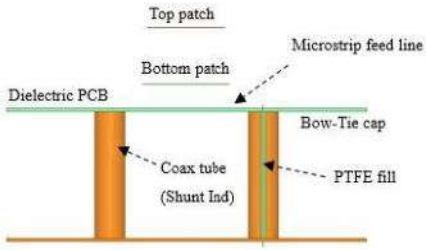

(b) Side view

Fig. 1. Dual-cell structure of the magneto-electric phased array

This array structure forms a basic composite-right-left-handed (CRLH) transmission line. Shunt inductors are simply metallic tubing (coax shield) connecting the bow-tie dipole grounds to the antenna ground sheet. Shunt inductors are simply metallic tubing (coax shield) connecting the bow-tie dipole grounds to the antenna ground sheet. Series capacitors are air gaps formed between bow-tie metallic grounds. Monopoles are microstrip feed lines connected directly to the center pins of coaxial lines, which also serves as feed line to the radiating slots.

With proper size of series capacitor gap and shunt coaxial tube the structure can be designed to further suppress unwanted surface waves from edges of the finite array structure.

Multiple layers of small metallic square patches are placed directly above the radiating slots and form layers of impedance-matching meta-surfaces. However, unlike an aperture-coupled stacked patch (ACP), sizes of these metallic patches are significantly smaller than half-wavelength. Together, these patches form layers of reactive meta-surfaces with the sole purpose of enhancing broadband impedance matching of the array. The principle and techniques of such method is well documented by Munk [5]. Fig. 2 shows an equivalent diagram of the broadband impedance matching using the meta-surfaces. Total impedance at the plane of radiating sources is a parallel sum of all discontinuity impedances in the transverse plane, including the complex element impedance, transformed impedance of ground plane, and transformed impedances of capacitive meta-surfaces, i.e.,

$$Z_{ANT} = Z_A + Z_c // Z_{GND} \quad (1)$$

Where,

$$Z_A = R_A + jX_A,$$
$$Z_c = Z_{c1}(d_1) // Z_{c2}(d_1 + d_2)$$
$$Z_{GND} = Z_{PEC}(d_0)$$

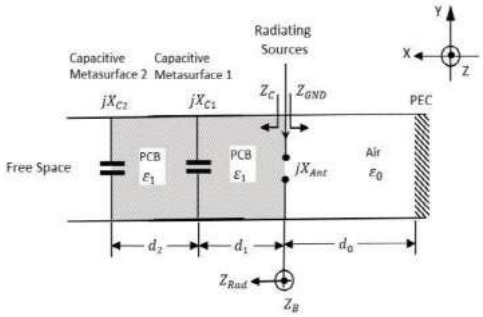

Fig. 2. Impedance matching scheme of the ME phased array

With proper tuning, combined characteristics of capacitive ME sources and meta-surfaces tend to cancel out the large inductive impedance of the PEC ground. This type of array is capable of producing a low constant real impedance near 50-75 ohm and low active VSWR over multi-octave of frequency bandwidth.

3. UWB millimeter-wave ME phased array

A 20-element linear ME phased array with periodicity of 3.7mm is modeled using the commercial EM simulation software ANSYS HFSS. Fig. 3 shows the magnitude of active VSWR for scan angles ±50º. The active VSWR is below 2:1 for scan angle below ±20º, and less than 3:1 for scan angle up to ±40º. However, frequency bandwidth (VSWR 3:1) is reduced to 12 to 37 GHz for scan angle above ±40º. The 4:1 frequency bandwidth is achieved over scan angle of ±40º for active VSWR of 3:1. Fig.4 shows typical co-polar and cross-polar radiation patterns (E-plane) with scan angles between 0 and 50deg. Cross-polar patterns are typically below -30 dB in the main lobes. Scan loss is in the order of 1dB for scan angle up to 50deg.

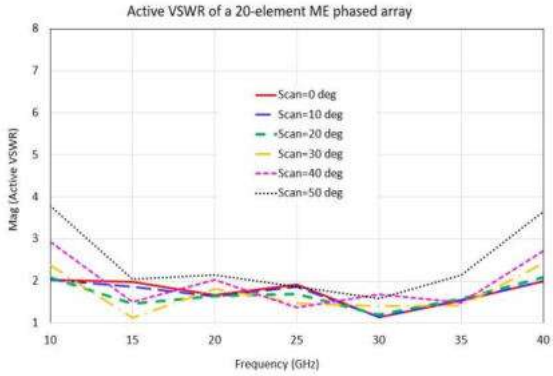

Fig. 3. Active VSWR of the 20-element ME phased array

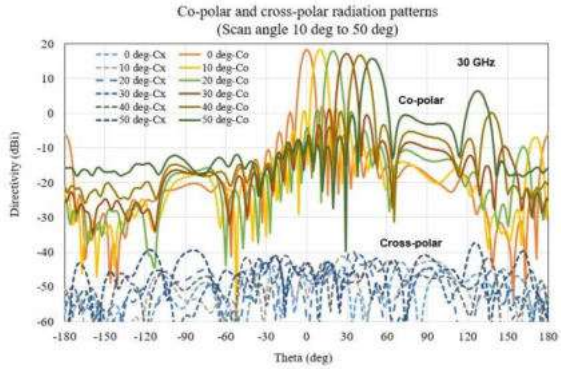

Fig. 4. Typical E-plane scanned patterns of the ME phased array

4. Conclusions

This paper presented an ultra-wideband millimeter-wave ME phased array. It is shown such array can be made to achieve an extremely wide impedance and radiation pattern bandwidth over a wide scan angle. A frequency bandwidth of 4:1 is achievable over scan angle of ±40º for active VSWR of 3:1. This enables beam steering over the entire frequency range from 10 GHz to 40 GHz.

References

[1] Y. Zhou, F. Zhu, Q. Luo, L. Wen, Q. Wang, X.X. Yang, Y.L. Geng, Z.Q. Cheng, "Tightly coupled array antennas for ultra-wideband wireless systems," *IEEE Access,* Vol. 6, 2018, pp.61851-61866.

[2] M. Jones, J. Rawnick, "A new approach to broadband array design using tightly coupled elements," *MILCOM 2007 IEEE Military Communications Conference,* 2007, pp. 1-7

[3] Johnson J.H.Wang, "Traveling-wave antenna array (TWAA) with multioctave scan-gain-bandwidth," *2016 IEEE International Symposium on Phased Array Systems and Technology (PAST),* 2016.

[4] S. Foo, "Ultra-wideband, tightly-coupled magneto-electric phased array," *15th European Conference on Antennas and Propagation (EuCap), 2021.*

[5] B. Munk, "Finite antenna arrays and FSS," *Wiley, IEEE Press*, 2003, pp. 181-213.

Characteristic Modes for the design of compact radiators on complex platforms

Simone Genovesi[1], Francesco Alessio Dicandia[2]

[1] Dipartimento Ingegneria dell'Informazione, Università di Pisa, Pisa, 56122, Italy.
[2]Greenwaves, Milan, Italy

Abstract

The placement of a communication system on a three-dimensional platform always poses a series of problems that the antenna designer has to solve or mitigate for guarantee the desired functional operability. Among the several challenges, the need of compact and conformal radiators is one of the hardest tasks to accomplish, especially if working on objects whose dimensions are comparable to the wavelength of interest. The solution to this problem can be pursued by using the Characteristic Mode Analysis.

1. Introduction

Small-size antennas are appealing solutions for managing communications on complex platforms where space is a scarce resource. However, due to intrinsic physical limits, the dimension of a resonant radiating element is directly proportional to the operative wavelength. This fact can have dramatic consequences for the designer if the addressed wavelength is comparable to the platform dimension. The interaction between the designed antenna and the platform need to be carefully evaluated as well. Moreover, if frequency or radiation pattern reconfigurability is a requested antenna feature [1],[2], then the goal is even tougher to tackle.

Characteristic Mode Analysis (CMA) can provide useful guidelines for the design of non-resonant elements that are able to exploit the hosting platform as the main radiating object. In CMA the current flowing on a conductive body surface is expressed in terms of a linear superposition of orthogonal current modes [3]. The selective excitation of these current modes can be advantageously exploited for several different tasks spanning from the design of small/conformal antennas, MIMO antennas as well as pattern and polarization reconfigurability. In addition to the small space required by this approach with respect to solutions resorting to resonant elements, the CMA allows to intrinsically consider the effect of the platform on the radiation properties of the antenna structure.

2. Characteristic Mode Theory

CMA determines the current modes that a conducting body is able to support. These modes are obtained by solving the generalized eigenvalue equation that is derived from the Method of Moments (MoM). The identified modes are found without considering any kind of excitation since they only depend on the shape and the size of the investigated structure. These modes are a convenient base where to expand the total surface current (J_{tot}) that can be found on a conducting body. More in detail, J_{tot} can be written as a linear superposition of current modes:

$$J_{tot} = \sum_n \alpha_n J_n \tag{1}$$

where α_n represents the modal weighting coefficients of the characteristic mode and J_n represent the current distribution of the nth mode. Furthermore, α_n can be calculated as:

$$\alpha_n = \frac{V_n^i}{1 + j\lambda_n} \tag{2}$$

where λ_n are the eigenvalues associated to the modes. The other two factors that contribute to the modal weighted coefficient of the modes are the modal significance (MS) of a mode, which is equal to:

$$MS = \left| \frac{1}{1 + j\lambda_n} \right| \tag{3}$$

and the modal excitation coefficient equal to:

$$V_n^i = \left\langle J_n, E^i \right\rangle = \oiint_S J_n \cdot E^i dS \tag{4}$$

where S is the surface of the conductive body and E^i the external excitation. Although the MS is independent of any kind of excitation, the terms V_n^i takes into account the effect of the external excitation applied, including the position, magnitude and phase. Consequently, the inner product $<J_n,E^i>$, represents the coupling between the exciter and the nth current mode, which quantifies the capacity of the applied source to excite a particular mode.

3. Discussion

A rough model of a vehicle is reported in Fig. 1a. (W = 2.1 m, L = 3.5 m, H = 1 m). The CMA is performed within a frequency range between 50 MHz and 80 MHz. It is interesting to observe that the relative wavelengths are comparable to the vehicle dimensions and therefore a

resonant antenna would require a significant space for its placement. The eigenvalues (λ_n) of the first eight characteristic modes as a function of the frequency are reported in Fig. 2. The eigenvalues are real numbers and a mode is considered at resonance when its associated value is equal to zero. The area highlighted in green corresponds to a MS greater than 0.8. By observing the results, it is apparent that in the frequency range of interest the most significant modes are Mode#1, Mode#3 and Mode#4 since they are the closest to zero over the whole bandwidth. The current distribution associated to each mode is illustrated at the center frequency of 65 MHz in Fig.1(b)-(e). The radiation pattern produced by a mode is, by definition, orthogonal to all the other ones and this property allows combining them in order to control the radiation pattern [4], [5]. However, each mode has to be properly excited and the kind, place and number of exciters requires careful study, especially on three-dimensional platforms [6],[7].

4. Conclusions

Example of CMA exploitation for designing the proper exciter on complex platforms will be provided as well as suitable design guidelines.

Acknowledgements

Work partially supported by the Italian Ministry of Education and Research (MIUR) in the framework of the Crosslab project (Departments of Excellence).

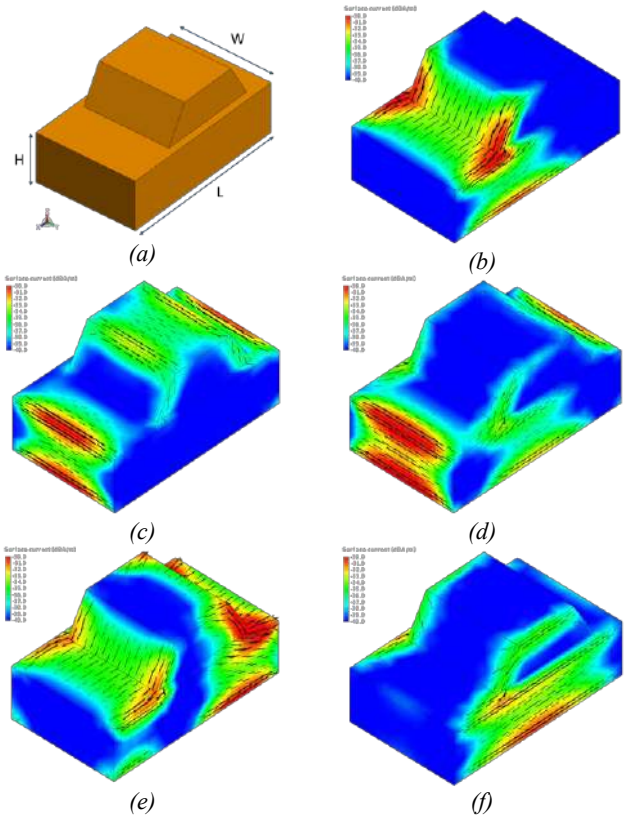

Figure 1: Rough model of the considered vehicle (a) and current distributions at 65 MHz of Mode#1 (a), Mode#2 (b), Mode#3 (c), Mode#4 (d), Mode#5 (e) and Mode#6 (f).

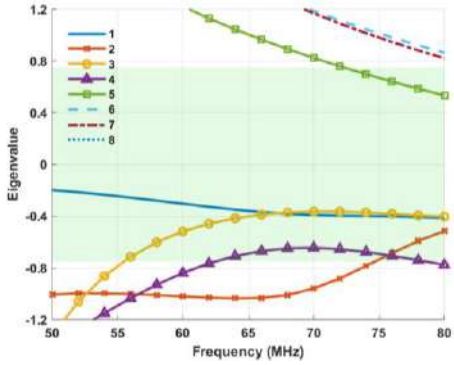

Figure 2: Plot of the first eight eigenvalues within the considered frequency bandwidth (50MHz-80 MHz).

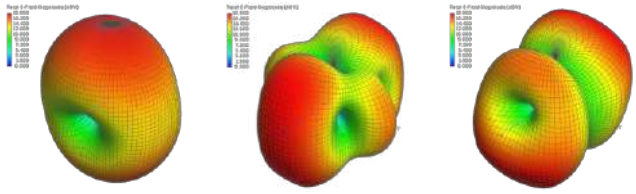

(a) *(b)* *(c)*

Figure 3: Radiation pattern associated with Mode#1 (a), Mode#3 (b) and Mode#4 (c).

References

[1] S. Genovesi, A. D. Candia, and A. Monorchio, 'Compact and Low Profile Frequency Agile Antenna for Multistandard Wireless Communication Systems', *IEEE Transactions on Antennas and Propagation*, vol. 62, no. 3, pp. 1019–1026, Mar. 2014, doi: 10.1109/TAP.2013.2272731.

[2] P.-Y. Qin, Y. J. Guo, A. R. Weily, and C.-H. Liang, 'A Pattern Reconfigurable U-Slot Antenna and Its Applications in MIMO Systems', *IEEE Transactions on Antennas and Propagation*, vol. 60, no. 2, pp. 516–528, Feb. 2012, doi: 10.1109/TAP.2011.2173439.

[3] R. Harrington and J. Mautz, 'Theory of characteristic modes for conducting bodies', *IEEE Transactions on Antennas and Propagation*, vol. 19, no. 5, pp. 622–628, Sep. 1971, doi: 10.1109/TAP.1971.1139999.

[4] F. A. Dicandia, S. Genovesi, and A. Monorchio, 'Null-Steering Antenna Design Using Phase-Shifted Characteristic Modes', *IEEE Transactions on Antennas and Propagation*, vol. 64, no. 7, pp. 2698–2706, Jul. 2016, doi: 10.1109/TAP.2016.2556700.

[5] F. A. Dicandia, S. Genovesi, and A. Monorchio, 'Advantageous Exploitation of Characteristic Modes Analysis for the Design of 3-D Null-Scanning Antennas', *IEEE Transactions on Antennas and Propagation*, vol. 65, no. 8, pp. 3924–3934, Aug. 2017, doi: 10.1109/TAP.2017.2716402.

[6] F. A. Dicandia, S. Genovesi, and A. Monorchio, 'Efficient Excitation of Characteristic Modes for Radiation Pattern Control by Using a Novel Balanced Inductive Coupling Element', *IEEE Transactions on Antennas and Propagation*, vol. 66, no. 3, pp. 1102–1113, Mar. 2018, doi: 10.1109/TAP.2018.2790046.

[7] F. A. Dicandia and S. Genovesi, 'A Compact CubeSat Antenna With Beamsteering Capability and Polarization Agility: Characteristic Modes Theory for Breakthrough Antenna Design', *IEEE Antennas and Propagation Magazine*, pp. 0–0, 2020, doi: 10.1109/MAP.2020.2965015.

Recent Advances in Conformal Transmitarrays

Pei-Yuan Qin*, Y. Jay Guo

University of Technology Sydney, Australia.
*corresponding author, E-mail: Peiyuan.qin@uts.edu.au

Abstract

For many wireless communication platforms, such as aircrafts and unmanned aerial vehicles (UAV), conformal transmitarray antennas, which are designed to follow the shapes of the platforms, are highly desired as they can achieve high gains, flexible radiation patterns and excellent aerodynamic performance. This talk will give an overview of research on conformal transmitarrays conducted in University of Technology Sydney, Australia. More specifically, it includes our latest progress in high efficiency conformal transmitarrays and multi-beam conformal transmitarrays.

Reconfigurable Intelligent Surfaces for Future Wireless Communication

Qammer H. Abbasi

James Watt School of Engineering, University of Glasgow, UK
*corresponding author, E-mail: qammer.abbasi@glasgow.ac.uk

Abstract

A novel idea of a smart reflector that is gaining a lot of interest is the Reconfigurable Intelligent Surface (RIS) which operates by reflecting the waves in the same way as a backscattering device. It consists of planar, low cost, nearly passive elements that would smartly manipulate EM waves in specific directions. As a result, this would boost the signal at the receiver with no added hardware cost. As compared to existing complex transceiver architectures with multiple RF chains and complex signal processing hardware, RIS practically has no RF chain, i.e., no power amplifier, phase shifters, attenuators, mixers and ADC components. This, in turn, eliminates the hardware complexity and the exorbitant cost of the RF equipment. Hence the overall potential impact of RIS is reduced deployment and hardware costs, network complexity and power consumption. In this talk, I will discuss about the work on this topic in our group and different testbeds and their results.

Decentralized Wireless Coordination for Distributed Antenna Arrays

Jeffrey Nanzer

Electrical and Computer Engineering, Michigan State University, East Lansing, MI, USA
E-mail: nanzer@msu.edu

Abstract

We present new approaches to wireless coordination of distributed antenna arrays using decentralized algorithms. Synchronization of the electrical states of elements in distributed arrays is necessary for distributed coherent operations such as beamforming. In large arrays, traditional centralized synchronization topologies yield susceptibilities to element failures and interference. Based on consensus averaging, we discuss new methods of synchronizing the relative phases and frequencies of distributed antenna array elements, and analyze the impact of residual errors on beamforming performance.

Broadband and multi-band antennas

Wideband Printed Planar Monopole Antenna Element for Wearable Application

Pedro Falcão, Custódio Peixeiro*

Instituto de Telecomunicações, Instituto Superior Técnico, University of Lisbon, Portugal
*corresponding author, E-mail: custodio.peixeiro@lx.it.pt

Abstract

The implementation of a wideband printed monopole antenna near a metallic shield is presented. A wearable antenna system application to probe the electromagnetic field, with frequency in the range 0.7-3.5 GHz (5:1 bandwidth), incident on a professional user is envisaged. A lossy foam layer is used between the shield and the antenna to absorb the shield reflection and avoid narrowing the bandwidth.

1. Introduction

Since the 90s there has been a permanent increase, with accelerated pace, in the deployment of mobile communication and Wi-Fi systems. With the advent of 5G a huge increase in the number of users and terminals as well as traffic is forecasted [1]. The deployment of new systems and the maintenance of existing ones demand the use of protective vests by professional workers. Moreover, the addition of new features in these vests, such as monitorization of the electromagnetic fields in the working space is under development [2].

To protect the workers from electromagnetic radiation hazard in their working environment their professional vests are lined with a protective metal shield. When the antennas are integrated in the vests near the shield their bandwidth decrease enormously. To avoid such bandwidth narrowing a layer of absorbing material is placed between the shield and the antenna. This papers presents the experimental characterization of the foam material used and the optimization of the corresponding layer thickness. Experimental reflection coefficient results are also included.

2. Antenna element configuration

The geometry of the single printed planar monopole element is shown in Fig. 1a. It consists on a modified octagonal patch monopole with coplanar waveguide (CPW) feeding [3]. It has been optimized to provide an input reflection coefficient below -10 dB in the frequency range 0.7-3.5 GHz. The typical monopole like radiation pattern is obtained with gain in the range 1.9-3.5 dBi [3]. Based on this element the dual-linearly polarized configuration composed of two orthogonal monopoles, shown in Fig. 1b, has been presented [3].

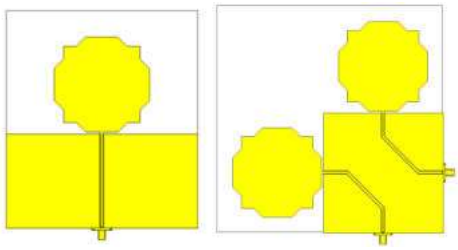

a) b)

Figure 1: Antenna geometry, a) single monopole, b) dual-linearly polarized monopole antenna.

The work described in the present paper corresponds to the integration of the dual-linearly polarized monopole antenna element (Fig. 1b) with the metal shield, as shown in Fig. 2.

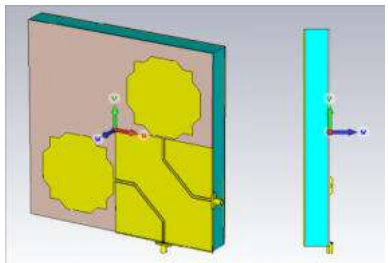

Figure 2: Dual-linearly polarized monopole antenna element with absorbing layer and metal shield.

3. Experimental characterization of the absorber

The absorber layer was obtained by slicing the planar region of an old anechoic chamber absorber panel. As the macroscopic characteristics (ε,μ,σ) of the panel are not homogeneous it was necessary to measure them. However, only ε and σ need to be measured since the panel material has normal magnetic behavior.

The real and imaginary parts of the relative (complex) electric permittivity, is defined as

$$\varepsilon_r' - j\varepsilon_r'' = \varepsilon_r - j\frac{\sigma}{\omega\varepsilon_0} = \varepsilon_r(1 - j\tan\delta) \qquad (1)$$

where ε_r is the relative electric permittivity, σ is the conductivity, ω is the angular frequency and tanδ is the loss tangent. ε_r' and ε_r'' were measured using the free-space transmission method, where the transmission coefficient (amplitude an phase) of a link between two horn antennas is

measured with a VNA (Fig. 3), with and without the absorber layer in the middle.

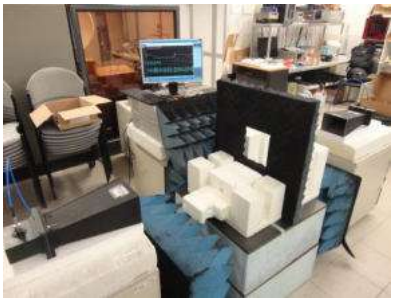

Figure 3: Setup for experimental characterization of the absorber.

The ε_r' and ε_r'' experimental results are shown in Fig. 4.

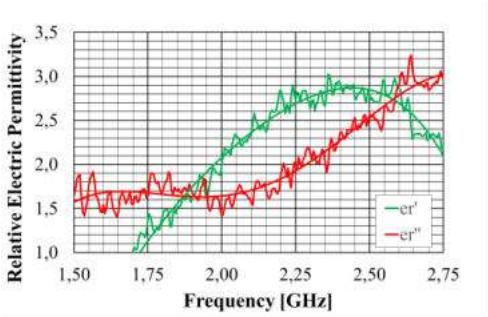

Figure 4: Experimental ε_r' and ε_r'' results.

These results have been used to calibrate the model of the absorber used in CST Microwave Studio. The ripple contained in the results is due to the reflections in the non-anechoic environment of the room.

4. Antenna optimization and test

The antenna geometry shown in Fig. 1b on top of the metallic shield and with the absorber layer in between them was simulated in CST Microwave Studio. Absorber thicknesses of 5, 10 and 15 mm have been simulated. The |S|-parameters' results obtained are shown in Fig. 5. The results of the free-space configuration (without shield and absorber) are also shown for reference.

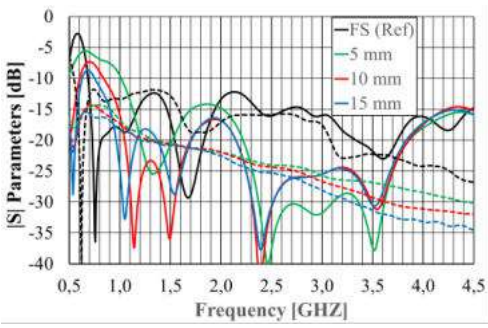

Figure 5: |S|-parameters simulation results for different absorber thicknesses, $|S_{11}|$-solid lines, $|S_{21}|$-dashed lines.

As it can be seen an absorber thickness of 10 mm provides and input reflection coefficient below – 10 dB, except in the range 700-750 MHz where it is slightly above (-8.7 dB).

Moreover, mutual coupling is very low (below -14.3 dB) in all the cases.

Radiation efficiency and gain have also been simulated. As expected, due to the losses in the absorber, there is a substantial reduction of the efficiency and gain. Both decrease as frequency increases. The decrease is about 6 dB at 700 MHz and 9 dB at 3.5 GHz.

An antenna prototype, with a 10 mm thick absorber layer, has been fabricated and tested. The corresponding experimental S-parameters' results are shown in Fig. 6.

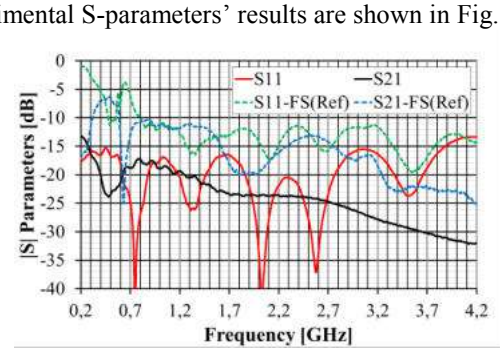

Figure 6: Experimental |S|-parameters' results.

The $|S_{11}|$ results of the antenna with metallic shield and absorber are considerably lower, compared with simulations, especially at low frequencies. This is due to a less accurate calibration of the absorber in that frequency region (a pair of horn antennas was not available for such frequency band). In the whole frequency band of interest both $|S_{11}|$ and $|S_{21}|$ are below -15 dB. This means it is possible to use a thinner (1 or 2 mm) absorber layer.

5. Conclusions

The paper presents the development of a dual-linearly polarized wideband monopole antenna element to be used in a professional vest lined with a protective metal shield. The use of an absorber layer is proposed to desensitize the antenna bandwidth from the presence of the shield. Input reflection coefficient and mutual coupling below -15 dB have been obtained with a 10 mm thick absorber layer sliced from and old anechoic chamber absorber panels. Naturally there is a substantial decrease (6 to 9 dB) in radiation efficiency and gain. However, this is not a problem for the envisaged application.

Acknowledgements

This work was partially supported by Instituto de Telecomunicações and Fundação para a Ciência e a Tecnologia under grant UIDB/50008/2020 and Instituto Superior Técnico, University of Lisbon

References

[1] CISCO Annual Internet Report (2018-2023). White paper C11-741490, 2020.

[2] https://www.centi.pt/en/projects/advanced-textiles/ipvest-

[3] P. Falcão, C. Peixeiro, Dual-Linearly Polarized Wideband Printed Planar Monopole Antenna, *Proc. EuCAP*, Madrid, Spain, pp. 1-5, 2022.

Design and Characterization of Compact Aspen Shape Multi-Element Antenna with Isolation Improvement for SWB Applications

N Suguna[1,*], S Revathi[1]

[1]School of Electronics Engineering, Vellore Institute of Technology, Vellore, India
*corresponding author, E-mail: reachsuguna@gmail.com

Abstract

Compact four - element Multiple – Input Multiple Output (MIMO) antenna is suggested to cover Ultra wide band (UWB: 3.1 – 10.6GHz), X-band (8 – 12GHz), Ku – band (12 - 18GHz) and K – band (18 – 26.5GHz) for future use in industrial, scientific and medical (ISM) systems as well satellite applications. Suggested design consists of four Aspen shape radiators with partial ground planes printed on Rogers RT / Duroid 5880™ substrate material having dielectric constant of 2.2, loss tangent 0.0009, thickness 0.787mm and its compact size is 43mm x 43mm. This design has been simulated using Ansys High Frequency Structure Simulator (HFSS) tool. The proposed antenna produces operating bandwidth at -10dB reflection coefficient is 23.66GHz (4.12 – 27.78GHz), having fractional impedance bandwidth (FBW) of 148.33%. Proposed antenna offers improvement in the isolation greater than -20dB in the operating super wideband (SWB) and voltage standing wave ratio (VSWR) is less than threshold value 2 in the obtained SWB range. Proposed antenna achieves peak gains within the operating band at selected frequencies 4.8GHz, 8GHz, 14.1GHz, 16.2GHz and 23.6GHz are 3.16dBi, 5.19dBi, 5.82dBi, 5.13dBi and 6.98dBi respectively. Furthermore, MIMO antenna parameters such as envelope correlation coefficient (ECC < 0.015), diversity gain (DG ≈ 10dB), total active reflection coefficient (TARC < 0.45), channel capacity loss (CCL < 0.30bits/sec/Hz) and mean effective gain (-4.5dB ≤ MEG ≤ -7dB) are investigated within the acceptable limits.

Keywords - Aspen shape, MIMO antenna, Irregular Isolating element, SWB, HFSS, Envelope Correlation Coefficient (ECC)

1. Introduction

With the advanced developments in the technology there is an enormous increase in the communication systems. Antenna plays a key role in the communications for the purpose of transmitting and receiving of the information. For designing an antenna [1], it should satisfy some of the requirements as high bandwidth, faster data rate, high efficiency, good resolution, high capacity. For designers it is a challenging activity to design a high-speed multimedia connectivity for wireless communication and also it requires covering wide bandwidth [2]. As, the signals gets weaker when it gets wider and also, it's harder to detect and send the wideband signals are the drawbacks. Due to this drawback ultra-wideband antennas [3] came into existence as it has the ability to provide the high data rate wireless communication systems. Its transmitting power is low, in multipath channels high performance; in adverse condition it delivers high signal strength. As it has some of the drawbacks like its adoption rate is slow, signal acquisition times is long, FCC has the limited emission, issues of co-existence and interference with other radio technologies, high cost. Due to its drawbacks, it has been recent trend to employ super wideband antenna [4] as it can offer high bandwidth by covering both long- and short-range communication. SWB has a bandwidth ratio greater than or equal to 10:1 and has a large BDR, high data rate, and electrical dimensions less, at faster rate data and video, increased channel capacity, greater time accuracy. It's now employed in monitoring systems, military and civil applications. To cover such large frequencies Multiple Input Multiple Output antenna is suitable as it is primarily utilized for the systems as multiple antennas employed for both source and destination in this case a single MIMO [5] antenna can be able to handle. With the help of the Spatial Multiplexing and multiple antennas high data rate achieved. MIMO based systems reduce fading effects, the systems with MIMO offers high Quality of Service and helps in achieving Bit Error Rate.

With the increase of technology there is a huge demand for the wideband communication. For the purpose of ultra – wide band applications MIMO antenna [6] designed with the size of 58.6 x 46mm^2 and it ranges entire UWB of 3.1-10.6GHz and has low correlational coefficient of < 0.02. In this article [7], with novel stub structure UWB-MIMO antenna is designed on FR4 substrate with the size of 40 x 68mm^2 and its frequency ranges from 3.2-10.6GHz and its IBW is 7.4GHz isolation less than -15dB and its gain is less than 2.5dB. In this paper [8], for the dual band MIMO system in the 5G smartphone an eight-antenna proposed. The overall dimensions of the antenna are about 145 x 75mm^2 on FR4 substrate and its frequency ranges from 3.3-3.6GHz and 4.8-5GHz and its ECC is less than 0.15. For the purpose of ultra-wideband systems an antenna which is uni-planar polarisation diversity is designed [9] with the size of 50 x 50mm^2 on Rogers RT/Duroid 6035HTC with the frequency ranges from 2.76-1075GHz. For the purpose of 5G smartphone application [10], MIMO antenna which is

dual band is designed and the size of the antenna is 130 x 74mm^2 on FR4 substrate as its frequency ranges from 3.3-3.6GHz, 4.8-5.0GHz. With WLAN band rejection a compact 4 x 4 UWB-MIMO antenna designed [11] with the size of 60 x 60mm^2 and its frequency ranges from 2.73-10.68GHz and its IBW is 7.95GHz. In this article [12], using carbon black film in UWB MIMO antenna system isolation improvement proposed and the overall size is of 50x40mm^2 and the frequency ranges from 2.5-11GHz and the gain of 2.11dBi and the efficiency of 69.2%. In this paper [13], with dual polarization UWB-MIMO antenna which is compact coradiator proposed on FR4 epoxy with the size of 48 x 48mm^2 which frequency ranges from 3-11GHz. MIMO antenna system [14], UWB Bi-planar Yagi-like which is miniaturized is proposed with the size of 50 x 80mm^2 and the frequency ranges from 4.183 – 6.584GHz and the efficiency of 80%. In this article [15], with 5.5GHz band-notched characteristics UWB diversity slot antenna which is compact printed on FR4 substrate which is 48 x 48mm^2 in which frequency ranges from 2.5-12GHz. In UWB-MIMO antenna using F-shaped stubs [16], mutual coupling reduction proposed and the size of the antenna is about 50 x 30mm^2 and has low mutual coupling of less than -20dB and ECC < 0.04, DG > 7.4dB. In this article [17], with WLAN band-rejection UWB MIMO antenna which is Koch fractal is proposed and the size of the antenna is about 45 x 45mm^2 and S_{11} < -10dB from 2-10.6GHz. For mobile platform based on the theory of characteristic modes planar UWB MIMO [18] antenna with the pattern diversity and isolation improvement designed. The overall size is about 85 x 50mm^2 and the bandwidth ranges from 2-9.5GHz and the gain is above 1.5dBi. High gain monopole antenna [19] which is triple band and fractal based is proposed and the overall size of the antenna is about 90 x 59mm^2 and the gain of the antenna is about 5dBi. In this article [20], coplanar strips rectangular spiral antenna which UWB coplanar waveguide in which its size about 50 x 40mm^2 on Rogers RO4003C substrate and its frequency ranges from 3.5-10.6GHz and gain about 4.7dBi. In this paper [21], for the purpose of Bluetooth/WLAN applications integrated wideband antenna which is multiband designed and the size of the antenna is about 60 x 50mm^2. For super wideband applications [22], circular monopole antenna which is elliptical slot loaded partially segmented proposed on Rogers RT/Duroid 5880 substrate.

In this paper, four – element Aspen shape multiple - input multiple - output (MIMO) antenna using irregular polygon shaped isolating element is used for developing SWB applications, which is printed on Rogers RT / Duroid 5880 ™ dielectric material having thickness of 0.787mm. Section 2 organizes as Aspen shape monopole antenna with partial ground plane and its characteristics. Furthermore, in order to improve the high data transmission rate and coverage area four – element MIMO antenna is implemented with and without isolating element. Simulation characteristics are analysed in the section 3. MIMO antenna parameters (ECC, DG, TARC, CCL and MEG) are investigated in the section 4. Section 5 shows the advantages of the proposed antenna with comparison of existed models [6 – 21] reported in literature. Finally this work is concluded with applications in section 6.

2. Aspen shape Monopole antenna design configuration and its performance characteristics

Conventional hexagonal microstrip patch antenna is designed using standard mathematical expressions [23-24]. Designed antenna is a three layer structure, Rogers RT / Duroid 5880 substrate material is sandwiched between the two perfect electric conductors (PEC) named as patch and ground layers. It has compact size of 20mmx 23mm. 50Ohm transmission line feeding is used for impedance matching with the characteristic impedance in free space. Proposed structure is designed and simulated using Ansys HFSS software.

2.1. Implementation of proposed Aspen geometry with partial ground

The proposed Aspen shape monopole antenna with partial ground and its development from conventional structure are shown in figure 1. Rogers RT/ Duroid 5880™ substrate is used to implement this proposed design due to it exhibits unique electrical properties, chemical resistance and low moisture absorption. Because of these properties, Rogers material is highly desirable for SWB applications. The proposed antenna is derived from conventional hexagon structure with radius (S) of 8mm as shown in figure 1(a). There are four derivation stages for the proposed Aspen structure: Iteration – 1, 2, 3 & 4. In the first stage, Iteration – 1 is 50ohm transmission line fed hexagon microstrip patch antenna is designed. Iteration – 2 is partial ground plane with the full hexagon radiator. Iteration – 3 is partial ground plane width is reduced with hexagonal radiator. Finally, iteration – 4 is Aspen structure derived from the hexagon geometry with width reduced partial ground plane. The optimized dimensions of the proposed design are L_s = 23mm, W_s = 20mm, L_f = 7.75mm, W_f = 2mm, L_g = 7.25mm, W_g = 16mm, S = 8mm. Three dimensional view of the proposed design is shown in figure 1(e).

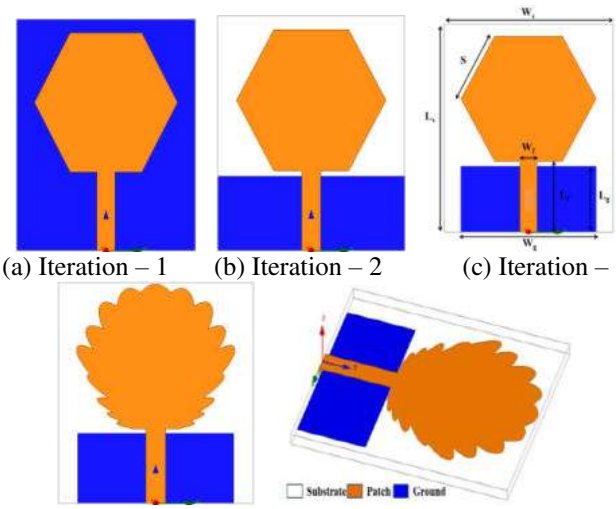

(a) Iteration – 1 (b) Iteration – 2 (c) Iteration – 3

(d) Iteration – 4 (e) 3D view

Figure 1. Evaluation of the proposed Aspen shape monopole antenna from conventional structure

2.2. Simulation results

The performance characteristics of the various iterations are evaluated from 3 – 30GHz interms of reflection coefficient (S_{11}) and voltage standing wave ratio (VSWR) as shown in figure 2 & 3. It is noticed that from figure 2, iteration – 1 is clearly resonates at the 19.30GHz with an impedance bandwidth (IBW) of 0.60GHz or 600MHz operating from 18.99GHz to 19.59GHz. By reducing the length of the ground plane, bandwidth can be improved to 16.99GHz from 0.60GHz for the 2nd iterative structure. Partial ground plane has been reduced to miniaturize the structure as shown in iteration – 3 and observed that there is an improvement in the IBW as well FBW. Iteration – 3 produces IBW of 21.67GHz at -10dB reflection coefficient and covers spectrum from 4.77 to 26.44GHz. Bandwidth ratio (BR) and fractional bandwidth (FBW) of iteration – 3 are 5.54 and 138.86%. Finally, regular hexagon structure is reshaped into Aspen shape structure with partial ground plane in case of iteration – 4. Impedance bandwidth, bandwidth ratio and FBW at -10dB are 24.03GHz, 6.25 and 144.88% respectively. VSWR signifies the designed antennas impedance matching condition with the characteristic impedance in free space. Ideal value of VSWR is 1 to infinity. Corresponding minimum VSWR values of the designed iterations 1 to 4 are 1.35, 1.01, 1.04 and 1.05 respectively as shown in figure 3. Table 1 reports the simulation characteristic parameters of the designed iterations.

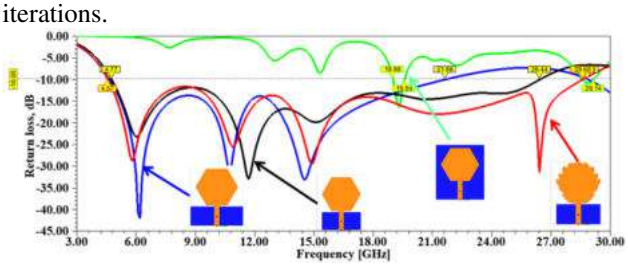

Figure 2. Reflection coefficient performance of designed antenna evaluations

Table 1. Simulated characteristic parameters of suggested Aspen monopole antenna

S.No	Parameter	I - 1	I – 2	I – 3	I - 4
1.	f_L, GHz	18.99	4.67	4.77	4.57
2.	f_H, GHz	19.59	21.66	26.44	28.60
3.	IBW, GHz	0.60	16.99	21.67	24.03
4.	S_{11}, dB	-16.2	-42	-34	-30
5.	BR	1.03	4.63	5.54	6.25
6.	FBW, %	3.11	129.05	138.86	144.88
7.	VSWR	1.35	1.01	1.04	1.05

(I – Iteration, f_L – Lowest operating frequency, f_H – highest operating frequency)

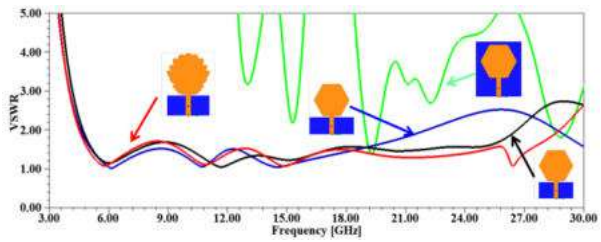

Figure 3. VSWR characteristics of the designed evaluations represented in figure 1(a – d)

3. Proposed MIMO antenna design and its characteristics

In order to improve the high date transmission rate and increasing the efficiency of the designed monopole antenna, multi - port antenna has been designed for provide efficient characteristics. Figure 4 shows the suggested four – element MIMO antenna configuration. Furthermore, to improve the isolation and reducing the mutual coupling between the two elements and to meet essential characteristics, the parameters are optimized and added isolating element in the ground plane as shown in figure 5. Three dimensional view of the proposed four element MIMO antenna with partial ground plane are configured in figure 6. The geometrical dimensions of the designed MIMO antenna are L_1 = 23mm, L_2 = 20mm, W_1 = 3mm, W_2 = 40mm.

3.1. MIMO antenna geometrical configuration

To address the high channel capacity, low latency and high data transmission rate, four – element MIMO antennas are considered as standard to obtain these characteristics. Figure 4 shows the geometrical configuration of the 4 – element MIMO antenna. Similar elements are placed orthogonally next to each element for its diversity characteristics. The reason behind this configuration is to reduce the mutual coupling between elements. Furthermore isolation between radiating elements is improved with adding the irregular polygon structure acts as decoupling structure as shown in figure 5. Three dimensional view of the proposed four – port MIMO antenna with isolating element is shown in figure 6. The geometrical dimensions of the designed MIMO antenna are L_1 = 23mm, L_2 = 20mm, W_1 = 40mm, W_2 = 3mm.

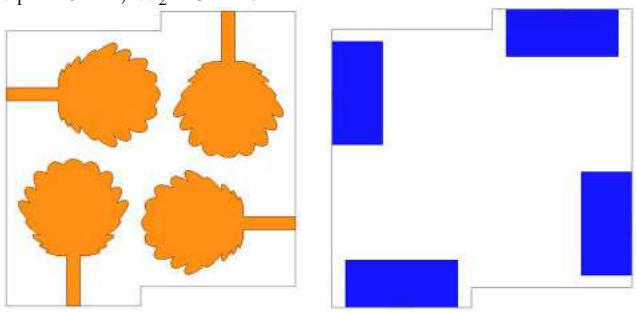

(a) Top view (b) Bottom view

Figure 4: Four element MIMO antenna without isolating element

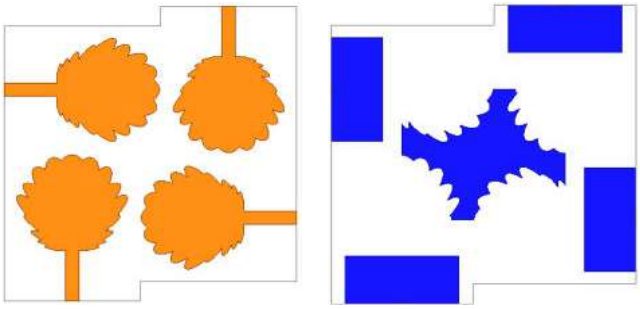

(a) Top view (b) Bottom view

Figure 5: Four element MIMO antenna with isolating element

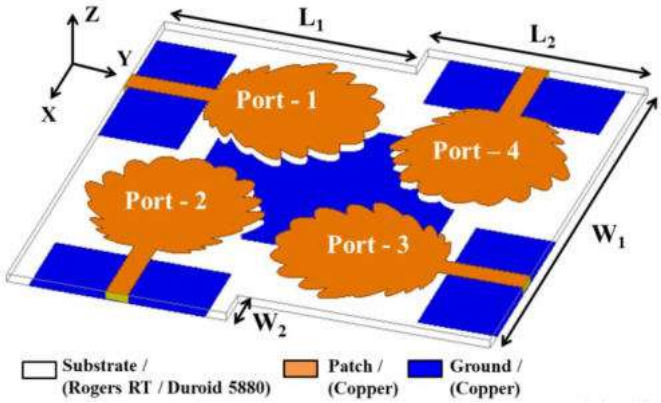

Figure 6: Three dimensional view of the proposed MIMO antenna

3.2. Simulated characteristics of the proposed design

Scattering parameters (S_{11} - reflection coefficient and S_{12} - insertion loss) of the designed four – element MIMO antenna with and without isolating elements are given in figure 7 and 8. From figure 7, MIMO antenna without isolating element operating from 4.38GHz to 26.72GHz at -10dB reflection coefficient with an IBW of 22.34GHz and its peak reflection coefficient is -29.98dB. Bandwidth ratio ($BR = f_H / f_L$) and fractional bandwidth ($FBW = \frac{2*(f_H - f_L)}{(f_H + f_L)}*100$) are 6.10 and 143.66%. Isolation between the MIMO elements is less than -15dB as shown in figure 8. According to the simulations of the proposed antenna (with isolating element), the proposed MIMO antenna operates frequency spectrum from 4.12GHz to 27.78GHz with S_{11} < -10dB. Due to the similarity of the antennas and its symmetrical arrangement, reflection coefficient characteristics of the suggested antenna are same. The corresponding BR and FBW are 6.74 and 148.33%. Figure 8 shows the insertion loss characteristics of the proposed MIMO antenna with isolating element. It can be noticed that by adding isolating / decoupling structure of the MIMO antenna, isolation factor has been increased by an average of 5dB. Proposed MIMO design has an isolation less than -20dB. The simulated VSWR Characteristics of the designed MIMO antenna with and without isolating elements are given in figure 9. The VSWR values of the designed MIMO antennas are 1.7:1 and 1.5:1 throughout the operating band respectively. The proposed antenna has very low VSWR value of 1.02 at 16.90GHz. Low value of VSWR indicates that very less impedance mismatch loss throughout the operating spectrum, which indicates the low power reflected and good impedance matching. Table 2 represents the simulated parameters such as lowest operating frequency, higher operating frequency, impedance bandwidth, reflection coefficient, bandwidth ratio, fractional bandwidth, VSWR and isolation value over the operating band for the designed MIMO antennas with and without isolating elements.

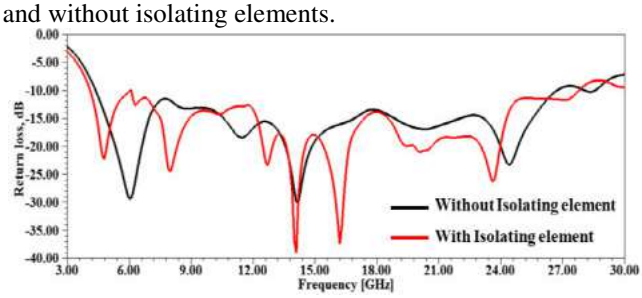

Figure 7. Reflection coefficient characteristics of the MIMO antenna design with and without decoupling structure

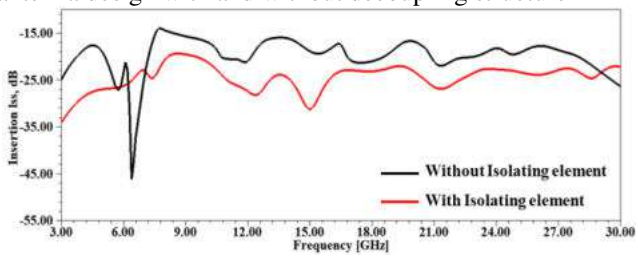

Figure 8. Insertion loss characteristics of the MIMO antenna design with and without isolating element

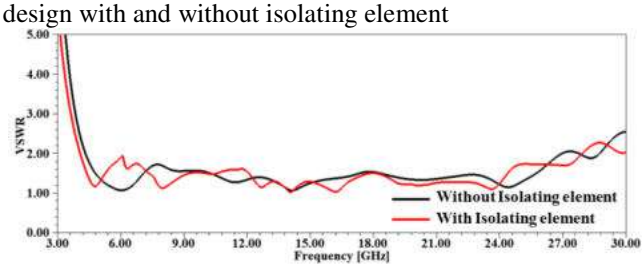

Figure 9. VSWR characteristics of the MIMO antenna design with and without isolating structure

Table 2. Simulated electrical parameters of the designed MIMO antennas

S. No	Parameter	MIMO without isolating element	MIMO with isolating element
1.	f_L, GHz	4.38GHz	4.12GHz
2.	f_H, GHz	26.72GHz	27.78GHz
3.	IBW, GHz	22.34GHz	23.66GHz
4.	S_{11}, dB	-29.98dB	-39.00dB
5.	BR	6.10	6.74
6.	FBW, %	143.66%	148.33%
7.	VSWR	1.06	1.02
8.	S_{12}, dB	< -15dB	< -20dB

Figure 10 shows the simulated gain characteristics of the proposed MIMO antenna designed on Rogers RT / Duroid 5880™ substrate material in 3D polar plots. Peak gains achieved at the selected resonant frequencies 4.80GHz, 8GHz, 14.1GHz, 16.2GHz and 23.6GHz are 3.16dBi, 5.19dBi, 5.82dBi, 5.13dBi and 6.98dBi respectively. Figure 11 represents two dimensional radiation patterns of the proposed MIMO antenna interms of elevation plane (E - plane) and azimuthal plane (H - plane) respectively.

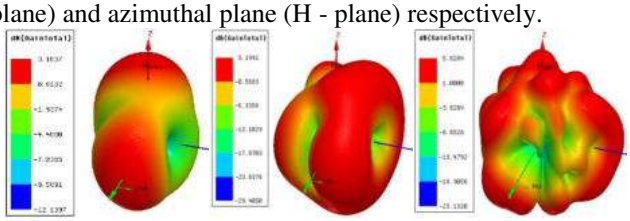

(a) 4.80GHz (b) 8.00GHz (c) 14.1GHz

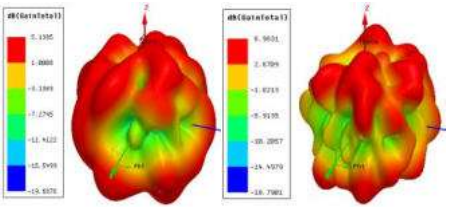

(d) 16.2GHz (e) 23.6GHz

Figure 10: 3D gain plots of proposed closely spaced MIMO antenna with isolating element

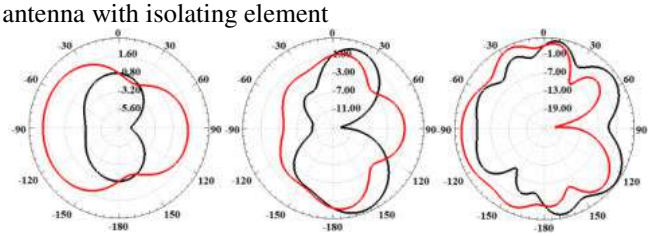

(a) 4.80GHz (b) 8.00GHz (c) 14.1GHz

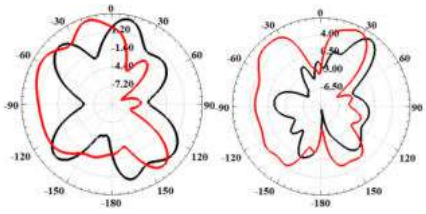

(d) 16.2GHz (e) 23.6GHz

Figure 11: 2D radiation characteristics of MIMO antenna (Red – Elevation, black - Azimuthal)

4. MIMO antenna parameters

Another important parameter to measure the mutual coupling between antenna elements is envelope correlation coefficient (ECC). ECC value is less than 0.015 (practically less than 0.5) over the operating band 4.12 – 27.78GHz, which indicates the low mutual coupling between antenna elements. ECC value is evaluated using S – parameters, given in [25-26]. Figure 12 shows the ECC between the individual antenna elements – 1&2, 1&3 and 1&4 respectively. Other parameter to measure the amount of power transmission without loss is diversity gain (DG). Diversity gain is evaluated from ECC, given in [25-26]. Lowest value of ECC indicates the high value of diversity gain. This value is closure to 10dB which is approximately equals to ideal value across the operating band. Figure 13 shows the diversity gain characteristics of the proposed MIMO antenna design. Total active reflection coefficient (TARC) measures the complete description of the proposed MIMO antenna potentiality. Ideal value of TARC is less than 0dB. From figure 14, it is observed that TARC is less than -8dB for the obtained bandwidth within the acceptable limits. Figure 15 shows the channel capacity loss (CCL) plot of the proposed MIMO antenna with isolating element. CCL measures the loss in channel capacity due to correlation between the MIMO antennas. Ideal value of CCL is less than 0.4bits/sec/Hz. From figure 15, it is observed that CCL is lower than 0.3bits/sec/Hz, which is within the limits. Mean effective gain (MEG) of individual elements in the proposed MIMO antenna characteristics are represented in figure 16. It is observed that practically proposed MIMO antenna achieves MEG within -4.5 to -7dB within the ideal acceptable range -3dB to -12dB.

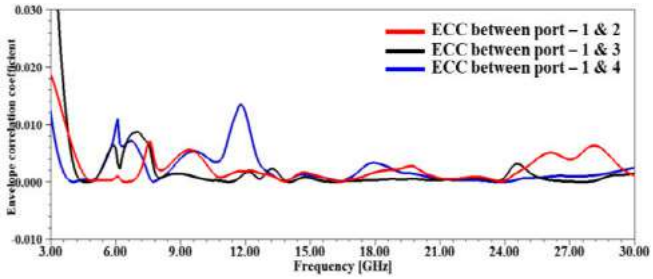

Figure 12. ECC vs frequency

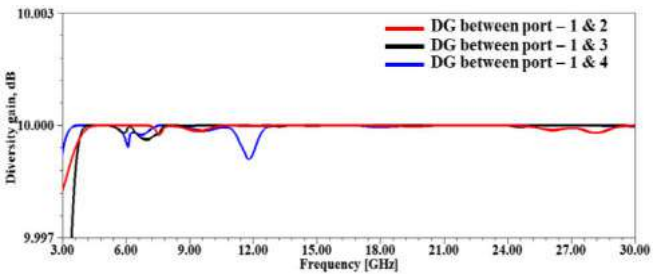

Figure 13. Diversity gain vs frequency

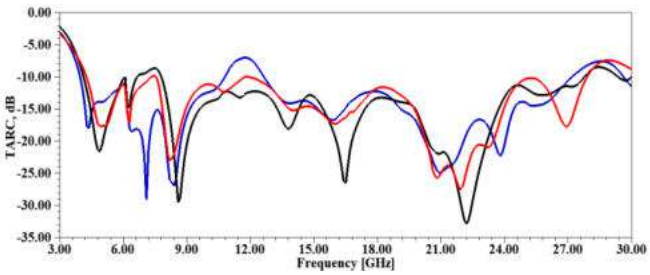

Figure 14. TARC vs frequency

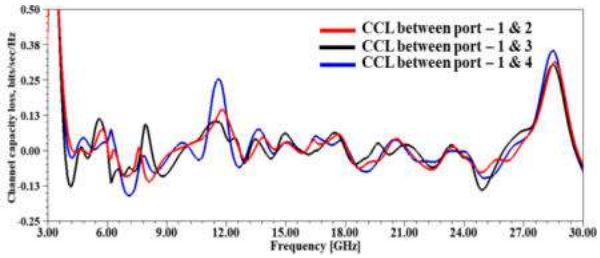

Figure 15. CCL vs frequency

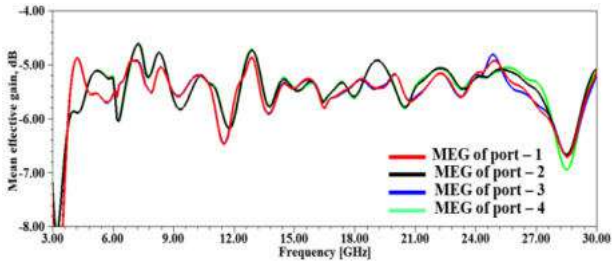

Figure 16. MEG vs frequency

5. Comparison of the proposed antenna

Simulation characteristics of the proposed MIMO antenna with some existed antennas [6-21] is shown in table 3. In this table proposed antenna has several advantages compared to the existing models. **i) Miniaturization** – smaller in size, 43mm x 43mm **ii) Better impedance** – Covers frequency band from 4.12 to 27.78GHz at S_{11} < -10dB **iii) Fractional bandwidth** – Proposed design obtains 148.33% **iv) Good isolation** – Proposed antenna has isolation between elements is less than -20dB **v) Peak gain** – It obtains peak gain of 6.89dBi with directional characteristics **vi) High radiation efficiency** – Suggested MIMO antenna with isolating element has higher efficiency 96%, which signifies that proposed design has efficient transmission / receiving capability **vii) ECC** – Mutual coupling between antenna elements is improved and its isolation is less than 0.015.

Table 3. Performance comparison of proposed MIMO antenna with other existed antennas

Ref.	Size, mm^2	f_L - f_H, GHz	IBW, GHz	FBW, %	Isolation, dB	Gain, dB	η, %	ECC
[6]	58.6 x 46	3.1 – 10.6	7.5	109.48	< -13	2.1-5.4	NR	< 0.02
[7]	40 x 68	3.2 – 10.6	7.4	107.24	< -15	< 2.5	70 - 85	NR
[8]	75 x 145	3.3 – 3.6 & 4.8 – 5.0	0. 3 & 0.2	8.69 & 4.08	< -10	NR	60-85	< 0.15
[9]	50 x 50	2.76 – 10.75	7.99	118.28	< -15	5.5	68	< 0.025
[10]	130 x 74	3.3 – 3.6 & 4.8 – 5.0	0.3 & 0.2	8.69 & 4.08	< -12	NR	> 50	< 0.1
[11]	60 x 60	2.73 – 10.68	7.95	118.56	< -15	7	NR	NR
[12]	50 x 40	2.5– 11	8.5	125.92	< -15	2.11	69.2	< 0.02
[13]	48 x 48	3 – 11	8	114.28	< -15	4	80-90	NR
[14]	50 x 80	4.183 – 6.584	2.501	46.02	< -17	6	80	< 0.056
[15]	48 x 48	2.5 – 12	9.5	131.03	< -15	< 3	NR	< 0.005
[16]	50 x 30	2.5 – 14.5	12	141.17	< -20	4.1	NR	< 0.04
[17]	45 x 45	2 – 10.6	8.6	136.5	< -17	3	NR	< 0.1
[18]	85 x 50	2 – 9.5	7.5	130.43	< -20	1.5	70	< 0.03
[19]	90 x59	3.34-14.96	11.62	126.99	NR	5	66	NR
[20]	50 x 48	3.5-10.6	7.1	100.70	NR	4.7	73	NR
[21]	60 x 50	2.05-10.86	8.81	136.48	NR	5.03	NR	NR
Proposed	43 x 43	4.12 – 27.78	23.66	148.33	< -20	6.89	96	< 0.015

6. Conclusion

Using HFSS simulation program, a new design of super wide band (SWB) planar monopole antenna loaded with Aspen shape and partial ground plane has been designed for serving SWB wireless communication systems. The antenna operates over the frequency range from 4.57GHz to 28.60GHz and its size is 20mm x 23mm x 0.787mm. A compact 4-port MIMO antenna with SWB is proposed to cover industrial – scientific – medical (ISM), satellite, radar, military and microwave applications. The proposed MIMO antenna covers impedance bandwidth (IBW) of 23.66GHz at -10dB reflection coefficient from 4.12 – 27.78GHz. The proposed antenna has bandwidth ratio (BR) of 6.74 and fractional impedance bandwidth (FBW) of 148.33%. Within this operating band, the mutual coupling / insertion loss / isolation between these antennas is purely greater than -20dB. All other parameters like mutual coupling, ECC, DG, TARC and CCL are depicted in results and discussed. During this entire band, the radiation pattern maintains stable characteristics and it has good diversity performance. Its planar footprint and SWB features make it a good candidate for wireless devices.

References

[1] Kishk, Ahmed. (2009). Fundamentals of Antennas. Antennas for Base Stations in Wireless Communications.

[2] Kurniawan, A., & Mukhlishin, S. (2013). Wideband Antenna Design and Fabrication for Modern Wireless Communications Systems. Procedia Technology, 11, 348–353.

[3] Saeidi, T., Ismail, I., Wen, W. P., Alhawari, A. R. H., & Mohammadi, A. (2019). Ultra-Wideband Antennas for Wireless Communication Applications. International Journal of Antennas and Propagation, 2019, 1–25.

[4] Dey, S., & Karmakar, N. C. (2020). Design of novel super wide band antenna close to the fundamental dimension limit theory. Scientific Reports, 10(1).

[5] Shiddanagouda, F. ., Vani, R. ., & Hunagund, P. V. (2018). Design and Analysis of Printed MIMO Antenna for Next Generation Wireless Applications. 2018 IEEE Indian Conference on Antennas and Propogation (InCAP).

[6] Mondal, S., Mandal, K., & Sarkar, P. P. (2018). Design of MIMO Antenna for Ultra-Wideband Applications. IETE Journal of Research, 64(4), 497–502.

[7] Najam, A. I., Duroc, Y., & Tedjni, S. (2011). UWB-MIMO ANTENNA WITH NOVEL STUB STRUCTURE. Progress In Electromagnetics Research C, 19, 245–257.

[8] Yan, K., Yang, P., Yang, F., Zeng, L. ., & Huang, S. (2018). Eight-Antenna Array in the 5G Smartphone for the Dual-Band MIMO System. 2018 IEEE International Symposium on Antennas and Propagation & USNC/URSI National Radio Science Meeting.

[9] Chacko, B. P., Denidni, T. A., & Augustin, G. (2013). Uniplanar polarisation diversity antenna for ultra-wideband systems. IET Microwaves, Antennas & Propagation, 7(10), 851–857. doi:10.1049/iet-map.2012.0732

[10] Zhang, W., Weng, Z., & Wang, L. (2018). Design of a dual-band MIMO antenna for 5G smartphone application. 2018 International Workshop on Antenna Technology (iWAT).

[11] Kiem, N. K., Phuong, H. N. B., & Chien, D. N. (2014). Design of Compact 4 × 4 UWB-MIMO Antenna with WLAN Band Rejection. International Journal of Antennas and Propagation, 2014, 1–11.

[12] Lin, G.-S., Sung, C.-H., Chen, J.-L., Chen, L.-S., & Houng, M.-P. (2017). Isolation Improvement in UWB MIMO Antenna System Using Carbon Black Film. IEEE Antennas and Wireless Propagation Letters, 16, 222–225.

[13] Mao, C.-X., & Chu, Q.-X. (2014). Compact Coradiator UWB-MIMO Antenna With Dual Polarization. IEEE Transactions on Antennas and Propagation, 62(9), 4474–4480.

[14] Jehangir, S. S., & Sharawi, M. S. (2017). A Miniaturized UWB Biplanar Yagi-Like MIMO Antenna System. IEEE Antennas and Wireless Propagation Letters, 16, 2320–2323.

[15] Peng Gao, Shuang He, Xubo Wei, Ziqiang Xu, Ning Wang, & Yi Zheng. (2014). Compact Printed UWB Diversity Slot Antenna With 5.5-GHz Band-Notched Characteristics. IEEE Antennas and Wireless Propagation Letters, 13, 376–379.

[16] Iqbal, A., Saraereh, O. A., Ahmad, A. W., & Bashir, S. (2018). Mutual Coupling Reduction Using F-Shaped Stubs in UWB-MIMO Antenna. IEEE Access, 6, 2755–2759.

[17] Tripathi, S., Mohan, A., & Yadav, S. (2015). A Compact Koch Fractal UWB MIMO Antenna With WLAN Band-Rejection. IEEE Antennas and Wireless Propagation Letters, 14, 1565–1568.

[18] Zhao, X., Yeo, S. P., & Ong, L. C. (2018). Planar UWB MIMO Antenna With Pattern Diversity and Isolation Improvement for Mobile Platform Based on the Theory of Characteristic Modes. IEEE Transactions on Antennas and Propagation, 66(1), 420–425.

[19] Pandey, S. K., Pandey, G. P., & Sarun, P. M. (2017). Fractal Based Triple Band High Gain Monopole Antenna. Frequenz, 71(11-12).

[20] Omar, A. A., Abu Safia, O., & Nedil, M. (2017). UWB coplanar waveguide-fed coplanar strips rectangular spiral antenna. International Journal of RF and Microwave Computer-Aided Engineering, 27(7), e21115.

[21] Srivastava, K., Kumar, A., Kanaujia, B. K., Dwari, S., & Kumar, S. (2018). Multiband integrated wideband antenna for bluetooth/WLAN applications. AEU - International Journal of Electronics and Communications, 89, 77–84.

[22] Okas, P., Sharma, A., Das, G., & Gangwar, R. K. (2018). Elliptical slot loaded partially segmented circular monopole antenna for super wideband application. AEU - International Journal of Electronics and Communications, 88, 63–69.

[23] Balanis CA (1992) Antenna theory and design, 3 edn.

[24] C. M. Krishna, M. Ravi and B. E. Raju, "Investigation of Hexagonal Antenna with Ring Resonators," 2020 4th International Conference on Electronics, Communication and Aerospace Technology (ICECA), 2020, pp. 569-574, doi: 10.1109/ICECA49313.2020.9297482.

[25] C. M. Krishna, M. Mamatha and J. P. Kumar, "Mickey Mouse Modeled MIMO Antenna for Extended UWB Applications," 2020 Fourth International Conference on Computing Methodologies and Communication (ICCMC), 2020, pp. 522-527, doi: 10.1109/ICCMC48092.2020.ICCMC-00097.

[26] Kommanaboyina V. Babu, Sudipta Das, Soufian Lakrit, Shobhit K. Patel, Boddapati T. P. Madhav, and Hicham Medkour, “Compact Dual-Band Printed MIMO Antenna with Very Low Mutual Coupling for WLAN, Wi-MAX, Sub-6GHz 5G and X-Band Satellite Communication Applications”, Progress In Electromagnetics Research C, Vol. 117, 99-114, 2021

A New Microstrip Sierpinski Carpet Antenna Using a Circular Pattern With Improved Performance

Abdelhakim Moutaouakil[1], Younes Jabrane[1], Abdelati Reha[2], Abdelaziz Koumina[3]

[1] Modelisation of Complex Systems Laboratory (LMSC), Cadi Ayyad University, Marrakech, Morocco
[2] Laboratory of Innovation in Management and Engineering for the Enterprise, ISGA, Marrakech, Morocco
[3] Nanostructures Physics Laboratory, ENS, Cadi Ayyad University Marrakech, Morocco
*corresponding author, E-mail: moutaouakilabdo@gmail.com

Abstract

In this work, we present the two first iterations design of the Sierpinski carpet fractal antenna by using a circular pattern. The proposed antenna is printed on FR4 substrate with a dielectric constant of 4.4. At the second iteration, the studied antenna has a multiband behavior with four resonant frequencies: 3.92, 4.89, 6.61 and 7.22 GHz with a good impedance matching. The simulated results performed by CADFEKO a Method of Moments (MoM) based Solver and measurement using Vector Network Analyzer (VNA) Anritsu MS2026C are in good agreement.

1. Introduction

For the wireless communication system, an antenna is one of the most critical components. A good design of the antenna can thus improve overall system performance. As the demand increases day by day to multi-band antennas, Thus, a major issue in multi-band communications concerns small or very small terminal dimensions, intended for short radio ranges and in association with sensors or networks for information transfer in a domestic, multimedia or professional context [1-3]. Low consumption, ease of integration, and above all cost are essential aspects that are not very compatible with performance, these antennas also have wide applications in long range of wireless systems.

Fractal Antennas Elements are currently beneficial to antenna designers & researchers. By applying fractals to antenna elements. The concept of fractal geometry was introduced for the first time by Mandelbrot in [4].

In this paper, we propose a new microstrip Sierpinski carpet antenna using a circular pattern.

2. The antenna geometry

Applying fractal theory for antenna design is a clever method of improving antenna performance thanks to the property of self-similarity that characterizes fractal geometries [5-7]. As shown in fig 1, the studied antenna is a microstrip patch antenna designed with the modification of the traditional fractal structure of Sierpinski Carpet by replacing the rectangular slots with circular ones.

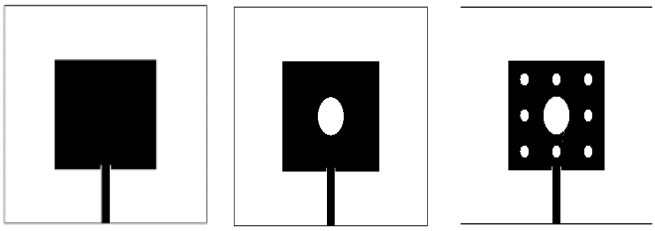

Iteration 0 Iteration 1 Iteration 2

Figure 1: Iteration steps to get Carpet geometry

to excite the patch. Here, the feed is applied through a microstrip inset feed.

The table below gives the corresponding values of design parameters.

Table 1: Design Parameters & Corresponding Values

Design Parameters	Value (mm)
Length of substrate	56.02
Width of substrate	72.44
Length of patch	28.01
Width of patch	36.22
Thickness of the substrate	1.6
Width of supply line	2.8
Length of inset point	1

3. Simulation Results using FEKO suite 5.5

The following figures represent a comparison of the reflection coefficient versus frequencies for different iteration numbers.

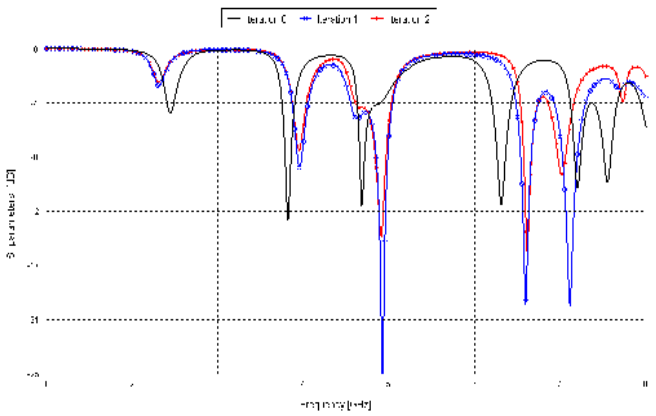

Figure 2: Simulated reflection coefficient (S11) versus frequencies for tree first iterations.

It is worth noting from the simulation that the resonance frequencies become lower when the iteration number increases. Also, for the higher frequencies, the bandwidth becomes larger.

Figure 3 shows the 3D gain pattern of the Simulated antenna for the resonance frequencies for each iteration.

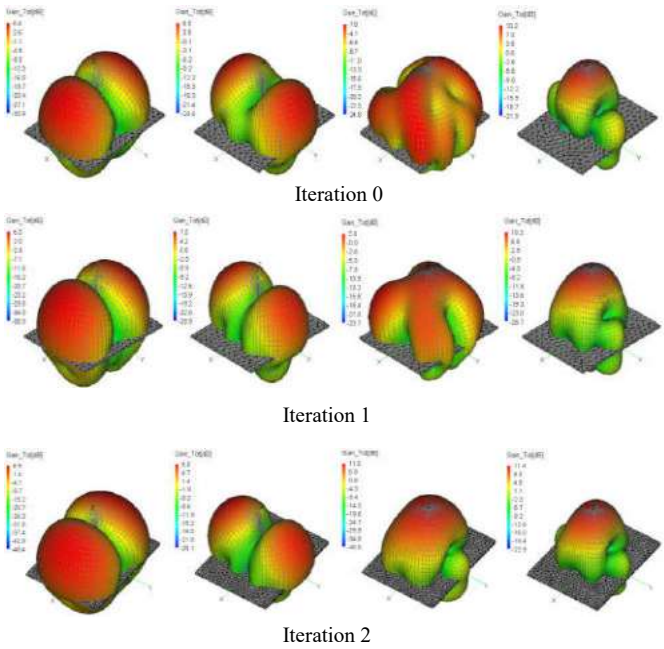

Figure 3: 3D Gain pattern of the Simulated antenna

According to the simulations, we see that the gains for all the resonance frequencies increase from one iteration to another, for example, for the first frequency F1 at iteration 0 we have the same gain 6.4dB and for the second iteration it is 6.9dB, for the third frequency the gain go from -1.8dB to 11dB at iteration 2, and for the fourth frequency F4, the gain equals 10.2dB at iteration 0 and 11.4dB at iteration 2.

.

4. Experimental results

The antenna is than fabricated and tested using Vector Network Analyzer (VNA Master, Anritsu MS2026C) to validate the simulated results. We confirm with measurements that resonance frequencies become lower when the iteration number increases. Also, for the higher frequencies, the bandwidth becomes bigger.

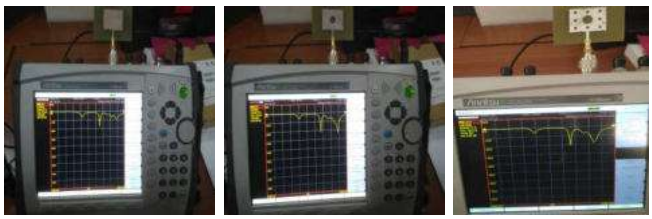

Figure 4: S_{11} Measurement by VNA for the tree antennas

5. Conclusions

In this paper, the setup of slots on the patch antenna using the Sierpinski Carpet Fractal structure allows the miniaturization of the antenna since the resonant frequency becomes smaller when increasing the number of iteration and the gain becomes higher. The simulated results performed by CADFEKO a MoM based Solver and measurement using Vector Network Analyzer (VNA) Anritsu MS2026C are in good agreement. The proposed antenna will be a good solution for many wireless telecommunications systems and especially for the embedded systems where easy integration, miniaturization, multi-band and broadband are the essential requirements.

References

[1] A. Reha, A. El Amri, O. Benhmammouch, A. Oulad said, A. El ouadih and M. Bouchouirbat, CPW-fed slotted CANTOR Set fractal antenna for WiMAX and WLAN applications, *International Journal of Microwave and Wireless Technologies*, page 1 of 7, 2016.

[2] J. Jayasinghe, A. Andújar, J. Anguera, On the properties of Sierpinski gasket fractal microstrip antennas, *Microw Opt Technol Lett,* 61: 772– 776, 2019.

[3] A. Moutaouakil, Y. Jabrane, A. Reha and A. Koumina, Effect Study of a Ring on the performances of a patch antenna, *2019 International Conference of Computer Science and Renewable Energies (ICCSRE),* Agadir, Morocco, 2019, pp. 1-3.

[4] B. B. Mandelbrot, The Fractal Geometry of Nature, San Francisco, 1983, 152–180.

[5] A. Constantine Balanis, Antenna Theory Analysis and Design, *John Wiley and Sons Inc*, 1997.

[6] W.L. Chen and G.M. Wang. Small size edge-fed Sierpinski carpet microstrip patch antenna, *PIERS C*, Vol.3, 2008.

[7] S. Gupta, P. Kshirsagar, and B. Mukherjee, Sierpinski fractal inspired inverted pyramidal DRA for wide band applications, *Electromagnetics, Taylor & Francis*, Vol. 38, No. 2, 103–112, 2018.

Engineering Highly Directive Optical Waveguide Antennas

Henna Farheen[1,*], Lok-Yee Yan[2], Till Leuteritz[2], Siqi Qiao[2], Florian Spreyer[3], Christian Schlickriede[3], Viktor Quiring[3], Christof Eigner[3], Thomas Zentgraf[3], Stefan Linden[2], Jens Förstner[1] and Viktor Myroshnychenko[1]

[1]Theoretical Electrical Engineering, Paderborn University, Paderborn, Germany
[2]Physikalisches Institut, Universität Bonn, Bonn, Germany
[3]Department of Physics, Paderborn University, Paderborn, Germany
*corresponding author, E-mail: henna18@campus.uni-paderborn.de

Abstract

We show the numerical and experimental realization of broadband optical traveling-wave antennas made from low-loss dielectric materials which exhibit highly directive patterns. The high directivity is a result of the interplay between two dominant TE- and leaky-modes present in the antenna director. These antennas possess near unity radiation efficiency at the operational wavelength of 780 nm, maintaining a broad bandwidth. We envision that our all-dielectric approach demonstrates a new class of antennas that are excellent candidates for optical-communication and sensing.

1. Introduction

Optical antennas provide a promising way to efficiently convert propagating light waves into localized modes and vice versa. The directed emission from these antennas can be used for a multitude of applications, in particular, on-chip communication can utilize different functionalities offered by antennas such as high directivity and front-to-back ratio, good radiation efficiency, low side lobe level, broadband and tunable capabilities, and a compact design [1]. These qualities can be pursued using dielectric structures, which furnish us with reduced dissipative losses and fabrication tolerances in comparison to the metals in the optical regime [2]. In the same context, it has also been shown recently that optical traveling wave antennas which support guided modes in addition to leaky modes exhibit excellent directional characteristics and a broadband nature [3]. The electromagnetic response and overall functionality of these antennas depend on the frequency of operation, structure geometry, material constituting the antennas and footprint of the structure. These enable the control over the modes excited and thus the angular radiation patterns, therefore providing a need for a meticulous designing and optimization strategy [4].

2. Results and Discussion

In this work, we report on a comprehensive numerical and experimental analysis of traveling-wave antennas made of different low-loss dielectric materials like hafnium dioxide (HfO_2), tantalum-pentoxide (Ta_2O_5) and Silicon (Si), furnishing a highly directive emission. Our dielectric antennas consist of two elements, namely, the reflector and director that are placed over a glass substrate. In particular, three different types of directors comprising the rectangular-, horn-, and tip-shaped geometries were designed and optimized. We utilize full-wave numerical simulations, which employ the particle swarm optimization in conjunction with the trust-region algorithm to realize robust antennas with high directive gains. The maximum directive gain (directivity D) is used as a cost function and defined as

$$D = \max D(\theta, \varphi) = \frac{4\pi U(\theta, \varphi)}{\int_0^{\pi} \int_0^{2\pi} U(\theta, \varphi) \sin(\theta) d\theta d\varphi}, \quad (1)$$

where $D(\theta, \phi)$ and $U(\theta, \phi)$ are, respectively, the directive gain and angular radiation intensity of the antenna in a direction defined by the polar angle θ, measured with respect to the optical axis (z-axis) and the azimuthal angle ϕ, measured with respect to the antenna axis (x-axis).

To give a deeper insight into our work, the schematic representation of the numerical setup and orientation of one of the antennas (rectangular-antenna) with respect to the xyz coordinates is illustrated in Fig. 1a, which also highlights the parameters used in the optimization process. Fig. 1c shows the calculated linear directive gain with tightly focused main lobe pointing at a polar angle of $\theta = 69°$ and azimuthal angle $\phi = 0°$ with a high directivity of 63.1. Our study reveals that the directivity and main lobe emission are majorly governed by two guided transverse electric modes that radiate from the end facet of the director. To validate our results, we also fabricated our optimized antenna using a two-step electron-beam lithography, whose scanning electron micrograph is depicted in Fig. 1b. The red box in the image indicates the area of quantum dot (QD) deposition. The measured far field intensity distribution in Fig. 1d is in good qualitative agreement with the numerical calculations. However, some discrepancies are observed in higher polar angles which can be attributed to the displacement of the quantum dots from the optimal position as well as the limited collection angle of the setup. Additionally, the ring-like feature at around $\theta = 41°$ stems from uncoupled QDs emitting directly into the substrate in all

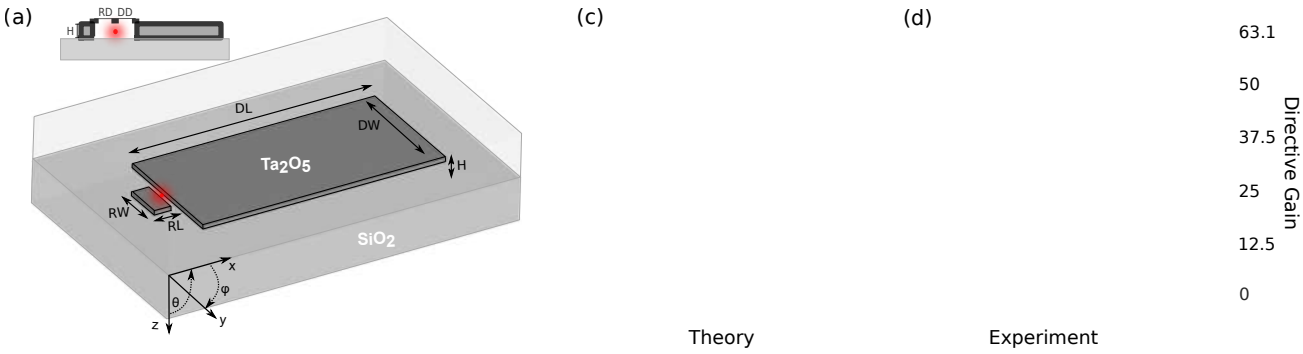

Figure 1: (a) Schematic representation of the Ta_2O_5 rectangular-antenna, highlighting the parameters used in the optimization. The antenna is excited by a dipole source emitting at 780 nm (red spot). (b) Scanning electron micrograph of the optimized antenna design with the red square marking the region of deposited QDs. (c) Calculated angular linear directive gain distributions of the antenna exhibiting an in-plane directivity of $D = 63.1$ at $\theta = 69°$. (d) Measured far-field intensity normalized to theoretical maximum.

azimuthal angles. A similar nature with a further enhanced performance is observed in the other antennas investigated in the scope of this work. These antennas are not just ultra directive, but they also showcase high efficiency and a wide operating frequency range while being robust with respect to fabrication tolerances. Furthermore, they also offer an opportunity to tailor the directivity and main lobe angle [4].

3. Conclusions

We present a series of optimized guided-wave optical antennas exhibiting high directivity. The antennas consist of a dielectric reflector and a director lying on a glass substrate, and a dipole emitter, placed in the feed gap between them serves as the source of excitation. In particular, we analyzed antennas with rectangular-, horn- and tip-shaped directors made of different low-loss dielectric materials. Our analysis of the optimized antennas reveals that their light emission is predominately governed by two TE guided modes in the director and show high linear directivity over a wide wavelength range. Our findings demonstrate the uniqueness and robustness of these optical antennas, which renders them excellent candidates for sensing applications and optical interconnects.

Acknowledgement

H.F., T.Z., J.F., and V.M. gratefully acknowledge financial support from the Deutsche Forschungsgemeinschaft (DFG) via TRR142 project C05. L.Y., T.L., and S.L. acknowledge financial support by the German Federal Ministry of Education and Research through the funding program Photonics Research Germany (Project 13N14150) and by the Deutsche Forschungsgemeinschaft, Cluster of Excellence ML4Q (EXC 2004/1–390534769). T.Z. acknowledges financial support by the European Research Council (ERC) under the European Union's Horizon 2020 research and innovation program (grant agreement No. 724306). The authors gratefully acknowledge the computing time support provided by the Paderborn Center for Parallel Computing (PC^2).

References

[1] N. Li, Y. Lai, S. H. Lam, H. Bai, L. Shao, J. Wang, Directional control of light with nanoantennas, *Advanced Optical Materials* 9(1): 2001081, 2021.

[2] P. Manuel, A. Hildebrandt, C. Schlickriede, K. Gharib, T. Zentgraf, J. Förstner, S. Linden, Directional emission from dielectric leaky-wave nanoantennas, *Nano Letters* 17(7): 4178–4183, 2017.

[3] T. Leuteritz, H. Farheen, S. Qiao, F. Spreyer, C. Schlickriede, T. Zentgraf, V. Myroshnychenko, J. Förstner, S. Linden, Dielectric travelling wave antennas for directional light emission, *Optics Express* 29(10): 14694–14704, 2021.

[4] H. Farheen, T. Leuteritz, S. Linden, V. Myroshnychenko, J. Förstner, Optimization of optical waveguide antennas for directive emission of light, *J. Opt. Soc. Am. B* 39(1): 83–91, 2022.

Wideband Design and Optimization of Reflectarray Antennas

Manuel Arrebola, Daniel R. Prado and Marcos R. Pino

Group of Signal Theory and Communications, Universidad de Oviedo, Gijón, Spain.
Email: {arrebola, drprado, mpino}@uniovi.es

Abstract

This paper describes a technique for the design and optimization of wideband reflectarrays based on the generalized intersection approach and a direct layout optimization using a method of moments based on local periodicity. Results for two very large dual-linear reflectarrays for direct-to-home applications are provided and discussed. The first is a reflectarray working in a 15% bandwidth with European coverage. The second antenna provides coverage to South America in two frequency bands with very tight requirements.

1. Introduction

Reflectarray antennas suffer from an inherent narrow bandwidth due the differential space delay with regard to a parabolic surface and the resonant nature of the reflecting elements [1, 2]. There are several solutions to overcome these limitations, including the use of broadband reflectarray elements with several resonances, sub-wavelength periodicity, faceted or curved reflectarrays, etc.

In this work we propose a wideband design technique based on the use of a multi-resonant unit cell with up to eight Degrees of Freedom (DoF) [3] and a optimization algorithm based on the generalized intersection approach [4] to compensate for the differential space delay at several frequencies. In addition, the process is divided in several stages to facilitate convergence towards a wideband performance. Both copolar and crosspolar requirements are taken into account. This technique has been applied to two large reflectarray antennas for space applications, improving the results of others works in the literature.

2. Wideband Design Procedure

Figure 1 shows a flowchart of the proposed design methodology. First, a Phase-Only Synthesis (POS) is carried out at central frequency to obtain an initial narrowband layout. Next, a wideband optimization is carried out. In order to facilitate convergence, the initial stages only deal with a copolar synthesis, starting with a limited number of degrees of freedom with are progressively increased. Later on, cross-polarization requirement may be included in the process as well.

The main idea behind this process is to solve increasingly difficult problems by first dealing with a single frequency design, then only with copolar requirements in a wideband and finally including both copolar and crosspolar

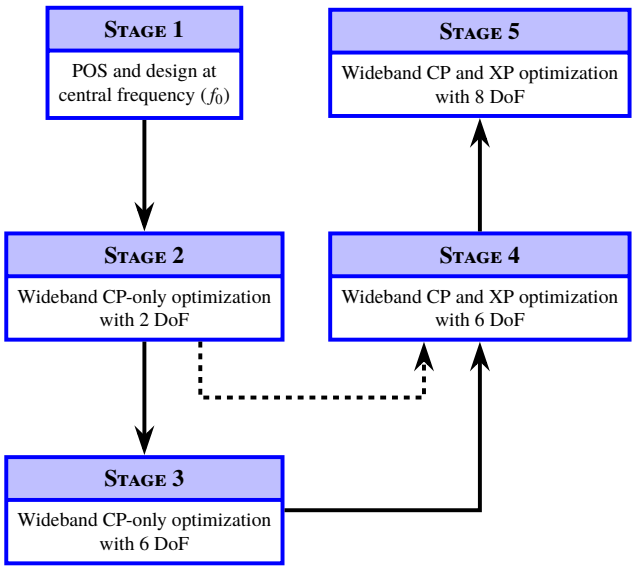

Figure 1: Flowchart of the wideband design procedure based on the generalized intersection approach. Stages three and five may be optional.

specifications. At the same time, by considering only a limited number of DoF per reflectarray element, the number of local minima is reduced, improving convergence [4]. However, to fully exploit the capabilities of the multi-resonant unit cell, the number of DoF is increased in successive stages to improve the performance of the optimized antenna.

This procedure has been applied to two large reflectarray for space applications, in particular for direct-to-home broadcast from satellites in geostationary orbit.

3. Reflectarray with European Coverage

For the first example, the same antenna as in [5] is considered here. It is a 1 meter reflectarray comprised of 5180 elements working in a 15% frequency band (10.95 GHz – 12.75 GHz). The goal is to achieve a minimum copolar gain of 28 dBi in the coverage zone and a minimum crosspolar discrimination (XPD_{min}) of 30 dB, both in dual-linear polarization in the 15% frequency band.

Table 1 shows the results of this wideband design. It can be seen how both the minimum copolar gain and XPD_{min} significantly improve after following the wideband design procedure described in Section II. In fact, compared to [5],

Table 1: Wideband performance of the reflectarray with European coverage for both linear polarizations in a 15% relative bandwidth, showing the minimum copolar gain (CP_{min}) and minimum crosspolar discrimination (XPD_{min}).

		10.95 GHz		11.40 GHz		11.85 GHz		12.30 GHz		12.75 GHz	
		X	Y	X	Y	X	Y	X	Y	X	Y
CP_{min} (in dBi)	**Initial layout**	25.99	25.94	28.79	28.59	30.11	30.06	26.03	28.21	15.15	23.69
	Optimized layout	28.23	28.32	28.77	28.83	28.48	28.83	28.56	29.09	28.04	29.27
XPD_{min} (in dB)	**Initial layout**	28.32	26.96	31.08	30.16	30.74	32.02	29.68	28.29	22.76	22.14
	Optimized layout	33.86	32.13	37.16	36.69	39.65	39.58	41.18	40.23	38.98	39.43

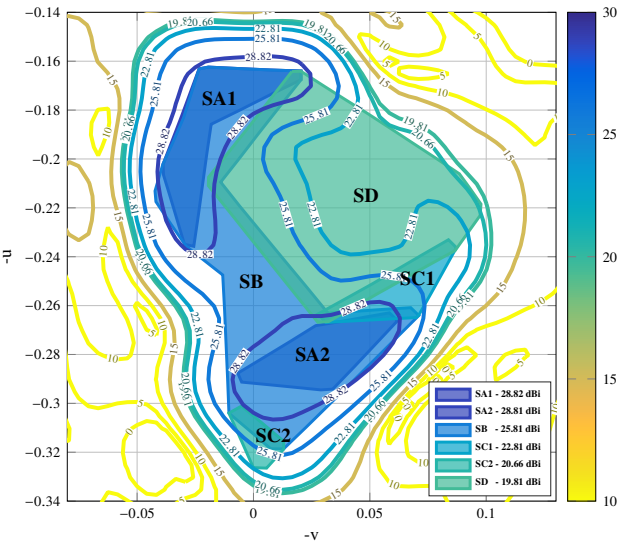

Figure 2: Copolar pattern for Y polarization at 11.70 GHz for the large reflectarray with South American coverage.

now a better cross-polarization is achieved in a wider band (11.3% vs. 15%), while using a simpler unit cell (three layers vs. two layers).

4. Dual-Band Reflectarray with South American Coverage

For the second example, the same reflectarray and requirements as in [6] is considered here. The coverage corresponds to the PAN_S mission of the Amazonas satellite, providing coverage to South America. The lower band (11.70 GHz – 12.20 GHz) is used for transmission while the upper band (13.75 GHz – 14.25 GHz) is used for reception.

Figure 2 shows the copolar pattern for Y polarization at 11.70 GHz with the South American coverage. All the requirements are met in both bands for dual-linear polarization with a loss budget of at least 0.59 dB. More results will be shown in the final paper and presentation.

5. Conclusions

A methodology to design wideband reflectarrays with improved copolar and crosspolar requirements has been presented. It is based on the generalized intersection approach and the use of a multi-resonant unit cell with several degrees of freedom. It is divided in several stages to facilitate convergence towards a wideband performance. It has been applied to the design of two large reflectarray antennas for space applications, obtaining excellent results.

Acknowledgement

This work was supported in part by the Ministerio de Ciencia, Innovación y Universidades under project IJC2018-035696-I; by the Ministerio de Ciencia e Innovación and the Agencia Estatal de Investigación within project ENHANCE-5G (PID2020-114172RB-C21 / AEI / 10.13039/501100011033); by Gobierno del Principado de Asturias under project AYUD/2021/51706.

References

[1] J. Huang and J. A. Encinar, *Reflectarray Antennas*. Hoboken, NJ, USA: John Wiley & Sons, 2008.

[2] D. M. Pozar, "Wideband reflectarrays using artificial impedance surfaces," *Electron. Lett.*, vol. 43, no. 3, pp. 148–149, Feb. 2007.

[3] R. Florencio, J. A. Encinar, R. R. Boix, V. Losada, and G. Toso, "Reflectarray antennas for dual polarization and broadband telecom satellite applications," *IEEE Trans. Antennas Propag.*, vol. 63, no. 4, pp. 1234–1246, Apr. 2015.

[4] O. M. Bucci, G. D'Elia, G. Mazzarella, and G. Panariello, "Antenna pattern synthesis: a new general approach," *Proc. IEEE*, vol. 82, no. 3, pp. 358–371, Mar. 1994.

[5] J. A. Encinar, M. Arrebola, M. Dejus, and C. Jouve, "Design of a 1-metre reflectarray for DBS application with 15% bandwidth," in *First European Conference on Antennas and Propagation (EuCAP)*, Nice, France, Nov. 6–10, 2006, pp. 1–5.

[6] J. A. Encinar, R. Florencio, M. Arrebola, M. A. Salas-Natera, M. Barba, J. E. Page, R. R. Boix, and G. Toso, "Dual-polarization reflectarray in Ku-band based on two layers of dipole arrays for a transmit-receive satellite antenna with South American coverage," *Int. J. Microw. Wirel. Technol.*, vol. 10, no. 2, pp. 149–159, 2018.

Dielectric resonator antennas, lens antennas and radomes

Design and Fabrication of ceramic-based antennas

Wenzhong Lu[1,2 *] , Xiaochuan Wang[1,2] , Yihui Lou[1,2]

[1] School of Optical and Electronic Information, Huazhong University of Science and Technology, Wuhan 430074, P. R. China

[2] Key Lab of Functional Materials for Electronic Information (B), Ministry of Education, Wuhan 430074, P. R. China

* email: lwz@hust.edu.cn

With the rapid development of modern wireless communication systems, ceramic antennas have received increasing attention due to their miniaturization, high durability, high power capacity and high sensitivity. For a long time, researchers are focusing on developing microwave dielectric ceramics with a high-quality factor, high permittivity and near zero temperature coefficient of resonate frequency for the use of antenna. Meanwhile, several advanced fabrication techniques such as low-temperature co-fired ceramic (LTCC) and 3D printing are emerging to satisfy the antenna fabrication demands, which help people to overcome the limitation of traditional manufacturing processes (for example, dry-pressing method) on ceramic antennas fabrication with complex structure.

LTCC technology, which is a multilayered fabrication method, has been widely applied in the field of ceramics antenna processing. Achieving blind via, buried via, through via, air cavity, and other complex structures by using LTCC technology is easier and more precise than using the traditional antenna preparation techniques, such as printed circuit board and metal machining technologies. In addition, the integration of antenna and other components in a small package is easily realized due to the high dielectric constant substrate and multilayer manufacturing process of LTCC technology.

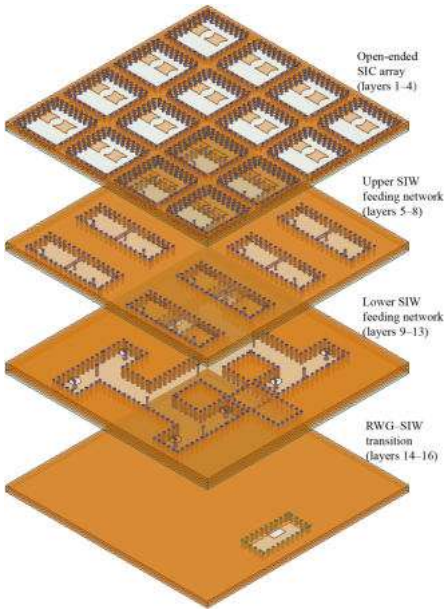

Fig. 1. Topology of the proposed antenna array.

Fig.1 shows a 4 × 4 high-gain substrate integrated cavity (SIC) antenna array using multilayered LTCC technology we proposed and designed for W-band applications. The TM_{211} mode of the SIC is utilized. Two parasitic patches are introduced on the top surface of the SIC to adjust the aperture electromagnetic field distribution of the TM_{211} mode in the cavity for obtaining a high-gain broadside radiation pattern. A bow tie shape is adopted for the parasitic patches to improve the matching

characteristic of the SIC. The SIC is modified to a stepped flared shape to improve the gain characteristic of the antenna element. Subsequently, a two-layer low-loss substrate integrated waveguide feeding network is designed for the 4 × 4 antenna array based on the proposed high-gain SIC radiating element. The proposed antenna array showed a wide measured bandwidth of 17.48% from 81.45 GHz to 97.05 GHz at |S11| < −10 dB and a measured gain of up to 20.3 dBi.

In recent time, as an emerging manufacturing technology, 3D printing, also known as additive manufacturing technology, shows great potential for the manufacturing of low-cost, low-weight complex structural components. It can create complex 3D structures such as photonic crystals which are not possible with traditional fabrication process. In addition, 3D printing can easily realize the integration of antenna and other components due to continuous forming capability, and it ensures antenna performance consistent with design for high manufacturing precision.

As shown in Fig.2, we presented a novel method for realizing flat Luneburg lenses for antenna applications. The method we described includes ceramic Stereolithography, metamaterial structure and optical coordinate transformation. We experimentally validate our design methodology by fabricating and characterizing a flat Luneburg lenses whose operation frequency is at Ku-band (12–18GHz) with antenna gains of 18dBi. The results demonstrate good agreement with electromagnetic simulations, and it shows the ability of passively beam steering over whole operating frequency.

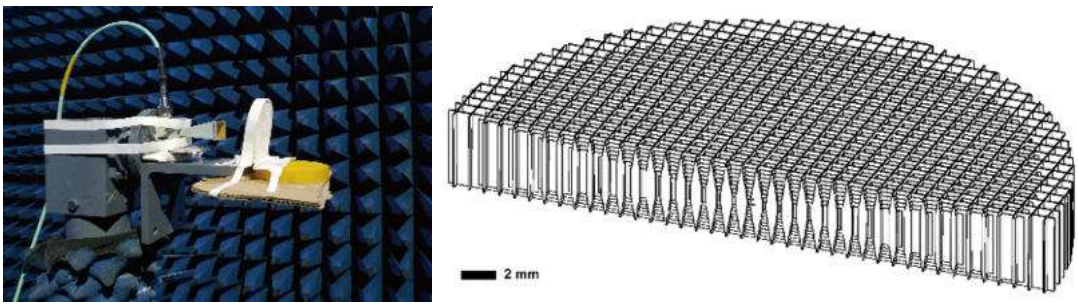

(a) (b)

Fig. 2. Test and structural profile of 3D printed Luneburg lens.

(a) Assembly of actual test system. (b) 3D printed Luneburg lens profile.

Millimeter/Terahertz and nano-optical antennas

60 GHz Planar Antenna Array on Glass Substrate for WiGig Communications

Jacqueline Damas[1,2]*, Niels Neumann[1], Klaus Wolf[1], and Dirk Plettemeier[1]

[1]Chair of Radio Frequency and Photonics Engineering, TU Dresden, Germany
[2]Department of Computer Science and Engineering, UDSM, Tanzania
*corresponding author, E-mail: jacqueline.damas@mailbox.tu-dresden.de

Abstract

A planar antenna array on the RF substrate increases the level of system integration and lowers the manufacturing cost for such systems. In this paper, the authors present the design and fabrication of a planar 2×2 antenna array for a 60 GHz Radio-over-Fiber (RoF) wireless system. The antenna is radiating at broadside and excited by microstrip line. For the measurement with RF probes on a wafer prober, a microstrip-to-coplanar waveguide transition is added. The measured gain of the antenna is 6 dBi and the matching is better than -20 dB at 60 GHz. The measurement and simulation results of gain and input return loss match very well at the resonance frequency.

1. Introduction

RoF systems integrate wireless and fiber optic networks, in order to utilize the immense bandwidth inherent with fiber optics. It is an affordable solution in environments such as conference centers, airports, hotels, shopping malls, and ultimately homes and small offices [1]. The RoF architecture consists of a central station (CS) where mm-wave signals are generated and transmitted over fiber to a base station (BS). At the BS, the transmitted signal is detected, preprocessed, amplified and wirelessly transmitted to the mobile station. Integrated planar antennas are essential components in mm-wave RoF systems. This is because for their small foot print, light weight, low cost and compatibility with integrated active radio frequency (RF) components, therefore representing the best choice for compact RoF systems. The 2×2 antenna array is designed on fused silica substrate, lightweight, and with excellent low loss ($\varepsilon_r = 3.75, \tan\delta = 0.0004$) characteristics up to 110 GHz [2]. It is fabricated on fused silica of 300 µm thickness with on top immersion silver/immersion gold (ISIG) surface plating of 5 µm thick excluding vias. In the following, we present the validation of the simulation as compared to the measurement results of the 2×2 antenna array.

2. Design, Fabrication and Measurements

The antenna should cover the 60 GHz ISM band in order to support IEEE 802.11ad signals. The RoF system design requires a realized gain of greater than 6 dBi and an input matching of lower than -10 dB at 60 GHz. The fabricated 2×2 antenna array on glass is shown in Fig. 1 with CPW-to-MS feed network.

Figure 1: A 2×2 60 GHz antenna array on glass substrate with CPW to MS transition feeding element.

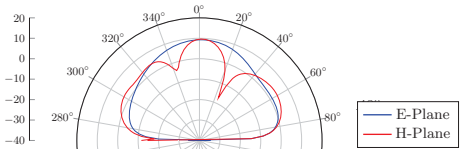

Figure 2: Simulation of the total radiation power pattern in E-Plane and H-Plane at 60 GHz of the 2×2 antenna array.

The simulated gain (EM full-wave simulation) of the microstrip antenna array at 60 GHz is 9.4 dBi, as shown in Fig. 2. The authors decided to use wafer-probes with the 400 µm pitch for the wafer prober measurements. Correspondingly, the microstrip antenna array requires a CPW transition to microstrip (MS). The CPW-to-MS transition feed network to the microstrip antenna array introduces loss of about 1 dB. As a result, the antenna array gain of 8.4 dBi is achieved. This gain meets the design criterion of 6 dBi gain and leaving some margin for implementation.

In this paper far field antenna measurements are carried out on a wafer prober using GGB Pico Probes Model 67A (ground-signal-ground (GSG) configuration, pitch of 400 µm) and a Network Analyzer up to 67 GHz connected to a receiving horn antenna with 20 dBi gain, see Fig. 3. The probe calibration was performed using thru-reflect-line (TRL) calibration structures fabricated on the fused silica substrate. The far-field region for the measurement setup can be determined by

$$R > \frac{2D^2}{\lambda} = 10.24\,\mathrm{cm} \tag{1}$$

taking into account the aparture $D = 16\,\mathrm{mm}$ of the Rx

horn antenna and the wavelength $\lambda = 5\,\mathrm{mm}$. Using the x-z-plane in a distance of 11 cm optimizes the measurable angle to $\pm 24°$ with the given scanning range of 10 cm×10 cm. Thus, the gain can be calculated from the measured data after polarization alignment of the Rx horn antenna and antenna array using the gain comparison method given by equation (2):

$$G_{\mathrm{AUT}}|_{\mathrm{dBi}} = S_{21,\mathrm{AUT}}|_{\mathrm{dB}} - S_{21,\mathrm{horn}}|_{\mathrm{dB}} + G_{\mathrm{horn}}|_{\mathrm{dBi}} \quad (2)$$

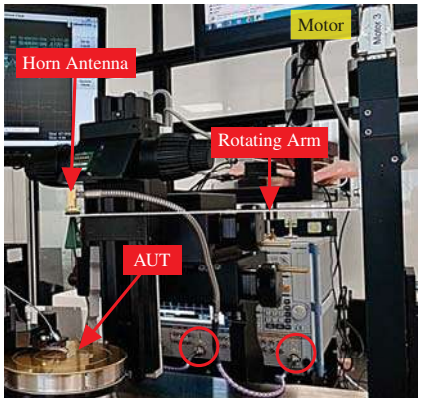

Figure 3: Overview of the AUT gain measurement at the middle of the chuck on wafer probing station with receiving horn antenna positioned on top.

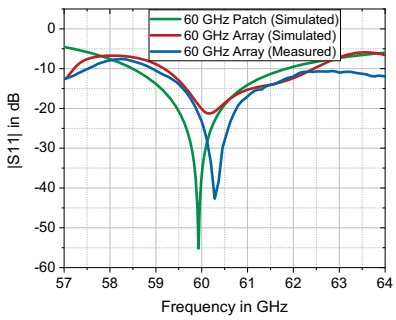

Figure 4: Simulated S11 of the 60 GHz patch element (green) compared with measured (blue) and simulated (red) S11 of the 60 GHz antenna array with CPW to MS feeding element.

The measurement and simulation results of gain and input return loss match well, as shown in Fig. 4 and Fig. 5. However, the measured gain is reduced by around 2 dB compared to the simulation. One of the reasons is the insertion loss of the CPW-to-MS transition that introduces about 1 dB loss. At these frequencies, fabrication tolerances and deviations in substrate material parameters have a huge influence [3]. Moreover, the reflections from the metal chuck induce interference effects in antenna measurements, especially around the axis perpendicular to the chuck which can be seen in the measurement curve in Fig. 5. It could be noted that the location of the minima and maxima on the

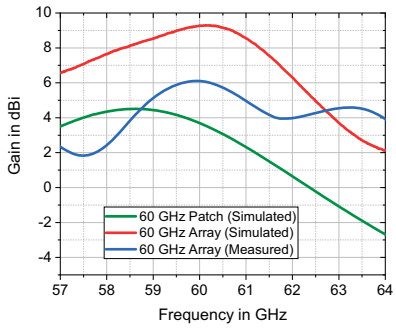

Figure 5: 60 GHz antenna array gain including losses (simulated, red) compared with measured (blue) and the patch element (simulated, green).

measured gain is very sensitive to the probe position relative to the x-z-plane of the Rx horn antenna movements. Reducing the reflectivity of either the Rx horn antenna or the antenna array on the chuck would drastically lower that influence. One improvement could be to use a plastic chuck. The measured gain of the antenna array at 60 GHz is $G_{\mathrm{AUT}} = 6\,\mathrm{dBi}$ whereas the measured input return loss is below -20 dB. This makes the antenna suitable for usage in aforementioned RoF system.

3. Conclusions

A 2×2 patch antenna array that can be manufactured on a simple two-layer process without vias has been successfully realized on a fused silica glass substrat that offers low-loss implementation. The characterization of matching and antenna gain shows that the antenna array covers the 60 GHz ISM band and has a gain of 6 dBi at 60 GHz. This allows the antenna to be used in a highly integrated BS for a RoF system. Further steps include the integration of the realized antenna into the RoF BS frontend design and system experiments.

References

[1] J. Damas, N. Neumann, and D. Plettemeier, "Cost Effective Printed Circuit Board Intermediate Frequency over Fiber Central Station," *International Journal of Microwave and Optical Technology*, vol. 10, no. 6-I, November, 2015.

[2] U. Arz, K. Kuhlmann, T. Dziomba, G. Hechtfischer, G. N. Phung, F. J. Schmückle, and W. Heinrich, "Traceable Coplanar Waveguide Calibrations on Fused Silica Substrates up to 110 GHz," *IEEE Transactions on Microwave Theory and Techniques*, vol. 67, no. 6, pp. 2423–2432, 2019.

[3] D. Titz, F. Ferrero, and C. Luxey, "Development of a millimeter-wave measurement setup and dedicated techniques to characterize the matching and radiation performance of probe-fed antennas [measurements corner]," *IEEE Antennas and Propagation Magazine*, vol. 54, no. 4, pp. 188–203, Aug. 2012.

Planar Terahertz Goubau-line Antenna with Endfire Radiation Based on Substrate Mode

Qing Le Zhang, Bao Jie Chen, Kam Man Shum, and Chi Hou Chan

State Key Laboratory of Terahertz and Millimeter Waves, Department of Electrical Engineering, City University of Hong Kong, Hong Kong SAR, China
*corresponding author, E-mail: eechic@cityu.edu.hk

Abstract

We present a planar terahertz goubau-line antenna with endfire radiation based on the substrate mode in this paper. As the antenna substrate thickness increases, the goubau line can excite the substrate mode and thus the truncated substrate will work as an antenna to generate endfire radiation. The proposed antenna operates from 325 GHz to 430 GHz on a 300 μm thick quartz substrate, and achieves the endfire radiation with 9.5-10.85 dBi gain.

1. Introduction

Terahertz technologies have received much attention in recent years as they hold many promising applications, like sensing, material detection, communications, etc. [1]. In these terahertz systems, antennas with endfire radiation are usually desired. In microwave and millimeter-wave bands, different types of antennas with endfire radiation have been proposed. Antennas with 3D structures (horns, dielectric lens and dielectric rod antennas) have wideband, high-gain and low cross-polarization advantages [2-4]. But in terahertz region, these 3D antennas are complicated to fabricate especially when integrated with other on-chip components. Some planar antennas (Yagi-Uda antennas and Vivaldi antennas) are usually fabricated on thin substrates with multiple metallic layers, which lead to the antenna deformation and difficult fabrication in terahertz band [5-6]. In this paper, we employ the goubau line on a thick quartz substrate, which can excite the substrate mode. Such thick substrate can support good mechanical stability and the truncated structure leads to endfire radiation. Meanwhile, this antenna only has one metallic layer and can be easily fabricated by photolithography.

2. Planar terahertz goubau-line antenna design

The geometry of the proposed planar terahertz goubau-line antenna based on the substrate mode is shown in Fig.1. It is fabricated on quartz substrate with ε_r = 3.75 and tanδ = 0.0004. Since the goubau line is a single-conductor line and propagates the transverse magnetic (TM) mode surface wave, a transition from 50 Ω coplanar waveguide (CPW) is required for the mode conversion and impedance matching. The tapered CPW ground plane provides a smooth conversion, where the exponential function is $y = f(\mathrm{x}) = A(\mathrm{e}^{\alpha x} - 1)$ with $A = L_g / (\mathrm{e}^{\alpha x} - 1)$ and α = 0.012. The antenna parameters are as follows: W_0 = 800 μm, W_c = 30 μm, L_c = 100 μm, L_1 = 500 μm, L_2 = 830 μm, L_3 = 350 μm, L_g = 230 μm and g_c = 4 μm. And the metallic material is copper with thickness 0.3 μm and conductivity $\sigma = 5.8\times10^7\ S/m$.

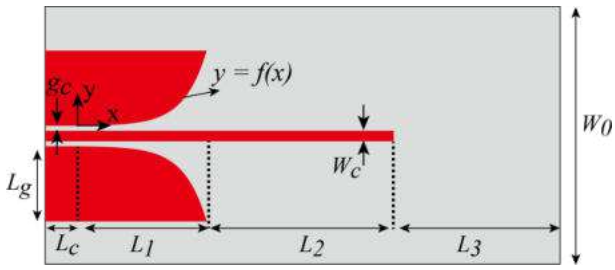

Figure 1: Geometry of the planar terahertz goubau-line antenna based on substrate mode.

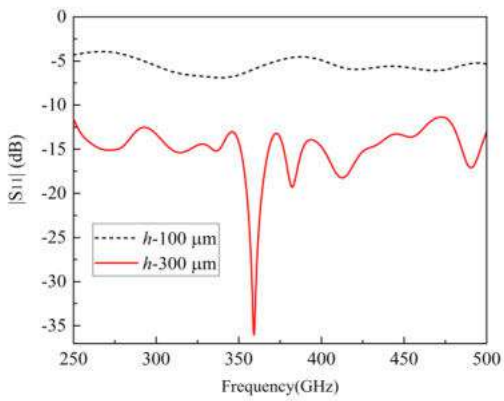

Figure 2: Reflection coefficients of the planar terahertz antenna on quartz substrate with different thicknesses.

The thickness of the quartz substrate plays an important role on the proposed terahertz goubau-line antenna. In Fig. 2, we compare the reflection coefficients of this antenna with different substrate thicknesses. When the thickness is 100 μm, the $|S_{11}|$ is about –5 dB, which means that the propagating wave is a standing wave and the field is reflected by the truncated goubau line. As the thickness

increases to 300 μm, the $|S_{11}|$ becomes below –10 dB in 250-500 GHz band and most of the energy radiates into free space. Therefore, the quartz thickness in this terahertz antenna is chosen as 300 μm. Fig. 3 displays the E_z field distribution of this terahertz antenna at 350 GHz. We can clearly observe that the TM-mode field along the goubau line is converted into the substrate mode and the truncated structure leak the energy into endfire direction. It also indicates that the polarization of this antenna is along z direction.

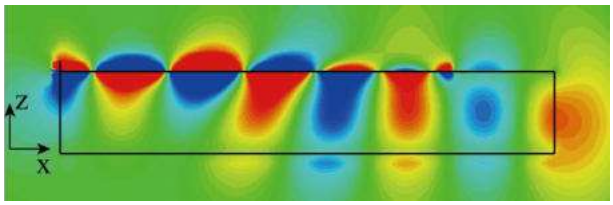

Figure 3: E_z field distribution of this terahertz antenna at 350 GHz.

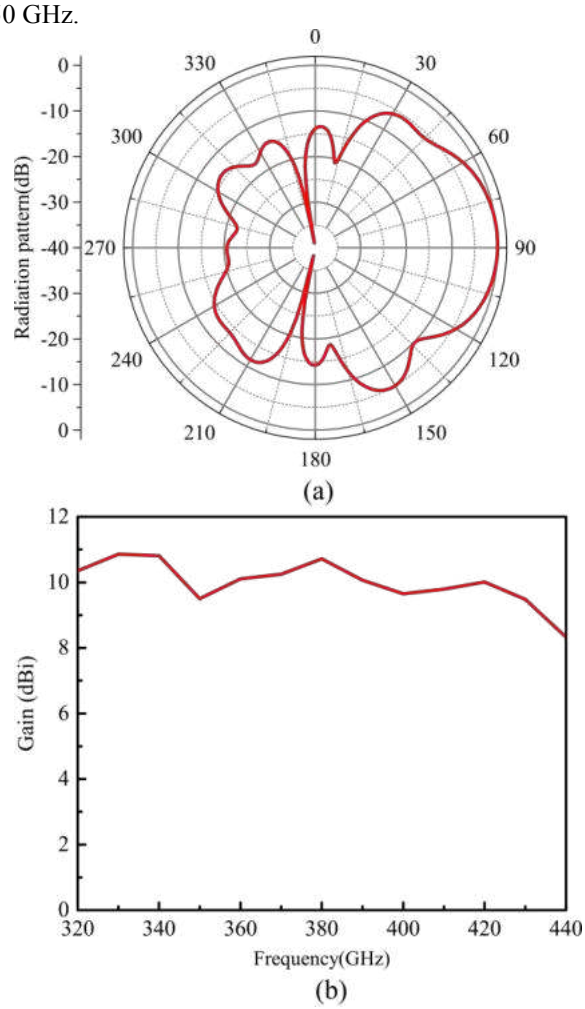

Figure 4: Radiation performance of the planar terahertz antenna, (a) E-plane radiation pattern (φ= 0◦) at 350 GHz and (b) gain versus frequency.

Fig. 4(a) gives the E-plane radiation pattern of the proposed terahertz antenna at 350 GHz. The main beam is in endfire direction and the 3dB beamwidth is 57◦. The cross-polarization is below -40 dB and not shown here. The gain versus frequency of this terahertz antenna is depicted in Fig. 4(b). In 325-430 GHz band, the gain can reach 9.5 to 10.85 dBi. Experimental validation of the design will be provided in the presentation.

3. Conclusions

In this paper, we propose a planar terahertz antenna with endfire radiation in 325-430 GHz. The goubau line is employed to excite the substrate mode on a 300 μm thick quartz substrate. The truncated structure leads to the energy radiation into the endfire direction. The gain can reach 9.5-10.85 dBi in the operating band.

Acknowledgements

This work was supported by the Hong Kong Research Grants Council Theme-Based Research Scheme Project T42-103/16-N.

References

[1] H. Song, T. Nagatsuma, Present and future of terahertz communications, *IEEE Trans. THz Sci. Technol.*, 1: 256-263, 2011.

[2] S. Sekiguchi, M. Sugimoto, S. Shu, Y. Sekimoto, K. Mitsui, T. Nishino, N. Okada, K. Kubo, T. Takahashi, T. Nitta, Broadband corrugated horn array with direct machined fabrication, *IEEE Trans. THz Sci. Technol.*, 7: 36-41, 2016.

[3] K. X. Wang, H. Wong, Design of a wideband circularly polarized millimeter-wave antenna with an extended hemispherical lens, *IEEE Trans. Antennas Propag.*, 66: 4303-4308, 2018.

[4] N. Ghassemi, K. Wu, Planar dielectric rod antenna for gigabyte chip-to-chip communication, *IEEE Trans. Antennas Propag.*, 60: 4924-4928, 2012.

[5] N. Kaneda, W. R. Deal, Y. X. Qian, R. Waterhouse, T. Itoh, A broadband planar quasi-Yagi antenna, *IEEE Trans. Antennas Propag.*, 50: 1158-1160, 2002.

[6] A. Z. Hood, T. Karacolak, E. Topsakal, A small antipodal vivaldi antenna for ultrawide-band applications, *IEEE Antennas Wireless Propag. Lett.*, 7: 656-660, 2008.

Graphene loaded 1 x 3 MIMO Terahertz Wideband Antenna with High Isolation for Medical and Short Indoor Applications

Ch. Murali Krishna[1,*], N Suguna[2], S Revathi[2]

[1]Department of ECE, PDPM IIIT Design and Manufacturing, Jabalpur, Madhya Pradesh, India
[2]School of Electronics Engineering, VIT University, Vellore, India
*corresponding author, E-mail: krishnasri780@gmail.com

Abstract

In this paper, novel approach tri – element Multiple – Input Multiple – Output (MIMO) terahertz (THz) antenna is designed to cover wide band characteristics from 2.44 – 3.09THz for medical, short – indoor and THz applications. The proposed MIMO antenna is designed on quartz glass dielectric material within compact size of 120µm x 60µm, offers of wide impedance bandwidth (IBW) of 0.65THz, isolation less than -20dB, peak gain 6.82dB and high radiation efficiency of 92 – 98%. Furthermore, in order to meet the high date transmission rate and channel capacity performance of MIMO antenna, MIMO antenna parameters envelope correlation coefficient (ECC < 0.07), diversity gain (DG ~ 10dB), total active reflection coefficient (TARC < 0.65), channel capacity loss (CCL < 0.75bits/sec/Hz) and mean effective gain (-4dB < MEG < -12dB) are investigated and which are within acceptable limits.

1. Introduction

In current years, the innovative increase of Wi-Fi technologies created the necessity of inexhaustible bandwidth to fulfill the demands of large statistics visitors charge, channel ability and interruption loose connectivity [1]. These needs have given researchers a compelling incentive to investigate a large new frequency band, the terahertz (THz) electromagnetic spectrum, which runs from 0.1 to 10 THz and has a wavelength of 0.03 to 3 mm [2-3]. The THz frequency spectrum (0.1-10 THz) has emerged as a viable alternative for meeting the demands of secure high-speed wireless communication applications by allowing for faster data transmission [4-5]. Due to various advantages of THz waves over millimetre waves, such as a wider useable frequency band, more spectral resolution, lower diffraction, and better anti-interference performance, the THz spectrum supports these diverse applications [6]. In the present day, better channel capacity and a fast data rate are required for wireless communication. MIMO-communication systems with THz range are necessary to meet these needs for high data speeds in Terabit/sec (Tbps). It also offers extremely high throughput per device (ranging from multiple Gbps to several Tera-bps), as well as per-area efficiency (bps/km^2). Some of the MIMO antenna designs in Terahertz region are reported by researchers for future wireless THz applications. Graphene based pattern diversity MIMO [7], graphene based reconfigurable structure [8], plasmonic reconfigurable MIMO antenna with beam forcing [9], THz MIMO for 3D medical imaging and radar [10], L – shaped decoupling MIMO structure for high isolation [11] and Micro scaled tree shaped MIMO antenna [12] are designed for various THz applications.

Now a days advancements in the communication requires high performable antenna, low cost, minimum weight. In THz a novel microstrip patch antenna on the photonic crystal is designed and analyzed. The size of the antenna is 800 x 600 µm^2 on polyamide substrate which operates at the frequency range from 0.615THz – 0.6514THz [13]. In this paper [14], for the purpose of short distance wireless communication systems at THz a rectangular microstrip patch antenna designed with the size of 1000 x 1000µm^2 on polyamide substrate. The operation frequency ranges from 0.7THz-0.85THz and the gain 3.497dB and the efficiency of 55.88%. In this paper [15], for the purpose of surveillance applications terahertz microstrip patch antennas designed with the frequency of 0.7THz-0.85THz and the IBW of 0.15THz. In this article [16], on polyimide substrate graphene nanoribbon-based terahertz antenna proposed and designed. The size of the antenna is about 208.98 x 433.2 µm^2 and the operating frequency of 0.725THz to 0.775THz and the gain of 4.93dB. For high-speed short range wireless communication applications THz antenna which is a micro-sized rhombus-shaped proposed with the size of 300 x 300 µm^2 and the frequency ranges from 0.445THz-0.714THz and the impedance bandwidth of 269GHz and the gain of 5.7dB [17]. In this paper [18], based on photonic crystals novel approach of a terahertz microstrip patch antenna designed and analyzed. The size of the antenna about 600 x 600 µm^2 and frequency of 0.5THz-0.8THz. In this article [19], for the purpose sub-terahertz short range wireless communication systems unslotted ultra-wideband microstrip antenna which is high efficiency designed. The size of the antenna is about 1000 x 1000 µm^2 and the frequency ranges from 0.093THz to 0.207THz. Based on a synthesized photonic bandgap substrate using BPSO a terahertz microstrip antenna is designed [20], and analyzed and the size of the antenna is about 500 x 500 µm^2 in which frequency ranges from 0.4THz-0.8THz. In this paper [21], for video rate imaging and homeland defense applications rectangular microstrip

patch antenna employing polyimide substrate which is THz proposed with the size of 208.9 x 422 μm^2 on polyimide substrate and the frequency ranges from 0.665THz-0.696THZ and the gain of 5.22dB. In this article [22], by using photonic band gap and defected ground structure THz patch antenna which is high performance designed on Rogers RO3003 with the size of 210 x 180 μm^2. For THz applications Bow-tie photoconductive antenna designed and performance analyzed[23], The gain obtained by the antenna is about 2.22dB.

In this paper, triple element MIMO antenna is designed using quartz dielectric material having dielectric constant of 3.78 and both sides of this material is layered with thickness of 0.5µm graphene layer acts as conducting layers. The proposed structure maintains IBW of 0.65THz (2.44 – 3.09THz) at S_{11} < -10dB. Further, isolation (S_{12}), voltage standing wave ratio (VSWR), group delay (t_d), radiation patterns, surface current analysis and MIMO parameters are evaluated and discussed in this paper.

2. Proposed Design Layout and Implementation

The MIMO antenna with wide band characteristics is designed and simulated using electromagnetic high frequency structure simulator (EM - HFSS) tool. The proposed evaluation is made from conventional rectangular shape patch antenna with graphene material loaded having thickness of 0.5µm within compact size of 60µm x 50µm. Geometrical parameters of the designed antenna (antenna - 1) shown in figure 1(a) are computed from standard mathematical equation [24]. 50Ohm characteristic impedance transmission feedline is used to feed the radiating graphene element. In order to meet the design essentials of the high – speed data communication rage and channel losses, MIMO antenna model has been proposed. Figure 1(b) represents the three element MIMO antenna designed on 120µm x 60µm quartz substrate for improving the impedance bandwidth. Furthermore, with respect to impedance bandwidth, reflection coefficient and mismatching losses, designed MIMO antenna has been altered to 45° inclination oriented elements are arranged to the mid element of the MIMO antenna design and spacing between elements (S) is 7.8µm is shown in figure 1(c). Geometrical dimensions of the designed antennas are reported in table 1.

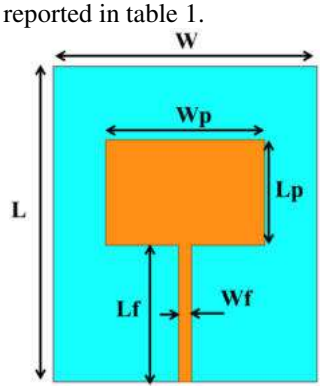

(a) Antenna – 1

Table 1: Geometrical dimension (units - µm)

L	W	Lp	Wp
60	50	20	30
Lf	**Wf**	**L_g**	
26	2.5	25	
Ls	**Ws**	**A**	**B**
60	120	0.9	2.65
L_1	**L_2**	**S**	
26	24.75	7.8	

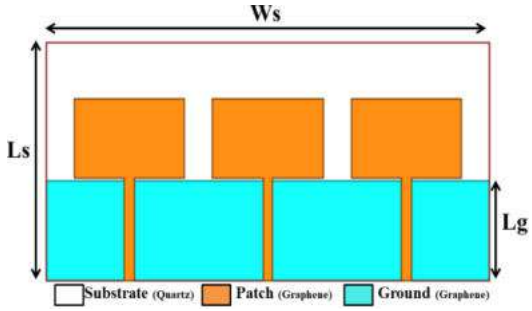

(b) Antenna – 2

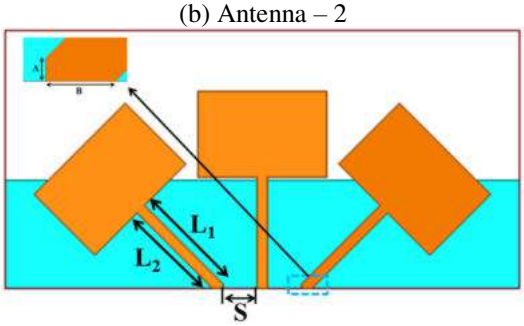

(c) Antenna – 3

Figure 1: Evaluation of tri – element planar MIMO antenna

3. Designed antenna performance characteristics

3.1. Electromagnetic simulation characteristics

The reflection coefficient (S_{11}) characteristics of the iteration wise proposed THz MIMO antenna is depicted in figure 2. It is observed that impedance bandwidth of antenna - 3 is better than antenna – 1 & 2. Conventional rectangular microstrip patch antenna resonates at 3.23THz with reflection coefficient of -35.19dB. This antenna – 1 achieves bandwidth of 0.19THz operating from 3.13 to 3.32THz. Three element MIMO antenna with partial ground plane (antenna – 2) produces Impedance bandwidth (IBW) of 0.40THz at S_{11} < -10dB covers frequency spectrum from 2.69 to 3.09THz. Inclined element MIMO antenna (antenna - 3) gives wide band characteristics with an IBW of 0.65THz (650GHz) covers 2.44 – 3.09THz spectrum for short – indoor and medical applications. Corresponding IBW, bandwidth ratio (BR) and fractional bandwidth (FBW) parameters of designed antennas are reported in table 2. Impedance matching with the free space characteristic impedance is the one of the prominent characteristics in antenna designing. VSWR measures the impedance matching in the bandwidth coverage. Figure 3 shows the VSWR characteristics of antenna – 1, 2 & 3 and obtained values are noted in table 2. Signal distortion between the MIMO elements are measured interms of group delay characteristics, which are presented in figure 4 and achieved peak delay values are included in table 2. The main objective of this work is to improve the isolation between elements. Figure 5 shows the isolation between MIMO elements of designed antenna – 2 & 3 respectively. Proposed antenna achieves isolation less than -25dB, compared to antenna – 2 it shows improvement in isolation.

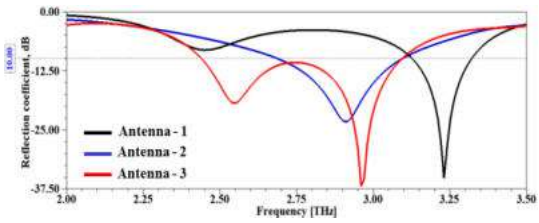

Figure 2: S_{11} characteristics of designed antennas

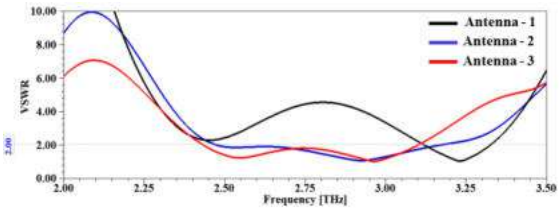

Figure 3: VSWR characteristics of designed antennas

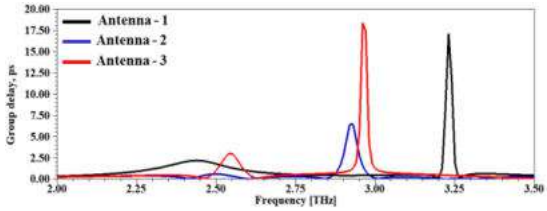

Figure 4: Group delay characteristics of designed antennas

Table 2: Design summary of electrical characteristics

A*	BW	IBW, THz	BR	FBW, %	VS WR	t_d, ps
1	3.13 - 3.32	0.19	1.06	5.89	1.03	17
2	2.69 – 3.09	0.4	1.14	13.84	1.07	6.4
3	2.44 – 3.09	0.65	1.26	23.5	1.02	19

(A* - Antenna)

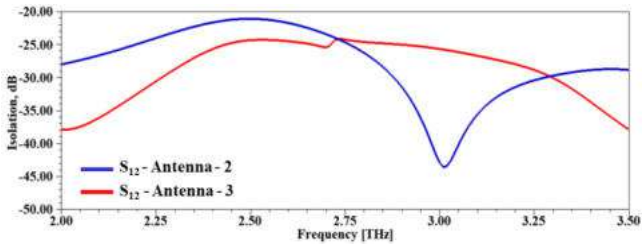

Figure 5: Isolation plots of antenna – 2 & antenna - 3

3.2. Far – field characteristics

Figure 6 shows the two dimensional radiation characteristics of suggested wide band antenna at 2.55THz and 2.96THz in E – plane and H – plane interms of co – polarization (Co –pol.) and cross – polarization (Cross – pol.) components. The proposed three element MIMO antenna exhibits almost unique characteristics at both resonant frequencies. The proposed antenna maintains omnidirectional patterns in co – polarization and low cross polarization is below -28dB are attained.

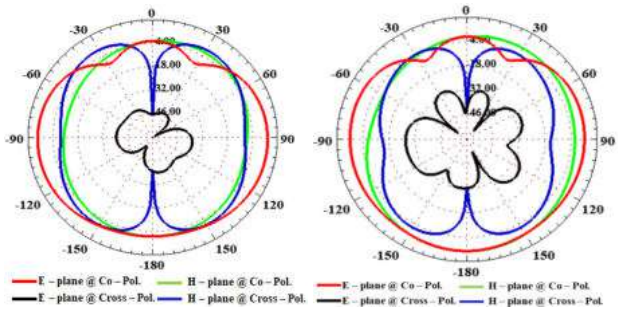

Figure 6: Radiation patterns of suggested antenna at 2.55THz and 2.96THz

3.3. Surface current analysis

Surface current distributions of the proposed antenna at resonant frequencies 2.55THz and 2.96THz are shown in figure 7. Figure 7(a) shows the current distribution of designed antenna – 3 at 2.55THz. In this very high surface current is concentrated at the feed lines of three elements and edges of graphene patches. Similarly figure 7(b) is more concentrated at the edges of elements at 2.96THz.

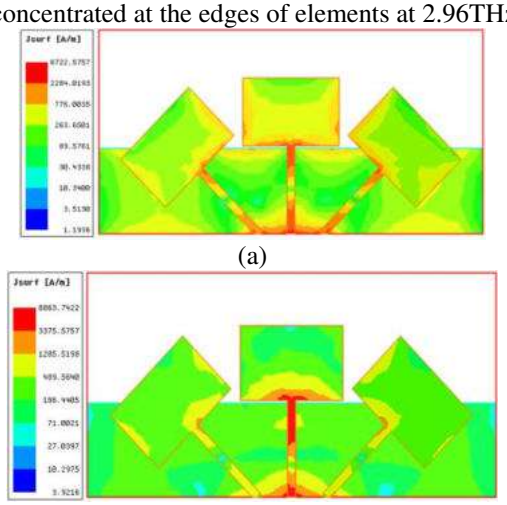

(a)

(b)

Figure 7: Magnitude surface current distribution of proposed antenna at a) 2.55THz b) 2.96THz

3.4. MIMO Antenna parameter analysis

In order to measure the similarity of the proposed tri – element MIMO antenna printed on Quartz material, MIMO parameters such as ECC, DG, TARC, CCL and MEG are evaluated [12, 25-26].

i. ECC is measured using S – parameters method of equation:

$$\rho_e = \frac{\left|S_{11}^* S_{12} + S_{21}^* S_{22}\right|^2}{\left(1-\left|S_{11}\right|^2-\left|S_{21}\right|^2\right)\left(1-\left|S_{12}\right|^2-\left|S_{22}\right|^2\right)} \quad (1)$$

ii. Diversity gain (DG) computed interms of ECC as:

$$DG = 10 * \sqrt{1-\rho_e^2} \quad (2)$$

iii. TARC can be computed interms of S – parameters as:

$$TARC = \sqrt{\frac{\left|S_{11}+S_{12}e^{j\theta}\right|^2+\left|S_{21}+S_{22}e^{j\theta}\right|^2}{2}} \quad (3)$$

iv. Channel capacity loss (CCL) can be computed interms of S – parameters as:

$$CCL = -\log_2^{|\psi^R|} = -\log_2^{\begin{vmatrix} \rho_{11} & \rho_{12} \\ \rho_{21} & \rho_{22} \end{vmatrix}} \quad (4)$$

Where ψ^R = Receiving antenna correlation matrix,

$$\rho_{ii} = 1 - |S_{ii}|^2 - |S_{ij}|^2 \quad (5)$$

$$\rho_{ij} = -\left(S_{ii}^* S_{ij} + S_{ij}^* S_{jj}\right) \text{ for all i, j = 1 \& 2} \quad (6)$$

v. MEG of three – port MIMO antenna can also be evaluated interms of S – parameters as

$$MEG_i = 0.5\left[1 - \sum_{j=1}^{N} |S_{ij}|^2\right] \quad (7)$$

The MIMO parameter evaluations are presented figure 8. From fig 8(a), it is evident that ECC is less than 0.07, which is acceptable within the ideal values and it signifies that efficient operating condition of two different elements on single substrate. Figure 8(b) represents the diversity gain characteristics of proposed MIMO antenna, it has constant 10dB value over the operating spectrum 2.44 – 3.09THz. TARC characteristics of the proposed MIMO antenna are obtained within the acceptable limit, which is less than 0.65 as shown in figure 8(c). The CCL value of the suggested MIMO design is less than 0.75bits/Sec/Hz over the entire bandwidth, which shows better diversity characteristics of the proposed MIMO are shown in figure 8(d). Idea value of MEG is in between -3dB to -12dB. Designed MIMO antenna achieves MEG characteristics in between -4dB to -12dB, which are represented in figure 8(e).

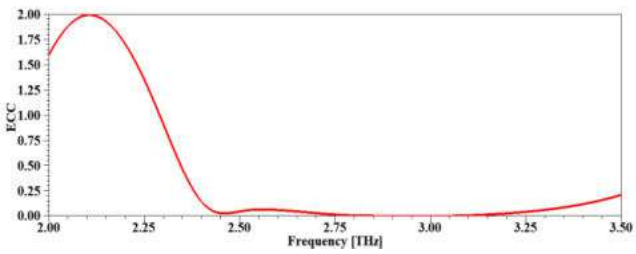

(a) Envelope Correlation Coefficient

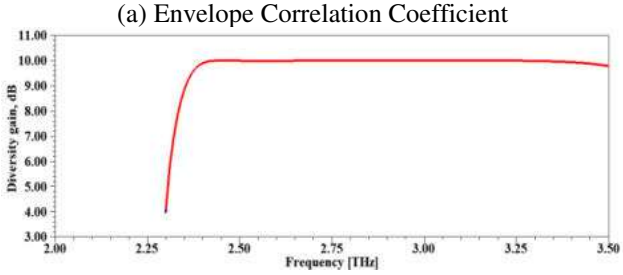

(b) Diversity gain (DG)

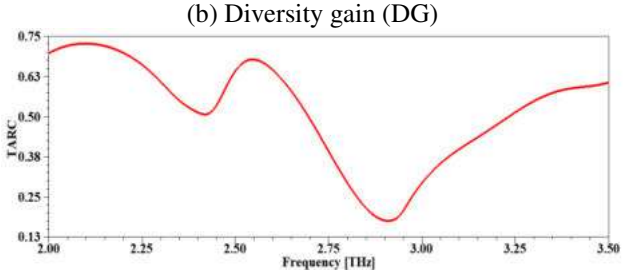

(c) Total active reflection coefficient (TARC)

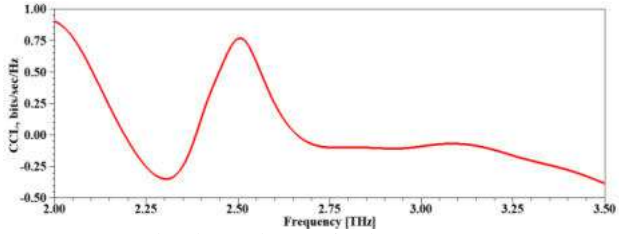

(d) Channel capacity loss (CCL)

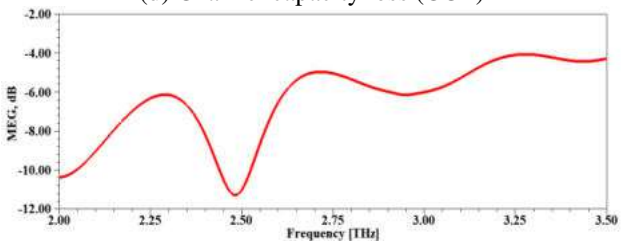

(e) Mean effective gain (MEG)

Figure 8: MIMO antenna parameters

3.5. Gain and Radiation efficiency

The gain and radiation efficiency of the proposed antenna are evaluated and presented in figure 9 & 10. The gain (G) of the proposed antenna is varied from 5.7 - 6.8dB over the operating bandwidth 2.44 – 3.09THz. Radiation efficiency (η) of the suggested graphene based antenna varies from 92 – 98%. The gain and radiation efficiency are prominent and justified that this antenna is suitable for THz communications.

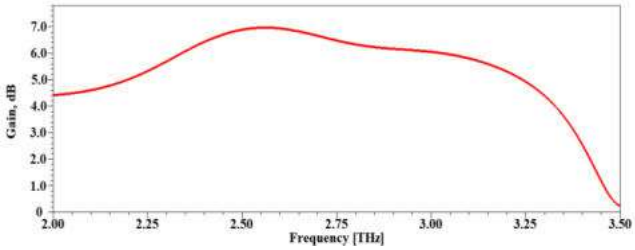

Figure 9: Gain characteristics of the suggested MIMO antenna

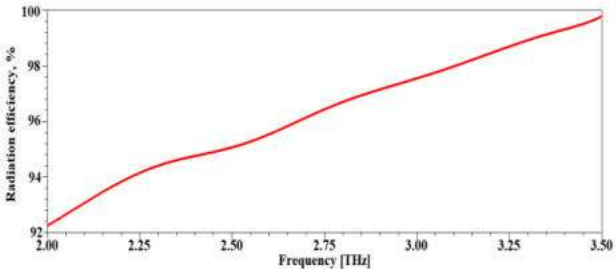

Figure 10. Radiation efficiency characteristics of the proposed MIMO antenna with partial ground plane

4. Comparison of proposed MIMO antenna with existed works

Table 3 summaries the analyzed performance comparison. In comparison to known single element THz antenna structures and recently announced MIMO antenna structures, the suggested antenna offers a wider impedance bandwidth and requires the shortest dimension, as shown in the comparison table. So, as stated in the preceding sections of the article, the novelty of the suggested design is a

broader impedance bandwidth in a comparatively smaller antenna size, as well as good impedance, radiation, and diversity properties.

Table 3: Performance comparison of proposed tri – element MIMO antenna with existed works

Ref.	Size, μm^2	Substrate	Operating range, THz	IBW, THz	Isolation, dB	Gain, dB	Radiation efficiency, %
[13]	800 x 600	Polyamide	0.615 – 0.6514	0.0364	-	7.934	85.71
[14]	1000 x 1000	Polyamide	0.7 – 0.85	0.15	-	3.497	55.88
[15]	700 x 600	Polyamide	0.7 – 0.85	0.15	-	6.4-9.7	75
[16]	433.2 x 208.98	Polyamide	0.725 – 0.775	0.05	-	5.09	86.85
[17]	300 x 300	Polyamide	0.445 – 0.714	0.269	-	5.7	97.3
[18]	600 x 600	polyimide	0.5 - 0.8	0.3	-	9.19	90.84
[19]	1000x1000	Rogers RO4835-T	0.093 - 0.207	0.114	< -17	4.4	94
[20]	500 x 500	Air cylinders embedded in a thick silicon	0.4 - 0.8	0.4	-	9.17	91.08
[21]	208.9 x 422	polyimide	0.665 - 0.696	0.031	-	5.22	-
[22]	210 x 180	Rogers RO3003	0.696	0.026	-	6.79	98
[23]	100 x 100	Grown GaAs	1.62 - 1.66	0.04	-	2.22	-
Proposed	**120 x 60**	**Quartz**	**2.44 – 3.09**	**0.65**	**< -20**	**5.7 – 6.8**	**92 - 98**

5. Conclusion

In this paper graphene based inclined three - element MIMO antenna is designed for improvement in isolation and high radiation efficiency. The achievements of designed antenna has been analyzed, studied and discussed interms of reflection coefficient (S_{11}), impedance bandwidth (IBW), isolation (S_{12}), VSWR, far – field characteristics, surface current distribution. Behalf of this, MIMO performance is investigated interms of ECC (< 0.07), DG (~ 10dB), TARC (< 0.65dB), CCL (< 0.75bits/sec/Hz) and -4dB < MEG < -12dB within the acceptable limits. The suggested antenna is suitable for security, medical imaging, sensing, radar, satellite, short – indoor and THz applications.

References

[1] F. Xu, Y. Lin, J. Huang et al., "Big data driven mobile traffic understanding and forecasting: a time series approach," IEEE Transactions on Services Computing, vol. 9, no. 5, 2016, pp. 796- 805.

[2] K. Guan, G. Li, T. Kürner, A. F. Molisch et al., "On millimeter wave and THz mobile radio channel for smart rail mobility," IEEE Transactions on Vehicular Technology, vol. 66, no. 7, 2017, pp. 5658-5674.

[3] I. F. Akyildiz, J. M. Jornet, and C. Han, "Terahertz band: next frontier for wireless communications," Physical Communication, vol. 12, pp. 16–32, 2014.

[4] Z. Chen, X. Ma, B. Zhang et al., "A survey on terahertz communications," China Communications, vol. 16, no. 2, 2019, pp. 1-35.

[5] H. Song and T. Nagatsuma, "Present and future of terahertz communications," IEEE Transactions on Terahertz Science and Technology, vol. 1, no.1, 2011, pp. 256-263.

[6] J. Federici, and L. Moeller, "Review of terahertz and subterahertz wireless communications," Journal of Applied Physics, vol. 107, 2010, pp.111101.

[7] Gaurav Varshney, Shailza Gotra, V.S. Pandey, R.S. Yaduvanshi, A proximity coupled two-port MIMO graphene antenna with pattern diversity for THz applications, Nano Communication Networks (2019).

[8] Zheng Xu, Xiaodai Dong, Jens Bornemann, Design of a reconfigurable MIMO system for THz communications based on graphene antennas, IEEE Transactions on Terahertz Science and Technology 4 (5) (2014) 609–617.

[9] Ian F. Akyildiz, Josep Miquel Jornet, Realizing ultra-massive MIMO (1024×1024) communication in the (0.06–10) terahertz band, Nano Communication Networks 8 (2016) 46–54.

[10] Sherif Adeshina Busari, Kazi Mohammed Saidul Huq, Shahid Mumtaz, Jonathan Rodriguez, Terahertz Massive MIMO for Beyond-5G Wireless Communication, ICC 2019-2019 IEEE International Conference on Communications (ICC) (2019) 1–6.

[11] Saxena, G., Awasthi, Y. K., & Jain, P. (2020). High Isolation and High Gain Super-Wideband (0.33-10 THz) MIMO Antenna for THz Applications. Optik, 165335. doi:10.1016/j.ijleo.2020.165335

[12] Vasu Babu, K., Das, S., Varshney, G. et al. A micro-scaled graphene-based tree-shaped wideband printed MIMO antenna for terahertz applications. J Comput Electron (2022). https://doi.org/10.1007/s10825-021-01831-3

[13] Kushwaha, R. K., Karuppanan, P., & Malviya, L. D. (2018). Design and analysis of novel microstrip patch antenna on photonic crystal in THz. Physica B: Condensed Matter, 545, 107–112.

[14] Sharma, A., & Singh, G. (2008). Rectangular Microstirp Patch Antenna Design at THz Frequency for Short Distance Wireless Communication Systems. Journal of Infrared, Millimeter, and Terahertz Waves, 30(1), 1–7.
[15] Mahmud, Rashad. (2020). Terahertz Microstrip Patch Antennas For The Surveillance Applications Article history. Kurdistan Journal of Applied Research. 5. 10.24017/science.2020.1.2.
[16] Anand, S., Sriram Kumar, D., Wu, R. J., & Chavali, M. (2014). Graphene nanoribbon-based terahertz antenna on polyimide substrate. Optik - International Journal for Light and Electron Optics, 125(19), 5546–5549.
[17] Krishna, C. M., Das, S., Nella, A., Lakrit, S., & Madhav, B. T. P. (2021). A Micro-Sized Rhombus-Shaped THz Antenna for High-Speed Short-Range Wireless Communication Applications. Plasmonics.
[18] Hocini, A., Temmar, M. N., Khedrouche, D., & Zamani, M. (2019). Novel Approach for the Design and Analysis of a Terahertz Microstrip Patch Antenna Based on Photonic Crystals. Photonics and Nanostructures - Fundamentals and Applications.
[19] Okan, T. (2021). High efficiency unslotted ultra-wideband microstrip antenna for sub-terahertz short range wireless communication systems. Optik, 242, 166859.
[20] Temmar, M. N. E., Hocini, A., Khedrouche, D., & Zamani, M. (2019). Analysis and design of a terahertz microstrip antenna based on a synthesized photonic bandgap substrate using BPSO. Journal of Computational Electronics.
[21] Dhillon, A. S., Mittal, D., & Sidhu, E. (2017). THz rectangular microstrip patch antenna employing polyimide substrate for video rate imaging and homeland defence applications. Optik, 144, 634–641.
[22] Ullah, S., Ruan, C., Haq, T. U., & Zhang, X. (2019). High performance THz patch antenna using photonic band gap and defected ground structure. Journal of Electromagnetic Waves and Applications, 1–12.
[23] Saurabh, L., Bhatnagar, A., & Kumar, S. (2017). Design and performance analysis of bow-tie photoconductive antenna for THz application. 2017 International Conference on Intelligent Computing and Control (I2C2).
[24] C. Balanis, Antenna Theory, Wiley Interscience, Hoboken, NJ, 2005.
[25] Ch Murali Krishna, M. Sai Prapoorna, K. Taruni Sesha Sai, M. Sai Teja, "Super Wideband 1 × 2 MIMO Antenna for Advanced Wireless Communication", Springer Advances in Electrical and Computer Technologies, https://doi.org/10.1007/978-981-15-9019-1_45
[26] C. M. Krishna, M. Mamatha and J. P. Kumar, "Mickey Mouse Modeled MIMO Antenna for Extended UWB Applications," 2020 Fourth International Conference on Computing Methodologies and Communication (ICCMC), 2020, pp. 522-527, doi: 10.1109/ICCMC48092.2020.ICCMC-00097.

Base Station and User Equipment Antennas for 60-GHz-Band Near-Field Wireless Communication System: GATE

Takashi Tomura[1], Jiro Hirokawa[1]

[1]Department of Electrical and Electronic Engineering, Tokyo Institute of Technology, Tokyo, Japan
*corresponding author, E-mail: tomura@ee.e.titech.ac.jp

Abstract

This paper presents base station and user equipment antennas for a 60-GHz-band near-field wireless communication system: gigabit access transponder equipment (GATE). The GATE uses electrically large antennas for base stations to provide a uniform field distribution and low interference between adjacent links.

1. Introduction

Demands for high-speed wireless communication have increased because of widespread mobile terminals such as smart phones and tablets. The 60-GHz band, 57 – 66 GHz, is allocated worldwide for wireless communication and can be used without a license [1].

The gigabit access transponder equipment (GATE) system [3] uses electrically large aperture or array antennas as antennas for base stations. Electrically large antennas realize long near-field areas where radio wave intensity does not attenuate by the square of the propagation distance. The GATE system uses the near-field region to provide stable field intensity and low interference between adjacent links. For user equipment such as mobile terminals or tablets, small linear polarized antennas [4], [5] are used. In this paper, base station and user equipment antennas for the 60-GHz-band GATE system are presented.

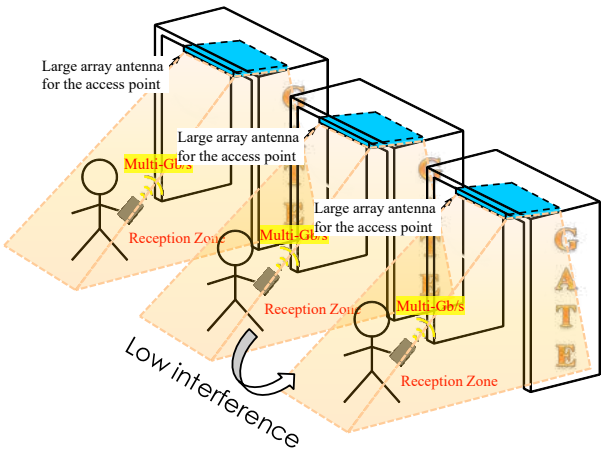

Figure 1: 60-GHz-Band Near-Field Wireless Communication System: GATE.

2. Base Station Antennas for GATE

A circularly-polarized slot array antenna [6], [7] for base stations of GATE is shown in Fig. 2. It consists of a corporate feed waveguide in the lower layer and a radiating part in the upper layer. The antenna is fed through an aperture (WR-15) from its backside, and the power divided equally by the corporate feed waveguide circuit. At the end of the feeding circuit, 2×2-element circular-polarized subarray is fed. The antenna was designed using a hybrid method of moments (MoM)/finite element method (FEM) [8].

The 128×64-element array was fabricated by diffusion bonding of 0.2-mm thickness aluminum (A6063) plates as shown in Fig. 2 (a). The aperture dimension of the arrays is 544 × 272 mm^2. The measured amplitude distribution of 128×64-element array shows uniform whereas the phase distribution shows non-uniformity. The reason for the non-uniformity may result from the incompleteness of the fabrication of the feeding circuit.

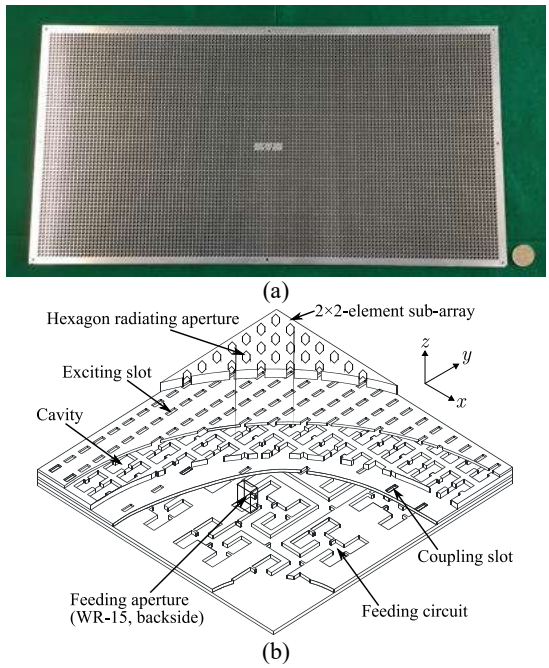

Figure 2: (a) 60-GHz-band 128×64-element slot array antenna by aluminum, (b) its structure.

3. User Equipment Antennas for GATE

A metal cap antenna for user equipment of GATE is shown in Fig. 3 [5]. The antenna is composed of a substrate and a metal cap antenna. The metal cap antenna is composed of a T-junction and two slots and fed by a post wall waveguide on the substrate. Two slots are employed to increase directivity and realize the same beamwidth in both E- and H-planes. The substrate is inserted into the metal cap until it touches the metal cap antenna. This structure realizes robustness against fabrication tolerance. Measured frequency characteristics of gain was more than 7.8 dBi from 57 to 66 GHz.

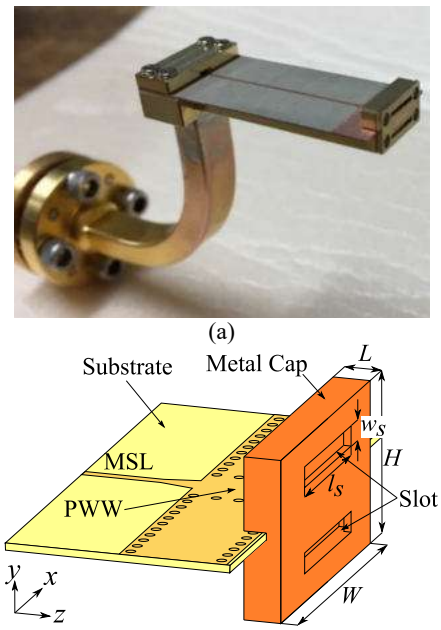

Figure 3: (a) Fabricated metal cap antenna with a waveguide feed, (b) its structure.

4. Conclusions

This paper has presented base station and user equipment antennas for the 60-GHz-band near-field wireless communication system: GATE. As a base station antenna, a 128x64-element circular-polarized waveguide slot array antenna was introduced and shows uniform amplitude distribution. As a user equipment, a metal cap antenna was described and shows wideband gain characteristics.

Acknowledgements

The authors would like to thank Dr. J. Iwasaki, Dr. K. Akiyama, and Dr. E. Sugisaki of Sony Semiconductor Solutions Corporation and Dr. T. Taniguchi, Dr. K. Akahori, and Dr. Y. Takekoh of Japan Radio Co., Ltd for their support on the GATE system.

References

[1] R. Fisher, “60 GHz WPAN standardization within IEEE 802.15.3c,” in Proc. Int. Signals, Syst. Electron. Symp., 2007, pp. 103–105.

[2] T. S. Rappaport et al., “Millimeter Wave Mobile Communications for 5G Cellular: It Will Work!,” IEEE Access, vol. 1, pp. 335-349, 2013.

[3] M. Zhang, K. Toyosaki, J. Hirokawa, M. Ando, T. Taniguchi and M. Noda, “A 60-GHz Band Compact-Range Gigabit Wireless Access System Using Large Array Antennas,” IEEE Trans. Antennas Propag., vol. 63, no. 8, pp. 3432-3440, Aug. 2015.

[4] R. Suga, H. Nakano, Y. Hirachi, J. Hirokawa, and M. Ando, “A small package with 46-dB isolation between Tx and Rx antennas suitable for 60-GHz WPAN module,” IEEE Trans. Microw. Theory Tech., vol. 60, no. 3, pp. 640–646, Mar. 2012.

[5] T. Tomura, H. Hirayama, J. Hirokawa, “A PCB-Integratable Metal Cap Slot Antenna for 60-GHz Band Mobile Terminals,” IEICE Trans. Commun., vol.E102-B, no.2, pp.317-323, Feb. 2019. doi: 10.1587/transcom.2018EBP3070

[6] Y. Miura, J. Hirokawa, M. Ando, K. Igarashi, and G. Yoshida, “A high-efficiency circularly-polarized aperture array antenna with a corporate-feed circuit in the 60GHz band,” IEICE Trans. Electron., vol.E94-C, no.10, pp.1618-1625, Oct. 2011.

[7] T. Yamamoto, M. Zhang, J. Hirokawa, T. Hirano and M. Ando, “Wideband design of a circularly-polarized plate-laminated waveguide slot array antenna,” 2014 International Symposium on Antennas and Propagation Conference Proceedings, Kaohsiung, 2014, pp. 13-14.

[8] T. Tomura, J. Hirokawa, T. Hirano and M. Ando, “Analysis of an x-shaped cavity-backed slot 2×2-element sub-array by hybrid MoM/FEM with numerical eigenmode basis functions,” Proceedings of the 2012 IEEE International Symposium on Antennas and Propagation, Chicago, IL, 2012, pp. 1-2.

Generation of high-quality tunable terahertz vortices based on difference frequency generation

Katsuhiko Miyamoto[1,2], Takashige Omatsu[1,2]

[1]Graduate School of Engineering, Chiba University, 1-33 Yayoi-cho, Inage-ku, Chiba 263-8522, Japan
[2]Molecular Chirality Research Center, Chiba University, 1-33 Yayoi-cho, Inage-ku, Chiba 263-8522, Japan
*corresponding author, E-mail: k-miyamoto@faculty.chiba-u.jp

Abstract

We demonstrate a high-quality tunable terahertz (THz) vortices generation based on difference frequency generation in combination with Gaussian and vortex modes. THz vortex outputs with a topological charge of $\ell_{THz} = \pm 1$ were obtained in a frequency range of 2-6 THz. The maximum average power of the THz vortex output reached up to ~3.3 μW at 4 THz.

1. Introduction

An optical vortex[1] carries an annular intensity spatial profile and an orbital angular momentum characterized by a topological charge, ℓ, which allows us to explore various research fields, including optical trapping, optical telecommunication, fabrication of structured materials[2] and super-resolution microscopy. In particular, terahertz (THz) vortex will provide new advanced spectroscopic technologies, such as 2-dimesional identification of the biomaterials with a high spatial resolution beyond the diffraction limit.

The generation of THz vortices was already demonstrated by using several optical devices based on wavefront conversion, such as a molded phase plate composed [3], and a spiral phase plate (SPP)[4,5]. However, these devices are typically designed for a specific frequency, which inherently constrains the wavelength tunability of the THz vortices.

In this presentation, we report a tunable THz vortices generation with a frequency range of 2-6 THz at a topological charge of $\ell_{THz} = \pm 1$, based on the 1.5μm optical vortex pumped difference frequency generation (DFG) from a 4'-dimethylamino-N-methyl-4-stilbazolium tosylate (DAST) crystal [6].

2. Experiments and Discussion

Figure 1 shows the experimental apparatus of a tunable THz vortex source consisting of the 1.5 μm dual-wavelength pumped DAST-DFG. A homemade picosecond laser (wavelength, 1064nm; average output power, ~5W; pulse width, 7.4ps; PRF, 1MHz) was used for a pump laser; its output was delivered to two injection-seeded optical parametric amplifiers (OPA1, 2) formed from periodically poled stoichiometric lithium tantalite (PPSLT) crystals (15 x

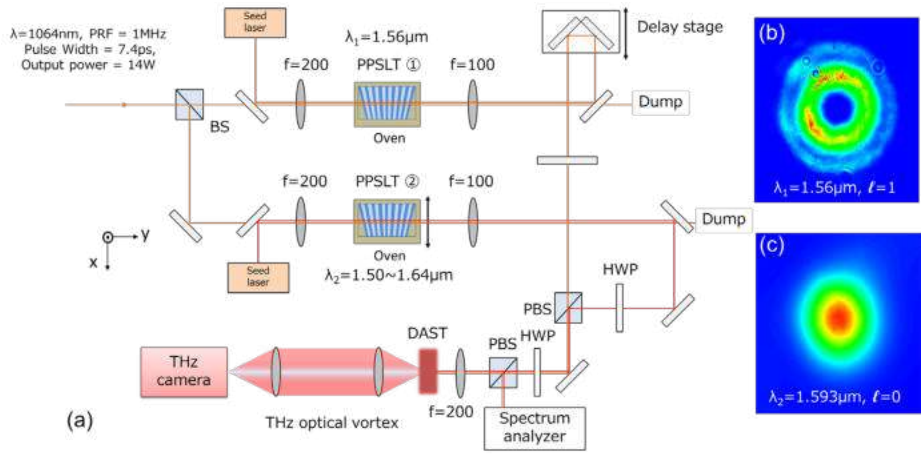

Fig.1 (a) Experimental setup for tunable THz vortex generation based on 1.5 μm dual wavelength pumped difference frequency generation in combination with a DAST crystal. (b) Spatial profile of λ_1, which was converted to an optical vortex using SPP at a topological charge of 1. Its wavelength was fixed to be 1.55μm. (c) Spatial profile of λ_2, at a wavelength of 1.583μm. Its tuning rage exhibited 1.50-1.64μm.

1 x 35mm, Λ = 29-31 μm). The OPA1 output was converted into an optical vortex (ℓ = 1) by using a SPP for 1.56 μm (Fig. 1(b)); its wavelength, λ_1, was then fixed to be 1.56 μm. The OPA2 output exhibited a Gaussian spatial form (Fig. 1(c)), and its wavelength, λ_2, was tuned within a wavelength range of 1.50-1.64 μm. The OPA1 and OPA2 outputs were then focused on to a DAST crystal, thereby generating a THz vortex output as a difference frequency mixing. The intensity distributions of the THz vortices were measured by a THz camera (NEC IRV-T0831).

Figure 2 (a) shows the frequency tunability of the THz vortices output from the optical vortex pumped DAST-DFG; the blue and red lines indicate the sign of the topological charge ℓ_{THz} = ± 1, respectively. In the case of λ_2 < 1.56 μm (λ_1 is fixed at 1.56 μm), the magnitude relation of the two pump wavelengths is switched; thus the sign of the topological charge of the THz vortices, ℓ_{THz}, is inverted according to the conservation law of the topological charge. By sweeping the wavelength of λ_2 in the range of 1.50-1.64 μm, THz vortices with positive and negative signs of the topological charge can be generated seamlessly between 2-6 THz. The THz vortex output with ℓ_{THz} = 1 is slightly lower than the negative sign (ℓ_{THz} = -1) due to the characteristic of λ_2 wavelength output spectrum. The frequency tuning range of the THz vortices output is mostly determined by the frequency tuning range of the OPA2 output. The maximum average power at the 4 THz vortex output was measured to be 3.3 μW at a 1.5 μm pump power of 1 W, corresponding to an optical-optical conversion efficiency (from 1.5 μm dual-pump output to THz vortex output) of ~3.3 x 10^{-4} %.

The experiment spatial distributions of the 4 THz vortex are summarized in Fig.3. The DFG output at the 4 THz exhibited an annular spatial profile with a topological charge of ℓ = ±1, as evidenced by a twin-lobed far-field rising to the left or right, observed by an astigmatic focusing method (Fig. 3 (c-d)). Also note that the undesired higher-order radial modes of the THz output were suppressed owing to soft-aperture effects in the DFG process.

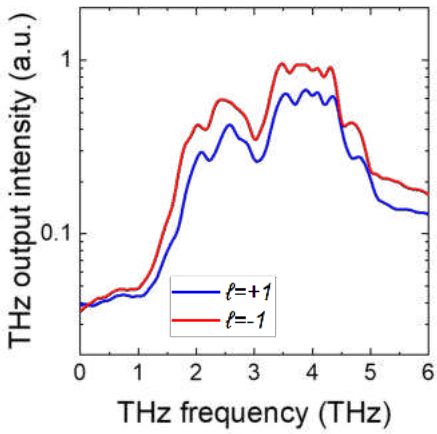

Fig. 2 Frequency tunabilities of the THz vortex output from DAST-DFG.

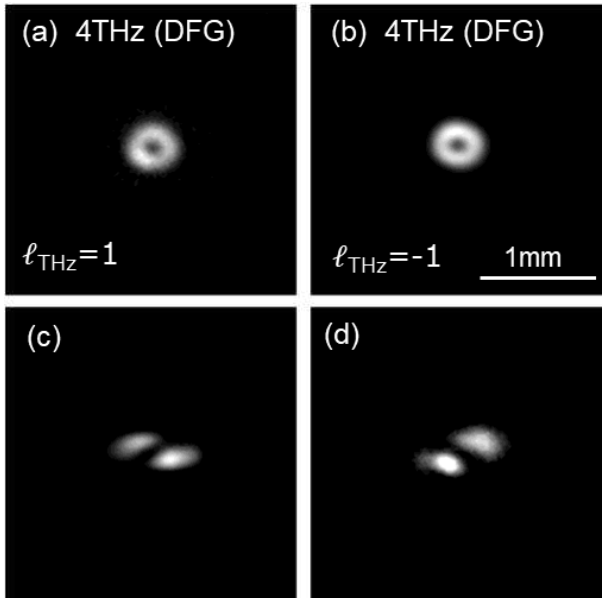

Fig. 3 Spatial distributions of the 4 THz vortex outputs focused by ((a), (b)), a conventional lens, and ((c), (d)), a tilted lens, at the topological the topological charge of ℓ_{THz} = ± 1, respectively.

3. Conclusions

We have demonstrated the generation of widely tunable THz vortices with high-quality formed of DFG of vortex and Gaussian beams. The system produced THz vortices output with ℓ_{THz} = ± 1, and continuously tuned within the frequency range of 2-6 THz. We also realized a seamless control of the sign of the THz vortices by merely sweeping the pump wavelength of λ_2.

Acknowledgements

This work was financially supported by Japan Society for the Promotion of Science, KAKENHI (JSPS-KAKENHI) Grant Number JP 19K05299.

References

[1] L. Allen, M. W. Beijersbergen, R. J. C. Spreeuw, and J. P. Woerdman, Phys. Rev. A 45(11), 8185–8189 (1992).

[2] K. Toyoda, K. Miyamoto, N. Aoki, R. Morita, and T. Omatsu, Nano Lett. 12(7), 3645–3649 (2012).

[3] J. He, X. Wang, D. Hu, J. Ye, S. Feng, Q. Kan, and Y. Zhang, Opt. Express 21(17), 20230–20239 (2013).

[4] K. Miyamoto, K. Suizu, T. Akiba, and T. Omatsu, Appl. Phys. Lett. 104(26), 261104 (2014).

[5] K. Miyamoto, B. J. Kang, W. T. Kim, Y. Sasaki, H. Niinomi, K. Suizu, F. Rotermund, and T. Omatsu, Sci. Rep. 6, 38880 (2016).

[6] K. Miyamoto, K. Sano, T. Miyakawa, H. Niinomi, K. Toyoda, A. Vallés, and T. Omatsu, Opt. Express 27(22), 31840–31849 (2019).

The physics of optical patch antennas

Antoine Moreau

Université Clermont Auvergne, CNRS, SIGMA Clermont, Institut Pascal,
F-63000 CLERMONT-FERRAND, FRANCE
*corresponding author, E-mail: antoine.moreau@uca.fr

Abstract

In the last ten years, optical patch antennas have emerged as a platform allowing for a complete control of light – from huge Purcell enhancement to wavefront control. We review here the rich physics of these antennas, ranging from plasmonic slowdown of light to the impact of nonlocality on the optical response and show that a "gap-plasmon optics" can be established, bringing a full and thorough understanding of such structures.

1. Plasmonic effects and optical patch antennas

In the past ten years, there has been a growing interest for optical patch antennas. Chemically synthesized nanoparticles can actually be used to form optical patch antennas when deposited on a metallic film[1]. Such self-assembled resonators have proven to be the tiniest optical cavities which can be realized[2], and the extreme miniaturization associated with plasmonic effects allows for an unprecedented control of the Purcell effect[3] for instance.

Optical patch antennas share a large number of properties with more classical patch antennas. They constitute resonant cavities, so that the formalism which is used to describe classical patch antennas can be applied to optical patch antennas[4]. The first and main difference between the two are plasmonics effects - the fact that the mode propagating under the patch in the case of an optical antenna is a gap-plasmon, a mode with a very high effective index because it propagates in the metal where the Poynting flux is negative[5]. Presenting such a high effective index leads to a dramatci reduction in the size of the patch, so that a $\lambda/10$ large resonator is able to support a resonance.

Such a miniturization has very important consequences. First, the Purcell effect should obvisouly be much stronger in such cavities, as has been several times proven. Then the ratio of the absorption cross-section over the geometrical cross-section reaches very high values, typically of the order of 30 – meaning only 3% of the surface needs to be covered with resonators to absorb 100% of the incoming light. Furthermore, the large cross-section, for the fundamental resonance, does almost not depend on the angle of incidence. This is very peculiar, and an interferometric model of the cavity, which is excited on both sides, allows to understand this point[6].

The large effective index of the gap-plasmons has finally a very important consequence: the resonators are so sensitive that they require an advanced description of the optical response of metals, able to take into account the fact that electrons repulse each other. Otherwise, experimental results can not be explained numerically[7, 8, 9, 10].

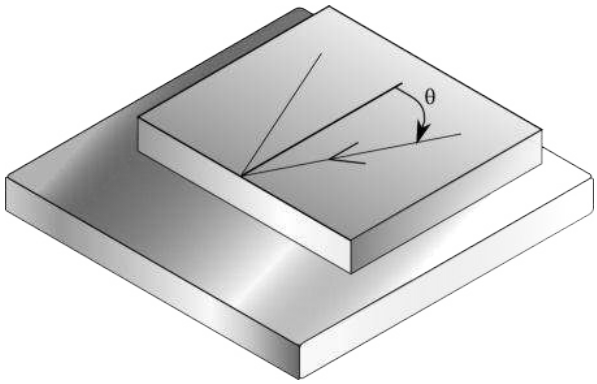

Figure 1: The incidence angle θ of the gap-plasmon propagating between the patch and the metallic film.

2. Total reflection of gap-plasmons

In order to completely understand what happens under an optical patch, we used a modal method[11] to retrieve the reflection coefficient of the gap-plasmon when the incidence angle (shown Fig. 1) is increased.

The modulus of the reflection coefficient is shown Fig. 2 and clearly shows that above a critical angle, there is a phenomenon which can be compared to total internal reflection - except for the losses. The angle θ_c for which such a response occurs is given by

$$\sin\theta_c = \frac{n_{sp}}{n_{gp}} \tag{1}$$

where n_{sp} is the effective index of the surface plasmon propagating along the metallic film, and n_{gp} is the effective index of the gap-plasmon. This shows that a gap-plasmon optics can be established – it is even possible to predict phenomenon like the Goos-Hnchen shift of the gap-plasmon total reflection.

This allows to understand the last properties of such patch antennas, like the fact that their emission can depend on the polarization for instance and how precisely their cross-section may vary with the distance between the patch

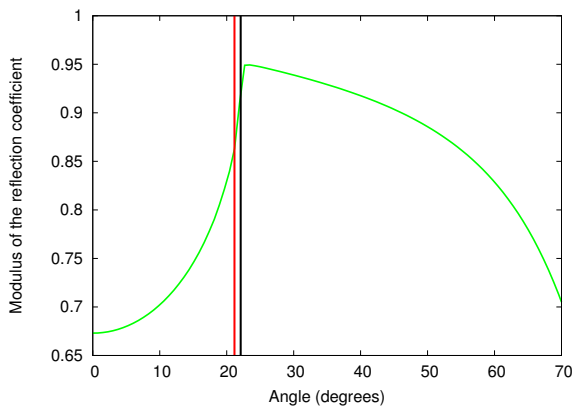

Figure 2: Modulus of the reflection coefficient of the gap-plasmon for a distance of 10 nm between the metallic film and the patch. The two vertical lines show the critical angle predicted when taking the index of air as the outside impedance (left) and the effective index of the surface plasmon (right). Definitely, the right impedance to consider is the

and the metallic film: the increase in the effective index of the gap-plasmon leads to an increase of the reflection coefficient. The patch thus forms a better cavity, which explains the increase in the cross-section. When the gap is below 5 nm however, the reflection coefficient is so high that coupling the cavity becomes difficult.

We underline in conclusion that the mechanisms which are explained here are actually not limited to such patch antennas and to the optical domain. It turns out that doped semi-conductors, in the close IR, present exactly the same kind of behaviour[12], including the sensitivity to spatial dispersion[13].

2.1. References

Acknowledgement

This work has been supported by the National Agency for Research, Project Physics of Gap-Plasmons No. ANR-13-JS10-0003 and the Académie CAP 20-25.

References

[1] A. Moreau, C. Ciracì, J. J. Mock, R. T. Hill, Q. Wang, B. J. Wiley, A. Chilkoti, and D. R. Smith, "Controlled-reflectance surfaces with film-coupled colloidal nanoantennas," *Nature*, vol. 492, no. 7427, pp. 86–89, 2012.

[2] J. J. Baumberg, J. Aizpurua, M. H. Mikkelsen, and D. R. Smith, "Extreme nanophotonics from ultrathin metallic gaps," *Nature materials*, vol. 18, no. 7, pp. 668–678, 2019.

[3] G. M. Akselrod, C. Argyropoulos, T. B. Hoang, C. Ciracì, C. Fang, J. Huang, D. R. Smith, and M. H. Mikkelsen, "Probing the mechanisms of large purcell enhancement in plasmonic nanoantennas," *Nature Photonics*, vol. 8, no. 11, p. 835, 2014.

[4] C. Ciracı, J. B. Lassiter, A. Moreau, and D. R. Smith, "Quasi-analytic study of scattering from optical plasmonic patch antennas," *Journal of Applied Physics*, vol. 114, p. 163108, 2013.

[5] R. Ajib, A. Pitelet, R. Pollès, E. Centeno, Z. Ajaltouni, and A. Moreau, "The energy point of view in plasmonics," *JOSA B*, vol. 36, no. 4, pp. 1150–1154, 2019.

[6] C. Lemaître, E. Centeno, and A. Moreau, "Interferometric control of the absorption in optical patch antennas," *Scientific Reports*, vol. 7, p. 2941, 2017.

[7] A. Moreau, C. Ciracì, and D. R. Smith, "Impact of nonlocal response on metallodielectric multilayers and optical patch antennas," *Physical Review B*, vol. 87, no. 4, p. 045401, 2013.

[8] A. Pitelet, E. Mallet, R. Ajib, C. Lemaître, E. Centeno, and A. Moreau, "Plasmonic enhancement of spatial dispersion effects in prism coupler experiments," *Physical Review B*, vol. 98, no. 12, p. 125418, 2018.

[9] C. A. Reynaud, D. Duché, J. Le Rouzo, A. Nasser, L. Nony, F. Pourcin, O. Margeat, J. Ackermann, G. Berginc, C. A. Nijhuis *et al.*, "Enhancing reproducibility and nonlocal effects in film-coupled nanoantennas," *Advanced Optical Materials*, vol. 6, no. 23, p. 1801177, 2018.

[10] A. Pitelet, N. Schmitt, D. Loukrezis, C. Scheid, H. De Gersem, C. Ciracì, E. Centeno, and A. Moreau, "Influence of spatial dispersion on surface plasmons, nanoparticles, and grating couplers," *JOSA B*, vol. 36, no. 11, pp. 2989–2999, 2019.

[11] G. Granet, "Reformulation of the lamellar grating problem through the concept of adaptive spatial resolution," *JOSA A*, vol. 16, no. 10, pp. 2510–2516, 1999.

[12] F. Omeis, R. Smaali, F. Gonzalez-Posada, L. Cerutti, T. Taliercio, and E. Centeno, "Metal-insulator-metal antennas in the far-infrared range based on highly doped inassb," *Applied Physics Letters*, vol. 111, no. 12, p. 121108, 2017.

[13] J. R. Maack, N. A. Mortensen, and M. Wubs, "Size-dependent nonlocal effects in plasmonic semiconductor particles," *EPL (Europhysics Letters)*, vol. 119, no. 1, p. 17003, 2017.

Phase control of THz-wave in multi-port waveguide structure coupled with bull's-eye antenna

Seigo Ohno*[1,2,3]

[1] Department of Physics, Graduate School of Science, Tohoku University, Sendai, Japan
[2] Division for the Establishment of Frontier Sciences, Organization for Advanced Studies, Tohoku University, Sendai, Japan
[3] Tera-Photonics Research Team, RIKEN Center for Advanced Photonics (RAP), RIKEN, Sendai, Japan
E-mail: seigo@tohoku.ac.jp

Abstract

We have analytically and numerically investigated phase control feature of terahertz wave in a waveguide structure coupled with a bull's-eye antenna via polarization state incident to the bull's-eye antenna. In this presentation, we will introduce the theoretical extension to the multiport waveguide aligned in parallel nearby the tiny hole of the bull's-eye antenna and show some numerical results.

1. Introduction

A terahertz (THz) wave has been attracted as a candidate of the carrier wave for wireless communications in the next generation with increasing the communication traffic. We have focused on a structure consists of a waveguide coupled with a bull's-eye antenna with bearing in mind the importance between collection of propagating waves in the air and the processing circuits. It was analytically and numerically turned out that, in such structure, the phase of the propagating wave in the waveguide can be controlled by the polarization direction of the incident wave to the bull's-eye antenna [1]. Furthermore, the propagation direction in the waveguide can be switched by the rotation direction of elliptically polarized wave incident to the antenna. This directional switching phenomenon can be understood as a similar one with the optical spin-momentum locking phenomenon discussed in the optical region [2,3].
In this presentation, we will introduce the extension of our analytical model to the multi-port waveguide and show its numerical results.

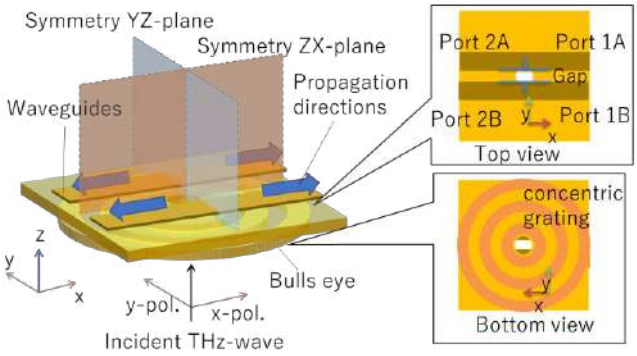

Figure 1: Concept of considering system.

2. Concept of system

Our conceptual system of waveguides coupled with a bull's-eye antenna is shown in Fig. 1. The bull's-eye antenna consists of a subwavelength scale hole and surrounding concentric grating is putted on a bottom of a metal substrate. Two parallel micro-strip waveguides are symmetrically aligned across the backside hole with a small gap. A THz wave normally incident to the bull's eye antenna is collected by the antenna and is focused to the center hole. Then the wave propagates to the back side of the substrate passing through the hole. When the hole is sufficiently close to the micro-strip and sufficiently smaller than the waveguide mode distribution on the micro-strip, the wave passing thorough the hall can couple to the each microstrip and the waves propagate to the ports labeled 1A, 1B, 2A, and 2B.

Here we consider the parity of the propagating mode depending on the polarization of the incident wave. When the polarization direction is x-direction, the parity of the propagating wave between the ports 1 and 2 is odd and that between A and B is even. In the y-polarized case, even and odd parities are respectively obtained between 1 and 2 and between A and B. This means there is phase controllability not only between 1 and 2, but also A and B when the polarization direction is changed as shown in our previous work [1].

In our presentation, we will show the analytical expression and numerical results.

Acknowledgements

The author would like to thank Dr. H. Minamide, Dr. Y. Tokizane, and Dr. Y. Takida in RIKEN, Prof. J. Shikata in Nihon University, and Prof. Y. Kanamori and Dr. T. Okatani in Tohoku university for their fruitful and constructive discussion.
This work was partly supported by JST A-STEP (JPMJTM20JX) and RIKEN Science and Technology Hub Collaborative Research Program.

References

[1] S. Ohno, Y. Tokizane, J. Shikata, H. Minamide, Phase and Direction Control of a Terahertz-Wave Propagating in a Waveguide Coupled with a Bull's-eye Structure, *URSI Radio Science Letters* 2: 1-4, 2020.

[2] J. Petersen, J. Volz, A. Rauschenbeutel, Chiral Nanophotonic Waveguide Interface Based on Spin-Orbit Interaction of Light, *Science* 346: 6205, 67-71, 2014.

[3] M. F. Picardi, A. V. Zayats, J. Rodríguez-Fortuño, Janus and Huygens Dipoles: Near-Field Directionality Beyond Spin-Momentum Locking, *Physical Review Letters* 120: 11, 117402, 2018.

Non Conventional Reflectarray and Transmitarray Configurations for Next Generation Applications

Paola Pirinoli

Department of Electronics and Telecommunications,
Politecnico di Torino, Torino, Italy
E-mail: paola.pirinoli@polito.it

Abstract

Reflectarrays (RAs) and transmitarrays (TAs) represent an efficient alternative to reflectors and arrays as high-gain antennas, since they posses nice features making them potentially suitable for several different applications. In view of these, some non-conventional, dielectric-only RA and TA configurations are here discussed.

1. Introduction

The next generation of wireless communication networks are demanded to offer and to support services such as virtual and augmented reality, portable video streaming, Internet of Things and on move communication, that also affect the radiating sub-system, and for this reason many effort are spending to face the challenge of designing innovative antenna configurations suitable for obtaining the required features. Among the different possible solutions, there are also those based on the use of Reflectarray (RA) [1, 2] or Transmitarray (TA) [3] technologies: they have been extensively studied, to develop configurations showing features as a broad-band behaviour [4, 5] and beam-scanning capabilities [6]. From the technological point of view, different solutions are considered, with the aim of improving the antenna performance, keeping as low as possible its complexity and the manufacturing cost. For this reason, the design of metal-only [7] or a completely dielectric structure [5, 9] are recently considered. In particular, this last solution gained interest since antennas of this type can be manufactured with 3D printing techniques, that allow to realize non-conventional shapes with a reduced cost. In the following, some recent results relatively to dielectric-only RAs and TAs designed to provide wide bandwidth, high efficiency and beam scanning capabilities, are discussed.

2. Dielectric-only RAs and TAs

In the following, two Additive Manufacturing (AM) techniques are addressed for the realization of RAs and TAs: the PolyJet and the FDM ones. The first one guarantees good resolution, important to manufacture structures at high frequencies, as the Ka-band considered here, but the material suitable for this type of 3D printers are characterized by rather high losses and low relative constant. The accuracy provided by FDM techniques depends on the size of the adopted nozzle, but in any case is lower; as a counter part, FDM-based printers can also work with materials showing lower losses and higher value of their relative dielectric constant.

Table 1: Performance of three different dielectric-only antenna configurations.

structure	thickness	max. Gain [dBi]	1-dB BW [%]	aperture efficiency [%]
TA unit-cell [8]	3.3 λ_0	30.7	21.5	38.6
RA unit-cell [10]	0.8 λ_0	31.3	24.5	39.3
RA unit-cell [11]	0.31 λ_0	31.9	15.4	54.5
TA unit-cell: 2 cylinders + square base	0.74 λ_0	32.0	16	51.6

Four different antennas are discussed here, two of which (a transmittaray and a reflectarray) are realized with PolyJet technique, using a material characterized by $\varepsilon_r = 2.77$ and $\tan\delta = 0.021$ at $f_0 = 30\,\text{GHz}$ while the unit-cell consists in a dielectric layer with a central square hole [10], eventually located between other two layers, presenting a pyramidal hole, acting as matching circuits and adopted to increase the bandwidth of the TA [8]. Both the antennas have an aperture size of $15.6\lambda \times 15.6\lambda$, at the design frequency $f_0 = 30\,\text{GHz}$; as it appears from the first two rows the data summarized in Table 1, the low value of ε_r forces to increase the thickness of the unit-cell, to reach good performance. The other two configurations are still a reflectarray and a transmitarray, both with size $15\lambda \times 15\lambda$ at f_0, designed to be manufactured with FDM technique, using a dielectric material with $\varepsilon_r = 10$ and $\tan\delta = 0.004$ [11]. Thanks to the high value of ε_r, the unit-cell, that consists in a cylindrical resonator over a square base in the case of the RA, while for the TA another cylinder is added on the other side of the base, is much thin, as it emerges from the first column and the rows 3, 4 of Table 1.

2.1. Bandwidth and efficiency

As it is shown from the data summarized in Table 1, all the four considered antennas are characterized by a wide band-

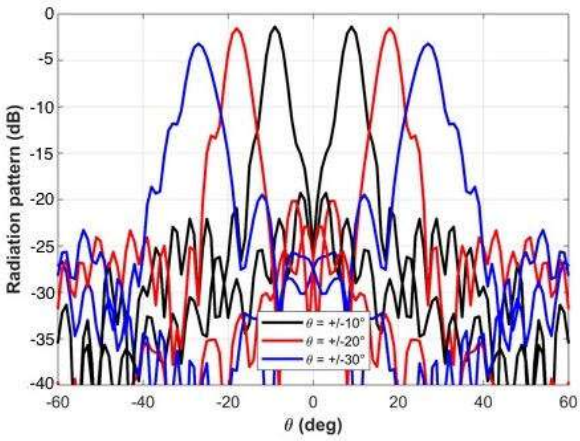

Figure 1: Radiation pattern of a beam-scanning RA, designed using the unit-cell in [10].

width and good efficiency. In particular, the RA and the TA manufactured with the PolyJet printer have a very large bandwidth, compensated by a lower efficiency. The other RA and TA have a smaller bandwidth, even though significantly larger than that obtained with more conventional configurations, but are characterized by two features that make them particularly attractive for many applications, i.e. their extremely reduced thickness, some flexibility that can be exploited especially in case of RAs, if it is convenient to mount them on a curved surface, and the efficiency, higher than $50\,\%$.

2.2. Beam-scanning capabilities

To reduce the complexity and the cost of beam-scanning RAs and TAs, a configuration in which the active part is just limited to the feed, keeping the reflecting/transmitting surface passive is more convenient. To improve the antenna performance, two aspects must be considered. The first one is the use of a proper unit-cell, as low as possible sensible to the direction of arrival of the field radiated by the feed: this improves the performance of the antenna, since it contributes to keep it constant over a large scanning range. An example of such a unit-cell is that introduced in [10], that is used to design a RA, in which the beam scanning is obtained changing the position of the feed. The obtained radiation patterns are plotted in Fig. 1: they stay almost the same over the entire scanning range, with a reduction of the maximum gain no larger than 1.8 dB. The steering beam capabilities of a passive RA or TA can be further enhanced through a suitable approach for their design; as described in [2] a possible solution is that of designing a non-parabolic phase aperture, as for instance a bifocal one: in this case, the antenna performance increase in proximity of the maximum scan angle, but at a cost of its degradation near the central direction of maximum radiation. To overcome this drawback, the use of a suitable optimization technique can be adopted [12].

3. Conclusions

Innovative solutions for the design and manufacturing of dielectric-only transmitarrays and reflectarrays are introduced, discussing their main advantages and drawbacks. Further results will be shown at the Conference.

Acknowledgement

The author thanks dr. Massaccesi for his central activity.

References

[1] J. Huang and J. A. Encinar, *Reflectarray Antennas, Hoboken*, NJ: John Wiley & Sons, 2007.

[2] P. Nayeri, F. Yang and A.Z. Elsherbeni, *Reflectarray Antennas: Theory, Designs, and Applications*, Hoboken, NJ: John Wiley & Sons, 2017.

[3] A.H. Abdelrahman et al., *Analysis and Design of Transmitarray Antennas*, Morgan & Claypool, 2017.

[4] J.A. Encinar and J.A. Zornoza, Broadband design of three-layer printed reflectarrays, *IEEE Trans. Antennas Propag.*, vol. 51, 2003.

[5] A. Massaccesi et al., 3D-printable dielectric transmitarray with enhanced bandwidth at millimeter-waves, *IEEE Access*, vol. 6, 2018.

[6] P. Nayeri, F. Yang, and A.Z. Elsherbeni, Beam-scanning reflectarray antennas: a technical overview and state of the art, *IEEE Antennas Propag. Mag.*, vol. 57, 2015.

[7] K.Q. Henderson and N. Ghalichechian, Circular-polarized metal-Only reflectarray with multi-slot elements, *IEEE Trans. Antennas Propag.*, vol. 68, 2020.

[8] A. Massaccesi et al., 3D-printable dielectric transmitarray with enhanced bandwidth at millimeter-waves, *IEEE Access*, vol. 6, 2018.

[9] B. Li, et al., A 3-D-printed wideband circularly polarized dielectric reflectarray of cross-shaped element, *IEEE Antennas Wirel. Propag. Lett.*, vol. 19, 2020.

[10] A. Massaccesi, M. Beccaria and P. Pirinoli, 3D-printable perforated dielectric reflectarray in Ka-band, *Proc. 2019 IEEE Int. Symp. Antennas Propag. and USNC-URSI Meeting*, Atlanta, GA, USA, 2019.

[11] A. Massaccesi, M. Beccaria and P. Pirinoli, High-efficiency Reflectarray Using Dielectric Resonator Elements, *Proc. 2021 IEEE Int. Symp. Antennas Propag. and USNC-URSI Meeting*, Singapore, 2021.

[12] A. Niccolai et al., Social Network Optimization Based Procedure for Beam-Scanning Reflectarray Antenna Design, *IEEE Open J. Antennas Propag.*, vol. 1, 2020.

THz transmission for fixed wireless services under severe weather conditions

Tetsuya Kawanishi

Faculty of Science and Engineering
Waseda University
Tokyo, Japan
kawanishi@waseda.jp

Abstract

Terahertz band systems are expected to be a means of achieving short-range, high-speed communications. However, there are concerns about the effects of rain attenuation and wind-induced vibration, and ensuring performance in adverse weather conditions is an issue. In this presentation, a link budget model of terahertz band fixed wireless systems under storm conditions will be presented and the feasibility of a highly stable system will be discussed.

Status and progress of millimeter-wave GaN transistors for next generation high-power radar systems

Kathia Harrouche[1], Sri Saran Vankatachalam[1], Elodie Carneiro[1], François Grandpierron[1], Farid Medjdoub[1*]

[1] CNRS-IEMN Institut d'Electronique, de Microélectronique et de Nanotechnologie, Lille, France
*corresponding author, E-mail: farid.medjdoub@univ-lille.fr

Abstract

With the development of wireless communication such as 5G or SATCOM, the need and requirements for millimeter-wave compact solid-state high power amplification has significantly increased. In this frame, high power densities have been demonstrated with GaN transistors up to the W-band, confirming the potential of this material system. However, achieving high power-added-efficiency (PAE) and output-power-density combination in the millimeter-wave range represents currently one of the key goal for the GaN technology despite some few initial results obtained so far. Indeed, higher PAE not only saves electrical power usage but also can reduce the size and cost of high power amplifiers (HPAs), due to the lower amount of heat dissipated. For instance, in space applications, the traveling wave tube amplifiers (TWTA) are still widely used, because of the high PAE while delivering high P_{OUT}. Even though attractive efficiencies on GaN devices (well-beyond 40%) have been already demonstrated up to Ka band, rather limited PAE has been reported so far in the Q band (40 GHz) and above. Furthermore, the device robustness and related reliability under high electric field ($V_{DS} \geq 20$ V) have not been yet demonstrated on ultrashort GaN power devices (sub-10 nm barrier thickness and sub-150 nm gate lengths). Actually, a number of parameters can be responsible for short GaN device degradation such as the gate leakage current, especially when using Al-rich ultrathin barriers, a poor electron confinement resulting in drain leakage current, the so-called current collapse and the self-heating due to a reduced thermal dissipation.

In this presentation, we will discuss some potential device design enabling to overcome the above-mentioned issues and properly operate in the millimeter-wave range under high drain bias > 20 V with high performance.

Gain and Efficiency Enhancement of mm-Wave On-Chip Antennas Through Artificial Magnetic Conductors

Atif Shamim

Electrical and Computer Engineering Program, King Abdullah University of Science and Technology (KAUST), KSA
corresponding author, E-mail: atif.shamim@kaust.edu.sa

Abstract

The emerging applications at millimeter wave frequencies have helped to achieve true System-on-Chip solutions by bringing the antennas on the Integrated Circuits (ICs that are also commonly known as chips). This is because the antenna sizes at these frequencies are small enough for practical on-chip realization. Though, there are a number of benefits of putting an antenna-on-chip (AoC), such as monolithic integration resulting in compact systems, and lower cost due to mass manufacturing in standard CMOS processes, etc, the major issue is dealing with silicon substrate's high conductivity and permittivity (resulting in poor radiation efficiency). Many off-chip techniques have been shown, such as etching the silicon substrate underneath the antenna, enhancing the resistivity of the substrate, and integrating a superstrate or lens, but all these techniques add processing steps, and eventually the cost of realization. A promising approach is to realize Artificial Magnetic Conductors (AMC) underneath the AoC to provide isolation from the lossy Si substrate as well as have in-phase reflections from the AMC. This talk describes AMC design steps in an on-chip environment and shows how it can be used to boost AoC radiation performance. Further, it also shows innovative techniques for AMC thickness reduction to make it more suitable with the traditional CMOS stack-ups.

Conformal Leaky-Wave Antennas for Terahertz Wireless Links

Hichem Guerboukha, Rabi Shrestha, Joshua Neronha,
Zhaoji Fang, and Daniel M. Mittleman*

School of Engineering, Brown University, Providence RI USA
*corresponding author, E-mail: daniel_mittleman@brown.edu

Abstract

We explore the performance of curved leaky-wave antennas in the terahertz range. We identify two distinct regimes in which the far-field emission pattern varies relative to that of a planar antenna. We show that a curved multi-aperture leaky-wave antenna can be used for agile far-field beam forming, and demonstrate high-gain wireless links at gigabit-per-second data rate with low bit error rate, in multiple directions simultaneously. This work lays the foundation for the implementation of terahertz leaky-wave structures in conformal geometries.

Novel resonant-tunneling-diode terahertz oscillators and applications

Safumi Suzuki[1]

[1]Department of Electrical and Electronic Engineering, Tokyo Institute of Technology, Tokyo, Japan
*corresponding author, E-mail: suzuki.s.av@m.titech.ac.jp

Abstract

The recent progress in resonant-tunneling diode (RTD) THz oscillators and applications is reviewed. For high-frequency and high output power, RTD oscillators integrated with cylindrical and rectangular cavities have been developed. Structure simplified RTD oscillators for easy device fabrication and good uniformity were proposed and fabricated. This simple structure has an extensibility for large-scale array, active metamaterial, and beam forming function. Novel THz radar systems using RTD oscillators were proposed, and a precise distance measurement and a three-dimensional imaging were demonstrated.

RFiD antennas/sensors and systems

Statistical Analysis of Matching Properties of Randomly Distributed Thin and Thick Dipoles

Imad Adjali[1], Benoit Poussot[1], Shermila Mostarshedi[1*], and Jean-Marc Laheurte[1]

[1]ESYCOM, Université Gustave Eiffel, CNRS UMR 9007, F-77454 Marne-la-Vallée, France
* E-mail: shermila.mostarshedi@univ-eiffel.fr

Abstract

A statistical analysis of the matching properties of a dipole surrounded by thin and thick randomly distributed loaded dipoles is presented. The input impedance and input reflection coefficient of the driven dipole is obtained by using the IEMF method and validated by NEC and measurements. The cumulative distributed functions are presented for different dipole densities and the mismatch of a surrounded thin or thick dipole is studied for different surrounding loads.

1. Introduction

UHF RFID (Radio Frequency IDentification) technologies are used for tracking and identification of objects and persons. In some applications, such as tracking in laundry, the density of RFID tags is high and this may give rise to an important electromagnetic coupling between tag antennas which modifies antenna's parameters, i.e. matching properties and radiation pattern. These electromagnetic modifications can alter and degrade the communication links between devices. Despite an initial description of the mutual coupling between RFID tags [1], the statistical modelling of the impact of the mutual coupling for high densities of RFID tags is still a new topic.

Following a series of previous publications [2] and [3], we model a set of randomly distributed tags by dipole-like antennas and we extract a statistical estimation of the behaviour of the straight dipoles in a randomly distributed set. In this paper, we will compare the statistical behaviour of thin and thick dipoles according to their mismatch properties. The electromagnetic coupling between thin dipoles can be easily modelled by IEMF method (Induced ElectroMotive Force) while a rigorous numerical simulation or measurement is time consuming for thick dipoles. The idea is to show that the rate of mismatch of realistic dipoles in a random set with a given density, can be estimated by the thin dipoles in the same set.

2. Simulation and measurement

The advantage of IEMF method [4] is its simplicity and reduced calculation time, the drawback is that this method gives accurate results only for thin dipoles (diameter less than 10^{-3} λ). As the aim of this paper is to make a statistical assessment of the mismatch behaviour of dipoles, the IEMF method is a good candidate to produce a rich database. If the statistical behaviour of thick dipoles are similar to that of the thin dipoles, then IEMF applied to thin dipoles would become the reference method. In order to prove this concept, some extra steps are necessary. Due to limited precision of IEMF for thick dipoles, we use NEC which is a numerical electromagnetic simulator based on MoM. The IEMF results are thus compared with NEC results for thin dipoles and NEC results are compared to measurements for thick dipoles.

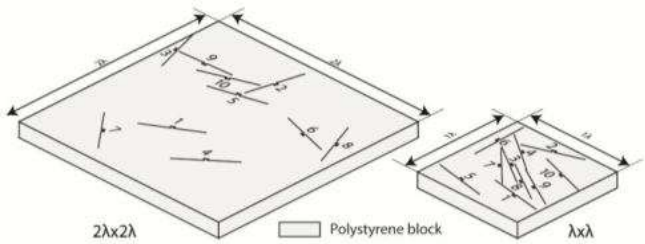

Figure 1: Set of randomly distributed dipoles on a polystyrene block of 2λ×2λ and λ×λ.

First the input impedance of an isolated thick dipole is measured. Then in a given set of randomly distributed dipoles, the input impedance of a driven dipole is measured while others are short-circuited. The thick dipoles are made of copper wires of length 17 cm (≃0.5 λ) and diameter 1 mm (≃3×10^{-3} λ). The set of dipoles are fixed in a block of polystyrene (Figure 1). The driven dipole is fed with a differential probe using a 2-port VNA.

Figure 2 presents the real and imaginary parts of the input impedance of an isolated dipole as a function of the frequency. NEC results for both thin and thick dipoles are in excellent agreement with IEMF and measurements, respectively. Figure 3 shows the input impedance of dipole no.1 in the highest distribution density λ×λ. The input impedance of surrounded dipoles deviates from that of an isolated dipole and the perturbation is globally more important in the highest density configuration but highly depends on the position of the driven antenna with respect to the others. As these given configurations are two examples among an infinite number of distribution possibilities, the mismatch of a surrounded dipole should be quantified statistically by taking into account an important

number of distribution profiles. Given the important number of samples, the results are only based on simulations.

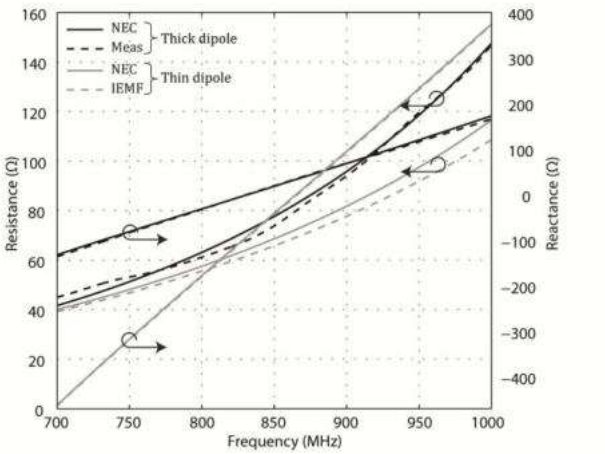

Figure 2: Input impedance of an isolated thin and thick dipole.

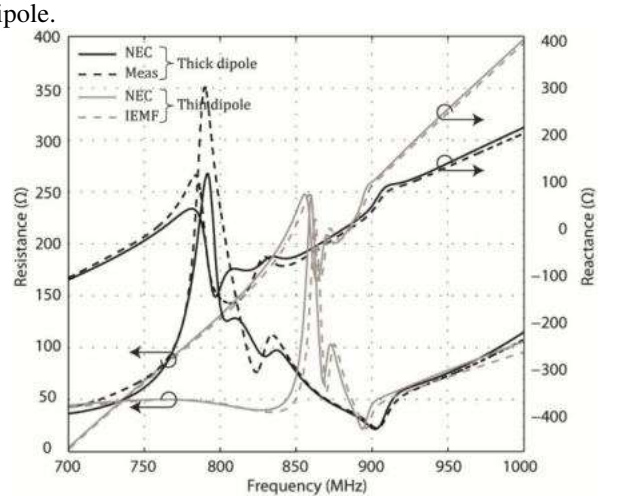

Figure 3: Input impedance of dipole no.1 in λ×λ distribution area.

3. Statistical analysis

In order to statistically assess the mismatch of a surrounded dipole in different random configurations, the reflection coefficient for the ith surrounded dipole is defined by: $\Gamma_{\text{in}\,i} = (Z_{\text{in}\,i} - Z^*_{\text{ref}})/(Z_{\text{in}\,i} + Z_{\text{ref}})$ where the reference impedance Z_{ref} is the complex conjugate of the self-impedance of an isolated dipole at the working frequency (892 MHz). The experimental data include 200 random configurations of 10 dipoles. The input reflection coefficient (Γ_{in}) for each dipole has been calculated when all others are either short-circuited or matched. The cumulative distribution functions (CDF) for the magnitude of the input reflection coefficient in dB are presented in Figure 4. For the two different loads, there is an excellent agreement between the CDF obtained by IEMF and NEC for thin and thick dipoles. This happens while the self or input impedance of an isolated or surrounded thin and thick dipole is different. Still the statistical behaviours of the two dipoles are very similar to each other and thus the amount of mismatch of thick dipoles for a given distribution density can be estimated by thin dipoles. By fixing a threshold for $|\Gamma_{\text{in}}|$, the percentage of dipoles having a smaller reflection coefficient can be estimated for both densities and terminating loads. Table 1 summarizes these results.

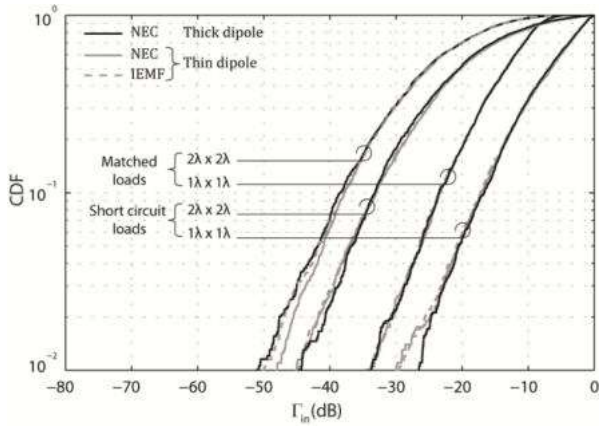

Figure 4: CDF of $|\Gamma_{\text{in}\,i}|$ of a dipole, surrounded by short-circuited or matched dipoles

Table 1: Percentage of matched dipoles.

Threshold	$\lvert\Gamma_{\text{in}}\rvert = -10$ dB		$\lvert\Gamma_{\text{in}}\rvert = -15$ dB	
Load	**Short**	**Matched**	**Short**	**Matched**
2λ×2λ	85%	96%	70%	87%
λ×λ	33%	77%	14%	40%

4. Conclusions

The behaviour of thin and thick dipoles, according to their matching properties, in a randomly distributed set is estimated and compared to each other. The results show that the realistic thick dipoles can be faithfully represented by thin dipoles when the goal is to have a global estimation of their behaviour and not the mismatch of one dipole in a particular configuration. In on-going works, our approach is extended to statistically assess the radiation pattern distortions of surrounded dipoles.

References

[1] G. Marrocco, RFID grids: Part I—Electromagnetic theory, *IEEE Transactions on Antennas and Propagation*, vol. 59, no. 3, pp. 1019-1026, 2011.

[2] I. Adjali, A. Gueye, B. Poussot, S. Mostarshedi, F. Nadal, J.-M. Laheurte, Statistical study of coupling in randomly distributed dipole sets," 12th European Conference on Antennas and Propagation (EuCAP), London, 2018.

[3] I. Adjali, A. Gueye, S. Mostarshedi, B. Poussot, F. Nadal, J.-M. Laheurte, Matching Evaluation of Highly Coupled Dipoles Quantified by a Statistical Approach, *IEEE Transactions on Antennas and Propagation*, vol. 68, no. unassigned, to be published in 2020.

[4] H. Baker, A. LaGrone, Digital computation of the mutual impedance between thin dipoles, *IRE Transactions on Antennas and Propagation*, vol. 10, no. 2, pp. 172-178, 1962.

RFID-UHF Tag Antenna for e-Healthcare Applications

Mohamed EL Khamllichi[1,2], Alejandro Alvarez Melcon[2], Mohamed-Ali Ennasar[3], Otman EL Mrabet[1], and Juan Hinojosa[2]

[1]System of Information and Telecommunications Laboratory (LaSIT), Faculty of Science, Abdelmalek Essaadi University, Tétouan 93000, Morocco
[2]Department of Information and Communications Technology, Universidad Politécnica de Cartagena, Plaza del Hospital nº. 1, 30202 Cartagena, Spain
3National Higher School of IT (ENSIAS), Rabat, Morocco
*Otman EL Mrabet, E-mail: o.elmrabet@uae.ac.ma

Abstract

This paper presents a novel low-cost and flexible passive RFID tag antenna for blood monitoring and tracking, which is in great demand by e-healthcare applications. The tag antenna consists of two compact symmetrical capacitive structures and works at the ultra-high frequency (UHF) European band (865 MHz–868 MHz). Measurement results show that the proposed design has a read range of 2.2 m, which is 4.4 times higher than commercial RFID tag antennas.

1. Introduction

Radio frequency identification (RFID) technology is rapidly developing and is becoming very important for monitoring and tracking applications [1,2,3]. Common applications with this technology include security identification, retail item management, access control, and tracking. Therefore, RFID technology has been found to be of great help in the healthcare sector and, especially for blood management in medical centers [4,5]. It may have some benefits with regards to optical technologies, such as quick response codes (QR) and barcodes [6], since it is possible to increase the automation level of stock, identification, tracking and monitoring tasks and, therefore, reduce possible human intervention errors. Passive tags working at the ultra-high frequency (UHF) European band (865 MHz–868 MHz) can be used for this type of applications. In this paper, a novel compact, low profile and flexible UHF RFID tag antenna for blood tubes tracking and monitoring is presented. While most of commercially available tags are based on inductive designs using the T-match technique, the proposed tag antenna consists of two compact coupled capacitive meandered structures. Due to the high relative permittivity value of the blood, inductive designs tend to have smaller sizes, leading to extra drop in the efficiency of the antenna. On the contrary, the proposed capacitive design exhibits reasonable size for the tube, and it represents a good compromise between compactness and radiation efficiency. In addition, the capacitive tag also presents higher sensitivity to the presence of blood. Thanks to this behavior, the reading range is increased when the tag antenna is attached to a clinic tube full of blood, while the reading range drastically drops when the tube is empty. The designed tag antenna covers the UHF band, and it is fabricated by using a DuPontTM Kapton polyimide film) [7]. It is expected that the development of this new tag will open new exciting perspectives in the design of future UHF RFID traceability systems for blood monitoring applications.

2. Proposed RFID tag antenna

The structure of the proposed design is depicted in Fig. 1. The tag consists of two symmetrical capacitive pads with two etched meandered substrate arms. Both pads are separated at the center by means of two different gaps s and g, which are placed at the left and right sides, respectively. The IC chip (NXP UCODE G2XL) is mounted across the gap s between the two pads, while the gap g is used to introduce a capacitive behavior to the tag antenna. The structure of the dipole antenna is meandered to achieve a compact design. Due to the good flexibility of the Kapton polyimide, the tag antenna can be easily conformed to the curved shape of the blood tube. The optimized geometrical parameters obtained by using CST Microwave studio are listed in Table. 1.

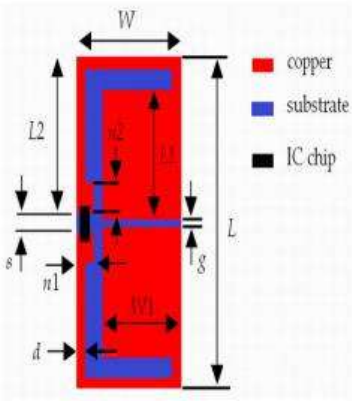

Figure 1: Schematic view of the proposed RFID tag antenna.

TABLE I
DIMENSIONS OF RFID TAG ANTENNA

Parameter	Value (mm)	Parameter	Value (mm)
L	49.5	*s*	5
W	15	*g*	2.25
*L*1	18.75	*n*1	5
*W*1	8.5	*n*2	3.5
*L*2	18.25	*d*	2

3. Results and discussion

Here, we will present only the results of the reading range which is a critical parameter that determines the performance of an RFID tag antenna. The simulated and measured reading ranges obtained for the proposed tag attached to a tube in the frequency range from 0.8 GHz and 0.9 GHz are shown in Fig.2. The measurements include the results obtained for the smallest and largest tube standards manufactured by the Becton Dickinson (BD) Company. It can be observed that the measurements are in good agreement with predictions. The measured reading range reaches a peak value of 2.2 m at the frequency of 867 MHz when the tag is attached to the smallest size tube full of blood, while the largest size tube has a peak value of 2.3 m at 860 MHz. At 867 MHz, the largest size tube presents a reading range of 2.25 m, which is similar to the measured value (2.2 m) for the smallest size tube. For both tube sizes, the reading ranges drastically decrease when the tubes are empty.

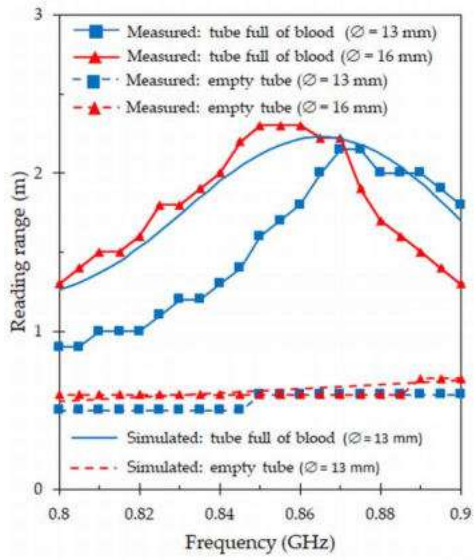

Figure 2: Simulated and measured reading ranges

This confirms that the proposed design can be applied to different tube standards, and that it is possible to detect the tag at reasonable distances when the tube is full of blood. In addition, in both cases the reading range drastically reduces for empty tubes.

4. Conclusions

In this work, a novel compact and high-performance tag antenna for blood tube traceability applications, working at the European RFID UHF system, is proposed. The proposed tag is based on a capacitive dipole design, which consists of two coupled compact capacitive meandered pads. Results have demonstrated that the new tag attached to a clinic tube full of blood exhibits reading ranges above 2 m. Moreover, its capacitive design has shown a strong sensitivity with the presence of the blood inside the tube. Therefore, reading ranges drastically drop when the tube is empty. This property may be interesting for many tracking applications, since it could reduce the amount of information generated from empty tubes.

Acknowledgements

The authors gratefully acknowledge financial support from Ministerio de Economía y Competitividad of Spain and the European Regional Development Funds for the financial support (grant no. TEC2016-75934-C04-4-R).

References

[1] Finkenzeller, K. RFID Handbook: Fundamentals and Applications in Contacless Smart Cards, Radio Frequency Identification and Near-Field Communication, 3rd ed.; John Wiley & Sons: Hoboken, NJ, USA, 2010.

[2] Rao, K.V.S.; Nikitin, V.; Lam, S. F. Antenna design for UHF RFID tags: a review and a practical application. *IEEE Trans. Antennas Propag., 53*, 3870-3876, 2005.

[3] Zhu, X.; Mukhopadhyay, S.K.; Kurata, H. A review of RFID technology and its managerial applications in different industries. *J. Eng. Technol. Manage.*, 29, 152-167, 2012.

[4] Zhang, J.; Tian, G.Y.; Marindra, A.M.; Sunny, A.I.; Zhao, A.B. A review of passive RFID tag antenna-based sensors and systems for structural health monitoring applications. *Sensors* **2017**, *17*, 265.

[5] Hohberger, C.; Davis, R.; Briggs, L.; Gutierrez, A.; Veeramani, D. Applying radio-frequency identification (RFID) technology in transfusion medicine. *Biologicals* **2012**, *40*, 209-213.

[6] Álvarez López, Y.; Franssen, J.; Álvarez Narciandi, G.; Pagnozzi, J.; González-Pinto Arrillaga, I.; Las-Heras Andrés, F. RFID Technology for management and tracking: e-health applications. Sensors 2018, 18, 2663.

[7] Ghodgaonkar, D.K.; Varadan, V.V.; Varadan, V.K. Free-space measurement of complex permittivity and complex permeability of magnetic materials at microwave frequencies. *IEEE Trans. Instrum. Meas.* **1990**, *39*, 387-394.

Radar Cross Section estimation of a set of randomly distributed dipoles as an application to RFID in a high density context

Aiman Mughal*, **Jithin Mudakkarappilli Sudersanan***, **Shermila Mostarshedi, Benoit Poussot, Jean-Marc Laheurte**

ESYCOM Lab, Univ Gustave Eiffel, CNRS, F-77454 Marne-la-vallee, France
*E-mail: aiman.mughal@univ-eiffel.fr, jithin.mudakkarappilli-sudersanan@univ-eiffel.fr

Abstract

Randomly distributed RFID tags are modeled by a set of short-circuited half-wave dipoles. Numerical Electromagnetics Code (NEC) simulator is used for the computation of mono-static radar cross section (RCS) following the two techniques based on the total field backscattered by the target and the radar equation. Different dipole configurations are studied to highlight the RCS distortion. The radar equation makes it possible to estimate RCS from measurements. The simulation results were found to be in good agreement with the experimental data.

Keywords: backscattered field, electromagnetic coupling, radar equation, mono-static RCS measurements

1. Introduction

RFID (Radio Frequency Identification) technology is widely deployed in several frequency bands and for different applications such as logistics, inventory tracking, supply-chain management and laundry management [1]. A passive UHF RFID system is composed of a tag and a reader, where the tag contains an antenna and an integrated circuit (the chip). The passive tag is powered up by the electromagnetic field received from the reader. The communication link between the reader and the tag is established by switching its chip impedance between two distinct states, resulting in a modulation of the signal scattered back towards the reader. The backscattered field of the tag can be analyzed in terms of its radar cross section.

Mono-static RCS is a key parameter used to assess the quality of an RFID communication link. Impedance matching between the tag antenna and the chip directly influences the RCS and thereby the performance parameters of the RFID system, such as read-range and read-rate. In high-density context, the tags are randomly distributed over a specified surface area which may result in significant electromagnetic coupling among them. This causes the radiation properties of an RFID tag to undergo random variations, which may be different from one configuration to another. Although the estimation of RCS in deterministic cases has been largely studied in literature [2], [3], to our knowledge the impact of introducing randomness in the system has not yet been studied.

The manuscript is organized as follows: in Section 2, an RFID system consisting of a set of N randomly distributed tags over an electrically small area, is modeled by a set of dipoles. Section 3 presents the two approaches used in this paper to compute the mono-static RCS of an RFID system and also NEC simulations to compute RCS for uniform and random configuration of dipoles. Simulation results are validated by measurements as discussed in section 4.

2. Dipole-based model for an RFID system

Figure 1(a) presents an RFID system consisting of a random distribution of N tags over a specific area in the yoz plane, illuminated by a reader positioned at a point in space (here on the x-axis).

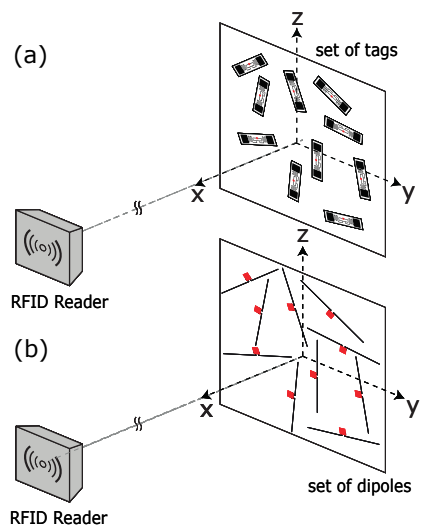

Figure 1: Set of RFID tags illuminated by the reader in (a) is modeled by a set of dipoles in (b)

The tag centers are assumed to be randomly distributed such that they do not overlap. On account of the statistical similarities discussed in [6], the tag antennas are modeled by half-wave dipoles. The dipoles representing the tags are loaded. The centers and orientations of the N dipoles are supposed to be the same as that of the randomly distributed tags. Thereby, it is assumed that studying the mono-static RCS of the set of N dipoles in Figure 1(b) could statistically represent the RCS of the N tags.

3. Mono-static radar cross section

The mono-static RCS (σ) in dBm^2 of a set of randomly distributed loaded dipoles acting as the target, is computed using the two methods explained in this section.

3.1. RCS using backscattered field

The reader antenna illuminates the dipoles (target) with an incident electromagnetic field (E_i). This field induces a voltage at the input of each of the dipoles which generates a backscattered field (E_s) in all directions. The total mono-static RCS from the set of dipoles is then calculated in the direction of the incident electromagnetic field by [4]:

$$\sigma = \lim_{r \to +\infty} 4\pi r^2 \frac{|E_s|^2}{|E_i|^2} \tag{1}$$

where r is the distance between the reader and target.

3.2. RCS using radar equation

The RCS can be determined from measurements in terms of the reflection coefficient by using the radar equation. The measurements are performed in an anechoic chamber by placing the dipoles (target) in the far-field of the transmitting horn antenna (reader). The reflection coefficient of the reader is measured in the presence and absence of the target. Following the detailed calculations in [5], RCS could be calculated using:

$$\sigma = \left| S_{11}^{+\text{target}} - S_{11}^{-\text{target}} \right|^2 \frac{(4\pi)^3 r^4}{G_t^2 \lambda^2} \tag{2}$$

where $S_{11}^{+\text{target}}$ and $S_{11}^{-\text{target}}$ are the reflection coefficients of the reader with and without the target respectively, G_t is the realized gain of the reader in free space including the mismatch losses, and r is the distance between the reader and the target.

3.3. Simulation results

NEC is used to simulate both approaches for the calculation of RCS. for the first approach, in order to estimate the backscattered field, a planewave is implemented in NEC. For the second approach, in order to use the radar equation, the reader is modeled by an excited dipole to create the incident electromagnetic field in order to illuminate the set of dipoles. We consider thin short-circuited ($Z_c = 0$) dipoles of length $\lambda/2$ and diameter $10^{-6}\lambda$ at an operating frequency of 866 MHz. Figure 2 presents the estimated RCS of an isolated dipole in (a) and of a configuration of two dipoles separated by a distance of $d = 0.2\lambda$, where one of them is inclined at an angle of 20° as shown in (b).

The two techniques show an excellent agreement in both cases. It is observed that the RCS of the second configuration presents a distorted form and different angular values for three planes (ϕ = 0°, ϕ = 90°, and θ = 90°) in comparison with that of the isolated case. This distortion is more visibly observed in ϕ = 90° plane, which leads us to investigate RCS in this plane by performing measurements. The two NEC-based methods discussed in this section can be used as a reference for the evaluation of the RCS in different dipole configurations (periodic and random). Further analysis on the distortion of RCS for random orientation of dipoles is done through experimental validation, especially in the case of a set of highly coupled dipoles (cf. Fig. 1).

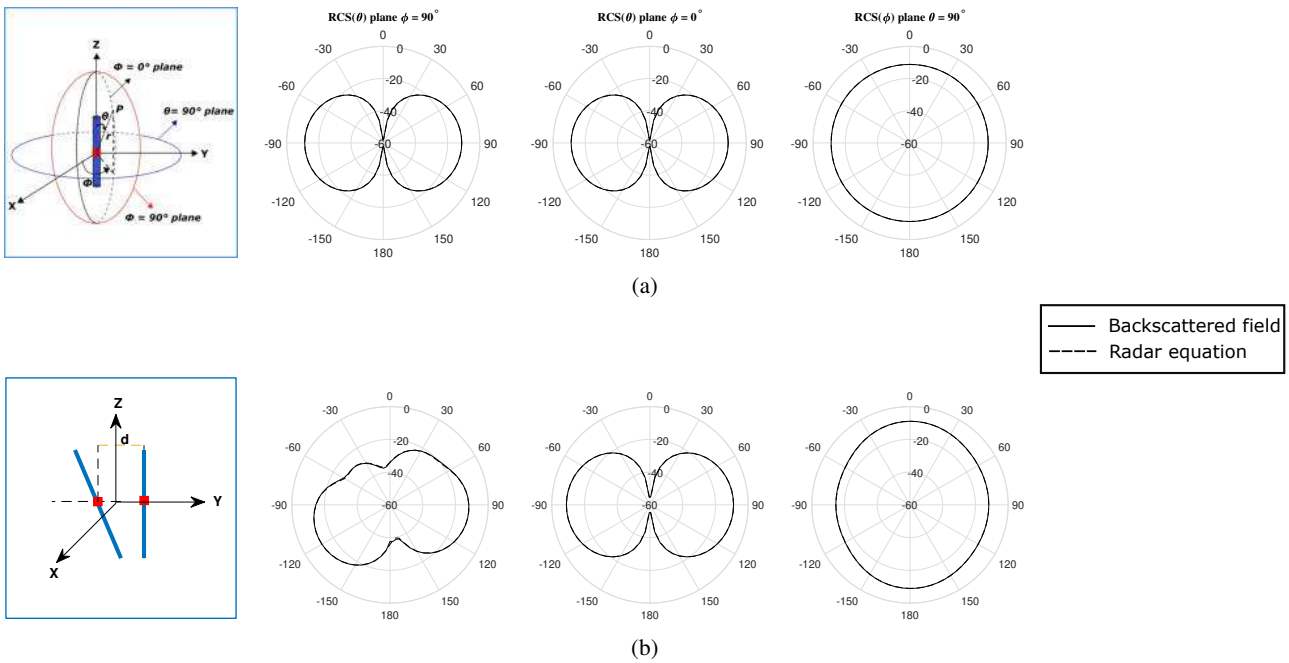

Figure 2: Mono-static RCS in three different planes (ϕ = 90°, ϕ = 0° and θ = 90°) for an isolated dipole in (a) and two dipoles with one inclined at 20° in (b)

4. RCS measurements

4.1. Measurement setup

This section elucidates the single-port network analyzer measurement used for estimating mono-static RCS in an anechoic chamber [2], [5]. A schematic representation of the measurement setup is shown in Figure 3.

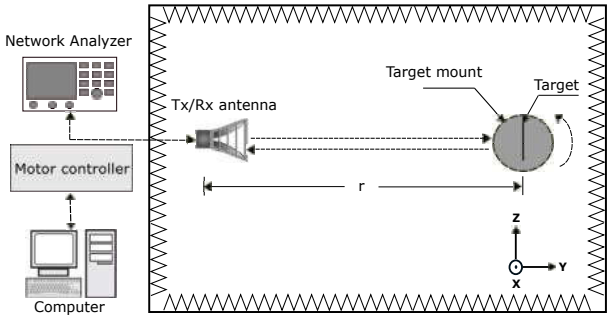

Figure 3: Experimental setup for measuring mono-static RCS in anechoic chamber

The measurement bench consists of E8361C PNA Microwave Network Analyzer (10 MHz - 67 GHz), a dual ridge horn antenna SH800 with an operational frequency range of 0.8 - 12 GHz acting as the Tx/Rx antenna, and a stepped motor which controls the rotation of the target mount. The target is mounted on a foam support to avoid any unwanted reflections which could interfere with the desired reflections from the target. The distance (r) between the Tx/Rx antenna and the target is fixed to 2.6 m, complying with the far-field conditions. It is measured from the input port of the Tx/Rx antenna to the center of the target mount. Only horizontal polarization of the antenna is employed as the study focuses on the $\phi = 90°$ plane. The key parameters used for measurements using the network analyzer is summarized in Table 1.

Parameter	Value used
Frequency range	0.8 - 4 GHz
IF bandwidth	5 kHz
Number of points	25601
Input power	7 dBm
Average factor	10

Table 1: Basic setup parameters used in network analyzer

The measurement procedure is carried out in two stages. First, the reflection coefficient of the reader antenna is measured in the absence of the target ($S_{11}^{-\text{target}}$). The measured value includes the effect of input port mismatch and unwanted reflections inside the anechoic chamber. Subsequently, the target is placed on the mount and the reflection coefficient ($S_{11}^{+\text{target}}$) is measured.

Data pre-processing techniques are employed to eliminate systematic errors from the measured data to obtain the correct RCS of the target [7], [8]. S-parameter calibration is performed at first to suppress errors of the measurement path, namely the PNA and cable connected to the Tx/Rx antenna. A background vector subtraction technique is used to coherently subtract the backscattered signals from the test range with and without the presence of the target, in order to eliminate effects of the background. Any residual reflections that remain from the background subtraction are filtered out using the time gating technique employing a suitable window. Kaiser–Bessel window is used in the context of this work. The parameter ($K = 4$) of the window is

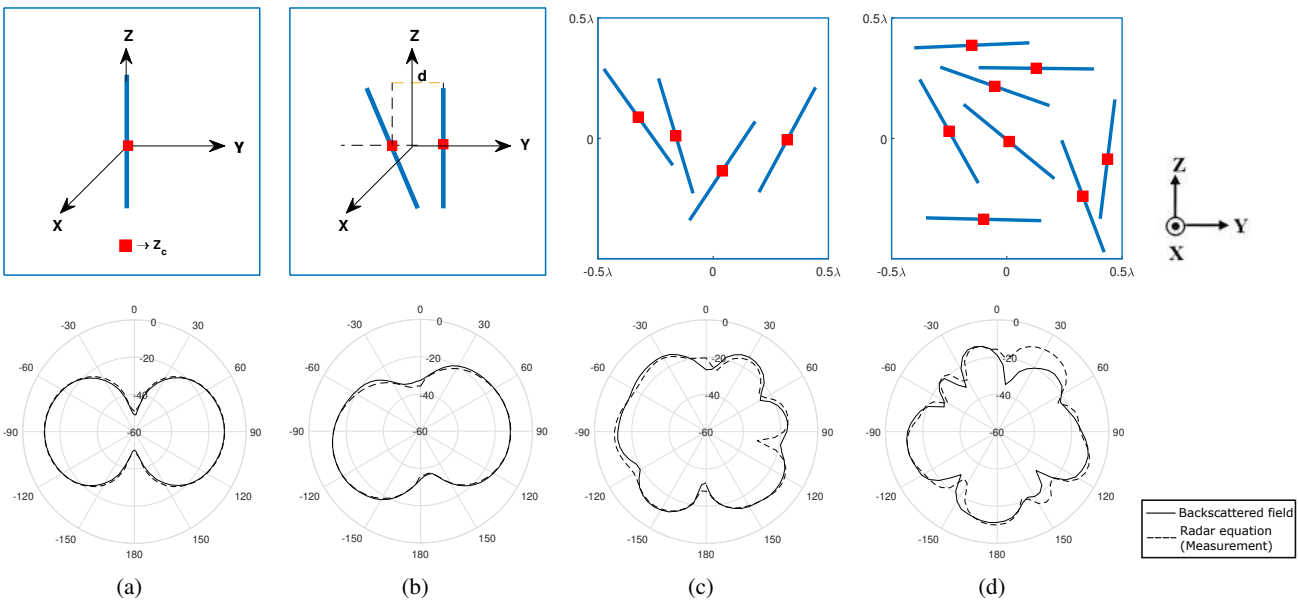

Figure 4: Mono-static RCS in $\phi = 90°$ plane for an isolated dipole in (a), two dipoles with one tilted at 20° in (b), a set of four randomly distributed dipoles in (c), and a set of eight randomly distributed dipoles in (d)

chosen so as to have sufficient suppression in the side lobe level. The width of time gate (gate span = 1.68 m) is chosen such that it covers the peak corresponding to the target.

4.2. Measurement results

Mono-static RCS of thick short-circuited ($Z_c = 0$) dipoles of length $\lambda/2$ and diameter of 1 mm is measured at the frequency of 866 MHz. The choice of short-circuit load is justified by the simplicity of its implementation for a preliminary study. The measurement results are compared with those obtained by the NEC electromagnetic simulator following the technique described in section $2.a$. Figure 4 presents the results of the RCS for a few different configurations and a good agreement is observed between the measurements and the simulations in ϕ = 90° plane. It is observed that the RCS of an isolated dipole gets deformed when a second dipole inclined at 20° is introduced at a distance d = 40 mm from it. Furthermore, the total RCS in the case of a set of 4 and 8 randomly distributed dipoles are measured and analyzed. The dipoles are distributed over a surface area of $1\lambda \times 1\lambda$. The results are more distorted and totally perturbed in the case of 4 and 8 dipoles.

The difference between the measured and simulated results could be potentially arising from the slight misalignment in position of dipoles on the plane and minor variations in the dipole lengths. Moreover, background subtraction followed by time gating may not suppress all errors. Even though the window function has a width covering most of the target reflection. There is not always a clear border of the target response while performing gating. In such a case, some part of the desired target response could be lost or some unwanted responses could be included in the time-gated signal, resulting in variations in the RCS response.

5. Conclusion

In this article, a set of RFID tags has been modeled by a set of randomly distributed half-wave dipoles. Total monostatic RCS in the direction of incident field has been computed to account for the total backscattering from the set of scattering elements (dipoles). We have shown that the two NEC-based methods can be employed to compute the RCS of randomly distributed dipoles, which is further validated by performing measurements in the anechoic chamber. Different dipole configurations were studied to analyze the distortion in RCS by varying the position and density of dipoles. The results show that when the target dipoles are randomly distributed, the deformation of the RCS is also random. Given the position and orientation of the dipoles, the corresponding distortion is difficult to predict using a purely deterministic approach and must be evaluated statistically, especially in the case of a set of strongly coupled dipoles. This requires a statistical model that can take into account the random aspect of the scenario to better analyze the RCS of a set of RFID tags in a high density context.

In ongoing works, RCS of commercial RFID tags will be measured in the UHF RFID frequency band. The measurements will also be extended to obtain the mono-static RCS in two other planes of interest which are discussed in section 3, i.e. ϕ = 0° and θ = 90° planes. Further, in order to get closer to a realistic scenario, the next step would be to study the differential RCS (ΔRCS) to model the response of an RFID tag while its impedance switches between two states [9]. Then, it would be an interesting parameter to compare the dipoles and tags in terms of ΔRCS. As the differential RCS is a key parameter to estimate the quality of an RFID communication link, the statistics of this output would be interesting to be established and analyzed. Consequently, in long term, this study could give a reliable prediction of an RFID system's performance comprising tags in a high-density context.

References

[1] S. A. Ahson and M. Ilyas, *RFID handbook: Applications, Technology, Security, and Privacy*. CRC press, 2017.

[2] P. V. Nikitin and K. S. Rao, "Theory and measurement of backscattering from RFID tags," *IEEE Antennas and Propagation Magazine*, vol. 48, no. 6, pp. 212–218, 2006.

[3] G. Marrocco, "RFID grids: Part I—Electromagnetic theory," *IEEE Transactions on Antennas and Propagation*, vol. 59, no. 3, pp. 1019–1026, 2011.

[4] K. Penttilä, M. Keskilammi, L. Sydänheimo, and M. Kivikoski, "Radar cross-section analysis for passive RFID systems," *IEE Proceedings-Microwaves, Antennas and Propagation*, vol. 153, no. 1, pp. 103–109, 2006.

[5] D. Hotte, R. Siragusa, Y. Duroc, and S. Tedjini, "Radar cross-section measurement in millimetre-wave for passive millimetre-wave identification tags," *IET Microwaves, Antennas & Propagation*, vol. 9, no. 15, pp. 1733–1739, 2015.

[6] I. Adjali, A. Gueye, S. Mostarshedi, B. Poussot, F. Nadal, and J.-M. Laheurte, "Matching evaluation of highly coupled dipoles quantified by a statistical approach," *IEEE Transactions on Antennas and Propagation*, vol. 68, no. 7, pp. 5044–5051, 2020.

[7] F. Babaeian and N. C. Karmakar, "Time and frequency domains analysis of chipless RFID back-scattered tag reflection," *IoT*, vol. 1, no. 1, pp. 109–127, 2020.

[8] V. Kabourek, "Objects characterization by means of wideband signals," Ph.D. dissertation, České vysoké učení technické v Praze, 2017.

[9] P. V. Nikitin, K. Rao, and R. D. Martinez, "Differential RCS of RFID tag," *Electronics Letters*, vol. 43, no. 8, pp. 431–432, 2007.

Analytical, Computational and numerical techniques

A fast hybrid approach to model roughness effects for 2D the tropospheric maritime long-range propagation

Thomas Bonnafont[1*], Othmane Benhmammouch[2], Ali Khenchaf[1]

[1]Lab-STICC UMR CNRS 6285, ENSTA Bretagne, 29806 Brest, France
[2]International University of Casablanca, Bouskoura 50169, Morocco
*corresponding author, E-mail: thomas.bonnafont@ensta-bretagne.fr

Abstract

This paper studies the long-range tropospheric electromagnetic wave propagation over the sea. An asymptotic model based on the parabolic wave equation is considered. This latter is solved using a fast and memory-efficient wavelet-based method. The roughness effects of the sea are introduced through a hybrid approach. Numerical experiments (in X-band) are provided to highlight the advantages of the wavelet-based method in the context of maritime propagation.

1. Introduction

Modeling the propagation of electromagnetic waves in a maritime environment is a problem of major interest for many applications, such as the optimization of coastal radar or the direct model of refractivity from clutter [1]. In this context, many effects can influence the propagation such as the refraction in the troposphere, or the sea state. Computational efficient methods are therefore needed to obtain the propagation over large distances.

The Parabolic Wave Equation (PWE) [2] is commonly used for this purpose. Indeed, this asymptotic method models the forward propagation allowing wide steps in the propagation direction. A convenient way to solve the latter is the Split-Step Fourier (SSF) [2] method that computes the propagation in two steps. First, the field is propagated in free-space in the spectral domain. Second, characteristics of the environment, such as refraction or relief, are considered in the space domain [2]. Ground composition is also incorporated through different methods [2]. In order to tackle the problem of the sea surface, a hybrid approach has been proposed for SSF [3].

Recently, a wavelet-based method, Split-Step Wavelet (SSW) [4, 5], has been proposed to solve the PWE. The method follows the same steps as SSF, but the free-space propagation is performed in the wavelet domain instead of the Fourier domain. Indeed, it has been shown that this method performs better in terms of memory and computation time efficiency [5].

The purpose of this paper is to introduce the sea's roughness effect in 2D SSW through the hybrid approach of [3], aiming at a complete deterministic and efficient method for the tropospheric long-range.

The remaining of this summary is organized as follows. Section 2 introduces the model and the discretization. Section 3 is devoted to a brief description of the SSW method and the introduction of the hybrid approach to consider the sea surface. Section 4 shows numerical experiments in the X-band. Section 5 concludes the paper.

2. Parabolic wave equation model and discretization

2.1. The parabolic wave equation

Throughout the paper, an $\exp(j\omega t)$ time dependence, with the angular frequency ω, and a slowly varying refractive index n are assumed.

Since it can consider the effects of the refraction, the relief, and the ground composition, the PWE model is adapted to our context. Besides, it is less burdensome in terms of boundary and mesh conditions, allowing wider steps in the propagation direction; thus, efficient schemes in terms of computation time. Taking into consideration the forward propagation, the Helmholtz equation is reduced to the wide-angle PWE [2] as follows

$$\frac{\partial u}{\partial x} = -j\left(\sqrt{k_0 + \frac{\partial^2}{\partial z^2}} - k_0\right) - jk_0\left(n^2 - 1\right)u, \quad (1)$$

with x the propagation direction, k_0 the free-space wavenumber and u the reduced field. The latter is only true in a paraxial cone of about $30°$.

In this article, we aim at solving equation (1) in an efficient way while accounting for the effects of the sea surface.

2.2. Discretization

The considered domain is of size $[0, x_{\max}]$ and $[0, z_{\max}]$. For obvious numerical reasons, this latter is discretized as follows. First, a sampling of N_z points along the z-direction is performed with $\Delta z = z_{\max}/N_z$ the step size. At a position x the field is, thus, denoted by $u_x[p_z]$ with $p_z \in \{0, \cdots, N_z\}$. Second, a discretization along x is applied with N_x points. The step is denoted by Δx.

3. Split-step wavelet above a rough sea surface

3.1. A brief overview of split-step wavelet

Split-step wavelet is an iterative computational scheme to compute the reduced field marching in on distances. This latter follows the same steps as SSF, but the free-space propagation is performed in the wavelet domain instead of the spectral domain. It can be summarized with the following equation

$$u_{x+\Delta x} = LRW^{-1}PC_{V_s}Wu_x, (2) \tag{2}$$

where W and W^{-1} denote respectively the fast wavelet transform and its inverse, C_{V_s} a compression operator with hard threshold V_s, P the compressed wavelet-to-wavelet propagator described in [5], R the phase screen operator that accounts for the refraction effects, and L the operator that accounts for the relief. The relief is considered through a staircase model [2]. The ground composition is accounted for using the local image method [4], which allows modeling the ground effects with a reduced number of points.

The overall complexity of the method has been shown to be lower than the complexity of SSF, if a good compression is performed. Besides the compression error is managed through a theoretical formula [6].

3.2. Propagation above the sea

To model the propagation above a rough sea surface, the hybrid approach proposed in [3] is introduced in SSW.

The idea of the method is to take both into account the effects of the roughness and of the geometry of the surface. To do so, the Elfouhaily sea spectrum [7] is cut into two. The lowest part of the spectrum is used to compute the surface, while the highest part allows to compute a new roughness parameter, which is introduced in the Fresnel coefficient [3]. The cutoff parameter of the spectrum is defined from the mesh size in the propagation direction as

$$k_{\max} = N_x \frac{2\pi}{x_{\max}}. \tag{3}$$

This technique allows to model more precisely the effects of the sea. Also, Monte Carlo simulations are performed since the sea surface geometries are randomly generated. Therefore, incorporating this method in a fast propagation scheme, such as SSW, allows for more simulations in a fewer time.

4. Numerical experiments

In this section, numerical experiments are presented to show that the method works well and highlight its advantages. The following results are computed in X-band (9 GHz). The source is a complex source point (CSP) of width $W_0 = 5$ m placed at 10 m above the ground and $z_s = -50$ m. The propagation is computed in a domain of size $[0, 60]$ km along x and $[0, 128]$ m along z with a mesh size of $\Delta x = 40$ m and $\Delta z = \lambda = 0.03$ m. An atmospheric duct of 40 m, modeled by a tri-linear profile of atmosphere, and a wind speed of 10 m/s are also considered. Furthermore, the sea dielectric parameters are as follows: $\varepsilon_r = 80$ and $\sigma_r = 5$ S/m.

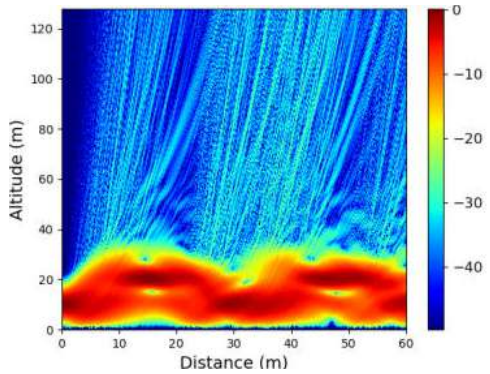

Figure 1: Normalized field u (dB) obtained with SSW

For the wavelet parameters, we use the symlet family with 6 vanishing moments and a maximum level of decomposition of $L = 3$. Also the thresholds for SSW are computed using the theoretical formula of [6] so as to obtain a maximum error of -20 dB.

The normalized field obtained with SSW is plotted in Figure 1.

Figure 1 shows both the effects of the rough sea, since the geometry induces interferences, and of the tropospheric duct. The error with SSF is of order -30 dB and in line with [3]. One can also note the shadow areas on the sea. Simulations on the antenna altitude could be performed to optimize the antenna position so as to have a better radiation patter to detect target on the sea.

5. Conclusions and perspectives

In this summary, the hybrid approach of [3] has been introduced in SSW, allowing to obtain a fast and memory-efficient method for long-range propagation in 2D.

Future works include a two-way version of the method for the propagation over different terrains, such as an island or with a ship. Besides Monte-Carlo simulations are needed in order to characterize the effects of the sea on the propagation medium. Furthermore, numerical experiments on the antenna position should be performed to optimize its altitude. Also, with the generalization of SSW in 3D [8, 9], including this hybrid approach would be an evolution of this work.

References

[1] P. Gerstoft, L. T. Rogers, J. L. Krolik, W. S. Hodgkiss, Inversion for refractivity parameters from radar sea clutter, *Radio Science*, 38(3), 2003.

[2] M. Levy, *Parabolic Equation Methods for Electromagnetic Wave Propagation*, London, IET, 2000.

[3] O. Benhmammouch, A. Khenchaf, N. Caouren, Modelling roughness effects on propagation of electromagnetic waves in maritime environment: a hybrid approach, *IET Radar, Sonar and Navigation*, 5(9), pp 1018—1025, 2011.

[4] H. Zhou, R. Douvenot, A. Chabory, Modeling the long-range wave propagation by a split-step wavelet method, *Journal of Computational Physics*, 402, pp 109042, 2020.

[5] T. Bonnafont, R. Douvenot, A. Chabory, A local split-step wavelet method for the long range propagation simulation in 2D, *Radio Science*, 56(2), e2020RS007114, 2021.

[6] T. Bonnafont, R. Douvenot, A. Chabory, Determination of the thresholds in split-step wavelet to assess accuracy for long-range propagation, *Radio Science Letters*, 3, 2022, in press.

[7] T. Elfouhaily, B. Chapron, K. Katsaros, D. Vandemark, A unified directional spectrum for long and short wind-driven waves, *Oceans 97*, 102, pp 15781—15796, 1997.

[8] T. Bonnafont, R. Douvenot, A. Chabory, 3D split-step wavelet method for the propagation over impedance ground condition, *XXXIVth General Assembly and Scientific Symposium of the International Union of Radio Science (URSI GASS)*, pp 1–4, 2021.

[9] Bonnafont, T., Douvenot, R., and Chabory, A., Split-step wavelet with local operators for the 3D long-range propagation, *15th European Conference on Antennas and Propagation (EUCAP)*, March 2021, pp. 1-5.

A TLM Algorithm for Wave Propagation In Human Fat and Muscle Tissues With a Cole-Cole Dispersion Model

Mohammed Kanjaa*,Otman El Mrabet, Mohsine Khalladi

[1]EMG Group, LaSIT Laboratory, Abdelmalek Essaadi University, Tetouan, Morocco.
*corresponding author, E-mail: mohammed.kanjaa@uae.ac.ma

Abstract

A transmission line method (TLM)algorithm is proposed for electromagnetic (EM) wave propagation in biological tissues with the Cole-Cole dispersion Model. A linear behavior of the polarization current during the time step is assumed. The polarization current density is approached using Lagrange extrapolation polynomial, and the fractional derivation is obtained according to Riemann definition. Reflection coefficients at an air/muscle interfaces simulated in a 1-D domain are found in good agreement with those obtained from the analytic model.

1. Introduction

In the last two decades there has been a renewed interest in the interaction between biological tissues and electromagnetic field at microwave frequencies due to new promising applications of this technology in biomedical engineering. the Cole-Cole modelproposed in [1] as:

$$\epsilon_r(\omega) = \epsilon_\infty + \sum_{p=1}^{p} \frac{\Delta\epsilon_p}{1 + (j\omega\tau_p)^{\alpha_p}} \tag{1}$$

where ϵ_∞ is the optical relative permittivity, $\Delta\epsilon_p = \epsilon_s - \epsilon_\infty$ is the amplitude of the $p-th$ pole, ϵ_s is the static relative permittivity, ω is ths angular frequency , τ_p is the relaxation time, α_p the parameter that indicates the broadening of the dispersion for this pole, which in the Cole-Cole model must satisfy $0 < \alpha_p < 1$, The consequence is a fractional order differentiation in the time domain[2].

2. FORMULATION AND EQUATIONS

In the Cole-Cole model the relationship between the polarization current related to the p_{th} pole and the electric field in time domain is given by:

$$\mathbf{J}_p(t) + \tau^{\alpha_p} D^{\alpha_p} \mathbf{J}_p(t) = \epsilon_0 \Delta\epsilon_p \frac{\partial \mathbf{E}(t)}{\partial t} \tag{2}$$

In order to obtain the descritized expression of $\mathbf{J}_p(t)$, the polarization current vector can be approached using a Lagrange interpolation in the time interval $t_i < t < t_j$ .Then performing a Reimann[3] fractional derivative the update equation for the polarization current is derived:

$$\mathbf{J}_p^{n+1} = -\frac{\phi_p}{\psi_p}\mathbf{J}_p^n + \frac{\zeta_p}{\psi_p}(\mathbf{E}^{n+1} - \mathbf{E}^n) \tag{3}$$

where the update parameters ψ_p, ϕ_p and ζ_p are:

$$\psi_p = \frac{1}{2} + \frac{\tau_p^{\alpha_p}}{\Delta t}\frac{\Gamma(2)}{\Gamma(2-\alpha_p)} t^{1-\alpha_p} - n\frac{\tau_p^{\alpha_p}}{\Gamma(1-\alpha_p)} t^{-\alpha_p} \tag{4}$$

$$\phi_p = \frac{1}{2} - \frac{\tau_p^{\alpha_p}}{\Delta t}\frac{\Gamma(2)}{\Gamma(2-\alpha_p)} t^{1-\alpha_p} + \frac{(n+1)\tau_p^{\alpha_p}}{\Gamma(1-\alpha_p)} t^{-\alpha_p} \tag{5}$$

$$\zeta_p = \frac{\epsilon_0 \Delta\epsilon_p}{\Delta t} \tag{6}$$

To get the update equation of the electric field components we start from the Maxwell-Ampere equation, and by including the conductivity term :

$$\nabla \times \mathbf{H} = \epsilon_0\epsilon_\infty \frac{\partial \mathbf{E}}{\partial t} + \sigma_0 \mathbf{E} + \sum_{p=1}^{p} \mathbf{J}_p \tag{7}$$

where σ_0 is the static ionic conductivity, the updated electric field is given by:

$$E_{x,y,z}^{n+1} = E_{x,y,z}^n (1 - \frac{2\sigma_0 \Delta t}{D}) - \sum_p \frac{(1 - \frac{\phi_p}{\psi_p})\Delta t}{D} J_{px,y,z}^n + \frac{2\Delta t}{D}(\nabla \times \mathbf{H})_{x,y,z}^{n+\frac{1}{2}} \tag{8}$$

$$D = 2\epsilon_0\epsilon_\infty + \sum_p \frac{\zeta_p \Delta t}{\psi_p} + \sigma_0 \Delta t \tag{9}$$

In the TLM method the simulation domain is discretized in cells where a series of uniform transmission lines model the propagation medium and the unit cell circuit referred to as symmetrical condensed node(SCN).

The voltage at the center of the SCN node, as deduced from the conservation laws[4], becomes :

$$V_{x,y,z}^{n+1} = V_{x,y,z}^n + \frac{1}{4 + Y_{ocx,y,z}}({}_sV_{x,y,z}^{n+1} + {}_s V_{x,y,z}^n) + \frac{4}{4 + Y_{ocx,y,z}} \frac{\Delta l \Delta t}{\epsilon_0} (\nabla \times \mathbf{H})_{x,y,z}^{n+\frac{1}{2}} \tag{10}$$

where $Y_{ocx,y,z}$ indicates the normalized admittance of the open circuit stub added to the node.

The update equation for voltage sources at the center of the node:

$${}_sV_{x,y,z}^{n+1} = -{}_sV_{x,y,z}^n + C_1 V_{x,y,z}^n + \sum_p C_{2p} J_{px,y,z} \tag{11}$$

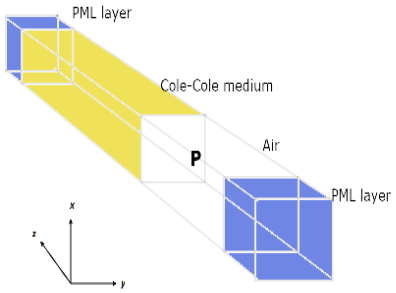

Figure 1: 3D view of the computation domain , incident and reflected fields are calculated at point P.

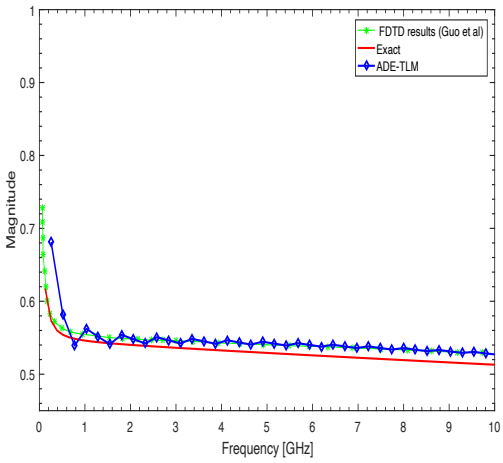

Figure 2: Reflection coefficient (dB) at normal incidence on an air/Fat interface obtained by the proposed algorithm compared to the FDTD results [2] and the exact solution

with update constants:

$$C_1 = -\frac{4\sigma_0 \Delta t}{\epsilon_0} \qquad C_{2p} = -\frac{2(1-\frac{\phi_p}{\psi_p})\Delta t \Delta l}{\epsilon_0} \qquad (12)$$

3. SIMULATION AND RESULTS

The simulation domain as depicted in Figure 1 consists of a grid of 1000 cells interconnected on the z axis truncated by an unsplit PML layer [5] of 10 cells at the beginning and the end.500 cells were used to model the Cole-Cole medium and the remaining cells were used to model the air is. The cell dimension Δl satisfies the stability condition $\Delta t = \Delta l/2c$, the time step is set as $\Delta t = 0.125ps$. The fourth order Cole-Cole parameters for Cole-Cole media are taken as in [2].

In Figures 2 and 3 the simulation results are compared to the theoretical reflection coefficient and to the FDTD results at the air/Cole-Cole medium interface A good agreement over the whole frequency band is observed.

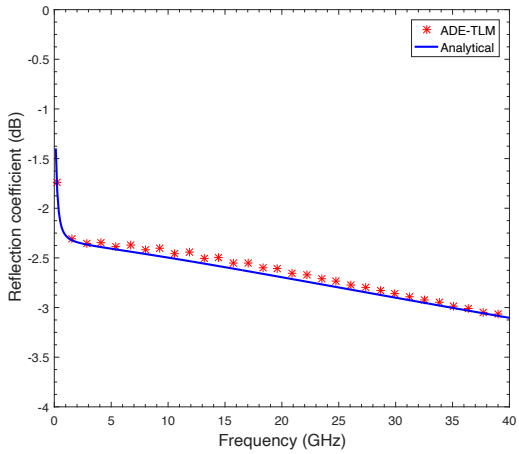

Figure 3: Reflection coefficient (dB) at normal incidence on an air/Muscle interface

4. CONCLUSION

In this paper, a TLM algorithm is presented to study the electromagnetic wave propagation in biological tissues using Cole-Cole dispersion model. A polynomial extrapolation is used to approach the polarization current and a Reimann definition iss used to perform the fractional derivation . This approximation reduces considerably both the numerical cost of the simulation since only two previous values of the J field are needed at each iteration. The presented results indicate the accuracy of our approach.

References

[1] Cole,K. S.,Cole,R.H.(1941).Dispersion and absorption in dielectrics I. Alternating current characteristics. The Journal of chemical physics,9(4), 341-351.

[2] Guo, B., Li, J. Zmuda, H. (2006). A new FDTD formulation for wave propagation in biological media with ColeCole model. IEEE Microwave and Wireless Components Letters, 16(12), 633-635.

[3] Engheta, N., On the role of fractional calculus in electromagnetic theory, IEEE Antennas and Propagation Magazine, Vol. 39, No. 4, 3546, Aug. 1997.

[4] Barba, I., Cabeceira, A. C. L., Panizo, M., Represa, J. (2001). Modelling dispersive dielectrics in TLM method. International Journal of Numerical Modelling: Electronic Networks, Devices and Fields, 14(1), 15-30.

[5] Yaich, M. I., M. Kanjaa, S. E. Adraoui, K. Mounirh, and M. Khalladi, An unsplit formulation of the 3D-PML absorbing boundary conditions for TLM-method in time domain, 2018 6th (ICMCS), 15, May 2018.

First-order perturbation theory for electromagnetic eigenmodes

Zoltan Sztranyovszky*, Wolfgang Langbein, Egor A. Muljarov

School of Physics and Astronomy, Cardiff University, Cardiff, United Kingdom
*corresponding author, E-mail: sztranyovszkyz@cardiff.ac.uk

Abstract

We present an accurate first order perturbation theory for the electromagnetic eigenmodes of a resonator, which is based on the spectral representation of the Green's dyadic. We show that when the resonator boundary is deformed, higher-order terms of the standard perturbation series can contribute to the eigenmode frequencies in first-order in the deformation depth. This is a consequence of the vectorial nature of the electromagnetic field and is technically due to the infinite degeneracy of static modes of the resonator.

1. Introduction

Resonant states (RSs) [1], also referred to as quasi-normal modes [2], are the eigenmodes of a resonator which determine its optical properties, such as the scattering cross-section or the Purcell enhancement [3]. For simple systems, such as a slab or a sphere, RSs can be found analytically [1]. For more complicated shapes they can be found numerically or via perturbative approaches [2, 3].

Here we study the role of static modes [4] in the perturbation theory for RSs, with specific focus on their contribution to the first-order approximation of the RS wavenumbers. Static modes describe the static pole of the Green's dyadic; they are infinitely degenerate and have the wavenumber eigenvalue $k = 0$. We develop a general perturbation theory that properly treats size or shape changes of the resonator. We will show that even though static modes appear only in second and higher order terms of the perturbation series, they contribute to the RS wavenumbers already in first order in the deformation depths.

2. Results

We start by considering an unperturbed system that can be solved analytically, such as a homogeneous dielectric sphere, and for simplicity we consider isotropic and non-magnetic materials only. Such system can be described by the electric Green's dyadic [5]

$$\mathbf{G}(\mathbf{r},\mathbf{r}') = \sum_{\nu} \frac{\mathbf{E}_\nu(\mathbf{r}) \otimes \mathbf{E}_\nu(\mathbf{r}')}{k - k_\nu} = \sum_{n} \frac{\mathbf{E}_n(\mathbf{r}) \otimes \mathbf{E}_n(\mathbf{r}')}{k - k_n} + \sum_{\lambda} \frac{\mathbf{E}_\lambda(\mathbf{r}) \otimes \mathbf{E}_\lambda(\mathbf{r}')}{k}\,, \tag{1}$$

where $\mathbf{E}_\nu$ is the electric field of the normalized eigenmodes, $\nu = n$ labels the RSs ($k_n \neq 0$), and $\nu = \lambda$ labels the static modes ($k_\lambda = 0$). The residue of the static pole of the Green's dyadic contains a delta-like singularity [5]. Using the Green's function we can find the matrix equation that links the unperturbed modes to the perturbed ones

$$(\varkappa - k_\nu)c_\nu = -\varkappa \sum_{\nu'} V_{\nu\nu'} c_{\nu'}\,, \tag{2}$$

where $\varkappa$ is the eigenvalue of the perturbed system, c_ν is the expansion coefficient for the perturbed field, and

$$V_{\nu\nu'} = \int \mathbf{E}_\nu(\mathbf{r}) \cdot \Delta\varepsilon(\mathbf{r}) \mathbf{E}_{\nu'}(\mathbf{r}) \mathrm{d}\mathbf{r}\,. \tag{3}$$

This procedure is called the resonant-state expansion [1, 5] which effectively treats perturbations to all orders. From the matrix equation one can extract corrections to the eigenvalue k_n in the form of a perturbation series

$$\varkappa = k_n - k_n V_{nn} + k_n V_{nn}^2 + k_n^2 \sum_{\nu' \neq n} \frac{V_{n\nu'} V_{\nu' n}}{k_n - k_{\nu'}} + \dots \tag{4}$$

from which it appears that $\varkappa^{(1)} = -k_n V_{nn}$ is the first-order correction to the wavenumber, being linear in the deformation depth δh. However, static modes are infinitely degenerate ($k_{\nu'} = 0$), and this allows the infinite sum in the second order term to lead to a correction linear in δh.

To extract such linear contributions from all orders, we reformulate Eq. (2) by moving all static modes into a matrix $W_{\lambda\lambda'}$ which is the inverse of $\delta_{\lambda\lambda'} + V_{\lambda\lambda'}$. Then the linear correction to $\varkappa$ can be found as

$$\varkappa^{(1)} = -k_n \tilde{V}_{nn}\,, \tag{5}$$

where

$$\tilde{V}_{nn} = V_{nn} - S_{nn}\,, \quad S_{nn} = \sum_{\lambda\lambda'} V_{n\lambda} W_{\lambda\lambda'} V_{\lambda' n}\,. \tag{6}$$

We now use a Neumann series expansion for W, then substitute the exact static pole residue of the Green's dyadic (which can written as a sum of regular and singular parts) into the series, and integrate out the delta functions from the singular part which is proportional to $\hat{\mathbf{r}} \otimes \hat{\mathbf{r}}'$ dyadic component [5]. Finally, after some algebra, we arrive at

$$S_{nn} \approx \int \mathbf{E}_n(\mathbf{r}) \cdot \frac{[\Delta\varepsilon(\mathbf{r})]^2}{\varepsilon(r) + \Delta\varepsilon(\mathbf{r})} \left(\hat{\mathbf{r}} \otimes \hat{\mathbf{r}}\right) \mathbf{E}_n(\mathbf{r}) \mathrm{d}\mathbf{r}\,, \tag{7}$$

where we have neglected the terms involving the regular part of the static pole and therefore not contributing in first

order. The expression for S_{nn} is clearly second order in $\Delta\varepsilon$; however it is of first order in the deformation depth δh, due to the single integral. The regular part in turn leads to multiple integrals, and thus to higher order terms in δh. Subtracting S_{nn} from V_{nn} we obtain

$$\tilde{V}_{nn} = \int \mathbf{E}_{n\parallel}(\mathbf{r}) \cdot \Delta\varepsilon(\mathbf{r}) \mathbf{E}_{n\parallel}(\mathbf{r}) \mathrm{d}\mathbf{r} + \int \mathbf{E}_{n\perp}(\mathbf{r}) \cdot \frac{\varepsilon(r)\Delta\varepsilon(\mathbf{r})}{\varepsilon(r) + \Delta\varepsilon(\mathbf{r})} \mathbf{E}_{n\perp}(\mathbf{r}) \mathrm{d}\mathbf{r}\,, \tag{8}$$

where the subscript $\parallel$ ($\perp$) labels the vector component parallel (normal) to the surface. The correct wavenumber to first order is thus given by $\varkappa \approx k_n - k_n \tilde{V}_{nn}$. Note that for a shape perturbation in vacuum we have $\varepsilon(r) + \Delta\varepsilon(\mathbf{r}) = 1$, rendering Eqs. (5) and (8) similar to the results in Ref. [2].

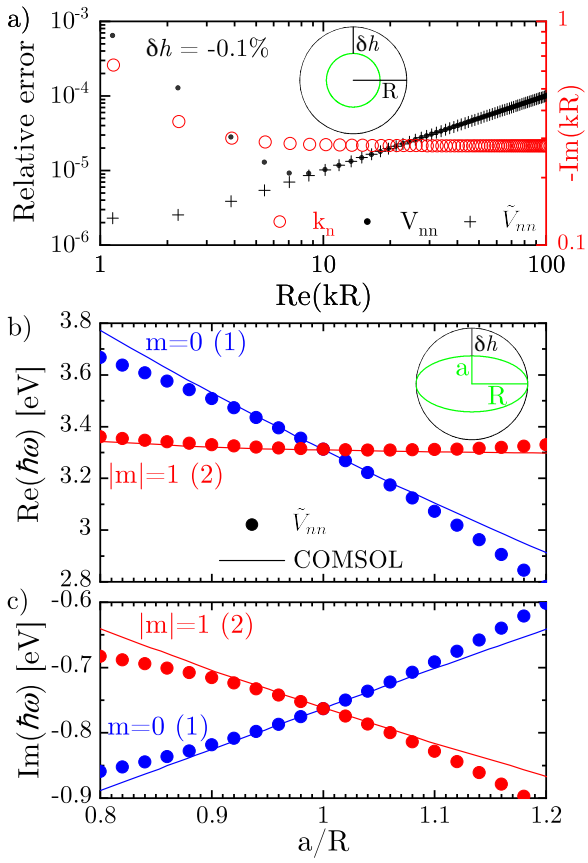

Figure 1: (a) RS wavenumbers (red) and relative errors (black) for the size perturbation of a dielectric sphere, with $\varepsilon = 4$ and radius R. (b) Real and (c) imaginary part of the surface plasmon frequency when a silver sphere is deformed into an ellipsoid, for angular momentum $l = 1$. The number in the brackets shows the degeneracy of the mode. The parameters for the silver sphere and the COMSOL data is taken from [2].

3. Discussion

When the permittivity change $\Delta\varepsilon(\mathbf{r})$ is small, for example, introducing a material change, one can neglect S_{nn} and use Eq. (3), which is a well known and tested result [3] and will not be discussed here further. When $\Delta\varepsilon(\mathbf{r})$ is large, which can be in case of a shape perturbation, the results of Eqs. (3) and (8) differ due to the contribution of the static modes S_{nn}. We show in Fig. 1(a) results for a size perturbation of a homogeneous dielectric sphere. For the modes with low wavenumbers, the relative error using Eq. (8) is a few order of magnitude smaller than using Eq. (3), showing the influence of the static modes on the first order correction. The first order results can also be extended to dispersive systems. Figures 1(b) and (c) show the real and imaginary part, respectively, for the surface plasmon mode of a silver sphere when it is being distorted into an ellipsoid as in [2]. We see good agreement between the perturbation theory results and the numerically calculated values for small changes, for both inwards ($a < R$) and outwards ($a > R$) perturbations.

4. Conclusions

We have shown that due to the static pole of the Green's dyadic higher order terms in the perturbation series can contribute in first order in the deformation depth. We have derived a general perturbation theory that can treat both material changes and shape perturbations. We have illustrated the importance of the static pole for size and shape changes of spherical resonators. This approach can be generalised to treat chirality and permeability perturbations.

Acknowledgement

Z.S. acknowledges the Engineering and Physical Sciences Research Council for his PhD studentship award (grant EP/R513003/1).

References

[1] E. A. Muljarov, W. Langbein, R. Zimmermann, Brillouin-Wigner perturbation theory in open electromagnetic systems, *Europhys. Lett.*, 92: 50010, 2010.

[2] W. Yan, P. Lalanne, M. Qui, Shape Deformation of Nanoresonator: A Quasinormal-Mode Perturbation Theory, *Physical Review Letters*, 125: 013901, 2020.

[3] S. Both, T. Weiss, Resonant states and their role in nanophotonics *Physical Review A*, 37: 013002, 2021.

[4] S. Lobanov, W. Langbein, E. A. Muljarov, Resonant-state expansion applied to three-dimensional open optical systems: Complete set of static modes *Physical Review A*, 100: 063811, 2019.

[5] E. A. Muljarov, Full electromagnetic Green's dyadic of spherically symmetric open optical systems and elimination of static modes from the resonant-state expansion *Physical Review A*, 101: 053854, 2020.

Accurate and Efficient Analysis of the Electromagnetic Scattering from a thin disk

Mario Lucido[1,*]

[1] Department of Electrical and Information Engineering "Maurizio Scarano" (DIEI), University of Cassino and Southern Lazio, 03043, Cassino, Italy
*corresponding author, E-mail: lucido@unicas.it

Abstract

An effective semi-analytical technique for the analysis of the scattering from a thin disk is briefly presented. The problem, formulated as sets of one-dimensional integral equations in the vector Hankel transform domain, is discretized by means of Helmholtz decomposition and Galerkin method with complete sets of orthogonal eigenfunctions of the most singular part of the integral operators, reconstructing the physical behavior of the fields, as expansion bases. In this way, fast-converging Fredholm second-kind matrix equations are obtained.

1. Introduction

The analysis of the electromagnetic scattering from finite objects is frequently carried out by means of integral equation formulations because the unknowns are defined on finite supports and the radiation condition is taken into account by a suitable choice of the Green's function of the problem. For such equations approximate solutions are generally obtained by resorting to discretization techniques. However, the existence of the solution of an arbitrary integral equation cannot be generally stated. Moreover, if the solution exists, the convergence of a discretization scheme cannot be generally established. Indeed, Fredholm's theory can be applied only if the operator is the superposition of a continuously invertible operator and a completely continuous operator [1].

When dealing with a first-kind integral equation or a hyper-singular second-kind integral equation, a Fredholm second-kind equation can be obtained by analytically inverting the most singular part of the integral operator [2], [3]. On the other hand, Fredholm theory can be applied to the matrix equation obtained by means of the Galerkin method with a complete set of orthogonal eigenfunctions of a suitable operator, containing the most singular part of the original integral operator, as expansion basis [2], [3]. Under such conditions, Galerkin-projection acts as a perfect analytical preconditioner for the considered integral equation. For this reason, this approach, called method of analytical preconditioning, has been widely used for the analysis of propagation, radiation, and scattering problems [4-12].

The aim of this paper is the analysis of the scattering from a thin disk in a homogeneous medium by means of a method recently developed by the author and belonging to the class of the methods of analytical preconditioning [13-17]. Surface integral equations for the effective electric and magnetic currents are obtained by imposing the generalized boundary conditions on the disk surface. Due to the revolution symmetry of the problem, all the involved functions are conveniently expanded in Fourier series and the surface integral equations are recast as sets of one-dimensional integral equations in the spectral domain for the harmonics of the vector Hankel transform (VHT) of the effective currents. The surface curl-free and divergence-free contributions of the effective currents are assumed as new unknowns in order to handle scalar unknowns in the VHT domain. Galerkin method with complete sets of orthogonal eigenfunctions of the most singular parts of the integral operators reconstructing the behavior of the fields at the edge and around the center of the disk as expansion bases are used to discretize the integral equations, thus leading to fast converging Fredholm second-kind matrix equations.

2. Formulation and Solution of the Problem

A disk of radius a and thickness τ immersed in a homogeneous medium is such that $\tau \ll a$ and $\tau \ll \lambda$, where λ is the wavenumber in the external medium. A cylindrical coordinate system (ρ,ϕ,z) with the origin at the center of the disk and the z axis orthogonal to it is introduced. An incident field $\left(\underline{E}^{inc}(\underline{r}),\underline{H}^{inc}(\underline{r})\right)$, where $\underline{r}=x\hat{x}+y\hat{y}+z\hat{z}$, impinges onto the disk surface generating a scattered field $\left(\underline{E}^{sc}(\underline{r}),\underline{H}^{sc}(\underline{r})\right)$ such that the tangential component of the total field satisfies the generalized boundary conditions on the disk surface, i.e., [18]

$$\hat{z}\times\left(\underline{E}^{inc}(\rho,\phi)+\underline{E}^{sc}(\rho,\phi)\right)\times\hat{z}=R\,\underline{J}(\rho,\phi), \quad (1)$$

$$\hat{z}\times\left(\underline{H}^{inc}(\rho,\phi)+\underline{H}^{sc}(\rho,\phi)\right)\times\hat{z}=S\,\underline{M}(\rho,\phi), \quad (2)$$

for $\rho\le a$, where

$$\underline{J}(\rho,\phi)=\hat{z}\times\left(\underline{H}^{sc}(\rho,\phi,0^+)-\underline{H}^{sc}(\rho,\phi,0^-)\right), \quad (3)$$

$$\underline{M}(\rho,\phi)=-\hat{z}\times\left(\underline{E}^{sc}(\rho,\phi,0^+)-\underline{E}^{sc}(\rho,\phi,0^-)\right), \quad (4)$$

are the effective electric and magnetic currents, respectively, and R and S are the electric and magnetic resistivities of the disk, respectively. The uniqueness of the solution is

guaranteed by requiring that the total field satisfies the edge conditions and the radiation condition.

The revolution symmetry of the problem allows to expand all the involved functions in series of orthogonal azimuthal harmonics. Hence, the surface integral equations for the effective currents can be equivalently reduced to infinite sets of independent one-dimensional integral equations in the spectral domain having as unknowns the VHT of the harmonics of the effective currents [13].

According to the Helmholtz decomposition, each current is written as the superposition of a surface curl-free contribution and a surface divergence-free contribution, which are assumed as new unknowns in order to handle scalar unknowns in the VHT domain [15].

The obtained integral equations are discretized by means of the Galerkin method. The behavior of the n-th harmonic of the effective currents at the edge and around the center of the disk is correctly reconstructed by expanding the unknowns in the following complete series of Bessel functions [16, 19], i.e.,

$$\tilde{f}^{(n)}(w) = \sum_{h=-1+\delta_{n,0}}^{+\infty} \gamma_h^{(n)} \sqrt{2p_h} \frac{J_{p_h}(aw)}{w^{\eta}}, \qquad (5)$$

where $\delta_{n,m}$ is the Kronecker delta, $\gamma_h^{(n)}$ denote the expansion coefficients, $p_h = |n| + 2h + \eta + 1$ and η depends on the edge behavior. With such a choice, the integral equations are reduced to fast converging Fredholm second-kind matrix equations. Moreover, the coefficient matrix elements, which are one-dimensional improper integrals of oscillating functions, are efficiently evaluated by means of the analytical procedure in the complex plane developed in [14, 15].

3. Numerical Results

An approximate solution of the problem can be obtained by truncating the infinite matrix equations. To show the fast convergence of the presented method, the following normalized truncation error is introduced

$$\mathrm{err}_N(M) = \sqrt{\sum_{n=-N+1}^{N-1} \left\| \mathbf{x}_{M+1}^{(n)} - \mathbf{x}_M^{(n)} \right\|^2 \Big/ \sum_{n=-N+1}^{N-1} \left\| \mathbf{x}_M^{(n)} \right\|^2}, \qquad (6)$$

where $2N-1$ is the number of considered harmonics estimated as in [20], $\|\cdot\|$ is the usual Euclidean norm and $\mathbf{x}_M^{(n)}$ is the vector of the expansion coefficients evaluated by using M expansion functions for each unknown.

In Figure 1a, $\mathrm{err}_N(M)$ is plotted for $N = 15$ in the case of a TM polarized plane wave, with incident angles $\theta_i = 30°$ with the z axis and $\phi_i = 0°$ with the x axis in the xy plane, impinging onto a resistive disk with $a = 2\lambda$ and $R = 100\Omega$. In this case, the generalized boundary conditions reduce to equation (1). As clearly shown, the convergence is very fast. Indeed, few expansion functions are needed to accurately reconstruct the solution. This behavior can be further appreciate in Figures 1b and 1c, where the effective electric current and the bistatic radar cross-section (BRCS) in the plane $\phi = 0°, 180°$, obtained for $M = 9$ so that the error is less than 10^{-3}, are plotted and compared with very good agreement with the results provided by CST Microwave Studio (CST-MWS). It is worth noting that, in reconstructing the solution in the case examined, the proposed method is 30 times faster than CST-MWS.

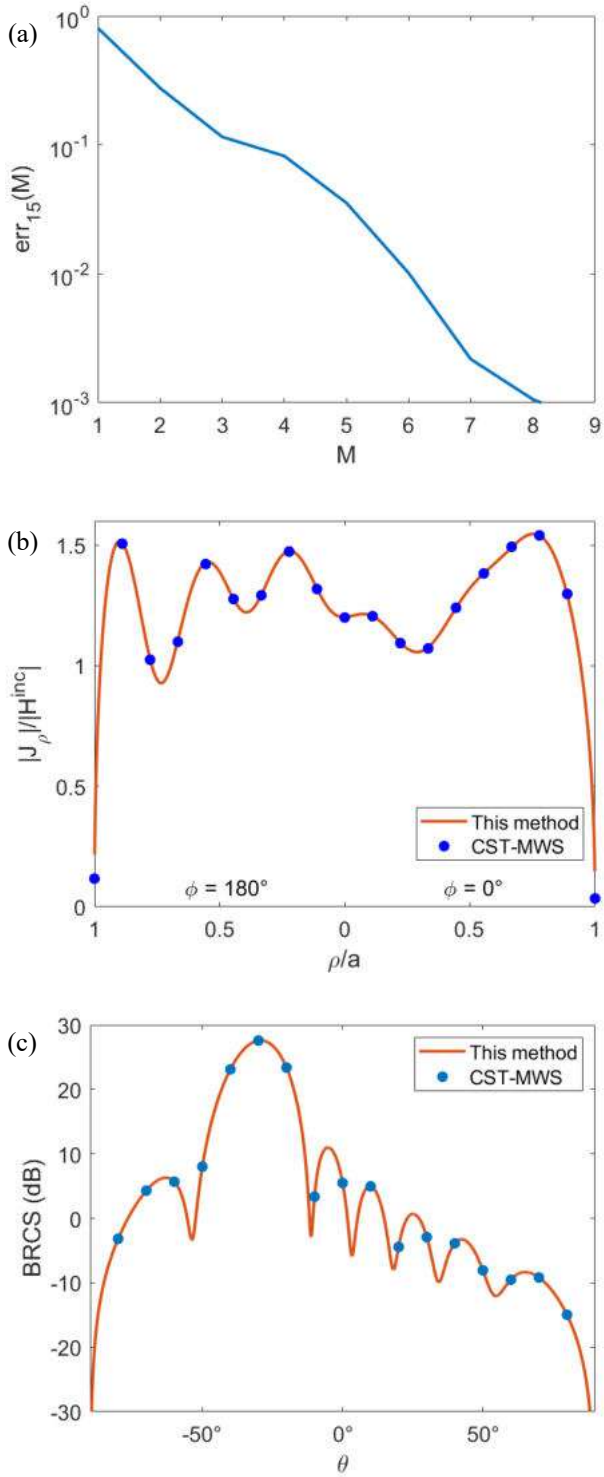

Figure 1. (a) Normalized truncation error, (b) effective electric current, and (c) bistatic radar cross section of a resistive disk with

$a = 2\lambda$ and $R = 100\Omega$ when a plane wave impinges onto the disk surface with $\theta_i = 30°$, $\phi_i = 0°$ and TM polarization.

In Figure 2a, $\mathrm{err}_N(M)$ for a dielectric disk of radius $a = 3\lambda/(2\pi)$, thickness $\tau = 0.05a$ and relative dielectric permittivity $\varepsilon_r = 10.5 - j0.3$, is plotted as a function of M for normal to the disk incidence, i.e., $\theta_i = 0°$, with $\underline{E}_0 = E_0\hat{y}$. In this case, only the harmonics for $n = \pm 1$ contribute to the field's representation, i.e., $N = 2$, and the resistivities can be approximated by means of the formulas devised for high-index contrast materials shown in [18]. The convergence is, again, very fast, and less than 1 min is needed to accurately reconstruct the solution. For the sake of completeness, in Figures 2b, 2c and 2d the effective electric current, the effective magnetic current and the BRCS, obtained for $M = 18$ so that the error is less than 10^{-3}, are plotted in the plane $\phi = 0°, 180°$ and compared with the results provided by CST-MWS. The agreement is quite good. It is interesting to note, however, that CST-MWS requires a computation time of 80 mins to reconstruct the plotted solution. After all, to the best of the authors knowledge, CST-MWS does not provide a 2D model for thin dielectric objects and an accurate 3D simulation has turned out to be time-consuming and particularly burdensome in terms of memory requirement.

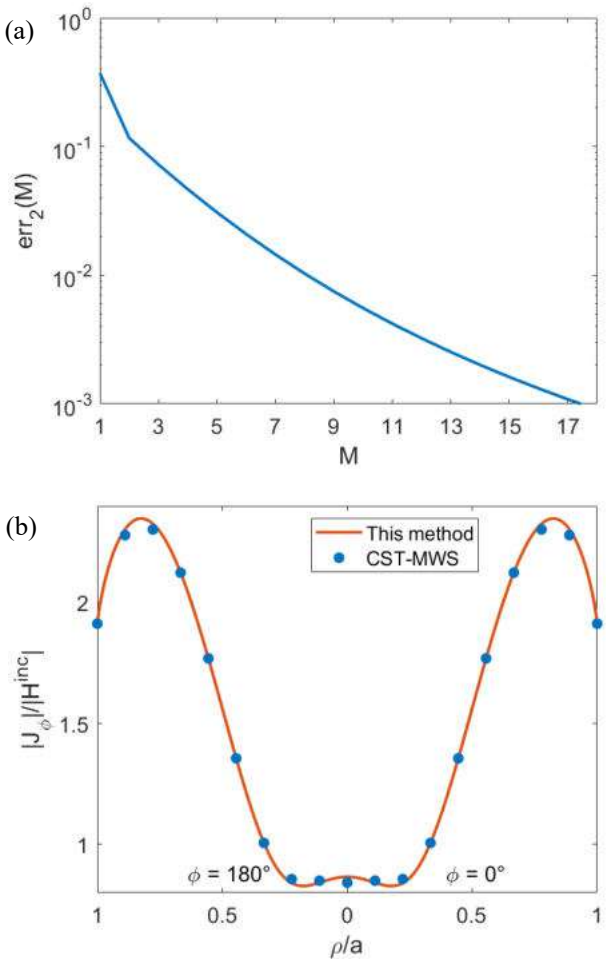

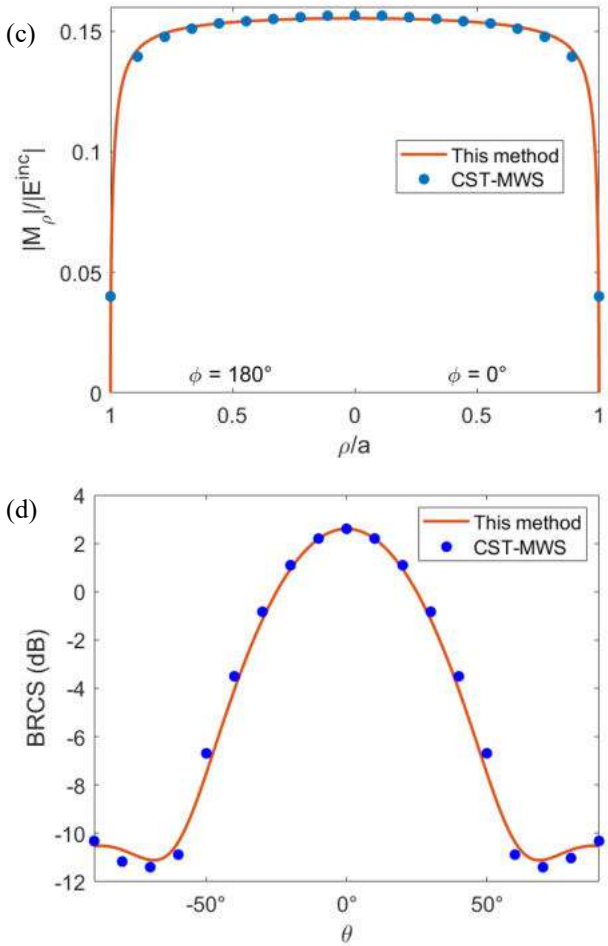

Figure 2. (a) Normalized truncation error, (b) effective electric current, (c) effective magnetic current, and (d) bistatic radar cross section of a dielectric disk with $a = 3\lambda/(2\pi)$, $\tau = 0.05a$ and $\varepsilon_r = 10.5 - j0.3$, when a plane wave normally impinges onto the disk surface with $\underline{E}_0 = E_0\hat{y}$.

4. Conclusions

The analysis of the electromagnetic scattering from a thin disk has been successfully carried out by means of a regularizing and fast converging method based on the Helmholtz decomposition and the Galerkin method. Comforting preliminary results show that the proposed method can be generalized to study more complex structures such as arrays of disks in non-homogeneous media.

Acknowledgements

This work was supported in part by the Italian Ministry of Instruction, University and Research program "Dipartimenti di Eccellenza 2018–2022" and under Grant 2017SAKZ78 (PRIN Project MIRABILIS).

References

[1] L. V. Kantorovich, G. P. Akilov, *Functional Analysis, 2nd ed.*, Pergamon Press, Oxford-Elmsford, NY, 1982.

[2] A. I. Nosich, Method of analytical regularization in computational photonics, *Radio Sci.* 51: 1421–1430, 2016.

[3] M. Lucido, K. Kobayashi, F. Medina, A. Nosich, E. Vinogradova, Guest editorial: Method of analytical regularisation for new frontiers of applied electromagnetics, *IET Microw. Antennas Propag*., 15: 1127–1132, 2021.

[4] K. Eswaran, On the solutions of a class of dual integral equations occurring in diffraction problems, *Proc. R. Soc. Lond. Ser. A*, 429: 399–427, 1990.

[5] E. I. Veliev, V. V. Veremey, Numerical-analytical approach for the solution to the wave scattering by polygonal cylinders and flat strip structures, in *Analytical and Numerical Methods in Electromagnetic Wave Theory*; Hashimoto, M., Idemen, M., Tretyakov, O.A., Eds.; Science House: Tokyo, Japan, 1993.

[6] M. J. Davis, R. W. Scharstein, Electromagnetic plane wave excitation of an open-ended finite-length conducting cylinder, *J. Electromagn. Waves Appl.*, 7: 301–319, 1993.

[7] K. Hongo, H. Serizawa, Diffraction of electromagnetic plane wave by rectangular plate and rectangular hole in the conducting plate, *IEEE Trans. Antennas Propag.*, 47: 1029–1041, 1999.

[8] J. L. Tsalamengas, Rapidly converging direct singular integral-equation techniques in the analysis of open microstrip lines on layered substrates, *IEEE Trans. Microw. Theory Tech.*, 49: 555–559, 2001.

[9] M. Lucido, Scattering by a tilted strip buried in a lossy half-space at oblique incidence. *Prog. Electromagn. Res. M*, 37: 51–62, 2014.

[10] F. Corsetti, M. Lucido, G. Panariello, Effective analysis of the propagation in coupled rectangular-core waveguides, *IEEE Photon. Technol. Lett.*, 26: 1855–1858, 2014.

[11] M. Lucido, F. Schettino, F., M. D. Migliore, D. Pinchera, F. Di Murro, G. Panariello, Electromagnetic scattering by a zero-thickness PEC annular ring: A new highly efficient MoM solution, *J. Electromagn. Waves Appl.*, 31: 405–416, 2017.

[12] M. Lucido, C. Santomassimo, G. Panariello, The method of analytical preconditioning in the analysis of the propagation in dielectric waveguides with wedges, *J. Light. Technol.*, 36: 2925–2932, 2018.

[13] M. Lucido, G. Panariello, F. Schettino, Scattering by a zero-thickness PEC disk: a new analytically regularizing procedure based on Helmholtz decomposition and Galerkin method, *Radio Sci.*, 52: 2-14, 2017.

[14] M. Lucido, F. Di Murro, G. Panariello, Electromagnetic scattering from a zero-thickness PEC disk: A note on the Helmholtz-Galerkin analytically regularizing procedure, *Progr. Electromagn. Res. Lett.*, 71: 7–13, 2017.

[15] M. Lucido, M. V. Balaban, S. V. Dukhopelnykov, A. I. Nosich, A fast-converging scheme for the electromagnetic scattering from a thin dielectric disk, *Electronics*, 9: 1451, 2020.

[16] M. Lucido, F. Schettino, G. Panariello, Scattering from a thin resistive disk: A guaranteed fast convergence technique, *IEEE Trans. Antennas Propag.*, 69: 387–396, 2021.

[17] M. Lucido, M. V. Balaban, A. I. Nosich, Plane wave scattering from thin dielectric disk in free space: Generalized boundary conditions, regularizing Galerkin technique and whispering gallery mode resonances, *IET Microw. Antennas Propag.*, 15: 1159–1170, 2021.

[18] Bleszynski, E., M. Bleszynski, T. Jaroszewicz, Surface-integral equations for electrmagnetic scattering from impenetrable and penetrable sheets, *IEEE Antennas Propag. Magazine*, 35: 14-24, 1993.

[19] J. E. Wilkins, Neumann series of Bessel functions, *Trans. Amer. Math. Soc.*, 64: 359-385, 1948.

[20] N. Geng, L. Carin, Wide-band electromagnetic scattering from a dielectric BOR buried in a layered lossy dispersive medium, *IEEE Trans. Antennas Propag.*, 47: 610-619, 1999.

Full-vectorial polynomial modal method for circular waveguides. Application to reflection and diffraction at the end of radially inhomogeous cylinders.

Gérard Granet

Université Clermont Auvergne,
CNRS,
SIGMA Clermont,
Institut Pascal,
F-63000 CLERMONT-FERRAND, FRANCE
E-mail: gerard.granet@uca.fr

Abstract

We develop a modal method for radially inhomenous waveguide. The formulation is derived with the two transverse components of the magnetic field. The algebraic eigensystem is solved by using Tchebycheff polynomials and a tau method.

1. Introduction

Cylindrical objects are the building blocks of photonic crystals, metamaterials, and fibers. Everyday components like waveguides, or resonators are created on their basis. More recently, plasmonic nano wires have also been studied [1]. Another promising area of research in nanophotonics is the tight focus that is formed using dielectric cylinders with diameters about wavelength [2], [3]. Nowadays, many efficient commercial codes are able to simulate efficiently such structures. However researchers often feel the need to develop in house codes in order to be able to completely master all the numerical parameters of a given simulation. Another reason to develop original codes is that one can get faster tools since they can be designed for a specific need. We are interested in the analysis of radially piece wise inhomogeneous circular waveguides using a polynomial modal method which is known to be robust with regards to materials properties because it enforces in an exact manner the interface boundary conditions. The originality of the method lies in the theoretical formulation of the spectral problem and its solution using a Galerkin method with Tchebychelf polynomials as expansion and test functions [4],[5],[6]. Once the eigen-solutions are computed, the rest of the solving follows the usual steps of any modal method. Fig 1 shows a typical structure that can be analysed with our code.

2. Theory

2.1. Eigenvalue equation

A quarter of the cross section of one step index circular wave-guide is shown in Fig.(2). In case a radial radiation condition is needed, PML may be introduced through complex coordinates. Let us consider a time-harmonic magnetic

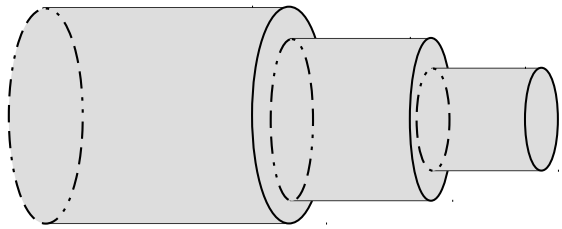

Figure 1: sketch of a multi sectional waveguide.

field such that:

$$\mathbf{H}(r,\phi,z) = \begin{bmatrix} H_r(r)\cos(m\phi) \\ H_\phi(r)\sin(m\phi) \\ H_z(r,\phi) \end{bmatrix} \exp j(\omega t - \gamma z) \quad (1)$$

In an homogeneous medium with relative permittivity ϵ_r and in the cylindrical coordinate system the vector wave equation for the magnetic field reduces to three scalar partial differential equations of the form

$$\begin{aligned} &\Delta H_r + \left(-\frac{H_r}{r^2} - \frac{2}{r^2}\frac{\partial H_\phi}{\partial_\phi}\right) = -k_0^2\epsilon_r \\ &\Delta H_\phi + \left(-\frac{H_\phi}{r^2} + \frac{2}{r^2}\frac{\partial H_r}{\partial_\phi}\right) = -k_0^2\epsilon_r \\ &\Delta H_z = -k_0^2\epsilon_r \end{aligned} \quad (2)$$

where k_0 is the wave number and where Δ represents the Laplacian of a scalar that in cylindrical coordinates takes the form of:

$$\frac{\partial^2\psi}{\partial r^2} + \frac{1}{r}\frac{\partial\psi}{\partial r} + \frac{1}{r^2}\frac{\partial^2}{\partial\phi^2} + \frac{\partial^2\psi}{\partial z^2} \quad (3)$$

Taking into account the special form of the field given by Eq(1), we get:

$$\left(\frac{\partial^2}{\partial r^2} + \frac{1}{r}\frac{\partial\psi}{\partial r} + k_0^2\epsilon_r\frac{K}{r^2}\right)\begin{bmatrix} H_r \\ H_\phi \end{bmatrix} = \gamma^2\begin{bmatrix} H_r \\ H_\phi \end{bmatrix} \quad (4)$$

$$K = -\begin{bmatrix} m^2+1 & 2m \\ 2m & m^2+1 \end{bmatrix} \quad (5)$$

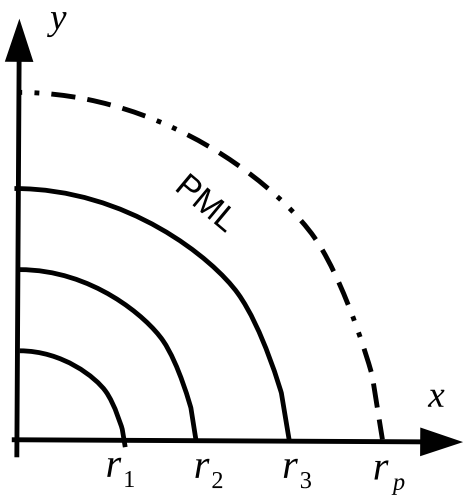

Figure 2: A quarter of the cross section of a radially piecewise inhomogeneous waveguide. The PML is backed by a PEC.

2.2. Boundary conditions

The magnetic field vector needs also to satisfy boundary conditions at coordinate surfaces $r = r_i$, at origin $r = 0$ and at $r = r_p$ which is the outer radius of the PML region.

At $r = r_i$

- H_r and H_ϕ are continuous
- $\dfrac{\partial H_r}{\partial r}$ is conthiinuous
- $\dfrac{1}{\epsilon_r}\left(\dfrac{\partial (rH_\phi)}{\partial r} + mH_r\right)$ is continuous

At $r = r_0$

- $H_r = H_\phi = 0$ if $m \neq 1$
- $\dfrac{\partial H_r}{\partial r} = \dfrac{\partial H_\phi}{\partial r} = 0$ if $m = 1$

At $r = r_p$

- $\dfrac{\partial (rH_\phi)}{\partial r} = 0$

2.3. Numerical solution

In a first step, in each homogeneous region, H_r and H_ϕ are approximated by a linear combination of Tchebycheff polynomials T_q:

$$\begin{array}{l} H_r(r) = \sum_{p=0}^{M-1} H_{rp} T_q(r) + \sum_{p=M}^{M+1} H_{rp} T_p(r) \\ H_\phi(r) = \sum_{q=0}^{M-1} H_{\phi q} T_q(r) + \sum_{q=M}^{M+1} H_{\phi q} T_q(r) \end{array} \quad (6)$$

Then Eq(4) is projected onto $2M$ Tchebycheff polynomials. Lastly an eigen-system, valid in the whole computational domain, is obtained by adding the relations which express the boundary conditions.

3. Conclusions

Our talk will be devoted to the detailed presentation of the polynomial modal method as applied to cylindrical structures. We will illustrate the effectiveness of the method through many examples. More specifically we will investigate the near field scattered at the end of a multi-sectional dielectric wave-guide

References

[1] T.Häyren, J.Rosenkrantz de Lasson, N.Gregersen, Open-geometry Fourier modal method:modeling nanophotonic structures in infinite domains, J. Opt. Soc. Am. A 33:1298–1306,2016.

[2] J.Zelgowski, A.Abdurrochman, F. Mermet, P. Pfeiffer, J. Fontaine, S. Lecler, Photonic jet subwavelength etching using a shaped optical fiber tip, Opt.Lett. 41:2073–2076,2016

[3] Y. Zhang 1, S. Li, Y. Zhu, Y. Zhuang, T. Suyama, C. Zheng ,Y. Okuno, Periodic transmission of circular binary Fresnel zone plates with etching depth and substrate, PIER Lett.,40:93–105,2013.

[4] R.Song, J.Zhu, X.Zhang, Full-vectorial modal analysis for circular optical wavegudes based on the multidomain Chebyshev pseudospectral method. J. Opt. Soc. Am. B 27:1722–1730,2010.

[5] K.Edee, M.Aboud, G.Granet, J.F. Cornet, J.Dauchet, Reformulation of the modal method based on Gegenbauer polynomial expansion for cylindrical structures with arbitrary cross sections, J. Opt. Soc. Am. A 31:2174–2178,2014.

[6] K.Edee, M.Aboud, G.Granet, J.F. Cornet, N.A. Gippius, Mode solver based on Gegenbauer polynomial expansion for cylindrical structures with arbitrary cross sections J. Opt. Soc. Am. A 31: 667–676,2014.

Fundamental limits to electromagnetic response across geometric, frequency, and configuration degrees of freedom

Owen D. Miller[1,*]

[1]Dept. of Applied Physics, Dept. of Physics, and Energy Sciences Institute, Yale University, New Haven, CT, USA
*corresponding author, E-mail: owen.miller@yale.edu

Abstract

Electromagnetic design problem are generically hard nonlinear problems that are computationally expensive and prone to getting trapped at low-quality optima. We reformulate electromagnetic-design problems as quadratically constrained quadratic programs (QCQPs). In this formulation, Maxwell's equations are replaced with a set of real- and reactive-power conservation laws, which enable identification of fundamental bounds across geometric, frequency, and configuration degrees of freedom. We show examples of fundamental limits for perfect absorbers, multi-frequency reflectivity sensors, and near-field radiative heat transfer.

Biophotonics, Biomedical Optics, and imaging

3D printed microrobots controlled by light – Towards environmental and biomedical applications

Ada-Ioana Bunea[1], Einstom Engay[1], Alexandre Emmanuel Wetzel[1], and Rafael Taboryski[1]

[1]DTU Nanolab, Technical University of Denmark, Kongens Lyngby, Denmark
*corresponding author, E-mail: adabu@dtu.dk

Abstract

Microrobots are rapidly developing as a valuable solution for performing microscale tasks, among which they seem particularly promising for biomedical and environmental applications. Two-photon polymerization enables the fabrication of microstructures with complex shapes, while focused laser beams allow for precise manipulation of such 3D printed objects. Whereas several challenges have yet to be overcome before microrobots can perform in the real world, many interesting laboratory applications have already been demonstrated, while others are being explored.

1. Introduction

Microrobots are raising enormous interest in the scientific community because of their potential for performing various tasks at the microscale. Among their target fields of use, biomedical and environmental applications are likely the most promising. Recently, we reviewed the literature on the use of microrobots for biomedical applications [1], and would like to highlight that, while the use of microrobots *in vivo* is a noble goal, there are yet numerous related challenges when it comes to e.g. deployment and retrieval strategies, control, or imaging. On the other hand, microrobots could in the near future become valuable tools for laboratory testing, where for example hyperlocalized sensing is particularly interesting for both biomedical and environmental applications.

2. 3D printing by two-photon polymerization

Two-photon polymerization 3D printing is a direct laser writing technique, where the structure is written layer-by-layer and voxel-by-voxel into a suitable negative photoresist using a highly focused femtosecond-pulsed laser beam. We use a Nanoscribe GT+ system for the microfabrication of polyacrylate robots amenable to optical trapping and manipulation. Typically, for producing microstructures with maximum resolution, we use a Plan-APOCHROMAT 63×/1.40 Oil DIC objective and the commercial photoresists IP-L 780 or IP-Dip. With optimal parameters, the resolution of the system is 100-200 nm in the XY plane and, because the laser focal spot is ellipsoidal rather than spherical, around 1.5-3.5 lower on the Z-axis [2,3]. An example of a 3D printed polyacrylate microrobot is shown in Fig. 1.

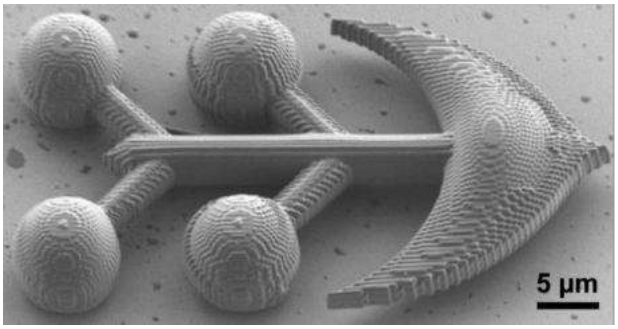

Figure 1: Scanning electron micrograph of a 3D printed microrobot including four spherical handles for optical manipulation and a large disk designed for a certain task.

3. Light-controlled micromanipulation

Among the many different approaches to microrobot propulsion and control, light offers unique opportunities in terms of precision, as highly focused near-infrared laser beams can be employed for simultaneous micromanipulation of multiple microrobotic components [2]. Furthermore, the use of light-responsive materials which deform when exposed to ultraviolet or visible light also offers interesting perspectives for introducing additional functionality (Fig. 2).

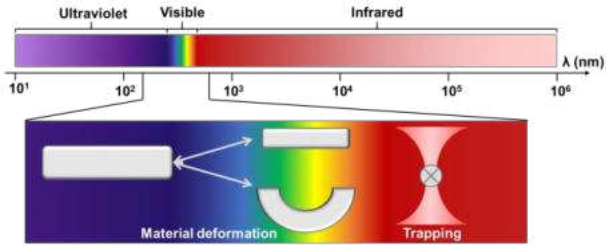

Figure 2: Light spectrum by wavelength. UV light with a wavelength above 200 nm and/or visible light can induce material deformation in photoresponsive materials. The nIR range is typically used for optical trapping, most commonly between 1060 and 1090 nm. Reproduced with permission [2], © 2021 The Authors. Advanced Intelligent Systems published by Wiley-VCH GmbH.

In our group, we employ a custom-made optical trapping setup called the Biophotonics WorkStation (BWS) for precise microrobot manipulation with six degrees of freedom (Fig. 3). The setup allows for visualizing the microrobots in motion both from the top and from the side.

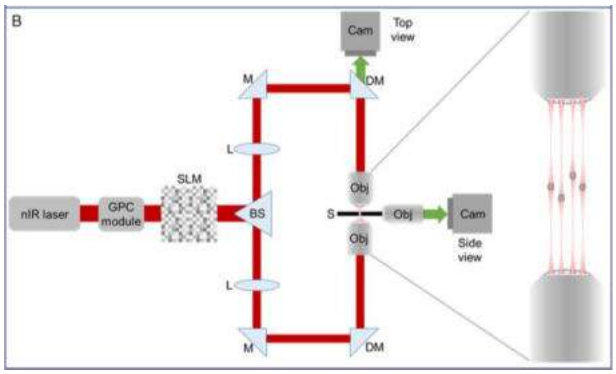

Figure 3: The Biophotonics Workstation (BWS) used for microrobot manipulation. The nIR light path used for trapping is shown in red, whereas the visible light source and light path are omitted to simplify the schematics. M—mirror; DM—dichroic mirror; L—lens; SLM—spatial light modulator; A—aperture; Cam—camera; Obj—objective; Cond—condenser; S—sample; BS—beamsplitter. The Gaussian beam coming from a 1080 nm laser is first shaped using a generalized phase contrast (GPC) module and then the SLM. The shaped beam is then split into two beams of equal intensity using a 50/50 beamsplitter, and relayed onto the sample from opposite directions using two 50× objectives with a NA of 0.55. This leaves space in the system for a 20× side-view objective. The microrobot handles are trapped in between the foci of the top and bottom counter-propagating beams. Reproduced with permission [2], © 2021 The Authors. Advanced Intelligent Systems published by Wiley-VCH GmbH.

4. Environmental and biomedical applications

Light-controlled microrobots are extremely precise and have therefore been employed for e.g. surface probing [4], localized micromixing [5], or indirect cell manipulation [6]. However, trapping in complex media, such as biological fluids or environmental samples, is rather challenging, particularly because of issues raised by the absorption and dispersion of light in such samples [7]. Nevertheless, there are several strategies for overcoming these challenges by e.g. wavefront engineering through wavefront correction algorithms, optical phase conjugation or metasurfaces. Furthermore, tailoring the microrobot surface chemistry can help reduce unwanted interactions between a microrobot and its environment, conferring "stealth" properties [8]. Recently, all-optic actuation of a microrobot in blood was demonstrated [9]. Overall, exploring combined solutions for improving light focusing in turbid media, as well as reducing the hindering interactions, should prove extremely beneficial for the future progress of microrobots in environmental and biomedical applications.

5. Conclusions

Although microrobots have yet to overcome several important challenges before they can become truly useful for real-world applications, current research is paving the way for such progress. Two-photon polymerization 3D printing enables the fabrication of microrobots with arbitrary and complex shapes and submicrometer critical dimensions. On the other hand, the use of focused beams for optical manipulation provides extreme precision for the micromanipulation of such objects. Implementing state-of-the-art solutions to improve light focusing in complex media while simultaneously tailoring the surface chemistry of the microrobots should foster applications in complex media, which is extremely relevant for many envisioned environmental and biomedical applications. Light-controlled microrobots with the ability to sense target analytes, deliver therapeutic agents, or neutralize toxic chemicals should soon become the go-to solution for laboratory experiments where such tasks need to be performed on the microscale with extreme precision. Ultimately, we envision that more complex microrobots will be able to perform microscale tasks in the real world, for example in lakes, rivers, or the human body.

Acknowledgements

The authors acknowledge support from VILLUM FONDEN (grants number 34424 and 00022918), and the Novo Nordisk Foundation (Grand Challenge Program NNF16OC0021948).

References

[1] A.-I. Bunea, R. Taboryski, Recent advances in microswimmers for biomedical applications, *Micromachines*. 11: 1048, 2020.

[2] A.-I. Bunea, D. Martella, S. Nocentini, C. Parmeggiani, R. Taboryski, D.S. Wiersma, Light-powered microrobots: Challenges and opportunities for hard and soft responsive microswimmers, *Adv. Intell. Syst.,* 3: 2000256, 2021.

[3] D. Sabaté Rovira, H.M. Nielsen, R. Taboryski, A.-I. Bunea, Additive manufacturing of polymeric scaffolds for biomimetic cell membrane engineering, *Mater. Des.* 201: 109468, 2021.

[4] D. B. Phillips, G. M. Gibson, R. Bowman, M. J. Padgett, S. Hanna, D. M. Carberry, M. J. Miles, S. H. Simpson, An optically actuated surface scanning probe, *Opt. Express*, 20: 29679, 2012.

[5] E. Engay, A.-I. Bunea, M. Chouliara, A. Bañas, J. Glückstad, Natural convection induced by an optically fabricated and actuated microtool with a thermoplasmonic disk, *Opt. Lett.,* 43: 3870-3873, 2018.

[6] S. Hu, R. Hu, X. Dong, T. Wei, S. Chen, D. Sun, Translational and rotational manipulation of filamentous cells using optically driven microrobots, *Opt. Express,* 27: 16475-16482, 2019.

[7] A.-I. Bunea, J. Glückstad, Strategies for optical trapping in biological samples: Aiming at microrobotic surgeons, *Laser Photon. Rev.,* 13: 1800227, 2019.

[8] P. Cabanach, A. Pena-Francesch, D. Sheehan, U. Bozuyuk, O. Yasa, S. Borros, M. Sitti,, Zwitterionic 3D-printed non-immunogenic stealth microrobots, *Adv. Mater.*, 32: 2003013, 2020.

[9] D. Li, C. Liu, Y. Yang, L. Wang, Y. Shen, Micro-rocket robot with all-optic actuating and tracking in blood, *Light Sci. Appl*., 9: 84, 2020.

Electromagnetic interaction and coupling

The Numerical Results of the Magnetic Behavior of the Thin-layers SFCL

Salah Belkhiri[1], F. Ben Mebarek[2], Mohamed. Lotfi. Khene[2]

[1] Department of Electrical Engineering, Faculty of technology, University of M'Sila, Algeria
[2] Department of Electrical Engineering, Faculty of technology, University of Biskra, Algeria
*corresponding author, E-mail: salah.belkhiri@univ-msila.dz

Abstract

The performance of superconducting current limiters associating the short-circuit phenomenon depends on the structure of the superconducting material envisaged and on the way of inserting it into the electrical network. The multi-layer structure, which uses thin "sandwich" layers, is found to be of interest in the search for fault current limiting power. In this paper, we present some numerical results of the magnetic behavior of superconducting fault current limiters (SFCLs). The numerical problem of this study is solved using the method of volume control (CVM). The electromagnetic and thermal coupling is ensured by an alternative algorithm. To describe the relationship between the electric field and the current density inside the thin-film superconductor, we chose to use the power law model widely used in simulation work.

1. Introduction

The object of the study is to design a thin-film superconducting current limiter capable of limiting short-circuit currents. Although thin-layers SFCL has certain favorable characteristics a priori (significant reduction in thermal stresses, relatively long service life, etc.). In this context, several simulation works have been proposed.

In this context, several simulation works have been proposed. In some of these works, the behavior of the superconductor is simulated as a vari-impedance [1-2], [3-4] where the superconducting material changes from non-dissipative state characterized by a zero impedance in the rated regime of the network to a very dissipative state characterized by a high impedance in the case of faults that can appear during the operation of the electrical network.

These simple models developed do not satisfactorily reflect the actual behavior of the superconductor in its intermediate state, particularly the flux-flow and flux-creep regimes [5,6,7]. For this, other microscopic models have been proposed in order to satisfactorily describe the flux-flow and flux-creep regimes [8-9]. In these models, the Maxwell equations are adopted and coupled to the heat diffusion equation, however the electromagnetic and thermal problems are solved in the case of one-dimensional [10] see bidimensional [11]. In these models, Maxwell's equations are adopted and coupled to the heat diffusion equation.

These models cannot correctly simulate superconducting current limiters, in particular, second generation superconducting current limiters.

The latter designed from several thin layers offer technical and economic advantages over conventional current limiter designed in a mass way is composed only of a superconducting material, usually type II. Thin-layers superconducting current limiters are essentially composed of three main layers (shunt, superconductor, substrate) [10], [9] and several buffer layers (Fig.2). Each layer has one or more functions defined [2]. They are produced by deposition on an assembly made up of a substrate and several buffer layers. The study of such a configuration requires the development of a three-dimensional computer code. For this, we propose in this article a three-dimensional mathematical-numerical model dedicated mainly to the modeling of thin-layers current limiters before and during the limitation process.

2. Formulation

To model the magnetic behavior of the presented problem, we adopted the formulation in magnetic vector potentials A and in electric scalar potential V, this one is described by the formulation below.

$$\nabla\times(\nu\nabla\times \mathrm{A})-\nabla(\nu\nabla\cdot \mathrm{A})+\sigma(E,T)\left(\frac{\partial \mathrm{A}}{\partial t}+\nabla V\right)=\mathrm{J}_s$$
$$\nabla.\left\{-\sigma(E,T)\left(\frac{\partial \mathrm{A}}{\partial t}+\nabla V\right)\right\}=0 \qquad (1)$$

$\boldsymbol{\upsilon}$ and $\boldsymbol{\sigma}$ represent respectively the magnetic reluctivity and the electrical conductivity of the superconductor. Concerning the apparent electrical conductivity of the superconducting material, in its non-dissipative state, it is defined by the ratio of J on E [12], this ratio is deduced from the characteristic E-J of the superconductor given by the relation.

$$\sigma_S(E,T) = \frac{J}{E} = \frac{J_c(T)}{E_c}\left(\frac{E}{E_c}\right)^{\frac{1}{n(T)}-1} \tag{2}$$

With

$$J_c(T) = J_{c0}\frac{(1-\frac{T}{T_c})}{(1-\frac{T_0}{T_c})}$$

This relation reflects the superconductors flux-flow and Flux-Creep regimes that is to say if the superconductor is in a non-dissipative state, to complete the expression of the electrical conductivity of the superconductor in the dissipative regime. Add an additional term σ_n which translates the increase in the resistance of the superconductor. Thus, the apparent electrical conductivity of the superconductor is deduced by the relation.

$$\sigma(E,T) = \sigma_s(E,T) + \sigma_n(T) \tag{3}$$

Where J_C and E_C respectively represent the density of the critical current and the critical electric field. According to relation (3), the apparent conductivity of the superconductor depends on the electric field E and the temperature T reached within the material. The electric field E will be determined from the resolution of the electromagnetic problem described by the partial differential equation presented by the formulation (1). The temperature will be determined from the resolution of the heat diffusion problem presented by

$$\rho C_p(T)\frac{\partial T}{\partial t} - \nabla.(\kappa(T)\nabla T) = W \tag{4}$$

Where *λ(T), ρ, Cp(T)* are respectively the thermal conductivity in (W / K / m), the density in (Kg / m^3) and the specific heat of the material in (J / K / Kg), W is a power density in (W / m^3), it expresses all the losses generated in the superconducting current limiter expressed by

$$W = E.J \tag{5}$$

In the results of the simulations presented, the thermal and the electrical properties depend on the temperature as mentioned in the equations (1), (2), (3), (4). The Models describing this dependence are presented in [12].

The resolution of the system of equations 1 and 4 solves electromagnetic and thermal problems. These are defined by strongly nonlinear equations. To solve such a problem, several methods have been used mainly finite element method [8-9], it cannot ensure the convergence of the problem to be solved especially during the presence of a superconducting material where have used a power type law to define electrical conductivity (Equation 2). To avoid this type of problem we used the finite volume method in its three-dimensional version. The adopted mesh is of Cartesian or structured type, it consists of elementary volumes of hexahedral or cubic form. For each volume Dp of hexahedral shape, we associate a so-called main node P and six facets: e and w in the direction x, n and s in the direction y, t and b in the z direction (Fig.1). The neighboring volumes of Dp are represented by their close neighboring nodes: E and W along the x, N and S axis along the y, T and B axis along the z axis [12].

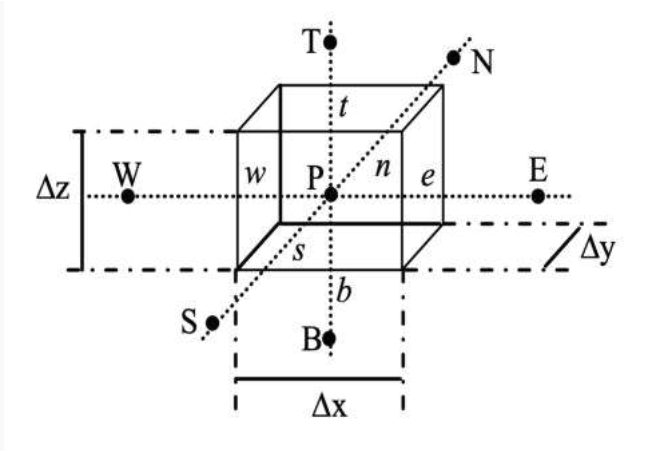

Figure 1: Elementary finished volume

$$\iiint_{D_P} \nabla\times(\upsilon\nabla\times A)\,d\tau - \iiint_{D_P} \nabla(\upsilon\nabla.A)d\tau + \iiint_{D_P} \sigma(\frac{\partial A}{\partial t} + \nabla V)\,d\tau = \iiint_{D_P} J_S\,d\tau$$

$$\iiint_{D_P} \nabla.\left\{-\sigma(\frac{\partial A}{\partial t} + \nabla V)\right\}d\tau = 0 \tag{6}$$

$$\iiint_{w\,s\,b}^{e\,n\,t} \rho C_p \frac{\partial T}{\partial t}d\tau =$$

$$\iiint_{w\,s\,b}^{e\,n\,t} \frac{\partial}{\partial x}\left(\kappa\frac{\partial T}{\partial x}\right)d\tau + \iiint_{w\,s\,b}^{e\,n\,t} \frac{\partial}{\partial y}\left(\kappa\frac{\partial T}{\partial y}\right)d\tau + \iiint_{w\,s\,b}^{e\,n\,t} \frac{\partial}{\partial z}\left(\kappa\frac{\partial T}{\partial z}\right)d\tau + \iiint_{w\,s\,b}^{e\,n\,t} W d\tau \tag{7}$$

To calculate the derivative terms in (6) and (7), we consider in our study a linear variation of the magnetic potential and the temperature across the integration facets of the finite volume. After integration, we arrive at a system of algebraic equation below that will be solved by an algebraic method such as the Gausse-Seidel method that will be adopted in our problem. The integral of equations (6) and (7) leads to the following algebraic equations [12]:

$$cpA_x^P + \sigma_p D_p A_x^{\bullet P} = \left[\sum_{m=e,w...} c_m A_x^M + \sum_{\substack{i=y,z \\ m=e,w...}} q_m A_i^M + \frac{\sigma_p D_p}{\Delta x_e + \Delta x_w} \left(V^E - V^W \right) + J_{sx} D_p \right] \quad (8)$$

$$cpA_z^P + \sigma_p D_p A_z^{\bullet P} = \left[\sum_{m=e,w...} c_m A_z^M + \sum_{\substack{i=x,y \\ m=e,w...}} q_m A_i^M + \frac{\sigma_p D_p}{\Delta z_t + \Delta z_b} \left(V^T - V^B \right) + J_{sz} D_p \right]$$

(9)

$$V^P = \frac{1}{u_p} \left[\sum_{m=e,w...} u_m V^M + \sum_{\substack{i=x,y,z \\ m=e,n...}} cv_m A_i^{\bullet M} \right] \quad (10)$$

$$[C][\dot{T}] + [K][T] = [Q] \quad (11)$$

The electromagnetic and thermal coupling is ensured by the alternating coupling model.

3. Modeling of SFCL

The device constituting the studied limiter is of the conductor type deposited with YBaCuO, it consists of three main layers (shunt, superconductor and substrate) and several buffer layers. It is true that these are poor electrical and thermal conductors but they have a major and important role in the functioning of the SFCL. They also make it possible to create a chemical diffusion barrier preventing pollution of the superconductor by the elements of the substrate and preventing oxidation of the latter during the YBaCuO deposition phase. The simplified architecture adopted for a ribbon of length L rub is described in Figure.1.

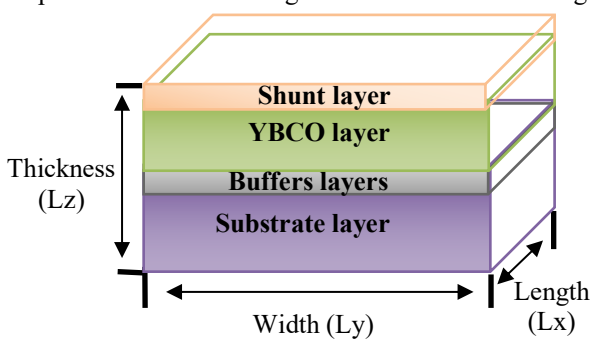

Figure 2: The description of the SFCL model.

Second-generation superconducting ribbons have been developed with the aim of getting as close as possible to the native properties of superconductors perfectly textured by epitaxial growth. The architecture of these ribbons is made in the form of a sandwich of four thin layers [15-16-17]: the substrate, the buffer layers, the superconducting layer and the shunt, (Fig. 1). Each layer has a role in the functioning of the limiter that we develop in the proposed model [14-16]. The substrate, which acts as a support, whose main function is to dissipate the excessive heat produced during the fault and thus protect the superconducting element. The thickness of the substrate is of the order of 100 µm [15-16-17], the alloys used are based on Nickel (NiCr, Inconel, Hastelloy, Constantan).

They make it possible to adapt the mechanical stresses, resulting on the one hand from the difference in thermal expansion coefficient between the superconductor and the substrate, on the other hand from the difference in the lattice parameter between these two materials. The buffer layers also provide a chemical diffusion barrier preventing pollution of the superconductor by the elements of the substrate and preventing oxidation of the latter during the YBaCuO deposition phase. They also make it possible to texturize the superconducting layer when the substrate has no orientation. To ensure a high critical current density for the YBaCuO, the buffer layer must provide a biaxial texture. The thickness of these layers varies between 0.5 µm and 3 µm [17], they are made up of YSZ, CeO, MgO or LZO. The superconducting layer generally of a thickness of the order of 1 µm (the YBaCuO) behaves like being a perfect conductor during the rated mode of the electrical network (R = 0) and in the blocked case limits the fault current by the insertion of a large resistance in the network [1]. The shunt has an average thickness of 200 nm, it acts as a thermal and electrical stabilizer in the blocked state of the limiter. Generally the materials used for this layer are noble materials such as gold or silver [16].

In the case without fault, only the YBCO is traversed by the current because its absence of resistance short-circuits the shunt, buffers and the substrate.

4. Simulation results

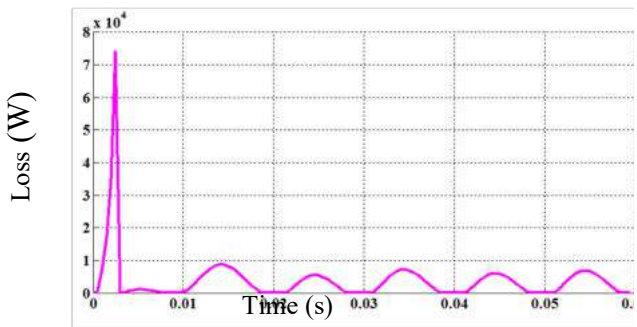

Figure 3: The variation of the average losses in the YBCO layer as a function of time.

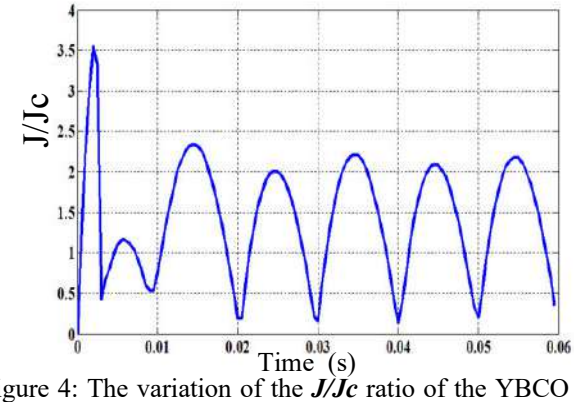

Figure 4: The variation of the ***J/Jc*** ratio of the YBCO layer as a function of time.

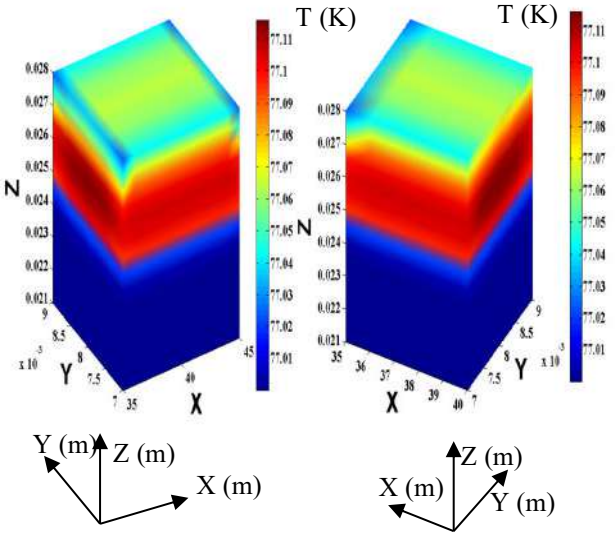

Figure 5: Spatial distribution of temperature within SFCL at t = 1 ms.

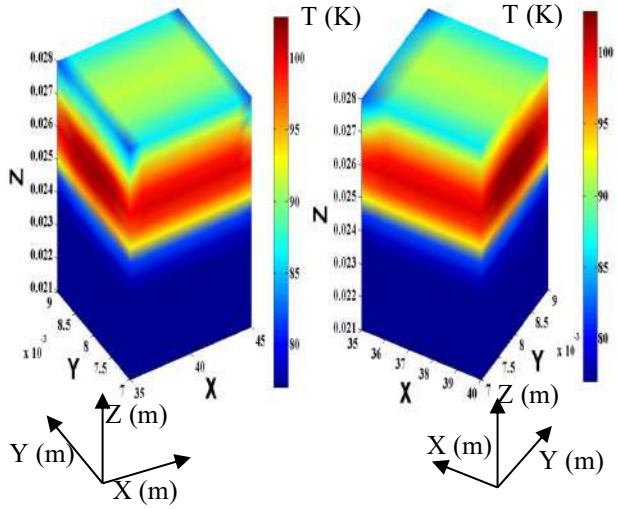

Figure 6: Spatial distribution of temperature within SFCL at t = 3 ms.

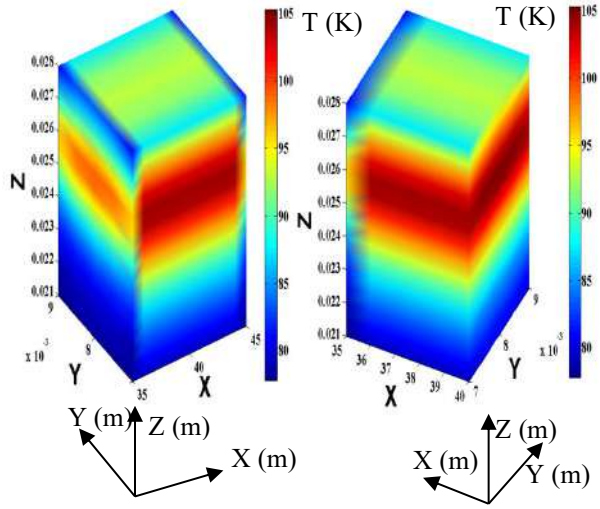

Figure 7: Spatial distribution of temperature within SFCL at t = 0.03s.

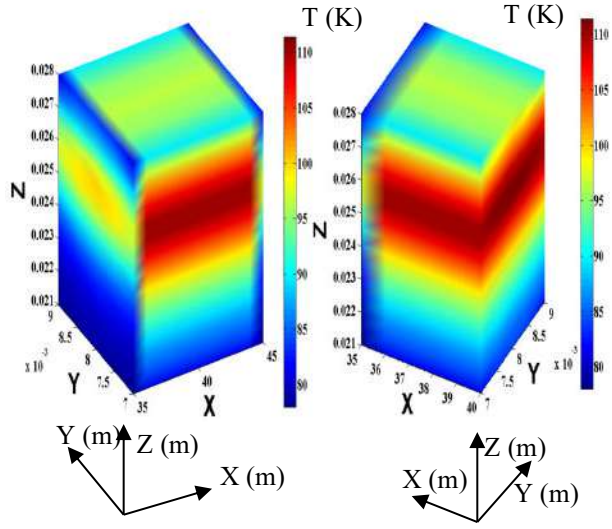

Figure 8: Spatial distribution of temperature within SFCL at t = 0.06s.

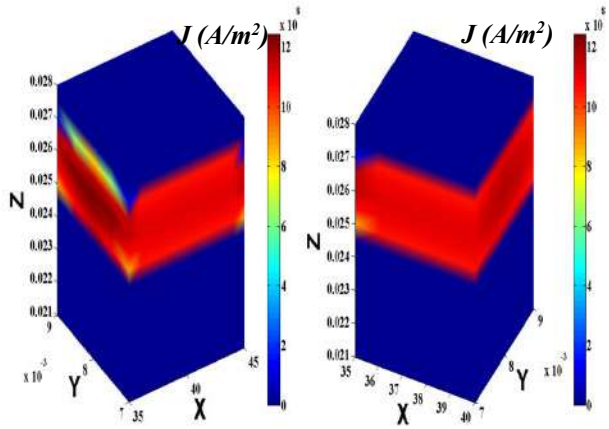

Figure 9: Spatial distribution of the density of current J within SFCL at t = 0.06s.

Figure (3) shows the temporal evolution of the average losses in the YBCO layer. The latter have evolved over time because of the energy dissipated per unit volume inside the superconducting zone (YBCO), there appears a strong increase in these losses at the start of the SFCL transition, and the amplitude reaches approximately 75KW. This is due to the heating caused by the increase in temperature within YBCO which is the site of considerably strong heat and which can damage the limiter. Then these losses are reduced, this is due to the substrate, whose main function is to dissipate the excessive heat produced during the short circuit fault and thus protect the superconducting layer.
According to the results presented in Fig. 5, we can say that the SFCL is always in a state supra at the instant t = 1 ms, that is to say that the current limiter cannot intervene at this time instant. The maximum temperature is almost 77.2 ° K below the critical temperature Tc = 92 ° K.

Figure 4 shows the variation of the J/Jc ratio as a function of time. It can clearly be seen that the superconducting limiter intervenes more quickly in a very short time even before the short - circuit current reaches its maximum during the first half-wave with a ratio of 3.5. The advantage of thin layers is their very rapid transitions, the current is limited for a J/Jc ratio generally less than or equal to two, through the substrate and the large specific surface area, the thin layers recover very quickly.

In Figs. 6-7, the temperature reached within the superconductor exceeds the value of the critical temperature (Tc = 92 ° K) at the instant t = 0.0025 s. Note also that this temperature is not homogeneous over the entire section of the limiter, in fact it is maximum at the center of the superconductor but it is minimal in the intermediate zones. The temperature which appears in the thin layers at the instant t> = 0.0025 s is mainly due to the transfer of heat between the superconducting layer and the thin layers. Indeed, during the time interval t <= 0.0025 s, all the current passes through the superconducting layer given its resistivity considered to be negligible compared to the resistivity's of the other layers. This means that the use of thin layers in the design of a current limiter has a great advantage as it significantly decreased the temperature within the current limiter during the process of fault current limiting. The decrease in temperature reached during the operation of the current limiter can extend the life of a superconducting current limiter. According to the results presented, we note that the use of thin layers has considerably improved the thermal behavior of the current limiter by significant reduction in temperature on the one hand, also the intermediate layers have improved the transition time or the current limiter intervenes in a shorter time. Also according to the results presented, it can be said that the presence of thin layers ensures that the temperature is maintained in the vicinity of 110 ° K (Fig. 8).

Fig. 9 shows the spatial distribution of current densities at SFCL breasts at time t = 0.06 s. It appears according to these results, that the current density reaches its maximum with a high concentration in the center of the YBCO layer, it is less in the other layers, and this is explained by the fact of its conductivities less low than that of YBCO even during the transition state.

5. Conclusions

The approach considered in this work takes into account the behavior of these layers according to their electromagnetic and thermal states. The different physical quantities and their spatial variations during the transition phase, current limitation and recovery are considered and widely exposed.

It is noted that when the short-circuit fault arises in the network, the current increases rapidly and exceeds the value of the critical current of the HTS which begins to transit. An electric field appears at its terminals and currents begin to flow through the shunt and the substrate.

The simulation results presented showed the interest and efficiency of thin films introduced in the design of a superconducting current limiter. These considerably improve the thermal stresses during the fault current limitation process by significantly reducing the temperature within the current limiter.

All these results will contribute to the optimization of the superconducting current limiter to obtain the best device for limiting the short-circuit currents and thus the best possible heat transfer. This is particularly important insofar as they can be used in the design of second generation limiters and installed in electrical networks.

References

[1] S.belkhiri, "Modeling a superconducting fault current limiter inserted in a nine-bus electrical network'', *AMSE. IIETA Journal*, Modelling. A, vol. 92, nº. 2-4, pp. 37-42, décembre 2019.

[2] S. Nemdili, S. Belkhiat, "Electrothermal Modeling of Coated Conductor for a Resistive Superconducting Fault-Current Limiter, " J Supercond Nov Magn doi10.1007/s10948-012-1895-4, 2012.

[3] J. Bae, Na and al, "Design and Tests of Prototype Hybrid Superconducting Fault Current Limiter WithFast Switch, " IEEE Trans. Appl. Supercond, vol. 22, no.3, pp. 5602604, 2012.

[4] H. Yamaguchi, and all. "Current Limiting Characteristics of Transformer Type Superconducting Fault Current Limiter With Shunt Impedance, " IEEE Trans. Appl. Supercond, vol.17, no. 2, pp. 1919-1922, 2007.

[5] S. Belkhiri, L. Alloui, F. B. Mebarek, "The influence of Geometrical Properties of Bulk Superconductors on Limiting Fault Current in an Electrical Network," ADVANCED ELECTROMAGNETICS, vol. 8, no.4, pp. 136-142, 2019.

[6] S. Belkhiri, M. Bouroubi, A. Harrabi, "Improvement of the Transient Stability of a 14-bus Network Using a

Superconducting Fault-Current Limiter SFCL," ADVANCED ELECTROMAGNETICS, vol. 9, no.2, pp. 75-83, 2020.

[7] S. Belkhiri, Z. Ghemari, "Comparative Study of Solid and Thin-Layers Superconducting Fault Current Limiters SFCL for Electrical Network Transient Stability Improvement," Journal of Superconductivity and Novel Magnetism. Vol. 35, Nº 3, pp.679-688, 2022. https://doi.org/10.1007/s10948-021-06128-x

[8] W. K. Chan, and al. "Three-Dimensional Micrometer-Scale Modeling of Quenching in High-Aspect-RatioYBa2Cu3O7−δ Coated Conductor Tapes—Part I: Model Development and Validation, " IEEE Trans. Appl. Supercond., vol. 20, no. 6, pp. 2370–2379, 2010.

[9] W. K. Chan, and al. "Three-Dimensional Micrometer-Scale Modeling of Quenching in High-Aspect-RatioYBa2Cu3O7−δ Coated Conductor Tapes—Part II: Influence of Geometric and Material Properties and Implications for Conductor Engineering and Magnet Design, "IEEE Trans. Appl. Supercond, vol. 21, no. 6, pp. 2628–2634, 2011.

[10] K. Nam, and al. "Thermal and Electrical Analysis of Coated Conductor Under AC Over-Current, " IEEE Trans. Appl. Supercond, vol. 17, no. 2, 1923-1926, 2007.

[11] Casali and al. "Two-Dimensional Anisotropic Model of YBCO Coated Conductors, " IEEE Trans. Appl. Supercond, vol. 25, no. 1, pp. 6600112, 2015.

[12] L. Alloui, F. Bouillault, and S.M. Mimoune, "Numerical Study of the Influence of flux creep and of Thermal Effect on Dynamic Behaviour of Magnetic Levitation Systems with a high-Tc superconductor using control volume method, " EPJ. App. Phys, vol. 37, no. 2, pp. 191-195, 2009.

[13] Y. Yoshida, M. Uesaka, and K. Miya, "Magnetic field and force analysis of high Tc superconductor with flux flow and creep, " IEEE Trans. Magn, vol.30, no. 5, pp. 3503-3506, 1994.

[14] C. Gandioli, P. Tixador, G. Mariani. "Tests and simulations of different YBCO tapes for FCL, " IEEE Transactions on Applied Superconductivity, vol. 22, no. 3, pp. 5603104–5603104, 2012.

[15] Y. Cointe, Doctorat Thesis, "Continuous superconductive limiter," Engineering Sciences [physics]. National Polytechnic Institute of Grenoble - INPG, 2007. French. <Tel-00300552>.

[16] L. Cavallucci, Doctorat Thesis, "Thermal stability and AC losses in high-field Superconducting magnets," Biomedical Electrical Engineering and IBES Systems Cycle XXX, 2018.

[17] W.T.B.d.Souse, Doctorat Thesis, " Transient simulations of superconducting fault current limiters," Electrical Engineering, Federal University of Rio de January, 2015.

Electromagnetic modelling of Leaf Water Potential under Ultra-Wide Band Microwaves Sensing

Youness Zaarour[1], Fatimazahrae Elarroud[1], Hafid Griguer[1], Rafiq El Alami[1], M'Hamed Drissi[1,2],

[1]Mohammed VI Polytechnic University, ILO, Benguerir, Morocco
[2]Univ Rennes, INSA Rennes, IETR, UMR CNRS 6164, F-35000 Rennes, France
*Corresponding author, E-mail: youness.zaarour@um6p.ma

Abstract

Noninvasive microwave sensor of plant that measure leaf concentration water is purposed. It is based on a microstrip structure where the loaded layer is represented by a mathematical model. The leaf is represented with the cellulose Cole-Debye model, that includes freshwater molecules which are simulated with different size to characterize the turgescence and plasmolysis behavior. The concept is validated and compared to Cole-Debye model for different situation of stress leaf, represented by an equivalent dielectric cell over the sensor.

I. Introduction

Agriculture is a significant economic sector in both Morocco and the rest of the globe. As a result, there is a continuing push to develop tools to aid activities in these industries. Individuals have obviously been investigating the application of remote sensing in this area for quite some time.

All remote sensing systems employ electromagnetic waves to bridge the distance between the sensor and the target to be observed. As a result, in microwave remote sensing, physical and/or biological variables must be determined from electromagnetic wave properties. The complex permittivity of the measured items is directly connected to the microwave signal received using microwave sensors. Thus, establishing a relationship between the targeted object's specific physical parameters and its complex permittivity is critical for the advancement of such technology, as well as a key method for obtaining quantitative information about the observed variables from microwave data [1].

Plant-based noninvasive microwave sensors show significant potential in informing farmers when to turn on the irrigation system, preventing water waste and plant drying. Our first purpose in this paper is using a microstrip structure line of a large frequency band combined to a mathematical model (Cole-Debye model) based on a multi-frequency dispersion to characterize the Turgescence and Plasmolysis behavior of a plant in the frequency band of 1-10GHz. This simply structure was chosen for its ability to generates several separate electric and magnetic resonant frequencies without the use of external resonant structures, this makes device design easier, and the requisite printed circuit board (PCB) production technology is simple and affordable. The electromagnetic (EM) fields in a microstrip line reside partially in the air above the dielectric substrate, which may be utilized to directly sense the subject above the sensor[2]. Generally, the central vacuole can take up to 90% of the cellular volume and, unlike intracellular organelles from animal cells, it can be studied successfully using the classic patch-clamp technique due to its large size (up to 40 m diameter)[3]. As a result, a standard model may easily simulate the electromagnetic properties of a leaf, which consist of two principal components, a cellulosic felt frame a water.

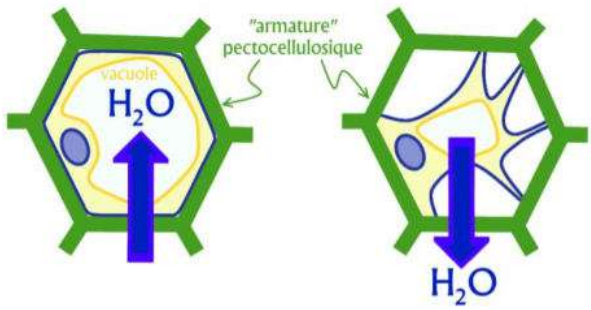

(a) Turgescent cell (b) plasmolyze cell

Figure 1: Principle of "Turgescence" in a Plant Leaf

II. Sensor design

The construction of the suggested microwave sensor and leaf model is shown in Figure 2. It includes a straightforward transmission line with w=3 mm strip width and l=120mm strip length connected to a 50Ω coaxial SMA connector to ensure the impedance matching. It is simulated on FR-4 substrate

with the relative permittivity of ε=4.3 and Tang=0.002, and the thickness of 0.79mm. The sensor has multi-resonance matched in a wide band (1GHz-10GHz) with -30dB. The choice of such simple structure (loaded line) was just to evaluate the efficiency of the proposed model. The loaded part using other type of resonators to improve the sensitivity will be the goal of the next work.

The plant leaf model positioned at the center of the microstrip line for detecting different water concentrations as shown in Fig.2. Dielectric constant of water in leaves depends on its concentration, thus, any changes in scattering matrix elements is relative to the change of water permittivity which is converted into the shift of the resonance frequency.

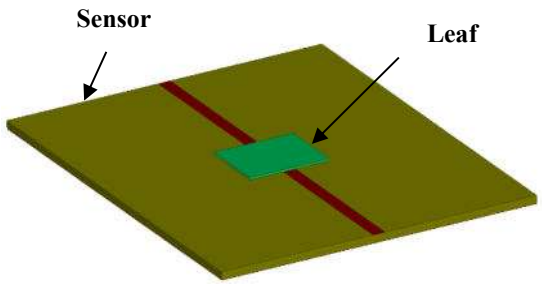

Figure 2: 3D electromagnetic model of leaf

III. EM model of the leaf

This section describes the EM modeling of plant leaves. The Leave tissues, as opposed to homogeneous dielectric materials, are made up of multiple layers of a complex inhomogeneous composition of bio-organic components with various electromagnetic qualities. The principal goal of non-invasive water concentration sensing is to detect changes in plant leaf permittivity caused by changes in water concentration. It suggests that the leaf's complex permittivity is a function of the amount of water present. This is the most important factor to keep in mind when performing any electromagnetic modeling for leaf water sensing. Although voxel-based techniques may yield excellent 3-D structural representations of plant leaves, the association between the permittivity of water and leaf concentration is difficult to account for in a voxel model.

The Debye-Cole model is widely used in electromagnetic modeling of various materials such as human blood or plant leaves as a function of frequency.

The Debye-Cole dual-dispersion established by Ulaby et al.,[4][5][6] and it is one of the most extensively used vegetation dielectric models in today's study area. The model was constructed based on observations of different kind of vegetation from 0.2 to 20 GHz via coaxial probe technique, in conjunction with theoretical models and actual data. The vegetation is represented in the model as a mix of mass vegetation, free water component, and bound water component. The model [7] may be represented as follows at room temperature (22°C):

$$\varepsilon_v = \varepsilon_r + v_{fw}\left[4{,}9\,\frac{75}{1+jf/18} - j\,\frac{18\sigma}{f}\right] + v_b\left[2{,}9 + \frac{55}{1+(\frac{jf}{0{,}18})^{0{,}5}}\right] \quad (1)$$

$$\varepsilon_r = 1.7 - 0.74M_g + 6.16M_g^2$$

$$v_{fw} = M_g(0.55M_g - 0.076)$$

$$v_b = 4.64M_g^2/(1 + 7.36M_g^2)$$

The relative permittivity of vegetation is expressed by ε_v. the nondispersive residual component is represented by ε_r, and the volume fraction of free water is represented by v_{fw}. v_b is the volume proportion of the average vegetation bound water mixture. f denotes frequency, measured in GHz. σ denotes free water conductivity, measured in S/m. M_g is the gravimetric moisture content.

Following the definition of water as a Debye-Cole material, a 3D layer-based simplified the EM model of the Leaf is created in HFSS, as illustrated in Fig. 3. The EM model is made up of homogenized cellulose and vacuoles that contains H_2O Debye model (exist in HFSS Analysis library). To focus on the variable, which is the water concentration, only the size of vacuoles is changed.

The homogeneous cellulose is characterized by a fixed permittivity. The dimension of the leaf model is 20 mm × 20 mm × 0.5mm (see Fig.4). Hv is the thickness of vacuoles, and it is changed from 10um to 140um to characterize turgescence and plasmolysis phenomena (see Fig.3), we supposed that the weight of filled leaf of water goes to Hv=140um. In general, we set the width of the vacuoles to 1mm.

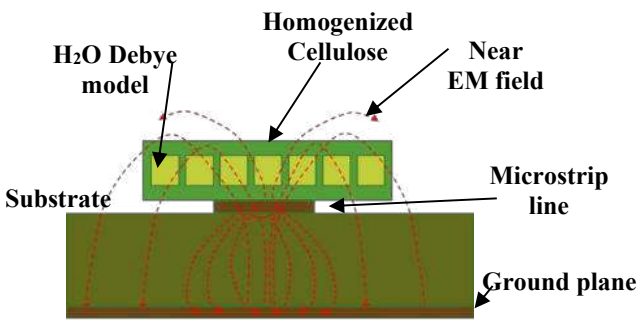

(a).

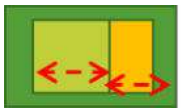

(b).

Figure 3: (a) Cross section of the loaded microstrip line with EM model. (b) vacuoles contain two targets

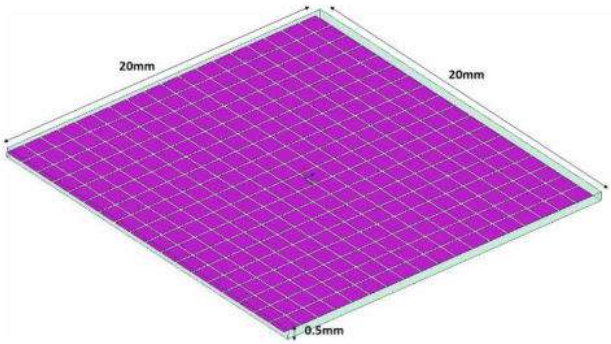

Figure 4: Side view of the Leaf

Each different level of the leaf while changing the vacuole size is correlated to a specific gravimetric moister Mg which can defined by equation (1):

$$Mg = \frac{M_f - M_d}{M_f} \quad (1)$$

where M_g is the vegetation gravimetric moisture, M_f is the weight of the moist vegetation (Hv=140um), and M_d is the dry weight of the vegetation (10um<Hv<140um).

Following that, a simulation is run with the water concentration level of the leaf varying by adjusting the size of

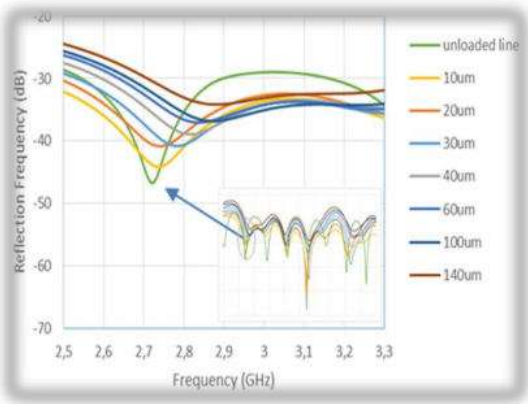

Figure 5: Reflection coefficient (S_{11}) versus frequency.

the vacuole, which ranges from 10um to 140um. It is noted in Fig. 3 that due to reduction of humidity (stress leaf) in the proposed model, the leaves permittivity decreases, and the resonance shifts towards the resonance of air (unloaded line). It is also shown that the shift frequency of the designed sensor shows linear changes to small variations of leaf size which is related to the changes of gravimetric moisture Mg as listed in table 1.

Table 1: Value of vacuole thickness versus the gravimetric moister Mg.

Hv(um)	10	20	30	40	60	100	140
Mg	0.92	0.85	0.78	0.71	0.57	0.28	0
F(MHz)	2740	2750	2790	2820	2845	2862	2890

As well as we can see from Fig.4, which plot the change of the reflection frequency described in equation (2) versus gravimetric moisture, we can predict and know for different sizes of vacuoles if plants need water or not. This model could be also used to determine irrigation efficiency by calculating the change in reflection frequency (frequency shift), thus avoiding water wastage, and drying out of plants.

$$\Delta f^{r_{min}}\% = \left(\frac{f_{leaf}^{r_{min}} - f_{unoaded\ line}^{r_{min}}}{f_{unoaded\ line}^{r_{min}}}\right) * \ 100 \quad (2)$$

Where $f_{leaf}^{r_{min}}$ is the minimum reflection frequency at the presence of leaf. $f_{unoaded\ line}^{r_{min}}$ is the free space minimum reflection frequency (unloaded line) and $\Delta f^{r_{min}}\%$ is the percentage change in the minimum reflection frequency.

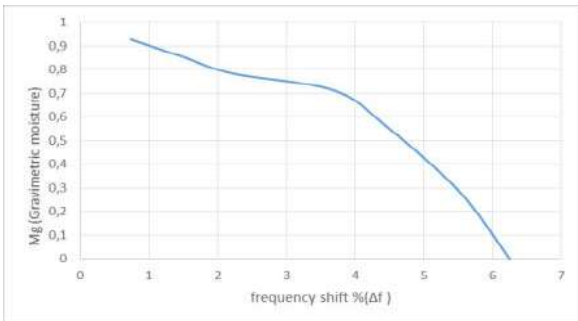

Figure 6: Gravimetric moisture versus the change of the reflection frequency (3D EM model)

III. Correlations and Verification

As Debye-Cole model might be applied to any vegetation, the proposed concept is compared to it for different situation of stress leaf, modeled with a homogeneous dielectric under the line that has different permittivity using equation (1). To define the properties (relative permittivity and loss Tand) of

the materiel under test that going to present the Cole Debye model, we used Matlab to solve the equation (1) and extract all value of ε_v, having followed that, we identified ε'(real part) and ε''(imaginary part) correspondent to different state of Mg, as the Electromagnetic Model. The obtained values are shown in Table 2:

Table 2: Value of vacuole thickness versus the gravimetric moister Mg.

Mg	0.92	0.85	0.78	0.71	0.57	0.28	0
ε'	44.23	38.45	33.09	28.29	20.2	10.07	7.9655
ε''	0.258	0.265	0.272	0.282	0.307	0.396	0.442
F(MHz)	3634	3000	3000	3000	3000	3000	3394

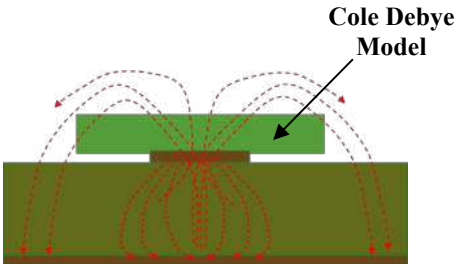

Figure 7: Cole Debye Model of the leaf

In accordance with resonance frequencies and their vacuole sizes, it is also possible to calculate the sensitivity of the sensor to compare the two models (3D electromagnetic and Cole Debye) using equation (3).

$$S = \frac{\Delta f}{\Delta hv} \text{MHz}/\mu\text{m} \quad (3)$$

Where:
ΔF= the frequency shift (MHz) between the frequency of driest and moister leaf
Δhv= the variation of vacuoles size.

The sensitivity of 3D EM model

$$S = \frac{2890 - 2740}{140 - 10} \text{MHz}/\mu\text{m}$$

$$S = 1.15 \text{ MHz}/\mu\text{m}$$

The sensitivity of Cole-Debye model

$$S = \frac{3634 - 3394}{140 - 10} \text{MHz}/\mu\text{m}$$

$$S = 1.84 \text{ MHz}/\mu\text{m}$$

As it can be seen, the results of the proposed loaded line with 3D EM model are more efficient and considerable than the homogeneous Debye-Cole model. It is an effective and general approach that gives a higher sensitivity and present closely the comportment and behavior of the leaf.

IV. Conclusion

The design and validation of the proposed 3D EM of the leaf is proposed in this paper. We used in this present paper a simple loaded line just to see how it is functional with proposed 3D EM mode and to get the intrinsic sensitivity. The uniform section of the microstrip line can be replaced by a sensor that contains specific resonator with large and high sensitivity. Microwave analysis and calibration of multi-material chemical matrix content models within a plant leaf (Application to two Micronutrients Fe, Cu see Fig3. (b)) will be introduced in the next part of this work.

V. References

[1] S. Trabelsi and S. O. Nelson, “Nondestructive sensing of physical properties of granular materials by microwave permittivity measurement,” *IEEE Trans. Instrum. Meas.*, vol. 55, no. 3, pp. 953–963, 2006, doi: 10.1109/TIM.2006.873787.

[2] L. G. Maloratsky, “Reviewing the basics of suspended striplines,” *Microw. J.*, vol. 45, no. 10, 2002.

[3] M. Festa, L. Lagostena, and A. Carpaneto, “Using the plant vacuole as a biological system to investigate the functional properties of exogenous channels and transporters,” *Biochim. Biophys. Acta - Biomembr.*, vol. 1858, no. 3, pp. 607–612, 2016, doi: 10.1016/j.bbamem.2015.09.022.

[4] F. T. Ulaby and R. P. Jedlicka, “Microwave Dielectric Properties of Plant Materials ITm jAe ’ I,” no. 4, pp. 406–415, 1984.

[5] M. A. El-rayes and F. T. Ulaby, “Dielectric Spectrum of Vegetation-Part I : Experimental Observations,” no. 5, 1987.

[6] F. T. Ulaby and M. A. El-rayes, “Dielectric Spectrum of Vegetation Part II : Dual-Dispersion Model,” no. 5, pp. 550–557, 1987.

[7] L. I. Zhen, Z. Jiangyuan, C. Quan, and B. I. Haiyun, “The measurement and model construction of complex permittivity of vegetation,” vol. 57, no. 4, pp. 729–740, 2014, doi: 10.1007/s11430-013-4691-5.

Enhancement of Light Emission Using ZnO Grating Nanowires: An Experimental and Numerical Study

Fatima Omeis[1*], Rafik Smaali[2], Aubry Martin[3,4], Audrey Potdevin[3], François Réveret[3], Emmanuel Centeno[2], Elena Silaeva[1], Yves Jourlin[1], Geneviève Chadeyron[3], Michel Langlet[4]

[1] *Laboratoire Hubert Curien, UMR 5516, Université Jean Monnet, Saint-Etienne, France*

[2] *Université Clermont Auvergne, Clermont Auvergne INP, CNRS, Institut Pascal, Clermont-Ferrand, France*

[3] *Université Clermont Auvergne, Clermont Auvergne INP, CNRS, Institut de Chimie de Clermont-Ferrand (ICCF), Clermont-Ferrand, France*

[4] *Université Grenoble Alpes, CNRS, LMGP, Grenoble, France*

*corresponding author, E-mail: `fatima.omeis@univ-st-etienne.fr`

Abstract

White Light Emitting Diodes (WLEDs) with improved light emission in the red region are highly desired for many applications especially for obtaining warm illumination rather than the conventional cold blue LEDs. In this work, we provide an experimental and theoretical study for a grating structure composed of ZnO nanowires (NWs) that proves to boost and directionally extract the visible and red light emission. The experimental results are compared with a theoretical and numerical model to understand this unique optical behavior.

1. Introduction

In recent years many research studies aimed to develop functional material structures to enhance light extraction in WLEDs. One way to accomplish this consists in structuring the most-common used phosphor in commercial white LEDs: $Y_3Al_5O_{12}:Ce^{3+}$ (or YAG:Ce) which emits mostly between 470 and 630nm under blue radiation[1]. Recently a study showed that light extraction from YAG:Ce can be improved using plasmonic nanocubes [2]. However, the combination of yellow to green photoluminescence of the phosphor with the blue light provides a white light with poor photometric parameters, in particular a low color rendering index (CRI). This is explained by the lack of red contribution in the emission spectrum of this association: blue LED and yellow phosphor. In the framework of the SMARTLEDs project, we propose an original approach that uses ZnO grating nanowires to add red light emission. The experimental measurement of the photoluminescence (PL) demonstrates that the micro structuring of the ZnO nanowire directionally extracts and enhances the ZnO light emission. Our theoretical and electromagnetic simulations show that trapped modes within the ZnO grating NWs are responsible for these behaviors.

2. Structure and design

The structure proposed is represented in Fig. 1. It consists of ZnO nanowires grown in a grating manner on a quartz substrate (Fig. 1(a)). The grating period is D=4µm, the width of the ZnO NWs gratings is w_{ZnO}=2µm, and its height is h_{ZnO}=0.6µm. The fabrication process is done by hydrothermal synthesis at ambient pressure according to Ref. [3-4]. The selective growth of NWs leading to grating ZnO NWs has been performed on a previously photo-patterned sol-gel derived ZnO-based resist. Fig. 1(b), shows the SEM images of the ZnO NWs, from the top while Fig.1(c) represents a cross section view.

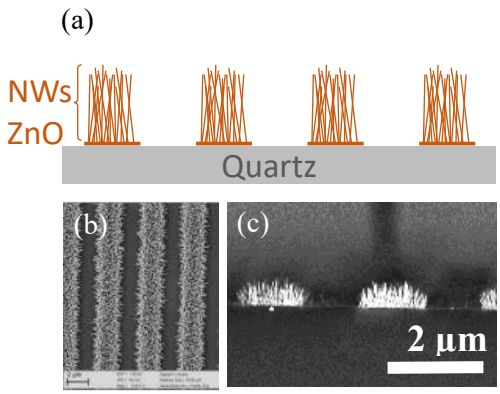

Figure 1: (a) Schematic representation of the grating ZnO NWs on a quartz substrate. (b-c) top and cross-sectional SEM images.

3. Experimental results

The room-temperature PL spectra of the structure are measured at several emitted angles when the grating structure is illuminated in normal incidence by blue radiation. Figure 2(a) shows the PL normalized vs the PL obtained at 0° as a function of the wavelength for three different angles 50°, 60°, and 75°. It can be observed that the PL is doubled at 60° near 650 nm (Fig.2 (a)). This shows that the light extraction is increased under oblique illumination compared to that at normal incidence. This is due to a resonant mode trapped inside the ZnO gratings at a certain angle, this aspect will be discussed in the last section. The comparison of the PL measured over the range 400-800 nm as a function of the extraction angle for the grating

structure and for an unpatterned ZnO coating demonstrates that the emission is clearly boosted around 65° (Fig.2 (b)). The periodic micro structuring of the ZnO NWs increases by 20% the total PL integrated between 0° and 90°. These results demonstrate that higher PL is achieved with twice less active material compared to an unpatterned coating.

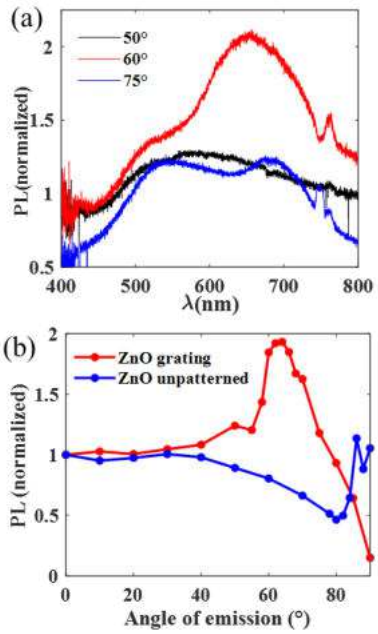

Figure 2: (a) Measured photoluminescence (normalized) under different angles of illumination (50°,60°,75°). (b) Average PL over the range 400-800nm for a ZnO grating and a coating of unpatterned ZnO on a quartz substrate.

4. Electromagnetic simulations

In this part we explain the origin of this enhanced light extraction in the grating structure. For this purpose, an effective model is adopted to substitute the spiky arrangement of the ZnO NWs by a homogeneous layer of effective index and width (neff=1.65, weff=1.6µm) (Fig. 3(a)). We found that this structure supports a resonant mode trapped within the effective ZnO ribbon (Fig 3(b)). The dispersion curve is calculated by following the eigen mode using Comsol Multiphysics (insert of Fig. 3(b)). This mode originates from the guided mode within the ZnO coating that resonates in the ribbon. Qualitatively, the angular dependence agrees with Bragg-scattering theory. The angle of emission is related to the wave vector of the guided mode, k_g, and the Bragg vector of the grating, $G = 2\pi/D$, by $k_0 \sin\theta = k_g + nG$. Finally, the experimental data (red dots) extracted from the PL measurements match with the numerical model (blue dots), which proves that the enhancement of the PL is attributed to the resonant trapped mode.

5. Conclusion

As a conclusion, we have shown that the grating ZnO nanowires proves to enhance light extraction up to two times more compared with an unpatterned layer of ZnO. This improved performance obtained with twice less active material is due to the localization of the resonant mode within the ZnO ribbon. We think that resonant ZnO gratings have a high potential for many applicative developments ranging from sensors to LEDs.

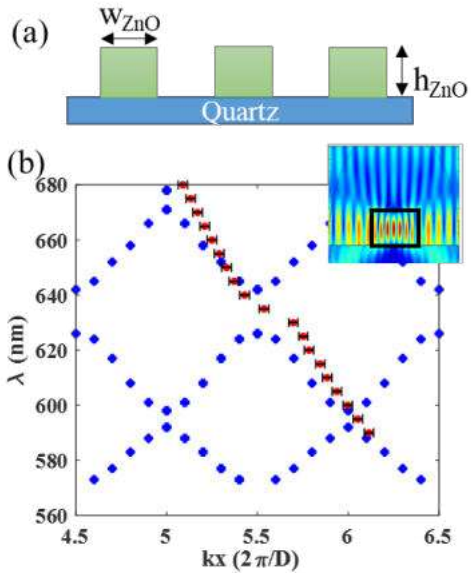

Figure 3: (a) Effective model of the ZnO grating NWs on a quartz substrate. (b) Dispersion curve of the mode resonating (inset) in the ZnO grating (blue dots). The red dots are the experimental data obtained from the measurement.

Acknowledgments

The authors acknowledge the French Agence Nationale de la Recherche for its financial support in the frame of the ANR SMARtLEDs project (ANR-19-CE08-0001)

References

[1] Tucureanu, V., Matei, A. & Avram, A. M. (2015). Synthesis and characterization of YAG: Ce phosphors for white LEDs. *Opto-electronics review*, *23*(4), 239-251.

[2] Khaywah, M., Potdevin, A., Réveret, F., Mahiou, R., Ouerdane, Y., Désert, A. & Moreau, A. (2021). Large and Versatile Plasmonic Enhancement of Photoluminescence Using Colloidal Metallic Nanocubes. *The Journal of Physical Chemistry C*, *125*(14), 7780-7790.

[3] Demes, T., Ternon, C., Riassetto, D., Stambouli, V., & Langlet, M. (2016). A comprehensive study of hydrothermally grown ZnO nanowires. *Journal of Materials Science*, *51*(23), 10652-10661.

[4] Amara, N., Martin, A., Potdevin, A., Riassetto, D., Messaoud, M., Réveret, F. & Langlet, M. (2020). ZnO nanowires/YAG: Ce functional heterostructure coatings with tunable optical properties. *Journal of Alloys and Compounds*, *842*, 155708.

Phonon-plasmon interaction in film-coupled metallic nanoparticles mediated by surface acoustic waves

A. Noual[1,2,*], R. Akiki[2], G. Lévêque[2], Y. Pennec[2], El. H. Boudouti[1] and B. Djafari-Rouhani[1]
[1]LPMR, Departement of Physics, Faculty of of Sciences, University Mohamed First, 60000 Oujda, Morocco.
[2]IEMN, UMR CNRS 8520, Département de Physique, Université de Lille, 59655 Villeneuve d'Ascq, France.
*corresponding author, E-mail: noualad@yahoo.fr

Abstract

We demonstrate by numerical analysis enhanced optomechanical interaction in a film-coupled gold nanoridges or pillars mediated by surface acoustic waves. The nanoparticles are placed atop a multilayer structure consisting of a thin dielectric spacer covering a gold film layer on a silicon dioxide/or silicon substrate. The design supports both localized surface plasmons (infrared range) confined under the nanoparticles and elastic phonons (sub-GHz) localized in the latters. Phonon-plasmon coupling is evaluated from the shift in the plasmon eigenfrequency.

1. Introduction

A great deal of interest has been sparked lately by nano-optomechanical (OM) components due to their capacity of controlling the flow of light in nanoscale photonic structures [1-2]. Such devices can also help providing utility in quantum information processing and control and/or enhancement of light-mater interaction [3-5]. The acousto-optical coupling is described by two main physical mechanisms namely, i) a volume photoelastic effect consisting in the local modulation of the dielectric constant of the material by the acoustic strain field [6], and a surface effect resulting from the deformations of the boundaries separating two adjacent media, referred to as moving-boundary effect [7]. An interesting class of structures that enable to reach strong OM interactions is based on cavities created in the so-called phoxonic crystals [8]. Band gaps exhibited for both photons and phonons by such structures, result in simultaneous highly localized light and sound which gives rise to enhanced OM coupling [9].

On the other side, surface plasmon modes localization effects are intensively employed in various fields of nano-optics such as for instance in waveguiding [10], for realizing the classical equivalent of electromagnetic induced transparency and related effects [11-12] and in enhanced inelastic Brillouin/Raman scattering [13-15]. In the latter process, the (enhanced) scattered signal enables to determine mechanical eigenmodes of metallic nanoparticles. The enhancement is due to strong coupling between the particles surface plasmon and mechanical eigenmodes. Employment of surface acoustic waves (SAWs) with high amplitudes (~ nm) enables to enhance the vibration amplitudes of the localized phonons in metallic nanoparticles, hence increasing acousto-plasmonic coupling [16, 17]. Within this spirit, we propose in this paper a high frequency (~ GHz) SAWs based device to investigate OM coupling in a film-coupled metallic nanoparticles (FCMN) structure.

2. Phonon-plasmon coupling in a pillared crystal

2.1. Acoustic properties

In this section, we study acoustic modes of the proposed structure made out of a film-coupled gold pillars (AuPls) system design. The pillars are set atop 50 nm polyamide thin layer covering a 100 nm gold film placed over a silicon substrate. A sketch of the studied structure is presented in Fig. 1(a). We chose for simplicity to set one dimensional periodic row of gold pillars roughly in the middle of the structure (on top), along y −axis. The system is finite along the propagation direction, ox. Perfect matched layers are placed all around the system in order to get rid of undesired reflections. Let us mention that the AuPls have radius $R = 165\ nm$ and height $h_{Au} = 300\ nm$, while the periodic row lattice constant is $a = 1000\ nm$. To excite the system, we employ a vertical force along a line source on top of the polymer material as shown in Fig. 1(a). Regarding elastic properties (elastic constants, mass, density etc.) of the involved materials, we employ the same parameters as in [17]. In Fig. 2(b), we show the displacement field $\sqrt{|u|^2 + |v|^2 + |w|^2}$ map within the structure for an incident plane wave at the frequency $f = 510\ MHz$.

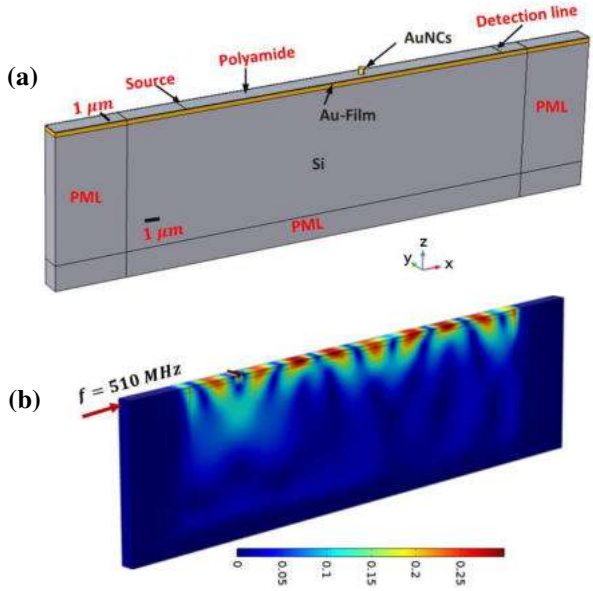

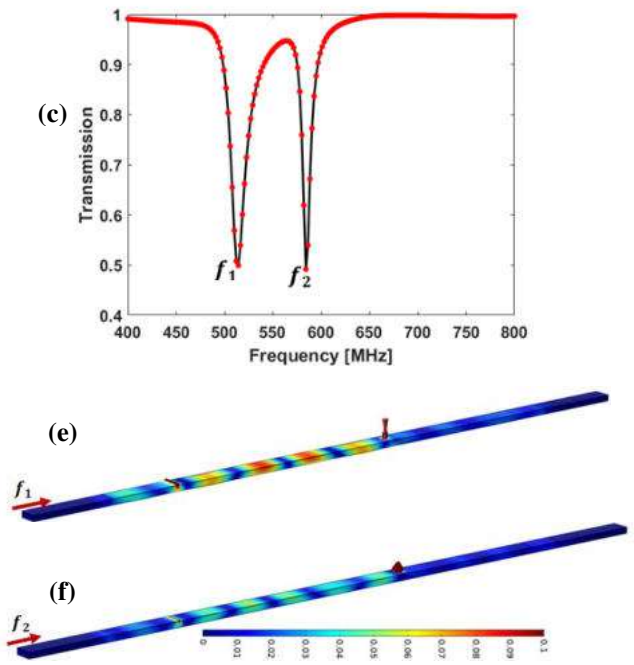

Figure 1: (a) Schematic of the SAWs-based geometry design. The structure is surrounded with PML domains, so to get rid of reflections. (b) Displacement field norm map within the structure associated with a Sezawa surface wave at the frequency, $f = 510\,MHz$. (c) Simulated transmission spectrum of the structure in (a). (e)-(f) Displacement field norm map at the frequencies of the observed dips in (c), that is, at $f_1 \approx 513\,MHz$ and $f_2 \approx 584\,MHz$, respectively.

We observe the strong confinement of the propagating waves close to the multilayer surface, indicating the excitation of a Sezawa surface wave. In order to study the interaction of the incident surface wave with the AuPls, we have simulated the transmission spectrum of the structure (of Fig. 1(a)); the frequency range extends from $400\,MHz$ up to $800\,MHz$. Figure 2(c), gives the corresponding results, where we note the excitation of two localized modes since two dips are observed in the transmission spectrum. The dips are situated at $f_1 \approx 513\,MHz$ and $f_2 \approx 584\,MHz$, and according to Figs. 5(e)-5(f), where we present the displacement field map within the upper layers of the system for clarity, the mode at f_1 (mode 1) correspond to a compressional mode while the mode at f_2 (mode 2) is a flexural mode.

2.2. Optomechanical coupling

In order to study optical quasi-eigenmodes (equivalent to eigenmodes in case of lossy materials [18]), we employ the geometry depicted in Fig. 1(a) but such as an air domain (surrounding the AuPls) is added on top of AuPls/Si-substrate. Then, we proceed to the search of localized surface plasmon modes near the AuPls in the infrared region. For that matter, we set the air-domain boundaries to scattering boundary conditions which absorb scattered waves, preventing unphysical reflections. It should be mentioned that optical properties of the materials (insulators refractive indices and gold dielectric constant) are set similarly to [17]. In Figs. 2(a) and 2(b), we give, respectively, the electric field norm map within ozx and oxy −cut planes of the simulated structure, of an optcial quasi-mode found at the eigen-wavelength $\lambda_{spp} \approx 1602\,nm$. It can be seen that such mode is well confined under the pillar within the dielectric layer and fits the so-called MIM-localized-surface plasmon (MIM-LSP) well described in [19]. In particular, the volume underneath the AuPls where the light is trapped acts as an actual effective MIM-cavity.

We study OM coupling between localized elastic phonons, mode 1 ($f_1 \approx 513\,MHz$) and mode 2 ($f_2 \approx 584\,MHz$), and the localized MIM plasmon supported by the structure, using the so-called moving interface effect. As mentioned earlier, such effect accounts for the acoustic induced deformations along each interface (between two materials) of the system. Due to the fact that an acoustic period $\sim 10^8\,/s$ is several orders of magnitude smaller than an optical cycle of the order of $10^{14}\,/s$, we use the quasi-static approximation in which at an instant of time of the deformed geometry we calculate the new resonance of the quasi-eigen plasmon mode frequency. Specifically, we simulate the latter for different phases $\varphi = 2\pi f t$ during an acoustic period, where f is the eigen-frequency of the elastic mode of interest and t is time. The deformation amplitude applied via the moving mesh effect is assumed to be such that the maximum elastic displacement inside the nanocylinder equals to 1% of its height, which yields $u_{max} = 3\,nm$. Such value though unrealistically high, it is yet convenient for numerical simulations. Also, it can be readily scaled down to smaller deformations assuming a linear dependence between the latters and the plasmon eigenfrequency modulations. In Fig. 2(c), we show the simulated MIM plasmon eigenwavelength plotted against the phase $\varphi \in [0 - \pi]$ of the compressional mode 1 (at $f_1 \approx 513$ MHz).

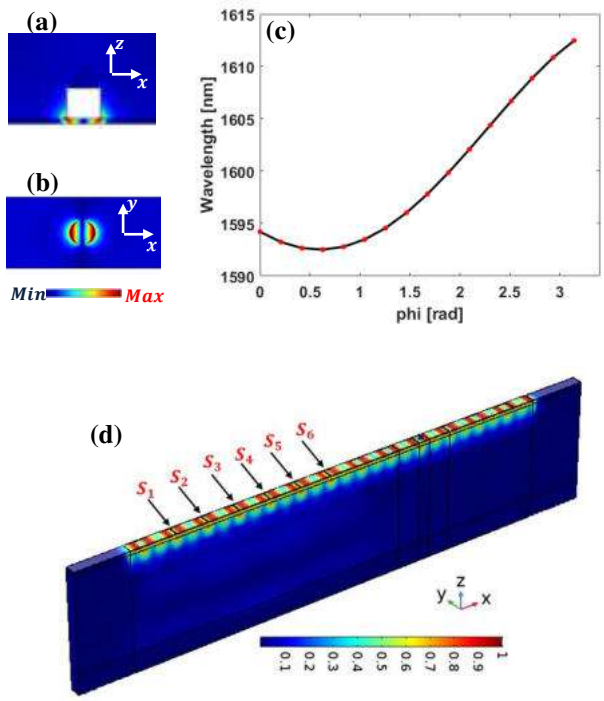

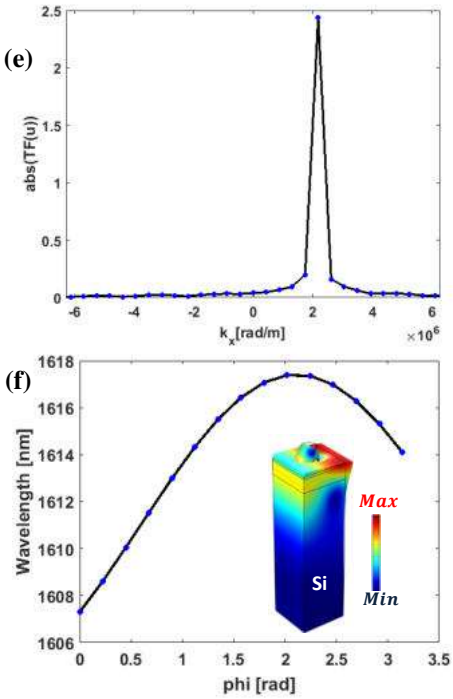

Figure 2: (a), (b) Electric field norm map in ozx and oxy −cut planes of the structure, respectively. (c) Plasmon mode eigenwavelength plotted versus an incident elastic surface wave phase $\varphi \in [0 - pi]$, excited at $f = 510\ MHz$ to match the compressional mode 1 frequency (Fig. 1(e)). (d) Displacement field map of a Sezawa mode of the system. The latter is excited by placing six linear sources on top, distant by $a_x = 2\pi/k_x$, where $k_x \approx 2.19.10^6\ rad/m$ is the wavenumber with the frequency $f = 0.8\ GHz$, according to the dispersion curve of the structure. (e) Fourier transform performed along (Ox) of $x-$component of displacement field (u) associated with Sezawa mode depicted in (d). (f) Same as (c) but for Sezawa mode in (d). Inset: displacement field map of such Sezawa mode depicted near the AuPls.

We can observe that the plasmonic mode eigenwavelength gets harmonically (following a sinusoidal form) modulated by the excited localized phonon via incident surface wave (Fig. 1(e)), with maximal oscillation amplitude of about $\Delta\lambda_{sppmax} \approx 19.9\ nm$. This value indicates the reach of strong OM coupling regime, which has been facilitated thanks to SAWs enhancing the localized phonon amplitude. As concerns the flexural mode, the plasmon modulation (not shown) is quite weak owing to such mode symmetry in which the volume of the effective MIM cavity under the pillar is nearly not affected. Conversely, in the compressional phonon (mode 1), the MIM cavity volume is strongly compressed and stretched, resulting in the observed plasmon modulation. We have also studied OM coupling between the plasmon by and a Sezawa mode of the system situated at $f = 0.8\ GHz$. As a matter of fact, in such mode the MIM cavity volume is rather strongly deformed, which hints at (possibly) intense OM coupling. The eigen-shape of this Sezawa mode is depicted in the inset of Fig. 1(f). In order to excite Sezawa modes one should set a well-defined value of wavenumber for a certain frequency due to these modes dispersion. According to dispersion curve of Sezawa modes supported by the structure (not shown), the considered Sezawa mode wavenumber at $0.8\ GHz$ is $k_x \approx 2.19.10^6\ rad/m$. To set the latter value at $f = 0.8\ GHz$, we place six linear sources parallel to each other on top of the structure at a distance equals to $a_x = 2\pi/k_x$. The employed method is illustrated in Fig. 2(d), where we plot the displacement field norm map of the Sezawa mode. In Fig. 2(e), we have plotted the Fourier transform along (Ox) of $x-$component of the displacement field (u) associated with this mode. We note the efficiency of the method as the excited wavenumber (at $0.8\ GHz$) is $\approx 2.191.10^6\ rad/m$. The plasmon eigenwavelength evolution versus the phase φ of the Sezawa mode is shown in Fig. 2(f), where we note its effective sinusoidal modulation with a maximum amplitude of oscillation of about $\Delta\lambda_{sppmax} \approx 10\ nm$. This shows a slightly lesser magnitude of OM coupling comparing with compressional mode, but yet a high phonon-plasmon interaction magnitude, reflecting strong OM regime.

3. Enhanced optomechanical coupling in film-coupled metallic dimer

3.1. Optical properties

A sketch of the proposed dimer film-coupled nanoparticles geometry design is showed in Fig. 3(a). It consists in a gold metal film lying under a polymer dielectric over which a gold ridge dimer is set. The metal film is deposited on a SiO_2 semi-infinite substrate. Due to symmetry, we perform numerical analysis in two-dimensional cross section of the design (in a ozx-cut plane). We set perfect matched layers (PMLs) around the design to prevent undesired reflections. The geometrical parameters are the ridges width D_{Au}, height h_{Au}, inter-dimer separation distance d_{dmr} and the polymer film thickness e_{pol}. The gold metal film thickness is to be set as $100\ nm$. We exclude SiO_2 substrate from optical simulations as the field would be fully absorbed within the metal film before reaching it. Materials refractive indices are $n_p \approx 1.5$ for the polymer, while for the gold material a Lorentz-Drude model is adopted [20]. In Fig. 3(b), we show the simulated scattering cross section spectrum of the dimer versus wavelength and incidence angle θ for $D_{Au} = 320\ nm$, $h_{Au} = 300\ nm$, $e_{pol} = 50\ nm$ and $d_{dmr} = 50\ nm$.

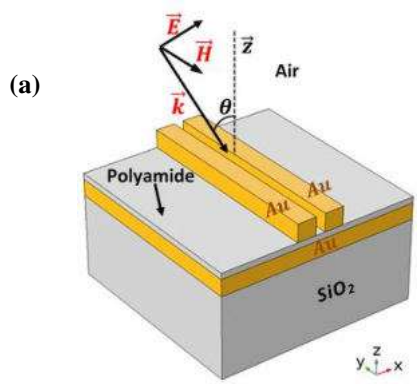

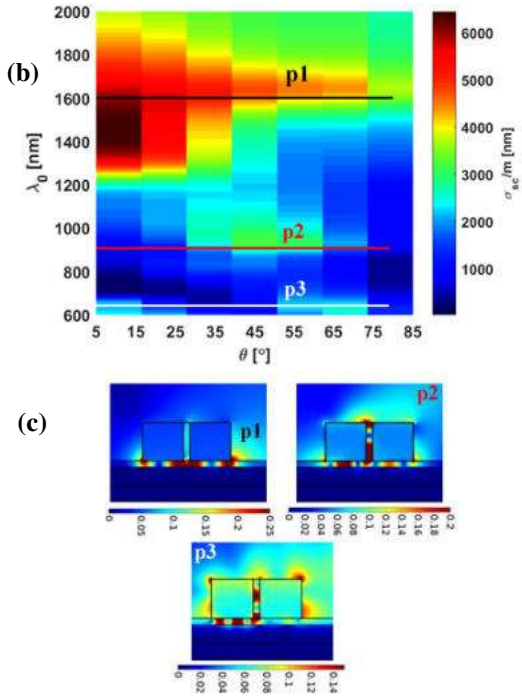

Figure 3: (a) Schematic of the proposed dimer-based FCMN design. Incoming light at oblique incidence is also illustrated. (b) Simulated extinction spectrum of the geometry of (a) versus wavelength and incoming light incidence angle. (c) Scattered field map norm near the dimer, at $\lambda_1 \approx 1638\,nm$, $\lambda_2 \approx 926\,nm$ and $\lambda_3 \approx 628\,nm$ for an incidence angle of $\theta \approx 51°$; the modes positions are referred to as p1, p2 and p3 in (b).

Three modes are observed for $\theta \gtrsim 51°$, where scattering (per unit length) increases at approximately $\lambda_1 \approx 1638\,nm$ (mode p1), $\lambda_2 \approx 926\,nm$ (mode p2) and $\lambda_3 \approx 628\,nm$ (mode p3). We also observe a strong excited scattering band near normal incidence at $\sim 1450\,nm$, with a higher FWHM comparing with modes p1, p2 and p3 (for $\theta \gtrsim 51°$). We shall focus mainly on these latter well-defined modes (at $\theta \sim 51°$), which are potentially useful for the purpose of optomechanical interactions. To better interpret such modes, we performed an eigen-frequency quasi normal mode study, where we searched for modes around λ_1, λ_2 and λ_3. The found eigenmodes are overlaid with the scattering spectrum with a black line for mode p1, a red line for mode p2 and a white line for mode p3. A good match can be noted. Scattered E_s-field norm map near the dimer is shown in Fig. 3(c) at λ_1, λ_2 and λ_3, respectively, for an incidence angle $\theta = 51°$. We see that mode p1 is a MIM-type localized surface plasmon (MIM-LSP) strongly confined in the space underneath the ridges acting as an effective MIM-cavity; mode p2 is a higher order MIM-LSP beneath the dimer but with an MIM-like component confined vertically between the ridges. Mode p3 on the other hand is a higher order MIM-LSP mode under the dimer with higher order vertically confined MIM-like component between ridges. Note that mode p2 and particularly mode p3 have antenna-like components associated with multipolar localizations at the edges. Overall, the three modes arise out of coupling of the two ridges, leading to new type of field localizations.

3.2. Dimer mechanical modes

In order to investigate OM coupling in a SAWs-based design we employ the geometry depicted in Fig. 4(a). Prior to this, we investigate SAW transmission properties in the structure, so to find the dimer mechanical modes. Perfect matched layers are set to surround the simulation domain preventing unwanted reflections. Geometrical parameters of the dimer and the FCMN structure are chosen as in Fig. 3(b). For symmetry reasons (invariance along y −axis), we perform 2D simulations within a section in the ozx-cut plane. Let us indicate that as far as elastic parameters of gold, polyamide and silicon dioxide materials, we took the same values as in [20]. An excitation line force is applied atop the system along the z −axis (Fig. 4(a)). The transmission spectrum is obtained by making an average of the displacement field magnitude $\langle\sqrt{|u|^2 + |w|^2}\rangle$ registered near at the output; the spectrum is normalized with respect to the structure in absence of the ridges. We should point out that the transmission spectrum is computed in the frequency range $[0.12\,GHz - 0.62\,GHz]$. Fig. 4(b) shows the corresponding simulated transmission, and as a matter of comparison, we have also plotted the transmission of a single gold ridge monomer atop the system (with the same dimensions). Regarding the monomer (black curve), we observe three dips in the spectrum indicating the existence of three resonance modes.

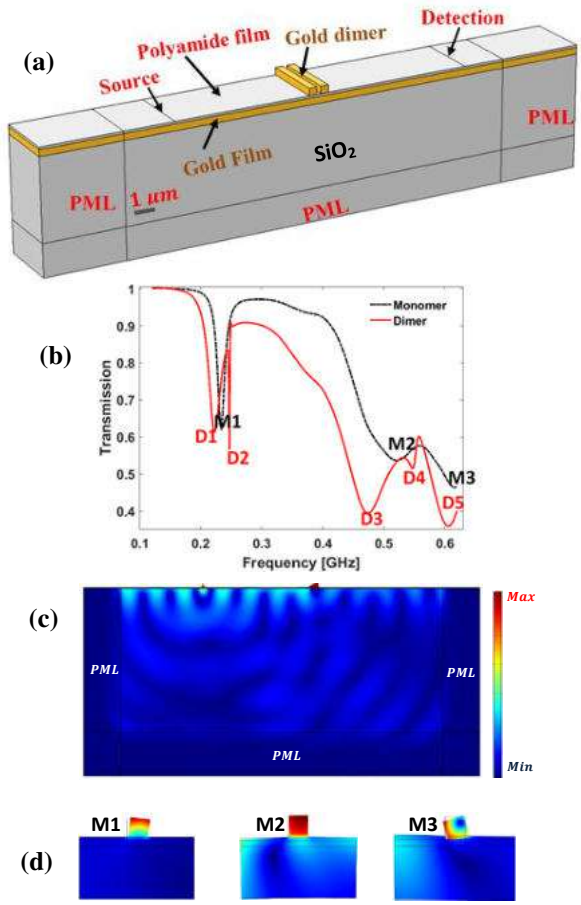

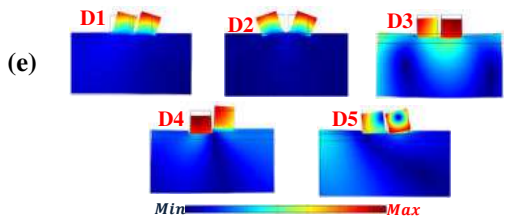

Figure 4: (a) Scheme of the SAW-based dimer-FCMN geometry. The structure is deposited on SiO_2 substrate and PMLs are employed to get rid of unwanted reflections. (b) Corresponding normalized transmission spectrum through a dimer (red curve) or a monomer (black curve). (c) Displacement field map in the system at the frequency, f_{D1} of the mode referred to as D1 in (b). (d)-(e) Zoom in of displacement map near the ridge (s) at the frequencies, f_{M1}, f_{M2} and f_{M3} of the modes referred to as M1, M2 and M3 in (b), and for the modes referred to as D1 up to D5 in (b). Note that the frequencies values are given in the main text.

These modes are found at, $f_{M1} \approx 0.234\ GHz$ (mode M1), $f_{M2} \approx 0.5218\ GHz$ (mode M2) and $f_{M3} \approx 0.615\ GHz$ (mode M3); and they correspond to a first flexural, a compressional and a higher order flexural mode, respectively. The identification here is based on the modes displacement field norm map plotted in Fig. 4(d). In case of a dimer (red curve), we note due to mechanical coupling in the dimer a split of the modes M1 and M2. Specifically, mode M1 splits, respectively, into in- and out-of-phase flexural modes namely, mode D1 at $f_{D1} \approx 0.222\ GHz$and mode D2 at $f_{D2} \approx 0.24724\ GHz$. Compressional mode M2 yields in- and out of-phase compressional modes, at $f_{D3} \approx 0.4748\ GHz$ (mode D3) and $f_{D4} \approx 0.548\ GHz$ (mode D4), respectively. This is seen in Fig. 4(e), where displacement maps near the dimer are depicted at these modes frequencies. Furthermore, the split of mode M3 is shifted out of the frequency range as concerns the higher frequency out-of-phase flexural mode whilst, the low frequency in-phase flexural mode (D5) is found at $f_{D5} \approx 0.6056\ GHz$ (Figs. 4(b), 4(e)).

3.3. Acousto-plasmonic coupling

Now, we study OM coupling between localized elastic phonons D2 and D3 and the plasmonic mode p1. The choice of the latter is justified by its stronger confinement under the ridges comparing with modes p2/p3, while concerning the formers namely the elastic modes, the choice is dictated by symmetry reasons. Indeed, in modes D2 or D3, resp., the volume where the plasmon is localized is symmetrically compressed/ stretched, leading possibly to important overlap between phonon and plasmon. Similar to OM coupling simulation in the previous section, we employ the moving mesh mechanism in order to simulate the plasmon eigen-wavelength shift due the phonon induced strain near boundaries/interfaces. Specifically, the maximum elastic displacement set around the ridges is $u_{max} \approx 1.55\ nm$, which indicates a small applied deformation rate of ~ 0.48 % the width of the ridge. We would like to point out that in order simulate the plasmon eigenfrequency shift an air domain is added on top, and PMLs are set to surround the added domain, so to minimize unwanted reflections. In Fig. 5(a), we present the shift in the plasmon eigen-wavelength caused by the in-phase compressional mode D3. To be more specific, we have plotted $\delta\lambda_1 = \lambda_1 - \lambda_{10}$ versus the temporal phase $\phi = f_a \times t \in [0 - 2\pi]$of the acoustic wave ($f_a$, being the frequency of the acoustic mode while t is the time), where λ_{10} is the original wavelength whilst λ_1 is the modulated wavelength. Similarly, in Fig. 5(b) we analyze the modulation of the plasmon (red curve) by the in-phase flexural dimer mode D2. We observe that mode D3 of the dimer clearly modulates the plasmon (Fig.5(a)) as the latter eigen-wavelength undergoes a sinusoidal oscillation with a maximal amplitude of $\delta\lambda_1 \approx 6.4\ nm$ around $\lambda_{10} \approx 1613$ nm. Concerning the coupling of mode D2 with the plasmon, we note the periodic modulated of the latter by the former, with the maximum modulation amplitude, $\delta\lambda_1 \approx 2.3\ nm$. This value though less intense as compared with the one caused by mode D3, it is yet quite significant especially considering the weak applied deformation rate of less than 0.5 %.

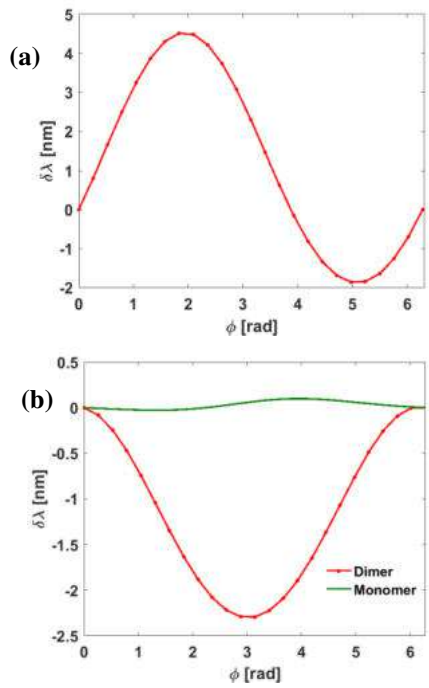

Figure 5: (a) The plasmon p1 eigenwavelength $\delta\lambda = \lambda - \lambda_{10}$ plotted versus the temporal phase of the in-phase compressional mode D3. The wavelength λ_{10} corresponds to the unmodulated plasmon resonance found at $\lambda_{10} \approx 1613\ nm$ by quasi-normal modes search. (b), Same as in (a) but in case where the modulating mechanical mode is the in-phase flexural mode D2. As for comparison of OM coupling rates between a dimer and monomer, we also plot in (b) in dark green curve, the modulation of the equivalent of plasmon p1 in case of a monomer by the flexural mode of a monomer (mode M1).

Such observed OM coupling rates between the plasmon p1 and modes D2 and D3 can be explained based on their

displacement norm maps plotted within the MIM-cavity under the dimer (not shown). One notes indeed that the latter volume undergoes strong compression/stretching movements in both mechanical modes, but with a lesser magnitude in mode D2. This certainly explains the observed plasmon modulation with such modes D2/D3, and also the different maximum modulation amplitudes they induce. In case of a monomer sitting atop the system, the equivalent plasmon of mode p1 with strong localization rate under the ridge is found by quasi-normal eigenfrequency simulations at $\lambda_0 \sim 1800\ nm$. We plot such plasmon modulation $\delta\lambda = f(\phi)$ by the monomer flexural mode M1 in dark green curve in Fig. 5(b). We see that the flexural mode M1 of the monomer seemingly inactive optomechanically becomes clearly active in case of a dimer in the mode D2.

4. Conclusions

In this work, we have investigated OM coupling in two film-coupled metallic nanoparticles structures namely, i) pillared crystal type, where a single gold pillar is set atop a multilayer design, and ii) gold ridges dimer-based device. In the latter geometry, the dimer is also placed atop a multilayer structure. We exploit SAWs in order to excite localized phonons in the with significant amplitudes magnitudes which, enables to enhance OM coupling strength. It is found in both designs that the compressional elastic mode yields the higher OM intensity with the localized MIM-type plasmon mode supported by the systems. We also found that the flexural mode optomechanically inactive for a single ridge (atop the system) turns on active in case of a dimer, when the latter vibrate in-phase. The findings in this paper could help design light acousto-optic modulators.

References

[1] D. A. Fuhrmann, M. T. Susanna, H. kim, D. Bouwmeester, P. M. Petroff, A. Wixforth, H. J. Krenner, Dynamic modulation of photonic crystal nanocavities using gigahertz acoustic phonons, *Nat Photoni*cs 5, 605–609, 2011.

[2] V. Laude, A. Belkhir, A. F. Alabiad, M. Addouche, S. Benchabane, A. Khelif and F. I. Baida, Extraordinary nonlinear transmission modulation in a doubly resonant acousto-optical structure, *Optica* 4 (10), 1245-1250, 2017.

[3] M. Sansa, M. Defoort, A. Brenac, M. Sansa, M. Defoort, A. Brenac, M. Hermouet, L. Banniard, A. Fafin, M. Gely, C. Masselon, I. Favero, G. Jourdan and S. Hentz, Optomechanical mass spectrometry, *Nat Commun* 11, 3781, 2020.

[4] H. Xiong, L. -G. Si, Y. Wu, Precision measurement of electrical charges in an optomechanical system beyond linearized dynamics, *Appl. Phys. Lett*, 110, 171102, 2017.

[5] J. Xia, Q. Qiao, G. Zhou, F. S. Chau and G. Zhou, Opto-Mechanical Photonic Crystal Cavities for Sensing Application, *Appl. Sci,* 10, 7080, 2020.

[6] D. Royer, E. Dieulesaint, Elastic Waves in Solids, *Springer*, New York, 2000.

[7] K. C. Balram, M. Davanço, J. Y. Lim, J. D. Song and K. Srinivasan, Moving boundary and photoelastic coupling in GaAs optomechanical resonators, *Optica*, 1, 414-420, 2014.

[8] B. Djafari-Rouhani, S. El-Jallal, Y. Pennec, Phoxonic crystals and cavity optomechanics, *C. R. Physique*, 17, 555–564, 2016.

[9] M. H. Aram and S. Khorasani, Optomechanical coupling strength in various triangular phoxonic crystal slab cavities, *J. Opt. Soc. Am. B* 35, 1390-1396, 2018.

[10] A. Aziz, A novel plasmonic waveguide for extraordinary field enhancement of spoof surface plasmon polaritons with low-loss feature*, Results in Optics*, 5, 100116, 2021.

[11] A. Noual, O.E. Abouti, E.H. El Boudouti et al., Plasmonic-induced transparency in a MIM waveguide with two side-coupled cavities. *Appl. Phys. A* 123**,** 49, 2017.

[12] J. Cheng, S. Xu, Learning Nonlinear Waves in Plasmon-induced Transparency. *ArXiv,* abs/2108.01508, 2021.

[13] A. Girard, H. Gehan, A. Mermet, C. Bonnet, J. Lermé, A. Berthelot, E. Cottancin, A. Crut, J. Margueritat, Acoustic mode hybridization in a single dimer of gold nanoparticles, *Nano Lett*, 18, 3800, 2018.

[14] A. Girard, J. Lermé et al., Inelastic light scattering by multiple vibrational modes in individual gold nanodimers, *J. Phys. Chem. C*, 123, 14834, 2019.

[15] A. Noual, E. Kang, T. Maji, M. Gkikas, B. Djafari-Rouhani and G. Fytas, Optomechanic Coupling in Ag Polymer Nanocomposite Films, *J. Phys. Chem. C*, 125 (27), 14854–14864, 2021.

[16] T.-R. Lin, C.-H. Lin and J.-C. Hsu, Strong Optomechanical Interaction in Hybrid Plasmonic-Photonic Crystal Nanocavities with Surface Acoustic Waves, *Sci Rep.* 5, 13782, 2015.

[17] A. Noual, R. Akiki, Y. Pennec, E. H. El Boudouti, and B. Djafari-Rouhani, Surface Acoustic Waves-Localized Plasmon Interaction in Pillared Phononic Crystals, *Phys. Rev. Applied*, 13, 024077, 2020.

[18] W. Yan, R. Faggiani and P. Lalanne, Rigorous modal analysis of plasmonic nanoresonators, *Phys. Rev. B*, 97, 205422, 2018.

[19] A. Mrabti, G. Lévêque, A. Akjouj, Y. Pennec, B. Djafari-Rouhani, R. Nicolas, T. Maurer, P. M. Adam, Elastoplasmonic interaction in metal-insulator-metal localized surface plasmon systems, *Phys. Rev. B* 94, 075405, 2016.

[20] A. Noual, R. Akiki, G. Lévêque, Y. Pennec, and B. Djafari-Rouhani, Enhanced phonon-plasmon interaction in film-coupled dimer nanoridges mediated by surface acoustic waves, *Opt. Express* 29, 43104-43123, 2021.

Electromagnetic theory

Symmetry protected and accidental bound states in the continuum in photonic-crystal structures, studied by the resonant-state expansion

Sam Neale and Egor A. Muljarov

School of Physics and Astronomy, Cardiff University, Cardiff CF24 3AA, United Kingdom

The resonant state expansion (RSE) is a novel rigorous method for calculating resonant states (RSs) of a photonic system [1]. These are the eigensolutions of Maxwell's wave equation (MWE) with outgoing boundary conditions. Using a complete set of the RSs of a simpler system as a basis, the RSE makes a mapping of the MWE onto a linear eigenvalues problem, determining the full set of the RSs of a complex system.

In addition to higher numerical efficiency [2,3] compared to other computational methods, the RSE provides an intuitive physical picture of resonant phenomena, capable of explaining features observed in optical spectra. So far, the RSE has been applied to finite open optical systems of different geometry and dimensionality, as well as to homogeneous and inhomogeneous planar waveguides [3]. Very recently, the RSE was generalized to magnetic, chiral and bi-anisotropic optical systems [4], enabling its further application to metamaterials. The RSE has also been used in first perturbation order for photonic crystal (PC) structures to describe sensing of the refractive index by a periodic array of plasmonic nano-antennas [5].

Very recently, we have developed a photonic-crystal RSE (PC-RSE) [6], a new rigorous approach to accurately calculate the RSs of planar PC systems, using a homogeneous slab as a basis system and treating the PC structure as a periodic modulation on top of the slab, see the inset in Fig.1. The periodicity of PC structures mixes all possible Bragg harmonics. Therefore, the basis RSs have to be taken with different in-plane wave numbers. As a result, the Green's function of MWE acquires branch cuts in the complex frequency plane, which must be taken into account in the PC-RSE along with the RSs. This presents the major complication of the PC-RSE which we have dealt with by splitting the cuts into a series of discrete, artificial cut states added for completeness to the basis of RSs, similar to what has been done in [3]. Using, for illustration, a dielectric slab periodically modulated in one direction, we demonstrate the accuracy and efficiency of the PC-RSE for finding the RSs of photonic crystals.

We use the advantages of the PC-RSE, namely its high efficiency and accuracy, as well as the analytical form of the eigenmode expansion, to study the origin of the optical modes of a PC system and their evolution with structural and material parameters, such as the period d, the thickness $2b$ of the periodic layer, and the permittivity contrast β, see Fig.1 and illustrations provided in [6]. This allows us to reveal the role of different basis states of the homogenous dielectric slab in the formation of the eigenmodes of the PC slab. We show in particular that the guided modes have the dominant contribution to the symmetry protected bound states in the continuum (BICs) and to high-quality (high-Q) quasi-guided modes (QGMs). We also study the contribution of different basis states to other types of modes, such as Fabry-Perot, leaky and cut modes.

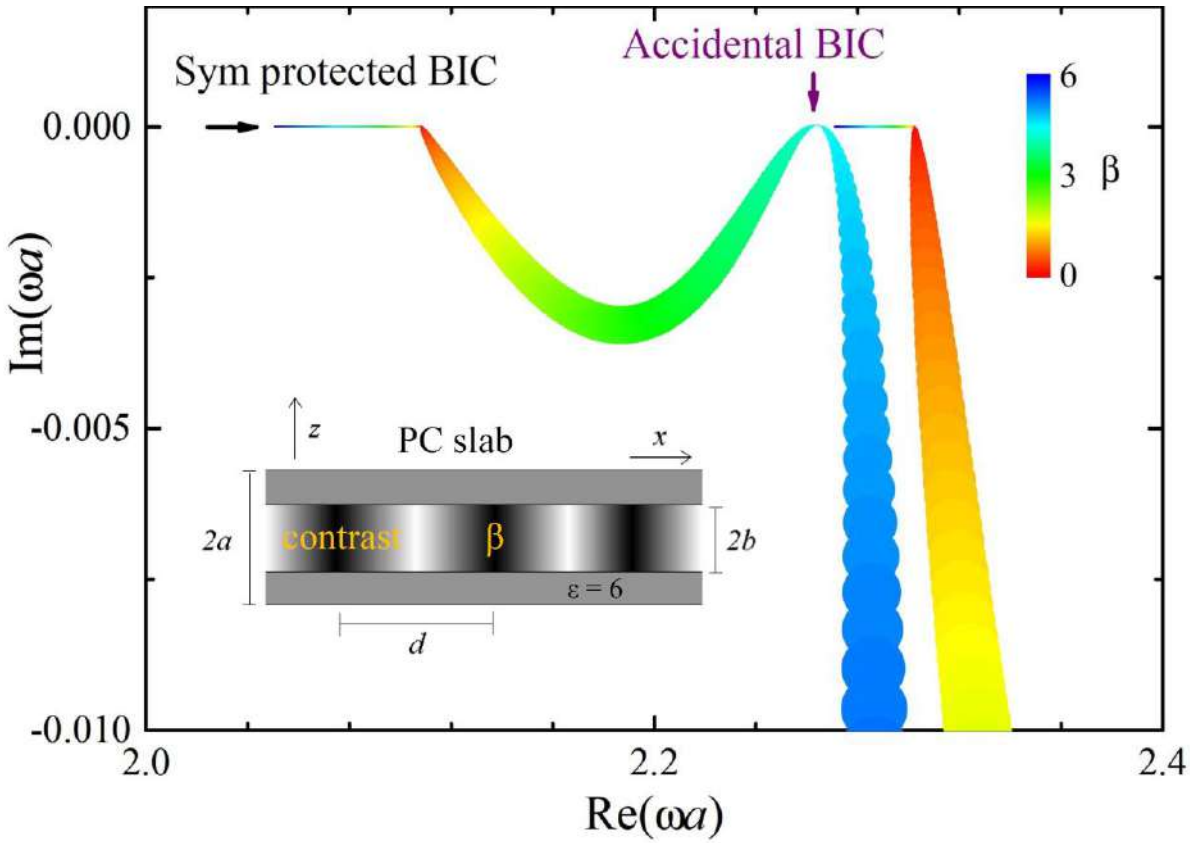

Figure 1: Evolution of the RSs of a PC slab (sketched in the inset) with the contrast β (color coded) of the periodic modulation of the permittivity of a homogenous dielectric slab with permittivity ε=6. The center of the circle shows the position of the RS frequency, while its area is proportional to the 0th Bragg channel contribution to the wave function. A doubly degenerate fundamental guided mode splits into a BIC-QGM pair. The BIC in this pair is protected by symmetry, having for any β a strictly vanishing contribution of the 0th Bragg channel. The evolution of the QGM is going through an accidental BIC.

We focus in this work on both symmetry protected and accidental BICs. Figure 1 demonstrates both types of BICs, tracing the evolution of the fundamental guided mode of a homogeneous slab with increase of the periodic modulation contrast β. Being doubly degenerate by symmetry at β=0 (no modulation), the guided mode splits for nonzero β into a symmetry-protected BIC and a quasi-guided mode (QGM), the latter having a high but finite Q-factor. These two modes are further separated as β increases. However, as can be seen in Fig. 1, for a certain value of β, the QGM transforms into an accidental BIC with an infinite Q factor. This transformation is accompanied by a morphological change of the wave function, which is further investigated and discussed in this work.

[1] E. A. Muljarov, W. Langbein, and R. Zimmermann, Europhys. Lett. **92**, 50010 (2010).
[2] M. B. Doost, W. Langbein, and E. A. Muljarov, Phys. Rev. A **90**, 013834 (2014).
[3] S. V. Lobanov, G. Zoriniants, W. Langbein, and E. A. Muljarov, Phys. Rev. A **95**, 053848 (2017).
[4] E. A. Muljarov and T. Weiss, Opt. Lett. **43**, 1978 (2018).
[5] T. Weiss, M. Mesch, M. Schäferling, H. Giessen, W. Langbein, and E. A. Muljarov, Phys. Rev. Lett. **116**, 237401 (2016).
[6] S. Neale and E. A. Muljarov, arXiv:1908.06916, Phys. Rev. B, accepted (2020).

Reflection and transmission coefficients at plane interfaces between transformation-optics media

Mircea Giloan

Faculty of Physics, Babes-Bolyai University, Cluj-Napoca, Romania
E-mail: mircea.giloan@phys.ubbcluj.ro

Abstract

The reflection and transmission phenomena occurring at the plane interface between two transformation-optics media are analyzed. In order to compute the reflection and transmission coefficients the wave vectors and the polarizations of the incident, reflected and transmitted waves are described inside the anisotropic and inhomogeneous media at the interface plane. The reflection and transmission coefficients are derived in terms of the coordinate transformations which are describing the transformation-optics media.

In this work the reflection and transmission at the interface between two transformation-optics media are theoretically studied. Two transformation media joined by a plane interface are considered. When an incident wave propagating inside the first medium arrives at the interface plane, usually, a transmitted wave propagating inside the second transformation medium and a reflected wave propagating inside the first medium will occur.

By heuristic means, was found that when the normal and parallel metrics of the joined transformation media are identical at interface, the incident wave passes into the second medium without being reflected [1]. The concept of transformation-optics was used to design different devices capable to manipulate both the wave paths and the wave vectors of the propagating waves. Some of these devices contain interfaces which have an important role in performing the desired manipulation of the wave paths and wave vectors [2-4]. Also, in the case of these devices, the normal and parallel metrics of the joined transformation media are different at interface. In order to describe the optical properties of these devices, the reflection and transmission coefficients have to be evaluated.

Following the steps of the method proposed in this theoretical study, one can compute the reflection and transmission coefficients at interfaces between two transformation-optics media. The reflection and transmission coefficients are described in terms of the coordinate transformations which are generating the transformation-optics media.

Acknowledgements

This work was partially supported by the Company for Applied Informatics through program POC – A2/221, project ID MySMIS:115641/2017.

References

[1] M. Rahm, S.A. Cummer, D. Schurig, J.B. Pendry, D.R. Smith, Optical Design of Reflectionless Complex Media by Finite Embedded Coordinate Transformations, *Phys. Rev. Lett.* 100: 063903, 2008.

[2] M. Giloan, Designing Devices for Wave-Vector Manipulation Using a Transformation-Optics Approach, *Phys. Rev. Appl.* 8: 014005, 2017.

[3] M. Giloan, R. Gutt, Optical imaging system based on transformation-optics lenses, *J. Opt.* 22: 015103, 2020.

[4] M. Giloan, R. Gutt, Designing flat optical devices for path and wave vector manipulation by space transformation along a fixed direction, *JOSA B* 38: 9 – 16, 2021.

GSTC formulation for Maxwell's equations

Agnès Maurel[1]*, Nicolas Lebbe[1], and Kim Pham[2]

[1] Institut Langevin, ESPCI Paris, Université PSL, Sorbonne Université, Université de Paris, CNRS, 75005 Paris, France
[2]IMSIA, ENSTA ParisTech - CNRS - EDF - CEA, Université Paris-Saclay, 828 Boulevard des Maréchaux, 91732 Palaiseau, France
*corresponding author, E-mail: agnes.maurel@espci.fr

Abstract

We revisit the classical zero-thickness Generalized Sheet Transition Conditions (GSTCs) which are a key tool for efficiently designing metafilms able to control the flow of light in a desired way. It is shown that it is more convenient to use an enlarged formulation of the GSTC in which the original metafilm is replaced by GSTCs that exclude the layer from the physical or computational domain. These new "layer" transition conditions have the same form as their "sheet" analogues hence they do not necessitate additional complications in their use; their advantage is that they provide a well-posed problem hence guaranty the stability of numerical schemes. These assessments are demonstrated for an all-dielectric structure; the effective susceptibility tensors are derived thanks to asymptotic analysis combined with homogenization technique and bounds for the susceptibilities entering the balance of energy are provided. Validation of the effective model is provided by means of comparison with direct numerics in two and three dimensions.

1. Introduction

Metasurfaces are smartly engineered two-dimensional structures that offer an attractive alternative to their bulk three-dimensional analogue. Because of their subwavelength thickness, they are less lossy, more compact and of relatively ease of fabrication. To describe metasurfaces, effective models have to encapsulate the microscopic distributions of currents and fields resulting in transition conditions relating the field differences at the two opposite sides of the film to their mean values. Through this homogenization process, the effects of the microscopic distributions are encoded in macroscopic parameters which can be interpreted in terms of effective surface currents and surface polarisations. In their most general form, these conditions are called General Sheet Transmission Conditions (GSTCs) [**?**].

2. The actual and the effective problems

2.1. The actual problem

We consider the Maxwell's equations in three-dimensions for dielectric materials with permittivities denoted $\varepsilon_0\varepsilon_{\rm r}^{\pm}$ in the two substrates, $\varepsilon_0\varepsilon_{\rm r}^{\rm sc}$ in the scattering particles and a uniform permeability $\mu = \mu_0$. The particles are evenly distributed at the interface $x = 0$ between the two substrates, with spacing d_y along y and d_z along z. We define $\mathcal{S} = d_y d_z$ the area of the periodic cell and $d = \sqrt{\mathcal{S}}$. In the time domain, the electric $\mathbf{E}$, displacement $\mathbf{D}$ and magnetizing $\mathbf{H}$ fields satisfy the Maxwell's equations in the actual problem (figure 1), namely

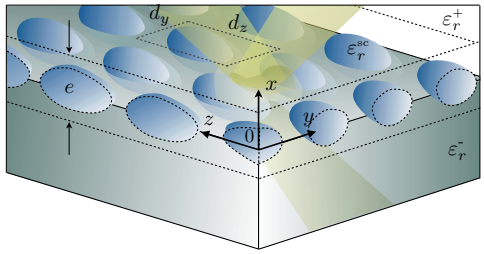

Figure 1: Actual problem of a metafilm composed by dielectric scattering particles evenly distributed at the interface between two dielectric substrates (with spacings d_y along y and d_z along z).

$$\begin{aligned} \mathbf{rot}\mathbf{H} &= \frac{\partial \mathbf{D}}{\partial t}, \quad \mathbf{D} = \varepsilon_0\varepsilon_{\rm r}(\boldsymbol{x})\mathbf{E}, \\ \mathbf{rot}\mathbf{E} &= -\mu_0\frac{\partial \mathbf{H}}{\partial t}, \quad \mathrm{div}\mathbf{H} = 0 \end{aligned} \tag{1}$$

where $\mathbf{H}$ and $\mathbf{E}\times\boldsymbol{n}$ are continuous at the interfaces. Mathematically, $[\![\mathbf{H}\times\hat{\boldsymbol{x}}]\!] = \mathbf{0}$ and $[\![\mathbf{E}\times\hat{\boldsymbol{x}}]\!] = \mathbf{0}$.

2.2. The effective problem, surfacic homogenization

Using an asymptotic analysis combined with homogenization tools, it is possible to obtain an effective model in which the metasurface is replaced by the following transition conditions:

$$\begin{aligned} [\![\mathbf{H}\times\hat{\boldsymbol{x}}]\!] &= -\varepsilon_0\frac{\partial \mathbf{P}_\parallel}{\partial t} - \nabla_\parallel M_x\times\hat{\boldsymbol{x}}, \\ [\![\mathbf{E}\times\hat{\boldsymbol{x}}]\!] &= \mu_0\frac{\partial \mathbf{M}_\parallel}{\partial t} - \nabla_\parallel P_x\times\hat{\boldsymbol{x}}, \end{aligned} \tag{2}$$

where for any field $\mathbf{A} = \mathbf{D}, \mathbf{E}, \mathbf{H}$ we have defined the jump $[\![\mathbf{A}]\!] = \mathbf{A}|_{e^+} - \mathbf{A}|_{-e^-}$ and mean $\mathbf{A}_{\rm av} = \frac{1}{2}\left(\mathbf{A}|_{e^+} + \mathbf{A}|_{-e^-}\right)$ operators across the metasurface's layer (figure 2). The vector $\hat{\boldsymbol{x}}$ is the unit vector along Ox, $\mathbf{P} = P_x\hat{\boldsymbol{x}} + \mathbf{P}_\parallel$, $\mathbf{M} = M_x\hat{\boldsymbol{x}} + \mathbf{M}_\parallel$(with $\mathbf{P}_\parallel\cdot\hat{\boldsymbol{x}} = \mathbf{M}_\parallel\cdot\hat{\boldsymbol{x}} = 0$), and the operator $\nabla_\parallel M_x\times\hat{\boldsymbol{x}} = \partial_z M_x\hat{\boldsymbol{y}} - \partial_y M_x\hat{\boldsymbol{z}}$ The vectors $\mathbf{P}$ and $\mathbf{M}$

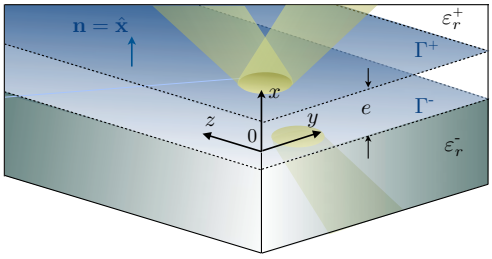

Figure 2: Effective problem in which the GSTCs (2) apply across $\Gamma^- = \{\boldsymbol{x} \in \Omega | x = -e^-\}$ and $\Gamma^+ = \{\boldsymbol{x} \in \Omega | x = e^+)$ with $e = e^- + e^+$.

refer to the electric and magnetic polarization densities, respectively. Expectedly, we obtain zero cross-susceptibility tensors hence we have

$$\mathbf{P} = \overline{\overline{\chi}}_{\text{ee}}\, \tilde{\mathbf{E}}_{\text{av}}, \qquad \mathbf{M} = \overline{\overline{\chi}}_{\text{mm}}\, \mathbf{H}_{\text{av}}, \tag{3}$$

where the subscript "av" refers to the average values of the fields at both sides of the interface, and where $\overline{\overline{\chi}}_{\text{ee}}$, and $\overline{\overline{\chi}}_{\text{mm}}$ are the electric-to-electric and magnetic-to-magnetic surface susceptibility tensors whose forms are

$$\overline{\overline{\chi}}_{\text{ee}} = \begin{pmatrix} \chi_{\text{ee}}^{xx} & \chi_{\text{ee}}^{xy} & \chi_{\text{ee}}^{xz} \\ \chi_{\text{ee}}^{xy} & \chi_{\text{ee}}^{yy} & \chi_{\text{ee}}^{yz} \\ \chi_{\text{ee}}^{xz} & \chi_{\text{ee}}^{yz} & \chi_{\text{ee}}^{zz} \end{pmatrix}, \quad \overline{\overline{\chi}}_{\text{mm}} = e \begin{pmatrix} -1 & 0 & 0 \\ 0 & 1 & 0 \\ 0 & 0 & 1 \end{pmatrix}, \tag{4}$$

and where the 6 effective susceptibilities are defined in terms of the solutions of so-called elementary problems (see details in [1]). The average electric field has to be understood as

$$\tilde{\mathbf{E}}_{\text{av}} = \frac{1}{\varepsilon_0} D_{x,\text{av}} \hat{\boldsymbol{x}} + \mathbf{E}_{\|,\text{av}}, \tag{5}$$

since it involves the fields being continuous at the dominant order corresponding to vanishing effect of the thin metafilm.

3. Validation of the effective model

We provide below illustrations of the efficiency of the effective model by means of comparisons between the results of the effective and actual problems (in the harmonic regime in two- and three-dimensions). For the actual and the effective problems, the Finite Element Method (FEM) has been used in Comsol Multiphysics (see details in [1]).

In figure 3, we report the comparaison of the actual field E_y for an ensemble of clover-like silicon particles (the source is indicated with a black circle) shown for $y < 0$ and the effective field for which the interface containing the particle has disappeared. The figure 4 show the same comparison in 3D for cuboid-shaped silicon particles with the air as unique substrate.

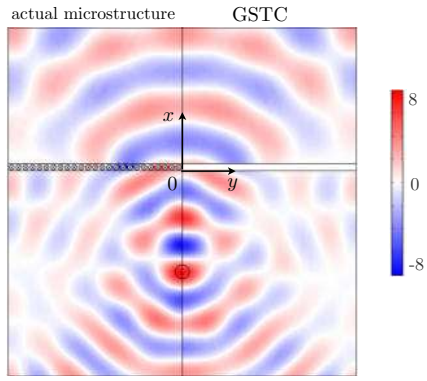

Figure 3: Real part of E_y for a layer comprising an array of clover-like silicon scattering particles. The field calculated in the actual problem is shown for $y < 0$ and the field calculated with the GSTCs is shown for $y > 0$.

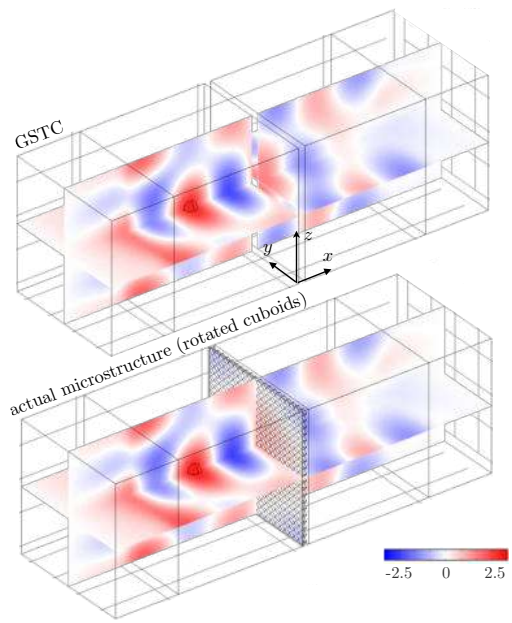

Figure 4: Real part of E_y in the effective problem (top) and in the actual problem (bottom) for the cuboid particles.

References

[1] N. Lebbe, K. Pham, A. Maurel, Stable GSTC formulation for Maxwell's equations, to appear in *IEEE Transactions on Antennas & Propagation* (2022).

imaging, inverse scattering and remote sensing

Cylindrical Microwave Imaging System with Extended Gap Ridge Horn Probes

Youness Akazzim[1,2], Luis Jofre Roca [2], Otman EL Mrabet[1],

[1]System of Information and Telecommunications Laboratory (LaSIT), Faculty of Sciences, Abdelmalek Essaadi University, Tetouan 93000, Morocco
[2]Department of Signal Theory and Communications, Technical University of Catalonia (UPC), Barcelona, Spain,
*Youness Akazzim, E-mail: yakazzim@gmail.com

Abstract

In this paper, we present a cylindrical microwave imaging system based on a multi-frequency bi-focusing (MFBF) imaging technique using Extended Gap Ridge Horn antenna (EGRH) probe for medical applications. The proposed probe antenna is designed to operate between 0.5 GHz to 1 GHz and filled with a high permittivity material to have an impedance match to the human body. This system has been successfully simulated using CST Microwave studio.

1. Introduction

Over the last two decades, microwave imaging (MWI) for medical applications has been investigated as a novel and promising imaging and diagnostics technique for tumor detection, due to the multiple advantages such as its noninvasive, non-ionizing, and penetrating characteristics. However, designing antennas for medical application present some challenges that should be solved such as the overall size and good impedance matching in low frequencies to ensure the penetrations of the wave in human body. In the last years, many ultra-wide band antennas(UWB) have been proposed in the literature for medical applications and other radar based microwave imaging such as Vivaldi antenna [1, 2], printed patch antenna, Bow-tie antenna, Horn antenna and Extended Gap Ridge Horn antenna (EGRH)[3]. In this paper, we present a EGRH for microwave imaging, the antenna is filled with a material of permittivity $\epsilon_r = 50$ which similar to the average permittivity of human body. The simulated results obtained by CST Microwave studio are then processed in Matlab to reconstruct the image using (MFBF) algorithm that allows us to detect the position of the target.

2. Imaging System Design

The key component of the proposed system is the EGRH, inspired from [3], depicted in Figure 1. The antenna consist of a double ridge waveguide that has a cut-off frequency close to $0.5GHz$. The technique of inserting ridges in the waveguide compared to the simple wave-guide of the same dimensions lowers the cutoff frequency and increase the cutoff frequencies of the next two higher modes to get an antenna that operate in ultra-wide band [4]. In our design f_c<$0.5GHz$, the EGRH feed with a coaxial cable of 50Ω by connecting the inner conductor of the coaxial to the lower ridge in the waveguide, then an horn with exponential ridge is added to the double ridge waveguide to match the antenna to the imaging area,and finally the antenna is filled with a material of $\epsilon_r = 50$ to match the impedance with human body. The imaging system of

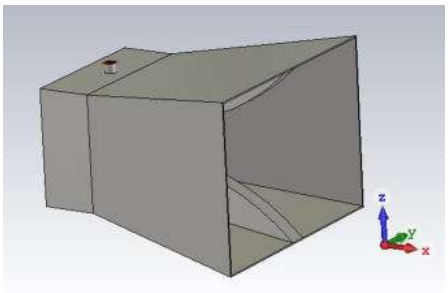

Figure 1: Simulated EGRH antenna.

figure 2 contains 8 EGRH displayed as a circular array of antennas along a cylinder with circumference radius of $100mm$ where the EGRH of figure 1 constitutes the basic element of the array, where one antenna works as transmitter and the other antennas receive the scattered signals; The principal step of microwaves imaging is getting the specific target response from the data, this process must be applied before starting the reconstruction of the image by simulating the model with the target and without the target. As result we get two matrices of 8*8 elements of scattered signals, with and without target. By using the equation 1 we get the target response, this direct problem is solved by the numerical software tools CST.

$$T_{targetresponse} = S_{target} - S_{notarget} \quad (1)$$

The S parameters result of the simulation are imported for processing in Matlab using an (MFBF) algorithm of image reconstruction (inverse problem) based on equation 2 from [5].

$$I(x_f, y_f) = \sum_{T_i} \sum_{R_j} E(\rho_{T_i}, \rho_{R_j}) * \frac{\sqrt{\rho_{R_j - f}}}{e^{-j*k*\rho_{R_j - f}}} * \frac{\sqrt{\rho_{T_i - f}}}{e^{-j*k*\rho_{T_i - f}}} \quad (2)$$

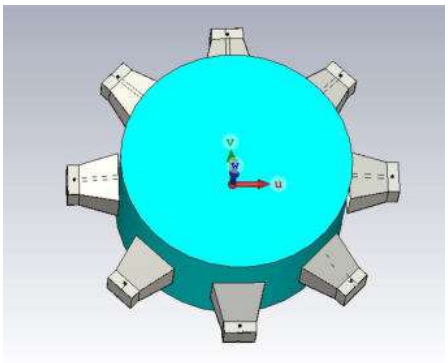

Figure 2: Microwave imaging system.

3. Results and discussion

The system in figure 2 has been simulated using the numerical software tools CST to test the performance of the (MFBF) algorithm developed, we inserted a metallic cylinder of radius 5mm as target in three different positions: ($x = 0mm$ & $y = 0mm$) figure 3, ($x = 50mm$ & $y = 0mm$) figure 4, and ($x = 50mm$ & $y = 50mm$) figure 5. To have a better accuracy on the detection of the target we used UWB signals to reconstruct the image, the addition of the phase and amplitude of each frequency which has the same amplitude and phase at the position of target we get as result an image with a size very close to the actual size of the target for tree different positions.

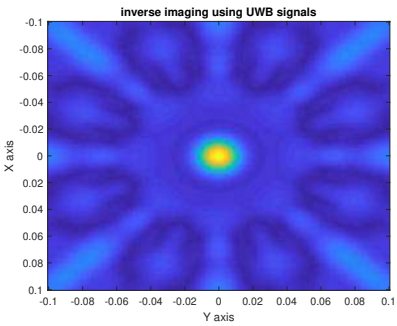

Figure 3: Target at the center.

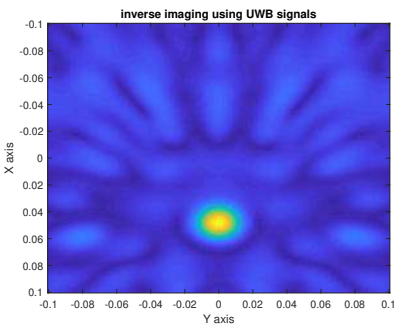

Figure 4: Target at $x = 50mm$.

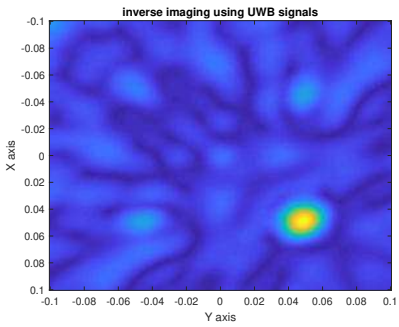

Figure 5: Target at $x = 50mm$ and $y = 50mm$.

4. Conclusions

In this work a microwave imaging System based on the Multi-Frequency Bi-Focusing technique is presented to be used for medical application such as brain and breast cancer detection using EGRH antennas.

Acknowledgement

This work was supported by the Moroccan Ministry of Higher Education (MESRSFC) and the CNRST under grant number PPR2/2015/36. This work was supported by the Spanish Comision Interministerial de Ciencia y Tecnologia (CICYT) under projects TEC2016-78028-C3-1-P, MDM2016-0600, and Catalan Research Group 2017 SGR 219.

References

[1] A. M. De Oliveira, M. B. Perotoni, S. T. Kofuji, and J. F. Justo, "A palm tree Antipodal Vivaldi Antenna with exponential slot edge for improved radiation pattern," *IEEE Antennas and Wireless Propagation Letters*, vol. 14, no. c, pp. 1334–1337, 2015.

[2] J. Bourqui, M. Okoniewski, and E. C. Fear, "Balanced antipodal vivaldi antenna with dielectric director for near-field microwave imaging," *IEEE Transactions on Antennas and Propagation*, vol. 58, no. 7, pp. 2318–2326, 2010.

[3] S. Rashid, L. Jofre, A. Garrido, G. Gonzalez, Y. Ding, A. Aguasca, J. O'Callaghan, and J. Romeu, "3-D Printed UWB Microwave Bodyscope for Biomedical Measurements," *IEEE Antennas and Wireless Propagation Letters*, vol. 18, no. 4, pp. 626–630, apr 2019.

[4] T. A. Milligan, *MODERN ANTENNA DESIGN Second Edition*, 2005.

[5] L. Jofre, A. Broquetas, J. Romeu, S. Blanch, A. P. Toda, X. Fàbregas, and A. Cardama, "UWB tomographie radar imaging of penetrable and impenetrable objects," *Proceedings of the IEEE*, vol. 97, no. 2, pp. 451–464, 2009.

Electromagnetic and Geophysical models to estimate wind speed from Sentinel 1 radar images - C band

Ali KHENCHAF[1]
[1]Lab-STICC, UMR CNRS 6285, ENSTA Bretagne, Brest, France
E-mail: ali.khenchaf@ensta-bretagne.fr

Abstract

SAR (Synthetic Aperture Radar) systems are commonly used to observe the globe, and in particular the sea surface, since they can offer high spatial resolution data. To exploit SAR data, a description of the relationship between electromagnetic backscatter and the sea surface is essential. Thus, it is possible to use empirical (geophysical) or EM models. In this paper, we investigated and presented models for sea surface radar backscatter calculations and then used to estimate wind speed from Sentinel-1 images.

Introduction

The sea surface wind field is a crucial input parameter for studies of other ocean parameters such as waves, currents, marine meteorology, etc. Likewise, it is one of the indispensable factors in the study of the observation of oil spills and the detection of ships. Among the various wind sources available, the estimation of wind speed from radar data (SAR) is particularly interesting since it can give high spatial resolution wind parameters. For this approach, it is possible to find many references on the estimation of the wind speed from the various SAR data in L, C, and X band. The common point of these studies is that the estimation of the speed of the wind is based on the geophysical model functions (GMFs) which empirically describes the dependence of the radar diffusion on the wind speed and the geometry of the observations. These GMFs are constructed and validated by the series of scatterometer missions. On the other hand, few studies use the GMFs built by electromagnetic (EM) calculations to estimate the wind speed since it is more complicated. However, EM models more generally describe the relationship between radar backscatter and sea state, as they include temperature, salinity, and wave spectrum in the equation, instead of only wind parameters as in empirical GMFs (EP). In order to evaluate the fidelity of the radar backscatter calculations by the EM models, and therefore the possibility of estimating the ocean parameters, we compare in this paper the wind speeds estimated by the EM and EP models for several cases in terms of polarization, angle of incidence and spatial resolution.

Description of several EM models

There are several EM models to describe radar backscatter from the sea surface, depending on the computational approach, such as quasi-exact methods, or asymptotic ones. Among different models, we distinguish the asymptotic methods which can be used for the inversion problem since they are simpler, and can give the results more quickly. There are two main categories in the asymptotic approach: i) models based on the Bragg resonance mechanism, and ii) those based on the low slope approximation.

Bragg resonance models

Models based on the Bragg mechanism include two types: i) one is based on the Small Perturbation Model (SPM) method [1] to describe small-scale sea surface backscatter, and ii) the other is based on the combination of Kirchhoff (KA) approximation for the large-scale surface and SPM, it is called composite two-scale model (CTSM) [1-2]. The principle to build these models is the Bragg resonance which is described as

$$K = 2k \times sin\theta \qquad (1)$$

where K is the spatial wave number of the waves, k is the radar wave number, and θ is the radar incidence angle.

The description of the two-scale composite model is presented in general as in [2]

$$\sigma_{comp}^{s} = \sigma_{KA}^{s} + \int W\left(\frac{\vec{k}}{k_z}\right)\sigma_{SPM}^{s}\left(\vec{k} - 2\overrightarrow{k_H}\right)d\vec{k} \qquad (2)$$

where W is the probability density function (PDF) of the large-scale wave surface slope.

Small Slope Approximation (SSA)

Like the composite model, the small-slope approximation uses the Kirchhoff approximation and the Bragg mechanism to calculate the large-scale and small-scale surface radar backscatter, respectively. Nevertheless, it handles the diffusion problem with a single processing process without the intervention of the arbitrary splitting parameter between the surface roughness structures, as observed in the composite two-scale model. In general, the SSA [3] is defined by

$$\sigma_{pq}^{s}(k, k_0) = \left|\frac{B_0(k,k_0)}{Q_z}\right|^2 \int e^{-Q_z^2[\rho(0)-\rho(r)]}\, e^{-iQ_H r} dr \qquad (3)$$

where $B_0(k, k_0)$ is the Bragg kernel, and $\rho(r)$ is the wave autocorrelation function.

Resonant curvature approximation (RCA)

The resonant curvature approximation (RCA) model is based on the SSA approximation to correct the radar backscatter calculation in horizontal polarization. Indeed, as presented in [4], the normalized radar cross section (NRCS) calculated by the CTSM and SSA is much lower than that given by the empirical models. The RCA equation [5] is defined as

$$\sigma_{pq}^{s}(k,k_0) = \left|\frac{K_0(k,k_0)}{Q_z}\right|^2 \int e^{-Q_z^2[\tilde{\rho}(0)-\tilde{\rho}(r)]}\, e^{-iQ_H r} dr \qquad (4)$$

The main difference between SSA and RCA is that the Bragg kernel $B_0(k,k_0)$ in (3) is replaced by that of Kirchhoff as shown in (4), and the autocorrelation function $\rho(r)$ is replaced by $\tilde{\rho}(r)$.

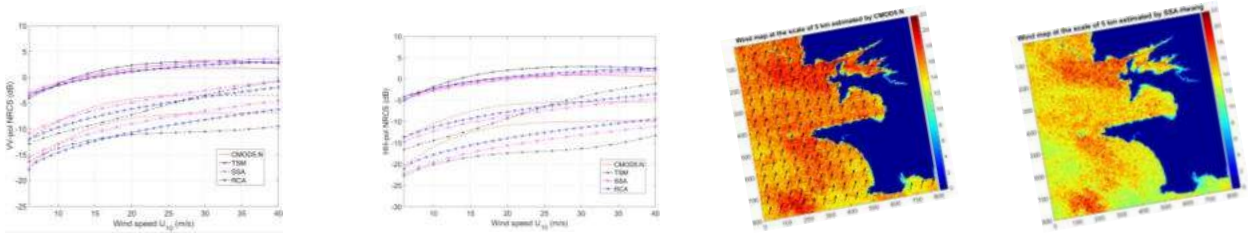

(a) (b) (c) (d)

Figure 1. Comparison of NRCS calculated by CMOD5.N, CTSM, SSA and RCA in (a) pol-VV and (b) pol-HH for the angle of incidence from 20° to 40°. And estimated wind map from the Sentinel-1 image in VV-pol, acquired in IWS mode on Nov. 29, 2015 from 18:13:00 to 18:13:25 UTC. Wind directions are retrieved by the LG method [7] at the scale of 5 km. (c) Wind estimates by CMOD5.N. (d) Wind estimates by SSA-Hwa+McD. The color bar represents estimated wind speed (m/s).

Sea surface roughness spectrum

In the above EM models, the sea surface roughness spectrum is a crucial parameter to accurately calculate the radar backscatter. In general, it includes two parts like

$$S(K,\Phi) = S(K,0) \times f(K,\Phi) \qquad (5)$$

where $S(K,0)$ is the omnidirectional part, and $f(K,\Phi)$ is the angular spread function. There are many studies on the modeling of the wave spectrum, but they can be divided into two categories: semi-empirical model (Elfouhaily, Donelan…) and the empirical one proposed by Hwang. In this paper we use the spectrum proposed by Hwang in [6], but other simulations are possible with other spectra.

Comparison of NRCS calculation models and estimation of wind speed from Sentinel 1 images

Figure 1 presents the NRCS calculated by CMOD5.N (empirical model), CTSM, SSA and RCA for the angle of incidence from 20° to 40°. For the lower angle of incidence (θ = 20°), the EP and EM models offer the same level of NRCS in pol-VV and pol-HH. Nevertheless, for a higher angle, in particular θ = 40°, only the asymptotic models give results similar to those given by the empirical reference model CMOD5.N. In particular, as indicated in [5], the level of the SERN calculated by RCA was improved compared to that given by SSA in pol-HH. In order to illustrate the wind speed estimation results, we present an example in Fig. 1 ((c) and (d)) where the wind maps estimated at the 5 km scale by CMOD5.N and SSA-1 from a sample of Sentinel-1 images in VV-pol.

Conclusion

We have presented in this paper the comparison between the EM and EP models for the calculations of the radar backscatter of the sea surface. Based on these models, the wind speed is estimated from the Sentinel-1 image in band C. The results obtained show that the asymptotic models give the level of NRCS closer to that given by CMOD5.N than the composite model at two scales. And the electromagnetic models were then used in the inversion problem in order to estimate the wind speed (which allows access to the sea state) from the SAR images. Other results will be presented at the conference with the presentation of ongoing and future work.

References

[1] A. Khenchaf, *« Bistatic scattering and depolarization by randomly rough surface: Application to natural rough surface in X-band »*, Wave in Random and Complex Media, Vol. 11, No. 2, pp. 61–89, 2001.

[2] D. R. Thompson, et al., *« Comparison of high-resolution wind fields extracted from TerraSAR-X SAR imagery with predictions from the WRF mesoscale model »*, J. Geophys. Res., Vol. 117(C2), pp. C02035, 2012.

[3] A. G. Voronovich, *« Small slope approximation in wave scattering from rough surfaces »*, J. of Experimental and Theoretical Physics, Vol. 62, pp. 65–70, 1985.

[4] T. V. La, et al., *« Study of wind speed retrievals from Sentinel-1 images using physical models »*, 10th EuCAP, pp. 1–4, Davos (Switzerland), Apr. 2016.

[5] A. A. Mouch, et al., « Importance of the sea surface curvature to interpret the normalized radar cross section », J. of. Geophysical Res., Vol. 112, C10002, 2007.

[6] P. Hwang, *« A note on the ocean surface roughness spectrum »*, J. Atmos. Oceanic Technol., Vol. 28, pp. 436–443, 2011.

[7] W. Koch, "Directional Analysis of SAR Images Aiming at Wind Direction," IEEE Trans. on Geo. & Rem. Sens., [Online] 42(4), pp. 702–710. Available: doi: 10.1109/TGRS.2003.818811.

A New Measurement Configuration for the Microwave Breast Cancer Imaging

İbrahim Akduman*, Aleksandar Janjic

Istanbul Technical University, Electrical and Electronics Engineering Faculty, Istanbul, Turkey
*corresponding author, E-mail: akduman@itu.edu.tr

Abstract

Microwave imaging offers both advantages and challenges as a medical imaging modality. Current research efforts mainly focus on two applications: (i) imaging of breast cancer for early diagnosis and (ii) continuous monitoring of brain after the stroke. As a rapidly evolving technology, medical microwave imaging has matured to reach clinical trials phases. Recent developments in the area are extensively shaped with the clinical outcomes such as increased importance of differential imaging techniques.

In this paper it will be presented a new microwave measurement configuration for the breast cancer imaging. The system consists of 36 modified Vivaldi antennas located circularly in an alumina matching medium. The operating frequency of the system is 0.4-8Ghz. The imaging system is clinically tested with 322 patients and now in the process of medical certification. During the talk the clinical results will be presented as well.

Laser, Laser Source and Application

Hybrid Photonic Crystal lasers for Refractive index Sensing

Liam O'Faolain[1,2]

[1]Centre for Advanced Photonics and Process Analysis, Munster Technological University, Cork, Ireland
[2]Tyndall National Institute, Cork, Ireland
*lofaolain@gmail.com

Abstract

We present results on a novel design of high Q-factor Silicon Nitride (SiN) 1D Photonic Crystal (PhC) cavities side-coupled to curved waveguides, operating with both silica and air cladding, which we then employ in a Hybrid External Cavity Laser (HECL) configuration. We demonstrate the operation of these lasers as novel transducers for refractive index changes that are induced by analyte specific absorption of infrared radiation by the target analytes present in gas or liquid phase.

Metamaterials, metasurfaces, FSS and EBG

On the propagation of surface plasmon polaritons at the interface of low-dimensional acoustic metamaterials

Tatjana Gric[1,2,3], Edik Rafailov[2]

[1] Department of Electronic Systems, Vilnius Tech, Vilnius, Lithuania
[2] Aston Institute of Photonic Technologies, Aston University, Birmingham B4 7ET, UK
[3] Semiconductor Physics Institute, Center for Physical Sciences and Technology, Vilnius, Lithuania
*corresponding author, E-mail: tatjana.gric@vilniustech.lt

Abstract

As a novel type of artificial media created recently, metamaterials demonstrate novel performance and consequently pave the way for potential applications in the area of practical engineering in comparison with the conventional materials. Acoustic metamaterials and phononic crystals possess a wide variety of exceptional physical features. These include effective negative parameters, band gaps, negative refraction, etc. Doing so, the acoustic properties of existing materials are extended. Acoustic metamaterials are periodic structures with the effective properties that can be tuned seeking for the dramatic control on wave propagation. Homogenization of the infinite periodic system is needed aiming to calculate permittivity of metamaterial. Dispersion properties of surface waves propagating at the interface between a nanocomposite made of a semiconductor inclusions systematically distributed in a transparent matrix and low-dimensional acoustic metamaterial, constructed by an array of nanowires implanted in a host material are investigated. We observed propagation of surface plasmon polaritons. It is demonstrated that one may dramatically modify properties of the system by tuning the geometry of inclusions.

1. Introduction

During the past years interest in creating materials allowing to control the flow of electromagnetic waves (e.g. light) in exceptional ways has increased dramatically. Novel engineering tools have opened the wide avenues to construct artificial materials possessing properties that are not possible in case of the naturally existing materials. The new design is possible due to the wide variety of inclusions. Moreover, the novel response appears because of the specific interactions with electromagnetic fields. These designs can be scaled down and constructed thanks to the nanotechnology. Hyperbolic metamaterials stand for as a multi-functional platform providing a fertile ground for realization of waveguiding, imaging, sensing, quantum and thermal engineering beyond conventional devices. This metamaterial utilizes the concept of engineering the basic dispersion relation of surface plasmon polaritons aiming to generate exceptional electromagnetic modes having a wide spectrum of applications. The hyperbolic metamaterial can be considered from the perspective of the polaritonic crystal. Doing so, the coupled states of light and matter provide a fertile ground for a larger bulk density of electromagnetic states.

Based on the frequency range, one may divide sound waves into the types as follows: low frequency, intermediate frequency and high frequency. Noise has strong penetrating power and dissipates slowly during propagation. Doing so, it is a challenging task to engineer the sound waves. Moreover, sound waves can also resonate with certain important organs of the human body. Consequently, health is dramatically affected. Hence, it is particular importance to focus on the investigation of the sound waves and vibration control. The study of surface waves and plasmonics stand for as another inherent part of nanophotonics. The former allows to reduce the length scales and dimensionality of various electromagnetic phenomena. Not surprisingly, nonreciprocity and unidirectional propagation of surface plasmon-polaritons (SPPs) have recently stimulated a tremendous interest. Magnetooptical nonreciprocity in the transverse Voigt geometry is mostly dealt with in these studies, including topological quantum-Hall-effect states. Herein we consider a novel approach allowing for propagation of SPPs at the acoustic metamaterial interface. It is worthwhile noting, that inclusions of the composites are fulfilled from the transparent conducting oxides (TCOs) making a stronger case towards implementation the properties of possible devices.

2. Geometry of the problem

Herein, we deal with the plane interface between a nanocomposite (NC) semi-infinite layer, which fills the half-space $x<0$ and an adjacent to it hypercrystal filling the half-space $x>0$ (Fig. 1). It is worthwhile mentioning, that the surface waves under consideration propagate along z axis. It is worthwhile noting, that the structure under the study can be constructed by means of molecular beam epitaxy [1], chemical vapor deposition, atomic layer deposition and sacrificial etching [2]. Nanocomposite is presented as a non-conductive transparent matrix with a

permittivity ε_n, in the volume of which regularly distributed semiconductor nanoparticles with permittivity ε_m. The dielectric function of the TCO based nanoparticles is of particular interest. An emerge of high-conducting metal being transparent has opened the wide avenues recently. The issue has attracted lots of interest within scientific community because of the metal being opaque for light. From the perspectives of the potential applications, transparent conducting metals described by high DC conductivity (σDC) are anticipated for optoelectronic devices, ranging from solar cells to electronic paper, touch screens and displays. Though, since $\sigma_{DC} = n_e e^2 \tau / m$ of a metal is associated with plasmon frequency $\omega_p^2 = n_e e^2 / \varepsilon_0 m$ through the free-electron density n_e, a high-conducting metal (with a high n_e) is naturally opaque for light due to its permittivity ε being usually very negative caused by its high ω_p. Typical techniques to produce transparent conducting metals include the decrease of the n_e, by utilizing transparent conducting oxides (TCOs).

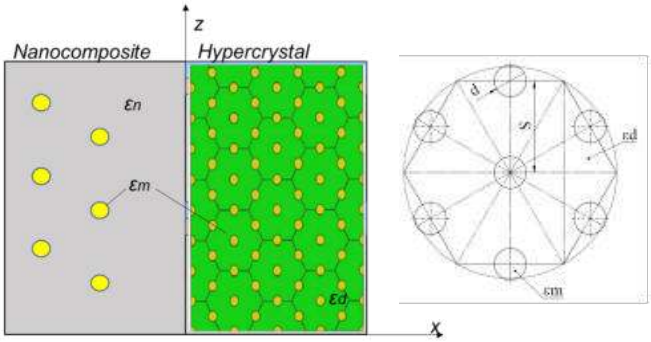

Fig. 1. Schematic geometry under study, consisting of a semi-infinite hypercrystal (x>0) and a nanocomposite with semiconductor inclusions (x<0), metamaterial (hypercrystal) unit cell (inset).

3. Discussion

Herein, the permittivity components of a hypercrystal and nanocomposite versus frequency are studied numerically aiming to identify the frequency ranges of Dyakonov surface waves (DSWs) and SPP waves existence (Fig. 2).

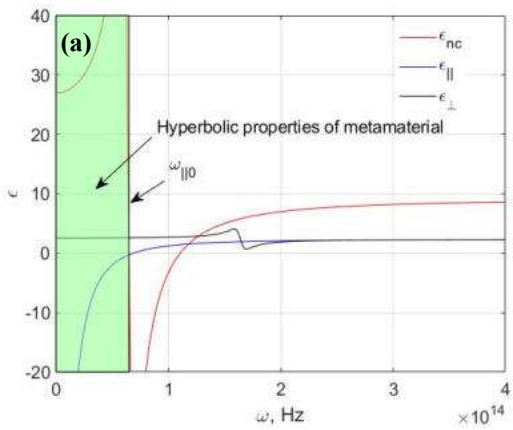

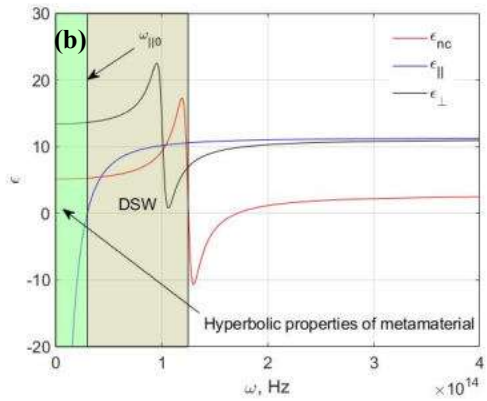

Fig. 2. Relative permittivity components of the nanocomposite and hypercrystal versus frequency. Herein, f=0.3. (a): $\varepsilon_n = 11.8$, $\varepsilon_d = 2.25$; (b) $\varepsilon_n = 2.25$, $\varepsilon_d = 11.8$. Herein AZO inclusions are employed in nanocomposite and hypercrystal.

In the frequency ranges below the frequency $\omega_{||0}$ the semiconductor-dielectric metamaterial possesses hyperbolic properties. It is worthwhile noting, that in this frequency range the presence of conventional surface plasmon polaritons waves with propagation parallel to the optical axis is feasible under specific conditions. One may conclude from Fig. 2, that propagation of DSW is possible in case of $\varepsilon_n = 2.25$, $\varepsilon_d = 11.8$. It is worthwhile noting, that regime of DSW propagation is possible in case of $\varepsilon_{||}, \varepsilon_{nc} > 0$.

4. Conclusions

Through theoretical derivation the excellent transmission characteristics of SPPs were analyzed and verified effectively in this paper. The dependence of the transmission characteristics on frequency for different filling ratios was obtained in this paper. Moreover, the possibilities to increase frequency ranges of DSW existence have been demonstrated. This work is of great significance to further research of optical devices based on SPPs.

Acknowledgements

This project has received funding from the European Union's Horizon 2020 research and innovation programme under the Marie Sklodowska Curie grant agreement No 713694 and from Engineering and Physical Sciences Research Council (EPSRC) (Grant No. EP/R024898/1). E.U.R. also acknowledges support and the Russian Science Foundation (Grant No. 18-15-00172).

References

[1] A. Hoffman, L. Alekseyev, S. Howard, K. Franz, D. Wasserman, V. Podolskiy, E. Narimanov, D. Sivco, C. Gmachl, Negative refraction in semiconductor metamaterials, Nat. Mater. **6** (2007) 946–950.

[2] J. Feng, Y. Chen, J. Blair, H. Kurt, R. Hao, D.S. Citrin, C.J. Summers, Z. Zhou, Fabrication of annular photonic crystals by atomic layer deposition and sacrificial etching, J. Vac. Sci. Technol. B: Microelectron. Nanometer Struct. **27** (2009) 568.

Single-shot quantitative phase imaging facilitated by a bifunctional metasurface

Einstom Engay[1,2], Dewang Huo[2,3], Radu Malureanu[2], Ada-Ioana Bunea[1], and Andrei Lavrinenko[2]

[1]DTU Nanolab, Technical University of Denmark, Kgs. Lyngby, Denmark
[2]DTU Fotonik, Technical University of Denmark, Kgs. Lyngby, Denmark
[3]Institute of Modern Optics, Harbin Institute of Technology, Harbin, China
*corresponding author, E-mail: einen@dtu.dk

Abstract

A bifunctional metasurface was fabricated to facilitate quantitative phase imaging. The silicon-based metasurface is made of elliptical nanopillars and acts as a polarization splitter allowing for the recording of two images, where one is shifted from the other. The two images were then used in an iterative calculation to retrieve the phase information of technical samples like lenses.

1. Introduction

Current image detectors are sensitive only to the intensity of an incoming light. As such, while the phase contains more crucial information about the optical path of the incident light before reaching the detector, the phase cannot be readily detected. Information about optical path, in turn, can be related to structural or morphological components of biological or technical samples. Quantitative phase imaging (QPI) aims to recover the phase from available intensity recordings by numerical calculation using multiple images of the sample as constraints [1]. One such calculation is based on the transport-of-intensity equation (TIE), which relates the phase of the field to the intensity variation along the propagation direction. In actuality, TIE-based QPI is implemented by recording a focused and a defocused image of the sample by detector displacement. Single-shot TIE refers to the simultaneous recording of the two images without the need to mechanically displace the camera, allowing for the QPI of dynamic events.

In this work, we present a bifunctional metasurface to facilitate single-shot TIE [2]. Metasurfaces are composed of subwavelength unit components that can control different properties of light including its wavefront [3]. Dielectric metasurfaces are particularly interesting due to the possibility to achieve multifunctionality while maintaining sufficient device efficiency. By introducing structural anisotropy to the unit components, the properties of multiple polarization components of the incident beam can be modulated simultaneously and independently. We exploit this interesting property in fabricating a bifunctional metasurface that splits the two orthogonal polarization components of a beam and creates two images of the sample, where one is shifted from the other, for use in phase calculation via TIE. We demonstrate the effectiveness of the metasurface in the QPI of technical samples.

2. Metasurface design and fabrication

2.1. Optical system

The QPI system consists of a 4*f* optical setup, where the sample is placed at the front-focal plane of the first lens or the input of the 4*f* and illuminated by a 45°-plane polarized light. The Fourier components are then modulated by the metasurface placed at the back-focal plane of the first lens. Here, the transmitted beam is angularly split into the TE and TM-polarized components by the metasurface, and the TM component gains an additional propagation phase shift also introduced by the metasurface. After Fourier transformation by the second lens, the output of the 4*f* setup consists of two laterally separated images, one of which is axially shifted, of the sample. To achieve such a function, the following polarization-dependent phase profiles are introduced by the metasurface:

$$\phi_{\mathrm{TE}}(\eta,\nu) = \frac{2\pi}{\lambda}\eta\tan\theta \tag{1}$$

$$\phi_{\mathrm{TM}}(\eta,\nu) = -\frac{2\pi}{\lambda}\eta\tan\theta + \frac{2\pi}{\lambda}\Delta z\sqrt{1-\frac{1}{f^2}\left(\eta^2+\nu^2\right)} \tag{2}$$

where θ is the magnitude of the angular displacement introduced by the metasurface, Δz is the axial defocus of the TM relative to the TE component, λ is the illumination wavelength, f is the focal length of the lenses in the and (η,ν) are the spatial coordinates in the Fourier plane.

2.2. Metasurface design and fabrication

The bifunctional metasurface is designed for an operating wavelength $\lambda = 850$ nm and is composed of elliptical nanopillars made of amorphous silicon ($n_{\mathrm{Si}} = 4.07 + 0.02i$). The height of the nanopillars is $h = 411$ nm and they are arranged in a square lattice with spacing $a = 350$ nm. The structural parameters (i.e. elliptical diameters: D_x and D_y) of the nanopillars necessary to introduce certain combinations of phase shifts for both polarizations were first determined. This was done by FDTD calculations of

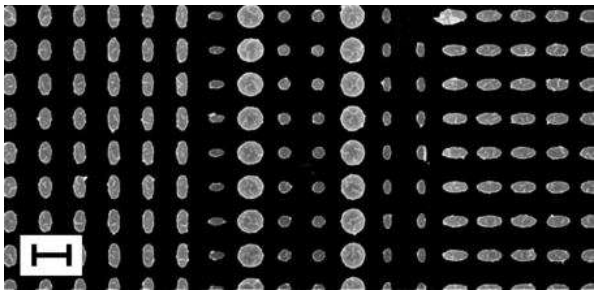

Figure 1: Scanning electron micrograph of the bifunctional metasurface based on elliptical nanopillars made of amorphous silicon. Scale bar: 400 nm.

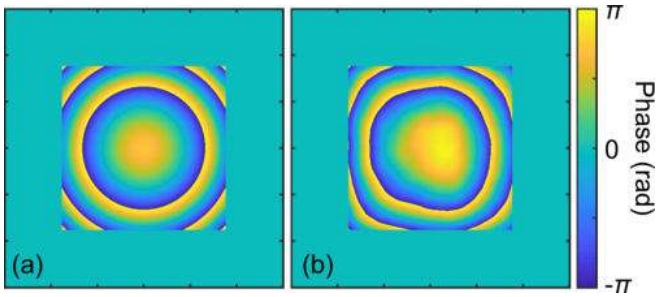

Figure 2: (a) Analytic phase profile o f a c onvex lens, $f = 250$ mm. (b) Reconstructed phase profile from the metasurface-based single-shot TIE.

periodically arranged uniform pillars, sweeping the diameters from 70-270 nm. The phase profiles in Eqns. 1 and 2 are then discretized by setting $\eta = ma$ and $\nu = na$, where m, n are the grid elements. In each grid, the phase value is converted to the optimal diameters of the nanopillar.

The metasurface is fabricated by first depositing amorphous silicon on a fused silica substrate by low power chemical vapor deposition. The patterning is then implemented using electron-beam lithography, followed by dry etch based on the Bosch process. For the complete details, interested readers are referred to the supplementary information of [2]. Figure 1 shows a scanning electron micrograph of the fabricated metasurface.

3. Results and Discussion

The overall transmission efficiency of the fabricated metasurface was found to be 68% and 65% for the TE- and TM-polarized incident beams, respectively, for $\lambda = 850$ nm. From *k*-space measurements, the angular deflections were verified to be as designed $\theta_{\mathrm{TE/TM,meas}} = 0.071$ rad, corresponding to a lateral separation of $d = 7.0$ mm between the centers of the two beams.

After the single-shot recording of the two laterally diplaced images, numerical post-processing was implemented to crop and center the two intensities. These were then used in an iterative calculation of the TIE [4], which is given by

$$-k\frac{\partial I(x,y)}{\partial z} = \nabla_\perp \cdot [I(x,y)\nabla_\perp \varphi(x,y)] \qquad (3)$$

where φ is the phase information to be recovered, $k = 2\pi/\lambda$, $\nabla_\perp$ is the gradient operator over the x and y coordinates and $\frac{\partial I}{\partial z}$ is the axial intensity gradient that is estimated by the finite difference of the two intensity recordings: $\frac{\partial I}{\partial z} = \frac{I_{\mathrm{TM}} - I_{\mathrm{TE}}}{\Delta z}$. The axial displacement was $\Delta z = 5$ mm.

The metasurface-based single-shot TIE is demonstrated in the QPI of a convex lens, $f = 250$ mm. Figure 2 (a) shows the analytic phase profile of such a technical sample. The phase map in Figure 2 obtained from our proposed technique show similarity with the analytic phase. We benchmarked our proposed technique with two other similar and established techniques: conventional TIE (C-TIE) and multiple-plane phase retrieval (MPPR). Qualitative comparisons show correspondence between our metasurface-based technique, and C-TIE and MPPR. Quantitatively, the root-mean-squared errors (RMSE) between the experimental reconstructions and the analytic were calculated as $\mathrm{RMSE}_{\mathrm{MS-TIE}} = 0.7804$, $\mathrm{RMSE}_{\mathrm{C-TIE}} = 0.6632$ and $\mathrm{RMSE}_{\mathrm{MPPR}} = 0.7772$. These comparisons demonstrate the viability of the metasurface-based TIE as an alternative for QPI.

4. Conclusions

In conclusion, we proposed a compact optical configuration for single-shot quantitative phase imaging. The system is based on a 4*f* optical setup integrated with a bifunctional dielectric metasurface at the Fourier plane. We demonstrated the effectiveness of our proposed technique in the wavefront reconstruction of technical samples. This represents a first important step towards rapid quantitative phase imaging of dynamic samples.

Acknowledgement

We would like to thank Novo Nordisk Fonden (NNF) (NNF16OC0021948)and VILLUM FONDEN (grant numbers 34424 and 00022918) for the funding support.

References

[1] T. Cacace, V. Bianco, P, Ferraro, Quantitative Phase Imaging Trends in Biomedical Applications. *Opt. Lasers Eng.* 135, 2020.

[2] E. Engay, et al, Polarization-dependent all-dielectric metasurface for single-shot quantitative phase imaging, *Nano Letters* 21: 3820–3826, 2021.

[3] P. Genevet, et al, Recent Advances in Planar Optics: From Plasmonic to Dielectric Metasurfaces. *Optica* 4:139, 2017.

[4] J. Zhang, et al, On a universal solution to the transport-of-intensity equation, *Optics Letter* 26: 586, 2020.

THz Range Perforated Metasurface-integrated Multiband Fabry-Perot Microstrip Patch Antenna

Garima Joshi[1] and R. Vijaya[1,2]
[1]Centre for Lasers and Photonics, Indian Institute of Technology Kanpur, Kanpur-208016, India
[2]Department of Physics, Indian Institute of Technology Kanpur, Kanpur-208016, India
*Corresponding author, E-mail: garimaj@iitk.ac.in

Abstract

We have proposed a THz range, multi-band, metasurface-integrated Fabry- Perot cavity antenna. The perforated single layer metasurface provides 40% wide stop bandwidth and it is used as superstrate. The metasurface integrated antenna resonates at the frequencies of 180.0 GHz, 189.46 GHz, 199.02 GHz and 208.82 GHz. The maximum peak gain of 13 dBi is at 189.46 GHz among the four bands. Nearly 5% of gain enhancement is achieved in all four bands after loading the metasurface on the antenna.

1. Introduction

The high demand for fast data transmission rates, low latency, high reliability and interference-free operation has heralded the use of millimetre-wave and terahertz- wave regimes [1]. In addition, multiband operation is also essential as most of the modern handheld wireless devices operate in multiple bands of frequency to provide multiple utilities with a single antenna. One of the main limitations of the THz regime arising from a high attenuation and atmospheric path loss of the signal can be overcome with bulky and expensive high-gain antennas. Therefore, in recent years, Fabry-Perot cavity (FPC) antennas are gaining in popularity as they are simpler in construction, economical and attain high gain and directivity at microwave, millimeter-wave, terahertz frequencies, and even at optical frequencies [2]. The FPC antenna can be designed using periodic structures such as frequency selective surfaces (FSS) and metasurfaces (MS) in different arrangements to increase the gain and directivity by placing it as superstrate [3,4].

Most low-profile FPC antennas consist of a multilayer cavity and/or multilayer configuration. Such designs increase the volume and make it more difficult to realize high-frequency integrated systems [2,4]. Recently, silicon and GaAs based microstrip patch antennas (MPA) are also fabricated to meet the monolithic integration requirements, but these are expensive, complex and high maintenance in profile [1,4]. To overcome some of these drawbacks, we present a simple, cost-effective, robust and mass-producible FSS based metasurface (MS-FSS) integrated with a multi-band MPA for THz range application. Our design of MS-FSS has 20x20 array of periodic holes in a square lattice arrangement on a dielectric substrate. It has 40% wide stop bandwidth ranging from nearly 175 GHz to 272 GHz. It is then used as a partially reflecting surface (PRS) by placing it above the antenna (as a superstrate) to make the FSS integrated MPA work as a FPC antenna. It helps to enhance the gain of the stand-alone MPA due to multiple reflections between the highly reflective FSS and the antenna ground plane, as in a Fabry–Perot (FP) resonator. Our design results in multiple resonances at 180.0 GHz, 189.46 GHz, 199.02 GHz and 208.82 GHz. Nearly 5% of peak gain enhancement is achieved in all the four bands after loading MS-FSS on MPA. An improvement of 2-3 dB is also seen in the reflection coefficient of FP-MPA.

2. Multi-band MPA and MS-integrated MPA

2.1. Stand-alone Multi-band MPA

Figure 1 (a) shows the schematic of THz-range multi-band MPA. The MPA is of conventional design and is made up with dielectric substrate backed by the metallic ground plane and the metallic patch is printed on the top of the substrate. We have used Rogers RT Duroid 5880 as the substrate (relative permittivity of 2.2, thickness 0.79 mm). The substrate has the length (Lg), width (Wg) and thickness of 12.00 mm, 12.00 mm and 0.79 mm respectively. The ground plane is of copper with comparable length and width, and a thickness of 0.35 mm. The rectangular patch is of length and width of W x L = 0.6mm x 1 mm. The rectangular patch has four slots in it as shown in Fig.1 (a). The length and width of slot 1 and 2 is a x b = 0.2 mm x 0.2 mm, whereas the length and width of slot 3 and 4 is c x d = 0.2 mm x 0.4 mm. The slots are inserted in the patch to achieve multiple resonances in the MPA. Four slots have been cut in the patch to provide additional resonance frequencies other than the natural resonance of the patch which is 180 GHz. The photograph of the prototype antenna is shown in Fig. 1(b).

2.2. THz Range FSS based Metasurface

The metasurface uses the same substrate with similar dimensions as in section 2.1 and is shown in Figs. 1 (c, d). The holes are of radius (*r*) 0.2 mm and hole-to-hole spacing (*a*) is 0.4 mm, arranged in square lattice arrangement. The FSS structure consists of 20 x 20 array. The perforation is of through holes of 0.79 mm thickness. The MS-FSS shown in Fig. 1(d) is fabricated using CNC drilling technique, which is easy, fast and simple to use. CST MW Studio^{TM} software is used for the design and analysis in time domain solver.

2.3. Metasurface-integrated Multi-band MPA

The MS-FSS is used as PRS for the multi-band MPA after loading it on the MPA at a distance of 1mm (0.5 λ_0), where λ_0 is the resonant wavelength (considered 180 GHz). The inset-fed multi band MPA (Fig. 1(a)) is selected as the primary source for the FPC antenna.

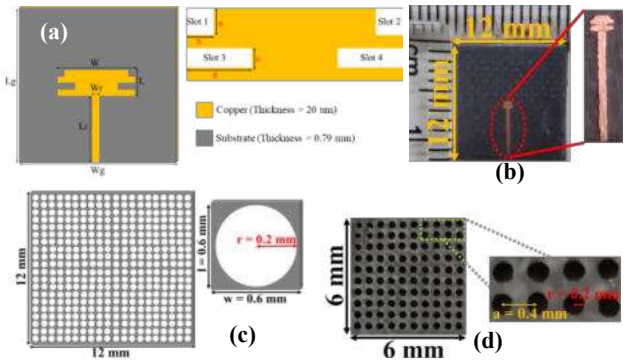

Figure 1. (a) Schematic of multi-band MPA, (b) photograph of multi-band MPA, (c) schematic of FSS-MS with its unit cell dimension in zoomed view and (d) photograph of a smaller-size FSS-MS with 10x10 array.

3. Results and Discussion

S-Parameters and Gain of Multi-band MPA, MS-FSS and integrated system

Figure 2 (a) is the simulated reflection coefficient of the stand-alone MPA. It shows four prominent resonance peaks indicated with star shapes. The MPA resonates at 180 GHz, 189.46 GHz, 199.02 GHz and 208.82 GHz, with reflection coefficients of -28.86 dB, -39.04 dB, -29.13 dB and -20.13 dB respectively. Figure 2(b) depicts the calculated reflection (S_{11}) and transmission (S_{21}) coefficients of MS-FSS in the frequency range of 100-300 GHz. The unit cell shows high reflection and low transmission coefficient in the frequency range of 174.70 GHz to 251.75 GHz as shown in with blue shaded region, which works as stop band, with a width of 39.8%. At 166.40 GHz and at 257.56 GHz, the structure has low reflection coefficient and high transmission coefficient, working as narrow pass bands.

Figure 2 (c) shows the reflection coefficient of MPA and superstrate loaded FP-MPA, and these are found to match exceedingly well. The reflection coefficients attained by FP-MPA are -33.57 dB at 180.0 GHz, -41.33 dB at 189.46 GHz, -32.00 dB at 199.02 GHz and -20.43 dB at 208.82 GHz, shown with black solid line in Fig. 2(c). The reflection coefficient improves by nearly 2-3 dB after loading the superstrate on MPA.

Figure 2(d) depicts the simulated peak gain for the MPA (in black solid line) in the direction of $\theta = 0^0$ (bore-sight). The stand- alone MPA attains peak gains of 7.45 dBi at 180 GHz, 7.93 dBi at 189.46 GHz, 7.13 dBi at 199.02 GHz and 6.53 dBi at 208.82 GHz. The maximum peak gain of nearly 8 dBi is obtained by the multiband stand- alone MPA at 189.46 GHz at bore sight. FP-MPA (shown with blue solid line) has peak gains of 12.22 dBi at 180.0 GHz, 13.02 dBi at 189.46 GHz, 12.24 dBi at 199.02 GHz and 11.19 dBi at 208.82 GHz. At all the four resonance frequencies, the FP- MPA has achieved a significant gain exceeding 11 dBi. On comparing the peak gains before and after loading the superstrate (FP-MPA), we note an increment in gain of nearly 4.7% at 180 GHz, 5.1% at 189.46 GHz, 4.9% 199.02 GHz and 4.7% at 208.82 GHz as shown by the arrows in Fig. 2(d).

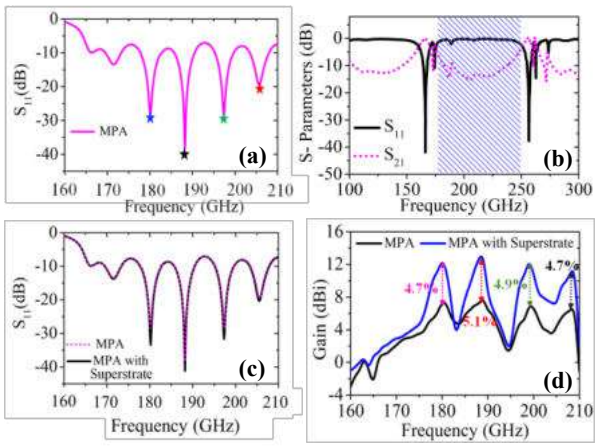

Figure 2. Simulated (a) reflection coefficient of stand-alone MPA, (b) S-parameters of the FSS, (c) reflection coefficient of MPA and MS-FSS superstrate loaded MPA and (d) peak gain as a function of frequency of the MPA and MS-FSS superstrate loaded MPA (the arrows represent the increment of peak gain).

4. Conclusion

A simple, cost-effective, robust and mass-producible FSS-MS integrated multi-band MPA for THz band is presented. The stand-alone MPA shows multiple resonances from 180 GHz to 209 GHz. The MS-FSS attains a wide stop bandwidth of 40% from 175 GHz to 272 GHz. This wide stop band is utilized by keeping the MS-FSS on the MPA as superstrate at a suitable height and making it work as a PRS for the MPA. This MS-FSS integration with MPA works as the FPC antenna and allows to enhance the gain of the stand-alone MPA. The antenna with MS-FSS structure has shown a significant peak gain improvement of nearly 5% in all the four resonating frequencies. Moreover, 2-3dB improvement in reflection coefficient is also attained for all the resonance frequencies of MS-FSS integrated FP-MPA. Our design for the prototype is novel, and is the first proposal for using perforated single layer metasurface as a superstrate in the THz regime. It is suitable for wireless communication, material characterization, and security applications in defense.

Acknowledgments

We acknowledge the fabrication facility and measurement facility of the RF and Antenna group of EE department at IIT Kanpur for granting permissions for our use. This work is sponsored by the ISRO-IIT Space Technology Cell (project number STC0168) and SERB (project no. CRG/2020/002353).

References

[1] K.B. Cooper, et al, A high-resolution imaging radar at 580 GHz, *IEEE Microw. Wirel. Compon. Lett.*, 18 (1): 64-66, 2008.

[2] Aqlan, B., et al. A 300-GHz low-cost high-gain fully metallic Fabry–Perot cavity antenna for 6G terahertz wireless communications, *Sci Rep*, 11: 7703, 2021.

[3] R. S. Anwar, L. Mao, H. Ning, Frequency Selective Surfaces: A Review, *Appl. Sci.,* 8: 1689, 2018.

[4] L. Qi and C. Li, Dual-band Frequency Selective Surface Bandpass Filters in Terahertz Band, *J. Opt. Soc. Korea,* 19: 673-678, 2015.

All-optical terahertz modulation with an epsilon near-zero material

E. Alvear-Cabezón*[1], E. Centeno*[1], R. Smaali[1], F. Gonzalez-Posada[2], S. Blin[2], T. Taliercio[2]

[1]1Univ. Clermont Auvergne, CNRS, Institut Pascal, F-63000 Clermont-Ferrand, France.
[2]2IES, Univ Montpellier, UMR CNRS 5214, Montpellier, France.
*corresponding author, E-mail:
emmanuel.centeno@uca.fr
eduardoalvear@alicantothz.com

Abstract

We theoretically and experimentally study the THz electromagnetic properties of an undoped-InAs slab whose permittivity is optically modified by a photo-generation process. We show a high modulation of the THz transmission up to 90% from 0.75 to 10 THz at very low pump fluence in the continuous wave regime. We also demonstrate a high-speed transmission modulation rate up to 2 MHz range with a modulated pump.

1. Introduction

The development of the technology based on terahertz (THz) electromagnetic radiation is crucial for many application domains such as security, medicine, non-destructive inspection, astronomical instrumentation, spectroscopy, imaging and wireless communication. To respond to the demand for versatile THz components operating in the THz gap (0.1–10 THz), artificial structures such as metasurfaces have been recently investigated to dynamically control THz waves.

2. Discussion

We have theoretically and experimentally studied the THz electromagnetic properties of photo-generated carriers in an undoped-InAs slab. The modifications of the permittivity induced by an optical pump are calculated by solving the ambipolar rate equation for the photo-carriers. Photo-carrier diffusion plays a crucial role in the search of an optimal geometry [1-2].

To understand and to reveal the real impact of the photo-carrier diffusion in the InAs material, we have created a multiphysics code to calculate the electromagnetic properties of the InAs slab illuminated by a THz plane wave. We have analyzed the electromagnetic properties of the InAs slab as a function of the thickness "*h*", the pump fluence and the polarization (TE and TM) of the THz wave and demonstrated a high modulation of the THz radiations [2].

We have carried out the experimental demonstration by measuring the transmission of a THz-wave through a micrometric-thick slab of undoped-InAs using a continuous-wave (CW) and modulated by an IR laser of around 800nm wavelength. In the experimental set-up, the collimated THz wave radiates the InAs membrane located in the sample holder of the optic set-up, which in turns is traversed by the IR laser. The maximum power is 500 mW and the spot diameter is 2 mm when it is collimated. The rest of the optic set-up is composed of a FTIR spectrometer for frequencies from 1 to 10 THz.

These experimental results reveals that a modulation depth of 90% at 1 THz is obtained with a continuous laser at irradiation lower than 10 W.cm^{-2} for a 6 µm thick InAs slab, Fig. 1. This strong modulation is demonstrated to originate from the photogenetation of an epsilon-near-zero (ENZ) material that boosts the absorption of the THz wave within a sub-wavelength thick (λ/50) InAs slab. Since the IR pump intensity drives the ENZ frequency, the ENZ absorption effect provides an efficient way to modulate the THz signal over a broadband from 1 to 10 THz.

In addition, the experimental results performed in the dynamic regime reveals that a cut-off frequency of 3 dB attains 2 MHz, Fig. 2.

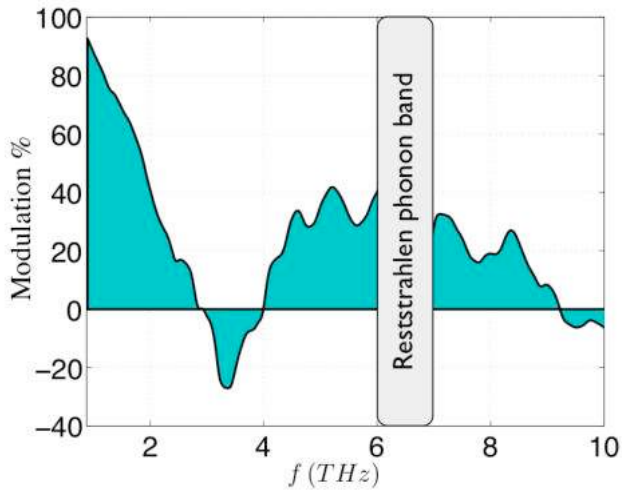

Figure 1: Modulation of an undoped 6 lm thick InAs slab irradiated with a pump irradiance of 8.1 W cm 2 at room temperature

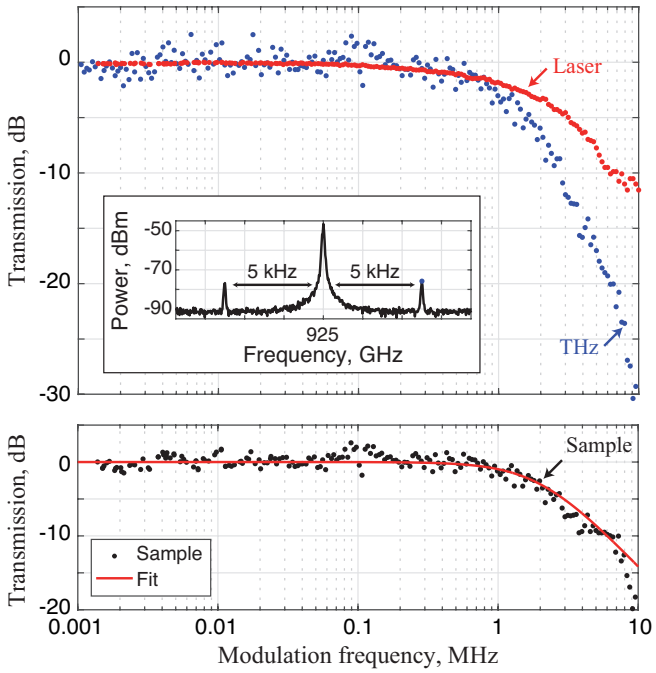

Figure 2: The transfer function of the InAs slab: the dots correspond to the experimental data and the solid line to their fit with a first-order low pass filter. The inset of the figure shows the THz spectrum measured using a 10 Hz resolution bandwidth for a laser amplitude modulation frequency 5 kHz.

3. Conclusions

We have demonstrated that the undoped-InAs is a promising semiconductor for the development of on-chip fast and efficiently THz components. A modulated pump at an irradiance of few W/cm^2 is enough to dynamically control the THz transmission over a frequency range from 1 THz to 10 THz and with a modulation rate up to 2 MHz range. These results open interesting routes for the design of advanced THz modulators.

Acknowledgements

Authors thanks J.-F. Roux from IMEP-LAHC (Univ. of Savoie) for the loan of the acousto-optic modulator.
This work was partially funded by the French Investment for the Future program (EquipEx EXTRA, No. ANR 11-EQPX-0016).
This work was funded by the French Labex IMOBS3.

References

[1] E. Alvear-Cabezón, R. Smaali, E. Centeno and T. Taliercio,« Photogenerated metasurfaces at terahertz frequencies induced by a continuous-wave low pump », Phys. Rev. B **98**, 035305 (2018).

[2] E. Alvear-Cabezón, T . Taliercio, S. Blin, R. Smaali, F. Gonzalez-Posada, A. Baranov, R. Teissier, E. Centeno, « Epsilon near-zero all-optical terahertz modulator », Applied Physics Letters 117, 111101, 2020.

[3] E. Centeno, E. Alvear-Cabezón, R. Smaali, A. Moreau, « Inverse-designed terahertz modulators based on semiconductor multilayers», Semiconductor Science and Technology, accepted manuscript online 22 June 2021.

Synthesis of Ultra-Wide Bandgaps for 2-D Photonic Crystals of Finite Thickness

Yuriy Sirenko[1,2], Kostyantyn Sirenko[1], Nataliya Yashina[1*], and Gerard Granet[3]

[1]O.Ya. Usikov Institute for Radio Physics and Electronics, National Academy of Sciences of Ukraine, Kharkiv, Ukraine
[2]V.N. Karazin Kharkiv National University, Kharkiv, Ukraine
[3]Université de Clermont-Ferrand, Institut Pascal, Clermont-Ferrand, 4 Impasse Blaise Pascal, France
*corresponding author Nataliya Yashina, E-mail: yashinanp@gmail.com

Abstract

The synthesis problem of 2-D photonic crystals of finite thickness providing the ultra-wide stopbands for the plane incident waves is solved on the base of EAC-method (method of exact absorbing conditions) [1–11].

1. Introduction

2-D photonic crystals of finite thickness having the same length of the period are able to produce clearly pronounced stopbands. Their position on the frequency axis can be effectively controlled by the variation of the geometric and material parameters of a unit cell of a periodic structure (see, for example, Fig. 1). This fact allowed proposing a simple, but quite effective scheme for the model synthesis of photonic crystals structures with ultra-wide stopbands.

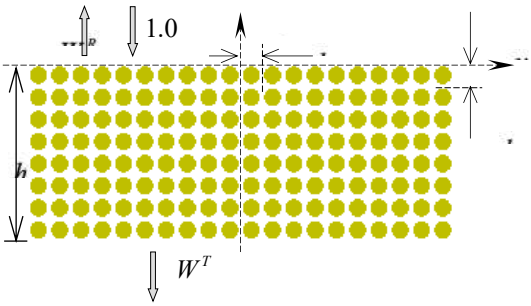

Figure 1: 2-D crystal of finite thickness.

The results presented for discussion have been obtained when working with models of the method of exact absorbing conditions (EAC) [1–11].

2. Formulation of the problem

The simple photonic crystal formed by circular dielectric cylindrical rods with various ε and $\sigma = 0$, oriented parallel to the axis x, had been considered. The intersection of the rods' axes with the planes $x = const$ defines the nodes of the infinite in the directions y and z rectangular grid; the cell size of such grid is $l \times l$. The radius of rods is r. Crystals of finite thickness h have been cut of from this crystal (Fig. 1).

The numerical results have been obtained within the framework of the approaches that had been implemented in [11]. Here we considered the case of H-polarization, that means that the vector $\mathbf{E}$ lies in the plane $y0z$.

The dimensions of all considered physical units are omitted: they correspond to the International System of Units, except the 'time' t that is the product of the real time and the velocity of light in vacuum, thus t is measured in meters.

3. Discussion of simulation

The wave number $k = 2\pi/\lambda$ is varying within the so-called single-wave frequency range, providing validity of the relation $W^T(k) + W^R(k) = 1$. Parameters ε and σ are the relative permittivity and conductivity of the rods' material; λ is a wavelength; $W^T(k)$ and $W^R(k)$ are the parts of the input energy carried by spatial harmonics propagating to the transmission ($z < -h$) and reflection ($z > 0$) zones of the periodic (along coordinate y) structure [4]. The process of band gaps formation in the structure was studied within numerical experiments consisting in the crystal's thickness h increase; that is, the process of formation of sufficiently wide bands of the parameter variation k, where $W^T(k) = 0$ has been simulated. It turned out that for the four- and five-layer crystals; the band gaps (BGs) or stopbands contours become clearer and finally formed for the crystals containing 10 or more layers.

Here is one of examples of synergetic operation of joint fifteen layers crystal designed by means of putting together three blocks of five-layer crystals. Each block is constructed of dielectric rods of the radius $r = 0.38l$ and permittivity varying from $\varepsilon = 10.9$ to $\varepsilon = 6.1$. Model excitation was performed by H-polarized pulse. Consider three values of ε, providing each corresponding crystal in the single-mode range $0.05 \le \kappa = l/\lambda = kl/2\pi \le 0.95$ with stopbands, covering such intervals of frequency range, that if these bandgaps are put in the same draft all together, they all

together cover without breaks a fairly wide range of the frequency parameter κ (see three upper fragments in Fig. 2). In such way we obtained a structure with a bandgap $0.357 \le \kappa \le 0.815$, having the width $B_\kappa = \left[2\left(\kappa_{upper} - \kappa_{lower}\right)/\left(\kappa_{upper} + \kappa_{lower}\right)\right] \cdot 100\%$, that is approximately equal to 78.16% Important, that the bandwidth of such stopband is practically insensible to the sequence of five-layer crystals blocks, see two lower fragments in the Fig. 2.

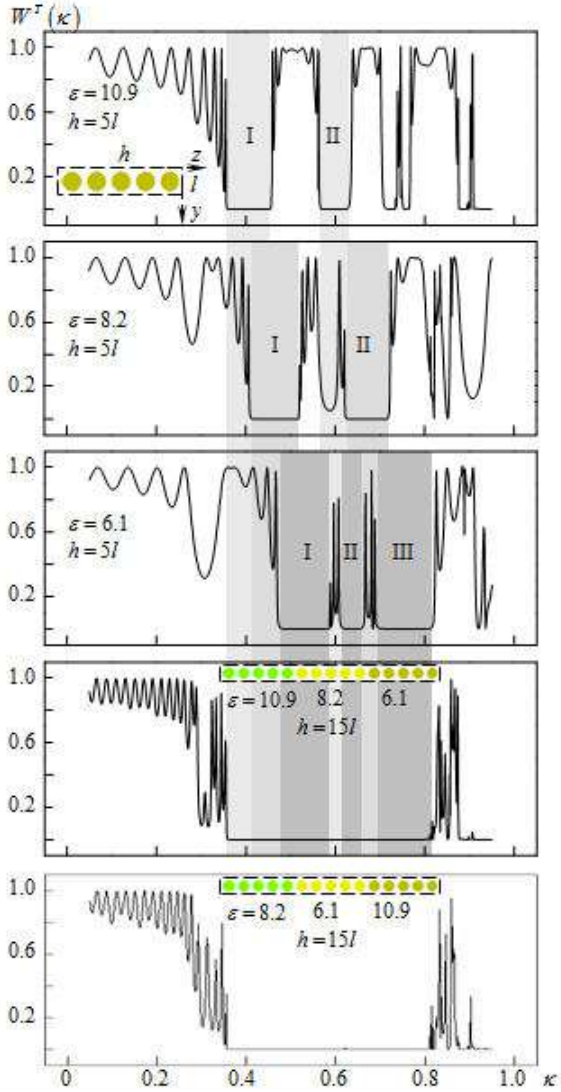

Figure 2: The synergistic effect of the joint operation of the three thick photonic crystals $h = 5l$.

4. Conclusions

The bottom-up approach for band gap photonic 2-D crystals construction is applied. It had been performed on the base of EAC.

The results of simulation proved: bandgaps (stopbands) of limited in thickness 2-D photonic crystals can be significantly increased due to the synergistic effect of the joint operation of several photonic crystals differing only in the internal structure of the crystal's unit cells.

References

[1] A. Perov, Yu. Sirenko, N. Yashina, Explicit conditions for virtual boundaries in initial boundary value problems in the theory of wave scattering, *Journal of Electromagnetic Waves and Applications*, 13(10): 1343–1371, 1999.

[2] K. Sirenko, Yu. Sirenko, Exact 'absorbing' conditions in the initial boundary value problems of the theory of open waveguide resonators, *Computational Mathematics and Mathematical Physics*, 45(3): 490–506, 2005.

[3] Yu. Sirenko, S. Strom, N. Yashina, *Modeling and Analysis of Transient Processes in Open Resonant Structures. New Methods and Techniques*, Springer, New York, 2007.

[4] Yu. Sirenko, S. Strom (eds), *Modern Theory of Gratings. Resonant Scattering: Analysis Techniques and Phenomena*, Springer, New York, 2010.

[5] K. Sirenko, Yu. Sirenko, N. Yashina, Modeling and analysis of transients in periodic gratings. I. Fully absorbing boundaries for 2-D open problems, *Journal of the Optical Society of America A*, 27(3): 532–543, 2010.

[6] V. Kravchenko, Yu. Sirenko, K. Sirenko, *Electromagnetic Wave Transformation and Radiation by the Open Resonant Structures. Modelling and Analysis of Transient and Steady-State Processes*, Fizmathlit, Moscow, 2011.

[7] O. Shafalyuk, Yu. Sirenko, P. Smith, Simulation and analysis of transient processes in open axially-symmetrical structures: Method of exact absorbing boundary conditions. Book chapter in Zhurbenko V. (ed), *Electromagnetic Waves*, 99–116, InTech, Rijeka, 2011.

[8] K. Sirenko, V. Pazynin, Yu. Sirenko, H. Bagci, An FFT-accelerated FDTD scheme with exact absorbing conditions for characterizing axially symmetric resonant structures, *Progress In Electromagnetics Research*, 111: 331–364, 2011.

[9] Yu. Sirenko, L. Velychko (eds), *Electromagnetic Waves in Complex Systems: Selected Theoretical and Applied Problems*, Springer, New York, 2016.

[10] K. Sirenko, Yu. Sirenko, H. Bagci, Exact absorbing boundary conditions for periodic three-dimensional structures: Derivation and implementation in discontinuous Galerkin time-domain method, *IEEE Journal on Multiscale and Multiphysics Computational Techniques*. 3(1): 108–120, 2018.

[11] M. Ney, K. Sirenko, Yu. Sirenko, H. Sliusarenko, N. Yashina, 2-D photonic crystals: Electromagnetic models of the method of exact absorbing conditions, *Telecommunication and Radio Engineering*, 76(3): 185–207, 2017.

Effective model of propagation across a metasurface with resonant Mie inclusions

Kim Pham[1] **and Agnès Maurel** [2]

[1] IMSIA, CNRS, ENSTA Paris, 828 Bd des Maréchaux, 91732 Palaiseau, France
[2] Institut Langevin, CNRS, ESPCI, 1 rue Jussieu, 75005 Paris, France,
*corresponding author, E-mail: kim.pham@ensta-paris.fr

Abstract

We study the scattering of waves by a single row of resonant inclusions, of the Mie type. An effective model based on matched asymptotic analyzed is used to account for the small thickness of the array. Hence, instead of the effective bulk parameters (permittivity and permeabilty), we end up with interface parameters entering in jump conditions for the electromagnetic fields; among these parameters, one is frequency dependent and encapsulates the resonant behavior of the inclusions. Our effective model is validated by comparison with results of full wave calculations.

1. Introduction

Starting in the 1990's with the pioneering work of [1] in the context of elasticity, resonant structures with subwavelength unit cells have been proposed in the context of electromagnetism [2], and in a unified mathematical context [3]. In this case, the resonances are attributable to an inclusion placed in the unit cell and presenting a high contrast in its material properties with respect to the surrounding matrix. These resonances often referred to as Mie resonances occur at frequencies producing a wavelength in the inclusion comparable to the inclusion size (and this size is much smaller than the incident wavelength). The ability of these so-called locally resonant structures to forbid the wave propagation has been exhibited and the forbidden band gaps have been interpreted in terms of an effective negative parameter being the mass density in elasticity and the permeability in electromagnetism. Since then, locally resonant materials have been intensively studied for applications including the design of efficient wave shields, see *e.g.* [3] or absorbers of small thicknesses, see *e.g.* [4].

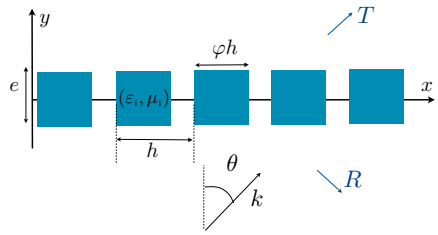

Figure 1: Scattering by an array of locally resonant inclusions with permittivity ε_i and permeability μ_i (in the air).

Motivated by the design of compact metamaterial devices and following the intuitive argument that each local resonator vibrates almost like an independent unit, structures involving a single row of resonators or few rows have been thought, see *e.g.* [5]. In this case, interrogating the bulk response of the device becomes questionable. Indeed, when the number of cells is too small, the metamaterial device is dominated by boundary layer effects and the response of its bulk, in terms of effective parameters, is not pertinent anymore; the failure of the effective medium theories for thick structures has been illustrated in [6]. Here, we extend these works to the case of an array composed of a single row of locally resonant inclusions (Fig. 1).

2. The actual and the effective problems

We consider transverse electric polarized waves propagating in the air and interacting with a row of inclusions with relative permittivity ε_i and permeability μ_i (and we set for the air $\varepsilon = \mu = 1$). In the case where $\varepsilon_i \mu_i \gg 1$, the wavelength inside the inclusions is much smaller than in the air, and resonances of the Mie type are possible. In this case, asymptotic analysis can be conducted which result in an effective interface model, see [7], where the array of resonant inclusions are replaced by jump conditions of the form

$$\begin{cases} [\![E]\!]_e = h\mathcal{B}\, \overline{\partial y E}, \\ [\![\partial_y E]\!]_e = h\mathcal{S}\, \overline{\partial_{yy} E} + h\mathcal{C}\, \partial_{xx}\overline{E} - h\mathcal{D}(k)\, k^2\, \overline{E}, \end{cases} \tag{1}$$

where we defined, for any field f, $[\![f]\!]_e \equiv f^+ - f^-$ and $\overline{f} \equiv (f^+ + f^-)/2$, with $f^\pm \equiv f(x, \pm e/2)$. The effective parameters $(\mathcal{B}, \mathcal{C}, \mathcal{S})$ depend only on the geometry of the inclusions while $\mathcal{D}(k)$ has an additional dependence on the frequency and it is the parameter which encapsulates the possible resonances of the Mie type. For instance, for rectangular shape of inclusion, as we shall consider in the numerical example, we have $\mathcal{S} = \frac{e}{h}(1-\varphi)$, $\mathcal{B} = \frac{e/h}{1-\varphi} - \frac{2}{\pi}\log\left(\cos\frac{\pi\varphi}{2}\right)$, $\mathcal{C} \simeq \frac{\pi}{8}(1-\varphi)^2\left(1 - e^{-\frac{8e}{(1-\varphi)\pi h}}\right)$ and

$$\mathcal{D}(k) = \varepsilon_i \frac{e\varphi}{h}\left[1 - \sum_n \alpha_n^2 \frac{k_i^2}{k_i^2 - k_{i,n}^2}\right], \tag{2}$$

with for $n = (n_1, n_2)$, $k_{i,n}^2 = \left(\frac{n_1\pi}{e}\right)^2 + \left(\frac{n_2\pi}{h\varphi}\right)^2$ the wavenumbers at the resonances and $\alpha_n = \frac{8}{\pi^2 n_1 n_2}$.

3. Fano resonances

In our homogenized problem, the region $|y| < e/2$ is disregarded and the wavefield satisfies (1) for $|y| > e/2$; a solution of this problem for an incident plane wave at oblique incidence θ reads

$$E = \begin{cases} \left[e^{\mathrm{i}k(y+e/2)\cos\theta} + Re^{-\mathrm{i}k(y+e/2)\cos\theta}\right] e^{\mathrm{i}kx\sin\theta}, \\ Te^{\mathrm{i}k(y-e/2)\cos\theta}\, e^{\mathrm{i}kx\sin\theta}, \end{cases} \tag{3}$$

for $y < -1/2$ and $y > e/2$ respectively. Next, applying the jump conditions (1) yields the scattering coefficient

$$\begin{cases} R = -\dfrac{1}{2}\left(\dfrac{z_1}{z_1^*} - \dfrac{z_2}{z_2^*}\right), \quad T = \dfrac{1}{2}\left(\dfrac{z_1}{z_1^*} + \dfrac{z_2}{z_2^*}\right), \\ z_1 \equiv 1 + \dfrac{ikh}{2}\,\mathcal{B}\cos\theta, \\ z_2 \equiv \cos\theta + \dfrac{ikh}{2}\left(\mathcal{S}\cos^2\theta + \mathcal{C}\sin^2\theta + \mathcal{D}(k)\right), \end{cases} \tag{4}$$

where z^* denotes the complex conjugate of z.

We report in Fig. 2 the variations of the reflection coefficients against the dimensionless frequency kh, R^{num} being computed numerically and R from (4) (the incidence is $\theta = 40°$). In the range $kh \in [0, 1]$, the first monopolar resonance for $n = (1, 1)$ in (2) is visible (it occurs for $k_{\text{i}}h = 8.9$ whence $kh \simeq 0.9$, resulting in a wavelength within the inclusions being about half the inclusion length). The agreement between R^{num} and its homogenized counterpart R is good, about 2% and this accuracy is the same for any incidence θ up the grazing incidence (results not reported). The resonance of the inclusions produces sharp variations of the reflection with a typical Fano resonance curve characterized by a perfect transmission followed by a perfect reflection. Results including the attenuation due to losses in the dielectric will be presented, with the same accuracy of the effective model to reproduce the scattering properties in the actual problem.

4. Concluding remarks

There are at least two natural extensions of the present study that we shall discuss. We have considered waves in a binary structures but the present work can be extended to ternary structure, as proposed in [8]. This extension may be of particular interest when locally resonant materials are considered in the acoustic case; as previously said, this is obtained in practice considering binary or ternary structures mixing fluids and elastic materials, thus for which the conversions between shear and longitudinal waves have to be accounted for. We believe that this is the key point to properly describe the negative index material reported in this context [9].

The second extension is technically much demanding. Our result has a serious limitation, already mentioned in [2]. The analysis holds for resonances with non zero mean value (namely, n_1 and n_2 odd in (2)). Although these resonances have a higher quality factor and thus are much more sensitive to losses, the accuracy of the homogenized solution would be enhanced if one is able to account for them. This requires to develop the model up to higher order and this is not incremental.

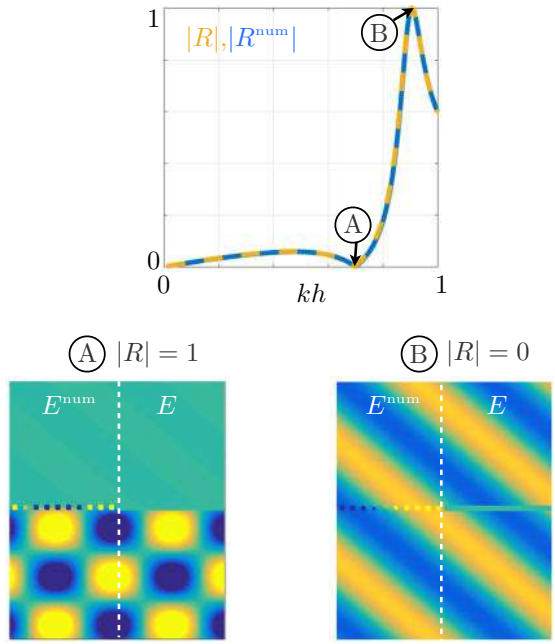

Figure 2: Fano resonance of a row of resonant Mie scatterers in the air ($\varepsilon = 100$, $\varphi = 0.5$, $e/h = 0.5$). Reflection coefficient $|R|$ against kh computed numerically (plain line) and from (4) (dotted line). The wavefields A at $kh = 0.7$ realizing perfect reflection and B at $kh = 0.9$ realizing perfect transmission (numerics and from (3) in both cases).

References

[1] J.-L. Auriault, Curr. Topics Ac. Res. I, 63-90, 1994.

[2] D. Felbacq and G. Bouchitté, PRL **94**(18),183902, 2005.

[3] V.V. Zhikov, Sbornik: Math., **191**(7), 973, 2000.

[3] C. Goffaux *et al.*, PRL, **88**(22), 225502, 2002.

[4] T. Brunet, J. Leng, and O. Mondain-Monval, **342**(6156), 323–324, 2013.

[5] H. Zhao, J. Wen, D. Yu and X. Wen, J. Appl. Phys., **107**(2), 023519, 2010.

[6] M. Lapine, R.C. McPhedran and C.G. Poulton, Phys. Rev. B, **93**(23), 235156, 2016.

[7] K. Pham, A. Maurel and J.-J. Marigo, JMPS, **106**, 80-94, 2017.

[8] Z. Liu, X. Zhang, Y. Mao, Y.Y. Zhu, Z. Yang, C.T. Chan, and P. Sheng, Science, **289**(5485, 1734-1736, 2000.

[9] Y. Ding, Z. Liu, C. Qiu, and J. Shi, Jing, Phys. Rev. Lett., **99**(9) 093904, 2007.

Spectral tuning of SPP reflection by quasi-symmetric metal nano-block arrays

Naoki Ichiji[1†], Atsushi Kubo[2*]

[1]Graduate School of Pure and Applied Science, University of Tsukuba, Ibaraki, Japan
[2]Division of Physics, Faculty of Pure and Applied Sciences, University of Tsukuba, Ibaraki, Japan
E-mail: †s2030036@s.tsukuba.ac.jp, *kubo.atsushi.ka@u.tsukuba.ac.jp

Abstract

We investigate the spectral tuning of the SPP wave packets by quasi-symmetric arrays composed of metal blocks with two different structural lengths. The FDTD simulations showed a resonance phenomenon in the gap between the blocks when the two blocks have different lengths in the longitudinal direction. Furthermore, the resonance of the gap resulted in a significant spectral modulation of the reflected SPP wave that depended on the structural length and positional relationship of the blocks.

1. Introduction

Metamaterials consisting of nanoscale structures have led to a significant development of optical manipulation techniques, such as polarization control and nonreciprocal transmission [1,2]. The artificial modulation of optical properties realized by metamaterials is one of the foundations for the control of light in free space and Surface Plasmon Polariton (SPP). SPP manipulation techniques, such as unidirectional excitation and wavelength selective focusing, have been demonstrated theoretically and experimentally by arranging nanorod and slit structures [3,4].

The specific optical properties of the metamaterial are determined by the design and arrangement of the individual resonator structure. In addition, when the distance between resonators is shorter than the wavelength of the incident light, mode coupling between resonators and near-field resonance can occur. Therefore, the interaction between resonators must be taken into account in metamaterials where the resonators are densely arranged.

In this work, we investigate the interaction between the SPP wave packet and a one-dimensional periodic structure of metal blocks. The periodic structure was constructed by periodically arranging Au blocks with two different structural lengths at intervals less than the wavelength of the incident SPP wave. An FDTD simulation reveals that the walls of the adjacent blocks behave as MIM resonators, with the gap between the blocks as an insulator layer only when the longitudinal length of the two blocks are different. This MIM resonator, referred to as gap MIM structure, caused spectral modulations in the transmitted and reflected wave, especially in the reflected wave. The spectral modulation observed in the reflected wave can be adjusted by arranging the two types of blocks.

2. Result

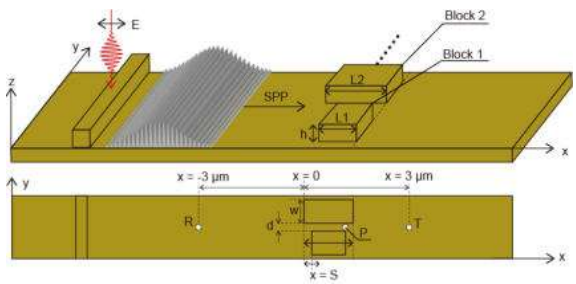

Figure 1: Schematic of periodic structure used for FDTD simulations.

Figure 1 (a) shows a schematic of the quasi-symmetric array constructed by Au blocks with two different lengths in the longitudinal direction. The height h and width w of the two blocks was fixed at 100 nm, and they were arranged periodically with a spacing d of 60 nm. In this study, we fixed the length L_1 of Block 1 at 200 nm, and the length L_2 of Block 2 was set as a variable. We defined the left edge of Block 2 as the origin of the x-axis. The left edge of Block 1 was placed at a distance S shifted from the origin. In this paper, we call the "left edge model" when the left edges of the blocks are coincident ($S = 0$ nm) and the "right edge model" when the right edges are coincident ($S = L2 - L1$ nm). The model with $L1 = L2 = 200$ nm was defined as the reference model. A Au ridge as a coupler for launching SPP WPs was placed on the same surface. The time evolution in the vertical component of the electric fields ($E_z(t)$) for reflected and transmitted waves of the array structure were recorded at points T and R, respectively. To analyze the effect of resonance between blocks, the horizontal component of the electric fields ($E_z(\mathrm{t})$) was also recorded at point P placed between blocks shown in Fig. 1.

Figs. 2 (a,b) show typical reflected and transmitted spectra calculated by the fast Fourier transform (FFT) of the $E_z(t)$ measured at points R and T. The reflected spectra obtained with the left edge model (red) and right edge model (blue) at the condition of L_2 = 290 nm show large modulation compared to the reference model (black). The modulation in the reflection spectrum occurs mainly at two wavelengths: an increase in intensity around 650 nm and an asymmetric shape around 820 nm. Compared with the reflected wave, which has a large difference in spectrum between the left- and right-edge models, there is almost no difference in the transmitted spectrum (Fig. 2 (b)).

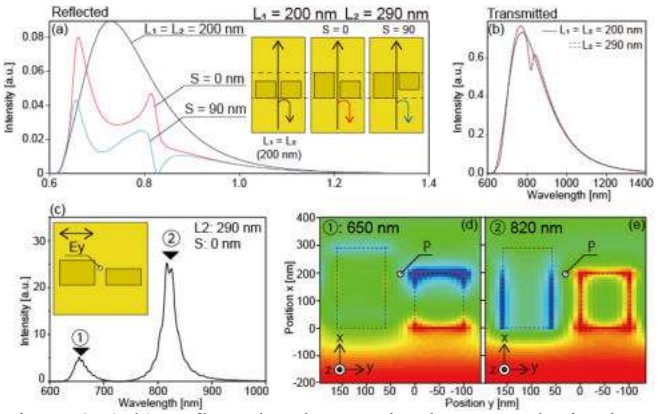

Figure 2: (a,b) Reflected and transmitted spectra obtained at point T and R. (c) Resonance spectra of the gap between blocks obtained at point P. (d,e) Electric field amplitudes E_z on the xy plane at the wavelength of 650 nm and 820 nm.

Fig. 2(c) shows the resonance spectra $F(\omega)$ calculated by the Fourier transform from the horizontal component of the electric field E_y(t) acquired at the P. This graph indicates clear peaks at 650 nm and 820 nm, which coincide with the characteristic spectral modulation in the reflected spectrum shown in Fig. 2 (a). These resonance peaks do not occur when the length of the two blocks is the same. Fig. 2(d,e) shows the vertical components of the electric field distributions $E_y(x, z)$ obtained at plane 8 nm above the Au surface. The blocks show two types of resonances at 650 nm and 820 nm. In this model, the two metal walls of adjacent blocks act as semi-open MIM nanocavities [5], with the gap between the blocks as an insulating layer.

3. Discussion

We attribute the spectral modulation with a characteristic asymmetric shape to the Fano resonance between the reflected wave from the block wall and the resonance in the MIM gap. Fano resonance is an asymmetric spectral modulation caused by the interference of a narrow discrete resonance with a broad spectral line or continuum [5]. The characteristic spectral shape of the Fano resonance $I(\omega)$ is described by the following equation [6].

$$I(\omega) = \left[\frac{(q+\Omega)^2}{1+\Omega^2}\eta + (1-\eta)\right]B^2, \qquad (1)$$

where q is the Fano asymmetry parameter, Ω is the dimensionless frequency, η is the interaction coefficient, and B is a constant. In this model, the reflection of the wall and resonance at the gap corresponds to the broad spectral line and narrow discrete resonance. In this model, Ω is determined by the resonance wavelength of the MIM resonance occurring in the gap (650 nm, 820 nm), and q is determined by the positions of blocks and the MIM gap. Figure 3 (a) shows the reflection spectrum obtained by varying S from 0 to 220 nm for the model with L_2 = 440 nm. A series of graphs indicate that a characteristic Fano-like spectrum modulation around 820 nm. As shown in Figs. 3 (b-d), varying S corresponds to varying the position of the MIM gap relative to Block 1. We performed a fitting based on the Fano resonance. The fitting curves were defined by multiplying the reflected wave spectrum in the reference model by Fano spectra (eq. (1)) with the center wavelength of 650 nm and 820 nm. The fitting results shown by the red lines in Fig. 3 (a) are well fitted with the simulation results.

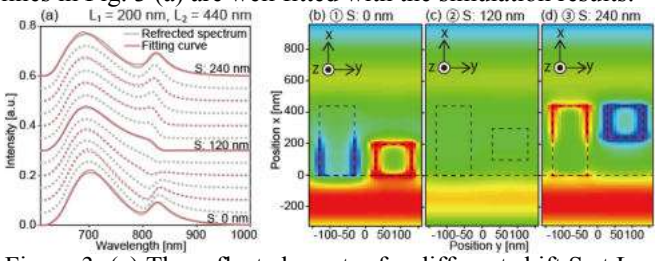

Figure 3: (a) The reflected spectra for different shift S at L_2 = 440 nm structures. (b-d) Related maps of the electric field amplitudes E_y at wavelength of 820 nm. S = 0 nm (b), S = 120 nm (c), S = 240 nm (d).

4. Conclusions

In conclusion, we numerically investigated a quasi-symmetric array structure composed of two metal blocks with different structural lengths. This structure revealed that the reflected wave has a spectral modulation highly depending on the positional relationship of blocks caused by Fano resonance. The incident direction dependence phenomenon observed in this study has potential applications to various optical devices, such as variable reflectivity structures and unidirectional excitation of SPP.

Acknowledgements

This work was supported by the JSPS KAKENHI ((JP14459290, JP16823280, JP18967972, JP20J21825), and MEXT Q-LEAP ATTO, Japan

References

[1] M. Lawrence, D. R. Barton, III, J. A. Dionne, Nonreciprocal flat optics with silicon metasurfaces, *Nano Lett.*, 18, 2, 1104-1109, 2018

[2] A. Arbabi, Y. Horie, M. Bagheri, A. Faraon, Dielectric metasurfaces for complete control of phase and polarization with subwavelength spatial resolution and high transmission, Nat. Nanotech., 10, 937-943, 2015

[3] J. S. Q. Liu, R. A. Para, F. Afshinmanesh, W. Cai, M. L. Brongesma, A submicron plasmonic dichroic splitter. *Nat Commun* **2,** 525. 2011.

[4] S. Wang, C. Zhao, X. Li, Dynamical Manipulation of Surface Plasmon Polaritons. *Appl. Sci. 9*, 3297, 2019.

[5] H. T. Miyazaki, Controlled plasmon resonance in closed metal/insulator/metal nanocavities, *Appl. Phys. Lett.,* 89, 211126, 2006.

[6] B. Luk'yanchuk, N. I. Zheludev, S. A. Maier, N. J. Halas, P. Nordlander, H. Giessen, C. T. Chong, Nat. Mater., 9, 707-715, 2010.

[7] M. V. Rybin, P. V. Kapitanova, D. S. Filonov, A. P. Slobozhanyuk, P. A. Belov, Y. S. Kivshar, M. F. Limonov, Fano resonances in antennas: General control radiation patterns, *Phys. Rev. B,* 88, 205106, 2013.

Mutual coupling Reduction in antenna arrays using Metasurface

Safia Jaouad[1], Mariem Aznabet[2], Otman EL Mrabet[1], Mohsine Khalladi[2]

[1]Information and Telecommunication Systems Lab, Faculty of Sciences, University of Abdelmalek Essaadi, Tétouan, Morocco.

[2]Department of Electrical and Computer Engineering, University of Wisconsin–Madison, Madison, WI 53706 USA.

*corresponding author, E-mail: safia.jaouad@gmail.com

ABSTRACT

In this paper, a meta-surface is developed as an effective solution for reducing mutual coupling between two adjacent antennas. The meta-surface comprises an array of omega shape resonators placed above two closely antennas. The simulated results show a 24 dB reduction in coupling when placing meta-surface over two adjacent antennas separated by a spacing of 1/5 wavelength at frequency of 2.85 GHz. Furthermore, the gain of antenna arrays with the meta-surface is also improved by 3dB.

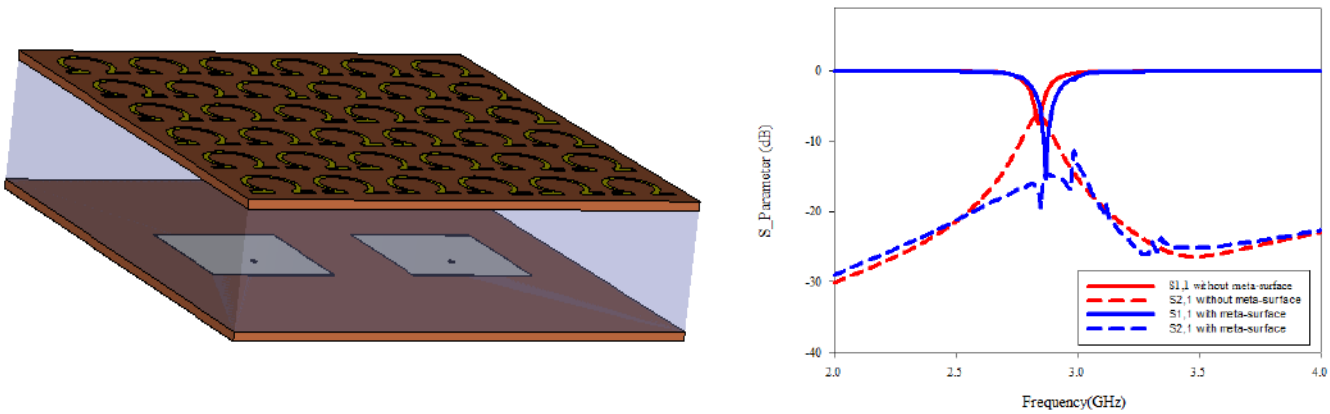

(a) (b)

Figure1: (a) Antenna Array with meta-surface; (b) simulated S-parameter with and without meta-surface

REFERENCE:

[1] Jensen, M. A. & Wallace, J. W. A review of antennas and propagation for MIMO wireless communications. IEEE Transactions on Antennas and Propagation 52(11), 2810–2824 (2004)

[2] Larsson, E. G., Edfors, O., Tufvesson, F. & Marzetta, T. L. Massive MIMO for next generation wireless systems. IEEE Communications Magazine 52(2), 186–195 (2014à

[3] Coetzee, J. C. & Yu, Y. Port decoupling for small arrays by means of an eigenmode feed network. IEEE Transactions on Antennas and Propagation 56(6), 1587–1593 (2008).

[4] Zhao, L., Yeung, L. K. & Wu, K. L. A coupled resonator decoupling network for two-element compact antenna arrays in mobile terminals. IEEE Transactions on Antennas and Propagation 62(5), 2767–2776 (2014).

[5] Wang, Z., Zhao, L., Cai, Y. et al. A Meta-Surface Antenna Array Decoupling (MAAD) Method for Mutual Coupling Reduction in a MIMO Antenna System. Sci Rep 8, 3152 (2018). https://doi.org/10.1038/s41598-018-21619-z

Design and optimization of holographic nonlinear metasurfaces

David Hähnel[1,*], Jens Förstner[1], and Viktor Myroshnychenko[1]

[1]Theoretical Electrical Engineering, Paderborn University, Paderborn, Germany
*corresponding author, E-mail: hdavid@mail.upb.de

Abstract

We present the design and optimization of all-dielectric nonlinear metasurfaces using a simple but effective sampling method combined with Monte Carlo simulation and demonstrate that the use of sophisticated optimization methods is not necessary. We apply this approach for the optimization of metasurface composed of silicon disks, which operates as a third harmonic beam deflector at a defined angle. Our results demonstrate a significant enhancement of radiated third harmonic intensity in the first diffraction order compared to that reported in literature.

1. Introduction

Various efficient methods for the design and optimization of linear metasurfaces have already been developed and reported in the past [1]. Among them, the most popular methods are gradient descent method, evolutionary and machine learning algorithms. Currently, attempts are being made to apply these techniques also for the design and optimization of nonlinear metasurfaces. However, this is quite a complex task due to the many degrees of freedom involved, the nontrivial functional dependencies, and complexity of the nonlinear processes. Many works in the literature employ sophisticated optimization algorithms for these purposes [2].

Here, we present a simple yet powerful sampling method in combination with the Monte Carlo simulation for the design and optimization of holographic nonlinear metasurfaces. The metasurfaces consist of silicon nanodisks of elliptical cross section deposited on a silicon dioxide substrate. The wavefront of the third harmonic signal is shaped through adjustment of the nanodisk's lateral dimensions. The robustness of our approach is illustrated through the design and optimization of a nonlinear beam deflector that directs the incoming linear polarized plane wave at the fundamental frequency into the first diffraction order at the third harmonic frequency. We reveal a capability of our approach to solve dynamic problems with a varying number of optimization parameters that are unknown in advance.

2. Results

Our metasurface is composed of silicon elliptical disks placed on a silicon dioxide substrate and generates a third harmonic signal under external illumination. To design the metasurface which produces a nonlinear beam deflection, a set of resonators with the required smooth phase gradient and constant amplitude has to be firstly found (Fig. 1). For this purpose, the phase and intensity maps of the third harmonic (TH) signal is calculated as a function of the disk's ellipse diameters. This is done independently for each resonator by modeling a unit cell with periodic boundary conditions and calculating the electromagnetic fields using COMSOL Multiphysics. The height of the resonators and periodicity are fixed and chosen to be $h = 285\,\text{nm}$ and $p = 916.67\,\text{nm}$, respectively. The corresponding phase map (color map) and the third harmonic intensity contour (black and white dashed lines) are shown in Fig. 2(a). By employing the sampling method, we then select six different resonators with equally spaced phase values and constant intensity in the parameter space. The disk parameters are determined by the intersections (white dots) of a predefined number of phase contours (solid black lines) with an intensity contour (dashed lines) that discretely covers the 2π phase range, as in [3]. We note that an arbitrary number of resonators with specified phase and constant intensity can be picked from the map, which provides the convenient flexibility to this method, especially, when the final number of resonators in the optimized application is unknown.

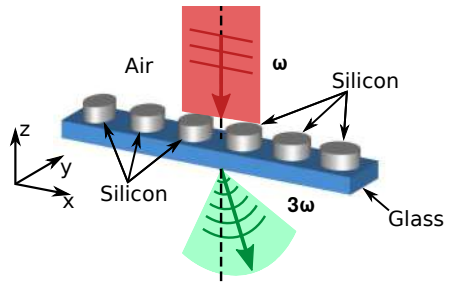

Figure 1: Sketch of the nonlinear beam deflection by a dielectric metasurface, illustrating the generated third harmonic beam deflection in transmission direction.

Finally, the diffraction spectrum for the presented parameter selection (Fig. 2(a)) is calculated and shown in Fig. 2(b). For orientation, the angle calculated with the equation of Bragg's law is inserted at the first diffraction order bar. The TH radiation of the first diffraction order is the maximum in the spectrum and in the near vicinity a suppression of about 80% can be achieved.

Aiming to further improve the TH radiation, we apply Monte-Carlo simulation to optimize the parameters of the individual resonators, by searching over a four-dimensional

parameter space including resonator height, x- and y-diameters, and periodicity. In comparison to Fig. 2(b), the enhanced TH radiation at the first positive diffraction order by a factor of 250 is achieved for the optimized parameter selection (not shown here).

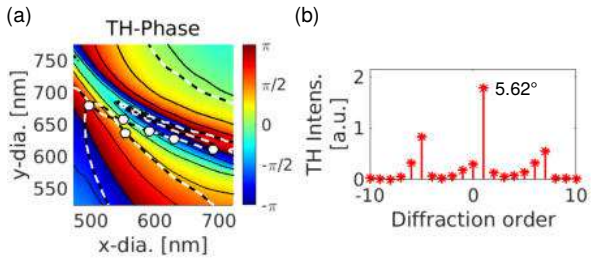

Figure 2: (a) Calculated third harmonic phase map with third harmonic intensity contour (black and white dashed lines). The resonators with selected parameters are marked by white dots. (b) Corresponding discrete diffraction spectrum of the radiated third harmonic intensity for the unit cell model composed of the selected six resonators and shown in Fig. 1.

3. Conclusions

In summary, we have shown that the proposed combination of the sampling method and Monte-Carlo simulation can be effectively used in the design and optimization of holographic nonlinear metasurfaces. We exemplarily use this approach to design and optimize a dielectric metasurface composed of silicon nanodisks for the nonlinear beam deflection application. The required phase gradient with a constant amplitude is engineered by varying the lateral dimensions of the nanodisks and thus exciting different electric and magnetic resonances. The selected set of the optimized resonators demonstrates a significantly enhanced intensity of the third harmonic beam radiated in the first diffraction order. Our approach can be used to design metasurfaces with other different functionalities.

Acknowledgement

The authors gratefully acknowledge financial support from the Deutsche Forschungsgemeinschaft (DFG) via TRR142 project C05 and computing time support provided by the Paderborner Center for Parallel Computing (PC^2).

References

[1] S. Chen, Z. Li, Y. Zhang, H. Cheng, and J. Tian, Phase Manipulation of Electromagnetic Waves with Metasurfaces and Its Applications in Nanophotonics, *Advanced Optical Materials* 6(13): 1800104, 2018.

[2] L. Wang, S. Kruk, K. Koshelev, I. Kravchenko, B. Luther-Davies, and Y. Kivshar, Nonlinear Wavefront Control with All-Dielectric Metasurfaces, *Nano Letters* 18(6): 3978–3984, 2018.

[3] E. Almeida, O. Bitton and Y. Prior, Nonlinear metamaterials for holography, *Nat. Commun.* 7: 12533, 2016.

Novel Sensing Technique for Non-destructive Composites Monitoring

Valentina Zhukova[1,2], Paula Corte-León[1,2], Aleksandra Allue[3], Koldo Gondra[3], Mihail Ipatov[1,2], Juan M. Blanco[2], Julian Gonzalez[1] and Arcady Zhukov[1,2,4]*

[1]Dpto. Fisica de Materiales, Fac. Quimicas, UPV/EHU, Paseo Manuel Lardizabal, 3, San Sebastian, 20018, Spain
[2]Dpto. de Física Aplicada, EIG, UPV/EHU, San Sebastian, Europa Plaza, 1,20018, Spain
[3]Gaiker Technological Centre, 48170, Zamudio, Spain
[4]IKERBASQUE, Basque Foundation for Science, Bilbao, 48011, Spain
*corresponding author, E-mail: arkadi.joukov@ehu.es

Abstract

We observed evolution of the transmission and reflection parameters of the composites containing magnetic microwire inclusions during the composites matrix polymerization. A remarkable change of the reflection and transmission in the range of 4-7 GHz upon the matrix polymerization is observed. Obtained results are considered as a base for novel sensing technique allowing non-destructive and non-contact monitoring of the composites utilizing ferromagnetic glass-coated microwire inclusions with magnetic properties sensitive to tensile stress and temperature.

1. Introduction

Amorphous magnetic materials can present an unusual combination of excellent magnetic properties (e.g. high magnetic permeability, giant magnetoimpedance, GMI, effect, magnetic bistability, Matteucci and Widemann effects,) and superior mechanical properties (plasticity, flexibility) making them suitable for numerous industrial applications [1]-[2]. Furthermore the preparation method involving rapid melt quenching is quite fast and cheap and above mentioned magnetic softness can be realized without any complex post-processing treatments [1].

The development of novel applications of amorphous materials requires new functionalities, i.e. reduced dimensions, enhanced corrosion resistance or biocompatibility [1]. Glass-coated microwires prepared using the Taylor-Ulitovsky method fit to most of aforementioned expectation: such magnetic microwires have micro-nanometric diameters (typically 0.5-50 μm) covered by thin, insulating, biocompatible and flexible glass-coating [1] and can present excellent magnetic softness or magnetic bistability [1],[3].

These features of glass-coated microwires allow development of new exciting applications in various magnetic sensors [1]-[3], as well as in smart composites with tunable magnetic permittivity [2]-[3]. A few years ago the stress dependence of the GMI effect is proposed for the mechanical stresses monitoring in fiber reinforced composites (FRC) containing microwires inclusions [2]-[4]. A novel sensing technique involving free space microwave spectroscopy utilizing ferromagnetic microwire inclusions presenting the high frequency impedance is quite sensitive to tensile stress and magnetic field [4].

In this work we provide our recent results on study of the stresses arising during the polymerization of the matrix in FRCs on permittivity of the FRC with embedded microwire inclusions.

2. Materials and methods

We used glass-coated $Fe_{3.8}Co_{65.4}Ni_1B_{13.8}Si_{13}Mo_{1.35}C_{1.65}$ (metallic nucleus diameter, d=18.8 μm, total diameter, D=22.2 μm, ρ =d/D= 0.88) microwires with low negative magnetostriction coefficients, λ_s, prepared by Taylor-Ulitovsky technique described elsewhere [2]. The temperature during the polymerization process has been measured by a standard thermocouple.

For the composite matrix we used a vinylester resin (DERAKANE 8084) resin, accelerated with Cobalt Octoate (0,3 pph) and catalyzed with Methyl Ethyl Ketona (MEK 60%, 1,5 pph).

We used the free space measurement system previously described in details in [4]. The reflection (*R*) and transmission (*T*) coefficients were measure in free-space. The experimental set-up consists of a pair of broadband horn antennas (1-17 GHz) and a vector network analyzer. The composite was placed in 20 x 20 cm^2 window to avoid the edge effects. This window limits the applicable frequency range in 4-17 GHz. More detailed description of the free space systems is given in our previous publications [4]. The composites with ordered glass coated amorphous wires embedded in the thermoset matrix polymerization were prepared (Fig.1).

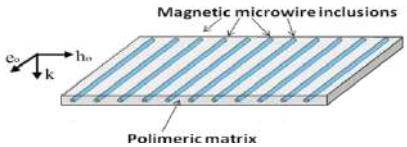

Figure 1 Sketch of a FRC with embedded microwires .

The polymerizing matrix provides external stimuli for the microwire inclusions (Fig. 1), which affects the magnetic properties and the GMI effect of microwires.

3. Results and discussion

During the polymerization process of the resin, volume shrinkage of about 8.2 % occurs and solid cured resin is obtained. The mechanical properties of the cured resin are the following: tensile strength of 76 MPa, tensile modulus of 2.9 GPa, and tensile elongation of 8-10%. However, apart of the matrix shrinkage considerable heating takes place. Therefore, in order to understand the processes during the polymerization of the composite that can affect the microwires we have measured the evaluation of temperature using a thermocouple. Obtained temperature changes during the polymerization represented at temperature, *T*, versus time, *t*, are sown in Fig.2.

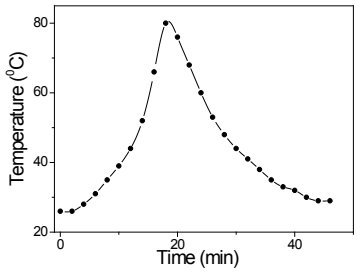

Figure 2. Evolution of temperature upon the polymerization.

As can be observed from the Fig.2, the matrix polymerization produces a heating of the composite up to 80 °C. As described above, we measured the transmission, *T*, and reflection, *R*, parameters of the composite containing Co-rich microwires ($Fe_{3.8}Co_{65.4}Ni_1B_{13.8}Si_{13}Mo_{1.35}C_{1.65}$) using the free space system.

As can be appreciated from Fig.3, considerable variation of the *T*-parameter is observed in the range frequency, *f*, of 4-7 GHz upon thermoset matrix polymerization (Fig.3). A non-monotonic variation of *T*-parameter upon polymerization is observed (Fig.3a). Additionally, some changes of *R*-parameter are also observed in a wide *f*- range (Fig.3b).

Observed changes of electromagnetic properties can be related to two main phenomena arising during the composite matrix polymerization: heating and mechanical stresses. As we mentioned above, apart of the matrix heating, the polymerization is accompanied by change of density and shrinkage. Therefore we can assume that the matrix shrinkage produces compressive stresses in magnetic nucleus of glass-coated microwires. Observed *T(f)* dependencies with are non-monotonic: some increase of *T* observed up to *t*=15 min (at *f* ≈4-7 GPa) followed by *T* decrease at *t*>15 min. Such evolution of *T*-parameter can be therefore associated to the heating and consequent cooling of the FRC.

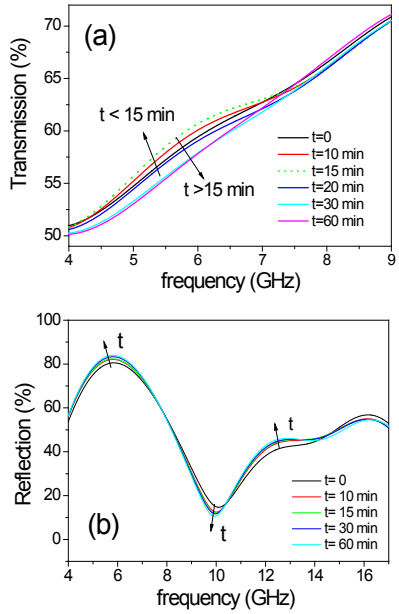

Figure 3. The Transmission, T (a) and reflection, R (a) parameters measured using free-space system during the composite polymerization.

4. Conclusions

We propose a novel sensing technique for non-destructive composites monitoring utilizing ferromagnetic microwire inclusions with magnetic properties sensitive to tensile stress and temperature. We have studied in-situ the impact of matrix polymerization on the evolution of the *T*- and R- parameters of the composites with microwire inclusions. We observed considerable variation of the *T*-parameter (in the range of 4-7 GHz) and *R*-parameter upon composite polymerization. Observed dependencies are discussed considering the matrix shrinkage during the polymerization and heating during the matrix polymerization and their influence on magnetic properties of glass-coated microwires.

References

[1] A. Zhukov, M. Ipatov and V. Zhukova, *Advances in Giant Magnetoimpedance of Materials*, Handbook of Magnetic Materials, ed. K.H.J. Buschow, Vol. 24, 2015, pp. 139-236 (chapter 2).

[2] K. Mohri, T. Uchiyama, L. P. Shen, C. M. Cai, L. V. Panina, Amorphous wire and CMOS IC-based sensitive micro-magnetic sensors (MI sensor and SI sensor) for intelligent measurements and controls, *J. Magn. Magn. Mater.* 249: 351-356, 2002.

[3] M.H. Phan, and H.X. Peng, Giant magnetoimedance materials: fundamentals and applications, *Prog. Mater. Sci.*, **53,** 323-420 (2008).

[4] D. Makhnovskiy, A. Zhukov, V. Zhukova, J. Gonzalez, Tunable and self-sensing microwave composite materials incorporating ferromagnetic microwires, *Advances in Science and Technology*, 54 (2008) pp. 201-210

Modeling of Spatially Dispersive Quadrupolar Metasurfaces

Karim Achouri[1], Ville Tiukuvaara[1] and Olivier J. F. Martin[1]

[1]Nanophotonics and Metrology Laboratory, Department of Microengineering,
École Polytechnique Fédérale de Lausanne, Route Cantonale, 1015 Lausanne, Switzerland
*corresponding author, E-mail: karim.achouri@a3.epfl.ch

Abstract

Metasurfaces are typically modeled using boundary conditions restricted to dipolar responses. While generally effective, this modeling approach suffers in the case of large incidence angles. To provide a better modeling accuracy, we derive a model that includes dipolar and quadrupolar responses as well as higher-order spatially dispersive effects. The effectiveness of this extended model is demonstrated by predicting the angular scattering of a dielectric metasurface up to grazing angles. This work is expected to be useful for designing spatial analog optical signal processing metasurfaces for incident beams with large angular spectra.

1. Introduction

In recent years, there has been a growing interest in the implementation of spatial optical analog processing metasurfaces [1–7]. To help designing such structures, one may employ conventional metasurface synthesis techniques, such as [8,9], which only include dipolar responses. As shown in [10], such dipolar models work well within the paraxial limit but start exhibiting significant errors for small wavelength-to-period ratios and/or large incidence angles. To overcome this limitation, we have extended the model to include multipolar responses and spatially dispersive interactions [11,12].

2. Metasurface Modeling

A common approach to model a metasurface is to replace it by a fictitious zero-thickness sheet, supporting electric and magnetic dipolar polarizations, for which convenient boundary conditions may be formulated [8,9,13]. To improve the angular scattering modeling accuracy of such a dipolar model, we have extended it to include quadrupolar responses. The new boundary conditions, for a metasurface lying in the xy plane, are given by [10]

$$\begin{aligned}\hat{\mathbf{z}}\times\Delta\mathbf{E} = &-j\omega\mu\mathbf{M}_{\parallel} + \frac{k^2}{2\epsilon}\hat{\mathbf{z}}\times\left(\overline{\overline{Q}}\cdot\hat{\mathbf{z}}\right)\\ &-\frac{1}{\epsilon}\hat{\mathbf{z}}\times\nabla\left[P_z - \frac{1}{2}(\nabla_{\parallel}\hat{\mathbf{z}}+\hat{\mathbf{z}}\nabla_{\parallel}):\overline{\overline{Q}}\right] \quad (1a)\\ &+\frac{j\omega\mu}{2}\left(\overline{\overline{S}} - S_{zz}\overline{\overline{I}}\right)\cdot\nabla_{\parallel},\end{aligned}$$

$$\begin{aligned}\hat{\mathbf{z}}\times\Delta\mathbf{H} = &\, j\omega\mathbf{P}_{\parallel} + \frac{k^2}{2}\hat{\mathbf{z}}\times\left(\overline{\overline{S}}\cdot\hat{\mathbf{z}}\right)\\ &-\hat{\mathbf{z}}\times\nabla\left[M_z - \frac{1}{2}(\nabla_{\parallel}\hat{\mathbf{z}}+\hat{\mathbf{z}}\nabla_{\parallel}):\overline{\overline{S}}\right] \quad (1b)\\ &-\frac{j\omega}{2}\left(\overline{\overline{Q}} - Q_{zz}\overline{\overline{I}}\right)\cdot\nabla_{\parallel}.\end{aligned}$$

where $\Delta\mathbf{E}$ and $\Delta\mathbf{H}$ are the differences of the fields on both sides of the metasurface, $\mathbf{P}$ and $\mathbf{M}$ are electric and magnetic dipolar responses, and $\overline{\overline{Q}}$ and $\overline{\overline{S}}$ are electric and magnetic quadrupolar responses. These multipolar quantities represent the response of the metasurface to an arbitrary excitation and include spatially dispersive interactions. They are related to the average fields and fields derivatives at the metasurface via

$$\begin{bmatrix} P_i \\ M_i \\ Q_{il} \\ S_{il}\end{bmatrix} = \overline{\overline{\chi}}\cdot\begin{bmatrix} E_{\text{av},j} \\ H_{\text{av},j} \\ \nabla_k E_{\text{av},j} \\ \nabla_k H_{\text{av},j}\end{bmatrix}, \quad (2)$$

where the hypersusceptibility tensor $\overline{\overline{\chi}}$ is given by

$$\overline{\overline{\chi}} = \begin{bmatrix} \epsilon_0\chi_{\text{ee}}^{ij} & \frac{1}{c_0}\chi_{\text{em}}^{ij} & \frac{\epsilon_0}{2k_0}\chi_{\text{ee}}^{'ijk} & \frac{1}{2c_0k_0}\chi_{\text{em}}^{'ijk} \\ \frac{1}{\eta_0}\chi_{\text{me}}^{ij} & \chi_{\text{mm}}^{ij} & \frac{1}{2\eta_0k_0}\chi_{\text{me}}^{'ijk} & \frac{1}{2k_0}\chi_{\text{mm}}^{'ijk} \\ \frac{\epsilon_0}{k_0}Q_{\text{ee}}^{ilj} & \frac{1}{c_0k_0}Q_{\text{em}}^{ilj} & \frac{\epsilon_0}{2k_0^2}Q_{\text{ee}}^{'iljk} & \frac{1}{2c_0k_0^2}Q_{\text{em}}^{'iljk} \\ \frac{1}{\eta_0k_0}S_{\text{me}}^{ilj} & \frac{1}{k_0}S_{\text{mm}}^{ilj} & \frac{1}{2\eta_0k_0^2}S_{\text{me}}^{'iljk} & \frac{1}{2k_0^2}S_{\text{mm}}^{'iljk}\end{bmatrix}. \quad (3)$$

These equations show that a quadrupolar metasurface provides a large number of additional degrees of freedom compared to a dipolar one. However, note that several important properties related to the symmetries of quadrupolar tensors, reciprocity and passivity/losslessness reduce the number of independent parameters in (3), as explained in [14].

In order to demonstrate the performance of our model, we compare its angular scattering predictive accuracy to that of the conventional dipolar model. Consider the simulation setup presented in Fig. 1a, where a metasurface made of dielectric cylinders is illuminated at oblique incidence by a TM-polarized wave. Its transmission coefficient is plotted versus wavelength and incidence angle in Fig. 1b. The performance of the dipolar model is first investigated by setting $\overline{\overline{Q}} = \overline{\overline{S}} = 0$ in (1), substituting the fields by those obtained from full-wave simulation at $\theta = 0°$ and solving for the remaining non-zero susceptibilities. The latter

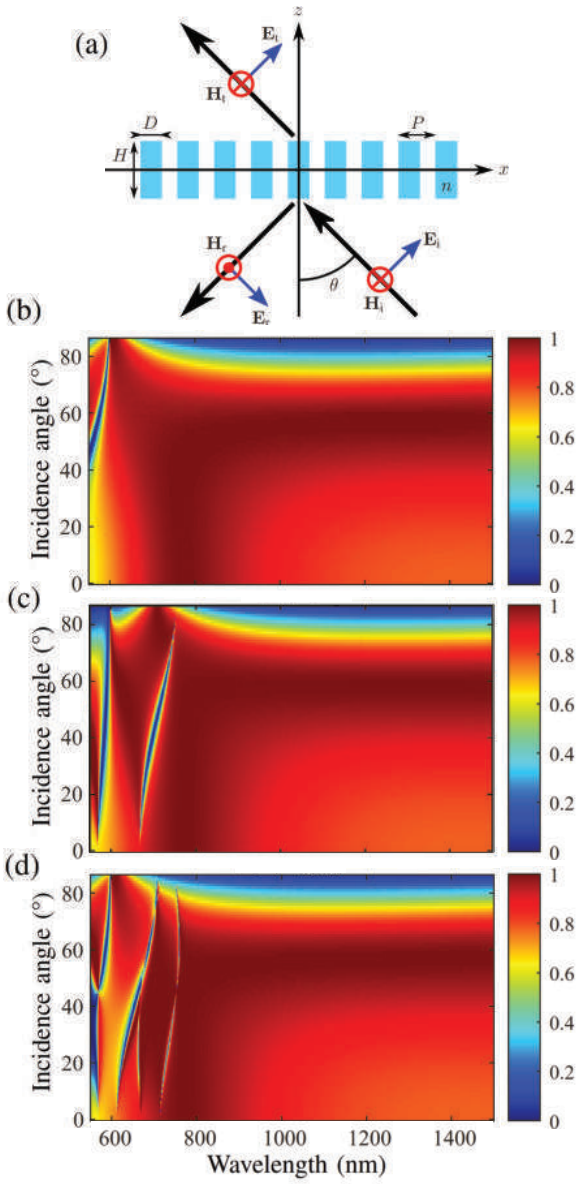

Figure 1: Multipolar modeling of an array of dielectric cylinders with $P = 225$ nm, $D = 200$ nm, $H = 200$ nm and $n = 2.55$. (a) Simulation setup. (b) Full-wave simulated transmission amplitude. Predicted transmission amplitude using a (c) purely dipolar and a (d) quadrupolar metasurface model. See [10] for more information.

are then used to predict the transmission coefficient in the range $\theta =]0°, 85°]$ and the resulting prediction is plotted in Fig. 1c. As expected, the model performs well for large wavelengths and small incidence angles but significant errors appear at lower wavelengths and higher angles. Now, the same approach is used for the quadrupolar model. Since more hypersusceptibility components must be solved, the full-wave simulated fields at $\theta = 0°, 45°$ and $85°$ are used to predict the transmission for all other angles. The result is plotted in Fig. 1d and, besides some undesired sharp features, show a much better agreement with the expected response, which is about 3.5 better than the dipolar model in Fig. 1c.

Acknowledgement

We gratefully acknowledge funding from the Swiss National Science Foundation (project PZ00P2_193221).

References

[1] A. Pors, M. G. Nielsen, and S. I. Bozhevolnyi, "Analog Computing Using Reflective Plasmonic Metasurfaces," *Nano Lett.*, vol. 15, no. 1, pp. 791–797, 2015.

[2] A. Chizari, S. Abdollahramezani, M. V. Jamali, and J. A. Salehi, "Analog optical computing based on a dielectric meta-reflect array," *Opt. Lett.*, vol. 41, no. 15, p. 3451, 2016.

[3] S. Abdollahramezani, A. Chizari, A. E. Dorche, M. V. Jamali, and J. A. Salehi, "Dielectric metasurfaces solve differential and integro-differential equations," *Opt. Lett.*, vol. 42, no. 7, p. 1197, 2017.

[4] H. Babashah, Z. Kavehvash, S. Koohi, and A. Khavasi, "Integration in analog optical computing using metasurfaces revisited: Toward ideal optical integration," *J. Opt. Soc. Am. B*, vol. 34, no. 6, p. 1270, 2017.

[5] T. Zhu, Y. Zhou, Y. Lou, H. Ye, M. Qiu, Z. Ruan, and S. Fan, "Plasmonic computing of spatial differentiation," *Nat. Commun.*, vol. 8, no. 1, p. 15391, 2017.

[6] A. Momeni, H. Rajabalipanah, A. Abdolali, and K. Achouri, "Generalized Optical Signal Processing Based on Multioperator Metasurfaces Synthesized by Susceptibility Tensors," *Phys. Rev. Applied*, vol. 11, no. 6, p. 064042, 2019.

[7] X. Zhang, Q. Li, F. Liu, M. Qiu, S. Sun, Q. He, and L. Zhou, "Controlling angular dispersions in optical metasurfaces," *Light Sci. Appl.*, vol. 9, no. 1, p. 76, 2020.

[8] C. L. Holloway, E. F. Kuester, J. A. Gordon, J. O'Hara, J. Booth, and D. R. Smith, "An Overview of the Theory and Applications of Metasurfaces: The Two-Dimensional Equivalents of Metamaterials," vol. 54, no. 2, pp. 10–35, 2012.

[9] C. Caloz and K. Achouri, *Electromagnetic Metasurfaces: Theory and Applications*. Hoboken, NJ: Wiley-IEEE Press, 2021.

[10] K. Achouri, V. Tiukuvaara, and O. J. F. Martin, "Multipolar modeling of spatially dispersive metasurfaces," *arXiv preprint arXiv:2103.10345*, 2021.

[11] R. E. Raab and O. L. De Lange, *Multipole Theory in Electromagnetism: Classical, Quantum, and Symmetry Aspects, with Applications*. No. 128 in Oxford Science Publications, Oxford University Press, 2005.

[12] C. Simovski, *Composite media with weak spatial dispersion*. Singapore: Pan Stanford, 2018.

[13] M. Idemen, *Discontinuities in the electromagnetic field*. Piscataway, NJ Hoboken, New Jersey: IEEE Press Wiley, 2011.

[14] K. Achouri and O. J. F. Martin, "Extension of lorentz reciprocity and poynting theorems for spatially dispersive media with quadrupolar responses," *Phys. Rev. B*, vol. 104, p. 165426, 2021.

Tunable Infrared Metasurface based on VO_2 for Anti-Counterfeiting and Adaptive Radiative Cooling

Junichi Takahara[1,2]

[1]Graduate School of Engineering, Osaka University, Suita, Osaka, Japan
[2]Photonics Center, Graduate School of Engineering Osaka University, Suita, Osaka, Japan
*corresponding author, E-mail: takahara@ap.eng.osaka-u.ac.jp

Abstract

We demonstrate tunable infrared metasurface by utilizing metal-insulator transition material of VO_2. Switching optical property between dielectric and negative dielectric opens new functionality of metasurface such as anti-counterfeiting and adaptive radiative cooling in wide range of spectra from near- to mid-IR range.

1. Introduction

Metasurface is two-dimensional ensemble of meta-atoms. The scattering and absorption of metasurface can be controlled by materials, shapes or arrangements of an individual meta-atom. Figure 1 shows schematic view of various meta-atoms showing different types of functions.

Dielectric structural colors based on an single crystal silicon (Si) Mie resonator (Fig. 1(a) and (b)) have been demonstrated with the resolution of 80,000 dots per inch (dpi) [1]. By adding a Cr cap layer to the top of Mie resonator (Fig. 1(b)), we are able to control the resonance of electric dipole, resulting in achieving the diffraction-limited resolution of 100,000 dpi. Such high resolution of structural colors is useful for applications to anti-counterfeiting color images [1]. However, the image can be easily observed by conventional optical microscope. Hence, it is natural to extend from visible image to near-infrared (IR) image in order to protect easy access by microscope.

In this paper, we report tunable IR pixels based on metal-insulator transition material of VO_2 and its application to tunable IR image and adaptive radiative cooling by changing temperature.

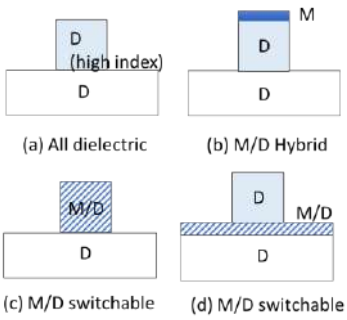

Figure 1: Cross sectional view of various meta-atoms: (a) all-dielectric, (b) M/D hybrid, and (c) and (d) M/D switchable (D: dielectric, M: metal).

2. Tunable metasurface based on VO_2

Since transition temperature of VO_2 is 340K, the permittivity of VO_2 ε can be changed from positive (ε >0) to negative (ε <0) drastically in near-IR range by temperature. Such change in ε induces great change of reflectance of the metasurface. Thus, by replacing the material of Mie resonator from Si to VO_2, we are able to realize tunable "color" pixels at near-IR [2]. Figure 1(c) and (d) show schematically tunable meta-atoms between dielectric (ε >0) and metal (ε <0).

Figure 2 shows scanning ion microscope image of cylindrical VO_2 metasurface. Here, at first 400nm-thickness VO_2 thin film was deposited by pulse laser deposition on the (0001) sapphire substrate. After that, we fabricated cylindrical array by electron beam lithography and reactive ion etching.

Figure 3 shows IR microscope image of VO_2 metasurface observed by IR objective lens through bandpass filter at 1.5μm. As seen in Fig. 3(b), hidden characters of "HOT" were clearly observed only above transition temperature of 340K. The resolution of the image exceeds 39,000 dpi at 1.5μm. We can embed hidden messages into the metasurface which can be observed only at near-IR.

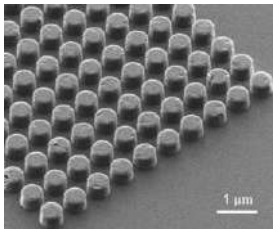

Figure 2 Scanning ion microscope image of cylindrical VO_2 metasurface formed on sapphire substrate.

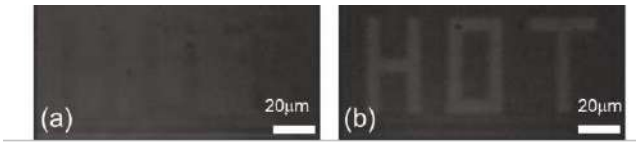

Figure 3: IR Microscope image of VO_2 metasurface at 1.5μm: (a)T=298K and (b) 348K [2].

In addition, we will propose and discuss about adaptive radiative cooling device based on Mie resonator in atmospheric window of 8-13μm utilizing VO_2 metasurface. In this device, we are able to control emissivity with depending on environmental temperature. Such devices are useful from the viewpoint of active thermal radiation control in mid-IR range [3].

Acknowledgements

This work was supported by JSPS KAKENHI Grant Number JP19H02630 and the JSPS Core-to-Core Program, A. Advanced Research Networks (Advanced Nanophotonics in the Emerging Fields of Nano-imaging, Spectroscopy, Nonlinear Optics, Plasmonics/ Metamaterials and Devices).

References

[1] Y. Nagasaki, I. Hotta, M. Suzuki, and J. Takahara, ACS Photonics 5, 3849 (2018).

[2] Y. Nagasaki, T. Kohno, K. Bando, H. Takase, K. Fujita, and J. Takahara, Appl. Phys. Lett. 115, 161105 (2019).

[3] H. Toyoda, K. Kimino, A. Kawano and J. Takahara, Photonics, 6(4), 105 (2019).

Conformable metasurface patches for mm-waves holographic application

Jianling Xiao[1], Simon Horsley[2], Robert I. Hunter[1], Sebastian A. Schulz[1], Graham Smith[1], Duncan A. Robertson[1], and Andrea Di Falco[1*]

[1]School of Physics and Astronomy, University of St Andrews, St Andrews, KY16 9SS, UK
[2]School of Physics and Astronomy, University of Exeter, Exeter, UK
*corresponding author, E-mail: adf10@st-andrews.ac.uk

Abstract

We present our work on the design, fabrication and characterisation of conformable metasurface patches in the mm-wave range for holographic applications.

1. Introduction

Metasurfaces Flexible metasurfaces merge the versatility of rigid metasurfaces with the practical advantages offered by a supple and conformable physical platform. In particular, they can be transferred onto virtually every target material or object, they can be mechanically tuned (statically or dynamically) after fabrication and they can exploit the mature manufacturing technology typical of printed electronics to scale up their area and manufacturing volume. These advantages are perhaps best exemplified by our recent demonstration that holographic metasurfaces can be placed on curved targets and, most importantly, that the designed holographic image depends on the specific shape of the target. [1, 2] Here we demonstrate that the flexible hologrphic metasurfaces (FHMS) can be scaled to the GHz range, for antennas and radar applications [3].

2. Results and Discussions

To design our metasurface we use the Gerchberg-Saxton iterative phase reconstruction algorithm (GSA). The inputs for the GSA are the required image and the source intensity. The output of the GSA, after many iterations, is a phase distribution which we encode into the metasurface. This is achieved by texturing at subwavelength scale the surface of the metasurface, defining suitably designed meta-atoms. Each meta-atom enforces a unique de-phasing to reflected radiation, between 0 and 360 degrees. In a recent paper [4] we demonstrated a modified GSA with the ability to tailor the holographic image to the shape of the FHMS, conformally coating a given target. The approach used a popular three layers geometry to create boradband and efficient reflection holograms. Here we show that the scheme can be adapted to the mm-wave range, choosing suitable substrates and c-ring meta-atoms designs. The fabrication procedure started depositing a sacrificial lift-off layer and a 5 μm thick polymeric substrate (SU8 in this case) on a rigid carrier (e.g. glass), followed by the deposition of 200 nm of gold via e-beam evaporation. The meta-atoms were then defined with an electron beam lithography step and trasnferred onto the gold layer with a dry etch process. The sacrificial lift-off layer was then dissolved to leave a free-floating membrane, which was placed on a 400 μm thick polymeric membrane, with a reflective backplane made of gold.

To characterise the FHMs we built a dedicated setup operating at 94 GHz. A mm-wave Gunn oscillator source is coupled to free space with a corrugated feedhorn and the beam is collimated with a suitable lens and directed at normal incidence towards the sample, via a polarising beam splitter (with the electric field parallel to the optical table). The FHMS is designed to create an image in reflection for the orthogonal polarisation. The reflection goes through the beam splitter, and is detected with a single mode waveguide X-Y scanning probe which is coupled to a heterodyne receiver. The intermediate frequency (IF) signal from the receiver is measured with a spectrum analyser. A laptop controls a beam scanner that records the power as a function of spatial position to map the output beam from the FHMS.

To demonstrate the successful realisation of a conformable holographic patch, we designed a FHMS for non-flat surfaces. Without loss in generality, we used on a non-flat cylindric design, using as the holographic image a focused spot displaced respect to the direction of geometric reflection. Fig. 1 shows a photograph of the FHMS patched applied to the target object and the raster scan image of the reflected beam, acquired at 10 cm distance from the metasurfaces, for the bare aluminum cylinder and for the patched case, both for the co- and cross-polarization cases.

In this communication we will discuss critically the limits and opportunities of the presented technology, placing particular emphasys on the novelty offered by an advanced design that allow to create different images for different curvatures and on the manufacturing of large scale holographic metasurfaces.

3. Conclusions

FHMS are a robust and credible platform to translate the metasurface technology out of the lab and deploy it in realistic environments. The ability to design at will the scattering of an object in the mm-wave range opens intriguing scenarios for antennas and radar applications. FHMS are conformable and tunable and can be used for novel de-

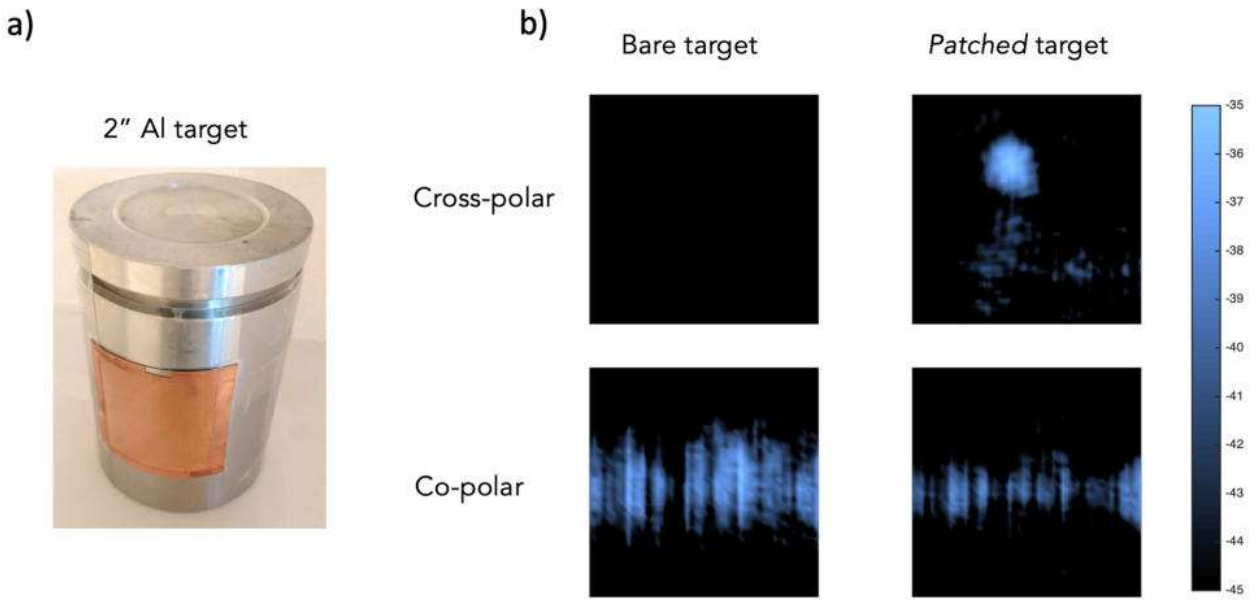

Figure 1: Figure 1. a) Photograph of a flexible holographic patch applied to an aluminum target. b) co- and cross-polar raster scan of the reflected beam for bare and patched cylinder.

signs or to retrofit existing devices with complex shapes and topologies.

Acknowledgement

We acknowledge Jing Ma's contribution for the design of the meta-atoms.

References

[1] J. Burch, D. Wen, X. Chen, and A. Di Falco, Conformable Holographic Metasurfaces, *Scientific Reports* 7, 501-7, 2017.

[2] A. M. Kamali, A. Arbabi, E. Arbabi, Y. Horie, and A. Faraon, Decoupling optical function and geometrical form using conformal flexible dielectric metasurfaces, *Nature Communications* 7, 11618, 2016.

[3] J. Burch, J. Ma, R. I. Hunter, S. A. Schulz, D. A. Robertson, G. M. Smith, J. Wang, and A. Di Falco, Flexible patches for mm-wave holography *Appl Phys Lett* 115, 021104, 2019.

[4] J. Burch, A. Di Falco, Surface Topology Specific Metasurface Holograms, *ACS Photonics* 5, 1762-1766, 2018.

Development of Three-Dimensional Fabrication Technologies Using Laser Processing and 3D Printing for Terahertz Optics Production

Kuniaki Konishi

Institute for Photon science and Technology, The University of Tokyo, Tokyo, Japan
E-mail: kkonishi@ipst.s.u-tokyo.ac.jp

Abstract

Lithography techniques conventionally used to make artifical strucutres can only make quasi-two-dimensional structures. We are developing new technologies which makes it possible to produce a three-dimensional artificial structure with a resolution of several tens of micrometers smaller than the wavelength of the THz wave. In this talk, I introduce the development of three-dimensional artificial structures for THz wave control fabricated by using laser processing and 3D printing technologies.

1. Introduction

Terahertz (THz) technologies have been gaining a great deal of interests, but current THz optics is still facing various challenges in their functionality and performance. Artificial structures consisting of many periodical units smaller than the wavelength of electromagnetic waves, such as metamaterials, are attracting attention as a tool for the development of THz optics because the optical properties of them can be controlled by appropriate designing of the structures. However, lithography techniques conventionally used to make such artifical strucutres can only make quasi-two-dimensional structures with thicknesses much smaller than the wavelength of THz waves (typically several hundred micrometer). This is a serious limiting factor, as the three dimensionality of the structure is important to extend the functionality as THz optical components.

In recent years, laser processing and 3D printeing have attracted attention as new techniques for producing three-dimensional structures. Laser processing is a top-down fabrication method that creates a three-dimensional structure by irradiating a bulk material with laser light to remove specific parts. Particularly, the use of an ultrashort pulse laser enables extremely high-precision processing. On the other hand, a 3D printer is a bottom-up modeling method that forms a three-dimensional structure by accumulating materials. Here, the use of laser light is also important for producing fine structures.

We are developing these technologies and it has become possible to produce a three-dimensional artificial structure with a resolution of several tens of micrometers smaller than the wavelength of the THz wave. In this talk, I introduce the development of three-dimensional artificial structures for THz wave control by using laser processing and 3D printing technologies.

2. THz moth-eye structure fabricated by femtosecond laser processing

A structure in which fine protrusion structures smaller than the wavelength are periodically arranged is called “moth-eye”, which eliminates the discontinuous change in the refractive index of the material interface that causes Fresnel reflection and functions as a broadband antireflection film [1]. For many THz applications, it should be important to use a moth-eye structure to suppress the Fresnel reflection loss. However, in the THz region where the characteristic size is on the order of several tens to several hundreds of micrometers, it has been difficult to fabricate using conventional processing methods. We have succeeded to fabricate a moth-eye structure of about 30 μm and a height of about 100 μm was formed in a 6 mm square area by scanning the focal point of the ultrashort pulse laser on the surface of a high-resistance silicon substrate, (Fig. 1). The transmission spectrum of the moth-eye structured subtracted on the both sides was evaluated by THz time-domain spectroscopy, and it was observed that the transmittance increased over a wide range from 0.5 to 2.5 THz, showing good agreement with the simulation results [2]. This revealed that the three-dimensional structure fabricated by this method functions as a broadband antireflection film in the THz region.

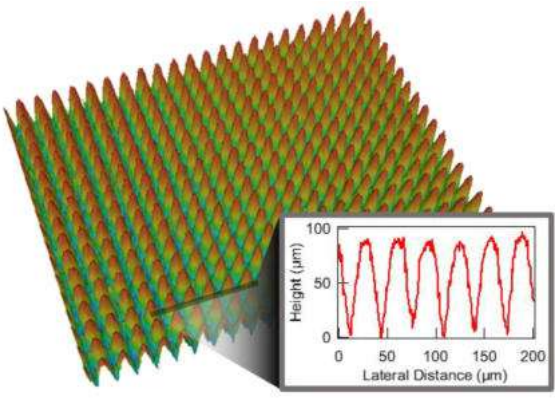

Figure 1: Microscopic image and cross-sectional profile of silicon moth-eye structure fabricated by femtosecond laser processing.

3. Fabrication of THz high-pass filter using 3D printing

Recently, the 3D printer has gained attention as a means to fabricate 3D structures. However, the typical resolution necessary to make THz metamaterial is smaller than several hundred micrometers, and this is still challenging for conventional metal 3D printers. In order to overcome this difficulty, we have developed a new 3D printing technology which can make metallic structures with sufficient resolution for making THz optics.

We have developed an ultra-high-definition 3D printer (RECILS) using a photocurable resin with a resolution of several tens of micrometers [3]. The material of the fine three-dimensional structure made with this printer is a polymer, but by coating the surface with a metal by using plating, a three-dimensional artificial structure that shows a metallic response to THz electromagnetic waves can be made [4]. It is known that by periodically arranging such a waveguide structure, it operates as a high-pass filter due to the cut-off characteristics of the waveguide [5]. In this study, as shown in Fig. 2 (a), we fabricated such a waveguide array structure in which rectangular waveguides with a side of 300 μm were arranged at a period of 400 μm by using the 3D printing technique. From the transmission spectrum measured by THz time-domain spectroscopy (Fig. 2 (b)), it was found that a clear cutoff characteristic was observed at 0.5THz as designed, which agreed well with the numerical simulation [6].

In order to induce such a THz waveguide effect, it is necessary that the artificial structure has a thickness greater than the THz, wavelength. For this purpose, our ultra-high-definition 3D printer becomes a very powerful tool.

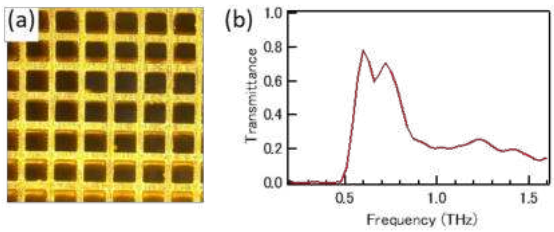

Figure 2: (a) Optical microscope image and (b) THz transmission spectrum of the THz high-pass filter fabricated by the 3D printer and gold plating.

4. Conclusions

As introduced in this talk, new fabrication technologies such as laser processing and 3D printing have sufficient performance for fabricating artificial structures for controlling THz waves. In the future, it may be a powerful new method for developing THz optical elements.

Acknowledgements

This research was supported by MEXT Photon Frontier Network Program, the Center of Innovation Program funded by the Japan Science and Technology Agency and New Energy and Industrial Technology Development Organization (NEDO).

References

[1] S. J. Wilson, M. C. Hutley, The Optical Properties of 'Moth Eye' Antireflection Surfaces, *Optica Acta* 29: 993-1009, 1982.

[2] H. Sakurai, N. Nemoto, K. Konishi, R. Takaku, Y. Sakurai, N. Katayama, T. Matsumura, J. Yumoto, M. Kuwata-Gonokami, Terahertz broadband anti-reflection moth-eye structures fabricated by femtosecond laser processing, *OSA Continuum* 2: 2764 – 2772, 2019.

[3] H. Yasukochi, US patent application: US2012045617 A1

[4] W. J. Otter, N. M. Ridler, H. Yasukochi, K. Soeda, K. Konishi, J. Yumoto, M. Kuwata-Gonokami, S. Lucyszyn, 3D printed 1.1 THz waveguides, *Electronics Letters* 53: 471-473, 2017.

[5] K. Sakai, T. Yoshida, Single mesh narrow bandpass filters from the infrared to the submillimeter region, *Infrared Physics* 18: 137-140, 1978.

[6] K. Konishi, H. Yasukochi, K. Soeda, Y. Takano, H. Niwa, J. Yumoto, M. Kuwata-Gonokami, “Thick THz Metamaterials fabricated by 3D printer for THz High-Pass Filter Application” CLEO®/Europe-EQEC 2017, CC-5.4 (June, 2017)

Bismuth-based Metamaterials: Fundamentals and Applications

Johann Toudert[1], and Rosalía Serna[1]

[1]Laser Processing Group, Instituto de Óptica, IO, CSIC, Madrid, Spain
*corresponding author, E-mail: johann.toudert@gmail.com

Abstract

Bismuth shows outstanding optical properties, including a metal-like response in the ultraviolet-visible and a dielectric character with a giant refractive index in the infrared. Herein, we explain how this enables bismuth-based metamaterials to show a remarkable optical response over these spectral regions. Such response can be tuned in a static way by suitable metamaterial design and in a dynamic way by harnessing the solid-liquid transition of bismuth. We discuss the applications of such metamaterials to information technology, energy harvesting and sensing.

1. Introduction

The semi-metal bismuth (Bi) is a non-conventional material platform for applications in photonics, because its optical properties strongly contrast with those of usual metals and semiconductors. These optical properties are driven by giant interband electronic transitions, which endow Bi with a metal-like response in the ultraviolet-visible and a dielectric character with a giant refractive index (n~10) in the infrared [1,2]. Thanks to that, Bi nanostructures can be used both as plasmonic and high index building blocks of metamaterials in the corresponding spectral regions [3,4]. Herein, we show how to tailor and assemble such building blocks to achieve Bi-based metamaterials showing an optical response tuned by design in a selected spectral range from the ultraviolet to the infrared. Besides such static tuning, we show how to harness the solid-liquid transition of the Bi nanostructures for an active tuning of the metamaterials' optical response. Finally, we discuss the applications of such metamaterials to information technology, energy and sensing.

2. Results

The considered metamaterials are built from Bi nanostructures: nanoparticles, nanorods, nanofilms with a three-dimensional distribution within a transparent matrix. By suitably selecting the nanostructure morphology and organization, their plasmonic and high-index response can be tailored and hybridized with cavity modes to tune the spectral response of the metamaterial. Such tuning can be achieved both in the ultraviolet-visible and infrared, to achieve ultranarrow resonances or a broadband perfect absorption of light.

These spectral features can also be tuned dynamically by harnessing the solid-liquid transition of the Bi nanostructures. In particular, upon controlled heating, a fraction of the nanostructures within the metamaterial can be melted to tune its optical response in an analog manner [4].

These properties make suitably designed Bi-based metamaterials appealing for several photonic applications: (i) they enable the analog tuning of the amplitude and phase of light in the visible regime, as needed for high density information processing [4]; (ii) they enable an efficient trapping of ultraviolet-visible and/or infrared light in subwavelength dimensions, as needed for photodetection or solar energy harvesting [3,5]; (iii) they enable optically-monitored sensing with a high figure of merit as needed for ultrasensitive non-invasive sensing applications.

References

[1] J. Toudert, R. Serna, I. Camps, J. Wojcik, P. Mascher, E. Rebollar, T.A. Ezquerra, Unveiling the far-infrared-to-ultraviolet optical properties of bismuth for applications in plasmonics and nanophotonics, *Journal of Physical Chemistry C* 121, 3511-3521, 2017.

[2] J. Toudert, R. Serna, C. Deeb, E. Rebollar, Optical properties of bismuth nanostructures towards the ultrathin film regime, *Optical Materials Express* 9, 2924-2936, 2019.

[3] J. Toudert, R. Serna, M. García Pardo, N. Ramos, R.J. Peláez, B. Maté, Mid-to-far infrared tunable perfect absorption by a sub-λ/100 nanofilm in a fractal phasor resonant cavity, *Optics Express* 16, 34043-34059, 2018.

[4] M. Garcia-Pardo, E.N. Pinero, A.K. Petford-Long, R. Serna, J. Toudert, Active analog tuning of the phase of light in the visible regime by bismuth-based metamaterials, *Nanophotonics, 2020 https://doi.org/10.1515/nanoph-2019-0502*.

[5] A. Ghobadi, H. Hajian, M. Gokbayrak, B. Butun, E. Ozbay, Bismuth-based metamaterials: from narrowband reflective color filters to extremely broadband near perfect absorber, *Nanophotonics* 8, 823-828, 2019.

Manipulating the Polarization of Electromagnetic Waves via Metastructures

Ruwen Peng*, and Mu Wang

National Laboratory of Solid State Microstructures, School of Physics, and Collaborative Innovation Center of Advanced Microstructures, Nanjing University, Nanjing 210093, China
*corresponding author, E-mail: rwpeng@nju.edu.cn

Abstract

In this work, we present our recent work on manipulating the polarization of electromagnetic waves with metastructures. We start from how to tune the polarization of electromagnetic waves via time retardation with a microstructured surface, and then to control them based on a dispersion-free metastructure. Further, we show a freely tunable polarization rotator for broadband terahertz waves by using a metastructure, and also an example on dynamically switching the polarization of the infrared light based on the phase transition of vanadium dioxide. The investigations provide some guidelines to control the polarization of electromagnetic waves at subwavelength scale.

References

[1] J. B. Pendry, A. J. Holden, D. J. Robbins, W. J. Stewart, *IEEE Trans. Microwave Theory Tech.* 1999, 47, 2075.
[2] Y. Liu, X. Zhang, *Chem. Soc. Rev.* 2011, 40, 2494.
[3] N. Yu, P. Genevet, M. A. Kats, F. Aieta, J.-P. Tetienne, F. Capasso, Z. Gaburro, *Science* 2011, 334, 333.
[4] S. C. Jiang, X. Xiong, P. Sarriugarte, S. W. Jiang, X. B. Yin, Y. Wang, R. W. Peng, D. Wu, R. Hillenbrand, X. Zhang, and Mu Wang, *Phys. Rev. B* 2013, 88, 161104(R).
[5] S. C. Jiang, X. Xiong, Y. S. Hu, Y. H. Hu, G. B. Ma, R. W. Peng, C. Sun, and Mu Wang, *Phys. Rev. X* 2014, 4, 021026.
[6] R. H. Fan, Y. Zhou, X. P. Ren, R. W. Peng, S. C. Jiang, D. H. Xu, X. Xiong, X. R. Huang, and Mu Wang, *Advanced Materials* 2015, 27, 1201.
[7] Zhi-Yong Jia, Fang-Zhou Shu, Ya-Jun Gao, Feng Cheng, Ru-Wen Peng, Ren-Hao Fan, Yongmin Liu, and Mu Wang, *Phys. Rev. Applied* 2018, 9, 034009.
[8] R. Fan, B. Xiong, Ru-Wen Peng, and Mu Wang, *Advanced Materials* 2019, 201904646, DOI: 10.1002/adma.201904646.

Tunable Carbon-Based Nanomaterials for THz Applications

Aleksandra Przewłoka[1,2], Nikolaos Xenidis[3], Serguei Smirnov[3], Aleksandra Krajewska[1], Piotr Drozdz[1], and Dmitri Lioubtchenko[1,3]

[1]CENTERA Laboratories, Institute of High-Pressure Physics PAS, Warsaw, Poland
[2]Institute of Optoelectronics, Military University of Technology, Warsaw, Poland
[3]Division of Micro and Nanosystems, KTH Royal Institute of Technology, Stockholm, Sweden
*corresponding author, E-mail: dml@kth.se

Abstract

In this work single-walled carbon nanotube tuning properties are studied for phase shifting applications. The dielectric rod waveguide with loaded carbon nanomaterials was experimentally studied in ultra-wide frequency band of 0.1-0.5 THz.

1. Introduction

The research and development in the frequency region of 0.1-1.0 THz is extremely significant for the wide range of applications, such as telecommunication and imaging systems, material spectroscopy, medical imaging and treatments, etc. Despite the problems in technology and high prices for basic components (phase shifters, directional couplers, etc.), the THz systems offer higher date rates for telecommunication, high spatial resolution in the visualization of objects, small size of antennas and other elements. The state-of-the-art of the THz devices reveals serious problems with radiation sources with continuous wave semiconductor-based source, electronically tunable phase shifters, amplifiers, etc.

Carbon nanotubes (CNT) offer unique properties due to their natural small dimensions and outstanding electrical properties. Their tunability properties makes them very attractive in application to the THz system [1-3]. Integration of CNTs with the dielectric rod waveguide (DRW) technology enables novel technology platform for tunable THz systems.

2. Results and Discussions

Phase shifter can be developed by introducing the optically controlled varactor to the DRW [4]. The phase change of 10-20 deg with almost negligible change in attenuation less than 0.1 dB can be achieved (Fig.1) in the frequency range of 75-500 GHz. Besides, DRWs have no cut-off frequency enabling broad band operation. In [5-6], the DRW antenna was proved to operate in the frequency band of 0.1-1.1 THz. The effect of the dielectric constant tuning of single-walled carbon nanotubes under light illumination is observed in the very wide frequency range of 0.1–1 THz. The optical absorption spectrum is not uniform and it consists of several absorption peaks related to electron transitions. Therefore, the change of capacity and resistance under different light wavelength illumination is different at different wavelengths (Fig. 3-4)

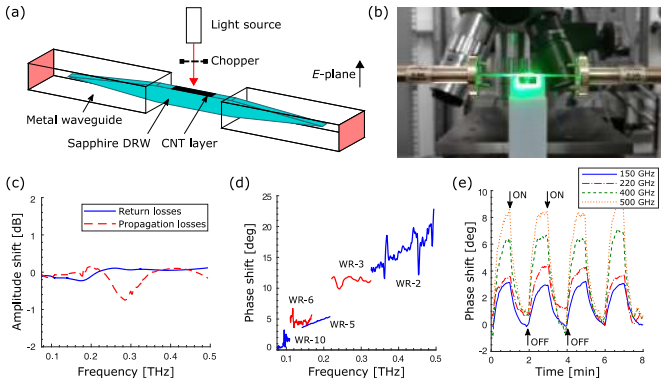

Figure 1: a) Schematic drawing of the two-port S-parameter measurement setup. DRW is loaded with a CNT layer and exposed to varying illumination conditions. b) Image of the measurement setup. c) Measured amplitude shifts due to the illumination of the CNT layer. d) Measured phase shift. e) Time dependence of the phase shift in the CNT-loaded DRW at 150, 220, 400 and 500 GHz.

3. Conclusions

CNTs are perspective materials for very wide applications in millimeter wave and THz frequency range. Phase shifter based on DRW loaded with CNT layer is a perspective candidate for ultra-wide band device application. The ultra-wide band optically controlled CNT-based phase shifter can enable THz beam steering.

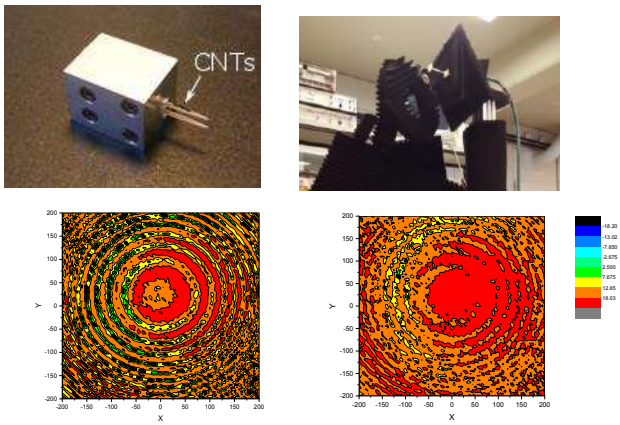

Figure 2: Radiation pattern measurements of DRW antenna array at 90 GHz without and with illumination of the CNT-loaded DRW.

Acknowledgements

The work was supported by Horizon 2020 Grant Agreement no: 862788, by the "International Research Agendas" program of the Foundation for Polish Science co-financed by the European Union under the European Regional Development Fund (No. MAB/2018/9).

References

[1] S. Smirnov, I.V. Anoshkin, P. Demchenko, D. Gomon, D.V. Lioubtchenko, M. Khodzitsky, J. Oberhammer, "Optically controlled dielectric properties of single-walled carbon nanotubes for terahertz wave applications" *Nanoscale*, vol. 10, pp. 12291 – 12296, 2018

[2] S. Smirnov, I.V. Anoshkin, A. Generalov, D.V. Lioubtchenko, J. Oberhammer, "Wavelength-dependent photoconductivity of single-walled carbon nanotube layers" *RSC Advances*, vol 9, pp. 14677-14682, 2019

[3] S. Smirnov, D.V. Lioubtchenko, J. Oberhammer, "Single-walled carbon nanotube layers for millimeter-wave beam steering", *Nanoscale* 11, pp. 14691-14697, 2019.

[4] D.V. Lioubtchenko, I. Anoshkin, I.I. Nefedova, J. Oberhammer, and A. V. Räisänen, "W-band Phase Shifter Based on the Optimized Optically Controlled Carbon Nanotube Layer", *2017 IEEE MTT-S International Microwave Symposium (IMS)*, Honololu, HI, pp. 1188-1191, 2017

[5] A.A. Generalov, D.V. Lioubtchenko, and A.V. Räisänen, "Dielectric rod waveguide antenna at 75-1100 GHz," in *Proc. 7th European Conference of Antennas and Propagation*, Gothenburg, Sweden, 8-11 April, 2013.

[6] A.A. Generalov, J.A. Haimakainen, D.V. Lioubtchenko, and A.V. Räisänen, "Wide Band mm- and Submm-Wave Dielectric Rod Waveguide Antenna", *IEEE Transactions on Terahertz Science and Technology*, vol. 4, no 5, pp.568-574, 2014.

Plasmonic and metamaterial devices based on highly doped semiconductors for infrared applications.

E. Centeno[1*], R. Smaali[1], F. Gonzalez-Posada[2], L. Cerutti[2], A. Moreau[1], F. Omeis[1], T. Taliercio[2]

[1]Universite Clermont Auvergne, CNRS, SIGMA Clermont, Institut Pascal, F-63000 Clermont-Ferrand, France
[2]IES, Univ Montpellier, UMR CNRS 5214, Montpellier, France

*corresponding author, E-mail: emmanuel.centeno@uca.fr

Abstract

Highly doped semiconductors are ideal materials to realize plasmonic and metamaterial based systems operating from the infrared to the THz frequencies. In this work, we show that nano-antennas, hyperbolic metamaterials and epsilon-near-zero metasurfaces can be designed with such materials. These systems are demonstrated to enhance light matter interactions and can be applied for infrared spectroscopy.

1. Introduction and Results

Owing to their control over the electromagnetic waves (EW), plasmonic and metamaterial devices are pivotal in a lot of applications such as for communication, security, and biomedical domains. There is an increasing demand for such photonics systems operating from the infrared to the THz range. The use of doped semiconductors is an interesting approach to couple infrared radiation with collective oscillations of electrons leading to the desired plasmonic resonances.

We theoretically and experimentally demonstrate that InAsSb is a suitable highly Si-doped semiconductor to realize: (i) ideal metal-insulator-metal antennas performing the strong coupling between gap-plasmon and phonon modes, Fig. 1 [1-2], (ii) miniaturized antennas based on hyperbolic metamaterials [3], and (iii) epsilon-near-zero metasurfaces for surface-enhanced infrared spectroscopy [4].

Acknowledgements

This work was partially funded by the French Investment for the Future program (EquipEx EXTRA, No. ANR 11-EQPX-0016). This work was funded by the French Labex IMOBS3.

References

[1] F. Omeis, R. Smaali, F. González-Posada, L. Cerutti, T. Taliercio, and E. Centeno, Metal-insulator-metal antennas in the far-infrared range based on highly doped InAsSb, Appl. Phys. Lett. 111: 121108, 2017.

[2] R. Smaali, F. Omeis, E. Centeno, T. Taliercio, F. González-Posada, L. Cerutti, Giant Rabi splitting at the phonon line within all-semiconductor metallic-insulator-metallic antenna, Phys. Rev. B Rapid Com. 100: 041302, 2019.

[3] R. Smaali, F. Omeis, A. Moreau, E. Centeno, and T. Taliercio, Miniaturizing optical antennas using hyperbolic metamaterial wires, Phys. Rev. B 95: 155306, 2017.

[4] R. Smaali, T. Taliercio, A. Moreau, E. Epsilon-near-zero enhancement of vibrationalsignals for infrared spectroscopy, submitted

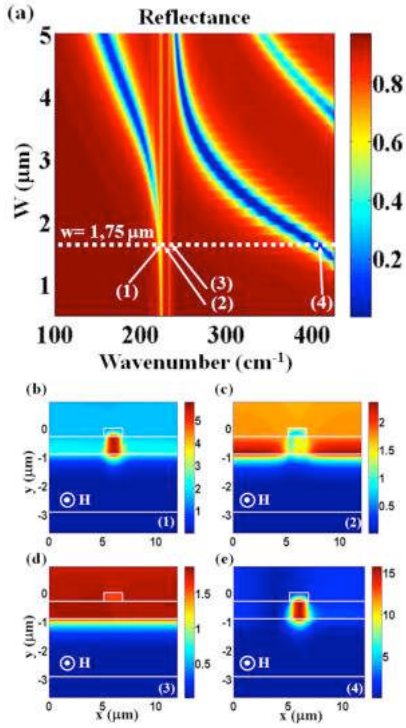

Figure 1: (a) Reflectance spectra as a function of the wavenum- ber and the antenna's width. (b-e) Maps of the magnetic field modulus calculated for each absorption lines labelled in the panel (a). Note that magnetic modulus scales are different.

Breaking the limit of emission suppression in low contrast 3D media

Meraj E. Mustafa[1], Lukas Maiwald,[1] Soumyadeep Saha[1,2], Mikhail S. Sidorenko[3,4], Ruslan R. Yafyasov[3,4], Mikhail V. Rybin[3,4], Manfred Eich[3,5] and Alexander Yu. Petrov[1,3,5] *

[1]Institute of Optical and Electronic Materials, Hamburg University of Technology, Germany
[2]Department of Electronics and Telecommunication Engineering, Jadavpur University, Kolkata
[3]Department of Physics and Engineering, ITMO University, Saint Petersburg, Russia
[4]Ioffe Institute, Saint Petersburg, Russia
[5]Institute of Material Research, Helmholtz-Zentrum Hereon, Germany

*corresponding author, E-mail: a.petrov@tuhh.de

Abstract

Light emission can be significantly suppressed in 3D photonic crystals at the frequency of a photonic band gap but a refractive index contrast above 1.8 is needed. We present 3D quasiperiodic structures that can significantly reduce the density of states even at lower index contrasts. The suppression of 10 dB is demonstrated in simulations with refractive index contrast of 1.4. A refractive index contrast of 1.6 is investigated experimentally in microwave regime.

1. Introduction

Complete suppression of light emission can be obtained in 3D photonic crystals at the frequencies of a photonic band gap. For that to occur the band gaps for light propagation in different directions should overlap in a certain frequency range. Structures that were proposed so far require a refractive index contrast of at least 1.8 to open a complete photonic band gap [1]. This excludes the application of glasses and polymers. For these materials directional band gaps have a smaller frequency range. Also the central frequencies of directional band gaps differ for different directions in photonic crystals and thus an overlap cannot be obtained.

This problem was successfully resolved in 2D photonic crystals using quasicrystal structures with higher than 6-fold symmetry [2]. Though the possibility to suppress emission in structures with an arbitrarily small refractive index was not investigated, the required contrast was significantly reduced in comparison with periodic structures. At the same time the progress with 3D quasicrystals was limited up to now and complete emission suppression was not demonstrated so far in low refractive index media [3].

Here we present quasiperiodic structures that allow an exact positioning of the Bragg peaks in reciprocal space [4]. Using this approach we demonstrate complete photonic band gaps with very small refractive index contrast in 2D and strong emission suppression in 3D structures [5]. Additionally, we present experimental characterization of the proposed structure produced by additive manufacturing for the microwave regime.

2. Results

The quasiperiodic structures were generated using the levelling of a random wave function. The random wave function is a sum of N sinusoidal gratings with constant wave number $|\vec{g}_i| = g$, optimized orientation and random phase ϕ_i. The refractive index perturbation is then obtained by levelling with a sign function:

$$\Delta n(\vec{r}) = \Delta n \cdot \mathrm{sgn}\{\textstyle\sum_{i=1}^{N} \sin(g_i \cdot \vec{r} + \phi_i)\} \quad (1)$$

The $\Delta n(\vec{r})$ represents the refractive index variation around the average index $\bar{n}$. The structure for 46 gratings is presented in Fig. 1, where 92 Bragg peaks are homogeneously distributed on the sphere keeping an icosahedral symmetry.

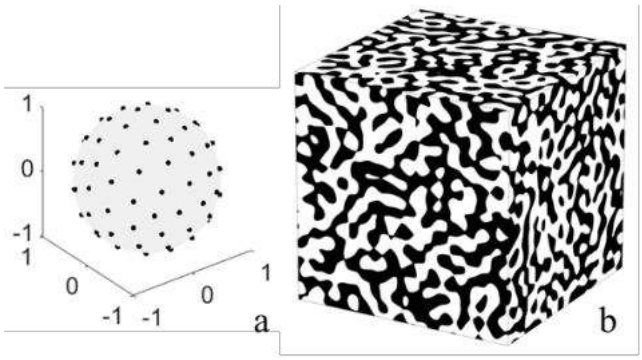

Figure 1: a) The distribution of the 92 Bragg peaks (46 gratings) on the sphere of radius 1. b) A small volume of the structure obtained by the overlap of the gratings from a).

The emission in the quasiperiodic structure is studied numerically by introducing a small dipole in the center of

the simulation volume. The emission is compared to the emission in a homogenous structure with the mean refractive index $\bar{n}$. The structure size is increased to evaluate the maximal emission suppression. In the case of a complete photonic band gap, the suppression should increase exponentially with the structure size. In our structures we observe a saturation of suppression at large volume sizes, approaching 10 dB maximal suppression (see Fig. 2). A similar behaviour is observed for a larger number of gratings and a smaller refractive index contrast of 1.38.

The proposed structures were also manufactured using a 3D printer for the 40 GHz microwave range. For that polylactide (PLA) plastic was used which has a refractive index of approximately 1.59 at this frequency. The transmission through the slab of structured material was measured at different angles indicating the original distribution of Bragg peaks in reciprocal space.

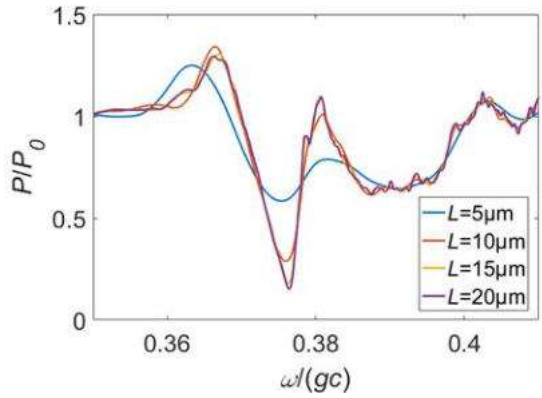

Figure 2: Normalized power emitted by a dipole antenna in the quasiperiodic structure with 46 gratings and a refractive index contrast of 1.6. The power is normalized to emission in the homogeneous medium with refractive index 1.3. The frequency is normalized by the wave number of the gratings and the speed of light. Different structure sizes *L* are shown, the lattice constant of the gratings was 220 nm.

3. Discussion and conclusion

The obtained results show that 10 dB suppression can be obtained in low refractive index media by careful reciprocal space design. Quasiperiodic structures allow an optimized distribution of Bragg peaks in reciprocal space which are not bound to periodic boundary conditions. The application of levelling and random phase distribution leads to homogenous structures out of two materials, where one material can be air.

The suppression of 10 dB in glasses and polymers opens the way for strong light manipulation with low refractive index media. Further investigations are required to improve the suppression beyond 10 dB.

Acknowledgements

We acknowledge the support from Dassault Systemes with their CST Studio Suite software. Funding: Deutsche Forschungsgemeinschaft (DFG) - Project number 278744289. The experimental studies have been supported by the grant of Russian Science Foundation (Grant No. 20-79-10316).

References

[1] H. Men, K. Y. K. Lee, R. M. Freund, J. Peraire, S. G. Johnson, Robust topology optimization of three-dimensional photonic-crystal band-gap structures. *Opt. Express* 22: 22632–22648, 2014.

[2] M. C. Rechtsman, H.-C. Jeong, P. M. Chaikin, S. Torquato, P. J. Steinhardt, Optimized structures for photonic quasicrystals. *Phys. Rev. Lett.* 101: 73902, 2008.

[3] W. Man, M. Megens, P. J. Steinhardt, P. M. Chaikin, Experimental measurement of the photonic properties of icosahedral quasicrystals. *Nature* 436: 993–996, 2005.

[4] L. Maiwald, S. Lang, D. Jalas, H. Renner, A. Yu. Petrov, M. Eich, Ewald sphere construction for structural colors. *Opt. Express* 26: 11352–11365, 2018

[5] L. Maiwald, T. Sommer, M. Schulz, M. Eich, A. Yu Petrov, The limits for complete photonic bandgaps in low-contrast media, *arXiv*:1909.09521, 2019

Fast Scattering Matrix Computation for Complex Media and Metasurfaces

Ho-Chun Lin, Zeyu Wang, and Chia Wei Hsu*

Ming Hsieh Department of Electrical and Computer Engineering, University of Southern California, Los Angeles, USA
*corresponding author, E-mail: cwhsu@usc.edu

Abstract

We use the Schur complement and partial factorization to compute the scattering matrices of large-scale complex optical systems and large-area metasurfaces, achieving orders-of-magnitude speed-up and reduced memory usage over existing methods.

1. Introduction and Background

The linear transport of any static optical system is fully characterized by its scattering matrix $\mathbf{S}$, which maps any incident wavefront β (expressed as a vector) to the corresponding outgoing wavefront α through $\alpha_n = \sum_m S_{nm}\beta_m$. Scattering matrices are used extensively in wavefront shaping and imaging in scattering media [1], and they also fully describe the incident-angle-dependent transmission and reflection from metasurfaces [2] and the input-output relations in photonic circuits [3], with no approximation. However, numerical computation of the S-matrix requires significant computing time and memory, so existing methods can only compute the S-matrix for small systems.

Electromagnetic scattering problems in frequency domain can be written as a system of linear equations $\mathbf{A}x = b$ where matrix $\mathbf{A} = -(\omega/c)^2\varepsilon_\mathrm{r}(\omega,\mathbf{r}) + \nabla\times\mu_\mathrm{r}^{-1}(\omega,\mathbf{r})\nabla\times$ is the electric-field Maxwell operator, and x and b are the electric field profile $\mathbf{E}(\mathbf{r})$ and the equivalent source profile respectively written as column vectors. Given one input b_m, solving the scattering problem reduces to the standard problem of solving for $x_m = \mathbf{A}^{-1}b_m$. However, this only yields the m-th column of the S-matrix. To characterize the system's response to $M \gg 1$ distinct input states, such computation needs to be repeated M times.

Iterative methods for solving $x_m = \mathbf{A}^{-1}b_m$ can minimize memory usage but do not scale well with M. Direct methods can reuse the LU factorization of matrix $\mathbf{A}$ but take more memory. Also, both methods involve repetition over the M input states so they are slow when M is large, and they both compute unnecessary information such as field profiles in the interior of the system. The recursive Green's function method (RGF) and rigorous coupled-wave analysis (RCWA) can compute the full S-matrix without looping over inputs but scale poorly with the system size as they do not make use of the sparsity of matrix $\mathbf{A}$ in the transverse directions.

Here, we propose and implement a new frequency-domain method that can compute the entire S-matrix in one shot with no repetition while making full use of the sparsity of all matrices involved. Our method is applicable to complex systems with arbitrary $\varepsilon_\mathrm{r}(\omega,\mathbf{r})$ and $\mu_\mathrm{r}(\omega,\mathbf{r})$ tensors, and for large systems it is orders of magnitude faster than all of the above-mentioned methods while using less memory.

2. Methods

We start by recognizing that the scattering matrix $\mathbf{S}$ can be concisely written as

$$\mathbf{S} = \mathbf{C}\mathbf{A}^{-1}\mathbf{B} - \mathbf{D}, \tag{1}$$

where the m-th column of matrix $\mathbf{B} = [b_1, \ldots, b_M]$ is the equivalent source profile that generates the m-th input state, the n-th row of matrix $\mathbf{C}$ is the conjugated profile of the n-th output state on the surface or a near-to-far-field transformation, and matrix $\mathbf{D}$ optionally subtracts incident fields from the input/output configuration. Under spatial discretization, matrices $\mathbf{A}$, $\mathbf{B}$, $\mathbf{C}$, $\mathbf{D}$ are all sparse.

Traditional iterative and direct methods compute $\mathbf{X} = \mathbf{A}^{-1}\mathbf{B}$, which contains much more information than is needed. To compute only what is needed, we directly evaluate the much smaller matrix $\mathbf{C}\mathbf{A}^{-1}\mathbf{B}$ by constructing a new sparse matrix $\mathbf{K}$ and performing a *partial* LU factorization on it,

$$\mathbf{K} \equiv \begin{bmatrix} \mathbf{A} & \mathbf{B} \\ \mathbf{C} & \mathbf{D} \end{bmatrix} = \begin{bmatrix} \mathbf{L} & \mathbf{0} \\ \mathbf{E} & \mathbf{I} \end{bmatrix} \begin{bmatrix} \mathbf{U} & \mathbf{F} \\ \mathbf{0} & \mathbf{H} \end{bmatrix}. \tag{2}$$

Here, $\mathbf{L}$ and $\mathbf{U}$ are lower-triangular and upper-triangular matrices, and $\mathbf{I}$ is the identity matrix. The factorization is partial as it stops after factorizing the upper-left block of $\mathbf{K}$ into $\mathbf{A} = \mathbf{L}\mathbf{U}$. Importantly, such $\mathbf{L}$ and $\mathbf{U}$ factors are *not* what we are interested in. By equating the middle and the right-hand sides of Eq. (2) for each of the four blocks, we can see that matrix $\mathbf{H}$, called the Schur complement, satisfies $\mathbf{H} = \mathbf{D} - \mathbf{C}\mathbf{A}^{-1}\mathbf{B}$ and gives the scattering matrix in Eq. (1). The Schur complement is often used in domain decomposition methods [4], but here we use it in an unconventional way to compute the scattering matrix $\mathbf{S}$ in a single step with no repetition and without evaluating $\mathbf{X} = \mathbf{A}^{-1}\mathbf{B}$.

The computing time of the proposed method only depends weakly on the number M of input states because the partial factorization time is dominated by the large matrix $\mathbf{A}$ instead of the smaller matrices $\mathbf{B}$ and $\mathbf{C}$; the number of non-zero elements in $\mathbf{B}$ and $\mathbf{C}$ can be further reduced through a change of basis. The sparsity patterns of all matrices are maintained and can be fully utilized in the partial factorization process. Furthermore, storing matrices $\mathbf{L}$

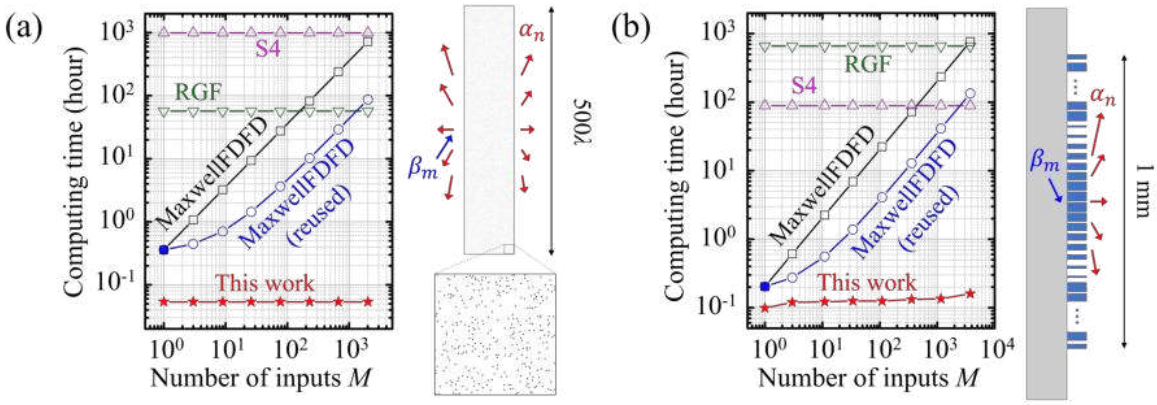

Figure 1: Computation time of the proposed method and other methods when solving for M columns of the scattering matrix, for (a) a $500\lambda \times 100\lambda$ disordered medium and (b) a 1 mm $\times$ 600 nm metalens. Solid symbols are raw data, and open symbols are data extrapolated from smaller M or smaller systems.

	This work	MaxwellFDFD	RGF	S4
Disordered medium	11.0	173.6	7.0	∼1200
Metalens	33.3	118.8	∼700	∼600

Table 1: Memory usage, in GB. The RGF and S4 values are extrapolated from smaller systems.

and **U** is typically the memory bottleneck for direct methods, but our method does not use **L** and **U** so we can drop them during the factorization process to significantly reduce memory usage.

3. Results

We implement this S-matrix solver for the transverse-magnetic waves in 2D under finite-difference discretization, with perfectly matched layer (PML) boundaries. We use the MUMPS package [5] with AMD ordering [6] to compute the partial factorization, with benchmarks done on an Intel Xeon Gold 6130 Processor with 184 GB memory, for two large-scale systems (Fig. 1). For the first system, we compute the full scattering matrix of a disordered medium with width $W = 500\lambda$ and thickness $L = 100\lambda$ using a coarse discretization ($\Delta x = \lambda_0/15$). For the second system, we compute the transmission matrix of a titanium dioxide metalens with parabolic phase profile [7, 8], with diameter $W = 1$ mm, thickness $L = 600$ nm, NA = 0.8, at wavelength $\lambda_0 = 532$ nm, using a finer discretization with $\Delta x = \lambda_0/40$.

Fig. 1 and Table 1 show the computation time and memory usage of the proposed method in comparison to (1) a conventional direct method implemented in MaxwellFDFD [9] where the full computation is repeated M times, (2) MaxwellFDFD modified to have the LU factors stored and reused for the M inputs, (3) RGF implemented in [10], and (4) RCWA implemented in S4 [11]. The proposed method achieves an almost M-independent computation time and is orders of magnitudes faster than the fastest alternative method, while also using much less memory.

The proposed method can readily apply to 3D vectorial simulations, with arbitrary discretization schemes, and can be generalized to compute other quantities such as force, torque, and differential scattering cross sections.

References

[1] S. Rotter and S. Gigan. *Rev. Mod. Phys.* **89**, 015005 (2017).

[2] Z. Lin *et. al. Appl. Phys. Lett.* **118**, 041104 (2021)

[3] W. Bogaerts *et. al. Nature* **586**, 207–216 (2020).

[4] F. Zhang. *The Schur Complement and Its Applications* (Springer, 2005).

[5] P. R. Amestoy, I. S. Duff, J.-Y. LExcellent, and J. Koster. *SIAM J. Matrix Anal. Appl.* **23**, 15–41 (2001).

[6] P. R. Amestoy, T. A. Davis, and I. S. Duff, SIAM J. Matrix Anal. Appl., **17**, 886–905 (1996).

[7] M. Pu *et. al. Opt. Express* **25**, 31471 (2017).

[8] A. Martins *et. al. ACS Photonics* **7**, 2073–2079 (2020).

[9] W. Shin and S. Fan. *Comput. Phys. Commun.* **231**, 3406–3431 (2012).

[10] C. W. Hsu, RGF, https://github.com/chiaweihsu/RGF.

[11] V. Liu and S. Fan. *Comput. Phys. Commun.* **183**, 2233–2244 (2012).

Multiphysics simulations for phase change material based nanophotonics

Dmitry N. Chigrin[1,2,*],

[1]DWI Leibniz Institute for Interactive Materials, Aachen, Germany,
[2]I. Physikalisches Institut (1A), RWTH Aachen University, Aachen, Germany
*corresponding author, E-mail: chigrin@dwi.rwth-aachen.de

Abstract

The growing demand on reconfigurability in neuromorphic computing, quantum computing and microwave photonics is attracting increasing attention towards design and optimization of active integrated photonic components. Phase change materials are materials in which phase transitions can be induced quickly and reversibly, resulting in pronounced changes of their physical properties. Phase change materials are becoming increasingly popular element of photonic components for manipulation of light. By changing a phase of the material near a localized electromagnetic element, being a part of an electronic or optoelectronic component or a functional element of a metamaterial, it is possible to realize non-volatile, reconfigurable, time dependent and (re)programmable functionality. Due to a drastic change of the material properties during the phase transition resulting in the time-dependent changes in the absorption rate and heat conduction near the switched element, one has to describe electromagnetic, thermal and phase transition processes in a self-consistent manner. In this presentation we report on recent developments and applications of a multiphysics description of phase change material based nanophotonic systems.

Radiation control with exceptional points in non-Hermitian plasmonic systems

Yuto Moritake*

Department of Physics, Tokyo Institute of Technology, Japan
PRESTO, Japan Science and Technology Agency, Japan
*corresponding author, E-mail: moritake@phys.titech.ac.jp

Abstract

In this paper, we introduce our research based on the singular eigenstates in EP. The first is formation of circular polarization eigenstates and the second is formation of Huygens dipoles at EPs. The studies introduced in this paper provide new photonic functionalities caused by the singular eigenstates at EP in NH systems.

1. Introduction

In recent years, the physics of systems described by non-Hermitian (NH) Hamiltonians has attracted a great deal of attention from researchers. The NH systems with PT symmetry exhibit PT phase transition from PT symmetric phase to PT broken phase across exceptional point (EP). The eigenvalues and eigenmodes coalesce at the EP, which is very unique property of NH system with PT symmetry [1].

Since photonic systems are naturally described by NH Hamiltonian due to radiation loss and material gain/loss, many photonic systems involving NH photonics have been reported and shown variety of intriguing phenomena [2].

So far, many studies have been reported on NH photonics, but only a few have focused on the phenomena occurring directly at the EP [3]. Especially, few studies have focused on *singular eigenstates* with $\pm\pi/2$ phase difference.

In this paper, we introduce our research focusing on *the singular eigenstates* in EP. The first is formation of circular polarization eigenstates [4] and the second is formation of Huygens dipoles [5] at EPs. The studies introduced in this paper provide new photonic functionalities caused by the singular eigenstates at EP in NH systems.

2. Singular eigenstate at EP

The simplest example of photonic systems described by NH Hamiltonian with PT symmetry is coupled two resonators described by 2x2 matrix as follows,

$$\mathcal{H} = \begin{pmatrix} i\gamma & \kappa \\ \kappa & -i\gamma \end{pmatrix}.$$

Here, γ is loss/gain rate of resonators and κ is a coupling constant. Eigenfrequency and eigenstates of the Hamiltonian are

$$\omega_{\pm} = \pm\sqrt{\kappa^2 - \gamma^2}$$

and

$$\begin{pmatrix} 1 \\ \dfrac{-i\gamma \pm \sqrt{\kappa^2 - \gamma^2}}{\kappa} \end{pmatrix}.$$

When $\kappa = \gamma$, the eigenvalues and eigenstates coalesce, which means only one mode can exist in spite of a coupled two resonator system. The singularity point is called an EP in NH systems. The eigenstate at EP can be written as,

$$\begin{pmatrix} 1 \\ -sign(\kappa)i \end{pmatrix},$$

which means the relative phase difference between two resonators is $\pm\pi/2$ and the sign is determined by the sign of the coupling constant κ. In this study, we investigate physical phenomena induced by the singular eigenstate with $\pm\pi/2$ phase difference in photonic systems.

3. Circular polarization eigenstates at EP

First, we introduce switchable polarization eigenstates in a NH plasmonic system by using GST phase transition. we discuss about circular polarization eigenstates induced by singular eigenstates at EP in Jones matrix [3]. Figure 1(a) shows the proposed coupled plasmonic resonators. Although the x- and y-bars cannot couple due to the symmetry in the case of d_x = 0 nm, symmetry breaking due to the shift d_x induces the coupling between the bars and coupling strength can be controlled through the value of d_x.

To achieve the system described by a NH matrix with (passive) PT symmetry, GST is put at the one end of the y-bar as an additional loss material (Fig. 1(a)), which introduces loss contrast between the x- and y-bars (difference in imaginary parts of diagonal terms). At 1.5 μm, crystal phase GST has finite loss while material loss is negligible in amorphous phase. Therefore, the system described by a NH matrix with (passive) PT symmetry is realized only by crystal phase GST. Once GST phase is changed to amorphous, the system becomes the system described by usual Hermitian matrix, which suggests that GST phase transition is applicable to reconfigurable NH photonic systems at near infrared frequency region.

Figure 1(b) shows trajectories of the polarization eigenstate derived from Jones matrix on Poincaré sphere in the case of crystal GST. As the shift d_x increases, two polarization eigenstates move from x-, y- polarization to ±45-degree polarization. Importantly, two polarization eigenstates

approach the same pole (left-circular polarization), which indicates PT phase transition through the EP occur in polarization space. The circular polarization eigenstate corresponds to the singular eigenstate (1, i) at EP in x, y basis. Therefore, the proposed plasmonic system loaded by crystal GST can be described by NH matrix with loss biased PT symmetry.

Figure 1(c) shows the trajectories for amorphous GST. In contrast to the results of crystal GST, the trajectories are always on the equator of the Poincaré sphere, which means polarization eigenstates are linear polarization regardless of the coupling strength. The results show that the system is described by usual Hermitian matrix because of negligible loss of amorphous GST. By using crystal-amorphous phase change of GST, polarization eigenstates can be switched from elliptical to linear polarization.

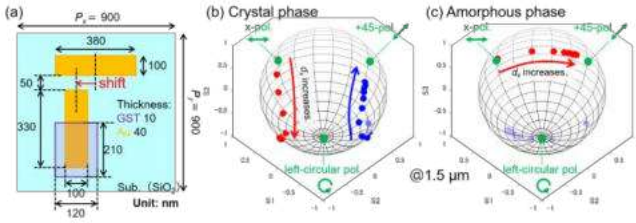

Figure1: (a) A schematic of the proposed structure. Trajectories of polarization eigenstates on Poincaré sphere for (b) crystal and (c) amorphous phases.

4. Huygens dipole formation at EP

Next, we introduce formation of Huygens dipole by the coupled SRRs described by NH Hamiltonian due to the difference in radiation losses. Huygens dipole is defined as a combination of electric and magnetic dipoles which arranged orthogonally each other [6]. Radiation fields from a Huygens dipole survives at only one direction and the radiation to the opposite direction is eliminated by destructive interference. Therefore, unidirectional radiation can be achieved by formation of Huygens dipole in artificial structures.

In order to mimic electric and magnetic dipoles in artificial structures, induced electric and magnetic dipoles in a split ring resonator (SRR) at the lowest resonance are employed (Fig. 2(a)). Different gap orientations of SRRs makes the system NH. Since phase of electric and magnetic dipoles are initially different by π/2, 0 or pi phase difference, which is necessary for Huygens dipole, can be obtained at the singular eigenstates with π/2 phase difference at EPs.

By sweeping geometrical parameters, we can observe two EPs, which is manifested by self-intersecting Riemann surface structure in complex eigenfrequencies (Fig. 2(b)). These EPs correspond to singular eigenstates by positive and negative coupling constants. We expect that unidirectional radiation due to the formation of Huygens dipoles should be observed at two EPs. To confirm this, we plot z-components of Poynting vector Pz at upper and lower surfaces of simulated models as shown in Fig. 2(c). Black arrows indicate direction and amplitude of Poynting vector in a log scale. Clear unidirectionality is observed at EP1 and EP2, which support the formation of Huygens dipoles. Furthermore, the radiation direction reverses between EP1 and EP2, meaning that the sign of the coupling constant flips from negative to positive.

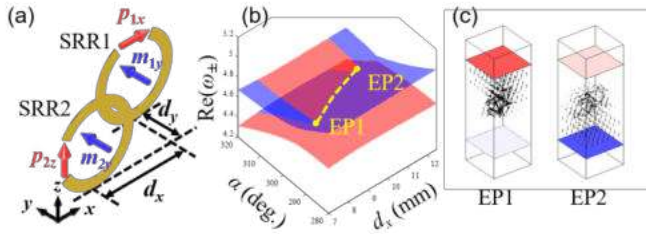

Figure2: (a) A schematic of the proposed structure. (b) Real eigen frequency surfaces for the coupled system. (c) Poynting vector flows at EPs.

5. Summary

In this study, we introduced photonic phenomena induced by singular eigenstates at EPs in NH systems. The singular eigenstate with π/2 phase difference is unique property of EP in NH system, which can not be achieved in usual Hermitian coupled systems. First, we proposed and numerically investigated the switchable polarization eigenstates in the NH plasmonic system by using GST phase transition. The loss contrast was introduced by adding crystal GST, and PT phase transition through the singular eigenstate at EP was demonstrated. Moreover, crystal-amorphous phase change of GST realized the switching of the polarization eigenstates from elliptical to linear polarization. Next, we theoretically and numerically investigated the coupled SRRs described by NH Hamiltonian due to the difference in radiation losses. Unidirectional radiation was observed at singular eigenstates at EPs, which support the formation of Huygens dipoles. Furthermore, the radiation direction reversed between EPs, meaning that the sign of coupling constats flip from negative to positive. The photonic functionalities originating from singular eigenstates at EPs would pave the way to realize reconfigurable NH based photonic devices.

Acknowledgements

This work has been supported by JST, PRESTO Grant Number JPMJPR18L9, Japan, by JSPS, Grant-in-Aid for Scientific Research (S), 20H05641, Japan, and by Grant-in-Aid for Early-Career Scientists, 21K14551.

References

[1] W. D. Heiss, J. Phys. A: Math. Theor. 45, 444016 (2012).
[2] L. Feng et al. Nat. Photon. 11, 752 (2017).
[3] M. Lawrence et al. PRL 113, 093901 (2014).
[4] Y. Moritake and M. Notomi, CLEO 2021
[5] Y. Moritake *in preparation*
[6] M. F. Picardi, A. V. Zayats, and F. J. Rodriguez-Fortuño, Phys. Rev. Lett. 120, 117402 (2018).

Simultaneously photonic and phononic metamaterials

Oliver B. Wright[1], Motonobu Tomoda[1], Osamu Matsuda[1], Ting Zhang[2], and Tetsuya Ueda[3]

[1]Division of Applied Physics, Faculty of Engineering, Hokkaido University, Sapporo 060-8628, Japan
[2]School of Electronic and Information Engineering, Nanjing University of Information Science and Technology, Nanjing 210044, China
[3]Department of Electronics, Kyoto Institute of Technology, Kyoto 606-8585, Japan
*corresponding author, E-mail: olly@eng.hokudai.ac.jp

Abstract

Metamaterials have been primarily studied in electromagnetics and acoustics to date. In the fields of photonic and phononic crystals, structures simultaneously exhibiting both photonic and phononic—so-called phoXonic—properties have been proposed, but this has not been done for metamaterials. Here we propose the concept of a phoxonic metamaterial, and demonstrate a working design in the GHz electromagnetic and kHz acoustic range that can simultaneously exhibit negative electromagnetic refraction at the same time as being a single-negative acoustic metamaterial. Possibilites for *quadruple-negative* phoxonic metamaterials, that exhibit dual double-negative behaviour, and applications to acousto-optic modulation are envisaged.

1. Introduction

Phoxonic crystals are periodic structures that are at the same time photonic and phononic crystals. First proposed theoretically,[1, 2] they were later verified experimentally.[3, 4] Simultaneously confining photons and phonons because of photonic or phononic band gaps, they show applications in sensing and cavity optomechanics.[4, 5]

Metamaterials are artificial media composed of unit cells much smaller than the wavelength. First developed for electromagnetic waves, they exhibit counterintuitive properties such as negative refractive index[6] and cloaking[7]. Such behavior is determined by the electrical or magnetic character of the constitutent meta-atoms. Over a similar period of time, acoustic metamaterials showing negative effective density and modulus were introduced.[8, 9] In the acoustic case, many studies have focused on various phenomena analogous to those in electromagnetism.

In spite of this progress, the obvious step of combining electromagnetic with acoustic metamaterials in one structure, i.e., the creation of a phoxonic metamaterial, does not appear to have been carried out. Such a system would have similar advantages to phoxonic *crystals*, but with the added convenience of easier miniaturization. Phoxonic metamaterials with simultaneously negative dielectric constant, magnetic permeability, density and modulus—which could be termed quadruple-negative phoxonic metamaterials—may make interesting candidates for acoustic-optic modulators in the form of flat superlenses.

Here we propose a realisable design for a phoxonic metamaterial, that exhibits negative electromagnetic refraction for GHz electromagnetic waves at the same time as a complete metamaterial band gap for kHz acoustic waves, and demonstrate its properties by numerical simulation.

2. Phoxonic metamaterial design

Our design is based on a modification of the double-negative microwave electromagnetic metamaterial proposed in Ref. [11], by incorporating a low elastic-modulus silicone rubber layer, as shown for a unit cell in Fig. 1. A central high-dielectric constant (ϵ=38, loss tangent γ=10^{-4}) ceramic disc (Murata Manufacturing, radius 2.33 mm, height 2.03 mm) of Young's modulus E=174 GPa, Poisson's ratio ν=0.31 (from resonant ultrasonic spectroscopy) and density ρ=5136 kg m^{-3} is embedded in an epoxy block (Rogers Corp. RT Duroid 5880, ϵ=2.2, γ=9×10^{-4}, E=965 MPa, ν=0.34, ρ=2200 kg m^{-3}), itself surrounded by a thin layer of silicone rubber (Ecoflex 00-30, ϵ=2.5, γ=0.01, E=71500 Pa, ν=0.44, ρ=1030 kg m^{-3}). Two copper layers of thickness 9 μm (conductivity 5.7×10^{-7} S m^{-1}, E=128 MPa, ν=0.36, ρ=8960 kg m^{-3}) containing hole arrays complete the unit cell, of dimensions $6\times6\times3.5$ mm^3. The electromagnetic properties refer to the $\sim$10 GHz regime. We carried out numerical simulations in both electromagnetism (ANSYS) and acoustics (COMSOL) to determine dispersion relations and propagation characteristics at selected points thereon. The unit cells and their internal elements are assumed to be in good acoustic contact (facilitated in practice, for example, by strong clamping or very thin adhesive), including disc-shaped gaps in the thin copper layers which we assume are filled with silicone rubber.

3. Dispersion relations

Figure 2 shows the electromagnetic and acoustic $\Gamma-X$ dispersion relations, both calculated in the absence of losses. We have marked with a red dot points on the dispersion relation to focus on. In the electromagnetic case, for a frequency of 11.7 GHz, this corresponds to a point in which the material exhibits negative permittivity and permeability

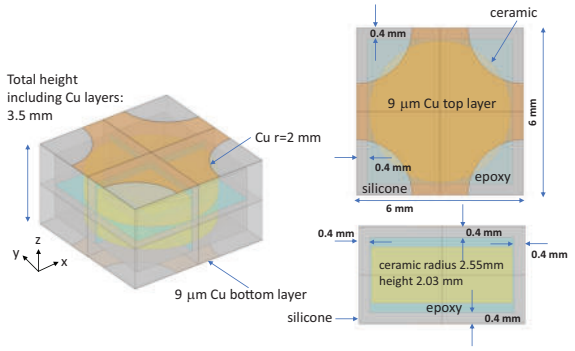

Figure 1: Schematic diagram of the phoxonic metamaterial. The thin Cu layers are not shown on the bottom-right.

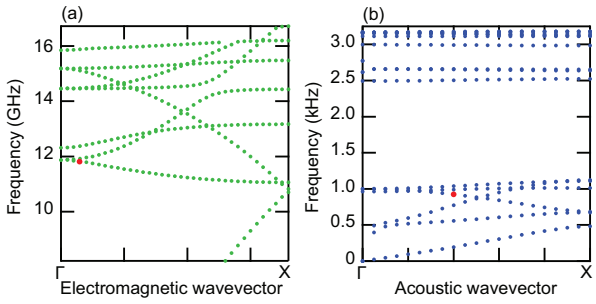

Figure 2: Numerically calculated (a) electromagnetic and (b) acoustic dispersion relations in the $\Gamma - X$ direction for the phoxonic metamaterial in the absence of losses. The red dots indicate particular points on the dispersion relation of interest.

with a y-polarized electric field. For the acoustic case, at a similar point on the dispersion relation, we can identify an xz-polarized wave at a frequency of 0.924 kHz, below a complete (i.e., for all propagation directions) metamaterial band gap that opens because of the introduction of the silicone rubber layer which supports vibrations of the central epoxy/ceramic mass. We suspect that the structure corresponds to a metamaterial with a negative effective density, i.e., a single-negative acoustic metamaterial, exhibited in the frequency range of the acoustic band gap.

Although we have not yet introduced elements in the design to produce a double-negative acoustic metamaterial, the existence of an acoustic metamaterial gap arising from a local mechanical resonance implies that our structure is an example of a phoxonic metamaterial with triple-negative character (i.e., single-negative acoustic and double-negative electromagnetic).

4. Conclusions

We have demonstated by numerical simulation a triple-negative phoxonic metamaterial. In the electromagnetic case a backward wave is identified for a chosen point on the dispersion relations below the band gap. For the acoustic case we have identified a band gap that arises because of a local resonance.

In future one would hope to demonstrate by calculation a metamaterial with the four negative effective parameters ϵ (permittivity), μ (permeability), B (bulk modulus) and ρ (density), i.e. a quadruple-negative phoxonic metamaterial.

Acknowledgement

We are grateful to Hirotsugu Ogi and Akira Nagakubo for resonant ultrasonic spectroscopy measurements. We also acknowledge Grants-in-Aid for Scientific Research from the Ministry of Education, Culture, Sports, Science and Technology (MEXT).

References

[1] M. Maldovan, E. L. Thomas, Simultaneous complete elastic and electromagnetic band gaps in periodic structures, *Appl. Phys. B* 83: 595-600, 2006.

[2] S. Sadat-Saleh, S. Benchabane, F. I. Baida, M.-P. Bernal, V. Laude, Tailoring simultaneous photonic and phononic band gaps, *J. Appl. Phys.* 106: 074912, 2009.

[3] A.V. Akimov, Y. Tanaka, A. B. Pevtsov, S. F. Kaplan, V. G. Golubev, S. Tamura, D. R. Yakovlev, M. Bayer, Hypersonic Modulation of Light in Three-Dimensional Photonic and Phononic Band-Gap Materials, *Phys. Rev. Lett.* 101: 033902, 2008.

[4] Y. Kawaguchi, T. Tsukahara, M. Motozawa, Phoxonic crystals–a new platform for chemical and biochemical sensors, *Anal. Bioanal Chem.* 405: 6497-6509, 2013.

[5] J. Chan, T. P. Mayer Alegre, A. H. Safavi-Naeini, J. T. Hill, A. Krause, S. Gröblacher, M. Aspelmeyer, O. Painter, Laser cooling of a nanomechanical oscillator into its quantum ground state, *Nature* 478: 89-92, 2011.

[6] R. A. Shelby, D. R. Smith, S. Schultz, Experimental verification of a negative index of refraction, *Science* 292: 77-79, 2001.

[7] D. Schurig, J. Mock, B. Justice, S. A. Cummer, J. B. Pendry, Metamaterial electromagnetic cloak at microwave frequencies, *Science* 314: 977-980, 2006.

[8] Liu, X. Zhang, Y. Mao, Y. Zhu, Z. Yang, C. T. Chan, P. Sheng, Locally resonant sonic materials, *Science* 289: 1734-1736, 2000.

[9] N. Fang, D. Xi, J. Xu, M. Ambati, W. Srituravanich, C. Sun, X. Zhang, Ultrasonic metamaterials with negative modulus, *Nat. Mater.* 5: 452, 2006.

[10] T. Ueda, S. Adachi, N. Michishita, M. Akiyama, T. Itoh, Multilayered volumetric composite right/left handed metamaterial structures composed of dielectric resonators and parallel mesh plates, *IEICE transactions on electronics* 93: 1063-1071, 2010.

Nonlinear Nanomechanical Photonic Metamaterials

Kevin F. MacDonald[1]*, Jinxiang Li[1], Dimitrios Papas[1], Jun-Yu Ou[1], Eric Plum[1] and Nikolay I. Zheludev[1, 2]

[1]Optoelectronics Research Centre & Centre for Photonic Metamaterials, University of Southampton, UK
[3]Centre for Disruptive Photonic Technologies, School of Physical and Mathematical Sciences & The Photonics Institute, Nanyang Technological University, Singapore
*corresponding author, E-mail: kfm@orc.soton.ac.uk

Abstract

By harnessing mechanical and optical resonances in tandem one can enhance the magnitude of actuation and optical response in dynamically reconfigurable nanostructures driven by microwatt optical signals and low-intensity acoustic vibrations. We review recent work on structures exhibiting profound opto-mechanical nonlinearity and bistability.

Summary

Nanomechanical metamaterials represent a highly adaptable platform of the engineering of profound electro-, magneto- and acousto-optic switching coefficients, and a range of optical phenomena that are vanishingly small, rare or non-existent in natural media. Here, we demonstrate systems in which coupling of near-infrared electromagnetic and MHz-frequency flexural resonances delivers strongly nonlinear optical properties.

Ponderomotive, non-thermal optical forces can control the structural configuration and thereby the optical response of an all-dielectric nanowire metamaterial, enabling all-optical transmission modulation at in a structure $<^1/_3$ of a wavelength thick, at low ($\mu W/\mu m^2$) intensities. This optomechanical nonlinearity is, moreover, strongly directionally asymmetric – i.e. dependent upon the direction of light propagation through the nanostructure.

Nanowires decorated with plasmonic resonators can be driven to provide a bistable optical response by acoustic signals modulated at their natural mechanical frequencies.

These hybrid nano-opto-mechanical systems opens new opportunities to develop low-power photonic switching devices.

Acknowledgements

This work is supported by the UK Engineering and Physical Sciences Research Council (Grant Nos. EP/M009122/1 and EP/T02643X/1) and the Singapore Ministry of Education (Grant No. MOE2016-T3-1-006). JL and TL would also like to acknowledge the support of the China Scholarship Council (grant nos. 201708440254 and 201806160012 respectively).

Software-defined reconfigurable metasurfaces for programmable wireless environments

Maria Kafesaki[1,2,*], O. Tsilipakos[1,2], Ch. Liaskos[1,3]

[1]Intitute of Electronic Structure and Laser, Foundation for Research and Technology Hellas, 70013 Heraklion, Greece
[2]Department of Materials Science and Technology, University of Crete, Heraklion, Greece
[3]Department of Computer Science and Engineering, University of Ioannina, Greece
*corresponding author, E-mail: kafesaki@iesl.forth.gr

Abstract

Programmable reconfigurable metasurfaces are expected to constitute a key element in the future programmable wireless environments. Here we discuss the design and fabrication of a programmable, reconfigurable and multifunctional metasurface able to operate as all-angle perfect absorber, beam steering and beam focusing device, accounting also for all aspects imposed by the programmability incorporation.

Reconfigurable intelligent metasurfaces are a subject of intensively increasing investigation in recent years, as they are associated with great potential in the realization of advanced wireless environments, important for 5G and beyond wireless communications. A key feature in such environments can be the programmability, i.e. the ability to dynamically control the wave propagation via software. To this extend software-defined metasurfaces, i.e. metasurfaces with multifunctional, reconfigurable response controllable (dynamically) via a software, are associate with unique potential. In this talk we will report our efforts to realize such a programmable reconfigurable metasurface. Our designed and fabricated metasurface is able to act as all-angle perfect absorber, beam steering and beam focusing device, being also compliant with all the practical restrictions imposed by the programmability incorporation. The reconfiguration of the metasurface is achieved via integrated circuits acting as varactor-varistor elements, able to offer local control and a continuously tunable impedance [1-3].

Acknowledgements

The work was performed in the framework of the EU-FET project VisorSurf - A Hardware Platform for Software-driven Functional Metasurfaces, www.visorsurf.eu. Other people contributed to the work presented are A. C. Tasolamprou, A. Pitilakis, F. Liu, X. C. Wang, S. Tretyakov, D. Manessis.

References

[1] F. Liu, O. Tsilipakos, A. Pitilakis, A. C. Tasolamprou, M. S Mirmoosa, N. V. Kantartzis, D. H. Kwon, M. Kafesaki, C. M. Soukoulis, S. A. Tretyakov, Intelligent metasurfaces with continuously tunable local surface impedance for multiple reconfigurable functions, *Phys. Rev. Appl.* 11, 044024 (2019).

[2] O. Tsilipakos, A. C. Tasolamprou, A. Pitilakis, F. Liu, X. C. Wang, M. S. Mirmoosa, D. C. Tzarouchis, S. Abadal, H. Taghvaee, C. Liaskos, A. Tsioliaridou, J. Georgiou, A. Cabellos-Aparicio, E. Alarcon, S. Ioannidis, A. Pitsillides, I. F. Akyildiz, N. V. Kantartzis, E. N. Economou, C. M. Soukoulis, M. Kafesaki, S. Tretyakov, Towards Intelligent Metasurfaces: The Progress from Globally Tunable Metasurfaces to Software-Defined Metasurfaces with an Embedded Network of Controllers, *Adv. Opt. Mat*. 8, 2000783 (2020). DOI: 10.1002/adom.202000783

[3] A. Pitilakis, O. Tsilipakos, F. Liu, K. M. Kossifos, A. C. Tasolamprou, D. H. Kwon, M. S. Mirmoosa, D. Manessis, N. V. Kantartzis, C. Liaskos, M. A. Antoniades, J. Georgiou, C. M. Soukoulis, M. Kafesaki, S. A. Tretyakov, A Multi-functional reconfigurable metasurface: Electromagnetic design accounting for fabrication aspects, *IEEE Trans. on Ant. and Propag.* 69, 1440 (2021). DOI: 10.1109/TAP.2020.3016479

Water-based metamaterials for advanced microwave control and sensing

Rasmus E. Jacobsen [1,2], Alex Krasnok [3], Andrea Alú [3,4], Samel Arslanagić [2], Andrei V. Lavrinenko [1*]

[1]Department of Photonics Engineering, Technical University of Denmark, Kgs. Lyngby, Denmark
[2]Department of Electrical Engineering, Technical University of Denmark, Kgs. Lyngby, Denmark
[3]Photonics Initiative, Advanced Science Research Center, City University of New York, New York, USA
[4]Physics Program, Graduate Center, City University of New York, New York, USA
*corresponding author, E-mail: alav@fotonik.dtu.dk

Abstract

With the increasing focus on ecological compatibility and recyclability of electromagnetic materials, immense efforts are applied to find cheap and bio-friendly alternatives. Such material at microwave frequencies can be just conventional water. Water in this range of interest has high dielectric permittivity, and can be used to engage strong Mie resonances in the devices performance for enhanced scattering and absorption of microwaves even in single inclusions. In the talk I review different water-based devices for microwave control and sensing. Among the effective implementation of water-based elements there are examples of metasurfaces, absorbers, dielectric resonance antennas, radio-frequency components and structures with a so-called bound state in the continuum as a sensor.

Optomechanics of ultra-thin photonic metasurfaces

Ognjen Ilic[1,2]

[1]Department of Mechanical Engineering, University of Minnesota, Minneapolis, USA
[2]School of Physics and Astronomy, University of Minnesota, Minneapolis, USA
*corresponding author, E-mail: ilic@umn.edu

Abstract

Metasurfaces have a remarkable capability to synthesize complex wavefronts, with diverse applications in beam focusing, imaging, and flat optics. Complementing established applications, we show how the ability to steer waves can be seen as a mechanical phenomenon, and how the underlying metasurface physics can be harnessed to shape optomechanical forces. We discuss the potential of metasurfaces as ideal platforms for optomechanics because of their large-area and ultra-lightweight form factor. Such metasurface control of optical forces can facilitate novel approaches to optical levitation and propulsion at the macro scale.

Exact, Feasible and Practical Cloaks for Static and Quasistatic Magnetic Fields

Alvaro Sanchez

Department of Physics, Universitat Autonoma de Barcelona, Catalonia, Spain

Abstract

Here we review how cloaks for dc and low-ac magnetic fields have been theoretically proposed and experimentally demonstrated using different approaches. They range from exact cloaks for uniform dc fields to actual cloaks being used in future particle accelerators. We also present how the cloak of static and quasistatic magnetic fields by metamaterials can be realized in very simplified situations, including the case of using only a single homogeneous and isotropic material.

We thank European Project MetaMagIC for support.

Generation of tunable order Bessel beams with cascaded metasurfaces

Yan Zhang[1], Guocui Wang[1,2], Bin Hu[2], and Xinke Wang[1]

[1]Department of Physics, Beijing Key Lab for Metamaterials and Devices, Key Laboratory for Terahertz Optoelectronics, Ministry of Education, Beijing Advanced Innovation Center for Imaging Theory and Technology, Capital Normal University, Beijing, China
[2]School of Optics and Photonics, Beijing Engineering Research Center for Mixed Reality and Advanced Display, Beijing Institute of Technology, Beijing, China,
*corresponding author, E-mail: yzhang@cnu.edu.cn

Abstract

A variorder Bessel beam generator is experimentally demonstrated with two metasurface devices. Two cascading metasurfaces are employed to generate Bessel beams in the terahertz range. The order of generated Bessel beam can be turned by rotating the metasurface. The order of the Bessel beam is changed from zero-order to fourth-order when the rotation angle of metasuface components from 20 degrees to 80 degrees.

Bessel beam which is a kind of diffraction-free beams with superior self-healing capability has many potential applications in the fields of optical particle control, microscopy, nonlinear optics, materials processing, and quantum communication [1-4]. Generally, an axicon is used to generate Bessel beam. In 2015, Wei et al. demonstrated a high-order terahertz Bessel beam using a polymer spiral axicons with different topological numbers, which is fabricated with 3D printing technique [5]. In 2017, Wu et al. further generated a zero-order terahertz Bessel beam by using a terahertz quarter wave plate and Teflon axicons [6]. However, this method is rather inefficient, because large size of axicon is unprofitable for devices miniaturization. Recently, rapid developments of metasurface provide new opportunities to realize ultracompact and high-efficiency terahertz devices. Metasurfaces are ultrathin artificial structures composed of sub-wavelength meta-atoms with arranged in a special sequence, which have extraordinary capabilities to control electromagnetic wavefront based on Huygens' principle [7-8]. In 2017, Chen et al. designed a wavelength-independently subwavelength Bessel beams using metasurfaces, they experimentally achieved the meta-axicons with a high NA up to 0.9 capable of generating Bessel beams with full width at half maximum about as small as $\sim\lambda/3$ [9]. Whereas, this device is static, which means that the order of Bessel beam is non-tunable once the opening angle of axicon is fixed.

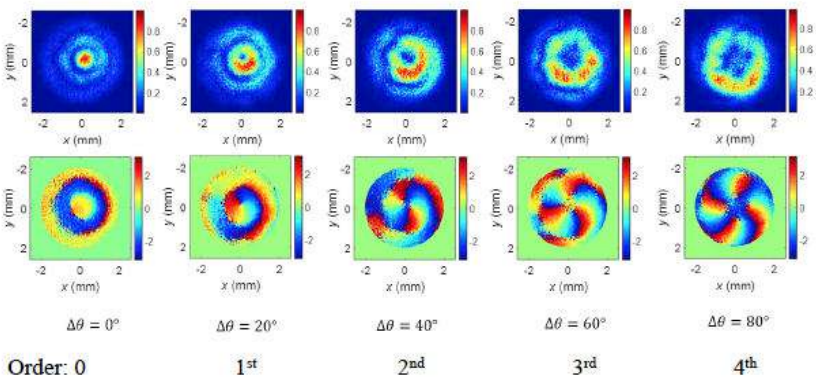

Fig. 1 Experimentally measured intensity and phase distributions of Bessel beams with different orders.

Here, a device which consists of two metasurface components placed face to face is designed to generate Bessel beams with tunable order in the terahertz range. The order of Bessel beam can be changed linearly by rotating one of metasurface relative to another metasurface. The basic elements of the designed metasurface are silicon pillar with heigh of 300 μm and

variable diameters changing from 30 μm to 160 μm, which was fabricated on a silicon substrate with heigh of 700 μm and periodic of 200 μm using the reactive ion beam etching technique. The performances of the device are measured with a home-build terahertz focal plane imaging system. Experimental results demonstrate that a zero order Bessel beam is obtained when the rotation angle between two metasurfaces is zero, and the order of Bessel beam can be changed from first-order to fourth-order when the rotation angle is increased from 20 degrees to 80 degrees with a step of 20 degrees. The measured intensity and phase distributions are shown in Fig. 1, it can be seen the Bessel beams with different order have been generated well.

This work demonstrates an approach to generate tunable special field distributions with radially symmetric and provide a way to construct active metasurface devices.

Reference:

[1]. Durnin J., Miceli J. J., Eberly J. H., Diffraction-free beams. Phys. Rev. Lett. 1987; 58: 1499-1501.

[2]. Bouchal Z., Wagner J., Chlup M., Self-reconstruction of a distorted nondiffracting beam. Opt. Commun. 1998; 151: 207-211.

[3]. Chen J., Ng J., Lin Z. F., Chen C. T., Optically pulling force. Nat. Photon. 2011; 5:531-534.

[4]. Dogariu A., Sukhov S., Jose J., Optical induced 'negative force'. Nat. Photon. 2013; 7: 24-27.

[5]. Wei X. L., Liu C. M., Niu L. T., Zhang Z. Q., Wang K. J., Yang Z. G., Liu J. S., Generation of arbitrary order Bessel beams via 3D printed axicons at the terahertz frequency range. Appl. Opt. 2015; 54: 10641-10649.

[6]. Wu Z., Wang X. K., Sun W. F., Feng S. F., Han P., Ye J. S., Zhang Y., Vector characterization of zero-order terahertz Bessel beams with linear and circular polarization. Sci. Rep. 2017; 7: 139329.

[7]. Yu N. F., Genevet P., Kats M. A., Aieta F., Tetienne J. P., Capasso F., Zeno G., Light propagation with phase discontinuities: generalized laws of reflection and refraction. Science 2011; 334: 333-337.

[8]. Sun S. L., He Q., Xiao S. Y., Xu Q., Li X., Zhou L., Gradient-index meta-surfaces as a bridge linking propagating waves and surface waves. Nat. Mater. 2012; 11:426-431.

[9]. Chen W. T., Khorasaninejad M., Zhu A. Y., Oh J., Devlin R. C., Zaidi A., Capasso F., Generation of wavelength-independent subwavelength Bessel beams using metasurfaces. Light Sci. Appl. 2017; 6:e16259.

Manipulating Circularly Polarized Optical Radiation with Functional Metasurfaces

Fei Ding

Centre for Nano Optics, University of Southern Denmark, Campusvej 55, DK-5230 Odense, Denmark
*corresponding author, E-mail: feid@mci.sdu.dk

Abstract

Metasurfaces have the potential to emerge as essential components for classical and nonclassical optical fields. In this talk, I will first present two examples on how to use metasurfaces to design quarter-wave plates that can not only allow broadband circular-to-linear polarization conversion but also generate vector vortex beams or function as a versatile beam splitter. After that, I will talk about a conceptually new approach to the room-temperature generation of circularly polarized, well-collimated single photons.

References

[1] F. Ding, A. Pors, and S. I. Bozhevolnyi, "Gradient metasurfaces: a review of fundamentals and applications," Rep Prog Phys. 81,026401 (2018).
[2] F. Ding, Y. Yang, R. Deshpande, and S. Bozhevolnyi, "A review of gap-surface plasmon metasurfaces: fundamentals and applications," Nanophotonics 7, 1129 (2018).
[3] J. T. Heiden, F. Ding, J. Linnet, Y. Yang, J. Beermann, and S. I. Bozhevolnyi, "Gap-Surface Plasmon Metasurfaces for Broadband Circular-to-Linear Polarization Conversion and Vector Vortex Beam Generation," Adv. Opt. Mater. 7, 1801414 (2019).
[4] Y. Deng, C. Wu, C. Meng, S. Bozhevolnyi, and F. Ding, "Functional metasurface quarter-wave plates for simultaneous polarization conversion and beam steering," ACS Nano 15, 18532–18540 (2021).
[5] C. Wu, S. Kumar, Y. Kan, D. Komisar, Z. Wang, S. I. Bozhevolnyi, and F Ding, "Room-temperature on-chip orbital angular momentum single-photon sources," Sci. Adv. 8, eabk3075 (2022).

Non-Hermitian THz metasurfaces based ultra-sensitive sensing

Teun-Teun Kim[1*], Soojeong Beak[2], Hosub Lim[3], Sang Hyun Park[4], Bumki Min[2]

[1]Department of Physics, University of Ulsan, Ulsan, Republic of Korea
[2]Department of Mechanical Engineering, Korea Advanced Institute of Science and Technology, Daejeon, Republic of Korea
[3]Renal Division and Division of Engineering in Medicine, Department of Medicine, Brigham and Women's Hospital, Harvard Medical School, Boston, MA, USA
[4]Department of Electrical and Computer Engineering, University of Minnesota, Minneapolis, Minnesota, United States
[5]Center for Integrated Nanostructure Physics, Institute for Basics Science, Sungkyunkwan University, Suwon, Republic of Korea
*corresponding author, E-mail: ttkim@ulsan.ac.kr

Abstract

Since the sensitivity around EPs is significantly enhanced, Non-Hermitian photonics has become an emerging research area that has been extensively studied in different spectral regions using various optical systems. Here, we demonstrate sensing of amyloid-beta (Aβ) protein, a well-known precursor for Alzheimer's disease by an abrupt phase transition near an exceptional point in non-Hermitian metasurfaces. The efficacy of the proposed sensing scheme is experimentally verified by detecting a minuscule amount of the monomer form of Aβ at the sub-picomole level.

Dragging and amplifying light with space-time metamaterials

P.A. Huidobro[1,3], M.G. Silveirinha[1], E. Galiffi[2] and J.B. Pendry[2]

[1] Instituto de Telecomunicações, Instituto Superior Tecnico-University of Lisbon, Avenida Rovisco Pais 1, Lisboa, 1049-001 Portugal
[2] The Blackett Laboratory, Department of Physics, Imperial College London, London, SW7 2AZ
[3]p.arroyo-huidobro@lx.it.pt

Abstract

In this talk I will consider space-time metamaterials of travelling-wave type and introduce the theory of homogenisation of these modulated media [1]. This framework provides analytical expressions for the effective permittivity, permeability and magnetoelectric coupling of these media in the long wavelength limit. From the derived parameters we will see how it is possible to achieve nonreciprocal effects away from the asymmetric band gaps, and even down to the quasistatic limit if both the permittivity and permeability are modulated, and how the synthetic motion present in these systems allow us to make a link to the Fresnel drag effect of light in moving media [2].

Our theory also unveils a regime when the modulation speed approaches that of waves in the background medium where homogenisation breaks down and a new mechanism for gain emerges [3], enabling a form of nonreciprocal broadband amplification that could be realised in graphene [4], or that could be chirally selective by implementing an Archimedes screw for light [5].

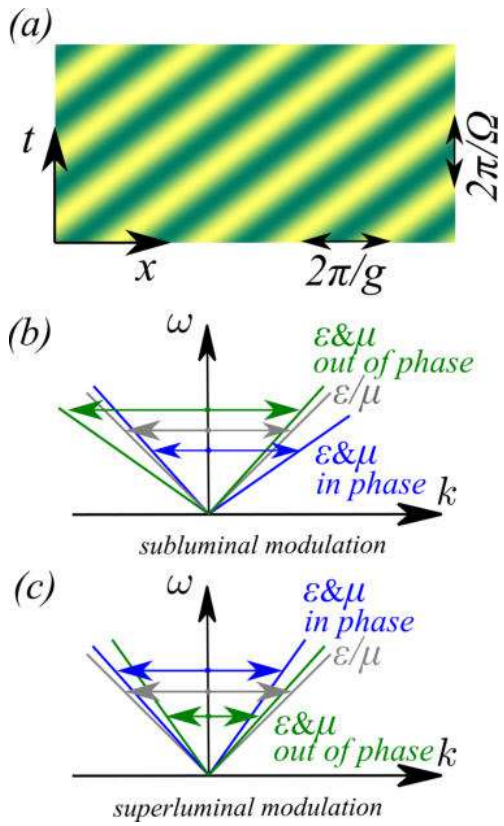

(a) Sketch of pace-time modulation of the permittivity and/or permeability of travelling wave kind. (b,c) The long wavelength dispersion relation of the electromagnetic modes is nonreciprocal if both the permittivity and permeability are modulated, and the sign and magnitude of the bianisotropic coupling can be tuned with the modulation parameters, e.g. by modulating the permittivity and permeability in or out-of phase, and by modulating at speeds larger or smaller than the speed of light in the medium. Reproduced from [1].

References

[1] Huidobro, P. A., Silveirinha, M. G., Galiffi, E., & Pendry, J. B. (2021). Homogenization theory of space-time metamaterials. Physical Review Applied, 16(1), 014044.

[2] Huidobro, P. A., Galiffi, E., Guenneau, S., Craster, R. V., & Pendry, J. B. (2019). Fresnel drag in space–time-modulated metamaterials. Proceedings of the National Academy of Sciences, 116(50), 24943-24948.

[3] Pendry, J. B., Galiffi, E., & Huidobro, P. A. (2021). Gain mechanism in time-dependent media. Optica, 8(5), 636-637.

[4] Galiffi, E., Huidobro, P. A., & Pendry, J. B. (2019). Broadband nonreciprocal amplification in luminal metamaterials. Physical review letters, 123(20), 206101.

[5] Galiffi, E., Huidobro, P. A., & Pendry, J. B. (2021). An Archimedes' Screw for Light. arXiv:2109.14460.

Recent progress in the frequency selective metasurfaces in mid infrared wavelength

Yoshiaki Nishijima[1*], Naoki To[1]

[1]Graduate school of engineering Yokohama National University
*corresponding author, E-mail: nishijima-yoshiaki-sp@ynu.ac.jp

Abstract

Mid infrared wavelength is unique to apply the detection of the small amount of molecules with molecular vibration or rotational modes. Especially absorption type of frequency selective meta surface can be used for the mid infrared light source, detectors according to the Kirchhoff's thermal ra- diation low. Here we summarized the recent progress of plasmonic meta surfaces in mid infrared wavelength region. The experimentally measured optical properties were com- pared with simulations by Finite difference time-domain calculations. Also, we demonstrate applications of these structures for the plasmonic IR-light sources and detec- tors.and another sensing devices.

Subwavelength waveguide arrays for spatial phase manipulation of microwaves

Dominic Palm[1], Marco Rahm[1]

[1]Department of Electrical and Computer Engineering, Research Center OPTIMAS,
Technische Universität Kaiserslautern, Kaiserslautern, Germany

Abstract

We design, fabricate and experimentally test waveguide arrays with subwavelength width and periodicity to manipulate the spatial phase of microwaves. The electromagnetic performance of the waveguide arrays is optimized by use of a particle swarm algorithm. For example, we implement a waveguide array wall that transmits microwaves with incidence angles between -80 and +80 deg with a transmittance of more than 88%, a spatial filter that refracts incident waves with incidence angles smaller than +/-20 deg at a refraction angle of 0 deg in the forward direction and a device that deflects normally incident waves at very large deflection angles in the backward direction.

Forward and Inverse Design of Electromagnetic Metasurfaces

Willie Padilla[1*], Simiao Ren[1], Jordan M. Malof[1],

[1]Department of Electrical and Computer Engineering, Duke University, Box 90291, Durham, NC 27708, USA
*corresponding author, E-mail: willie.padilla@duke.edu

Abstract

The demonstration of exotic electromagnetic metasurfaces has benefited from the advance of computational electromagnetic simulations and the continued maturation of nanolithography. Recently, deep learning has shown a unmatched ability for the forward and inverse design of electromagnetic metasurfaces. I will overview this exciting and rapidly expanding area of research, highlighting novel examples and provide an outlook.

1. Introduction

Electromagnetic (EM) metasurfaces, or simply metamaterials (MMs), have demonstrated novel electromagnetic phenomena that is difficult or impossible to achieve with naturally occurring materials. [1] One reason for the success of MMs was their simple underlying design principles. Specifically, one could design relatively advanced EM response through specification of only a few unit-cell geometrical parameters. The unit-cell was then replicated to form a larger surface or volume, and since metamaterial are sub-wavelength, the larger arrays maintained unit-cell EM properties. The underlying sub-wavelength design principles afforded another salient MM property – that of electromagnetic similitude. That is, since metamaterial design requires conductive sub-wavelength resonant elements, they could be scaled to any band of the electromagnetic spectrum where these requirements could be met.

Although great success has been achieved with the metamaterial approach, it is fundamentally a forward design process. That is, one is guided by theory, computational EM simulations (CEMS), experiments, and intuition. As more advanced metamaterial structures are sought, including all-dielectric metasurfaces – as well as their combination with exotic natural materials – a trade between design simplicity and exotic EM properties arises. Theory may be incomplete and insufficient to guide design of the desired EM response. Further the parameter space may be too large to permit an exhaustive search, with little guidance from the intuition afforded to the simpler classical metamaterial designs. [2]

Ideally, one would like to specify some desired electromagnetic response, and then to have some design process give the metamaterial geometry and constituent materials for such a response. [3] Such a design process is called an inverse problem, and is an outstanding problem in many fields including electromagnetic metamaterials and metasurfaces. We overview deep learning based forward and inverse design of metasurfaces.

2. Results

In this work we investigate deep inverse methods for design of metamaterials and metasurfaces with the goal of achieving a desired scattering property, such as reflectivity, transmissivity, or absorptivity. Our approach uses a forward trained deep neural network which is specially designed to solve ill-posed inverse problems. Here we compare several inverse methods based on deep learning on three metamaterial design problems. Our results indicate that deep learning inverse methods produce accurate designs to achieve a custom desired scattering. [4] We also demonstrate that not all metamaterial design problems are ill-posed, and in such cases a conventional deep neural network is the best choice.

Acknowledgement

We acknowledge funding from the Department of Energy

under U.S. Department of Energy (DOE) (DESC0014372).

References

[1] Filippo Capolino. *Theory and phenomena of metamaterials*. CRC Press/Taylor & Francis, Boca Raton, FL, 2009. ISBN 978-1420054255.

[2] Omar Khatib, Simiao Ren, Jordan Malof, and Willie J Padilla. Deep learning the electromagnetic properties of metamaterials—a comprehensive review. *Advanced Functional Materials*, page 2101748, 2021.

[3] Yang Deng, Simiao Ren, Kebin Fan, Jordan M. Malof, and Willie J. Padilla. Neural-adjoint method for the inverse design of all-dielectric metasurfaces. *Optics Express*, 29(5):7526, February 2021.

[4] Simiao Ren, Ashwin Mahendra, Omar Khatib, Yang Deng, Willie J. Padilla, and Jordan M. Malof. *Inverse deep learning methods and benchmarks for artificial electromagnetic material design*. Nanoscale, volume 14, pages 3958–3969, 2022.

Wideband metamaterial absorber: from concept to naval applications

Xavier Begaud[1*], Anne Claire Lepage[1], Michel Soiron[2], André Barka[3] and Sarah Laybros[4]

[1] LTCI, Télécom Paris, Institut Polytechnique de Paris, Palaiseau, France
[2] SART, Boulogne Billancourt, France
[3] ONERA-DEMR, Université de Toulouse, Toulouse, France
[4] NAVAL GROUP, Ollioules, France
*corresponding author, E-mail: Xavier.Begaud@telecom-paris.fr

Abstract

This presentation focuses on the results obtained during the two projects SAFAS and SAFASNAV, which highlight the evolution from the concept of broadband absorber with metamaterials to a realization of this concept in structural material for naval application. The French Ministry of Defense (DGA), through the National Research Agency (ANR) and the Astrid and Astrid Maturation programs, funded the research that led to these results. The simulation results were obtained using GENCI's HPC resources (Grant c2016107558).

Meta-waveguides: a marriage between metasurface and integrated photonics enabling subwavelength control of guided waves

Xingjie Ni

Department of Electrical Engineering and Material Research Institute, The Pennsylvania State University, University Park, PA, USA
*corresponding author, E-mail: xingjie@psu.edu

Abstract

Metasurfaces with unparalleled light controllability have shown great potential to revolutionize conventional optics. However, they mainly require free-space light excitation, making it challenging to integrate them on-chip fully. Here, we present metasurface-incorporated waveguides that synergize subwavelength metaphotonic architectures with photonic integrated waveguide platforms. Such meta-waveguides achieve various functions in a completely integrated platform, such as steering and focusing guided waves into free space, projecting holograms with controlled phase and amplitude control, and generating laser emission carrying orbital angular momenta. Our study shows a viable route toward complete control of light across integrated photonics and free-space platforms and paves the way for creating multifunctional photonic integrated devices with agile access to free space.

Nanophotonics, plasmonics and quantum optics

Interplay between nonlinear effects at the nanoscale in engineered optical nanoantennas

A. Zilli,[1] A. Locatelli,[2] D. Rocco,[2] L. Carletti,[2] P. Biagioni,[1] L. Duò,[1] X. Wu,[3] S. Grossman,[3] C. Gigli,[4] G. Marino,[4] G. Leo,[4] C. De Angelis,[2] B. Hecht,[3] M. Celebrano,[1] and M. Finazzi[1*]

[1] Politecnico di Milano, Physics Department, 20133 Milano, Italy
[2] University of Brescia, Department of Information Engineering, 25123 Brescia, Italy
[3] University of Würzburg, Nano-Optics & Biophotonics Group - Department of Physics - Experimental Physics 5, 97074 Würzburg, Germany
[4] Université de Paris, Physics Department, Rue A. Domon et L. Duquet 10, 75013 Paris, France
*corresponding author, E-mail: marco.finazzi@polimi.it

Abstract

Nnanostructures can be exploited to enhance nonlinear optical processes via the strong light confinement by their resonant modes. The sensitive dependence of these modes on the geometry and material composition offers ample opportunities for tailoring the optical response of the system. I report about sum-frequency generation (SFG) by individual dielectric and plasmonic nanocylinders, pumped by two pulsed beams with different photon energies. A rich size- and polarization-dependent behavior is observed, disclosing strategies to manipulate the nonlinear properties of nanoscale systems.

1. Introduction

Nanoscale optical integration is nowadays a strategic technological challenge and the ability of generating and manipulating nonlinear optical processes in sub-wavelength volumes is a key-enabling asset for the realization of efficient probes for sensing and photonic sources for the next-generation communication technologies. Yet, to date, confining nonlinear processes beyond the diffraction limit remains a challenging task because phase-matching conditions, which ensure efficient energy transfer from the fundamental to the nonlinear wave in the bulk, cannot be realized at the nanoscale.

Significant efforts have been recently devoted to the investigation of nonlinear optical processes in plasmonic nanoantennas [1,2]. The strong local field enhancement they exhibit makes them promising candidates to overcome the lack of phase-matching at the nanoscale. In this framework, we devised a plasmonic nanoantenna working in the near-infrared region of the electromagnetic spectrum, which allows boosting the second-harmonic generation (SHG) efficiency. This is achieved by optimizing the nanoantenna geometry to feature (i) a doubly resonant response at both the fundamental and emission wavelengths; (ii) a spatial overlap between the modes involved in the process; and (iii) a broken symmetry, to enable efficient SHG through electric dipole emission. We found that this nanoantenna concept behaves like a strongly coherent nanoscale light source, featuring low photoluminescence in the visible range and a marked third-harmonic generation (THG) along with an intense SHG [3]. We recently applied this concept to an extended array of non-centrosymmetric nanoantennas demonstrating its potential for nonlinear sensing [4].

Due to the relatively low nonlinear conversion efficiencies in these nanoscale systems, a widely accepted approach consists in treating independently different order nonlinear processes such as, for instance, THG and SHG. We show that this paradigm can dramatically fail in these non-centrosymmetric plasmonic nanoantennas, highlighting a SHG-mediated cascaded pathway in THG [5]. This mechanism can be unveiled thanks to the commensurate emission yields of SHG and THG in this nanostructure. We have disentangled this cascading effect from bulk mediated THG based on the characteristic nonlinear emission fingerprint of these processes, which can be identified through the analysis of the overall emission polarization.

2. Results

In this context, I will also present the evidence of interference effects between THG and degenerate sum-frequency generation (SFG), produced by combining the original pump beam with a frequency-doubled beam, both on AlGaAs nanopillars and on asymmetric Au nanoantennas. We recently demonstrated that both these nanoscale systems can sustain intense SHG associated with the bulk second-order susceptibility of the material [6]. I will show that, in coincidence with the first order anapole configuration of the AlGaAs system [7], SFG can be controlled by the polarization of the impinging beams, obtaining signal yields higher than THG generated by the original pump beam alone. Conversely, the polarization state of the nonlinear radiation emitted by Au nanoantennas depends by the interplay between SFG and THG. For both systems, due to the degeneracy in the output wavelength,we are able to observe a marked interference between the two

processes, which is mediated by the resonances in these nanosystems.

These results demonstrate the possibility of tailoring the coupling efficiency between nonlinear processes in nanoscale systems nanoantennas and represent a crucial step towards the realization of nanoscale photon conversion and manipulation at room temperature, thereby opening new possibilities in quantum optics and in nonlinear optical sensing.

Acknowledgements

A.Z., D.R., C.D.A., and M.C. acknowledge financial support by the Italian Ministry of Education, University and Research (MIUR) through the PRIN project “NOMEN" (2017MP7F8F). G.L., acknowledges financial support by the French National Research Agency (ANR) through the project NANOPAIR (ANR-18-CE92-0043). All authors thank Aristide Lemaîatre for the epitaxial growth of the sample.

References

[1] M. Kauranen, A. V. Zayats. Nature Photonics 6, 737–748, 2012.
[2] J. Butèt et al. ACS Nano 9, 10545–10562, 2015.
[3] M. Celebrano et al. Nature Nanotechnology 10, 412–417, 2015.
[4] L. Ghirardini et al. J. Phys. Chem. C 122, 11475–11481, 2018.
[5] M. Celebrano et al. Nano Letters 19, 7013–7020, 2019.
[6] V. Gili et al. Opt. Exp. 24, 15965, 2016.
[7] A. E. Miroshnichenko, et al. Nature Communications, 6 (2015).

Analytical and numerical study of T-shaped plasmonic demultiplexer based on Fano and induced transparency resonances

Madiha Amrani[1], Soufyane Khattou[1,*], Adnane Noual[1], Abdelkader Mouadili[2], El Houssaine El Boudouti[1] and Bahram Djafari-Rouhani[3]

[1]LPMR, Département de Physique, Faculté des Sciences, Université Mohammed I, Oujda, Morocco
[2]LPMCER, Département de Physique, Faculté des Sciences et Techniques de Mohammedia, Université Hassan II, Casablanca, Morocco
[3]IEMN, Université de Lille, 59650 Villeneuve d'Ascq, France
*corresponding author, E-mail: s.khattou@ump.ac.ma

Abstract

We give both analytically and numerically a demonstration of the possibility to realize a simple plasmonic demultiplexer based on Fano and electromagnetic induced transparency resonances. The demultiplexer consists in a T-shaped waveguide with an input line and two output lines. Each output line contains two stubs attached at two positions far from the input line. We derive in closed form the expressions for a selective transfer of a single propagating mode through one line keeping the other line unaffected. The analytical results obtained by the Green's function method are confirmed by numerical simulation using Comsol Multiphysics Software.

1. Introduction

The interaction of incident electromagnetic waves propagating through different paths in a composite material in presence of scatterers, may result in constructive or destructive wave phenomena giving rise to resonances or anti-resonances in the transmission spectra. When a resonance falls near an anti-resonance, we obtain an asymmetric line profile called Fano resonance [1], however when the resonance falls between two anti-resonances, we obtain the so-called electromagnetic induced transparency (EIT) resonance [2]. These resonances are the consequence of the interaction of a discrete localized state with a continuum of propagating states. Even though these resonances have been first observed in quantum systems, it was shown that Fano and EIT resonances can be also obtained in classical systems such as: coupled micro resonators [3], photonic crystal waveguides coupled to cavities [4], metamaterials [5] and photonic circuits [6].

In a recent paper [7], we have shown the possibility to realize a photonic demultiplexer based on induced transparency resonances. The demultiplexer consists of a Y-shape waveguide with an input line and two output lines. Each line contains two grafted resonators in a given position away from the input line. The idea consists in coinciding at a given frequency a resonance on one line with a transmission zero on the other line. The necessary conditions for realizing selective transfer of a single mode through one line while keeping the other line unaffected are deduced and an experimental confirmation of these results has been performed [7]. However, these circuits operate in the radio-frequency domain which renders their usefulness less important.

In this communication, we use plasmonic nano-waveguides to realize a T-shaped plasmonic demultiplexer operating in the telecommunication domain. Such system is based on metal-insulator-metal structures which support surface plasmon polaritons. Hence, the proposed device enables to confine and manipulate the propagation of light below the classical diffraction limit [8]. The demultiplexer consists in an input waveguide and two output waveguides. Each line contains two grafted resonators at two different positions (Fig. 1 (a)) away from the input line. Our goal is to use the properties of Fano and plasmon induced transparency (PIT) resonances in order to get the analytical expressions that should be satisfied by the different lengths of the waveguides in order to realize a reasonable transmission in one line whilst keeping the other line unaltered. The analytical results obtained by means of the Green's function method [9] are confirmed by numerical results using Comsol Multiphysics Software. The waveguides are filled with air, whereas the surrounding metal is made of silver, the corresponding permittivity is given in [10].

2. Analytical and numerical results

From the transmission and reflection coefficients [7], we get the expressions of the different waveguides lengths which should be satisfied in order to realize a complete filtering in one line while the other line is kept unperturbed. In the case of a lossless demultiplexer based on PIT resonances, the geometrical parameters should be taken such that:

$$d_1 = \frac{d}{2} - \frac{\delta}{2}; d_2 = d_5 = \frac{d}{2} + \frac{\delta}{2}; d_3 = d_6 = \frac{d}{2}; d_4 = \frac{d}{2} + \delta \quad (1)$$

Where, $d = d_1 + d_2$ and $\delta = d_2 - d_1$. Similarly, in the case of a lossless demultiplexer based on Fano resonances, the lengths of the waveguides should be chosen such as:

$$d_1 = d_2 = \frac{d_0}{2} - \varepsilon;\ d_3 = d_4 = \frac{d_0}{2} - \frac{\varepsilon}{2};\ d'_0 = d_0 - 3\varepsilon;\ d_5 = d_2$$
$$\text{and } d_6 = d_3. \qquad (2)$$

Figure 2 gives the transmission coefficients T_1 and T_2 through both lines as well as the reflection coefficient R in the input line for the structure depicted in Fig. 1 (a), with $d_0 = d_1 + d_2 = 520$ nm and $\delta = d_2 - d_1 = 100$ nm. The waveguide lengths are given by Eq. (1). One clearly notices that when the transmission in the first output (red curve) is maximal ($T_1 = 0.8$) around 194.12 THz, both the transmission in the second output T_2 (blue curve) and the reflection R (black curve) becomes close to zero (i.e. $T_2 = R \cong 0$). Similarly, when the transmission in the second output (blue curve) is maximal ($T_2 = 0.8$) around 238.82 THz, the transmission in the first output T_1 (red curve) and the reflection R (black) becomes close to zero (i.e., $T_1 = R \cong 0$). Both resonances are of PIT type as they are squeezed between two transmission zeros. Figure 3 gives similar results but for the geometrical parameters given by Eq. (2) (see Fig. 1(a)) with $d_0 = 520$ nm and $\varepsilon = 150$ nm. Equivalently, we observe that when the transmission in the first output (red curve) is maximal ($T_1 = 0.8$) around 134.62 THz, the transmission in the second output T_2 (blue curve) and the reflection R (black curve) vanish (i.e., $T_2 = R = 0$). Similarly, when the transmission in the second output (blue curve) is maximal ($T_2 = 0.8$) around 156.03THz, the transmission in the first output T_1 (red curve) and the reflection R (black curve) vanish (i.e. $T_1 = R = 0$). Both resonances are of Fano type as each of them fall near a transmission zero. Both analytical (full curves) and numerical results (circles) are in good agreement. Figures 1 (b) and (c) give the H_z-field maps in both lines for two filtered PIT resonances at f_1=194.12 THz and f_2=238.82 THz respectively. These modes correspond respectively to a filtered resonance in one line and a stopped resonance in the second line (blue and red curves in Fig.2). Each mode is transmitted in its own line.

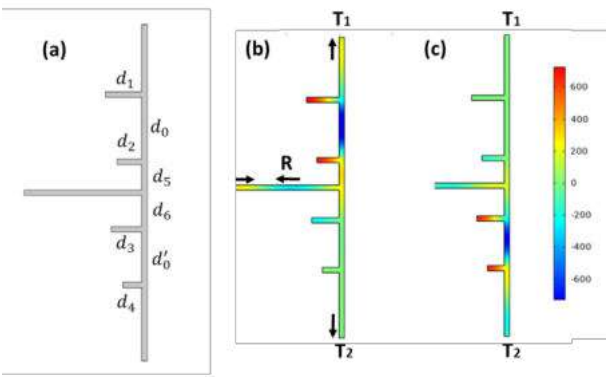

Figure 1: (a) Schematic representation of T-shaped demultiplexer. H_z-field map in both lines for two filtered PIT resonances at f_1=194.12 THz (b) and f_2=238.92 THz (c) in Fig.2.

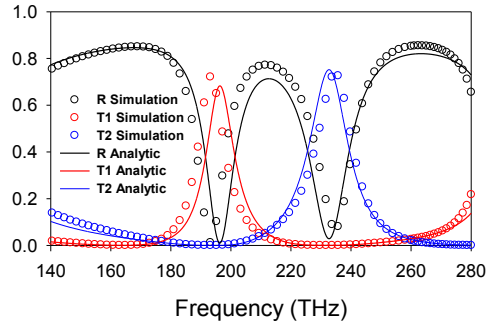

Figure 2: Transmission and reflection coefficients in different outputs for the demultiplexer depicted in Fig. 1 (a) with $d_0=d_1+d_2$= 520 nm and $\delta= d_2-d_1$ = 100nm.

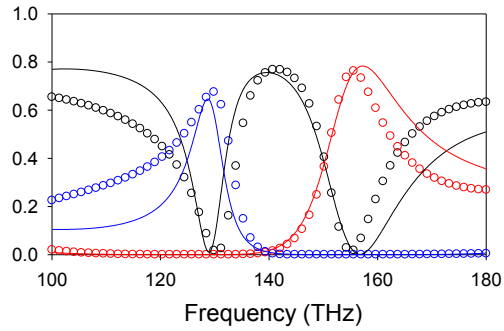

Figure 3: Transmission and reflexion coefficients in different outputs for the demultiplexer depicted in Fig .1 (a) with d_0 = 520 nm and ε = 150 nm.

References

[1] A. E. Miroshnichenko, S. Flach, and Y. S. Kivshar, *Rev.Mod. Phys.* 82, 2257 (2010).

[2] M. Fleischhauer1, A. Imamoglu, and J. P. Marangos, Rev. *Mod. Phys*. 77, 633 (2005).

[3] Q. Xu, S. Sandhu, M. L. Povinelli, J. Shakya, S. Fan, and M. Lipson, *Phys. Rev. Lett*. 96, 123901 (2006).

[4] Y. Sato, Y. Tanaka, J. Upham, Y. Takahashi, T. Asano, and S. Noda, *Nat. Photonics* 6, 56 (2012).

[5] B. Luk'yanchuk, N. I. Zheludev, S. A. Maier, N. J. Halas, P. Nordlander, H. Giessen, and C. T. Chong, *Nature Mater*. 9, 707 (2010).

[6] A. Mouadili, E.H. El Boudouti, A. Soltani, A. Talbi A, Akjouj and B. Djafari-Rouhani, *J. Appl. Phys.* 113, 164101 (2013)

[7] A. Mouadili, E.H. El Boudouti, A. Soltani, A. Talbi, K. Haddadi, A. Akjouj and B. Djafari-Rouhani, *J. Phys. D: Appl. Phys*. 52 075101(2019).

[8] S.X. Xia, X. Zhai, L.L. Wang, B. Sun, J.Q. Liu, S.C. Wen, Opt. Express. 24, 17886 (2016).

[9] J. O. Vasseur, A. Akjouj, L. Dobrzynski, B. Djafari-Rouhani and E. H. El Boudouti, *Surf. Sci. Rep*. 54 1 (2004).

[10] M. Zhang and Z. Wang, Opt. Express 27, 1 (2019).

Near-field spectroscopy of a phonon polariton infrared metasurface

Andrea Mancini[1, *], Christopher R. Gubbin[2], Rodrigo Berte[1], Alberto Politi[2], Yi Li[3], Simone De Liberato[2], and Stefan A. Maier[1]

[1]Chair in Hybrid Nanosystems, Nanoinstitute Munich, Faculty of Physics, Ludwig-Maxilimians-Universität München, 80539 München, Germany
[2]School of Physics and Astronomy, University of Southampton, Southampton, SO17 1BJ, United Kingdom
[3]School of Microelectronics, MOE Engineering Research Center of Integrated Circuits for Next Generation Communications, Southern University of Science and Technology, Shenzhen 518055, China
*corresponding author, E-mail: A.Mancini@lmu.de

Abstract

Surface Phonon Polaritons (SPhPs) can be excited in the Reststrahlen band of polar dielectrics where the dielectric function is negative. Antennas supporting surface phonon polaritons are an alternative to plasmonic resonators in the infrared, due to their reduced losses and higher field confinement. We investigate the near-field response of arrays of Silicon Carbide antennas by means of scattering scanning near field microscopy. Knowledge of the near-field response is needed for many applications requiring coupling of the antennas to other elements.

1. Introduction

The lifetime of plasmonic excitations depends on the material properties of the metal employed, and is related to the typical electron-electron scattering rate. As a consequence, plasmon dephasing happens in the range of tens of femtoseconds, and the quality factor of plasmonic resonances for isolated antennas is rather low. The loss in metallic antennas at optical frequencies has limited their employment in a variety of applications where high quality factors and low losses are required [1]. In the mid-IR polar dielectrics can also behave, from an electromagnetic point of view, as metals due to the presence of a region called the Reststrahlen (RS) band where the real part of the dielectric function ε_1 is negative. The RS band is enabled by the strong dispersive lineshape of ε_1 around a TO phonon. Antennas made of polar dielectrics allow subwavelength confinement and the lifetime of their localized SPhPs resonances are higher than in metals (on the order of picoseconds, two orders of magnitude higher than for plasmons) due to the smaller phonon-phonon scattering rate which determines SPhPs decay. Consequently, SPhPs antennas provide much stronger field confinement and lower losses if compared to analogous plasmonic structures in the IR. Many possible photonic applications require knowledge of the near-field spectral behavior of the system under investigation, which cannot be obtained or easily inferred from far-field measurements. Scattering scanning near field optical microscopy (sSNOM) has been demonstrated as a powerful tool to investigate the near-field properties of optical resonators [3]. Here, we report on the near-field study a metasurface composed of Silicon Carbide (SiC) cylindrical antennas [4].

2. Results and Discussion

One limitation of SPhPs is the narrow frequency band in which they can be excited. SiC is particularly interesting as its RS band is one of the largest of known polar dielectrics, spanning from ω_{TO}=796 cm^{-1} to ω_{LO}=973 cm^{-1}. Moreover, SiC is already employed in power electronics and its processing is CMOS-compatible. Among different geometries, arrays of SiC pillars have attracted considerable attention thanks to their rich electromagnetic response, including broadly tunable modes [5] and nonlinear response [6]. In Fig. 1(a) a SEM image of a portion of one of the arrays is reported, along the experimental FTIR (b) and simulated (c) reflectance spectra for different metasurfaces with varying spacing *P*.

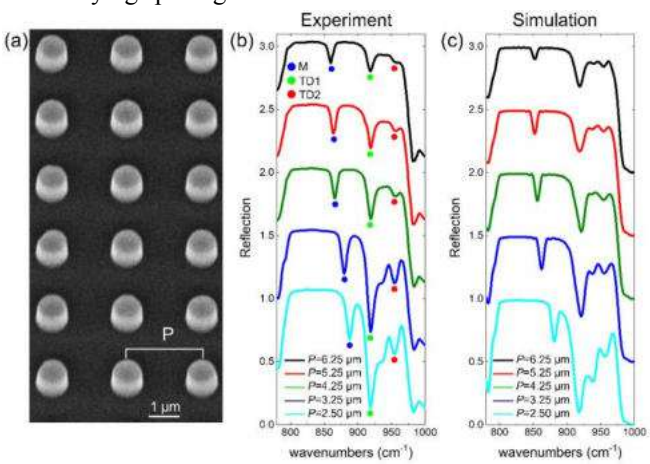

Figure 1: (a) SEM of a portion of a SiC pillars array. Experimental (b) and simulated (c) reflectance spectra for different array spacing *P*. The different modes are highlighted by dots.

The modes of the structure can be described from the coupling of simple longitudinal and transverse resonances of a single pillar to the bare SiC surface supporting SPhPs at ω=951 cm^{-1} [6]. Three main resonances can be identified from the spectra, a monopolar mode (M) redshifting with increasing P and two transverse dipolar resonances (TD1 and TD2) at ω_{TD1}=921 cm^{-1} and ω_{TD2}=955 cm^{-1} independent of P. For P=2.5 μm the field enhancement simulations for the three resonances are reported in Fig. 2.

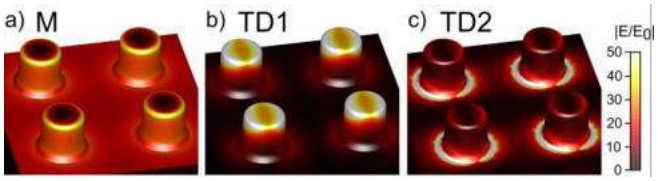

Figure 2: Simulated field profiles for the M mode (a) the TD1 mode (b) and the TD2 mode (c).

We study the near-field response of the arrays by positioning the sSNOM tip either on top of one of the pillars, or on the substrate between them, as shown in Fig. 3.

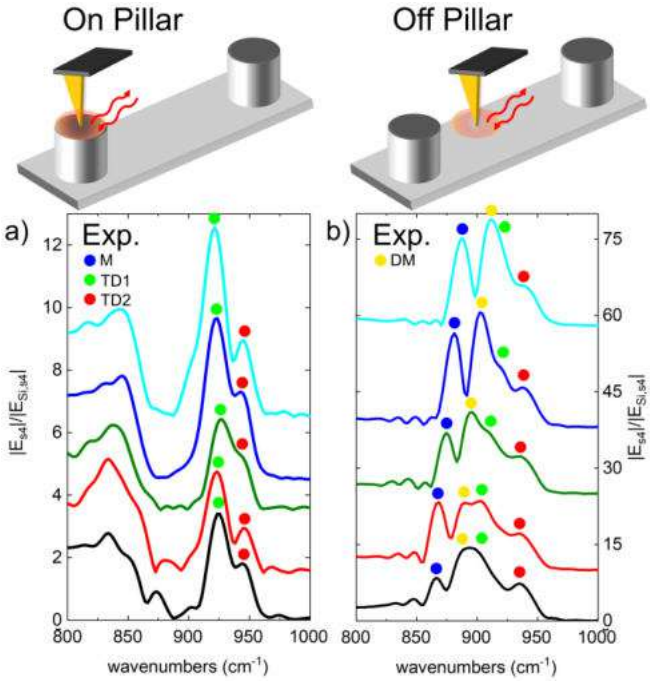

Figure 3: Near-field measurements of the different arrays when placing the AFM tip on top of a pillar (a) or on the substrate between pillars (b).

The response on the pillars is independent of P, as two peaks, marked with green and red dots, at ω_{TD1}=920 cm^{-1} and ω_{TD2}=945 cm^{-1} can be individuated for all P with frequencies matching the far-field measurements. When measuring off pillars the monopolar mode can be identified as the lower energy peak, closely matching the frequency reported in the FTIR far-field data. An additional peak appears in the spectra (yellow dot in Fig. 3(b)), redshifting with the monopolar mode, which has no counterpart in the far-field. This mode arises from the near-field illumination of the tip, which allows excitations of modes that are otherwise "dark" due to having net zero dipole moment. We confirm this with simulations where we take into account the presence of the AFM tip in the form of a metallic sphere located on top of a pillar. To isolate the contribution of the tip we first solve for the pillar in the absence of the sphere with plane wave excitation, and then we use this field as a background that we subtract from the full simulation including the sphere. An additional peak analogous to what observed in the experiments is found in the tip-induced scattering cross section [4].

3. Conclusions

In conclusion, we reported on the near-field study of the spectral response of arrays of SPhPs SiC pillar resonators in the mid-IR by means of sSNOM. The understanding of the near-field spectral response of SPhPs resonators is of critical importance for their employment in any application requiring near-field interaction. We further employ 3D electromagnetic simulations to understand the effect of the sSNOM tip in modifying the response of the SPhPs antennas.

References

[1] J. B. Khurgin, "How to deal with the loss in plasmonics and metamaterials," *Nat. Nanotechnol.*, vol. 10, no. 1, pp. 2–6, 2015.

[2] J. D. Caldwell *et al.*, "Review article Low-loss , infrared and terahertz nanophotonics using surface phonon polaritons," pp. 44–68, 2015.

[3] R. Hillenbrand, T. Taubner, and F. Keilmann, "Phonon-enhanced light-matter interaction at the nanometre scale," *Nature*, vol. 418, no. 6894, pp. 159–162, 2002.

[4] Mancini, Andrea, et al. "Near-field spectroscopy of cylindrical phonon-polariton antennas." ACS nano 14.7, 8508-8517, (2020).

[5] Y. Chen *et al.*, "Spectral Tuning of Localized Surface Phonon Polariton Resonators for Low-Loss Mid-IR Applications," *ACS Photonics*, vol. 1, no. 8, pp. 718–724, 2014.

[6] I. Razdolski *et al.*, "Resonant Enhancement of Second-Harmonic Generation in the Mid- Infrared Using Localized Surface Phonon Polaritons in Subdi ff ractional Nanostructures," 2016

[7] C. R. Gubbin, S. A. Maier, and S. De Liberato, "Theoretical investigation of phonon polaritons in SiC micropillar resonators," vol. 035313, pp. 1–9, 2017.

Large-area self-assembly of anisotropic Palladium nanostructures for SERS applications

Mohammad Navvabpour[1], Pierre Michel Adam[2], Safi Jradi[3], Suzanna Akil[4]

[321]Light, nanomaterials, nanotechnology (L2N - CNRS-EMR 7004), University of Technology of Troyes, Troyes, France
[4]Institute Chemistry Physical and Materials, LCP-A2MC, University of Lorraine, Metz, France
*corresponding author, E-mail: suzanna.akil@univ-lorraine.fr

Abstract

Here, we report for the first time a facile one-step fabrication route of anisotropic palladium nanoparticles (Pd NPs) with high SERS performance by polymer self-assembly.

1. Introduction

Recently Akil et .al have reported ring like structure and also nano cube particles for gold/silver nano particles obtained by a self-assembly shape-controlled technique, simple, fast and independent of reducing agent in two different researches. In this technique, MNPs are formed in a "one step" upon spin coating, on conductor or n doped semi-conductor substrate, of a dispersion of homopolymer (Polymethyl methacrylate) and metallic salt as precursor. There is neither reducing agent or copolymer nor preliminary functionalization of the surface in this fabrication method. In this project we aim to extend this synthesis way to Pd nanomaterials due to the potential of Pd in photocatalysis and the difficulty to produce anisotropic Pd nanoparticles by simple synthesis methods [1-5].

2. Discussion

Anisotropic Pd NPs are spontaneously formed upon the spin coating of Pd precursor-PMMA (polymethyl methacrylate) dispersion on N-doped silicon wafer/ITO due to a rapid evaporation of the volatile solvents from PMMA. Precisely, the spin coating leads first to a self-assembly of PMMA into micelles containing Pd^{2+}, and then the solvents' evaporation leads to the formation of nano porous PMMA film, where Pd NPs are localized inside holes. The substrate conductivity plays a major role in the synthesis mechanism since it allows a spontaneous reduction of the Pd precursor into Pd nanoparticles. The repulsive interaction force between the couple (hydrophilic Pd phase /hydrophobic PMMA phase) and the substrate allows us to control the final size and morphology of the produced nanostructures. In addition, the number of Pd NPs can also be modulated by adjusting the synthesis parameters such as precursor concentration and PMMA solution. A high number of NPs (Figure 1) separated by small gaps was obtained at high Pd precursor concentration and led to high SERS performance substrate despite the weak plasmonic properties of Pd.

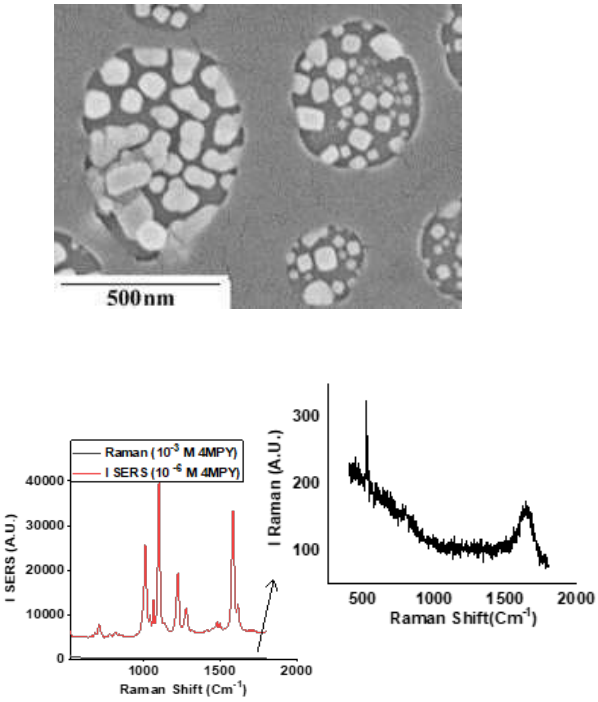

Figure 1. a) SEM images of high-density substrate of closely separated anisotropic Pd NPs. b) SERS of 4-Mercaptopyridine 10-6 M and average Raman spectra of 4-Mercaptopyridine 10-3 M obtained with self-assembly synthesis.

3. Conclusions

In summary, Mono-dispersed anisotropic Pd nano particles has been synthesized using a simple one-step method without any surfactant or reducing agent. With adjusting of synthesis parameters, different morphologies with high SERS performance were obtained.

References

[1] I. Shahine, N. Beydoun., J. J. Gaumet, E. E. Bendeif, H. Magri and S. Akil "Pure, size tunable ZnO nanocrystals assembled into large area PMMA layer as efficient catalyst," Catalysts, Vol. 9, No. 2, 162-186, 2019.

[2] R. Omar, A. E. Naciri and S. Jradi, "One-step synthesis of a monolayer of monodisperse gold nanocubes for SERS substrates." J. Mater. Chem, vol. 5, No. 41, 10813-10821, 2017.

[3] M. Khanafer, A. Issa., S. Akil., T. Hamieh., P. M. Adam and S. Jradi, "A general strategy to incorporate a wide range of salts into ring-like organized nanostructures via polymer self-assembly," RSC Adv, No. 105, Vol. 6, 102843-102852, 2016.

[4] A. Fahes, A. E. Naciri, M. Navvabpour, S. Jradi and S. Akil, "Self-assembled Ag nanocomposites into ultra-sensitive and reproducible large-area SERS-Active opaque substrates," Nanomaterials, No. 8, Vol. 11, 2055-2076, 2021.

[5] S. Akil, R. Omar, D. Kuznetsov, V. Shur, A. E. Naciri and S. Jradi "Advanced large-scale nanofabrication route for ultrasensitive SERS platforms based on precisely shaped gold nanostructures," Nanomaterials, No. 7, Vol. 11, 1806-1824, 2021.

Excitation and Modulation of Surface Plasmon Polaritons at PN++ Junctions

D. A. Genov[1]*, R. K. Vinnakota[2], Z. Dong[3], A. F. Briggs[3], L. Nordin[3], S. R. Bank[3], D. Wasserman[3]

[1] Louisiana Tech University, Department of Physics, Ruston, USA
[2] Troy University, Department of Chemistry and Physics, Troy, USA
[3] University of Texas Austin, Department of Electrical and Computer Engineering, Austin, USA
*corresponding author, E-mail: dgenov@latech.edu

Abstract

We present excitation and active modulation of Surface Plasmon Polaritons (SPPs) at degenerately doped PN++-junction based on lattice matched Indium Gallium Arsenide. The device is experimentally characterized, showing far-field voltage assisted reflectivity modulation for mid-IR wavelengths. Numerical simulations of the device have confirmed the experimental findings and predict data rates of up to 1Gbits/s. Decreeing the device physical dimensions can lead to data rates in excess of 50Gbits/s, thus providing a new pathway toward fast plasmotronic devices.

1. Introduction

Photonics and in particular plasmonics has been recognized as a key technology for fast data communication and computing [1-3]. In this work we present an optoelectronic switch for functional plasmonic circuits based on active control of Surface Plasmon Polaritons (SPPs). The device, which we refer to as Surface Plasmon Polariton Diode (SPPD), consists of a degenerate PN++ semiconductor junction with an active drift-diffusion region formed between two control electrodes (see Fig. 1). Under forward bias minority carriers (electrons) are injected in the P- doped layer and for applied voltage higher than a critical value Vc the P-layer acquires a metal like characteristics impeding the propagation of the SPP across the active region and establishing the OFF state of the device. The lattice matched Indium Gallium Arsenide ($In_{0.53}Ga_{0.47}As$) is identified as the best semiconductor material for the practical implementation of the optoelectronic switch providing high optical confinement, reduced system size and fast operation. A steady-state SPP signal modulation higher than -20dB is predicted, and responsivities in excess of -1000 dB/V for Si and -500 dB/V are expected for applied bias close to a critical values Vc=1.14V for Si and Vc=0.81V for $In_{0.53}Ga_{0.47}As$. The numerical results show a well-defined distinction between the OFF and ON response times, with the former being substantially faster. Consistently, a faster response is observed for the In0.53Ga0.47As device with 3dB data rates in excess of 50Gbit/s. A proof of concept experimental study has been performed to assess the main switching mechanism behind the SPPD operation. Degenerate p-n++ junctions are grown epitaxially on InP and fabricated by spin-doping on Si-on-insulator (SOI) wafers. The devices are characterize both electrically and optically as a function of applied forward bias, with the measured change in reflectivity compared to the theory, see Figure 1.

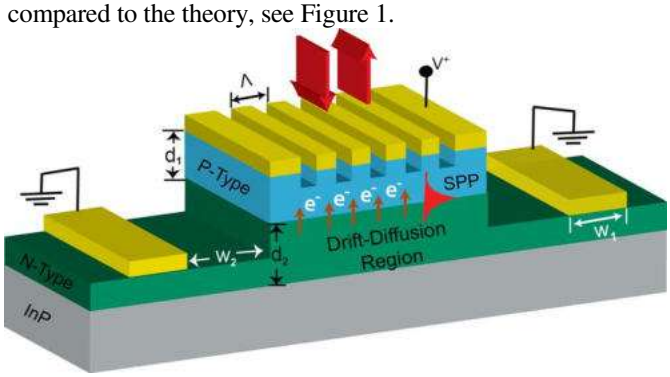

Figure 1: Schematic of the Surface Plasmon Polariton Diode (SPPD). The device consists of a lattice matched Indium Gallium Arsenide PN++-junction grown epitaxially on Indium Phosphide (InP) substrate. A grading with period Λ=2.4 μm is used to couple far-IR incident light to the SPP modes propagating the junction interface.

2. Device characterization

The SPPD device fabrication involves standard UV lithography, dry-etching, and metal deposition. A degenerately doped PN++- junction was grown by molecular beam epitaxy with doping concentrations N_A=1×10^18 [1/cm^3] and N_D=3.4×10^19 [1/cm^3]. Upon fabrication, the SPPD is characterized through polarization-dependent reflectivity measurements using a Bruker v80V Fourier transform infrared (FTIR) spectrometer working in fast-scan mode and normalized to reflection of a gold surface. Figure 2a shows the TE and TM polarization reflectivity spectra of the unbiased device obtained experimentally and compared to the theory. The reflectivity spectra for the TM polarized light shows distinctive dips at λ~6.7μm and λ~11.4μm, whereas for TE polarized light a dip in reflectivity is observed at λ~8.2μm. The observed dip in the TM reflectivity at λ~11.4μm is attributed due to excitation of a SPP at the junction interface, while the dips in the TM reflectivity at λ~6.7μm and TE reflectivity at λ~8.2μm correspond to Fabry-Perot resonances in the dielectric P- layer. As expected, only in the case of TM polarization do we observe an SPP mode propagating at the PN++- junction. To the best of our knowledge this result is

the first experimental demonstration of SPPs at doped semiconductor junctions.

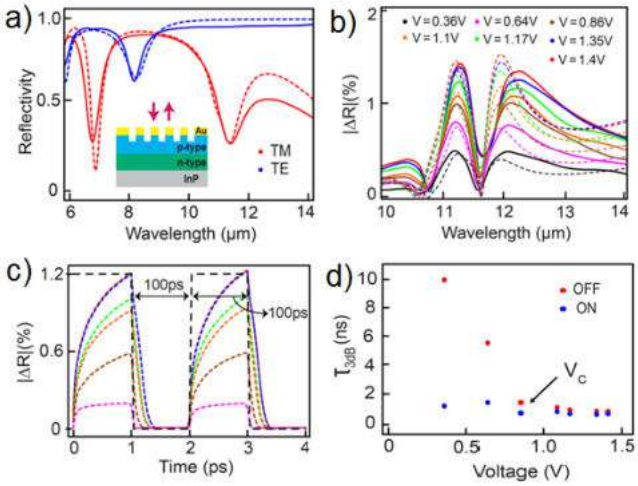

Figure 2: (a) Transverse magnetic (TM) and transverse electric (TE) polarized reflectivity spectra of the SPPD grating device (see insert) under zero bias. (b) The absolute change in reflectivity is experimentally obtained under various forward bias voltages (solid lines) and compared to the self-consistent electro-optic simulations (dashed lines). (c) Far field reflectivity (dashed lines) under step-type of input voltage (dashed black line) with various maximum forward bias voltages. SPPD 3dB response times as function of the applied external bias. In the calculations the operation wavelength is set at λ=12μm.

To assess the SPPD signal modulation, we have performed reflectivity studies under applied forward voltage bias. The numerical (dashed line) and experimental (solid lines) results are depicted in Figure 2b where we plot the absolute change in reflectivity $|\Delta R(\lambda,V)|=|R(\lambda,V)-R(\lambda,0)|$ for a set of forward voltages. As the external forward bias is increased, a far-field reflectivity modulation with respect to the unbiased device is observed. This behavior is consistent with expectations and is revealed both in the experimental data and numerical results. In our earlier theoretical studies [3] we have shown that semiconductor based Surface Plasmon Polariton Diodes (SPPDs) can provide excellent switching rates. To assess the response times of the experimental device, we have used the already validated self-consistent electro-optic model and performed a transient analysis under the input voltage biases used in the reflectivity studies (see Figure 2c). As the SPPD is forward biased, the far-field reflectivity is modulated corresponding to SPP switching OFF. The modulation of the signal increases with increasing bias. A well-defined distinction between the OFF and ON times is observed, with the latter being substantially faster. This distinction can be attributed to the different physical mechanisms that are involved when the device is under forward and zero bias. Namely, the OFF times are governed predominantly by the time of flight of minority carriers (electrons) across the PN++ depletion region while the ON times are facilitated by charge diffusion and recombination in the quasi-neutral regions. The 3dB ON/OFF times as functions of the applied bias are shown is Figure 2d. Close inspection reveals that the OFF times are inversely proportional with the applied external bias for V<Vc=0.87 V, and saturate at ≈0.5ns for V>Vc. This is because the electron injection rate into the P-layer is proportional to the applied bias. The ON times are weakly dependent on the external bias since excess minority carriers in the P-layer are removed by the process of diffusion and charge recombination. Overall, our data shows that for moderate applied voltages (V~Vc), 3dB data rates in excess of 1Gbit/s can be achieved. Finally, it should be noted that further improvement in the switching rates and minimization of the power dissipation can be accomplished by reducing the size of the SPPD drift-diffusion region and varying the P and N++- layers doping concentrations while keeping the SPP operation frequency within the mid-IR spectral range. The potential for such speed up was already studied theoretically [3] where we have shown that optimal SPPD device architectures can provide data rates in excess of 50Gbits/s.

3. Conclusions

We have demonstrated excitation and modulation of Surface Plasmon Polaritons (SPPs) at degenerate semiconductor interfaces. The modulation of the SPP modes under the presence of an external forward bias was studied experimentally and compared to numerical simulations, validating the switching mechanism underlying the device operation. The observed SPP modulation is the result of minority carrier injection across the metallurgical junction. Based on the excellent match between theory and experiment, we have perform time-dependent numerical studied of the SPPD response times under step-type of input bias. Our results show that the current device can support data rates of up to 1Gbit/s, which can be further improved for optimized geometries. Overall, the presented results indicate that SPP modes on degenerate semiconductor junctions can be utilized as signal carriers, an important step toward realization of fast optoelectronic circuit elements.

Acknowledgements

This work has been supported by the National Science Foundation (Award numbers ECCS-1610200 and ECCS-1611231).

References

[1] R. Zia, J. A. Schuller, A. Chandran, and M. L. Brongersma, "Plasmonics: the next chip-scale technology," Mater. Today 9, 20 (2006).

[2] E. Ozbay, "Plasmonics: merging photonics and electronics at nanoscale dimensions," Science 311, 189 (2006).

[3] R. K. Vinnakota, and D. A. Genov, "Active Control of Charge Density Waves at degenerate Semiconductor Interfaces", Scientific Reports 7, 10778 (2017).

[4] Z. Dong, A. Briggs, L. Nordin, R. K. Vinnakota, D. A. Genov, S. Bank, and D. Wasserman, "Electrical modulation of degenerate semiconductor plasmonic interfaces", Journal of Applied Physics 126, 043101 (2019).

Inverse Design of Plasmonic Nano-Antenna

Zhou Zeng[1], Prabhukumar Venuthurumilli[1], Xianfan Xu[1,*]

*corresponding author, E-mail: xxu@ecn.purdue.edu

Abstract

We develop a new method for inverse design of plasmonic nano-antennas. We demonstrate the accuracy of this method for a plasmonic antenna used for heat-assisted magnetic recording (HAMR). We also use non-linear material interpolation to counter the non-physical field amplification, and filtering-and-projection regularization to ensure manufacturability of the design. Successful design of a plasmonic aperture to produce an electric field as small as 60 nm x 30 nm is presented.

1. Introduction

Inverse design of plasmonic structures has only been reported in recent years and is almost exclusively based on frequency-domain solvers such as the Finite Element Method (FEM). FDTD method is not a popular choice in the inverse design of plasmonics due to the problem rooted in plasmonics where numerical error in electromagnetic simulations of plasmonic structures is highest at the metal-dielectric interfaces. we develop a new method of calculating discrete sensitivity with the FDTD method and incorporate this method into the density-based topology optimization framework [1]. The method accepts any objective function that is only dependent of frequency-domain variables, i.e., solutions of Maxwell's equations at a designated frequency. As a result, the method solves similar problems as the wide-spread FEM-based approach which also gives solutions in frequency domain. The accuracy of the method is illustrated through design of a plasmonic nano-antenna to produce a field as small as 60nm x 30 nm.

2. Results and Discussion

Bowtie aperture antennas are known to produce highly localized fields and have potential applications in optical lithography [2] and high density data storage [3]. The enhanced electric fields are confined within only a tiny region of the nanometer length scale near the surface of the nanostructures and decay significantly thereafter. As an example, we use our method to design an antenna to produce a field with a size of 60nm x 30 nm in magnetic material.

Figure 1 shows the evolution of the antenna during the inverse calcuation, for generating an electric filed of the size of 60nm x 30 nm. The material used is gold film of 60 nm thick, and the field is produced in magnetic recording medium whose properties are given in [3]. Figure 2 shows the obtained filed from such an antenna. It is seen that the design can produce a desired field of nanometer size.

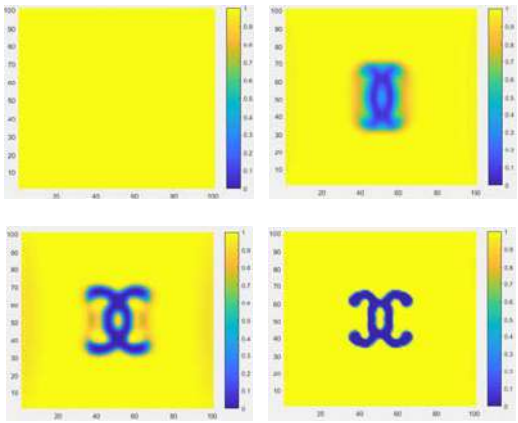

Figuer 1: 1st (top left) 14th (top right) 24th (bottom left) and 34th (bottom right, and final) iterations of the inversion calculation of the antenna for producing a confined field.

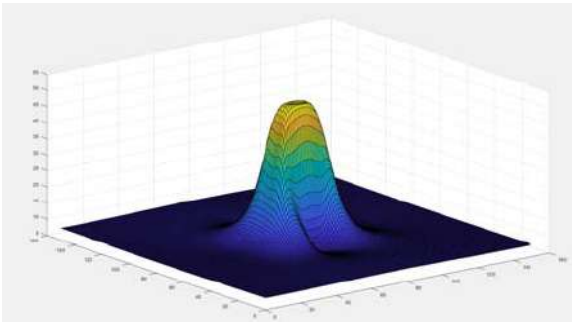

Figure 2: Final field distribution in magnetic recording medium.

3. Conclusions

We present a method for inverse design of plamonic antennas using the FDTD method as the direct solver. A density-based topology optimization method with the FDTD method and the filtering-and-projection regularization is carried out to successfully recover near field patterns of a plasmonic bowtie aperture antenna.

Acknowledgements

Support to this work by ASTC – Advanced Storage Technology Consortium and the National Science Foundation is acknowledged.

References

[1] T. Borrvall, J. Petersson, Topology optimization using regularized intermediate density control, Comput. Methods Appl. Mech. Eng. 190 (2001) 4911–4928. doi:10.1016/S0045-7825(00)00356-X.

[2] X. Wen, A. Datta, L.M. Traverso, L. Pan, X. Xu, E.E. Moon, High throughput optical lithography by scanning a massive array of bowtie aperture antennas at near-field, Sci. Rep. 5 (2015) 16192. doi:10.1038/srep16192.W.M. Kays, M.E. Crawford, *Heat transfer*, Wiley, New York, pp.256-258, 1990.

[3] N. Zhou, X. Xu, A.T. Hammack, B.C. Stipe, K. Gao, W. Scholz, E.C. Gage, Plasmonic near-field transducer for heat-assisted magnetic recording, Nanophotonics. 3 (2014) 141–155. doi:10.1515/nanoph-2014-0001.

Surface Enhanced Visible Absorption of Dye Molecules in the Near-Field of Gold Nano-Antennas

Siham Refki[1] and Zouheir Sekkat[1,2]

University Mohammed V, Rabat, Morocco;
[2]MAScIR-UM6P, Rabat, Morocco;

Surface enhanced absorption was clearly reported to occur in the infrared region of the spectrum of light. In this presentation, we show that it also occurs in the visible region of the spectrum by using a dye, i.e. an azo-dye, which exhibits a good light absorption in that region, and gold nanoparticles, which act as plasmonic nanoantennas, when the azo-dyes and the nanoparticles are incorporated in the bulk of solid films of polymer.

Emergent $\mathcal{PT}$ symmetry and quantum fluctuations in a double-quantum-dot circuit QED set-up

Archak Purkayastha[1], **Manas Kulkarni**[2], , **Yogesh Joglekar**[3],

[1]Trinity College Dublin, The University of Dublin, College Green, Dublin, Ireland
[2]International Center for theoretical Sciences, Tata Institute of Fundamental Research, Bangalore, India
[3]Department of Physics, Indiana University Purdue University Indianapolis (IUPUI), Indianapolis, Indiana, USA

Abstract

Open classical and quantum systems with effective parity-time ($\mathcal{PT}$) symmetry have shown tremendous promise for advances in lasers, sensing, and non-reciprocal devices. However, the microscopic origin of such effective, non-Hermitian models is not well under-stood. In this work, by microscopically modelling a double-quantum-dot-circuit-QED set-up that is realizable in state-of-the-art experiments, we show that a non-Hermitian Hamiltonian emerges naturally, which can be controllably tuned to observe both $\mathcal{PT}$-transition, as well as the effect of quantum fluctuations.

1. The set-up

The schematic diagram of the set-up is given in Fig. 1. The main parts of the set-up consist of the DQD and the two cavities. These are described by the following Hamiltonians

$$\hat{\mathcal{H}}_{DQD} = \frac{\varepsilon}{2}(\hat{c}_1^\dagger\hat{c}_1 - \hat{c}_2^\dagger\hat{c}_2) + t_c(\hat{c}_1^\dagger\hat{c}_2 + \hat{c}_2^\dagger\hat{c}_1) + V\hat{c}_1^\dagger\hat{c}_1\hat{c}_2^\dagger\hat{c}_2,$$
$$\hat{\mathcal{H}}_C = \omega_0(\hat{b}_1^\dagger\hat{b}_1 + \hat{b}_2^\dagger\hat{b}_2) + \lambda(\hat{b}_1^\dagger\hat{b}_2 + \hat{b}_2^\dagger\hat{b}_1),$$
$$\hat{\mathcal{H}}_{DQD-C} = g_0\Theta(t)(\hat{c}_1^\dagger\hat{c}_1 - \hat{c}_2^\dagger\hat{c}_2)(\hat{b}_1^\dagger + \hat{b}_1), \quad (1)$$

where $\Theta(t)$ is the Heaviside function. Here, $\hat{c}_{1,2}^\dagger$ denote fermionic creation operators for sites 1 and 2 that model the DQD, ε is the energy difference between the two sites, t_c is the hopping amplitude between the two sites, and $V > 0$ denotes the capacitive charging energy between the two sites. $\hat{b}_{1,2}$ represent the bosonic creation operators for the two cavities, each with frequency ω_0, that are coupled via a number-conserving hopping process with amplitude λ. Closely following the experimental set-ups, the DQD is dipole-coupled to the (first) cavity it is in with strength g_0 when the cavity is switched on at time $t = 0$. Thus, Eq.(1) captures the microscopic model of the DQD and the two cavities.

Each of the three main components is connected to multiple baths. All baths are modelled by Hamiltonians quadratic in bosonic or fermionic creation and annihilation operators. Each cavity is coupled to its own bosonic bath at inverse temperature β, with $\beta\omega_0 \gg 1$. The presence of these baths lead to a cavity decay rate of κ_1 (κ_1) for the first (second) cavity. Each site of the DQD is coupled to its own

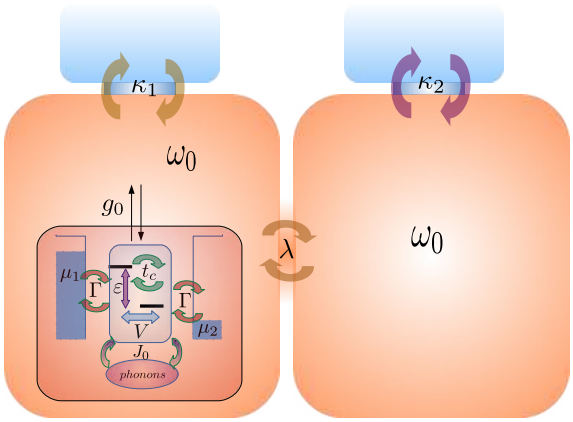

Figure 1: The set-up consists of two cavities connected to each other, with the left cavity having a double-quantum-dot out-of-equilibrium. The double-quantum-dot is configured to give a gain to the left cavity. If the gain is same as the loss of the right cavity, the bosonic system of the cavities have an effective $\mathcal{PT}$ symmetric dynamics.

fermionic lead. The lead coupled to the first (second) site has inverse temperature β and chemical potential μ_1 (μ_2). The strength of coupling to both leads is taken to be same and denoted by Γ. The entire set-up is realizable in state-of-the-art experiments with DQD coupled to circuit-QED cavities. However, to model experimental set-up consistently, we also have to consider that the DQD is dipole-coupled to a phononic bath in the substrate on which it is located [1].

We look at the parameter regime that ensures a resonant DQD, i.e $\omega_0 = \omega_q$; a weak cavity-DQD couplng, i.e. $g_0\sqrt{n_{\text{photons}}} \lesssim \Gamma$ (n_{photons} is the average number of photons in the cavity coupled to the DQD), and

$$\omega_q/2 \ll -\mu_2, \mu_1 \ll V,$$
$$\kappa_1, \kappa_2, \lambda \ll \Gamma \ll \omega_0. \quad (2)$$

In this parameter regime, the it can be shown that, for $\varepsilon > 0$, the DQD will be population inverted in the steady state in the absence of the cavities. The DQD thus acts as a controllable gain medium [2].

2. The effective $\mathcal{PT}$ symmetry

After integrating out the fermionic part and the bosonic baths, we have the effective equations of motion for the bosonic system,

$$i\frac{d}{dt}\begin{pmatrix}\hat{b}_1\\ \hat{b}_2\end{pmatrix} \simeq \mathbf{H}_{\text{eff}}\begin{pmatrix}\hat{b}_1\\ \hat{b}_2\end{pmatrix} + \begin{pmatrix}\hat{\xi}_A\\ 0\end{pmatrix}. \quad (3)$$

The 2×2 non-Hermitian Hamiltonian is given by

$$\mathbf{H}_{\text{eff}} = \begin{bmatrix}\omega_0 - i\kappa_1 + i\Gamma\delta & \lambda(1-\delta)\\ \lambda & \omega_0 - i\kappa_2\end{bmatrix}, \quad (4)$$

where $\delta = 2g^2\Delta N_{ss}/\Gamma^2 \ll 1$ by the choice of our parameters and $\Delta N_{ss} = \langle\hat{N}_1\rangle_{ss} - \langle\hat{N}_2\rangle_{ss}$, is the steady-state population inversion in the DQD in the absence of cavities. Here $\langle\hat{N}_1\rangle_{ss}$ ($\langle\hat{N}_2\rangle_{ss}$) is the population of the higher (lower) energy state of the DQD in steady state in absence of the cavity. The time-dependent quantum noise operator $\hat{\xi}_A(t)$, resulting from the DQD gain, has almost zero mean value, $\langle\hat{\xi}_A(t)\rangle \approx 0$, and a Lorenzian power spectrum for the variance, i.e.

$$\langle\hat{\xi}_A^\dagger(t)\hat{\xi}_A(t')\rangle \simeq g^2\langle\hat{N}_1\rangle_{ss}\int_{-\infty}^{\infty}\frac{d\omega}{2\pi}\frac{2\Gamma e^{i\omega(t-t')}}{(\omega-\omega_0)^2+\Gamma^2}. \quad (5)$$

In all of the equations above, the expectation value represents quantum statistical average, i.e. $\langle O\rangle = \text{Tr}(\rho_{\text{tot}}O)$ where ρ_{tot} is the density matrix for the initial state of the whole set-up. The effective Hamiltonian in Eq. 4 can be tuned to observe both active and passive $\mathcal{PT}$ transition just by tuning the parameters ε and t_c of the DQD and by tuning the parameter λ of the cavities. As can be easily seen from Eq. 3, the effect of the various phases will be observed in the dynamics of the complex quadratures $\langle\hat{b}_\ell(t)\rangle$ ($\ell = 1, 2$). However, our complete microscopic derivation has lead to occurrence of the additional noise term $\hat{\xi}_A(t)$, in consistency with fluctuation-dissipation theorem. The presence of $\hat{\xi}_A(t)$ lets us study the effect of quantum fluctuations on the dynamics of $\mathcal{PT}$-symmetric and $\mathcal{PT}$-broken phases.

As an example, here, in Fig. 2, we show the effect of quantum fluctuations on the active $\mathcal{PT}$-symmetric phase where the eigenvalues of $\mathbf{H}_{\text{eff}}$ are real. The dynamics is shown starting from a state where the cavity with the DQD (gain cavity) is in a coherent state with the other cavity (loss cavity) is empty. The amplitudes of the complex quadratures show periodic oscillations characteristic of the $\mathcal{PT}$-symmetric phase. However, the quantum fluctuations of the quadratures, given by $\langle\hat{n}_\ell(t)\rangle - |\langle\hat{b}_\ell(t)\rangle|^2$, where $\hat{n}_\ell(t) = \hat{b}_\ell^\dagger(t)\hat{b}_\ell(t)$, show linear growth superimposed with oscillations. Similar behavior is seen in the photon current $I(t) = \lambda\text{Im}(\langle\hat{b}_2^\dagger(t)\hat{b}_1(t)\rangle)$, where Im() refers to imaginary part.

3. Conclusions and further work

The set-up of two coupled cavities with a voltage biased DQD in one of them provides a perfect test bed for exploring effective $\mathcal{PT}$-symmetry in the quantum regime, and explore the effect of quantum fluctuations. While not discussed in the above summary, we have also explored the effect of passive $\mathcal{PT}$-transition in input-output experiments. Further, we have been able to show that as a consequence of the passive $\mathcal{PT}$-transition, loss induced lasing can be observed in the set-up.

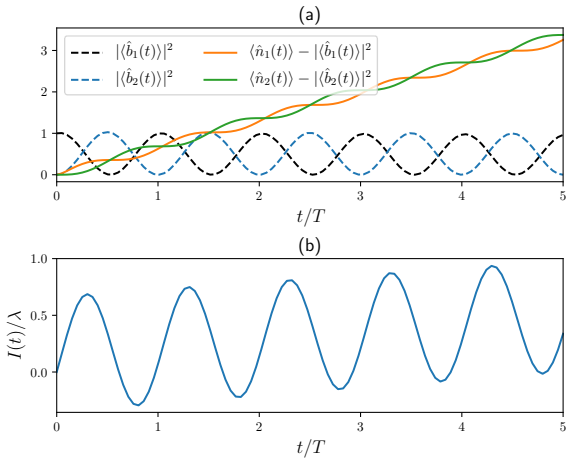

Figure 2: Oscillatory dynamics of the cavity operator expectation values in the $\mathcal{PT}$-symmetric regime with empty loss cavity and a coherent state in the gain cavity. (a) The quadrature magnitudes show oscillations with period $T_\Lambda = 2\pi/\Delta\Lambda$. On the other hand, quantum fluctuations show a linear growth with superimposed oscillations with the same period. (b) Dynamics of the photonic current $I(t)$ also shows linear growth with superimposed oscillations.

4. Acknowledgements

A.P acknowledges funding from European Research Council Starting Grant ODYSSEY (Grant Agreement No.758403) of Prof. John Goold, Trinity College, Dublin.

References

[1] T. R. Hartke, Y.-Y. Liu, M. J. Gullans, and J. R. Petta, Phys. Rev. Lett. **120**, 097701 (2018).

[2] Y.-Y. Liu, J. Stehlik, C. Eichler, M. J. Gullans, J. M. Taylor, and J. R. Petta, Science **347**, 285 (2015).

Integrated single photons sources based on tapered optical nanofibers

Alberto Bramati[1]

[1]Laboratoire Kastler Brossel, Sorbonne Université, CNRS UMR8552, Ecole Normale Supérieure, Collège de France, 75005 Paris, France
*corresponding author, E-mail: alberto.bramati@lkb.upmc.fr

Abstract

We present the optical and quantum properties of highly efficient perovskite nanocubes and discuss our strategy towards a compact integrated single photon source.

1. Introduction

The interest in perovskite nanocrystals such as CsPbBr3 for quantum applications has rapidly increased, after the demonstration that they can exhibit very efficient single photon emission. The main drawback of these emitters is their photostability under optical excitation.

2. Discussion

We present a full characterization of the quantum properties of highly efficient perovskite nanocubes synthesized with a method which ensures an increased photostability. These emitters exhibit reduced blinking together with a strong photon antibunching. Remarkably these features are almost not affected by the increase of the excitation intensity well above the emission saturation levels.

3. Conclusions

We will discuss the different strategies we are pursuing to develop hybrid photonic devices by coupling single nanoemitters with photonic structures such as deep parabolic mirrors [1] and tapered nanofibers [2]. In particular the deposition of a single emitter on a nanofiber and the observation of single photon statistics through the guided mode of the fiber will be reported, showing the high potential of this platform for the realization of a compact integrated single photon source.

Finally we will show how this hybrid system is a very promising playground for novel chiral optics experiments, including a spin-orbit coupling effect for light [3].

References

[1] V. Salakhutdinov. M. Sondermann, L. Carbone, E. Giacobino, A. Bramati, G. Leuchs, Single photons emitted by nanocrystals optically trapped in a deep parabolic mirror, *Phys. Rev. Lett.* 124, 013607 (2020)

[2] S. Pierini, M. D'Amato, M. Goyal, Q. Glorieux, E. Giacobino, E. Lhuillier, C. Couteau, A. Bramati, Highly photo-stable Perovskite nanocubes: towards integrated single photon sources based on tapered nanofibe *ACS Photonics* 7, 2265-2272 (2020)

[3] M. Joos, C. Ding, V. Loo, G. Blanquer, E. Giacobino, A. Bramati, V. Krachmalnikoff and Q. Glorieux, Polarization Control of Linear Dipole radiation using an Optical Nanofiber, *Phys. Rev. Applied,* 9, 064035 (2018)

Plasmonic nanoantennas and their applications

Pierre Berini

School of Electrical Engineering and Computer Science, University of Ottawa, Ottawa, Canada
Department of Physics, University of Ottawa, Ottawa, Canada
Centre for Research in Photonics, University of Ottawa, Ottawa, Canada
*corresponding author, E-mail: berini@eecs.uottawa.ca

Abstract

We review recent work on plasmonic nanoantennas and their applications in nonlinear optics and in optoelectronics.

1. Introduction

Nanometallic structures, such as resonant plasmonic nanoantennas, are essential to the conversion of light to surface plasmon-polaritons (SPPs) localized to ultra-small volumes [1]. Such structures can provide highly enhanced fields, strong confinement, high surface sensitivity, and can double as a device electrode for applying voltages or passing currents to active regions in optoelectronic devices. Here we review some of their many applications, in the areas of plasmon-enhanced nonlinear optics [2-5] and opto-electronics [6-9].

2. Applications in nonlinear optics

In nonlinear optics, plasmon enhancement can be applied to the pump [2], or to the nonlinear emission [3-5], through spectral alignment. An advantage of the former is that all nonlinear processes involving the pump are enhanced, but a disadvantage is that the pump, typically of high intensity, can damage the nanostructures. Nonetheless, such enhancement was exploited in high-harmonic generation via re-collision radiation in Si [2], where a 10× enhancement was observed for all harmonics emitted up to the 9th.

Alternatively, applying plasmon enhancement to the nonlinear emission by designing them to be resonant with the emission is advantageous because the latter is typically weak, and the structures are non-resonant with the pump so are less susceptible to damage. Such enhancement was exploited in Raman scattering experiments [3-5], where the nanoantennas were spectrally-aligned with the Stokes wavelengths of graphene. Under this scenario, single-antenna scattering cross-section enhancements of over 500× were observed [5].

3. Applications to optoelectronics

In optoelectronics, plasmon enhancement can be exploited to improve the performance of, *e.g.*, electro-optic modulators [6], photodetectors [7], and beam-steering devices [8-10]. A key requirement is for the plasmonic enhancement to overlap strongly with the active region of the device, which requires that the nanostructure also operate as a device electrode. Fig. 1 shows such a structure, consisting of an array of Au nanoantennas contacted perpendicularly by electrical contact lines. The contact lines are centred on the nanoantennas (dipoles), which ensures that they are minimally invasive optically, due to their orthogonal alignment relative to the incident polarisation which is along the nanoantenna axes. Structures such as these are very promising for beam steering, as each row can be routed to an individual contact such that a 1D phase gradient is applied over the array [8]. Nanostructures that consist of holes in a metal film are also of significant interest, especially arrangements of nanoholes (*e.g.*, heptamers), which can be fabricated via focussed ion beam milling because they exhibit interesting and useful Fano resonances [11, 12].

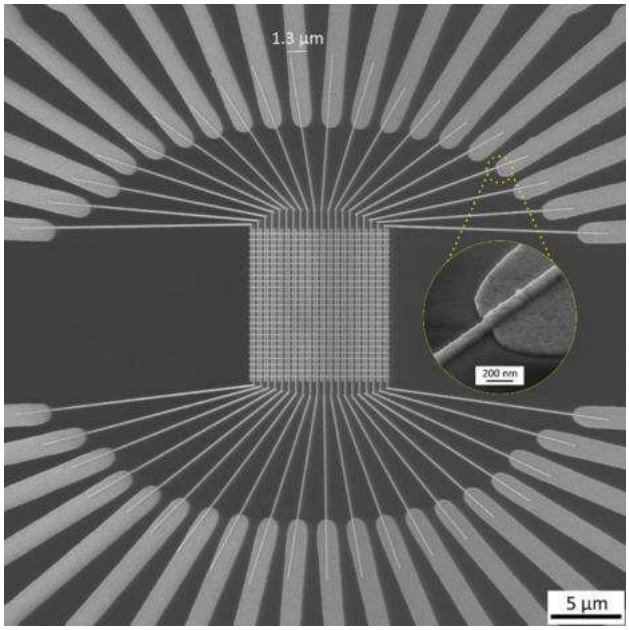

Figure 1: HIM image demonstrating overlay alignment of a 10 × 10 µm^2 gold nanoantenna array and its connection to 40 gold fingers on a pre-existing fan-out microstructure. Inset: Magnified image acquired at a tilt angle of 54° reveals step-height coverage of a fan-out finger by a nanoscale connector. The structures were fabricated on a fused silica substrate.

4. Conclusions

Resonant plasmonic nanoantennas are useful for the conversion of light to SPPs localized to ultra-small volumes. They provide highly enhanced fields, strong confinement, high surface sensitivity, and can double as a device electrode for applying voltages or passing currents to active regions in optoelectronic devices.

References

[1] Bharadwaj, P., Deutsch, B., Novotny, L., *Adv. Opt. Photonics* 1, 438-483, 2009

[2] Vampa, G., Ghamsari, B. G., Siadat Mousavi, S., Hammond, T. J., Olivieri, A., Lisicka-Skrek, E., Naumov, A., Villeneuve, D. M., Staudte, A., Berini, P., Corkum, P. B., *Nature Physics* 13, 659, 2017

[3] Ghamsari, B. G., Olivieri, A., Variola, F., Berini, P., *Nanophotonics* 3, 363, 2014

[4] Ghamsari, B. G., Olivieri, A., Variola, F., Berini, P., *Phys. Rev. B* 91, 201408, 2015

[5] Al-Shehab, M., Ghamsari, B. G., Berini, P., *J. Opt. Soc. Am. B*, 36, F49, 2019

[6] Olivieri, A., Chen, C., Hassan, S., Lisicka-Skrzek, E., Tait, R. N., Berini, P., *Nano Letters* 15, 2304-2311, 2015

[7] Alavirad, M., Olivieri, A., Roy, L., Berini, P., *Optics Express* 24, 22544-22554, 2016

[8] Calà Lesina, A., Goodwill, D., Bernier, E., Ramunno, L., Berini, P., *IEEE J Sel. Top. Quant. Electr*. 27, 4700116, 2021

[9] Calà Lesina, A., Goodwill, D., Bernier, E., Ramunno, L., Berini, P., *Optics Exp.* 28, 31637, 2020

[10] Rashid, S., Walia, J., Northfield, H., Hahn, C., Olivieri, A., Calà Lesina, A., Variola, F., Weck, A., Ramunno, L., Berini, P., *Nano Futures* 5, 025003, 2021

[11] Hahn, C., Hajebifard, A., Berini, P., *Nanophotonics* 9, 393-399, 2020

[12] Hajebifard, A., Hahn, C., Walia, J., Suleman, H., Variola, F., Weck, A., Berini, P., *J. Appl. Phys*. 129, 033103, 2021

Large scale metasurfaces: from plasmonics to photon harvesting in 2D semiconductor layers

Maria Caterina Giordano[1*], Matteo Gardella[1], Matteo Barelli[1], Giorgio Zambito[1], Giulio Ferrando[1], Pham Duy Long[2], Nguyen Si Hieu[2], Francesco Buatier de Mongeot[1]

[1] Dipartimento di Fisica, Università di Genova, I-16146 Genova, Italy
[2]Institute of Materials Science, Vietnam Academy of Science and Technology, Hanoi, Vietnam
*corresponding author, E-mail: giordano@fisica.unige.it

Abstract

The nanofabrication of large-area optical metasurfaces with tunable optoelectronic response is crucial in many fields ranging from plasmonics to energy conversion. Here the engineering of self-organized plasmonic nanostripe antennas will be demonstrated, showing their performances in photo-degradation of polluting molecules. In parallel, the capability to strongly couple light to large area (cm^2 scale) ultra-thin semiconductor layers will be shown. Thanks to nanoscale re-shaping of the interface to form flat-optics nanogratings superior photon harvesting performances can be achieved with strong impact in photonics and energy conversion.

1. Introduction

The engineering of metasurfaces based either on plasmonic nanoantennas or on atomic two-dimensional (2D) materials is currently a very active field of research with a strong impact in optoelectronics, sensing, and nanophotonics [1,2]. A recent trend in the field aims to increase the complexity of lithographically designed metasurfaces for sensing and optical spectroscopies to photo-conversion. However, in order to scale-up these promising configurations to real-world devices and applications, alternative large-area approaches are attracting an increasing attention. Here we demonstrate the engineering of large-scale metasurfaces based on self-organized plasmonic nanoantennas [3,4]. The plasmonic response of self-organized arrays of nanoantennas is tuned in order to boost the photo-degradation of polluting molecules in solution, with strong impact in photochemistry [5]. Within a parallel research line, large-scale flat-optics MoS_2 nanogratings are developed demonstrating broadband photon harvesting [6,7] with strong impact in new-generation photonic and energy conversion devices.

2. Results and discussion

Self-organized plasmonic metasurfaces are fabricated with a novel large area (cm^2) approach exploiting the ion beam induced wrinkling in glass substrates for the synthesis of transparent faceted nanopatterns [1]. These templates are ideal for the maskless confinement of quasi-one dimensional (1D) arrays of plasmonic nanostripes (Fig. 1). Controlled tuning of localized plasmon resonances from the visible to the Near- and Mid-IR can be achieved by tailoring nanoantennas shape and/or light polarization, thus demonstrating competitive sensing performances in SEIRA [2], SERS [3], and plasmonic color routing [4]. Very recently, the plasmon-enhanced photobleaching of dye molecules has been shown, thus opening new avenues in phochemistry and energy storage [5].

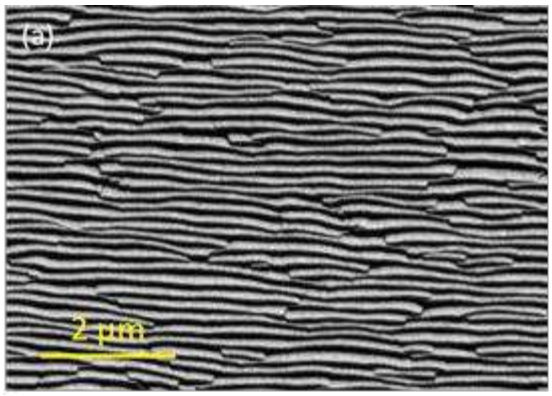

Figure 1 Self-organized plasmonic nanostripe arrays (top-view SEM image).

3. Conclusions

In conclusion, we demonstrated the self-organized engineering of anisotropic arrays of plasmonic nanoantennas supporting tunable plasmonic response and near-field enhancement for sensing. We have shown the possibility to engineer plasmonic antennas featuring plasmon enhaced photobleaching, paving the way for color routing in novel large-scale flat-optics components.

Acknowledgements

M.C. Giordano, F. Buatier de Mongeot and, P. D. Long acknowledge support from MAECI within the bilateral Italy – Vietnam project, Progetti di Grande Rilevanza 2021-2023 and from Università di Genova within BIPE 2020 project.

References

[1] M.C. Giordano, F. Buatier de Mongeot, Anisotropic Nanoscale Wrinkling in Solid State Substrates. *Adv. Mater.* 30.30, 1801840, 2018.

[2] M.C. Giordano et al. Self-Organized Nanorod Arrays for Large-Area Surface-Enhanced Infrared Absorption. *ACS Appl. Mater. Interf.* 12(9), 11155, 2020.

[3] M. Barelli, et al. "Self-organized nanogratings for large-area surface plasmon polariton excitation and surface-enhanced Raman spectroscopy sensing." *ACS Applied Nano Materials* 3 (9) , 8784, 2020.

[4] M. Barelli et al. Color Routing via Cross-Polarized Detuned Plasmonic Nanoantennas in Large-Area Metasurfaces. *Nano Lett.*, 20(6), 4121, 2020.

[5] M. Barelli et al. Wavelength-Dependent Plasmonic Photobleaching of Dye Molecules by Large-Area Au Nanostripe Arrays, Under review

[6] C. Bhatnagar et al., Ultra-broadband photon harvesting in large-area few-layer MoS_2 nanostripe gratings. *Nanoscale* 12(48), 24385, 2020.

[7] C. Bhatnagar et al., Tunable Light Harvesting in Nanorippled MoS2 Ultrathin Films." *ACS applied materials & interfaces* 13 (11) 13508, 2021.

Towards efficient detection and spectroscopy of photons emitted by Er^{3+} ions in silicon

A Zilli[1], M. Castriotta[1], M. Celebrano[1], G. Ferrari[1], L. Duò[1], M. Finazzi[1], and E. Prati[2]

[1] Politecnico di Milano, Physics Department, 20133 Milano, Italy
[2]Istituto di Fotonica e Nanotecnologie, Consiglio Nazionale delle Ricerche, Italy
*corresponding author, E-mail: marco.finazzi@polimi.it

Abstract

We develop a highly sensitive apparatus for efficient room temperature detection of the emission by Er^{3+} ions co-implanted with oxygen atoms in a Si substrate. Our setup proves to be capable of detecting a lower bound value for the emission intensity of about 10^4 photons/s, corresponding to an ion surface concentrations down to 10^{12} cm^{-2}. Yet, the open challenge we aim here is to retrieve the spectroscopic fingerprint of Er^{3+} with high resolution at these low concentrations.

1. Introduction

The demand for single photon sources at the telecom wavelength, which follows from the consistent development of quantum networks based on commercial optical fibers, makes $Er:O_x$ centers in silicon still a viable resource thanks to the optical transition of Er^{3+}: $^4I_{13/2} \rightarrow {}^4I_{15/2}$. Ultra-low doses of implanted atoms in semiconductor nanostructures for both electronic [1–5] and optoelectronic devices [6-9] can achieve the limit of single atom doping by single ion implantation method. Yet, to date, the investigation and implementation of such systems remains hindered by its extremely low emission rate. We have recently observed room temperature photoluminescence [9] resonant at 1550 nm at concentrations down to 10^{12} cm^{-2}. Here, we report on the development of a state-of-the art microscpectroscopy which allows to retrieve the spectral fingerprint of extremely low concentration of Er^{3+} ions.

2. Results

We recently reported on the room-temperature photoluminescence (PL) at the telecom wavelength ($\lambda_{PL} \approx 1540$ nm) of very low implantation doses of Er:Ox in Si. The emitted photons, excited by a laser centered at $\lambda_{EX} = 792$ nm, are collected by a custom-made inverted confocal microscope. The lower-bound number of detectable emission centers within our diffraction-limited illumination spot was estimated to be down to about 10^4 using an InGaAs single photon avalanche diode (SPAD) [8]. This has allowed us estimating an emission rate per individual ion of about 4×10^3 photons/s, which is in good agreement with other values reported in literature [10]. Yet, retrieving the spectroscopic fingerprint of Er3+ at these extremely low concentrations and in confined devices remains to date an open challenge [11]. Here, we will report on our last experimental efforts obtained using our inverted confocal microscope equipped with a reflective high numerical aperture (NA) objective (NA = 0.65) and coupled with a Short-Wave InfraRed (SWIR) spectrometer equipped InGaAs CCD camera (Andor Kymera 328i + iDus 490).

We will show electroluminescence maps and emission spectra from photodiodes based on Er-doped silicon realized within the QUASIX project funded by the Italian Space Agency.

These preliminary studies are conducted with the aim of realizing Er-based single photon source for quantum information technology applied in space.

Acknowledgements

This work was carried out within the QUASIX project (2019-5-U.0) funded by the Italian Space Agency (ASI) through the call “Nuove idee per la componentistica spaziale del future”.

References

[1]E. Prati; T. Shinada “Atomic scale devices: Advancements and directions., 1.2.1–1.2.4 *[In Proceedings of the 2014 IEEE International Electron Devices Meeting, San Francisco, CA, 2014]*

[2]E. Prati and T. Shinada Eds., *Single-atom nanoelectronics* Singapore: Pan Stanford Publishing, 2013.

[3] E. Prati, M. Hori, F. Guagliardo, G. Ferrari, and T. Shinada, *Nature Nanotechnology*, vol. 7, pp. 443, 2012.
[4] E. Prati, K. Kumagai, M. Hori, and T. Shinada, *Scientific Reports*, vol. 6, pp. 19704, 2016.
[5] E. Prati, Y. Chiba, M. Yano, K. Kumagai, M. Hori, G. Ferrari, T. Shinada, and T. Tanii, in 2015 *Silicon Nanoelectronics Workshop* (SNW) (IEEE, 2015)
[6] E. Prati et al. "Revisiting room-temperature 1.54 μm photoluminescence of ErOx centers in silicon at extremely low concentration", in 2017 *Silicon Nanoelectronics Workshop* (SNW) (IEEE, 2017)
[7] Y. Shimizu, et al"Atom probe study of erbium and oxygen co-implanted silicon", in 2017 *Silicon Nanoelectronics Workshop* (SNW) (IEEE, 2017)
[8] M. Celebrano et al., "1.54 μm photoluminescence from Er:Ox centers at extremely low concentration in silicon at 300 K." Opt. Lett. vol. 42, pp. 3311–3314, 2017.
[9] M. Celebrano et al. "Room Temperature Resonant Photocurrent in an Erbium Low-Doped Silicon Transistor at Telecom Wavelength." Nanomaterials vol. 9, no.3, pp. 416, 2019.
[10] G. N. van den Hoven, J. H. Shin, A. Polman, S. Lombardo and S. U. Campisano. J. Appl. Phys. Lett. 78, 2642-2650, 1995.
[11] B. Kalinic, T. Cesca, S. Mignuzzi, A. Jacassi, I. G. Balasa, S. A. Maier, R. Sapienza, and G. Mattei "All-Dielectric Silicon Nanoslots for Er^{3+} Photoluminescence Enhancement" Phys. Rev. Applied 14, 014086, 2020.

Magnetoplasmonic nanocavities for the enhanced magnetic control of light polarization via hybridization with dark plasmons

Paolo Vavassori[1,2,*], Andrey Chuvilin[1,2], Alberto López-Ortega[3], Nicolò Maccaferri[4], Mario Zapata-Herrera[5], Matteo Pancaldi[6]

[1]CIC nanoGUNE BRTA, Donostia–San Sebastian 20018, Spain
[2]IKERBASQUE, Basque Foundation for Science, Bilbao 48013, Spain
[3]Universidad Pública de Navarra, Campus de Arrosadía, Pamplona 31006, Spain
[4]Umeå University, Sweden and University of Luxembourg
5 Materials Physics Center, Donostia-San Sebastian 20018, Spain
[6]Elettra Synchrotron Trieste, AREA Science Park 34149 Basovizza, Trieste, Italy
* corresponding author, E-mail: p.vavassori@nanogune.eu

Abstract

Magneto-optical (MO) effects are widely used in studying magnetic materials as well as to realize optical devices exploiting non-reciprocal propagation of light. Enhancing MO effects is crucial for size reduction of key photonic devices based on non-reciprocal propagation of light and to enable active nanophotonics. Here, we disclose an approach that exploits multipolar Fano resonances excitable in symmetry broken magnetoplasmonic nanocavities and arising from the hybridization of dark plasmons with dipolar plasmonic resonances to achieve an unprecedented amplification of magneto-optical activity.

Controlling the PT Symmetry of Non-Hermitian Graphene Dirac Plasmons and its Application to Terahertz Lasers

Taiichi Otsuji[1]*

[1]Research Institute of Electrical Communication, Tohoku University, Sendai. Japan
*Corresponding author, E-mail: otsuji@riec.tohoku.ac.jp

Abstract

Graphene has a unique electronic band structure that is linearly dispersed and gapless. As a result, both electrons and holes behave as relativistic charged particles of massless Dirac fermions. The quantum of plasma oscillation of these Dirac electrons is called the graphene Dirac plasmon (GDP), which can dramatically enhance the interaction of terahertz (THz) photons with graphene Dirac fermions. We have proposed an original current-injection graphene THz laser transistor, demonstrated single-mode THz laser oscillation at 100 K[1-3)], and discovered and demonstrated the THz giant gain enhancement effect by graphene Dirac plasmons[4-6)]. However, in order to realize room temperature high intensity THz lasing and ultrafast modulation operation, which are necessary for the next generation 6G and 7G wireless communication systems, further breakthroughs are needed. We introduce completely new physics and principles to simultaneously break through the limits of quantum efficiency and high-speed modulation operation by actively controlling the parity and time-reversal (PT) symmetry[6)] of GDPs with nanostructures and applied voltages. In quantum mechanics, even if the system is non-Hermitian, real solutions are obtained if it preserves the PT symmetry. The PT symmetry is expressed by a pair of complementary gain and loss elements. This gain-loss balance leads to the existence of exceptional points at the real frequency axis in the exact PT-phase, resulting in the extraordinary frequency response of spectral singularity like 'unidirectionality'; the incident from the gain port gives normal transmission/reflection whereas the incident from the loss port gives a perfect transmission without reflection[7)]. This extraordinary anisotropic wave propagation behavior has opened a new paradigm in laser physics like active control of the laser cavity Q values in various materials[8)] including graphene metamaterials[9-11)]. In this talk, we will present new ideas on the operating principle and device structure of graphene plasmonic laser transistors[12)] with high radiation intensity and ultrafast modulation capability operating at room temperature in the THz frequency band.

This work was supported by JSPS KAKENHI #16H06361 and #20K20349, Japan.

References

1) V. Ryzhii, M. Ryzhii, and T. Otsuji, J. Appl. Phys. 101, 083114 (2007).
2) T. Otsuji, S. Boubanga Tombet, A. Satou, M. Ryzhii, and V. Ryzhii, IEEE J. Sel. Top. Quantum Electron. 19, 8400209 (2013).
3) D. Yadav, G. Tamamushi, T. Watanabe, J. Mitsushio, Y. Tobah, K. Sugawara, A.A. Dubinov, A. Satou, M. Ryzhii, V. Ryzhii, and T. Otsuji, Nanophoton. 7, 741-752 (2018).
4) T. Watanabe, T. Fukushima, Y. Yabe, S.A. Boubanga Tombet, A. Satou, A.A. Dubinov, V. Ya Aleshkin, V. Mitin, V. Ryzhii, and T. Otsuji, New J. Phys. 15, 075003 (2013).
5) S. Boubanga-Tombet, W. Knap, D. Yadav, A. Satou, D.B. But, V.V. Popov, I.V. Gorbenko, V. Kachorovskii, and T. Otsuji, Phys. Rev. X 10, 031004 (2020).
6) M.-A. Miri, and A. Alu, Science 363, eaar7709 (2019).
7) H. Ramezani and T. Kottos, Phys. Rev. A 82, 04383 (2010).
8) M.-A. Miri, and A. Alu, Proc. IEEE 108, 628-654 (2020).
9) W. Zhang, T. Wu, and X. Zhang, Sci. Rep. 7, 11407 (2017).
10) M. Sakhadari, M. Farhat, and P.Y. Chen, New J. Phys. 19, 065002 (2017).
11) O.A. Zhernovnvkova, O.V. Popova, G.V. Deynychenko, T.I. Dynichenko, and Y.V. Bludov, J. Phys.: Condens. Matter 31, 465301 (2019).
12) T. Otsuji et al., Nanophoton. (2022) early access. doi: 10.1515/nanoph-2021-0651

Scalable quantum dot single-photon sources

L. Midolo*

Center for Hybrid Quantum Networks (Hy-Q), Niels Bohr Institute,
University of Copenhagen, Blegdamsvej 17, DK-2100 Copenhagen, Denmark
*corresponding author, E-mail: midolo@nbi.ku.dk

Abstract

Deterministic sources of single photons are key elements for quantum information processing, simulation, and computing. Implementing a scalable photonic integrated platform featuring quantum emitters and circuits is, however, challenging. I will present a photonic integrated circuit based on dual-mode waveguides for the resonant excitation of two self-assembled InAs quantum dots, paving the way to the integration of multiple sources on a chip. Our plug-and-play waveguide-based source can generate streams of pure and indistinguishable single photons on-demand, so that a planar platform for quantum photonic integrated circuits can be realized.

Light induced exotic chiral surface reliefs in azo-polymers

Takashige Omatsu[1,2]

[1]Graduate School of Engineering, Chiba University, Chiba, China
[2]Molecular Chirality Research Center, Chiba University, Chiba, Japan
*corresponding author, E-mail: omatsu@faculty.chiba-u.jp

Abstract

We review the formation of exotic chiral surface reliefs of azo-polymers by irradiation of structured light beams with optical angular momentum, that is orbital and spin angular momentum. Such chiral surface relief will be applied to be advanced chiral metasurfaces.

Structured light beams, including Laguerre-Gaussian (LG), Helical Ince-Gaussian (HIC), and Bessel beam (BB) modes, possess an annular intensity spatial form and an orbital angular momentum (OAM), associated from a helical wavefront with an on-axis phase singularity, as well as non-diffraction property, and self-healing wavefront. Thus, they have been widely studies in a myriad of fields, including optical manipulation, super-resolution microscope, and quantum/optical communications [1,2]. Furthermore, the structured light field allows the orbital motion of the irradiated materials to form nano/micro-scale helical structures [3-6].

Azo-polymers exhibit photo-induced mass transport, originating from an optical gradient force, anisotropic photo-fluidity, and trans-cis photo-isomerization, thereby enabling the formation of photo-induced reversible reliefs which reflect the spatial intensity profile and polarization of the irradiated light [7,8]. Thus, they provide a myriad of applications, for instance, the development of rewritable photonic circuits, including photonic/plasmonic crystals, metasurfaces, and optical data storages.

To date, it is found that stuructured light beams with OAM twist azopolymers to form chiral surface reliefs, reflecting helical wavefronts of the irradiated structured light fields, with the help of spin angular momentum (SAM) associated with circular polarization [9-11]. Furthermore, it is discovered that the structured light beams even without OAM and only with SAM enable the formation of chiral relief [12].

In this work, we review the formation of exotic chiral surface reliefs of azopolymers by employing versatile structured light beams. Also, we address two-photon induced chiral surface reliefs by ultrafast structured light beams.

This study was funded by a Japan Society for the Promotion of Science (JSPS) fellowship (ID: P19352), JSPS KAKENHI (JP16H06507, JP17K19070, JP18H03884, G21K14549), and JST Core Research for Evolutional Science and Technology (CREST) (JPMJCR1903).

References

[1] L. Allen, M. W. Beijersbergen, R. J. C. Spreeuw, J. P. Woerdman, *Phys. Rev. A* **45**, 8185 (1992).
[2] M. J. Padgett, *Opt. Express* **25**(10), 11265–11274 (2017).
[3] K. Toyoda, K. Miyamoto, N. Aoki, R. Morita, T. Omatsu, *Nano Lett.* **12**, 3645−3649 (2012).
[4] K. Toyoda, F. Takahashi, S. Takizawa, Y. Tokizane, K. Miyamoto, R. Morita, T. Omatsu, *Phys. Rev. Lett.* **110**, 143603/1-5 (2013).
[5] J. Lee, Y. Arita, S. Toyoshima, K. Miyamoto, P. Panagiotopoulos, E. M. Wright, K. Dholakia, T. Omatsu, *ACS Photonics* **5**(10) 4156-4163 (2018).
[6] T. Omatsu, K. Miyamoto, K. Toyoda, R. Morita, Y. Arita, K. Dholakia, *Advanced Optical Materials*, **7**(14), 1801672 (2019).
[7] A. Natansohn, P. Rochon, *Chem. Rev.* **102**, 4139 (2002).
[8] H. Ishitobi, M. Tanabe, Z. Sekkat, S. Kawata, *Opt. Express* **15**, 652 (2007).

[9] A. Ambrosio, L. Marrucci, F. Borbone, A. Roviello, P. Maddalena, *Nat. Commun.* **3**, 989 (2012).
[10] M. Watabe, G. Juman, K. Miyamoto, T. Omatsu, *Sci. Rep.* **4**, 4281 (2014).
[11] D. Barada, G. Juman, I. Yoshida, K. Miyamoto, S. Kawata, S. Ohno, T. Omatsu, *Appl. Phys. Lett.* **108**, 051108 (2016).
[12] K. Masuda, S. Nakano, D. Barada, M. Kumakura, K. Miyamoto, T. Omatsu, *Opt. Express* **25**, 12499 (2017).

Dipole-Dipole Coupling Mediated by Lattice Resonances

Alejandro Manjavacas[1,2,*]

[1]Instituto de Óptica (IO−CSIC), Consejo Superior de Investigaciones Científicas, 28006 Madrid, Spain
[2]Department of Physics and Astronomy, University of New Mexico, Albuquerque, New Mexico 87106, United States
*corresponding author, E-mail: a.manjavacas@csic.es

Abstract

Ordered arrays of metallic nanostructures support collective modes known as lattice resonances, which give rise to very strong and spectrally narrow optical responses. Here, we show that, thanks to their collective nature, the lattice resonances of a periodic array of metallic nanoparticles can mediate an efficient long-range coupling between two dipole emitters placed near the array.

Scalable and efficient photonic designs using disordered metamaterial nanounits

Ekmel Ozbay

Electrical and Electronics Engineering Department, Bilkent University, 06800 Ankara, Turkey

Abstract. Subwavelength metamaterial nanounits can efficiently harvest electromagnetic (EM) waves, resulting in near unity light absorption in the narrow or broad frequency range. Thus, in last decades, many applications are interested for these metamaterial-based perfect light absorbers. Although advancements in nanofabrication have allowed for the realization of strong light–matter interaction in a variety of optical nanostructures, the reproducibility and upscaling of these nanounits for large scale applications has remained as a challenge. The most widely employed tool for fabrication of nanounits is electron beam lithography (EBL), a high-cost and large-scale incompatible route. Although nanoimprint lithography (NIL) can be used to pattern nanounits in large areas but this tool is also high-cost, complex and fabrication of packed, high aspect ratio nanodesigns is generally challenging. Bottom-up approaches can be also adopted to obtain these 3D designs, however, these techniques have also material limitation. Due to their ease of manufacture and excellent functionality, the concept of lithography-free planar light perfect absorbers has gotten a lot of interest in recent years in many parts of the EM spectrum. To address this issue, my group has pioneered numerous fabrication techniques over the previous five years.The i) strong interference in planar ultrathin designs[1–3], ii) dewetting induced surface texturing[4], nanohole[5] and nanoparticle formation[6], and iii) oblique angle deposition of nanorods with deep sub-wavelength gaps[7–10], and iv) utilization of densely packed chemical synthesized trapping scaffolds[11–13] are examples of these studies. Later, this disorder tightly packed nanounits have been brought into novel applications.

For this purpuse, first, we explored the material and architecture requirements for the realization of light perfect absorption using these metamaterial designs from ultraviolet (UV) to far-infrared (FIR) wavelength regimes. We show that, by the use of proper material and design configuration, it is possible to realize these lithography-free light perfect absorbers in every portion of the EM spectrum[14]. This, in turn, opens up the opportunity of the practical application of these perfect absorbers in large scale dimensions. In last couple of years, we adopted these lithography-free techniques in many applications including photoelectrochemical water splitting, photodetection, light emission, sensing, filtering and thermal camouflage[2,7–9,11,13,15,16]. This presentation will summarize our recent accomplishments in scaleble photonic and photoelectronic designs for various applications.

References:

1. Ghobadi, A., Hajian, H., Soydan, M. C., Butun, B. & Ozbay, E. Lithography-Free Planar Band-Pass Reflective Color Filter Using Series Connection of Cavities. *Sci. Rep.* **9**, 1–11 (2019).
2. Ghobadi, A. *et al.* Spectrally Selective Ultrathin Photodetectors Using Strong Interference in Nanocavity Design. *IEEE Electron Device Lett.* **40**, 1–1 (2019).
3. Kosger, A. C., Ghobadi, A., Rashed, A. R., Caglayan, H. & Ozbay, E. Generation of additive colors with near unity amplitude using a multilayer tandem Fabry–Perot cavity. *Opt. Lett.* **46**, 3464 (2021).
4. Ghobadi, A. *et al.* Ultra-broadband , wide angle absorber utilizing metal insulator multilayers stack with a multi- thickness metal surface texture. *Sci. Rep.* **7**, 4755 (2017).
5. Ghobadi, A. *et al.* Disordered Nanohole Patterns in Metal-Insulator Multilayer for Ultra-broadband Light Absorption: Atomic Layer Deposition for Lithography Free Highly repeatable Large Scale Multilayer Growth. *Sci. Rep.* **7**, 1–10 (2017).
6. Ghobadi, A., Hajian, H., Rashed, A. R., Butun, B. & Ozbay, E. Tuning the metal filling fraction in metal-insulator-metal ultra-broadband perfect absorbers to maximize the absorption bandwidth. *Photonics Res.* **6**, 168–176 (2018).
7. Yildirim, D. U. *et al.* Disordered and Densely Packed ITO Nanorods as an Excellent Lithography-Free Optical Solar Reflector Metasurface. *ACS Photonics* **6**, 1812–1822 (2019).
8. Eftekhari, Z., Ghobadi, A. & Ozbay, E. Lithography-free disordered metal–insulator–metal nanoantennas for colorimetric sensing. *Opt. Lett.* **45**, 6719 (2020).
9. Eftekhari, Z. *et al.* Strong light emission from a defective hexagonal boron nitride monolayer coupled to near-touching random plasmonic nanounits. *Opt. Lett.* **46**, 1664 (2021).
10. Soydan, M. C., Ghobadi, A., Yildirim, D. U., Erturk, V. B. & Ozbay, E. Deep Subwavelength Light Confinement in Disordered Bismuth Nanorods as a Linearly Thermal-Tunable Metamaterial. *Phys. Status Solidi - Rapid Res. Lett.* **2000066**, 1–6 (2020).
11. Ghobadi, T. G. U. *et al.* Strong Light–Matter Interactions in Au Plasmonic Nanoantennas Coupled with Prussian Blue Catalyst on BiVO4 for Photoelectrochemical Water Splitting. *ChemSusChem* **13**, 2577–2588 (2020).
12. Ulusoy Ghobadi, T. G., Ghobadi, A., Karadas, F. & Ozbay, E. Large scale compatible fabrication of gold capped titanium dioxide nanoantennas using a shadowing effect for photoelectrochemical water splitting. *Int. J. Hydrogen Energy* **45**, 1521–1531 (2020).
13. Soydan, M. C. *et al.* Lithography-Free Random Bismuth Nanostructures for Full Solar Spectrum Harvesting and Mid-Infrared Sensing. *Adv. Opt. Mater.* **8**, 1–11 (2020).
14. Ghobadi, A., Hajian, H., Butun, B. & Ozbay, E. Strong Light − Matter Interaction in Lithography-free Planar Metamaterial Perfect Absorbers. *ACS Photonics* **5**, 4203–4221 (2018).
15. Ghobadi, A., Hajian, H., Gokbayrak, M., Butun, B. & Ozbay, E. Bismuth-based metamaterials: From narrowband reflective color filter to extremely broadband near perfect absorber. *Nanophotonics* **8**, 823–832 (2019).
16. Soydan, M. C. *et al.* Lithography-Free Random Bismuth Nanostructures for Full Solar Spectrum Harvesting and Mid-Infrared Sensing. *Adv. Opt. Mater.* **8**, (2020).

Universal light encoders: artificial intelligence hardware for light processing components and integrated systems

A. B. Lopez[1], F. Getman[1], M. Makarenko[1], Q. Wang[1], A. Fratalocchi[1]
[1]PRIMALIGHT, Faculty of Electrical and Computer Engineering; Applied Mathematics and Computational Science, King Abdullah University of Science and Technology, Thuwal 23955-6900, Saudi Arabia
Andrea.fratalocchi@kaust.edu.sa

Abstract

In this invited talk, I will review our recent theoretical and experimental results in the field of Universal Light Encoders (ULE) artificial intelligence (AI) hardware for a new class of flexible ultra-flat components (thickness < 100nm) for high efficiency (close to unitary) vectorial control of light [1-4]. These devices are supported by a layer of "physical" neural network units in suitably engineered optical nanoresonators. These systems act as universal approximators of arbitrary defined input-output responses, processing information at the speed of light. I will discuss basic optical components and new integrated systems for the real-time processing of high-dimensional visual information.

References

[1] Getman, F., Makarenko, M., Burguete-Lopez, A. *et al.* Broadband vectorial ultrathin optics with experimental efficiency up to 99% in the visible region via universal approximators. *Light Sci Appl* **10,** 47 (2021). https://doi.org/10.1038/s41377-021-00489-7

[2] Makarenko, M., Wang, Q., Burguete-Lopez, A., Getman, F. and Fratalocchi, A. (2021), Robust and Scalable Flat-Optics on Flexible Substrates via Evolutionary Neural Networks. *Adv. Intell. Syst*. **2100105**. https://doi.org/10.1002/aisy.202100105

[3] A. Fratalocchi, A. B. Lopez, M. Makarenko, Q. Wang, F. Getman, HOCULUS Imaging system, US Pat. Appl. No. **63/277,741**

[4] F. Getman and A. B. Lopez and M. Makarenko and A. Fratalocchi, Light processing device based on multi-layer nano-elements, US. Pat. Appl. No. **62/844,416**

Temporal dynamic of strongly coupled epsilon-near-zero media

Mehdi H. Ebrahim[1], Andrea Marini[2], Nathaniel Kinsey[3], Jacob B. Khurgin[4], Lucia Caspani[5], Marcello Ferrera[6], Vladimir M. Shalaev[7], Alexandra Boltasseva[7], Daniele Faccio[8], Matteo Clerici[1]

[1]James Watt School of Engineering, University of Glasgow, G12 8QQ Glasgow, UK
[2]Department of Physical and Chemical Sciences, University of L'Aquila, Via Vetoio, 67100 L'Aquila, Italy
[3]Department of Electrical and Computer Engineering, Virginia Commonwealth University, Richmond, Virginia 23284, USA
[4]Department of Electrical and Computer Engineering, Johns Hopkins University, Baltimore, Maryland 21218, USA
[5]Institute of Photonics, Department of Physics, University of Strathclyde, G1 1RD, Glasgow, UK
[6]Institute of Photonics and Quantum Sciences, Heriot-Watt University, SUPA, Edinburgh EH14 4AS, UK
[7]School of Electrical and Computer Engineering, Purdue University, West Lafayette, Indiana 47907, USA
[8]School of Physics and Astronomy, University of Glasgow, G12 8QQ Glasgow, UK

*corresponding author, E-mail: `matteo.clerici@glasgow.ac.uk`

Abstract: We shall present an overview of our recent investigations into the time-dependent effects observed in transparent conductive oxides photoexcited at the epsilon near zero point. We will then discuss the role of the epsilon-near-zero mode in establishing the temporal dynamics in strongly coupled plasmonic systems.

Dynamically Tuneable Conducting Polymer Nanooptics

Magnus Jonsson[1]

[1]Organic Photonics and Nanooptics Group, Laboratory of Organic Electronics, Linköping University, Sweden
*corresponding author, E-mail: magnus.jonsson@liu.se

Abstract

I will present our recent research showing that organic conducting polymers can be used as a new type of materials for dynamically tuneable nanooptics, including chemically and electrically controlled plasmonic nanoantennas.[1,2]

References:
1. Conductive polymer nanoantennas for dynamic organic plasmonics
S. Chen et al. **Nature Nanotechnology** 2020, 15, 35-40

2. Electrical Tuning of Plasmonic Conducting Polymer Nanoantennas
A. Karki, et al. **Advanced Materials** 2022, 2107172

Quantum dynamics in structured photonic fields

Jonas Wätzel[1], Jamal Berakdar[2]

[1]Institute of Physics, Martin-Luther-Universität Halle-Wittenberg, Germany
*corresponding author, E-mail: jamal.berakdar@physik.uni-halle.de

Abstract

Phase- and polarization-textured laser pulses have been realized in a wide range of frequencies spanning the XUV to the THz regimes. This contribution presents few examples on how to use these pulses or combination thereof to induce new types of optical quantum transitions and/or laser-dressed states. For instance, it is found that electronic toroidal states can be triggered and controlled on the picosecond time scale using polarization-structured THz vector beams [1]. As well, micrometer size gas samples can be magnetized within femtoseconds using a combination of XUV pulse from a free-electron laser combined with an IR laser pulse carrying orbital angular momentum [2,3].

[1] J. Wätzel *et al.* Adv. Quantum Technol., 2: 1800096. https://doi.org/10.1002/qute.201800096 (2019).
[2] J. Wätzel *et al*. Physical Review Letters (2022) at press.
[3] G. De Ninno *et al.* Nature Photonics 14, 554–558 (2020).

Tunable Mie resonances in silicon nanostructures probed with electron energy-loss spectroscopy

Søren Raza

Department of Physics, Technical University of Denmark, Fysikvej, DK-2800 Kongens Lyngby, denmark
E-mail: sraz@dtu.dk

Abstract

In this talk, I will present results on thermo-optic and electromechanical tuning of optical Mie resonances in high-refractive-index silicon nanostructures. Using in situ electron energy-loss spectroscopy, we show that the high thermo-optic coefficient of silicon enables tuning between the near field of Mie resonances supported by silicon nanoparticles in the visible. We also demonstrate an electromechanical platform composed of a silicon nanobeam dimer to electrically tune the optical response.

Riesz-projection based simulation and analysis of resonant photonic devices and machine-learning based parameter optimization

Fridtjof Betz[1], Felix Binkowski[1], Matthias Plock[1], Lilli Kuen[1,2], Phillip Manley[2], Philipp-Immanuel Schneider[2], Martin Hammerschmidt[2], Lin Zschiedrich[2], Sven Burger[1,2]

[1]Computational Nano Optics, Zuse Institute Berlin, Takustrasse 7, 14195 Berlin, Germany
[2]JCMwave GmbH, Bolivarallee 22, 14050 Berlin, Germany
https://www.zib.de/cno
*corresponding author, E-mail: burger@zib.de

Abstract

We present Riesz projection based methods relying on contour integration for efficiently computing quasi-normal modes and modal expansions of near-field and far-field physical quantities. We use a finite-element method based implementation of these methods for the analysis of nanophotonic resonators for quantumoptics applications. We use Bayesian optimization methods for finding best geometry parameters yielding, e.g., resonators with maximized quality factor.

Optoinduced magnetization from the spin and orbital angular momenta of light

Vage Karakhanyan, Clément Eustache, Yannick Lefier, Thierry Grosjean*

FEMTO-ST Institute, CNRS, University of Bourgogne - Franche-Comté, Besançon, France
*corresponding author, E-mail: thierry.grosjean@femto-st.fr

Abstract: We provide a spin and orbital angular momentum representation of the inverse Faraday effect in a metal. We analytically show the role of the spin and orbital angular momenta of light (SAM and OAM, respectively), as well as the spin-orbit interaction (SOI), in the generation of an optoinduced magnetization. We also show that resonances in plasmonic nanoantennas enhance and confine the IFE on the nanoscale, thereby leading to static magnetic fields directly applicable in a vast application domain including all-optical magnetization switching and spin-wave excitation.

Light is known to possess polarization and spatial degrees of freedom, manifested by its linear momentum as well as spin and orbital angular momenta[1]. Remarkably, the SAM of light can be transferred to electrons in matter, a phenomenon which refers to as the IFE [2, 3]. The IFE has attracted much attention for its ability to generate light-induced magnetization, thereby opening the prospect of an ultrafast magnetic data storage and a non-contact excitation of spin-waves. On the basis of a hydrodynamic model of the conduction electron gas [4, 5], we provide a spin and orbital angular momentum representation of the IFE in a metal [6]. The OAM and SOI of light provide additional degrees of freedom in the control of the IFE usually solely attributed to the SAM. We also investigate a resonant IFE within individual nanoantennas [7, 8]. Upon illumination, individual subwavelength gold coaxes and cylinders are shown to develop a strong optomagnetic field on the nanoscale that is controllable by the helicity of the light. In pulse optical regime, this magnetic field is found to reach 0.3 T upon excitation at a light intensity below damage threshold.

Our model shows that both the SAM and OAM contributions to the IFE in the metal bulk rely on an optical drag effect [9]: the underlying optoinduced current densities are proportional to the Poynting energy flow (optical momentum) inside the metal. In the case of an axisymmetric optical system, we find a direct proportionality between the optoinduced drift current at metal surfaces and the radial component of the SAM of light. In the paraxial approximation, the contribution of the SAM vanishes, and the IFE is driven solely by the OAM of light, which is consistent with the interpretation of the spin and orbital angular momenta of purely transverse light fields [10, 11]. We also show that the SOI of light [12] plays a significant role in the IFE. Finally, we numerically quantify the relative contributions of the SAM and OAM to the IFE in a thin gold film illuminated with four different focused beams carrying SAM and/or OAM (see table 1). We find that the SAM of light is the main source of drift current density regardless of the helicity of the incident light. However, the compensation effects between SAM-driven surface and bulk currents of opposite handedness reduce the contribution of the SAM to the observable optoinduced magnetization. Except for circular polarization, the OAM of light is found to be the main contributor to the IFE. We also numerically confirm the importance of the SOI of light in the IFE, which manifests both via SAM-to-OAM and OAM-to-SAM conversions at the focus. The OAM of light thus opens new degrees of freedom in the control of the IFE in metals, thus potentially impacting various research fields, including all-optical magnetization switching and spin-wave excitation.

	l=0,s=1	l=1,s=0	l=1,s=1	l=-1,s=1
SAM	78%	0.2%	36%	49%
OAM	22%	99.8%	64%	51%

Table 1: The table shows relative contribution of OAM and SAM of light into the IFE for four different combinations of the l and s parameters defining the incoming beam entering the microscope objective.

We also investigate the generation of an optomagnetic field in plasmonic nanoantennas upon illumination with a circularly polarized light (Fig. 1). We predict an optomagnetic field reaching 0.3 T at laser fluence below nanostructure damage threshold. We also show that the substrate introduces an important asymmetry of the optomagnetic response of plasmonic nanoantennas fabricated via a top-down technological approach. For a 50-nm thick gold coaxial nanoantenna (Fig. 1b), the optomagnetism is mainly localized within the substrate, which appears to be advantageous for many applications involving magnetic material within the substrate. Optomagnetism in resonant plasmonic nanoantennas may impact a broad field of applications and techniques including spintronics, magnonics and data storage via the development of on-chip nanoscale plasmonic-magnetic architectures. Optomagnetism may also provide new degrees of freedom in nano-object tweezing based on the combination of optomagnetic and pure optical forces.

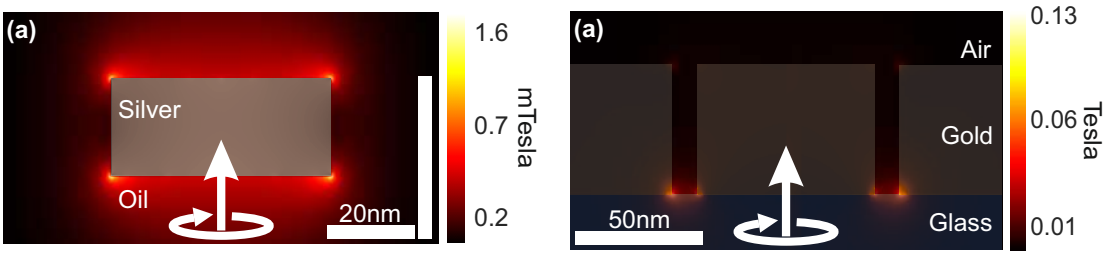

Figure 1: Optically-induced static magnetic field generated by (a) a gold nanocylinder (diameter: 50 nm, thickness: 12 nm) in oil (n=1.45), and (b), a coaxial nanoaperture in a 50-nm thick gold film on a glass substrate (n=1.5). The inner and outer diameters of the coax are of 50 nm and 70 nm, respectively. The wavelength is equal to 800 nm for each configuration.

The authors are indebted to Ulrich Fischer for helpful discussions. This work is funded by Conseil régional de "Bourgogne Franche-Comté"; EIPHI Graduate School (ANR-17-EURE-0002); Agence National de le Recherche (ANR-18-CE42-0016).

References

[1] Les Allen, Marco W Beijersbergen, RJC Spreeuw, and JP Woerdman. Orbital angular momentum of light and the transformation of laguerre-gaussian laser modes. *Phys. Rev. A*, 45(11):8185, 1992.

[2] PS Pershan, JP Van der Ziel, and LD Malmstrom. Theoretical discussion of the inverse faraday effect, raman scattering, and related phenomena. *Physical review*, 143(2):574, 1966.

[3] Riccardo Hertel. Theory of the inverse faraday effect in metals. *J. Magn. Magn. Mater.*, 303(1):L1–L4, 2006.

[4] Jérôme Hurst, Peter M Oppeneer, Giovanni Manfredi, and Paul-Antoine Hervieux. Magnetic moment generation in small gold nanoparticles via the plasmonic inverse faraday effect. *Phys. Rev. B*, 98(13):134439, 2018.

[5] Yannick Lefier. *Etudes du couplage spin-orbite en nano-photonique. applications à l'excitation unidirectionnelle de modes plasmoniques guidés et à la génération d'opto-aimants nanométriques contrôlables par l'état de polarisation de la lumière*. PhD thesis, Université de Franche-Comté, 2016.

[6] Vage Karakhanyan, Clément Eustache, Yannick Lefier, and Thierry Grosjean. Inverse faraday effect from the orbital angular momentum of light. *Phys. Rev. B*, 105(4):045406, 2022.

[7] Vage Karakhanyan, Yannick Lefier, Clément Eustache, and Thierry Grosjean. Optomagnets in nonmagnetic plasmonic nanostructures. *Opt. Lett.*, 46(3):613–616, Feb 2021.

[8] Vage Karakhanyan, Clément Eustache, Yannick Lefier, and Thierry Grosjean. Plasmon-induced 0.13 t optomagnetic field in a gold coaxial nanoaperture. *OSA Continuum*, 4(5):1598–1608, May 2021.

[9] N Noginova, AV Yakim, J Soimo, L Gu, and MA Noginov. Light-to-current and current-to-light coupling in plasmonic systems. *Phys. Rev. B*, 84(3):035447, 2011.

[10] Michael V Berry. Optical currents. *J.Opt. A*, 11(9):094001, 2009.

[11] Konstantin Y Bliokh, Aleksandr Y Bekshaev, and Franco Nori. Extraordinary momentum and spin in evanescent waves. *Nat. commun.*, 5:3300, 2014.

[12] KY Bliokh, FJ Rodríguez-Fortuño, F Nori, and AV Zayats. Spin-orbit interactions of light. *Nat. Photonics*, 9(12):796–808, 2015.

ENSEMBLE3 - Novel materials for photonics - possibilities provided by crystal growth

Dorota A. Pawlak

ENSEMBLE3 Centre of Excellence (Poland),
*corresponding author, E-mail: dorota.anna.pawlak@gmail.com

Abstract

Possibilities of producing novel photonic materials provided by the crystal growth will be discussed including examples of materials exhibiting various interesting optical and electromagnetic properties.

The authors thank ENSEMBLE3 project (GA no. MAB/2020/14) carried out within the International Research Agendas program of the Foundation for Polish Science and Teaming for Excellence project (GA no. 857543) for support of this work

Strong Light-Matter interaction in nanohybrid architectures

Andrea Toma[1]

[1]Istituto Italiano di Tecnologia, Via Morego 30, 16163 Genova, Italy
*corresponding author, E-mail: andrea.toma@iit.it

Abstract

The fabrication of hybrid systems composed by optical nanocavities and quantum dots represents a key approach to induce new and distinctive physico-chemical properties, with significant implications in fields ranging from cavity quantum electrodynamics to polariton chemistry [1,2]. Here, strong coupling between surface plasmon polaritons and nanocrystal quasiparticles such as excitons [3,4] and phonons [5] has been investigated through steady-state and time resolved spectroscopies, thus confirming the possibility of altering the intrinsic nanomaterial response by means of properly tailored optical nanoresonators.

References

[1] J. Flick, N. Rivera, and P. Narang, *Strong Light-Matter Coupling in Quantum Chemistry and Quantum Photonics*, Nanophotonics **7**, 1479 (2018).
[2] E. Cortés, L. V. Besteiro, A. Alabastri, A. Baldi, G. Tagliabue, A. Demetriadou, and P. Narang, *Challenges in Plasmonic Catalysis*, ACS Nano **14**, 16202 (2020).
[3] H. Wang, H.-Y. Wang, A. Toma, T. Yano, Q.-D. Chen, H.-L. Xu, H.-B. Sun, and R. Proietti Zaccaria, *Dynamics of Strong Coupling between CdSe Quantum Dots and Surface Plasmon Polaritons in Subwavelength Hole Array*, J. Phys. Chem. Lett. **7**, 4648 (2016).
[4] H. Wang et al., *Dynamics of Strongly Coupled Hybrid States by Transient Absorption Spectroscopy*, Adv. Funct. Mater. **28**, 1801761 (2018).
[5] X. Jin et al., *Reshaping the Phonon Energy Landscape of Nanocrystals inside a Terahertz Plasmonic Nanocavity*, Nat. Commun. **9**, (2018).

Optics and Photonics

Laser scanners with rotational Risley prisms: A graphical method to determine and study exact scan patterns [Invited]

Virgil-Florin Duma[1,2] *, Alexandru-Lucian Dîmb[2]

[1]3OM Optomechatronics Group, Aurel Vlaicu University of Arad, 77 Revolutiei Ave., 310130 Arad, Romania,
[2]Doctoral School, Polytechnic University of Timisoara, 1 Mihai Viteazu Ave., 300222 Timisoara.
*corresponding author, E-mail: duma.virgil@osamember.org

Abstract

We report on a novel, graphical method, using a 3D mechanical design program, CATIA V5R20, to obtain and analyze exact scan patterns or a pair of rotational Risley prisms - in comparison to other scanning modalities, produced by the most common galvanometer laser scanners.

1. Introduction

Optical and laser scanners are built in a variety of solutions. The most important are [1]: galvanometer scanners (GSs)-oscillatory, polygon mirrors (PMs)-rotational, Risley prisms-both oscillatory and rotational, as well as acousto- or electro-optical scanners-both without moving parts (which is an advantage), but with lower resolutions (which is a clear drawback). Scanning applications have a wide range, from commercial to industrial and remote sensing, as well as to high-end biomedical systems such as confocal microscopy and optical coherence tomography (OCT) [2].
The different systems above and their combinations produce several types of scanning modalities with different characteristics which make them appropriate for a certain application. The aim of this paper is to present some of our contributions in optimizing scanners and scanning modalities, from the point of view of their parameters. The focus is on passing from the slower GS-based raster scanning to the faster but non-linear Risley prisms scanning.

2. Scanners and scanning modalities

The main scanning modalities are:
(i) *Raster scanning* is produced with the most common dual axis 2D GSs or Micro-Electro-Mechanical Systems (MEMS). The fast GS produces a laser line which is positioned by the slow GS with a step-by-step or with a continuous movement. For the fast GS, a trade-off must be made between the scan frequency and amplitude, as studied in detail in [3] and optimized with a new mathematical model for 1D GSs in [4], considering the three most common input signals (i.e., sinusoidal, triangular, and sawtooth). For 2D scanning, we demonstrated that, when a GS- or MEMS-based system is used, the step-by-step movement (with certain, *optimized* functions) is better than the continuous movement of the slow GS [5]. The latter is convenient when the slow scan axis is provided by a moving (for example, airborne) platform-as in remote sensing, for which only the issues of the fast scan axis must be solved. Raster scanning has the major advantage of equally-spaced pixels on both axis (when properly optimized), but it is still rather slow. The scan speed can be increased by using a PM for the fast scan axis [6], but with the non-linearity issues of PMs, studied with the novel theory developed in [7]. Because of the above issues of raster scanning, other scanning modalities have been developed, including:
(ii) *Spiral scanning* can be produced with 2D GSs or with MEMS, but with the advantage that both scan axis are faster. The most convenient is to use archimede spiral [8], because resolution can still be constant for such as spot trajectory.
(iii) *Lissajous scanning* is much faster than both of the above, but also highly non-linear, which is a drawback. However, it has been explored lately with interesting advances in high-definition scanning [9]. It also has the disadvantage that it is still produced with oscillatory GSs (or MEMS), therefore it has limitations in both speed and Field-of-View (FOV).
(iv) *Risley prisms scanning* is a much better alternative to Lissajous scanning, because in its most common variant it uses rotational Risley prisms (i.e., usually optical wedges), which do not have to stop-and-turn like oscillatory mirrors – Fig. 1. This is an advantage compared to all scanning modalities presented above.

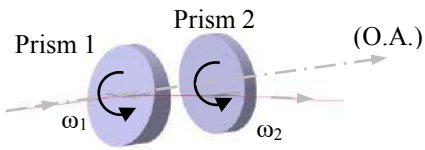

Figure 1: Laser scanner with rotational Risley prisms: modeling with a 3D mechanical design program, CATIA V5R20 to obtain scan patterns (Fig. 2). Configuration *ba-ab* ("a", diopter perpendicular to the optical axis (O.A.); "b", inclined diopter), considered from the four configurations of a pair of prisms.

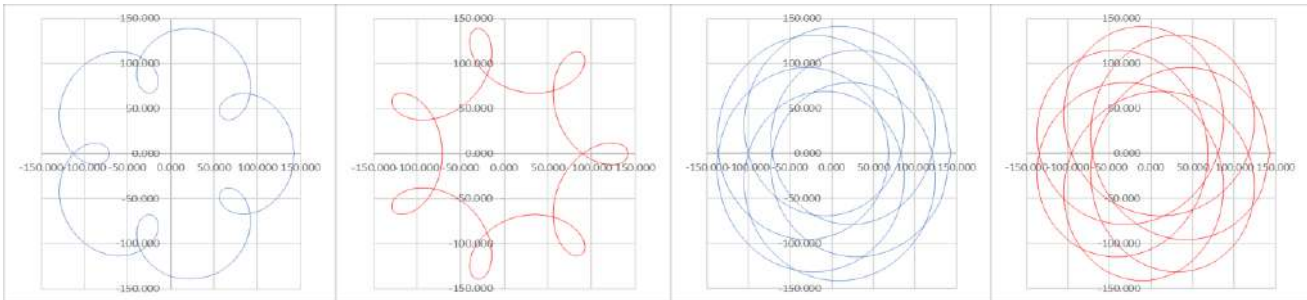

(a1) (a2) (b1) (b2)

Figure 2: Simulated scan patterns of a pair of rotational Risley prisms, for (a) k=2/6 and (b) k=6/2 and for (1) M=6 and (2) M=-6. The patterns are obtained in a plane perpendicular to the optical axis.

Risley laser scanning systems can be of several types [1]: rotational or translational; with two, three or double prisms. The main applications of these systems are: laser scanning, precision pointing, interferometry, holography, polarimetry, light attenuation and biomedical imaging. The main advantage of the exact scan patterns with the graphical method is that they are accurate, compared to the scan patterns obtained with the analytical method.

3. Graphical simulation of scan patterns of rotational Risley prisms

We have and developed a novel, graphical method to generate and study exact scan patterns of rotational Risley prisms, using only common prisms equations and a mechanical design program, CATIA V5R20 [10]. With regard to approximate method (e.g., using the paraxial domain), our method has the advantage of providing exact scan pattern. With regard to exact, analytical approaches, our method has the advantage of being easy-to-use and fast.
A few examples are presented in Fig. 2. A multi-parameter analysis has been carried out with regard to all the possible parameters of a pair of rotational prisms: prisms angles (respectively deviations); distance from the 'a' diopter to the screen where patterns are formed; distance between the 'a' diopters; Marshall's parameters, i.e. M, ratio of angular speeds and k, ratio of angles of the prisms [10].

4. Conclusions

We compared the four most common scanning modalities and we reported the graphical method developed to obtain fast exact scan patterns of Risley prisms. The example of a pair of rotational prisms was considered, for different values of the parameter k and for two (equal in module, but one positive and the other one negative) values of the parameter M. Scanning with Riley prisms is nonlinear and complicated, which is a drawback; pixels in a scanned plane are not equally spaced as obtained with raster or (appropriate) spiral scanning. However, the FOV is larger, the speed is much higher, and if fill factors can be limited (for example in remote sensing), such scanners are the appropriate system to use. Current work in our group include applications, as well as studies of other configurations of Risley prisms, as well as comparisons to other scanning systems.

Acknowledgements

This research is supported by the Romanian Ministry of Research, Innovation and Digitization, CNCS/CCCDI–UEFISCDI, project PN-III-P4-ID-PCE-2020-2600, within PNCDI III (http://3om-group-optomechatronics.ro/).

References

[1] G.F. Marshall, G.E. Stutz, Eds. *Handbook of optical and laser scanning*, 2nd ed.; CRC Press: London, 2011.

[2] A.Gh. Podoleanu, R.B. Rosen, Combinations of techniques in imaging the retina with high resolution, *Progress in Retinal and Eye Research* 27: 464-499, 2008.

[3] V.-F. Duma, K.-S. Lee, P. Meemon, J.P. Rolland, Experimental investigations of the scanning functions of galvanometer-based scanners with applications in OCT, *Appl. Opt.* 50(29): 5735-5749, 2011.

[4] V.-F. Duma, P. Tankam, J. Huang, J.J. Won, J.P. Rolland, Optimization of galvanometer scanning for Optical Coherence Tomography, *Appl. Opt.* 54(17): 5495-5507, 2015.

[5] V.-F. Duma, Laser scanners with oscillatory elements: Design and optimization of 1D and 2D scanning functions, *Appl. Math. Modelling* 67(3): 456-476, 2019.

[6] Y. Li, Beam deflection and scanning by two-mirror and two-axis systems of different architectures: a unified approach, *Appl. Opt.* 47: 5976-5985, 2008.

[7] V.-F. Duma, Polygonal mirror laser scanning heads: Characteristic functions, *Proc. of the Romanian Academy Series A* 18(1): 25-33, 2017.

[8] O.M. Carrasco-Zevallos, C. Viehland, B. Keller, R.P. McNabb, A.N. Kuo, J.A. Izatt, Constant linear velocity spiral scanning for near video rate 4D OCT ophthalmic and surgical imaging with isotropic transverse sampling. *Biomed. Opt. Express* 9: 5052, 2018.

[9] K. Hwang, Y.-H. Seo, J. Ahn, P. Kim, K.-H. Jeong, Frequency selection rule for high definition and high frame rate Lissajous scanning, *Sc. Rep.* 7: 14075, 2017.

[10] V.-F. Duma, A. Schitea, Laser scanners with rotational Risley prisms: Exact scan patterns, *Proc. of the Romanian Academy Series A* 19(1): 53-60, 2018.

High-Speed Fiber–Wireless–Fiber Bridge System for Fixed Wireless Link in Millimeter-Wave Band Using Photonic Technology

Pham Tien Dat

National Institute of Information and Communications Technology, Tokyo 184-8795, Japan
corresponding author, E-mail: ptdat@nict.go.jp

Abstract

We present photonics-enabled technologies to realize high-speed fiber–wireless–fiber bridge systems in the millimeter-wave band, including a photonics-enabled receiver and an all-photonic receiver. In the former method, the millimeter-wave signal is down-converted to the microwave band before being converted to the optical signal for further transmission using an optically generated local oscillator signal. In the latter method, the millimeter-wave signal is directly converted to the optical domain without any frequency conversion using a broadband optical modulator. Using the proposed technologies, we successfully transmitted high-speed signal over both systems.

1. Introduction

Fiber–wireless–fiber bridge systems in high-frequency bands are promising for interconnections, disaster recovery, and fixed access networks for indoor environments. In these systems, wireless receivers are normally installed outdoors, such as on rooftops or windows, and the received wireless signal should be further transmitted to end users, typically indoor residents, over a second fiber link. In addition, encoding radio signals collected at antenna sites to the optical backbone is essential for the uplink mobile fronthaul. In this application, the evolution of radio access networks, which are expected to continue beyond 71 GHz towards the terahertz band, poses significant challenges to transport networks, particularly the uplink fronthaul. In both scenarios, the simplification of antenna sites and fiber transport systems is vital to satisfying the rapid increase in the number of small cells. Currently, systems based on electronic receivers for radio-to-optical conversion at the antenna sites are widely used [1]. However, the inclusion of electrical local oscillator (LO) sources at antenna sites complicates the system configuration, operation, and management. In this paper, we present two different approaches based on photonic technology to simplify the antenna sites and the second fiber transmission link. The first method is based on a photonics-enabled receiver to convert a millimeter-wave (mmW) signal to the microwave band before converting it to the optical domain for further transmission to the receiver. In addition, for the further fiber link transmission, an optical phase modulation and direct detection technology using an optical filter is employed to simplify the system and the receiver. In the second method, an all-photonic receiver using a broadband optical modulator is used to directly convert an mmW signal to an optical signal without any frequency conversion. A photonic down-conversion technology is also utilized to down-convert the signal to the microwave band. Both the systems can simplify the antenna sites and the second fiber link transmission, rendering them a simple and efficient method for high-speed bridge and uplink mobile fronthaul in ultra-high frequency bands.

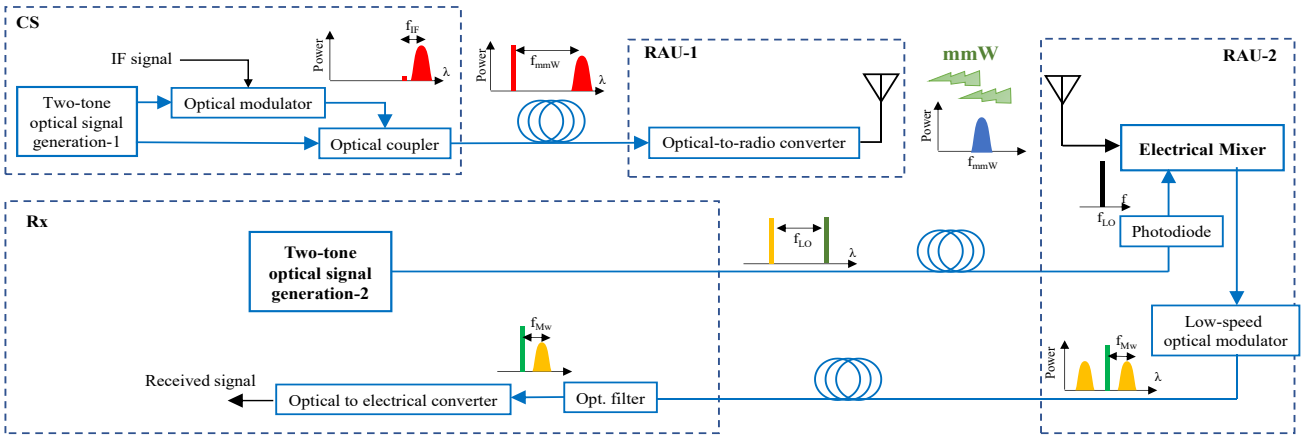

Figure. 1: Schematic diagram of fiber–wireless–fiber system using photonics-enabled receiver.
CS: central station; RAU: remote antenna unit; Rx: receiver; mmW: millimeter-wave; Mw: microwave; IF: intermediate frequency; LO: local oscillator.

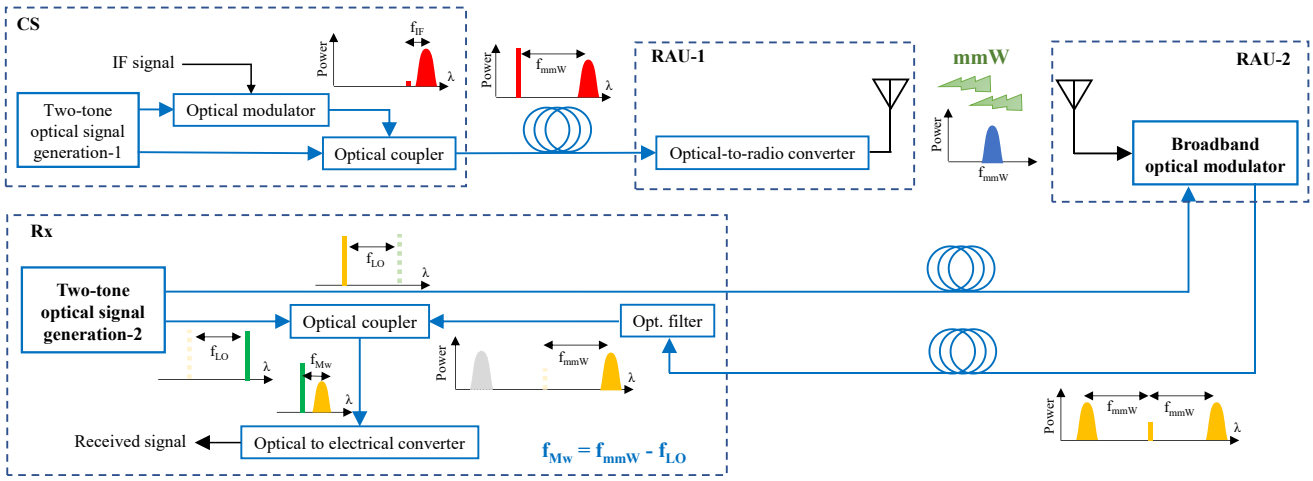

Figure. 2: Schematic diagram of fiber–wireless–fiber system using optical modulator and photonic down-conversion.

2. Photonics-enabled receiver

The system concept of a fiber–wireless–fiber system using a photonics-enabled receiver is shown in Fig. 1. The system consists of four main blocks: a central station (CS), remote antenna unit 1 (RAU-1), remote antenna unit 2 (RAU-1), and receiver (Rx). The CS generates and modulates the data on the optical signal. A two-tone optical signal consisting of two coherent optical sidebands is generated using optical modulation technology. The two optical sidebands are separated, and one of them is modulated by a data signal using an optical modulator. The modulated and unmodulated sidebands from the two-tone optical signal are combined to construct a radio-over-fiber (RoF) signal. At RAU-1, the RoF signal is up-converted to an mmW radio signal using a high-speed photodetector. The generated signal can be further amplified to increase the power level before transmitting to RAU-2. At RAU-2, the mmW signal is received and down-converted to the microwave band using an electrical mixer. To simplify RAU-2, a local oscillator signal is optically generated at the Rx and sent to RAU-2 for the signal down-conversion. The down-converted signal is converted to an optical signal using a low-speed optical modulator. The signal is transmitted to the Rx and detected using a low-speed photodiode. To prove the system concept, we successfully transmitted 80-Gb/s line rate signal over the system [2].

3. All-photonic receiver

The system concept of a fiber–wireless–fiber system using an all-photonic receiver is shown in Fig. 2. Similar to the first method, the system consists of four main blocks, including a CS, RAU-1, RAU-1, and Rx. The CS and RAU-1 are same as in the first case. At RAU-2, the mmW signal is received and converted to an optical signal using a broadband optical modulator. For the mmW-to-optical conversion, the optical carrier signal is directly modulated by the mmW signal. Compared with the electronics-based conversion method, which needs to down-convert the signal to a low-frequency band before converting to the optical signal, the direct mmW-optical conversion method can significantly simplify the antenna site. The Rx performs signal reception, detection, and down-conversion to the microwave band. A direct photonic down-conversion method can also be used to simplify the receiver and reduce the frequency offset and phase noise of the detected signal. Another two-tone optical signal is generated, and the two sidebands are separated. One of them is transmitted to RAU-2 for data modulation. The other sideband is used for signal detection and down-conversion. The received optical signal from RAU-2 is filtered to select only one of the sidebands using an optical filter. The filtered signal is then combined with the unmodulated sideband from the generated two-tone optical signal. The combined signal is input to a photodiode for conversion to a microwave signal. As a proof-of-concept demonstration, we successfully transmitted more than 70 Gb/s line rate over the system [3].

4. Conclusions

We present high-speed fiber–wireless–fiber systems in the millimeter-wave band using a photonics-enabled and an all-photonic receiver. The proposed systems significantly simplify the antenna sites and optical receivers. We successfully demonstrated high-speed signal transmission over the proposed systems with a line rate of over 70 Gb/s. The proposed systems are promising for fiber–radio bridges and uplink fronthaul systems in ultra-high frequency bands in beyond-5G networks.

References

[1] A. Kanno et al., "Evaluation of Frequency Fluctuation in Fiber-Wireless Link with Direct IQ Down-Converter," ECOC, We.3.6.3 (2014).

[2] P. T. Dat et al., "High-speed fiber–wireless–fiber system in the 100-GHz band using a photonics-enabled receiver and optical phase modulator", Optics Lett., Early Access (2022).

[3] P. T. Dat et al., "Transparent Fiber–Millimeter-Wave–Fiber System in 100-GHz Band Using Optical Modulator and Photonic Down-Conversion," J. Light. Technol., Early Access (2022).

Giant Pockels Effect in Thin Film Barium Titanate for Reconfigurable Photonics

Aaron Danner[1,*]

[1]Dept. Of Electrical and Computer Engineering, National University of Singapore, Singapore
*corresponding author, E-mail: adanner@nus.edu.sg

Abstract

In this talk I will introduce the barium titanate photonics platform. The Pockels effect is what enables GHz-level switching speeds in optical modulators and switches, so materials which exhibit strong Pockels coefficients are advantageous as they maximize light-matter interaction. Using pulse laser deposition, we have grown single crystal barium titanate on various low index substrates and measured an r-parameter over 600 pm/V, which is nearly 20 times that of the commonly used lithium niobate. We then experimentally demonstrated polarization modulation.

Shapeshifting diffractive optical elements

Antonio Ambrosio[1]

[1]Istituto Italiano di Tecnologia, Via Pascoli 70/3, 20133, Milano, Italy
*corresponding author, E-mail: antonio.ambrosio@iit.it

Abstract

We have proved that it is possible to realize optical elements with theory-matching efficiency and practical use, reconfigurable on demand right where and when needed. I will present diffraction optical elements with efficiency equal to the theoretical efficiency, realized by direct structuring of the surface of a photosensitive polymer, avoiding any further development step. The realized gratings and lenses can be reshaped completely while aligned in the optical setup. Grating periodicity can be changed; lenses focal length can be tuned; one optical element can be morphed into another optical element with completely different optical functionality, without affecting the alignment of the specific optical setup.

Integrated microresonator frequency comb source for massive-parallel optical communication

Takasumi Tanabe[1,*], Soma Kogure[1], and Shun Fujii[1,2]

[1]Departament of Electronics and Electrical Engineering, Faculty of Science and Technology, Keio University, Yokohama, Japan
[2]RIKEN Center for Advanced Photonics, 2-1, Hirosawa, Wako, Saitama 351-0198
*corresponding author, E-mail: takasumi@elec.keio.ac.jp

Abstract

We demonstrated ultra-dense wavelength-division multiplexing (WDM) data transmission using an intensity modulation and direct detection (IM-DD) scheme. We discuss the feasibility of SiN and MgF_2 microresonators for WDM applications regarding output power, bandwidth, and required pumping power. In addition, we discuss that IM-DD communication is relevant to the next-generation optical communication that requires ultra-low latency.

1. Introduction

We believe that massively parallel wavelength division multiplexed (WDM) optical communications are required to support high transmission rates and low latency. Optical frequency comb using optical microresonators, now known as a microcomb, is being actively studied as a possible candidate that replaces existing single wavelength lasers.

Microcomb is based on the four-wave mixing (FWM) that occurs in a tiny microresonator. When a continuous wave (CW) laser with a single wavelength is injected into an optical microresonator, degenerate and non-degenerate FWMs occur, resulting in the generation of different wavelength components. In order to obtain FWM efficiently, a high-Q cavity is needed. Various platforms exist, including magnesium fluoride (MgF_2) whispering gallery mode (WGM) resonators [1] and silicon nitride (SiN) microring resonators.

In this paper, we first explain our experiments on the generation of the soliton combs and then discuss the feasibility of the modulation instability comb for optical data transmission.

2. Comparison between MgF_2 and SiN microresonators

Before we show the transmittance experiment, we would like to discuss which microresonators are advantageous for WDM applications.

Figure 1 shows the output power per longitudinal line (i.e., channel) for SiN (Fig. 1(a)) and MgF_2 (Fig. 1(b)) microresonators, in function to the Q, free-spectral range (FSR), and input power, when soliton comb is generated [2]. Typical Q and FSR for the SiN microring are a few million and a few hundred GHz. It means that we can obtain –10 dBm/channel output at a pumping power of ~100 mW. On the other hand, Fig. 1(b) is a map for the MgF_2 WGM microresonator, of which Q is usually much higher. The Q is typically 10^9, and FSR is > 10 GHz. It suggests that a soliton is obtained at much lower power of ~10 mW, but the output is as low as –25 dBm. It shows that these platforms have pros and cons.

The following is a very simplified discussion: If we need a dense WDM with channel spacing of 10 to 40 GHz, a MgF_2 resonator is advantageous. It also allows us to generate a comb with much lower pump power. On the other hand, if we need a WDM light source with much higher power per channel, SiN microring is advantageous. It also allows us to build an on-chip integrated system, but the FSR is as sparse as > 100 GHz.

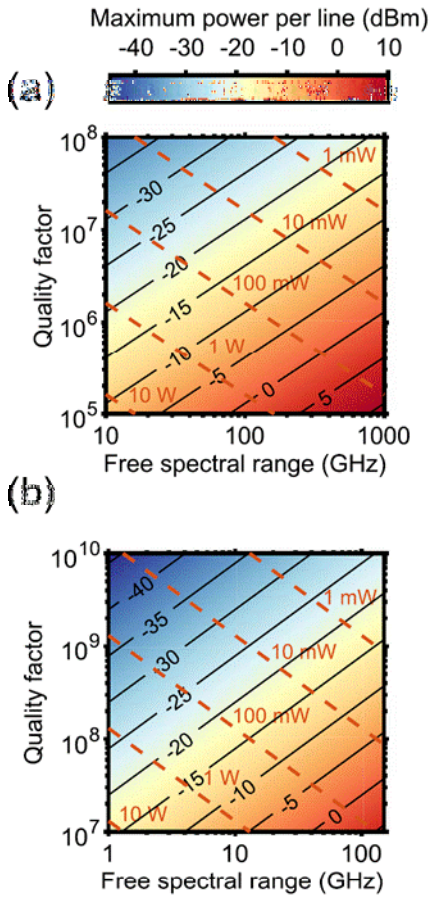

Figure 1: This color map shows the maximum power output per comb line when a soliton comb is generated. The red dotted lines are the required pump power to obtain a soliton comb. (a) SiN microring. (b) MgF_2 WGM microresonator. [2]

3. Optical transmittance experiment

Here we will show our experimental results of ultra-low latency optical transmission using the IM-DD scheme. We want to note that coherent digital communication requires powerful electrical signal processing, and the delay caused by the signal processing is not negligible. Forward error correction (FEC) is also often used, which further increases the delay in the electrical stage.

Therefore, to construct an ultra-low latency transmission system, it is necessary to reduce the electrical signal processing load by utilizing FEC-free transmission. It is expected to achieve massively parallel transmission and high transmission capacity as the overall system performance.

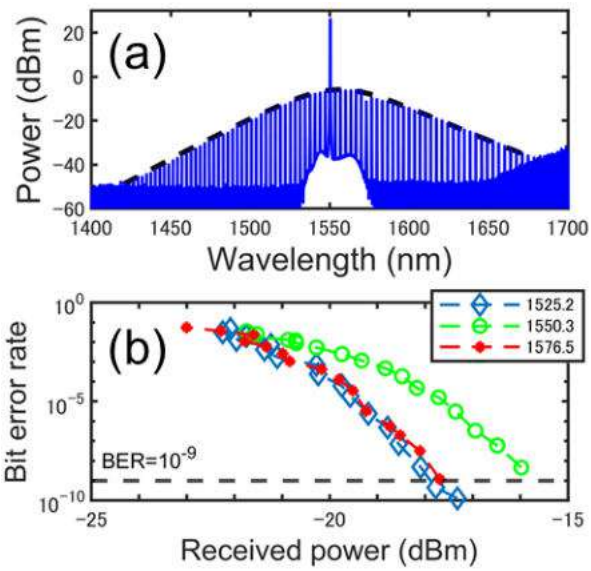

Figure 2: Optical spectrum of a soliton comb from SiN resonator with FSR of 400 GHz. (b) Bit error rate curves for three different comb lines at the wavelength of 1525.2, 1550.3, and 1576. nm.

Figure 2(a) shows the spectrum of the soliton comb generated with a SiN microring. The FSR is 400 GHz. We use a fast-scan method to generate the soliton comb. Comb lines at wavelengths of 1525.2, 1550.3, and 1576.5 nm were filtered out by a BPF, and the signal light is modulated at 10 Gbps with an intensity-modulator. Note that 1550.3 nm is the CW pump light. The modulated light propagated through a 40-km single-mode optical fiber. Figure 2(b) shows the BER at different received power. All three comb lines achieved a BER < 10^{-9} (error-free), which is necessary for FEC-free transmission.

Next, we show the results of transmission experiments using an MgF_2 resonator with an FSR of 10 GHz (Fig. 3(a)). The spectrum's full width at half maximum is 1.22 THz, with 386 comb lines in the C-band. Figure 3(b) shows the lowest BER values for the transmission for each comb line. The 145 comb lines achieved error-free transmission with a total transmission capacity of 1.45 Tbit/s. The BERs are degraded near the pump wavelength due to the spontaneous emission of amplified light at the optical fiber amplifier. The BER is also degraded at both wings of the spectrum due to the small output power of the comb line. The spectral efficiency was 1 bit/s/Hz, the highest spectral efficiency achieved to our knowledge for microcomb-based transmission without FEC.

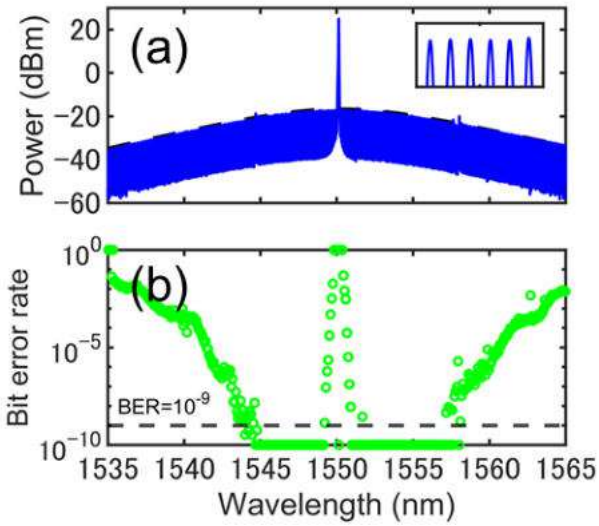

Figure 3: Optical spectrum of a soliton comb from MgF_2 resonator with an FSR of 10 GHz. Inset: Enlarged spectrum between 1549.0 and 1549.5 nm. (b) Bit error rate spectrum of 386 comb lines across the C-band. 145 comb lines exhibit error-free operation (BER < 10^{-9}).

4. Conclusions

We discussed the feasibility of the microresonator frequency combs generated with MgF_2 WGM microresonator and SiN microring for WDM application. We demonstrated massive-parallel FEC free transmittance which is needed for high-capacity low-latency optical transmittance.

Acknowledgments

This work is based on results obtained from a project, JPNP16007, commissioned by the New Energy and Industrial Technology Development Organization (NEDO).

References

[1] S. Fujii, Y. Hayama, K. Imamura, H. Kumazaki, Y. Kakinuma, and T. Tanabe: Optica 7 (2020) 694.

[2] S. Fujii, S. Tanaka, T. Ohtsuka, S. Kogure, K. Wada, H. Kumazaki, S. Tasaka, Y. Hashimoto, Y. Kobayashi, T. Araki *et al.*: Opt. Express **30** (2022) 1351.

Photothermal effects in nanostructures: from ultrafast optical symmetry breaking to extreme heat dissipation

Alessandro Alabastri[1]

[1] Department of Electrical and Computer Engineering, Rice University, 6100 Main Street MS-378, Houston, TX 77005
E-mail: alabastri@rice.edu

Abstract

Electromagnetic radiation is absorbed inhomogeneously in differently shaped nanostructures. I will show how this phenomenon leads to a space-dependent out-of-equilibrium hot carrier population that breaks the optical symmetry of otherwise symmetrical nanostructures. The resulting asymmetric hot-carrier time dynamics can be exploited to manipulate light-matter interaction in the ultrafast regime. Electron-phonon scattering eventually induces heating, and I will show how properly designed large scale ultrathin (~250nm) metasurfaces allow extremely large (~GW/m^3) and broadband (~90% of solar spectrum) dissipated power densities.

Optoelectronics, Photonic Materials and Devices

Electronic and optoelectronic properties of black phosphorous

Vivek Chaudhary,[1,2*] P. Neugebauer,[3] O. Mounkachi,[2,4] S. Lahbabi,[2,5] A. El Fatimy[1,3*]

[1]Institute of Applied Physics, Mohammed VI Polytechnic University, Lot 660, Hay Moulay Rachid Ben Guerir, 43150, Morocco.
[2]Modeling, Simulation and Data Analysis (MSDA), Mohammed VI Polytechnic University, Lot 660, Hay Moulay Rachid Ben Guerir, 43150, Morocco.
[3]Central European Institute of Technology, CEITEC BUT, Brno University of Technology, Purkyňova 123, Brno 61200, Czech Republic.
[4]Laboratoire de Matière Condensée et Sciences Interdisciplinaires (LaMCScI), B.P. 1014, Faculty of Science, Mohammed V University in Rabat, Morocco.
[5]Equipe Modélisation, Applications, Mathématiques et Informatiques (EMAMI), Laboratoire de Recherche en Ingénierie, ENSEM, University Hassan II of Casablanca, Morocco.
Email: vivek.chaudhary@um6p.ma and Abdelouahed.ELFATIMY@um6p.ma

Abstract

The optoelectronic and photonic devices based on two-dimensional (2D) materials are of great importance in the technological development of efficient devices for various applications including ultrafast computing, imaging, environmental monitoring, security systems, optical communication, and health care, etc., is vitally important. After the invention of graphene, the past decade witnessed a rapid development and amelioration of several 2D materials. These newly discovered materials have the capability to emit and or detect the electromagnetic radiation from visible to radio frequency waves which is an essential need for daily life applications. Herein, we present the enormous capabilities of the most recent rediscovered 2D material named black phosphorous (BP). It offers a solution for several technological limitations that appears in conventional 2D materials such as transition metal dichalcogenides/oxides etc. In the present work, we have demonstrated the electronic and optoelectronic properties of BP via realizing field effect transistors.

Towards far-field multipole retrieval with a reconfigurable photonic integrated circuit

Johannes Bütow[1], Jörg S. Eismann[1,2,3], Varun Sharma[1], Dorian Brandmüller[1], and Peter Banzer[1,2,3,*]

[1]Institute of Physics, University of Graz, NAWI Graz, Austria
[2]Max Planck Institute for the Science of Light, Erlangen, Germany
[3]Institute of Optics, Information, and Photonics, University Erlangen-Nuremberg, Germany
*corresponding author, E-mail: peter.banzer@uni-graz.de

Abstract

Controlled excitation and measurement of multipoles in nanoscatterers is an important task of increasing interest in nano-optics and nano-metrology. Here, we discuss the implementation of a far-field approach for the retrieval of multipolar contributions to particle scattering. We utilize a reconfigurable photonic integrated circuit capable of measuring spatial phase, polarization and intensity information. We introduce the multipole retrieval scheme and discuss the main concepts of this novel detector, paving the way towards intriguing applications in nano-metrology, microscopy and imaging.

1. Introduction

In the last decade, the study of electric and magnetic dipole excitation in photonic nano-structures has attracted tremendous attention with applications ranging from dipole-interference-based directional scattering [1], tunable waveguide coupling [2,3] to nano-metrology [4,5]. Recently, also the role and additional capabilities of higher order multipoles in the context of directional scattering have been studied theoretically [6]. However, although very important, the experimental study of such higher order multipoles is far from trivial. A far-field approach for experimentally retrieving the multipolar response of individual scatterers would be desirable. For the unambiguous experimental determination from far-field scattered light, the intensity distribution is not sufficient and needs to be complemented with phase and/or polarization information.

2. Measuring higher order multipolar contributions to particle scattering using novel detectors

For the study of far-field multipole retrieval, tightly focused and polarization engineered light beams represent an excellent and versatile tool. They have been utilized to selectively and controllably excite multipoles in nanoparticles [1,4,7,8].

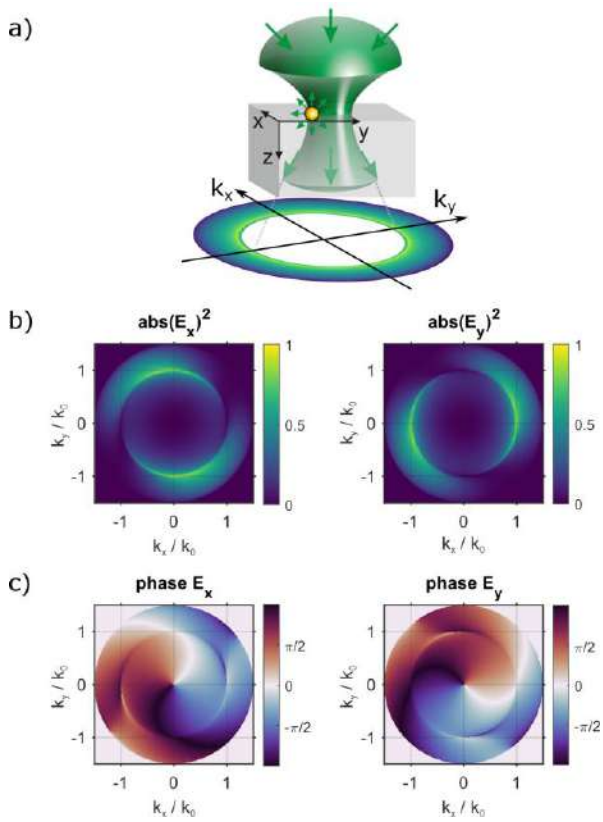

Figure 1: a) Excitation scheme of an individual nanoparticle using tightly focused polarization tailored light. Far-field imaging of the back focal plane (BFP) of a collection objective onto a camera provides access to the angular emission spectra. b) Exemplary electric field intensity and c) phase information for the emission of an electric quadrupole (l=2, m=2) placed near a dielectric interface (substrate). Far-field measurement of this information can grant access to the identification of electric and magnetic dipoles as well as quadrupoles.

Experimentally, the light scattered by a nanoparticle can be collected with a high numerical aperture (NA) objective

(Figure 1 a). The back focal plane (BFP) of this objective contains information about the scattered field in k-space. If excitation and collection NA are chosen properly, an angular region can be isolated, which contains scattered light only (see ring-like intensity distribution in Figure 1 a). It has been shown that by measuring the polarization of this region in the BFP based on a Stokes analysis with a camera, full information about the dipole contributions to the scattering (electric and magnetic) can be extracted [8]. However, this method requires an elaborate polarization measurement.

Here, we now extend this approach to also enable the retrieval of all electric and magnetic quadrupolar contributions (in addition to dipoles) based on intensity, polarization and phase information (Fig. 1 b) and c). Furthermore, we develop and utilize a novel detector capable of measuring the spatial distributions of intensity, phase and polarization information simultaneously, simplifying and speeding up the measurement process substantially.

This novel detector consists of a reconfigurable photonic integrated circuit processing the input field. On-chip grating couplers and meshes of Mach-Zehnder interferometers serve as an interface – referred to as Super-Pixels – between the incoming light and on-chip waveguide modes [9,10]. After calibration of the system based on a known input field, the relative intensity and phase information between all pixels can be measured for arbitrary input beams [11]. The architecture of the grating couplers themselves also provides for additional information about the polarization.

We discuss the concept of this novel detector, its building-blocks, and its calibration, and we elaborate on one of its main applications in the field of nano-optics, i.e., the multipole retrieval. As an example we show that even low-resolution 'Super-Pixel' detectors with only 16 pixels can be used to unambiguously measure the complete sets of electric and magnetic dipole and quadrupole moments without any a-priori knowledge.

3. Conclusions

Novel integrated detectors capable of simultaneously measuring intensity, phase and polarization of a field distribution or light beam offer exciting new possibilities in nano-optics and related fields, e.g., in the context of far-field multipole retrieval. The underlying method for multipole retrieval, the 'Super-Pixel' architecture, its building-blocks, and its calibration will be introduced.

Acknowledgements

We acknowledge the support by the Super-Pixels Consortium. This project has received partial funding from the European Commission Horizon 2020 research and innovation programme under the Future and Emerging Technologies Open Grant Agreement Super-Pixels No. 829116.

References

[1] M. Neugebauer, P. Wozniak, A. Bag, G. Leuchs, P. Banzer, Polarization-controlled directional scattering for nanoscopic position sensing, *Nature Commun*. 7, 11286, 2016.

[2] S. Nechayev, J. S. Eismann, M. Neugebauer, P. Woźniak, A. Bag, G. Leuchs, P. Banzer, Huygens' dipole for polarization-controlled nanoscale light routing, *Phys. Rev. A* 99, 041801, 2019.

[3] M. F. Picardi, A. V. Zayats, F. J. Rodríguez-Fortuño, Janus and Huygens dipoles: near-field directionality beyond spin-momentum locking, *Phys. Rev. Lett*. 120, 117402, 2018.

[4] A. Bag, M. Neugebauer, P. Wozniak, G. Leuchs, P. Banzer, Transverse Kerker scattering for Angström localization of nanoparticles, *Phys. Rev. Lett*. 121, 193902, 2018.

[5] J. S. Eismann, M. Neugebauer, K. Mantel, P. Banzer, Absolute characterization of high numerical aperture microscope objectives utilizing a dipole scatterer, *Light: Science & Applications*, 10(1), 1-7, 2021.

[6] J. E. Vazquez-Lozano, A. Martinez, F. J. Rodriguez-Fortuno, Near-Field Directionality Beyond the Dipole Approximation: Electric Quadrupole and Higher-Order Multipole Angular Spectra, *Phys. Rev. A*. 12, 024065, 2019.

[7] P. Woźniak, P. Banzer, G. Leuchs, Selective switching of individual multipole resonances in single dielectric nanoparticles, *Laser & Photonics Reviews* 9.2, 231-240, 2015.

[8] M. F. Picardi, M. Neugebauer, J. S. Eismann, G. Leuchs, P. Banzer, F. J. Rodriguez-Fortuno, A. V. Zayats, Experimental demonstration of linear and spinning Janus dipoles for polarisation- and wavelength-selective near-field coupling, *Light: Science & Applications* 8.1, 1-7, 2019.

[9] D. A. B. Miller, Self-aligning universal beam coupler, *Opt. Express* 21, 6360-6370, 2013.

[10] D. A. B. Miller, Self-configuring universal linear optical component, *Photonics Res*. 1, 1-15, 2013.

[11] J. Bütow, J. S. Eismann, M. Milanizadeh, F. Morichetti, A. Melloni, D. A. B. Miller, P. Banzer, Spatially resolving amplitude and phase of light with a reconfigurable photonic integrated circuit, *Submitted*, 2022.

Towards Robust Optical Data Processing with Photonic Integrated Circuits

Jian Wang[1,2*]

[1] Wuhan National Laboratory for Optoelectronics and School of Optical and Electronic Information, Huazhong University of Science and Technology, Wuhan, Hubei, 430074, China
[2] Optics Valley Laboratory, Wuhan 430074, Hubei, China

*Corresponding author, E-mail: jwang@hust.edu.cn

Abstract

Photonic integrated circuits (PICs) that are compatible with the complementary metal-oxide-semiconductor (CMOS) technology are promising candidates for ultracompact data management. In this talk, we review recent advances in robust optical data processing using silicon PICs: 1) On-chip reconfigurable optical full-field manipulation for grooming photonic signal processor (reconfigurable optical add/drop multiplexer, filter); 2) On-chip mesh-structure-enabled programmable multi-task photonic signal processor (filter, delay, router, switch); 3) On-chip multi-dimensional (mode, polarization, wavelength) selective switch; 4) On-chip intelligent mode switching in fiber-chip-fiber communication systems.

Long Wavelength Infrared Detection by Combining Nano-Thermoelectrics and Sub-Wavelength Absorbers

Aapo Varpula, Anton Murros, Kuura Sovanto, Jonna Tiira, Kirsi Tappura, and Mika Prunnila*

VTT Technical Research Centre of Finland Ltd, Tietotie 3, FI-02150 Espoo, Finland
*corresponding author, E-mail: mika.prunnila@vtt.fi

Abstract

Detection of infrared (IR) radiation is required in numerous applications from spectroscopic gas sensing to thermal imaging. Obtaining high speed and sensitivity, low-power operation, and cost-effectiveness with a single technology remains to be a challenge in the field of IR sensing. By combining nano-thermoelectric heat-to-voltage transduction and sub-wavelength absorbers, we demonstrate uncooled IR bolometer technology that provides fast and high sensitivity response to long-wavelength IR (LWIR) around 8 - 12 μm and is material-compatible with large-scale CMOS fabrication.

The state-of-the-art optical detectors are either bolometers or quantum photodetectors. In the infrared (IR) range, the state-of-the-art bolometers convert the IR signal into an electric signal using either temperature-dependent resistors or thermoelectrics. Quantum IR photodetectors have high performance, but they require cooling, and exotic materials at longer wavelengths. Compared to quantum IR photodetectors, IR bolometers offer lower cost without need for cooling, but they are typically much slower and less sensitive.

Nano-thermoelectrics has been mainly driven by applications in thermal energy harvesting with very little attention to detectors until recently when it was postulated [1,2] and demonstrated [3] that nano-thermoelectrics can provide an attractive low noise transduction method for bolometers. When nano-thermoelectric beams are combined with nanomembrane IR absorbers with inherently low thermal mass, they can be utilized as fast and sensitive infrared detectors [3] (see also Fig. 1). The nano-thermoelectric transducer-support approach benefits from enhanced phonon scattering in the beams, which enhances the sensitivity. We have demonstrated different size nano-thermoelectric bolometric photodetector pixels with LWIR responsitivities, specific detectivities, and time constants in the ranges 179 V/W–2930 V/W, 1.5×10^7 cm $Hz^{1/2}$/W–3.1×10^8 cm $Hz^{1/2}$/W, and 66 μs–3600 μs, respectively. We have also benchmarked the technology against different LWIR detector solutions and showed how nano-thermoelectric detector technology can reach the fundamental sensitivity limits posed by phonon and photon thermal fluctuation noise [3].

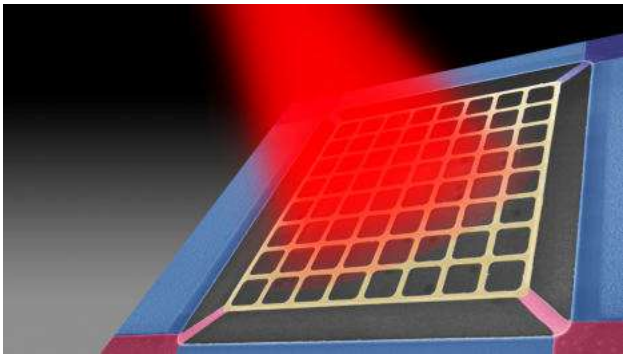

Figure 1: Nano-thermoelectric LWIR bolometer [3].

[1] A. Varpula et al., Appl. Phys. Lett. 110, 262101 (2017).

[2] A. Varpula et al., Proceedings 2 (13), 894 (2018).

[3] A. Varpula, K. Tappura, J. Tiira, K. Grigoras, O.-P. Kilpi, K. Sovanto, J. Ahopelto, and M. Prunnila, “Nano-thermoelectric infrared bolometers”, APL Photonics 6, 036111 (2021).

Scattering and diffraction

Effective Scattering Control of Graphene Micro-disks Utilizing the Fundamental Plasmon Resonances

Stamatios Amanatiadis[1*], Vasileios Salonikios[1], Michalis Nitas[1], Theodoros Zygiridis[2], Nikolaos Kantartzis[1], and Traianos Yioultsis[1]

[1]Department of Electrical and Computer Engineering, Aristotle University of Thessaloniki, Thessaloniki, Greece
[2]Department of Electrical and Computer Engineering, University of Western Macedonia, Kozani, Greece
*corresponding author, E-mail: samanati@auth.gr

Abstract

The plane wave scattering on graphene micro-disks is investigated numerically in the present work. Initially, the propagation properties of the supported surface waves on the 2D material are studied theoretically. Then, the plasmonic resonant frequencies of a circular graphene scatterer are identified via the broadband analysis of the absorption cross-section. Finally, the radar cross-section of the same setup is examined, indicating that the resonant frequencies are optimal for forward propagation, thus enabling the effective beam manipulation.

1. Introduction

Several years have passed since the first report of a stable graphene layer, but various different aspects regarding this truly 2D material are still challenging. Specifically, the capability of graphene to support surface waves at the far-infrared regime has enabled the design of various devices [1]. However, the theoretical analysis is limited on infinite layers, while numerical solvers are required for the characterization of plasmonic waveguides [2, 3].

This paper focuses on a circular graphene scatterer to identify its resonant frequencies. This is achieved through the absorption cross-section numerical examination of a plane-wave that propagates towards our device. Moreover, the radar cross-section is investigated at various frequencies, indicating that forward propagation is maximized at resonances. This knowledge is important since an effective beam manipulation is enabled via the appropriate combination of graphene scatterers on 2D arrays [4].

2. Theoretical aspects and setup

2.1. Graphene surface conductivity

In our work, graphene is considered as a thin layer, characterized via its surface conductivity σ_{gr}. The latter depend on the chemical potential μ_c, the scattering rate Γ , and the temperature T and it is evaluated by the compact expression resulting from the Kubo formula [5], involving only the dominant, at the far-infrared spectrum, intraband term:

$$\sigma_{\mathrm{gr}} = \frac{e^2 k_B T}{\pi \hbar^2 (j\omega + 2\Gamma)} \left[\frac{\mu_c}{k_B T} + 2\ln(e^{-\frac{\mu_c}{k_B T}} + 1) \right]. \quad (1)$$

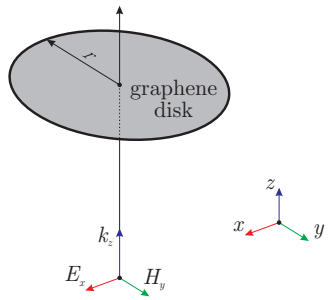

Figure 1: Linearly polarized plane-wave propagating towards a graphene circular scatterer.

2.2. Surface wave propagation properties

The propagation properties of the surface wave onto graphene are evaluated via the complex wavenumber k_ρ that is extracted via [6]:

$$k_\rho = k_0 \sqrt{1 - \left(\frac{2}{\sigma_{\mathrm{gr}} \eta_0} \right)^2}, \quad (2)$$

with k_0 and η_0 the free space wavenumber and wave impedance, respectively. An additional, more intuitive feature of the SPP wave is its wavelength λ_{SPP} that is related to k_ρ via $\lambda_{SPP} = 2\pi/\Re\{k_\rho\}$.

2.3. Setup description

The main device of this work is a circular graphene scatterer of radius r, as depicted in Fig. 1. The selection of such a simple apparatus initiates from its symmetrical configuration. Therefore, the scattering effects are independent of the plane wave polarization that is propagating perpendicularly to the surface.

3. Numerical Analysis

3.1. Computational setup

Our setup is investigated using the popular FDTD method, and the computational domain is divided into $100 \times 100 \times 400$ cells with $\Delta x = \Delta y = \Delta z = 2\,\mu$m. Moreover, a time-step of $\Delta t = 3.8$ fs is selected and open boundaries are terminated with an 8-cell perfectly matched layer. The sim-

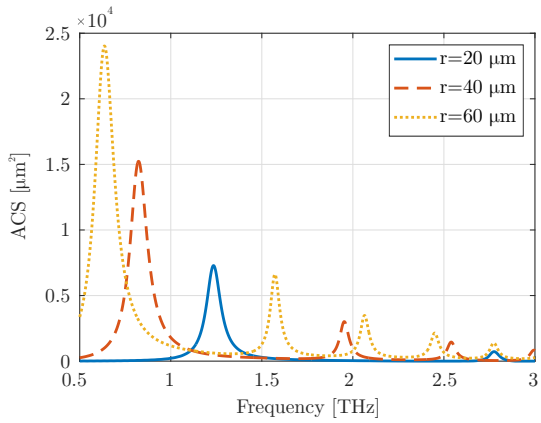

Figure 2: Absorption cross-section of graphene circular scatterers with different radii.

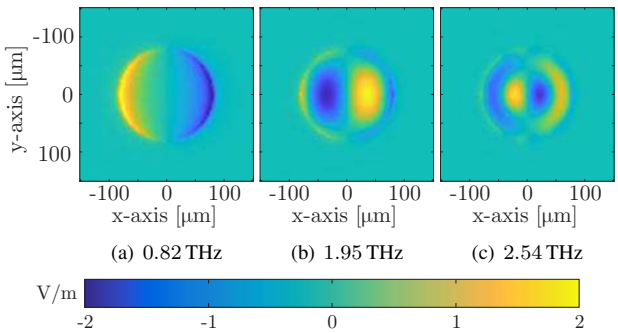

Figure 3: Distribution of the normal, to graphene disk, electric component at different resonance frequencies.

ulations are conducted within the range $0.5 - 3$ THz, where graphene plasmonic waves are strong, while the radius of the circular scatterer varies from $r = 20\,\mu$m to $60\,\mu$m. Finally, graphene parameters are set to $\Gamma = 0.1$ meV and the chemical potential varies from low to moderate values, specifically $0.1 - 0.3$ eV.

3.2. Numerical results

Initially, the broadband absorption cross-section (ACS) is extracted for the graphene disks. This operation facilitates the identification of the resonant frequencies since the ACS peaks highlight the regions of increased absorption. The numerical results for the involved graphene disks are depicted in Fig. 2 and it is evident that various resonances are present. Moreover, their number increases with the radius.

Interestingly, the first mode appears at the frequency that $\lambda_{\rm SPP}$ is equal to the disk's circumference. Additionally, the subsequent modes are at $r = n\lambda_{\rm SPP}/4$ with $n = 3, 5, 7, \ldots$. The electric field distribution at the resonant frequencies, in Fig. 3, indicates that the first mode is concentrated along the edge of the disk, while the higher-order ones are stronger at its interior.

Finally, the radar cross-section is sketched in Fig. 4 for the graphene disk with $r = 40\,\mu$m. Although the back-scattered wave is independent of the frequency, the forward scattering differentiates. Specifically, at the resonant frequencies, 1.95 THz and 2.54 THz, the initial direction is preserved, in contrast to the non-resonant ones that the plane-wave is scattered sideways.

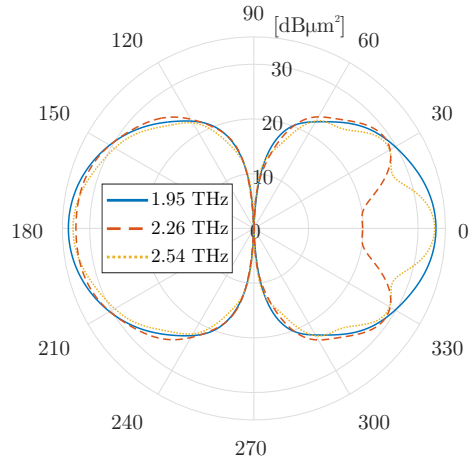

Figure 4: Radar cross-section of a graphene circular scatterer ($r = 40\,\mu$m) at different frequencies.

Acknowledgement

The research project was supported by the Hellenic Foundation for Research and Innovation (H.F.R.I.) under the "2nd Call for H.F.R.I. Research Projects to support Post-Doctoral Researchers" (Project Number: 756).

References

[1] J. Garcia de Abajo, Graphene plasmonics: challenges and opportunities, *ACS Photonics* 1(3): 135–152, 2014.

[2] V. Salonikios *et al.*, Modal analysis of graphene microtubes utilizing a two-dimensional vectorial finite element method, *Appl. Phys. A* 122(4): 1–7, 2016.

[3] V. Salonikios *et al.*, Computational analysis of graphene-based periodic structures via a three-dimensional field-flux eigenmode finite element formulation, *Prog. Electromagn. Res. M* 92: 157–167, 2020.

[4] O. Tsilipakos *et al.*, Toward intelligent metasurfaces: the progress from globally tunable metasurfaces to software-defined metasurfaces with an embedded network of controllers, *Adv. Opt. Mater.* 8(17): 2000783, 2020.

[5] V. P. Gusynin, S. G. Sharapov, and J. P. Carbotte, Magneto-optical conductivity in graphene, *J. Phys. Condens. Matter* 19(2): 026222, 2006.

[6] G. W. Hanson, Dyadic Green's functions and guided surface waves for a surface conductivity model of graphene, *J. Appl. Phys.* 103(6): 064302, 2008.

Scattering by a dielectric cylinder with arbitrary cross section using Pseudo-spectral Modal Method

Tsirinantenaina A. Rafalimanana[1], Gérard Granet[2*], Karyl Danielson Raniriharinosy[1]

[1]LAPAUF, Université de Fianarantsoa, Fianarantsoa, Madagascar
[2]Université Clermont Auvergne, CNRS, SIGMA Clermont, Institut Pascal F-63000 Clermont-Ferrand, France
*corresponding author, E-mail: gerard.granet@uca.fr

Abstract

We present a new semi-analytical formulation for diffraction by structured cylinders. A pseudo-spectral modal method is used to solve the Maxwell equations written in curvilinear coordinates. The program is compared with the numerical results obtained with finite element method using Comsol Multiphysics.

1. Introduction

The last two decades have been marked by the study and fabrication of structured materials to control light. To solve complex electromagnetic problems, numerical methods are widely used. We propose a semi-analytical model based on the pseudo-spectral method using the Chebyshev differentiation matrix [1, 2, 3]. In this method, Maxwell's equations are written in their covariant form and a change of coordinates is used to transform an arbitrary cross section cylinder into a circular cross section one. Since the boundary of the cylinder coincide with a coordinate surface, writing the boundary conditions is very easy.

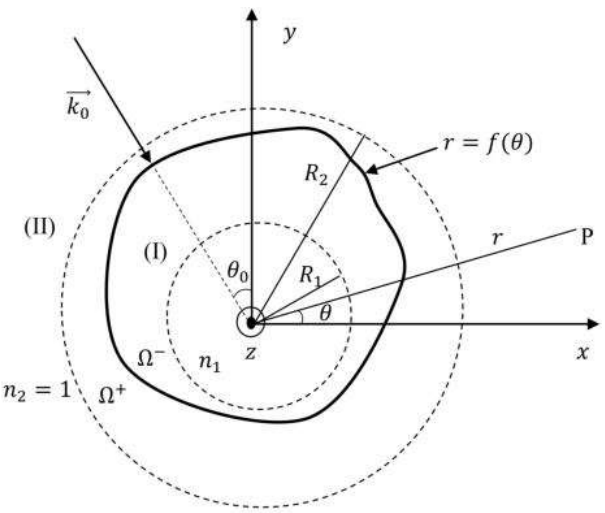

Figure 1: Geometry of the problem.

Since the structure has cylindrical symmetry and 2π periodic with θ, in the usual cylindrical coordinate the incident field is given by :

$$E_z^i(r,\theta) = E_0 \exp[ik_0 r \sin(\theta - \theta_0)] \tag{1}$$

2. resolution

2.1. New Coordinates

The change of coordinates transforms a section with arbitrary contour into a circular section. In the new coordinates, the space is divided into four regions separated by circles with radii $u_1 = R_1$ and $u_3 = R_2$. The circle with radius u_2 coincides with the profile under study. We have :

$$a(u,\theta) = \begin{cases} R_1 + [f(\theta) - R_1]\dfrac{u-u_1}{u_2-u_1} & \text{for} \quad u_1 \le u \le u_2 \\ f(\theta) + [R_2 - f(\theta)]\dfrac{u-u_2}{u_3-u_2} & \text{for} \quad u_2 \le u \le u_3 \end{cases} \tag{2}$$

In order to respect the non singularity of the field at $r = 0$ and the radiation condition for $r \to +\infty$, the field inside the region $r < R_1$ and outside the region $r > R_2$ are respectively developed in Fourier-Bessel and Hankel series.

$$E_z^{(1)}(r,\theta) = \sum_{m=-M}^{M} A_{1m} J_m(k_0 n_1 r) \exp(im\theta) \tag{3}$$

$$E_z^{(3)}(r,\theta) = \sum_{m=-M}^{M} \left\{ \left[(-i)^m J_m(k_0 r) + A_{3m} H_m^{(2)}(k_0 r) \right] \exp(im\theta) \right\} \tag{4}$$

2.2. Maxwell's Covariant Equations

In a source free homogeneous medium, considering the angular frequency ω in the harmonic regime $\exp(-i\omega t)$ and with Einstein's convention, the Maxwell-Minkowski equations are written.

$$\begin{cases} \xi^{ijk}\partial_j E_k = +i\omega B^i \\ \xi^{ijk}\partial_j H_k = -i\omega D^i \end{cases} \tag{5}$$

where $i, j, k = 1, 2, 3$. ξ^{ijk} is the Levi-Civita indicator.

The constitutive equations are given by :

$$\begin{cases} B^i = \mu^{ij} H_j \\ D^i = \varepsilon^{ij} E_j \end{cases} \tag{6}$$

where the μ^{ij} and the ε^{ij} depend on the metric associated with new coordinates and on the medium.

2.3. Pseudo spectral method

In regions $\Omega^- = [u_1, u_2]$, $\Omega^+ = [u_2, u_3]$, the unknown function $E_z(u)$ is approximated by the product of a set of suitable Lagrange-interpolating functions C_n and unknown grid point values $E_z(u_n)$ at collocation points u_n as follows [4]:

$$E_z(u) = \sum_{n=0}^{N} C_n(u) E_z(u_n) \tag{7}$$

Considering Tchebycheff polynomials T_n and Gauss- Lobatto points u_n as basis functions and collocation points, respectively, the explicit form of C_n is:

$$C_n(u) = \frac{(-1)^{n+1}(1-u^2)T'_N(u)}{\sigma_n N^2 (u - u_n)}, \quad u \neq u_n \tag{8}$$

with $\sigma_0 = \sigma_N = 2$ and $\sigma_n = 1$ for $1 \leq n \leq N-1$. The above expansion is matched with (3) at $u = u_2$ and with (4) at $u = u_3$ which allows to compute the A_{3m} which correspond to the expansion coefficients of the diffacted field. Lastly, we may compute the radar cross defined as.

$$\sigma = \lim_{r \to \infty} 2\pi r \frac{|E^{diff}|^2}{|E^{inc}|^2} \tag{9}$$

3. Results

For z-invariant cylinders equation (5) reduces to two independent scalar problems with E_z or H_z as unknowns according to the incident plane wave polarization. Numerically, we obtain a matrix equation which is solved for the A_{3m}. For illustrative purpose, we consider the profile defined as $r = \lambda[1 + 0.5\sin(10\theta)]$. The refractive index is $n_1 = 1.5$.

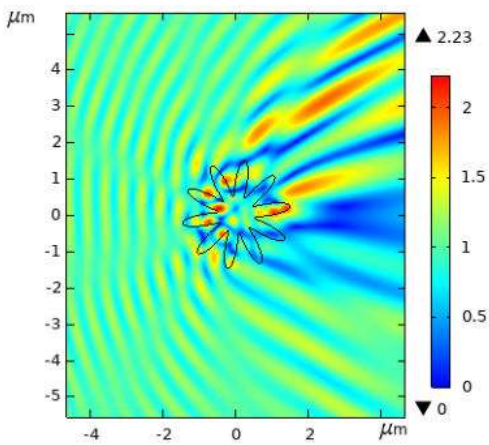

Figure 2: Spatial distribution of the E_z ($\lambda = 1\mu m$).

4. Conclusions

We have proposed a pseudo-spectral modal method for electromagnetic diffraction. We could solve the problem of diffraction by cylinder with arbitrary section which is very difficult with other method. The specificity of this method lies in the fact that the field at infinity can be handle without any Perfect Matched Layer.

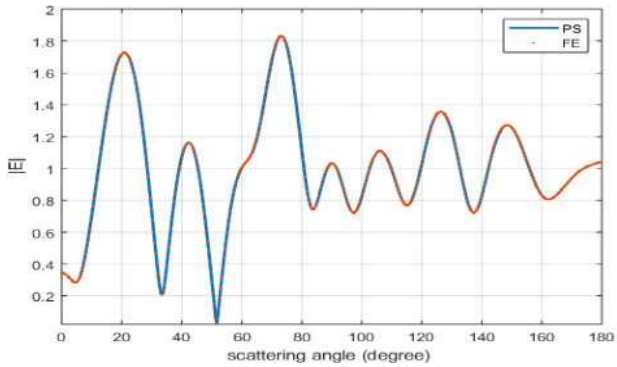

Figure 3: Comparison of the total field surrounding the cylinder at a distance of $r = 2.5\lambda$.

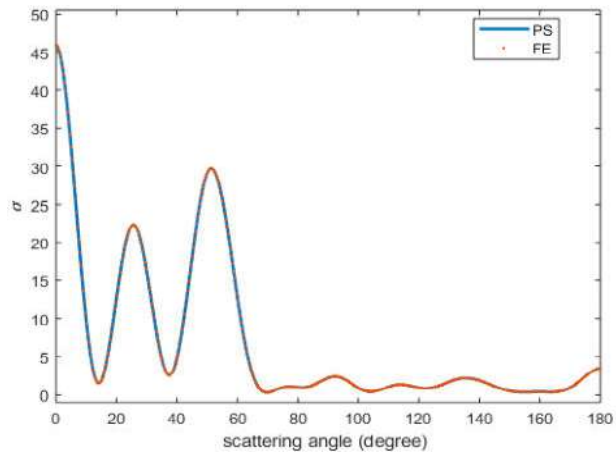

Figure 4: Comparison of the Radar Cross Section obtained with our method and with Comsol.

References

[1] Gérard Granet, Fourier-matching pseudospectral modal method for diffraction gratings : comment *Optical Society of America*, pp. 1843-1845, 2012

[2] Kofi Edee, Mira Abboud, Gérard Granet, Jean François Cornet, Nikolay A. Gippius, Mode solver based on Gegenbauer polynomial expansion for cylindrical structures with arbitrary cross sections. *Optical Society of America*, pp. 667-676, 2014

[3] Denis Prémel, Gérard Granet, François Caire, Matching curvilinear coordinates for the computation of the distribution of eddy currents in a cylindrical tube described by an arbitrary longitudinal internal/external profile. *The European Physical Journal Applied Physics*, 2016

[4] Lloyd N Trefethen, Spectral methods in matlab. *SIAM*, 2000

Limits on Electromagnetic Scattering

Pengning Chao[1], Benjamin Strekha[1], Rodrick K. Defo[1], Sean Molesky[2], and Alejandro W. Rodriguez[1*]

[1]Department of Electrical and Computer Engineering, Princeton University, Princeton, NJ, USA
[2]Department of Engineering Physics, Polytechnique Montreal, Montreal, Quebec, Canada
*corresponding author, E-mail: arod@princeton.edu

Abstract

Much of the continuing appeal and challenge of electromagnetism stems from the same root: given some desired objective (enhancing radiation from a quantum emitter, the field intensity in a photovoltaic cell, the radiative cross section of an antenna) subject to some physical constraints (material compatibility, fabrication tolerances, or system size) there is currently no method for finding or assessing uniquely best wave solutions. While improvements in nanofabrication and computational methods have driven dramatic progress in expanding the range of achievable optical characteristics, they have also greatly increased design complexity [1]. These developments have led to heightened relevance for the study of fundamental limits on optical response. Here, we review recent progress in our understanding of these limits with special focus on an emerging theoretical framework that combines computational optimization with conservation laws to yield physical limits capturing all relevant wave effects [2]. Results pertaining to canonical electromagnetic problems such as thermal emission (Fig. 1), scattering cross sections, Purcell enhancement, and power routing are presented.

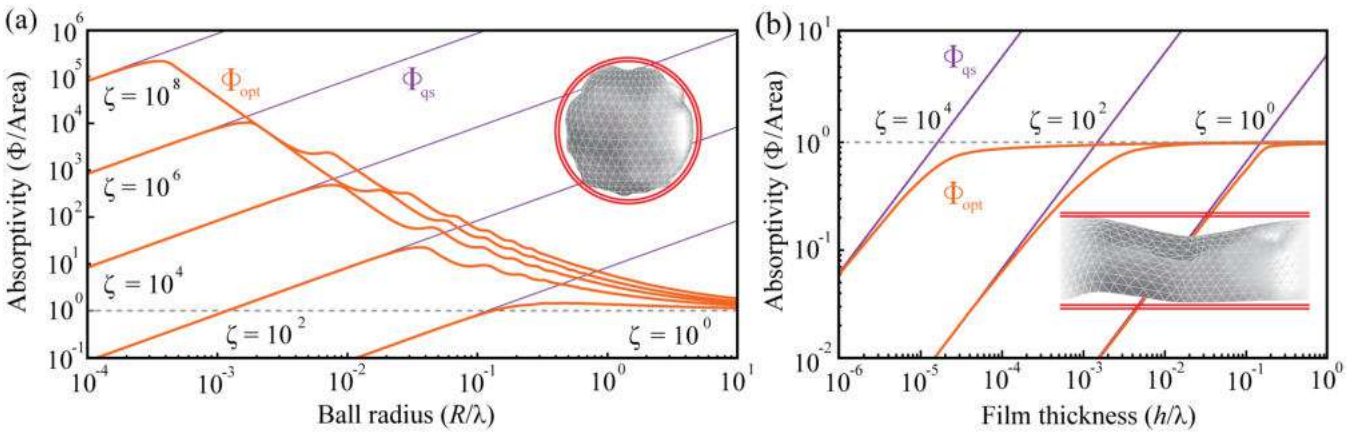

Fig. 1. Representative maximum scattering bounds for integrated absorption and incoherent emission. Both panels display upper bounds on area-normalized absorptivity Φ_{opt} (orange lines) for several values of the material efficacy figure of merit $\zeta = |\chi|^2/\mathrm{Im}[\chi]$ at a fixed wavelength λ. These quantities are shown as a function of the wavelength normalized radius R of an enclosing sphere (left) or thickness h of an enclosing slab (right).

References

[1] Sean Molesky, Zin Lin, Alexander Y Piggott, Weiliang Jin, Jelena Vuckovic, and Alejandro W Rodriguez. Inverse design in nanophotonics. *Nature Photonics*, 12 (2018) pp. 659–670.

[2] Pengning Chao, Benjamin Strekha, Rodrick Kuate Defo, Sean Molesky, and Alejandro W. Rodriguez. Physical limits on electromagnetic response. *arXiv*:2109.0566 (2021).

5G propagation

Design of Multiband-Filters for Mobile Radio Applications

Mohamed Karim LAOUFI [1], Slimane MEKAOUI[1], Mohamed Lamine TOUNSI [2]

[1] Laboratoire LCPTS, Faculty of electrical engineering, USTHB University, Algiers, Algeria
[2]Laboratoire LCDEP, Faculty of electrical engineering, USTHB University, Algiers, Algeria
E-mail: mltounsi@ieee.org

Abstract

In this paper, a new multi-standard filter with four resonance frequencies is proposed for radio-mobile including GSM/4G LTE, WLAN and 5 G applications. The design and synthesis is resolved using a new formulation of the FDTD method. The metal finite conductivity and thickness are rigorously taken into account. The FDTD computed results are in good agreement with simulated data obtained with CST electromagnetic tool.

1. Introduction

With the increasing development of multi-service wireless communication networks, it has become essential to synthesize microwave systems and components with various modern communication standards [1]. Furthermore, in order to satisfy the strict constraints related to high-speed and high-capacity transmission, future mobile communication systems must use simultaneously several frequency bands in a single circuit [2]. Thus, transceivers operating on multiple bands are highly preferred [3]. Recently, there has been a strong demand for planar filters with multiple resonances, compact size, low insertion losses and low integration cost [4],[5]. Several prototypes of two-, three-, and four-band planar filters have been proposed [3]. However, without increasing the effective size of the filter, it becomes difficult to combine multiple frequencies on a single circuit [6]. Therefore, using a single multi-band filter operating at different frequencies can only reduce the overall size of system [7],[8]. In [9], the frequency transformation method is employed. The authors are based on the parallel association of one band-pass resonator and three band-stop ones to generate four resonance frequencies in a lumped-element configuration. In [10], quad band band-pass filters (BPFs) was presented using stub loaded resonators (SLR). The proposed resonator has been analyzed using even–odd mode approach. In [11], quad-band (BPFs) were realized by using stepped-impedance coupled-line quad-mode resonators (SICLQMRs). Multi-section parallel and interdigital coupling structure are used in this design.

In this paper, we propose a new topology of a multi-band filter that can be used simultaneously for GSM/4G LTE (around 1.8 GHz), 5G (3.5 GHz) and WLAN (5.42 GHz) applications. The design of the proposed filter is resolved in fullwave-mode using a new FDTD formalism which simultaneously takes into account the finite conductivity as well as the thickness of the metallic thin film. We note also that the proposed update equations remain applicable for any planar structure with an imperfect thin film conductor with an arbitrary number of metallization levels.

2. Modified FDTD Algorithm

First, we present a modified FDTD formulation to model imperfect metallic thin films [12], which consider the finite conductivity and thickness. The tangential components (parallel to the plane of the circuit) are given by:

$$E_x^{n+1}(m+\frac{1}{2},p_c,q) = AE_x^c.E_x^n(m+\frac{1}{2},p_c,q) + E_{x1}^n(m,p_c,q) + E_{x2}^n(m,p_c,q) \quad (1.1)$$

$$E_z^{n+1}(m,p_c,q+\frac{1}{2}) = AE_z^c.E_Z^n(m,p_c,q+\frac{1}{2}) + E_{z1}^n(m,p_c,q) + E_{z2}^n(m,p_c,q) \quad (1.2)$$

$$E_{x1}^n(m,p_c,q) = BE_x^c.[H_z^{n+\frac{1}{2}}(m+\frac{1}{2},p_c+\frac{1}{2},q) - H_z^{n+\frac{1}{2}}(m+\frac{1}{2},p_c-\frac{1}{2},q)] \quad (2.1)$$

$$E_{x2}^n(m,p_c,q) = CE_x^c.[H_y^{n+\frac{1}{2}}(m+\frac{1}{2},p_c,q+\frac{1}{2}) - H_y^{n+\frac{1}{2}}(m+\frac{1}{2},p_c,q-\frac{1}{2})] \quad (2.2)$$

$$E_{z1}^n(m,p_c,q) = BE_Z^c.[H_y^{n+\frac{1}{2}}(m+\frac{1}{2},p_c,q+\frac{1}{2}) - H_y^{n+\frac{1}{2}}(m-\frac{1}{2},p_c+\frac{1}{2},q)] \quad (2.3)$$

$$E_{z2}^n(m,p_c,q) = CE_Z^c.[H_x^{n+\frac{1}{2}}(m,p_c+\frac{1}{2},q+\frac{1}{2}) - H_x^{n+\frac{1}{2}}(m,p_c-\frac{1}{2},q+\frac{1}{2})] \quad (2.4)$$

The coefficients AE_u^c, BE_u^c and CE_u^c (u=x or z) are given in [13]. Equations (1) are expressed at instant (n+1)Δt. Δt is the time step, while m and q denote the mesh indices along the x and z directions respectively, p_c refers to the index corresponding to the metalized interface [14].

3. Design of multi-band filters

In this part, the proposed FDTD algorithm is applied to the synthesis of a shielded filter with four pass bands. Two forms of resonators (S and L shaped) are considered. The inter-resonator coupling essentially depends on the distance S separating them. The resonators are parallel coupled and judiciously placed in order to obtain the desired specification filter. The chosen substrate and conductor are respectively alumina (ε_r=9.4) and copper (σ=5.8. 10^6 S/m, thickness t= 5 µm). The shield height is b=9.92 mm. The dimensions of the filter are (figure 1): L_x=2.54 mm, L_z=10.04 mm, L=26.77 mm, w=1.42 mm, s=0.87 mm, G=1.9 mm, a=23.18 mm, h=1.86 mm. Figures 2 and 3 illustrate respectively the insertion loss and the return loss versus frequency. A good agreement is obtained compared to data simulated with CST commercial software. Table 1 shows better performance especially in terms of return loss (RL) compared to some 4-band filters [15] [16].

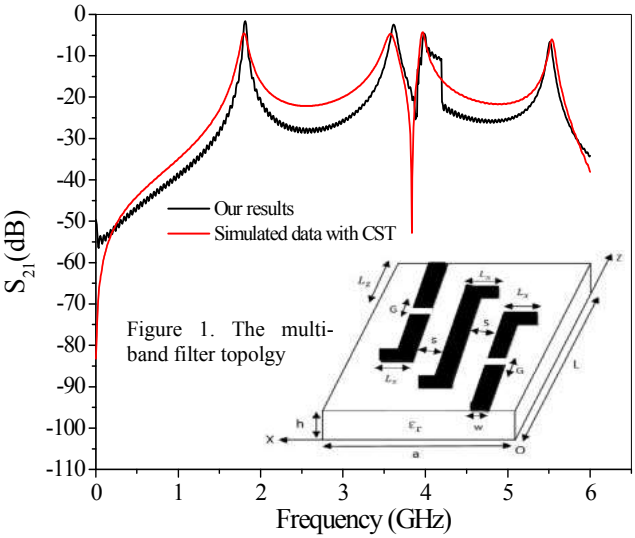

Figure 2: Insertion losses versus frequency

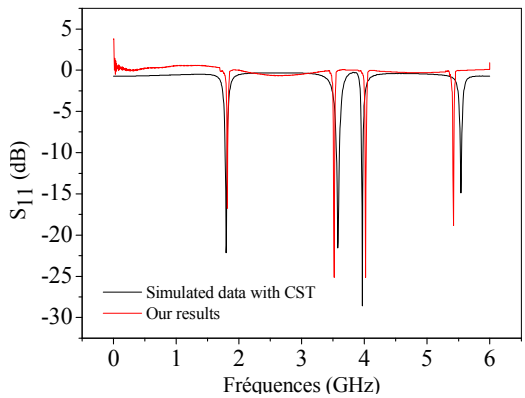

Figure 3: Return loss versus frequency

Table 1: Comparison results with other works

Réf	$f_1/f_2/f_3/f_4$ (GHz)	IL (dB)	ISO (dB)	RL (dB)	Size/λ_g
[15]	1.55/2.2 3.45/5.3	2.9	12	10	0.5x0.36
[16]	2.46/3.41/ 6.65/9.09	2.23	26	14	0.59x0.26
Our results	1.78/3.5 3.88/5.42	3.5	31	15	0.42x0.48

(IL: insertion losses, ISO: minimum isolation between bandwidths, RL : minimum return loss)

4. Conclusion

In this paper, a new design of quad-band shielded BPFs was proposed for GSM/4G LTE, WLAN and 5G applications. Good performances have been obtained comparing to other works: the filter is compact, the isolation between resonances is greater than 31 dB, the insertion losses do not exceed 3.5 dB. A good matching is also signaled (greater than 15 dB). In addition, the particularity of the proposed filter is that the topology is relatively simple than those reported in the literature. Finally, a modified formulation of the FDTD algorithm has been proposed to rigorously taking into account the finite conductivity of the metallic thin film as well as its thickness. Note that this technique can be further extended to any planar structure with an imperfect thin film conductor and an arbitrary number of metallization levels.

References

[1] E. H. Liu et al., "Triband high-temperature superconducting bandpass filters using multimode resonators", *IEEE Transactions on Applied Superconductivity* vol. 26, N°5, August 2016.

[2] T. Unno et al. "Compact high-pole hts triband bandpass filters using a new feeding structure," *in IEEE Transactions on Applied Superconductivity,* vol. 28, no. 4, pp. 1-5, June 2018.

[3] F. Song et al.,"Quad-Band superconducting bandpass filter using quad-mode stub-loaded resonators with controllable frequencies and bandwidths", *IEEE Transactions on Applied Superconductivity*, vol. 26, Issue: 6, 2016.

[4] J. Tang et al. "Miniaturized multiband hts bandpass filter design using a single-perturbed multimode resonator with multitransmission zeros", *IEEE Transactions on applied superconductivity,* vol. 28, No. 4, June 2018.

[5] X. Guan et al., "Compact triple-band high-temperature superconducting filter using coupled-line stepped impedance resonator", *IEEE Transactions on Applied Superconductivity,* vol. 26, N°. 7, October 2016.

[6] P. Ranjan et al.,*"Triple band microwave filter using stepped impedance line (SIL) and stub loaded resonator with five transmission zeroes", 2017 IEEE International Microwave and RF Conference (IMaRC)* , Dec. 2017.

[7] D. K. Choudhary and R. K. Chaudhary, ''A compact CPW-based dualband filter using modified complementary split ring resonator,'' *AEU-Int. J. Electron. Commun*., vol. 89, pp. 110–115, May 2018.

[8] X. Guo, L. Zhu, and W. Wu, ''Design method for multiband filters with compact configuration in substrate integrated waveguide,'' *IEEE Trans. Microw. Theory Techn*., vol. 66, no. 6, pp. 3011–3018, Jun. 2018.

[9] S. W. Lan et al., "A triband bandpass filter with wide stopband using asymmetric stub-loaded resonators," *IEEE Microwave and Wireless Components Letters,* vol. 25, no. 1, 2015.

[10] J. Tang, H. Liu, Q. Zhang, B. Ren, and Y. Liu,"Miniaturized multiband hts bandpass filter design using a single-perturbed multimode resonator with multitransmission zeros", *IEEE Transactions on Applied superconductivity,* Vol. 28, No. 4, June 2018.

[11] F. Song et al., "Quad-band superconducting bandpass filter using quad-mode stub-loaded resonators with controllable frequencies and bandwidths" *IEEE Transactions on Applied Superconductivity,* Vol 26, No. 6, June 2016.

[12] T. Xia et al., *"A Full wave integral equation analysis of conductors", Progress in Electromagnetic Research Symposium (PIERS),* Shanghai, China, pp. 291–295, August 2016.

[13] M. K. Laoufi, S. Mekaoui, M. L. Tounsi, "A Novel FDTD algorithm for analyzing imperfect microwave filters", *11th IEEE Annual Information Technology, Electronics and Mobile Communication Conference (IEMCON).* Vancouver, BC, Canada 4-7 Nov. 2020

[14] M. K. Laoufi, S. Mekaoui, M. L. Tounsi, and M.C.E. Yagoub, "Modified FDTD algorithm for analysis of anisotropic stratified waveguides and multilayered microwave filters", *19th Mediterranean Microwave Symposium,* Hammamet- Tunisia, 31 Oct.-2 Nov. 2019.

[15] C.W. Cui et al., "Quad-band bandpass filter design by embedding dual-band bandpass filters with dual-mode notch elements", *Electronics Letters*, Nov. 2014, Vol. 50 No. 23 pp.1719–1720.

[16] B. H. Zhu et al. "A quad-band bandpass filter using sept-mode double square-ring loaded resonator", *Microwave Optical Technology Letters*, Wiley 2020.

Body-centric propagation

A Biomedical Implantable Patch Antenna with X-shaped slot for Wireless Communication Networks

Sarosh Ahmad[1,2] *, Shuvra Barua[3], Ayesha Akram[4], and Bilal Manzoor[5]

[1]Department of Electrical Engineering and Technology, Government College University Faisalabad (GCUF), Faisalabad, Pakistan
[2]Department of Signal Theory and Communications, Universidad Carlos III de Madrid (UC3M), Madrid, Spain
[3]Department of Electrical and Electronic Engineering, Ahsanullah University of Science & Technology (AUST), Dhaka, Bangladesh
[4]Department of Computer Science and Information Technology, University of lahore, Pakistan.
[5]Department of Telecom Engineering University of Engineering and Technology (UET), Taxila, Pakistan
*corresponding author, E-mail: saroshahmad@ieee.org

Abstract

Since biomedical implanted antennas play a crucial role in biomedical telemetry applications, this study gives an overview of an Industrial, Scientific, and Medical (ISM) band at the range of 915 MHz with a compact size, implantable, and low-profile antenna. This antenna was described with a feature of simple slotted patch equipped by a coaxial probe with an impedance value of 50-ohm. There are four slotted resonators in this patch, which are simulated on a flexible substrate of Roger Duroid RT5880 with a typical thickness of 0.254 mm. The suggested antenna's overall dimensions are 7mm × 7mm × 0.254 mm, and it spans a frequency range between 800 MHz and 1 GHz (200 MHz) within the skin tissue. Finally, the simulation resolved the value of the Specific Absorption Rate (SAR) within the skin over 1 g of bulk tissue was found to be 8.17 W/kg, which shows that, the recommended SAR values were below the Federal Communications Commission's limit (FCC). Miniaturization has been achieved, and it is a good candidate for biomedical implant applications.

1. Introduction

To ameliorate the living conditions of the patients the Implantable Medical Devices (IMD) possess a crucial role and with the help of this antenna the telemetry system has an advantageous feature in terms of higher rate of data and long-distance communications of the wireless communications system among the IMDs as well as the off-body monitoring gadgets [1]. The IMDs are the key elements of this proposed model [2]. In case of in-body antenna, the gadget is supposed to be thin in size, less quantity of SAR and should offer a great deal of flexibility [3]. Hence, while designing an antenna it should be congruent and its features are to be in accordance with the human corps. Human body tissues can be exposed to the antenna's operational frequency which can create an impact on the body tissues. For this reason, a broader bandwidth should be a feature of the antenna which can facilitate the necessary frequency bands after the trial on body tissues [4]. An antenna's radiation properties can vary with respect to the multifarious layers and structures of the human corps. The human tissue structure is different in different part and since the tissues have diverse dielectric property, it is really a challenging task to design a biocompatible antenna for medical application [5]. Generally, the in-body antennae are of the range between 402 MHz- 405 MHz [6-8] and 2.4 GHz - 2.48 GHz at the range of ISM when it comes to the wireless communication [9-12]. The realized gain in the reported frequency was found to be -34.9 dB and operating bandwidth was 14.9% respectively. A tiny in-body polarized antenna with circular-shape with an ameliorated impedance congruent for the medical applications was presented in [13].

The radiational patch which is rounded-shape has a X-shaped slot within the ground plane. Rogers 3010 substrate was the material utilized with a reported height of 0.634 mm. Since there is a double-layered substrate for which the antenna profile becomes hefty. However, the antenna was less human congruous with a higher value of SAR of 649 W/kg that tends to be bigger than that of the standard limitation of IEEE/IEC 6270-1 over the mass tissue of 1g. [14] reported an implantable antenna which was at 915 MHz for the purpose of wireless power transfer. The overall dimension was 11 × 11 × 1.27 mm^3 with the substrate of Roger 3010 which demonstrated an impedance bandwidth of 3.8% as well as its realized gain was -29 dB. Nevertheless, the calculation of the SAR values was not performed as the size was larger with respect to the less bandwidth [15]. The complete volume of this reported antenna was 15 × 15 × 1.27 mm^3, that was printed on a substrate of Roger 3010, and it was operational at the range of 915 MHz possessing a bandwidth of 10.6%. Having performed the experiment on the body tissue, 517 W/kg was the SAR value of the antenna which was a bigger value than that of our proposed one.

The article presents a compact sized implantable antenna made in pursuit of the biomedical applications which is operated in ISM band at the range of 915 MHz with a

volume of at 7 × 7 × 0.254 mm^3 (0.08λg × 0.08λg × 0.003λg) on the substrate of Rogers RT5880 whose εr = 2.2 and tanδ = 0.0009. At the range of 915 MHz, the radiation pattern of the antenna is reported to be omnidirectional in both E and H plane. This design has a configuration of full ground planar shape along with four slotted resonators, that helps the bandwidth to response and a decreased back-radiation is available on the skin tissue. For example, the dimension of the skin is maintained 20× 20 mm^2. Due to the novel and compact modified patch, a greater bandwidth at the range of 915 MHz is covered and the peak gain is estimated to be analogous to the previous research. Basically, the performance and the efficacy of the designed antenna in the vicinity of the human body are improved and the SAR values were significantly minimized. a minimum amount of SAR values was reported and better results in accordance with measurement and simulation. This paper is comprised of five parts, for instance: section 1, which firstly introduces the research task as well as covers the background of the proposed work, the problem statement, significance, and our objectives of this proposed research. Section 2 refers to the design analysis and section 3 emphasizes the fabrication as well as measurement outcomes. Section 4 reports the test within the human skin tissue and finally, section 5 draws the conclusion.

2. Procedure for Designing the Antenna

A slotted patch antenna, compact in nature including the radiator having a novel shape, that is fed by a coaxial type of probe. Our proposed antenna has different layers such as a full planar ground, a thickness of 0.254 mm, low-profiled substrate of Roger RT5880, whose ε_r = 2.2 and tanδ = 0.0009 along with a slotted patch demonstrated in Fig. 1. The complete dimensions of the antenna are reported to be 7 × 7 × 0.254 mm^3 (0.08λg × 0.08λg × 0.003λg). The HFSS (High-frequency structure simulator) software has been used to simulate the antenna and -25dB was found to be the value of S_{11} at a working frequency and 21.85% was the operating bandwidth of the proposed antenna. The optimized values were reported in Table 1. Fig. 2 depicts the implanted antenna's current density. The current circulates mostly around the top and bottom sides of the resonators, as well as the feed patch. The red arrows represent which part of the antenna contributes the most to functioning in the intended frequency band.

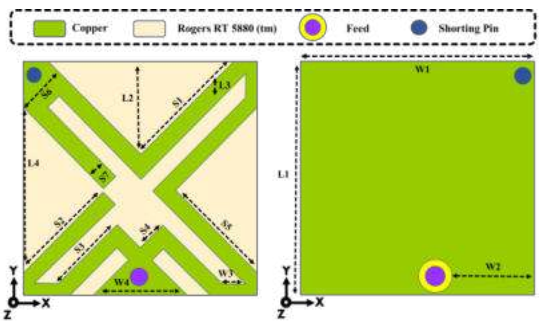

Figure 1: Proposed dimensions of the low-profile antenna, (a) front view, (b) back view.

Table 1. Optimized parameters of the proposed design.

Dimensions	Values (mm)	Dimension	Values (mm)
S1	3.94	W1	7.0
S2	3.34	W2	3.0
S3	1.9	W3	0.7
S4	0.7	W4	2.7
S5	3.4	L1	7.0
S6	1.4	L2	2.79
S7	0.5	L3	0.7
S8	3.5	L4	4.8

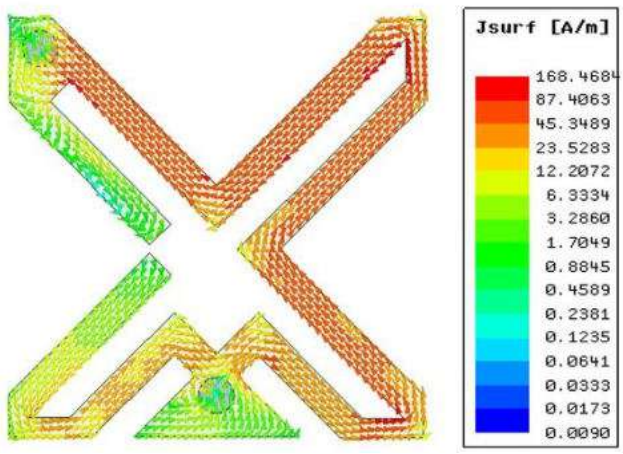

Figure 2: Current distribution all over the patch at the range of 915 MHz

2.1 Proposal for the procedure of Antenna Design

The procedure for designing the proposed Antenna is explained as per the following:

Step I: A slot of the shape of triangle is initiated (Fig. 3(a)) on left of the patch due to the generation of a frequency band at the range of 1.5 GHz. However, the return loss is reported to be bigger than -10 dB as per Fig. 4.

Step II: For keeping the S_{11} value below -10 dB (Fig. 3(b)) as well as for altering the frequency band towards a lower frequency band, A "T"-shaped slot has been initiated in a truncated patch for the operation of the Antenna at the range of 1.4 GHz

Step III: Within the patch, the introduction of the X-shaped slot (Fig. 3(b)). This slot shifts the band to 0.7 GHz from 1.4 GHz (700 MHz)

Step IV: For assisting the resonation of the antenna, the proposed novel shape is made (Fig.3(c)) for obtaining the desired frequency at 0.915 GHz.

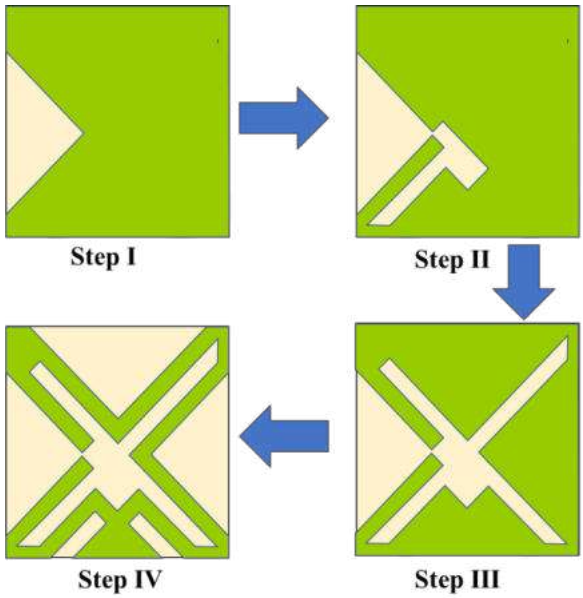

Figure 3: Design procedure of the Implantable antenna; (a) (STEP I) Truncated patch, (b) (STEP II) Slotted truncated patch, (c) (STEP III) X-shaped slotted patch, (d) (STEP IV) Proposed design.

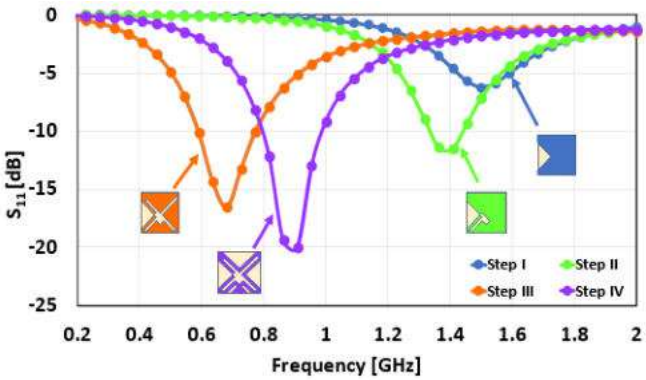

Figure 4: Comparison of the Simulation results: S_{11} for the design steps shown in Fig. 3.

2.2 Proposed Antenna's Parameter Analysis

Here, the parameter analysis of the antenna is explained. At 0.915 GHz range, by altering the values of key parameters the reflection coefficient can be fine-tuned. For instance: the feed patch width 'S4', the patch resonator length 'S2', the upper left resonator length of the patch 'S8', the patch slot length at a 45º angle 'S3', as well as the via position as illustrated in Fig.5. From Fig.5(a), we can see how the frequency band shifted to 0.915 GHz from 1.6 GHz by shifting the value of 'S2' from 2.5mm to 3.34mm (685 MHz). The frequency spectrum switched to 0.915 GHz from 1.5 GHz (585 MHz) when the value of the 'S4' was altered to 0.7mm from 0.3 mm, as shown in Fig.5(b). According to Fig.5(c), the frequency band increases to 0.75 GHz from 0.60 GHz (150 MHz) when the values of the 'S3' are changed to 1.8 mm from 1.6 mm. Fig.5(d) shows the frequency shifts to 0.9 GHz from 1.7 GHz (800 MHz) in case the value of 'S8' is altered to 3 mm from 2mm. By shifting the via position in our proposed patch antenna the frequency band has been altered to be higher than our intended frequency band. Fig.5(e) demonstrates that positioning the via at position 1, the frequency band was found 1.4 GHz, and when the via was displaced to position 2 from position 1, the frequency band was found 0.8 GHz, and when the via was moved from position 2 to position 3, we were able to achieve our desired frequency band of 0.915 GHz.

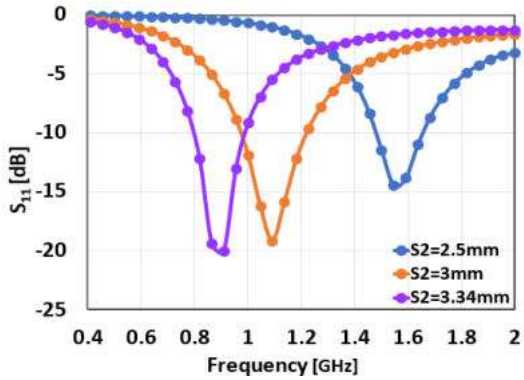

(a)

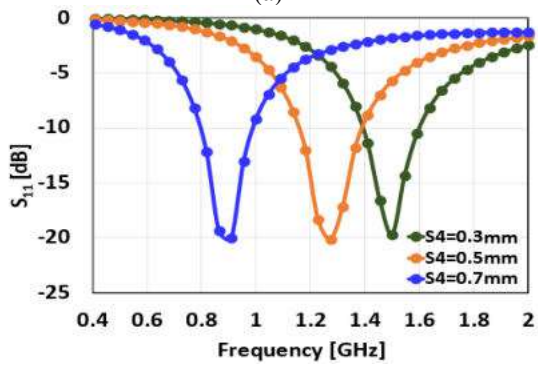

(b)

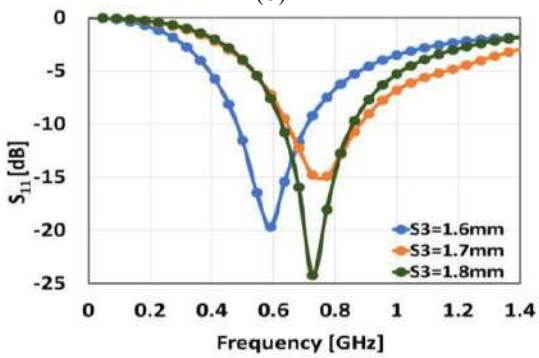

(c)

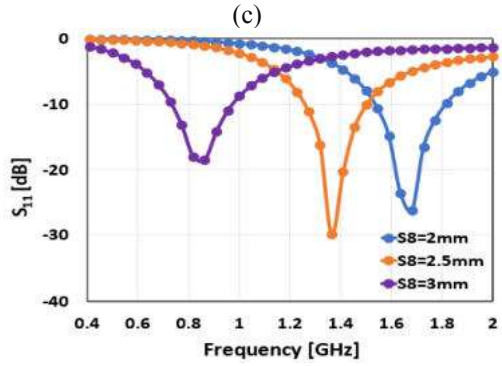

(d)

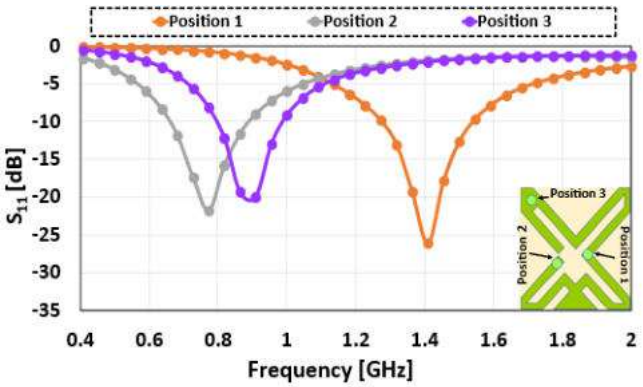

(e)

Figure 5: Proposed antenna's parametric study; (a) change in *'S_2'*, (b) change in *'S_4'*, (c) change in *'S_3'*, (d) change in *'S_8'*, (e) changing the position of the Via.

3. Results and Discussion

In this section, our antenna design is simulated and experimented within the body tissue to see if it is suitable for biomedical telemetry applications. As a result, when making a design of an antenna for biotelemetry applications for high accurate feature, the existence of human body phantoms is to be taken into consideration in case of calculating the SAR. The performance of our antenna in the proximity of the human phantoms, as well as the SAR values at 915 MHz, are assessed as well for this objective. As per Fig. 6, the surface area of the phantoms box is of 20 x 20 mm^2. Simulation of the proposed antenna is done with HFSS Studio.

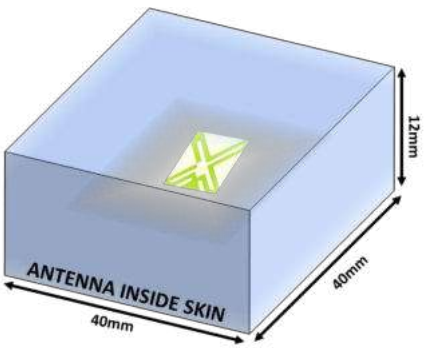

Figure 6: Skin phantom box's perspective view.

In case of an ideal situation, in-body antennae would be designed to minimize substantial coupling effects caused because of the body tissues. This antenna is implanted 2 mm deep inside the epidermal tissue of the human corpse during the experiment, as presented in Fig. 7. This reported design is kept inside a 40 mm x 40 mm of body tissue to check these impacts. Due to the same qualities of human skin tissue, a skin-mimicking gel having the properties like the relative permittivity (ε_r) of 43 and an electrical conductivity (σ) of 1.40 was involved.

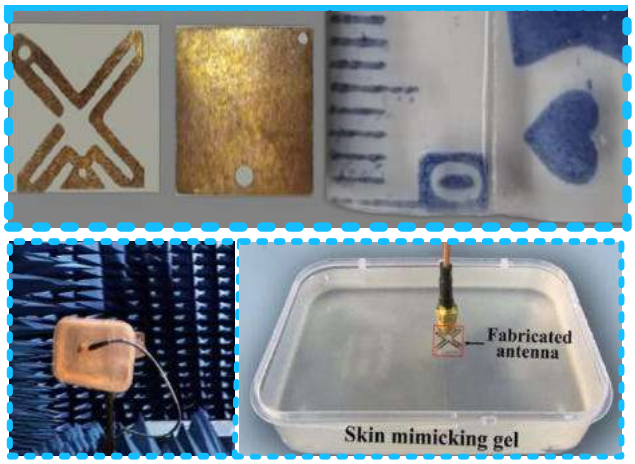

Figure 7: Fabricated prototype and the experimental setup system of the proposed antenna.

Fig.8 shows the contrast between the measured and simulated results of S_{11} of the antenna within the skin. The biomedical antenna is found operational between 780 MHz and 1000 MHz (220 MHz) at the range of 915 MHz, as per the simulated S_{11} beneath the skin, whereas the proposed antenna inside the mimicking gel had a bandwidth range varies between 785 MHz and 998 MHz (213 MHz). It demonstrates that the measured and simulated findings are in well-matched with each other.

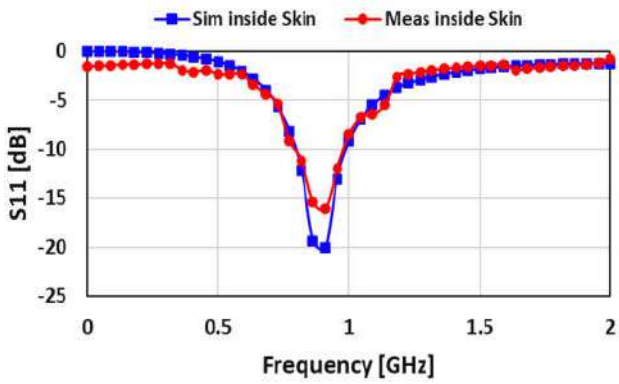

Figure 8: Juxtaposition between the measured and simulated S_{11} within skin tissue.

The (E & H)-planes obtained from the measurement and simulation findings of the pattern of radiation within the skin tissues are presented in Fig. 9. The function of the antenna within the skin is presented by the 2D radiation pattern. At the range of 915 MHz, these far field data reveal that the antenna within the skin tissue has an omni-directional radiation pattern feature in both planes. At the range of 915 MHz and within the skin, the simulation obtained realized gain is determined to be -22 dB, but measurement findings illustrate a realized gain of -28 dB. Fig.10 represents the measured and simulated efficacy as well as a gain graph. According to the graph, the antenna's measured efficiency of 2.1% inside the skin and a simulated efficiency is 2.2%.

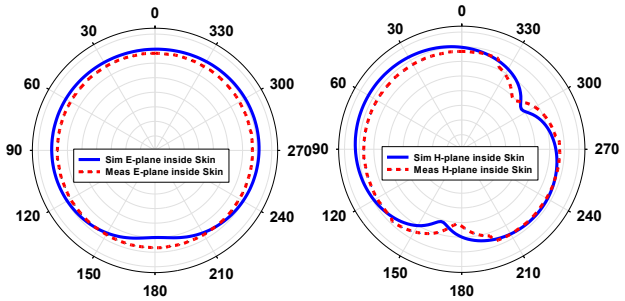

Figure 9: Far field results in measurement and simulation at 915 MHz within skin tissue.

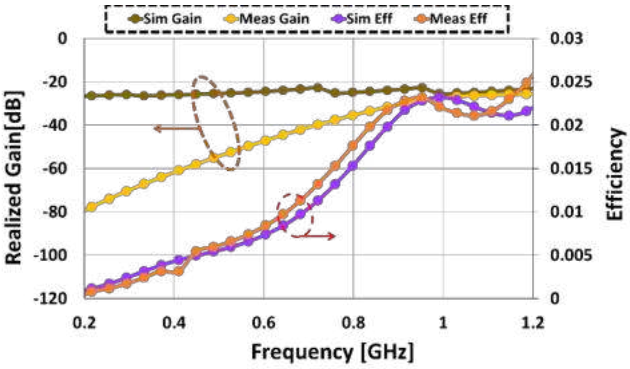

Figure 10: Efficiency and gain and graph of simulation and measurement inside skin.

3.3. SAR Analysis

Any emission of electromagnetic waves might expose the human health, and this menace is measured in terms of the SAR. The following is the relationship between the SAR and input power [10]:

$$SAR = \frac{\sigma|E^2|}{\rho} \quad (1)$$

where 'ρ' and 'σ' denote the mass density (kg/m3) and the thermal conductivity (S/m) respectively. On the other hand, E denotes the electric field intensity (V/m). The signal power which involves to the electric power intensity is the following [13]:

$$\text{Power } (W/m^2) = \frac{(E(V/m))^2}{377} \quad (2)$$

When the planned antenna was preserved inside skin as well as inside muscle, SAR simulations were completed. The SAR is calculated using the IEEE/IEC 6270-1 standard, averaged over 1 g of mass tissue, with the input power Pin kept constant at 0.5 W. From Fig.11, within the skin the SAR values are determined as 8.17 W/kg at the range of 915 MHz.

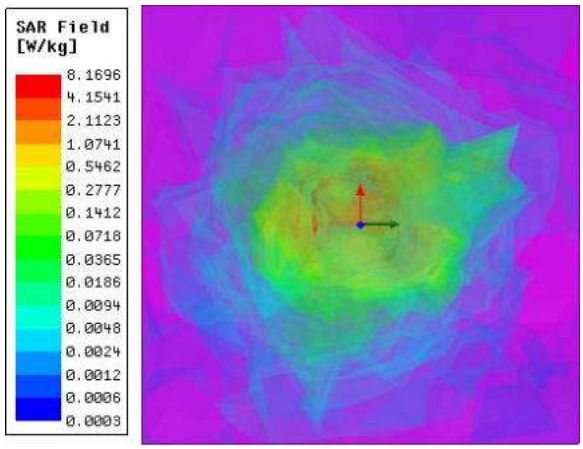

Figure 11: Distribution of the SAR of the reported antenna within body tissue is over 1 g at 915 MHz

Table 2: Performance comparison of the proposed antenna with our proposed work.

Ref. No.	Dimensions (mm^3)/ (λ_g^3)	Operating Frequency (GHz)	Realized Gain (dB)	Operating Bandwidth (%)	SAR (W/kg) @ 1g
[6]	(23×16.4×1.27) (0.098×0.070×0.005)	0.402	-34.9	12.9	284.5
[7]	(25×20×0.07) (0.34×0.27×0.00095)	2.45	-16.8	1.22	1.0
[8]	(15×21.5×1.5748) (0.39×0.56×0.039)	2.45	<-15	3.2	Not Calculated
[9]	(3.14×100×2.54) (0.082×2.6×0.066)	0.4 / 2.45	-33.1/ -14.55	38.1/17.6	241.5/ 149.7
[10]	(14×14×0.5) (0.365×0.365×0.013)	2.45	-15.96	18.36	0.494
[11]	(3.14×28.6×1.34) (0.082×0.748×0.035)	0.402 / 2.45	-41 / -21.3	41/27.8	666/ 676
[12]	(3.14×23×0.634) (0.082×0.60×0.016)	2.45	-20.3	18.3	649
[13]	11×11×1.27 (0.107×0.107×0.0123)	0.915	-29	3.8	Not Calculated
[14]	15×15×1.27 (0.14×0.14×0.0123)	0.915	-27	10.6	517
[15]	3.14×22.09×1.27 (0.030×0.22×0.0123)	0.915	-32.8	12.2	778
[This work]	**7×7×0.254 (0.08×0.08×0.003)**	**0.915**	**-28**	**21.85**	**8.1**

4. Conclusion

The following work presents a low-profiled ISM band patch antenna where with a small footprint is to be used for biomedical implants. The HFSS software performed the simulation of the proposed work. In the ISM band, this suggested antenna resonates at the range of 915 MHz and the antenna is fabricated with the substrate of Rogers RT/Duroid 5880 (ε_r = 2.2, tanδ = 0.0009) and has a total dimension of 7 mm × 7 mm × 0.254 mm. At the range of 915 MHz, the antenna's measured gain inside the skin-mimicking gel is -28 dB, while the measured bandwidth of the antenna is found to be 21.85% dipping into the skin-mimicking gel. Within the skin tissue, the SAR value is found to be 8.1 W/kg. Biocompatibility as well as safety issues in the medical design applications were also explored. This antenna is tiny and compact, making it perfect for use in Biomedical sectors.

References

[1] M. Yousaf et al., "An Ultra-Miniaturized Antenna with Ultra-Wide Bandwidth Characteristics for Medical Implant Systems," IEEE Access, vol. 9, pp. 40086-40097, 2021.

[2] D. Nguyen and C. Seo, "An Ultra-Miniaturized Antenna Using Loading Circuit Method for Medical Implant Applications," in IEEE Access, vol. 9, pp. 111890-111898, 2021.

[3] M. Yousaf et al., "Compacted Conformal Implantable Antenna with Multitasking Capabilities for Ingestible Capsule Endoscope," IEEE Access, vol. 8, pp. 157617-157627, 2020.

[4] Moirangthem Santoshkumar Singh, Jeet Ghosh, Soumendu Ghosh, Abhishek Sarkhel, "Miniaturized Dual-Antenna System for Implantable Biotelemetry Application", IEEE Antennas and Wireless Propagation Letters, vol. 20, no. 8, pp. 1394-1398, 2021.

[5] Z. Xia et al., "A Wideband Circularly Polarized Implantable Patch Antenna for ISM Band Biomedical Applications," IEEE Transactions on Antennas and Propagation, vol. 68, no. 3, pp. 2399-2404, 2020.

[6] R. Li, B. Li, G. Du, X. Sun, and H. Sun, "A compact broadband antenna with dual-resonance for implantable devices," Micromachines, vol. 10, no. 1, p. 59, 2019.

[7] Ketavath Kumar Naik, Seelam Chaithanya Satya Teja, Bokkisam Venkata Sailaja, and Pasumarthi Amala Sri, "Design of Flexible Parasitic Element Patch Antenna for Biomedical Application," Progress in Electromagnetics Research M, vol. 94, pp. 143-153, 2020.

[8] N. H. Sulaiman, N. A. Samsuri, M. K. A. Rahim, F. C. Seman, and M. Inam, "Compact Meander Line Telemetry Antenna for Implantable Pacemaker Applications," Indonesian Journal of Electrical Engineering and Computer Science, vol. 10, no. 3, 2018.

[9] Loktongbam, P., Pal, D. & Koley, C. "Design of an implantable antenna for biotelemetry applications," *Microsystem Technology*, vol. 26, pp. 2217–2226, 2020.

[10] W. Lei, H. Chu and Y. Guo, "Design of a Circularly Polarized Ground Radiation Antenna for Biomedical Applications," IEEE Transactions on Antennas and Propagation, vol. 64, no. 6, pp. 2535-2540, 2016.

[11] Shekhawat, Sumita & Gunaram, & Sharma, Vijay & Bhatnagar, D. "CPW fed implantable elliptical patch antenna for biomedical application," AIP Conference Proceedings. vol. 2220. p.130068, 2020.

[12] Luo, Lingzhi & Hu, Bing & Wu, Jiahui & Yan, Tianwen & Xu, Li-Jie. "Compact dual-band antenna with slotted ground for implantable applications," Microwave and Optical Technology Letters. vol. 61, no. 5, pp. 1314-1319, 2019.

[13] L. Xu, J. Xu, Z. Chu, S. Liu and X. Zhu, "Circularly Polarized Implantable Antenna with Improved Impedance Matching," IEEE Antennas and Wireless Propagation Letters, vol. 19, no. 5, pp. 876-880, 2020.

[14] Changrong Liu, Yudi Zhang, and Xueguan Liu, "Circularly polarized implantable antenna for 915 MHz ISM-band far-field wireless power transmission," IEEE Antennas and Wireless Propagation Letters, vol. 17, no. 3, pp. 373-376, 2018.

[15] Ke Zhang, et al, "Miniaturized circularly polarized implantable antenna for ISM-band biomedical devices," International Journal of Antennas and Propagation, 2017.

Millimeter/terahertz and UWB propagation

A Terahertz Polarization Splitter Using a Hybrid Plasmonic Waveguide

Jun Shibayama, Arata Yamamoto, Junji Yamauchi, and Hisamatsu Nakano

Faculty of Science and Engineering, Hosei University, Tokyo, Japan
*corresponding author, E-mail: shiba@hosei.ac.jp

Abstract

We investigate a waveguide-based polarization splitter in the terahertz (THz) region, in which a hybrid plasmonic waveguide and a dielectric waveguide are placed in parallel. The eigenmode analysis of each waveguide shows that the phase matching condition is satisfied for the quasi-TE mode and not for the quasi-TM mode, leading to a TM-pass polarizer. The device length is also predicted with the analysis of the supermode of the parallel waveguide.

1. Introduction

It is known that a surface plasmon polariton (SPP) propagates along a metal/insulator interface at optical frequencies [1]. Note, at terahertz (THz) frequencies, that a metal/insulator interface cannot support the SPP, due to negligible penetration of the electromagnetic waves into metal. In contrast, a semiconductor material, such as indium antimonide (InSb), has a negative permittivity at THz frequencies, leading to supporting SPP waves. We have proposed a surface plasmon resonance (SPR) waveguide sensor, in which a thin InSb layer is adopted for the sensing section [2]. This THz SPR waveguide sensor utilizes only a TM wave as an input source. In this article, we investigate a waveguide-based polarization splitter in the THz region to extract the TM wave.

2. Discussion

The splitter is composed of a parallel waveguide, in which a hybrid plasmonic waveguide (HPW) with an InSb layer and a dielectric waveguide (DW) are placed in parallel. The HPW and DW are respectively shown in Fig. 1(a) and (b). The core width is denoted by w_1 and w_2, the heights of Si and SiO_2 are respectively chosen to be $h_{\mathrm{Si}} = 50$ μm and $h_{\mathrm{SiO_2}} = 10$ μm. For the HPW, an InSb layer is added on the top of the waveguide ($h_{\mathrm{InSb}} = 20$ μm). The permittivities of Si and SiO_2 are $\varepsilon_{\mathrm{Si}} = 3.4^2$ and $\varepsilon_{\mathrm{SiO_2}} = 1.94^2$ and the permittivity of InSb [3] is $\varepsilon_{\mathrm{InSb}} = -36.54 - j13.05$ at 1 THz and 293 K.

The eigenmode analysis is performed to know the mode characteristics of the two waveguides. The Yee-mesh-based imaginary-distance beam-propagation method [4] is used to calculate the effective indices of the waveguides. Figure 2 shows the real part of the effective indices of the HPW and DW, as a function of w_1 and w_2. It is shown that the difference of the effective indices of the quasi-TE modes is

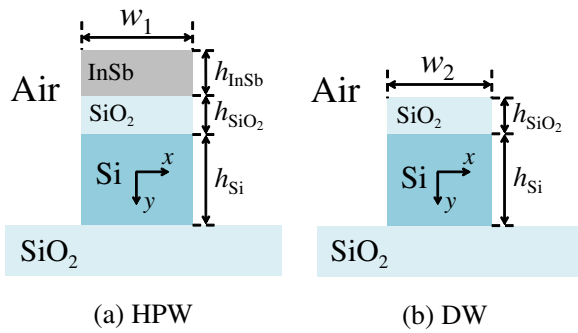

Figure 1: Waveguide structures. (a) HPW and (b) DW.

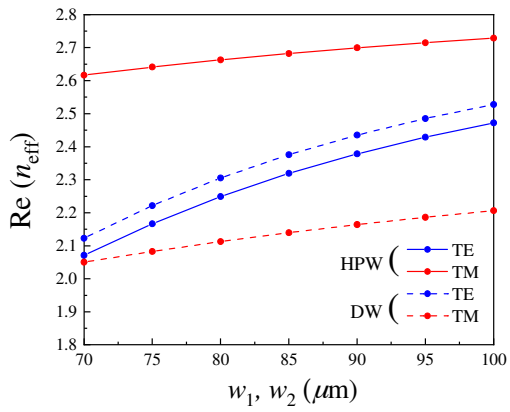

Figure 2: Effective indices.

small between the HPW and DW. In contrast, the difference of the quasi-TM mode is found to be large, when compared to the TE case. This is because for the HPW the SPP is excited and localized in the SiO_2 layer under the InSb one, leading to the increase of the effective index.

It should be noted that the phase matching condition is satisfied only for the quasi-TE mode with slightly different core widths in Fig. 2. For example, the effective indices for the TE mode is $n_{\mathrm{eff}} = 2.37$, when the widths of the HPW and DW are respectively chosen to be $w_1 = 90$ and $w_2 = 85$ μm. On the other hand, for the quasi-TM mode, the phase matching condition is not satisfied. As a result, a polarization splitter can be realized with these waveguides being placed in parallel, in which the TE wave is coupled

to the other waveguide and the TM one is obtained from the original input waveguide.

Finally, we perform the eigenmode analysis of the splitter, in which the HPW and DW are placed in parallel with a gap of 40 μm. The even and odd modes of the quasi-TE mode are calculated for the splitter. The coupling length is obtained using the real parts of their propagation constants as $L = \pi/(\beta_{\mathrm{even}} - \beta_{\mathrm{odd}})$. For the above case, i.e., $w_1 = 90$ μm for the HPW and $w_2 = 85$ μm for the DW, the device length is calculated to be $\simeq 8600$ μm, while it is reduced to be $\simeq 2700$ μm for $w_1 = 73$ and $w_2 = 70$ μm.

3. Conclusion

We have investigated a THz polarization splitter with a hybrid plasmonic waveguide and a dielectric waveguide being placed in parallel. It is shown that the phase matching condition is satisfied for the quasi-TE mode, while it is not satisfied for the quasi-TM mode. As a result, the polarization splitter can be realized, in which the TE wave is coupled to the other waveguide and the TM one is obtained from the original input waveguide. The propagating beam analysis using the simple frequency-dependent FDTD method [5] will be shown at the presentation.

Acknowledgement

This work was supported in part by JSPS KAKENHI under Grant JP19K04537.

References

[1] M. Miyata and J. Takahara, "Excitation control of long-range surface plasmons by two incident beams," *Opt. Exp.*, vol. 20, no. 9, pp. 9493-9500, 2012.

[2] J. Shibayama, K. Shimizu, J. Yamauchi, and H. Nakano, "Surface plasmon resonance waveguide sensor in the terahertz regime," *IEEE/OSA J. Lightw. Technol.*, vol. 34, no. 10 , pp. 2518-2525, 2016.

[3] Q Wang, Q. Tang, D. Zhang, Z. Wang, Y. Huang, "Tunable terahertz spectral filter based on temperature controlled subwavelength InSb grating," *Superlattice. Microst.*, vol. 75, pp. 955-961, 2014.

[4] M. Ito, J. Shibayama, J. Yamauchi, and H. Nakano, "Imaginary-distance beam-propagation method based on Yee's mesh in cylindrical coordinates," *Microw. Optical Tech. Lett.*, vol. 60, no. 12, pp. 2918-2922, 2018.

[5] J. Shibayama, R. Ando, A. Nomura, J. Yamauchi, and H. Nakano, "Simple trapezoidal recursive convolution technique for the frequency-dependent FDTD analysis of a Drude-Lorentz model," *IEEE Photon. Technol. Lett.*, vol. 21, no. 2, pp. 100-102, 2009.

Non-linear THz studies at the TeraFERMI beamline

Andrea Perucchi[1*]

[1]Elettra - Sincrotrone Trieste, S.S. km 163. 5 in AREA Science Park, I-34149 Basovizza, Trieste, Italy
*corresponding author, E-mail: andrea.perucchi@elettra.eu

Abstract

TeraFERMI is the THz beamline of the FERMI Free Electron Laser providing intense and broadband THz pulses. The THz fields are used to achieve THz control of matter and to push materials well into their nonlinear regime. THz nonlinearities are particularly pronounced in Dirac materials, because of their non-conventional band-structure properties. We report here on the THz nonlinear electrodynamics of the topological insulator Bi_2Se_3 and on layered black phosphorus, thus highlighting the role of band dispersion in shaping the nonlinear properties.

Propagation for vehicular communications

A Stochastic Ray-Based Model for UAV-to-Ground Radio Channels in Built-Up Environments

Claude Oestges

ICTEAM UCLouvain (Université catholique de Louvain), Louvain-la-Neuve, Belgium
E-mail: claude.oestges@uclouvain.be

Abstract

A stochastic ray-based model is applied to model the UAV-to-ground radio channel in urban areas. The modeling method relies on simple input data, such as input distribution parameters (e.g. mean building height, building height variance). The physical part of the model being based on ray-tracing, it is also applicable over very wide parameter ranges at a very low computation time thanks to a pre-calculation procedure.

1. Introduction

Unmanned Aerial Vehicle (UAV) communications have attracted a significant interest over the past years [1], as UAVs can be used as surrogate base stations or flying mobile terminals. Yet, important challenges still need to be investigated. In particular, radio channel models have mostly focused on the Air-to-Ground (A2G) path loss [2], with very results dealing with large- and small-scale fading. In this paper, a fading model is presented that tackles the fading model while linking the geometrical parameters with the fading statistics in a physical way, as detailed in Section 2. Experimental validations are outlined in Section 3.

2. UAV-to-Ground Fading Model

2.1. Generic Modeling Setup

In most cases [3], stochastic geometrical predictions can be analytically formulated. In this paper, the narrowband fading s is modelled by means of the following distribution:

$$p(s) = \int_{\Psi} p(s|\psi)p(\psi)d\psi \tag{1}$$

where ψ is a vector of input geometrical parameters, Ψ representing the whole set of possible parameters (building height and spacing, street width, link elevation angle, etc.). The conditional distribution $p(s|\psi)$ represents the (Ricean) fading distribution for a given realization of ψ. Such given realization of ψ generates a simulation area, described in Figure 1.

The geometrical parameters are defined as follows:

- w [m] is the street width at the terminal location (the width of other streets is taken as the average street width and denoted as w_0),

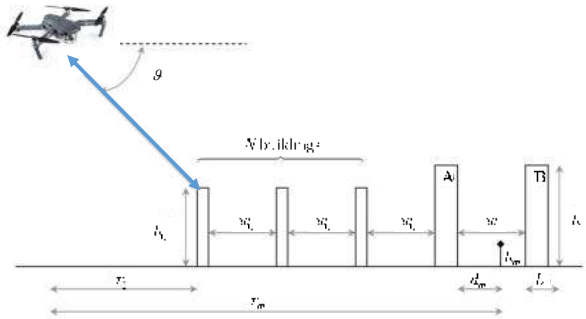

Figure 1: Simulation setup.

- d_m [m] is the perpendicular distance from the terminal to the nearest building,
- h [m] is the nearest building height (the height of remote buildings is taken as the average building height h_0),
- h_m [m] is the height of the terminal antenna,
- r_m [m] is the UAV-to-terminal distance,
- r_1 [m] is the distance between the UAV and the first building,
- ϕ is the link azimuth angle relative to the street axis (this angle is not represented in Figure 1, which corresponds to $\phi = 0$),
- L [m] is the width of the nearest buildings (which can be fixed without loss of generality, e.g. $L = 5$ m), while the N other buildings are assumed to have a null width.

2.2. From an Electromagnetic Ray-Based Model to Ricean Fading

The conditional relationship $p(s|\psi)$ is evaluated from the application of a physical ray-based model. Four propagation mechanisms are included: (1) line-of-sight (LOS) transmission, (2) rooftop to street single wedge diffraction

by rooftop wedge **A**, (3) rooftop to street single wedge diffraction by rooftop wedge **B**, (4) multiple diffraction caused by successive building knife-edges, and (5) contributions arising from single and double reflections from the ground and/or the nearest building walls, which might also possibly include diffuse components.

The radio signal transmitted from the UAV is assumed to be a plane wave with a given polarization to be specified. The above-listed field contributions can then be estimated by means of geometrical optics as well as the Uniform Theory of Diffraction. Regarding multiple diffraction, it is recommended to use $N = 10$ and 15, respectively in suburban and urban areas [3]. From the electromagnetic simulations, which can be pre-processed and tabulated for every set of parameters $\psi \in \Psi$, a Ricean fading model is considered, i.e. $p(s|\psi)$ is Ricean, with a dominant path amplitude equal to contribution (1) or (2) (the latter being considered when the LOS transmission is blocked), whereas the scattered multipath power is obtained as the non-coherent addition of all other power contributions (i.e. (2) to (5) or (3) to (5), in LOS and non-LOS respectively).

2.3. Geometrical Parameter Distributions

Street width or building height can be associated with known analytical probability density functions. As an example, building height has been found to be lognormally-distributed [3],

$$p(h) = \frac{1}{\sqrt{2\pi}\sigma h} \exp\left[-\frac{\log^2(h/\mu)}{2\sigma^2} \right] \tag{2}$$

with parameters outlined in Table 1.

Table 1: Building height lognormal fitting parameters.

Environment	μ [m]	σ
Suburban	7.1	0.25
Urban (London)	20.6	0.44
Urban (Athens)	15.0	0.30
Urban (Brussels)	17.6	0.31

3. Experimental Validation

First-order fade statistics provided by the model are compared with measurements from an airborne campaign carried out by the European Space Agency [4] at 1.6 GHz. In the experiment, the mobile platform moved parallel to the measurement vehicle, at various elevation angles, in a suburban residential area with detached two/three-storeyed houses, 10-20 meters distant from the road. Hence, a suburban building height profile and constant values for $w = w_0 = 30$ m and $\phi = 0$ (ϑ depends on the experiment) are chosen as input parameters (note that the building height data are not taken directly from the measurement site). The receiver is assumed to be located in the middle of the street (so that $d_m = w/2$) at a height $h_m = 2$ m.

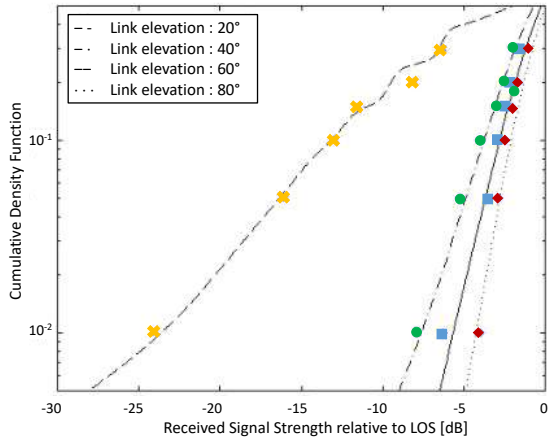

Figure 2: Comparison between simulation (dashed, dot-dashed, solid and dot lines) and experimental (crosses, circles, squares and diamonds) results at various elevation angles.

In Figure 2 , an excellent agreement between the measured statistics and the model can be observed, and that the model is quite robust to small deviations in the input data (as the chosen building height is a generic suburban profile).

4. Conclusions

A physical-statistical model of the UAV-to-Ground channel has been described and experimentally validated. The fading model relies on the combination of ray-based pre-processed simulations and stochastic input data corresponding to the (sub)urban setup. The model is able to represent the variation of fading statistics with the link elevation angle and is robust with respect to the exact distribution of physical parameters.

References

[1] M. Mozaffari, W. Saad, M. Bennis, Y.-H. Nam, and M. Debbah, "A tutorial on UAVs for wireless networks: Applications, challenges, and open problems," *IEEE Communications Surveys and Tutorials*, vol. 21, no. 3, pp. 2334–2360, 2019.

[2] C. Yan, L. Fu, J. Zhang, and J. Wang, "A comprehensive survey on UAV communication channel modeling," *IEEE Access*, vol. 7, pp. 107 769–107 792, 2019.

[3] C. Oestges, "A stochastic geometrical vector model of macro- and megacellular communication channels," *IEEE Transactions on Vehicular Technology*, vol. 51, no. 6, pp. 1352–1360, November 2002.

[4] M. Sforza and S. Buonomo, "Characterisation of the LMS propagation channel at L and S bands: narrowband experimental data and channel modelling," in *Proc. NAPEX 17*, 1993, pp. 183–192.

Propagation theory

Critical distances for near-ground propagation: application to dipole antennas

Hocine Belaid*, Shermila Mostarshedi, Benoit Poussot and Jean-Marc Laheurte
Univ Gustave Eiffel, CNRS, ESYCOM, F-77454 Marne la Vallée, France
E-mail* : hocine-anis.belaid@univ-eiffel.fr

Abstract

This paper deals with the problem of near-ground wave propagation, in particular with the assessment of the region in which the near-ground wave becomes the dominant component. The critical distances are estimated as a function of the link parameters in the case of half-wave dipole antennas.

1. Introduction

In the context of smart cities, wireless sensor networks (WSN) have been widely deployed for environment purposes or surveillance. In some cases, the sensors are placed close to a conductive interface in order to collect data of interest. The radiation of a near-ground sensor invokes the famous Sommerfeld half-space problem. The Sommerfeld formulation is widely accepted in the community and can be validated by rigorous mathematical treatment [1–5]. The steepest descent technique provides an infinitesimal model describing the electric field radiated by an elementary vertical electric dipole (VED) over a lossy interface [6]. Recently, in [6] the existence of a region of interest for the surface component has been highlighted. According to [1,2,6], the E_z component of the electric field follows a two-phase decay: a region where the attenuation is about 10 dB/decade and a second where it is about 20 dB/decade. Analytical expressions of the two critical distances have been proposed for a VED case [1, 2, 6]. In this paper, we propose an extension for the propagation model of the infinitesimal vertical dipole near the ground. We also introduce an empirical method to determine the critical distances in the case of a half-wave dipole antenna. Finally, the conditions of emergence of the surface component are determined, in order to verify the possibility for the two-ray method [7] to predict the field in certain cases with a good precision.

2. Infinitesimal vertical dipole

The Sommerfeld half-space problem [1] for dipole antennas involves image theory. As we can see in fig. 1, the model of the problem is composed of an infinite lossy surface dividing the space into two different media, the emitting and the receiving antennas are placed in medium 1. The interface is further replaced by the image of the emitting antenna with respect to the interface.

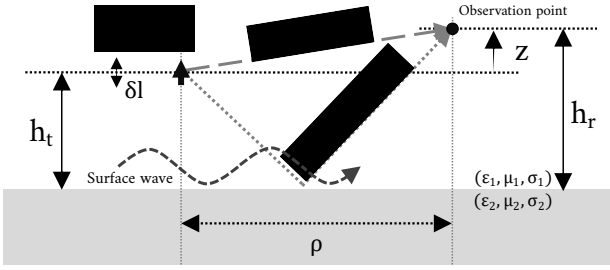

Figure 1: VED radiating over a lossy half-space

Here δl is the infinitesimal length of the emitting VED, h_t the height of the emitting VED, h_r the height of the observation point, ρ the radial distance between the emitting VED and observation point, z the vertical distance between the emitting VED and the observation point ($z \in]-h_t, \infty[$), and finally ε_i, μ_i and σ_i are the electromagnetic characteristics of the propagation medium ($i = 1$) and the lossy medium ($i = 2$). Fig. 1 suggests that besides the classic direct and reflected waves, one needs to include a third component in order to model the wave propagation properly. This term which is due to the proximity to the interface may commonly be called the "surface wave" which attenuates rapidly above the interface.

As described in [6], the z component of the electric field radiated by an infinitesimal vertical dipole (E_z^{VED}) is given by the asymptotic approximation below:

$$E_z^{\mathrm{VED}} = -jI_0\delta l\eta_1 k_1 \left(\sin^2(\theta)\frac{e^{-jk_1 r}}{4\pi r} + \Gamma\sin^2(\theta_I)\frac{e^{-jk_1 r_I}}{4\pi r_I} \underbrace{-jF\sqrt{2\sin^7(\omega_p)}\frac{n^2}{1-n^2}\cos(\omega_p)\frac{e^{-jk_1 r_I}}{4\pi r_I}}_{\text{Surface component}}\right) \quad (1)$$

where the first two terms can be provided by the classic two-ray model as below :

$$E_{z\ \mathrm{two-ray}}^{\mathrm{VED}} = -jI_0\delta l\eta_1 k_1 \left(\sin^2(\theta)\frac{e^{-jk_1 r}}{4\pi r} + \Gamma\sin^2(\theta_I)\frac{e^{-jk_1 r_I}}{4\pi r_I}\right) \quad (2)$$

In (1) and (2), the angles and radiuses (r, θ) and (r_I, θ_I) are functions of ρ and z and are related to the relative positions of the observation point, the VED and the VED image (see fig. 1). The other parameters are summarized in table 1.

Table 1: Parameters in equation (1)

Parameter	Description
Γ	Reflection coefficient of the interface
F	Sommerfeld attenuation term [6]
$I_0 \delta l$	Dipolar moment of the VED
η_1	Medium impedance
k_1	Wavenumber
$\omega_p = \arccos(\sqrt{\frac{\varepsilon_1}{\varepsilon_1+\varepsilon_2}})$	Pole of the reflection coefficient
$n = \sqrt{\varepsilon_2/\varepsilon_1}$	Refractive index (provided that the first medium is vacuum)
$\tau = jk_1 r_I[\cos(\omega_p - \theta_I) - 1]$	Numerical distance [6]

3. Half-wave vertical dipole

3.1. Current distribution

The accurate current distribution on a finite-length vertical dipole (VD) above an interface should be obtained by a rigorous numerical method such as the Method of Moments (MoM) [8]. In the case of a half-wave thin dipole in free space, a sinusoidal approximation can describe the current distribution with a good precision [9]. If the half-wave dipole is fed by a 1 A current, the current distribution along the dipole would be as follows:

$$I(z') = \sin\Big(k_1\big(\frac{\lambda}{4} - |z'|\big)\Big) \tag{3}$$

where $z' \in [-\lambda/4, \lambda/4]$ is the vertical position over the dipole.

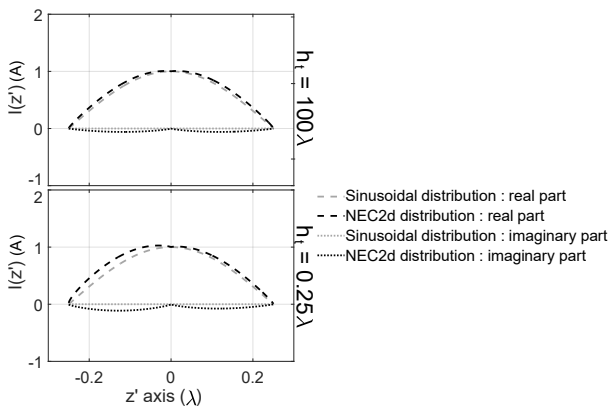

Figure 2: Current distribution on a half-wave vertical dipole above a PEC

In order to check the validity of the sinusoidal approximation to predict the current values over a half-wave dipole above an interface, the current distribution computed by NEC2d [10] is compared with the sinusoidal one. We consider a working frequency of 100 MHz and a Perfect Electric Conductor as interface. The results are given by Fig. 2 and the Relative Root Square Errors (RRSE) (described by eq. 4) are summarized in Table 2 for two different heights.

$$\mathrm{RRSE} = \frac{\|I_{\mathrm{NEC}}(z') - I(z')\|_2}{\|I_{\mathrm{NEC}}(z')\|_2} = \sqrt{\frac{\int_{-\lambda/4}^{+\lambda/4} |I_{\mathrm{NEC}}(z') - I(z')|^2 \, dz'}{\int_{-\lambda/4}^{+\lambda/4} |I_{\mathrm{NEC}}(z')|^2 \, dz'}} \tag{4}$$

Table 2: RRSE on the current distribution of the half-wave VD at two different heights

Configuration	RRSE
$h_t = 100\lambda$	**8.713%**
$h_t = 0.25\lambda$	**14.42%**

Fig. 2 and Table 2 show that there is a slight difference between NEC2d current distribution and the sinusoidal one. This difference is mainly due to the fact that the sinusoidal distribution is omitting the imaginary part of the current. In addition to this, we notice that the RRSE increases as the dipole gets closer to the interface while the current tends to get asymmetric.

3.2. Extension of the infinitesimal model

Fig. 3 shows that the VD of length $L = \lambda/2$ is decomposed into a infinite set of VEDs of length δl, the current of each weighted according to the sinusoidal distribution given in (3). Their radiated electric fields using (1) are summed up at the reception point based on the superposition principle.

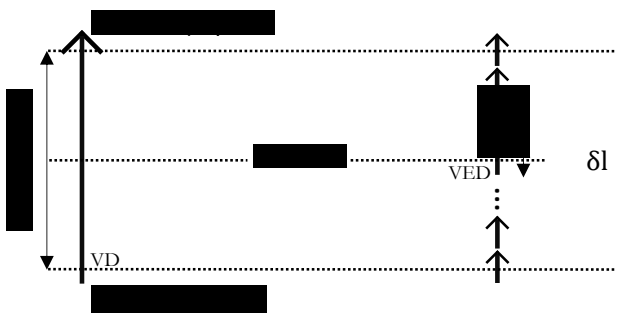

Figure 3: Approximation of a half-wave VD by a set of VEDs

The computation of the total electric field radiated by a half-wave VD, following the superposition principle, leads us to an integral. By rewriting (1) in the following compact form $E_z^{\mathrm{VED}} = I_0 \delta l f(\rho, z)$, the expression of E_z^{VD} is consequently given by:

$$E_z^{\mathrm{VD}} = \int_{-\lambda/4}^{+\lambda/4} I(z') f(\rho, z - z') dz' \tag{5}$$

The extended model would be comparable to the infinitesimal model in terms of the electric field levels (especially in far-field) provided that the dipolar moments of both dipoles are equivalent. This equivalence is established by the following equation:

$$I_0 \delta l = \int_{-\lambda/4}^{+\lambda/4} I(z')dz' \tag{6}$$

By applying (3) to (6), we finally obtain:

$$I_0 \delta l = \frac{\lambda}{\pi} \tag{7}$$

In the following sections, this equivalence is automatically used to estimate the dipolar moment of the VED.

3.3. Comparison between the infinitesimal and the extended models

In order to highlight the differences between the infinitesimal and extended models, both models are tested and compared. We choose a working frequency of $f = 868$ MHz, at the emitting and receiving heights of $h_t = h_r = 0.5\lambda$, the characteristics of the lossy medium being $\varepsilon_r = 1$ and $\sigma_2 = 100\ \mathrm{S/m}$. The results are shown in Fig. 4.

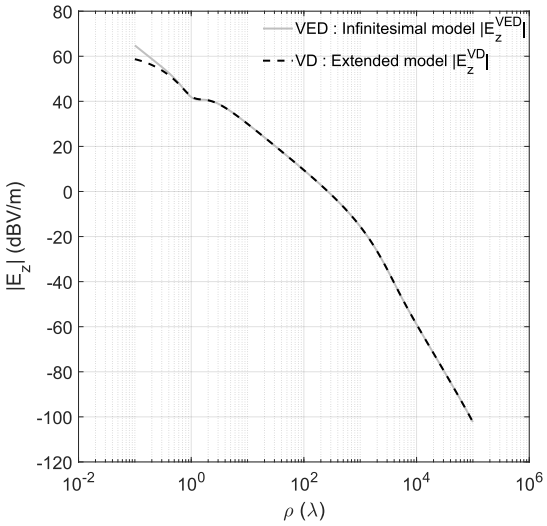

Figure 4: Evolution of $|E_z|$ of both models according to ρ

This result shows that as long as the equivalence seen in (6) is applied, both models overlap over a large range of ρ distances, especially in far-field. As a first conclusion, we can say that a half-wave VD shows the same radiation behavior in far-field as a VED, provided that the dipolar moments are equivalent. This result will be subject to further investigations in future works.

4. Critical distances

4.1. Definition

In order to identify the effect of the surface component on the E_z field, we introduce the critical distances and the region of interest. The determination of theses distances is based on an empirical approach, relying on the two-ray propagation model, and allowing us to mark out a region of interest, where the surface component becomes predominant.

We define the region of interest as to be the region delimited by the critical distances, i.e. the region starting from the distance where $|E_{z\ \mathrm{surface}}|$ becomes greater than $|E_{z\ \mathrm{two-ray}}|$ to the distance where $|E_{z\ \mathrm{surface}}|$ attains $|E_{z\ \mathrm{surface}}|_{\mathrm{max}}$. We also define the quantity $\Delta\rho$, representing the extent of the region of interest, and ΔE_z being the maximum gap between $|E_z|$ and $|E_{z\ \mathrm{two-ray}}|$.

4.2. Parametric study

In this section, we expose a parametric study using the extended model in the case of a half-wave dipole. The output parameters, i.e. $\Delta\rho$ and ΔE_z, are computed according to the simultaneous variation of the problem's parameters. The main goal is to bring out the conditions of emergence of the surface component. Having these conditions in hand, one knows in advance in which case the use of the two-ray model could guarantee a good precision and thus be sufficient. The parametric study is carried out by considering two configurations for a half-wave VD ($L = \lambda/2$) shown in Table 3.

Table 3: Parameters of the test configurations

	f (MHz)	h_t (λ)	z (λ)	ε_r	σ_2 (S/m)
Config. 1	100	$[0.25, 1.25]$	0	1	$[5, 500]$
Config. 2	$[1, 100]$	$[0.25, 1.25]$	0	1	5

The results, in the form of maps, are given by Fig. 5.

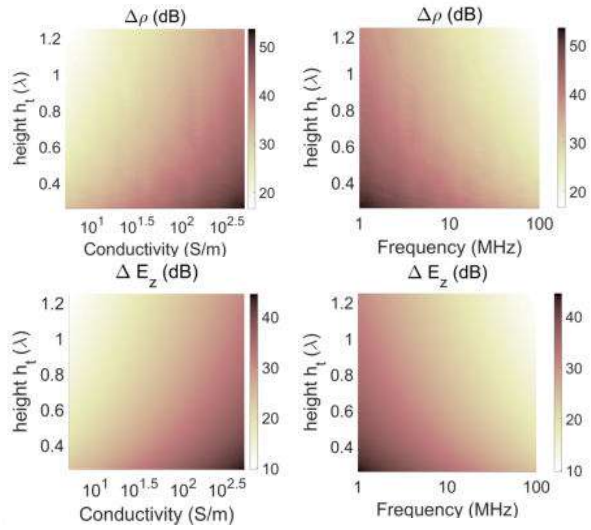

Figure 5: Evolution of the output parameters according to the two configrations (Config. 1: left, Config. 2: right)

The results related to Config. 1 show that the region

of interest shrinks as σ_2 decreases or h_t increases, and this comes with the decrease of ΔE_z. On the other hand, the region of interest is further enlarged as σ_2 increases or h_t decreases, and we notice a clear reduction of ΔE_z.

According to the results related to Config. 2, the region of interest tightens up as f or h_t increases, and this comes with a drastic decrease of ΔE_z. Contrarily, the region of interest is further expanded as f or h_t decreases, and we observe a noticeable rise of ΔE_z.

5. Conclusion

In this paper, an extension of the infinitesimal model given in [6] has been obtained for a half-wave dipole. Both infinitesimal and extended models have been compared and have shown similar behavior in far-field if the dipolar moment equivalence is respected.

In addition to this results, we proposed a new way to compute critical distances which was used in the case of the extended model. Consequently, Section 4 highlights the scenarios in which the two-ray model could be sufficient for the link estimation. By the means of the maps shown in Fig. 5, it is possible for a radio-link designer to decide whether to use the model in (1) or the one in (2), depending on the range of $\Delta\rho$ and ΔE_z. Should the region of interest and the gap between the two models are large enough, the use of a complete model to predict the surface component would become necessary.

References

[1] K. Michalski and J. Mosig, "The sommerfeld halfspace problem redux: Alternative field representations, role of zenneck and surface plasmon waves," *IEEE Transactions on Antennas and Propagation*, vol. 63, no. 12, pp. 5777–5790, 2015.

[2] ——, "The sommerfeld half-space problem revisited: from radio frequencies and zenneck waves to visible light and fano modes," *Journal of Electromagnetic Waves and Applications*, vol. 30, no. 1, pp. 1–42, 2016.

[3] R. W. King, "Electromagnetic field of a vertical dipole over an imperfectly conducting half-space," *Radio Science*, vol. 25, no. 2, pp. 149–160, 1990.

[4] R. Moore and W. Blair, "Dipole radiation in a conducting half space," *Journal of Research of the National Bureau of Standards.*, vol. 65D, no. 6, pp. 547–563, 1960.

[5] W. C. Chew, *Lectures on Electromagnetic Field Theory*. Purdue University, 2019.

[6] M. H. B. Cardoso, S. Mostarshedi, G. Baudoin, and J.-M. Laheurte, "Analytical expressions of critical distances for near-ground propagation," *IEEE Transactions on Antennas and Propagation*, vol. 66, no. 5, pp. 2482–2493, 2018.

[7] S. S. Haykin and M. Moher, *Modern wireless communications*. Pearson Education India, 2011.

[8] W. C. Gibson, *The method of moments in electromagnetics*. Chapman and Hall/CRC, 2021.

[9] C. A. Balanis, *Antenna theory: analysis and design*. John wiley & sons, 2015.

[10] G. J. Burke and A. J. Poggio, "Numerical electromagnetics code (nec) - method of moments," 1981.

Radar systems, target detection, localization, and tracking

Target DOA Estimation using GLRT and Crosstalk Reduction for MIMO Radar

Oscar Gómez[1], Florence Nadal[1], Benoit Poussot[2*], Pascale Jardin[1], and Geneviève Baudoin[1]

[1]Univ Gustave Eiffel, CNRS, ESYCOM, 2 Bd Blaise Pascal, F-93162 Noisy-le-Grand, France
[2]Univ Gustave Eiffel, CNRS, ESYCOM, F-77454 Marne-la-Vallée, France
*corresponding author, E-mail: benoit.poussot@univ-eiffel.fr

Abstract

Multiple-Input Multiple-Output (MIMO) radars with colocated antennas have been shown to have higher resolution and better accuracy in target localization than standard phased-array radars. However, due to the proximity of the antenna elements, direct coupling between the transmitters and the receivers (crosstalk) may exist and degrade in the narrowband case the performance of some detection techniques, such as the Generalized Likelihood Ratio Test (GLRT) based one. This paper presents a crosstalk reduction technique for MIMO radar.

1. Introduction

A Multiple-Input Multiple-Output (MIMO) radar is a system employing multiple spatially distributed transmitters and receivers in which the waveforms to be transmitted can be totally independent. There are two basic configurations of MIMO radar depending on the location of the transmitting and receiving elements. In the first one, known as statistical MIMO radar, the transmitting and receiving elements are widely distributed over an area, achieving spatial diversity by exploiting the different (and independent) scattering responses for each antenna pairing [1], [2], [3]. In the second one, known as MIMO radar with colocated antennas, the transmitting and receiving antenna elements are closely spaced and the target response is approximately the same for each antenna pairing with different time delays due to the different propagation paths. While this configuration does not provide spatial diversity, spatial resolution can be increased by combining the information from all of the transmitting and receiving paths. This configuration also has other benefits such as a good interference rejection and a good flexibility for transmitting a desired beampattern [2], [4], [5]. In this paper we focus on MIMO radar with colocated antennas which might be applied to medicine [6] and environmental issues [7] among others.

Among the existing target parameter estimation techniques proposed for MIMO radar with colocated antennas, we can mention Capon and APES (Amplitude and Phase Estimation) which allow estimating the target Direction-Of-Arrival (DOA) and the reflected signal amplitudes [8]. Another technique, based on the use of the Generalized Likelihood Ratio Test (GLRT) has also been proposed in [8]. Despite its lower spatial resolution compared to Capon, the GLRT technique is of particular interest since it is able to reject very effectively strong interferences which are uncorrelated with the transmitted signals [8], [9]. However, as a result of the small separation between the antenna elements, the performance of the above-mentioned techniques might be affected by undesired phenomena such as mutual coupling and crosstalk. The former designates the electromagnetic interactions between the antennas affecting their radiation patterns and matching characteristics and the latter is a result of the direct coupling between the transmitter and the receiver elements. These two phenomena can be addressed separately.

In this paper, we introduce a new signal model of MIMO radar with colocated antennas which takes crosstalk into account, and we propose a crosstalk reduction technique based on a signal processing approach. An experimental platform previously developed by the authors in [10] has been used to obtain some experimental results using the GLRT detection technique.

The paper is organized as follows: The signal model is presented in Section 2, followed by the description of the GLRT in Section 3. Next, we propose a crosstalk reduction technique in Section 4. Some experimental results showing the efficiency of this method are presented in Section 5.

2. Signal model

Consider a MIMO radar system with colocated antennas composed of L_t transmitting and L_r receiving closely spaced elements. If the K targets are located in the far-field region at $\{\theta_k\}_{k=1}^{K}$, the baseband signal at the lth element of the receive array will be given by [11]

$$x_l(t) = \sum_{k=1}^{K} \beta_k e^{-j2\pi f_c \tau_r(l,k)} \sum_{i=1}^{L_t} e^{-j2\pi f_c \tau_t(i,k)} c_i\big(t - \tau_t(i,k) - \tau_r(l,k)\big) + z_l(t) \quad (1)$$

where $c_i(t)$ denotes the baseband signal transmitted by the ith antenna element, f_c is the carrier frequency, β_k is the complex reflection coefficient of the kth target, $\tau_t(i,k)$ and $\tau_r(l,k)$ are the time delays from the ith transmitter element to the kth target and from this target to the lth receiver element respectively (their dependence on θ_k has been omitted for notational simplicity), and $z_l(t)$ models the interference and noise. If the transmitted signals $\{c_i(t)\}_{i=1}^{L_t}$ are narrowband, the signal model in (1) can be written in vector notation as [4]

$$\boldsymbol{x} = \sum_{k=1}^{K} \beta_k \boldsymbol{a}_r^*(\theta_k) \boldsymbol{a}_t^H(\theta_k) \boldsymbol{c} + \boldsymbol{z} \quad (2)$$

where $\boldsymbol{x} = \left[x_1(t) \cdots x_{L_r}(t)\right]^T$,

$\boldsymbol{c} = \left[c_1(t) \cdots c_{L_t}(t)\right]^T$,

$\boldsymbol{a_t}(\theta_k) = \left[e^{j2\pi f_c \tau_t(1,k)} \ldots e^{j2\pi f_c \tau_t(L_t,k)}\right]^T$,

$\boldsymbol{a_r}(\theta_k) = \left[e^{j2\pi f_c \tau_r(1,k)} \ldots e^{j2\pi f_c \tau_r(L_r,k)}\right]^T$.

Symbols $(\cdot)^*$, $(\cdot)^T$ and $(\cdot)^H$ designate respectively the complex conjugate, the transpose and the Hermitian operators.

3. The Generalized Likelihood Ratio Test (GLRT) detection technique

The GLRT detection technique for narrowband MIMO radar was derived in [8] assuming that the columns of the noise term $\boldsymbol{z}$ are i.i.d. circularly symmetric complex Gaussian random vectors with zero mean and unknown covariance matrix. The GLR is given by

$$\rho(\theta) = 1 - \frac{\boldsymbol{a}_r^T(\theta) \widehat{\boldsymbol{R}}_{xx}^{-1} \boldsymbol{a}_r^*(\theta)}{\boldsymbol{a}_r^T(\theta) \widehat{\boldsymbol{Q}}^{-1} \boldsymbol{a}_r^*(\theta)} \quad (3)$$

where $\widehat{\boldsymbol{R}}_{xx}$ is the estimated auto-covariance matrix of the received signals, $\widehat{\boldsymbol{Q}}$ is defined as

$$\widehat{\boldsymbol{Q}} = \widehat{\boldsymbol{R}}_{xx} - \frac{\widehat{\boldsymbol{R}}_{xc} \boldsymbol{a_t}(\theta) \boldsymbol{a_t}^H(\theta) \widehat{\boldsymbol{R}}_{xc}^H}{\boldsymbol{a}_t^H(\theta) \widehat{\boldsymbol{R}}_{cc} \boldsymbol{a_t}(\theta)}, \quad (4)$$

$\widehat{\boldsymbol{R}}_{cc}$ is the estimated auto-covariance matrix of the transmitted signals, and $\widehat{\boldsymbol{R}}_{xc}$ is the estimated cross-covariance matrix between the received and the transmitted signals. The fractional part of (3) is the ratio between two likelihood functions; the one at the numerator under the noise-alone hypothesis (without any target) and the one at the denominator under signal-plus-noise hypothesis (with a target in direction θ). Thus, the target directions can be found by searching for the maxima of the spectrum $\rho(\theta)$.

This technique is of particular interest because of its potential in rejecting interferences which are uncorrelated with the transmit signals [8]. However, the real performance of GLRT may differ from the one shown in the literature due to various phenomena, e.g. the non Gaussianity of the noise or the existence of interference correlated with the transmitted signals, such as crosstalk.

4. Crosstalk modeling and reduction

4.1. Signal model in the presence of crosstalk

In a MIMO radar with colocated antennas, the transmitting (Tx) and receiving (Rx) antenna elements are closely spaced. Due to this proximity, a part of the transmitted power may be directly transferred to the receiver elements which can deteriorate the detection performance. The signals directly transmitted from Tx to Rx can be modeled as a mixture of the different transmitted symbols $\boldsymbol{c}$. Thus, the signal model taking crosstalk into account can be written as

$$\boldsymbol{x} = \sum_{k=1}^{K} \beta_k \boldsymbol{a_r}^*(\theta_k) \boldsymbol{a_t}^H(\theta_k) \boldsymbol{c} + \boldsymbol{M}\boldsymbol{c} + \boldsymbol{z} \quad (5)$$

where $\boldsymbol{M}$ is a L_rxL_t crosstalk matrix in which each element $m_{i,j}$ is the complex transmission coefficient between the jth element of the Tx array and the ith element of the Rx array.

Based on a signal processing approach, we present thereafter a method to estimate the crosstalk matrix and the straightforward crosstalk reduction technique.

4.2. Crosstalk reduction

The crosstalk matrix can be estimated from a first measurement in an environment without any target. This estimation can be performed during a calibration phase previous to any operational task. In that case the signal model is

$$\tilde{\boldsymbol{x}} = \boldsymbol{M}\tilde{\boldsymbol{c}} + \boldsymbol{z}, \quad (6)$$

where $\tilde{\boldsymbol{c}}$ denotes the transmitted symbols in the calibration phase. We need to determine the matrix $\boldsymbol{M}$ which minimizes the Mean Square Error (MSE) criterion

$$J = E[\|\tilde{\boldsymbol{x}} - \boldsymbol{M}\tilde{\boldsymbol{c}}\|^2]. \quad (7)$$

By denoting $\boldsymbol{m}_i^H$ the ith row of $\boldsymbol{M}$ and $\tilde{x}_i(t)$ the ith element of $\tilde{\boldsymbol{x}}$, this criterion can be written as

$$J = E\left[\sum_{i=1}^{L_r} |\tilde{x}_i(t) - \boldsymbol{m}_i^H \tilde{\boldsymbol{c}}|^2\right]. \quad (8)$$

Finally, the ith row of $\boldsymbol{M}$ will be the one that minimizes

$$J_i = E[|\tilde{x}_i(t) - \boldsymbol{m}_i^H \tilde{\boldsymbol{c}}|^2]. \quad (9)$$

Assuming that the noise $\boldsymbol{z}$ is white and independent from the transmitted signals $\tilde{\boldsymbol{c}}$, the solution is that of a classical Wiener filtering: $\widehat{\boldsymbol{m}}_i^H = E[\tilde{x}_i(t)\tilde{\boldsymbol{c}}^H]E[\tilde{\boldsymbol{c}}\tilde{\boldsymbol{c}}^H]^{-1}$. Consequently, the optimal crosstalk matrix according to the MSE criterion is given by

$$\widetilde{\boldsymbol{M}} = \boldsymbol{R}_{\tilde{x}\tilde{c}} \boldsymbol{R}_{\tilde{c}\tilde{c}}^{-1} \quad (10)$$

where $\boldsymbol{R}_{\tilde{x}\tilde{c}} = E[\tilde{\boldsymbol{x}}\tilde{\boldsymbol{c}}^H]$ and $\boldsymbol{R}_{\tilde{c}\tilde{c}} = E[\tilde{\boldsymbol{c}}\tilde{\boldsymbol{c}}^H]$. In practice we can estimate this matrix as $\widehat{\boldsymbol{M}} = \widehat{\boldsymbol{R}}_{\tilde{x}\tilde{c}} \widehat{\boldsymbol{R}}_{\tilde{c}\tilde{c}}^{-1}$, where $\widehat{\boldsymbol{R}}_{\tilde{x}\tilde{c}}$ and $\widehat{\boldsymbol{R}}_{\tilde{c}\tilde{c}}$ are estimated versions of $\boldsymbol{R}_{\tilde{x}\tilde{c}}$ and $\boldsymbol{R}_{\tilde{c}\tilde{c}}$ respectively.

Once the crosstalk matrix has been estimated, the contribution of crosstalk to the received signals (5) can be reduced by calculating

$$\boldsymbol{y} = \boldsymbol{x} - \widehat{\boldsymbol{M}}\boldsymbol{c}. \quad (11)$$

In the next section, we present some experimental results showing the benefits of this crosstalk reduction technique when applying the GLRT to $\boldsymbol{y}$.

5. Experimental results

5.1. Description of the experimental platform

In order to study the real performance of a MIMO radar, a dedicated reconfigurable measurement platform was previously developed and tested [10]. In a conventional MIMO system, each antenna element is associated with a separate RF architecture and the overall system has to be synchronized. The requirements for such implementations are difficult to maintain especially for large MIMO systems and lead to a high cost and complex hardware at the radio

frequency level. In contrast, the proposed platform represented in Fig. 1 works with only one RF transceiver.

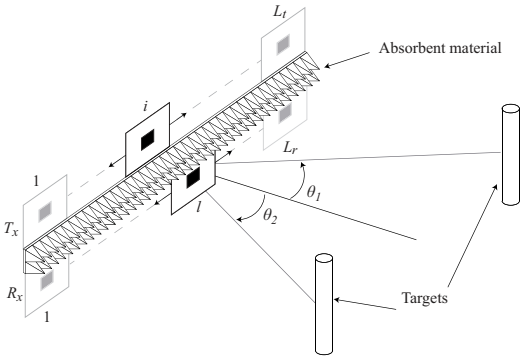

Figure 1: Scheme of the measurement platform.

In this configuration, the transmitter and the receiver become movable due to the positioning of each antenna on an automated mechanical system containing two rails. A series of measurements are performed for a given position of the transmitter, while the receiver takes the different positions of a Uniform Linear Array (ULA). The same procedure is repeated for different positions of the transmitter antenna. In this way, all possible configurations between the transmitter and the receiver in a MIMO system are covered. By applying the superposition principle, the received signals at each position can be wisely combined to construct the received signals matrix $\boldsymbol{X}$ of the MIMO system. As the superposition principle is valid provided that the environment is stationary, the measurements are done in an anechoic chamber. It is important to note that, unlike a real MIMO system, our configuration does not take into account the mutual coupling between the transmitter elements and the receiver elements respectively.

Both antennas are coaxially-fed vertically polarized rectangular patch antennas. The signals are transmitted at a carrier frequency of 5.88 GHz (wavelength $\lambda_0 = 51.02$ mm) with a total bandwidth of $F_s = 1.28$ MHz. The different positions of the antenna elements ($L_t = L_r = 10$) are separated by $\lambda_0/2$ whereas the distance between the rails is about $8\lambda_0$. In order to reduce crosstalk levels between the antennas, the space separating the rails is filled with absorbent material. The tested targets are metallic cylinders of diameter of 6 cm with a height of 1.5 m.

5.2. Estimation of the crosstalk matrix

The crosstalk matrix has been estimated in a first measurement process in the environment without any target using (10). In order to test the reliability of this estimation, the same process has been performed 100 times, using a different set of transmit signals at each time. Every transmitted signal has a duration of N/F_s seconds, where $N = 512$. The standard deviations of the coefficients of $\widehat{\boldsymbol{M}}$ are shown in amplitude and phase in Fig. 2 and Fig. 3 respectively. We can see that the relative standard deviations of $|\widehat{m}_{i,j}|$ are lower than 3.5% and the circular standard deviations [12] of $\arg(\widehat{m}_{i,j})$ are lower than 0.035 which indicates that the estimates of the coefficients of $\widehat{\boldsymbol{M}}$ are reliable.

When the mean transmitted power is fixed to 25 dBm, the mean power of the estimated crosstalk term $\widehat{\boldsymbol{M}}\boldsymbol{c}$ is found to be equal to -49 dBm.

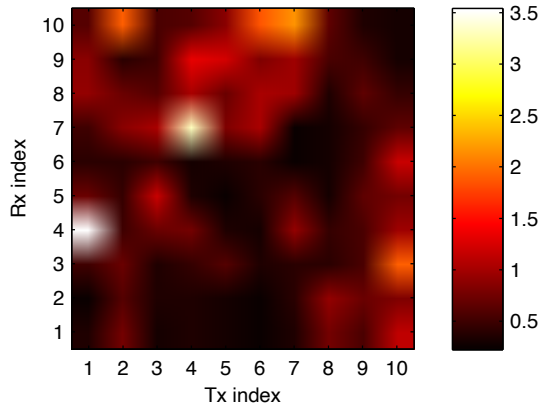

Figure 2: Relative standard deviation of the magnitude of the coefficients of $\widehat{\boldsymbol{M}}$ (in %).

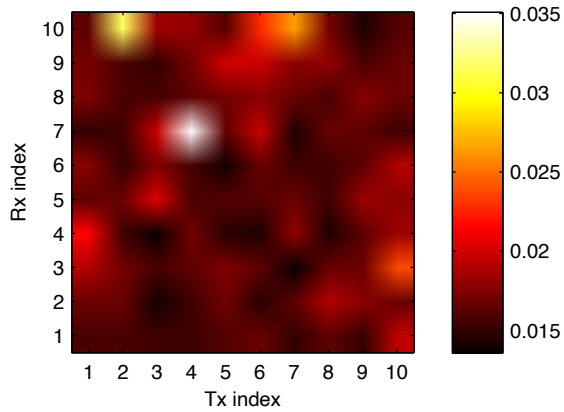

Figure 3: Circular standard deviation of the phase of the coefficients of $\widehat{\boldsymbol{M}}$.

5.3. Target detection using GLRT and crosstalk reduction

The GLRT was used to detect two targets located at -15° and 18°. Fig. 4(a) shows the GLRT spectrum computed from the received signals $\boldsymbol{x}$ (without any additional processing). Even though we have filled the space separating the transmitter and the receiver with an absorbent material, a residual crosstalk level appears to affect the GLRT detection technique, which explains the secondary lobes we observe around the target locations. Moreover, the characteristics of the actual noise, which are usually unknown, might also deteriorate the GLRT detection performance either if the noise level is too low (leading to ill-conditioning issues) or if the noise is not Gaussian.

In order to solve the noise characteristics problem, we first add a white Gaussian noise to the received signals $\boldsymbol{x}$ (see Fig. 4(b)). The power of this additive noise is chosen to be 70 dB below the received signals power (the latter being of

-36 dBm). Compared to the previous spectrum, we can see that several side lobes are attenuated. However, several false peaks due to crosstalk are still present around the target locations.

To overcome the negative effects of crosstalk, we next apply the technique proposed in Section 4.2 using the previously estimated crosstalk matrix $\widehat{\boldsymbol{M}}$ according to (11), where $\boldsymbol{x}$ includes the previously added white Gaussian noise. Fig. 4(c) shows the impact of this crosstalk reduction technique on the GLRT. We observe that the side lobes due to crosstalk are greatly reduced, which allows us to clearly identify the target directions.

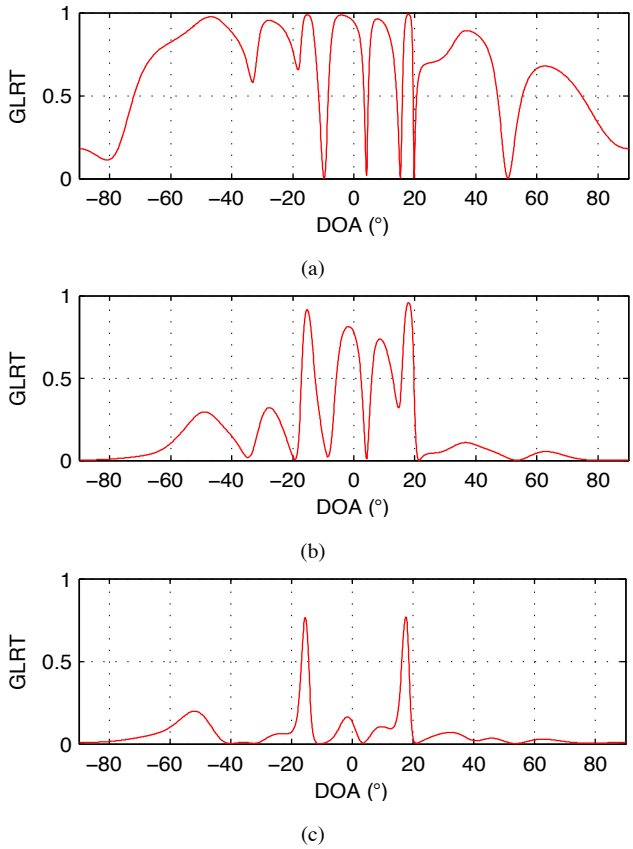

Figure 4: GLRT spectrum (a) without post-processing, (b) after addition of white Gaussian noise, and (c) after addition of white Gaussian noise and crosstalk reduction.

6. Conclusion

We have proposed a new signal model which takes crosstalk into account and we have shown that the existence of this phenomenon, due to the proximity between the transmitters and the receivers, can seriously affect the detection performance of MIMO radars with colocated antennas. Even if some absorbent material is used to reduce the crosstalk level, the remaining crosstalk can still affect some detection techniques such as GLRT. To solve this problem, we have proposed a crosstalk reduction technique and we have demonstrated its validity with some experimental results using real hardware.

References

[1] A. M. Haimovich, R. S. Blum, and L. J. Cimini, "MIMO radar with widely separated antennas," IEEE Signal Processing Magazine, vol. 25, no. 1, pp. 116-129, Jan. 2008.

[2] D. W. Bliss, K. W. Forsythe, S. K. Davis, G. S. Fawcett, D. J. Rabideau, L. L. Horowitz, and S. Kraut, "GMTI MIMO radar," in Int. Waveform Diversity and Design Conf., 2009, pp. 118-122.

[3] N. H. Lehmann, A. M. Haimovich, R. S. Blum, and L. J. Cimini, "High resolution capabilities of MIMO radar," in Proc. 40th Asilomar Conf. Signals, Systems and Computers, 2006, pp. 25-30.

[4] J. Li, and P. Stoica, "MIMO radar with colocated antennas," IEEE Signal Processing Magazine, vol. 24, issue 5, pp. 106-114, Sep. 2007.

[5] A. Hassanien, and S. A. Vorobyov, "Transmit/receive beamforming for MIMO radar with colocated antennas," in IEEE ICASSP, 2009, pp. 2089-2092.

[6] J. Li, and P. Stoica, "MIMO radar – Diversity means superiority," in MIMO Radar Signal Processing. Hoboken: John Wiley & Sons, 2009, ch. 1, sec. 1.6, pp. 49-52.

[7] N. W. D. Le Marshall, and A. Z. Tirkel. "MIMO radar array for termite detection and imaging," in Progress in Electromagnetics Research B, vol. 28, pp. 75-94, 2011.

[8] L. Xu, J. Li, and P. Stoica, "Radar imaging via adaptive MIMO techniques," in Proc. EUSIPCO, 2006.

[9] P. Stoica, J. Li, and Y. Xie, "On probing signal design for MIMO radar," IEEE Trans. Signal Processing, vol. 55, no. 8, pp. 4151-4161, Aug. 2007.

[10] O. Gomez, B. Poussot, F. Nadal, P. Jardin, and G. Baudoin, "An experimental platform for MIMO radar with colocated antennas," in IEEE APMC, Kaohsiung, Taiwan, 2012, pp. 1085-1087.

[11] P. Jardin, F. Nadal, and S. Middleton, "On wideband MIMO radar: Extended signal model and spectral beampattern design," in Proc. EuRAD Conf., Paris, France, 2010, pp. 392-395.

[12] N. I. Fisher, "Descriptive methods," in Statistical Analysis of Circular Data. Cambridge, UK: Cambridge Univ. Press, 1995, pp. 31-34.

Object reconstruction via radar detection behind walls

Aihua Wood[1], Ryan Wood[2], Matthew Charnley[3]

[1]Department of Mathematics and Statistics, Air Force Institute of Technology
[2]Department of Statistics, Harvard University, Cambridge, MA, USA
[3] Department of Mathematics, Rutgers University, Piscataway, NJ, USA
*corresponding author, E-mail: aihua.wood@afit.edu

Abstract

This paper explores the through-the-wall inverse scattering problem via machine learning. The reconstruction method seeks to discover the shape, location, and type of hidden objects behind simulated walls. We use radar frequency (RF) sources and receivers placed outside the room to generate observation data with objects randomly placed inside the room.

1. Introduction

Inverse problems have always been a highly researched area of mathematics due to their obvious physical and engineering applications. One important example of this type of problem is through-the-wall radar imaging. In this problem, one wishes to use scattered data from receivers positioned outside of a walled room, where a transmitter is also positioned, to locate and analyze an object inside the room. Previous work has used Doppler-type radar to detect and analyze humans where there is no direct line of sight, whether it be studying human motion with standard Doppler radar, noise forms, or micro-Doppler radar, which looks for smaller scale movements such as arm movement and heartbeats. In [1], a Support Vector Machine approach was used to discriminate between child and adult in a through-the-wall setting. More recently, neural networks were exploited to estimate human pose through walls.

In this presentation, we discuss the behind walls setting and a process for numerically reconstructing obstacles from scattered data. The main feature of this reconstruction is that it uses a source within the numerical field, so that the incoming field is not generated by a plane wave, and that the object is located within a set of walls that will interfere with the ability to analyze the object normally. The data used for performing this reconstruction is generated numerically, but it is also only assumed that the scattered field can be known at certain locations outside of the walled area, instead of known as a function. All of these changes violate the assumptions of the theoretical reconstructions, so a different approach is needed. We develop an appropriate adjustment to the theoretical methods presented in the literature to analyze obstacles in this setting, and present some numerical results towards this end. The reconstruction method seeks to discover the shape, size, and conductivity of the obstacles using a behind walls analysis. Specifically, in [2], locations of hidden objects behind walls were estimated by observing the time difference between signals from an empty room and that when an object was present. Based on the physics of electromagnetic wave propagation, ellipses with foci at the source and receiver pairs were constructed to provide the contour of the objects. In [3], a form of linear sampling method was used for the reconstruction. Specifically, a reciprocity gap functional to the electromagnetic field solution and the fundamental solution of the Helmholtz equation was used to derive an integral equation; the properties of whose solution gave indication of the location of the objects. We also explore machine learning using similar RF data as in [2-3], which was generated by numerically modeling the Maxwell's equations. We experiment with two types of neural networks and use an 80-20 train-test split for both reconstruction and classification.

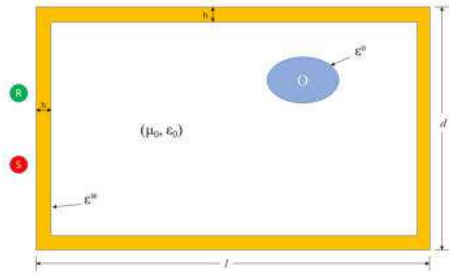

Figure 1: Model setup

2. Problem Setup

To model the actual physical problem, we will record and use data that could be gathered from a set of antenna transmitters and receivers. Thus, for any given simulation, we will assume that the electromagnetic waves are generated from a source antenna (S) positioned outside of the room and the data is recorded from a (finite) set of receivers (R), also positioned outside the room as shown in Figure 1.

We consider a two-dimensional radar imaging problem, assuming that all materials are invariant in the z-direction. The room is rectangular of size l by d. The walls are of a uniform thickness h, with relative electric permittivity

ϵ^w. The object that is to be detected is a convex domain $O \subset [0, l] \times [0, d]$ that has relative electric permittivity ϵ^o and is away from the boundaries of the room. We assume the medium throughout is nonmagnetic, thus $\mu_r = 1$. The source will be a pulse wave and monochromatic, emitting two full cycles of the wave before turning off. We observe that $k = \omega\sqrt{\mu\epsilon}$ and $\lambda = c_0/\sqrt{\epsilon_r}\omega$, where k is the wavenumber, ω frequency, λ wavelength, and c_0 free space speed of light.

3. Experiments

Here we present an example of object reconstruction using a simple pattern recognition algorithm, the k-NN. The main reason for this choice is its ease of adaptation. Since our data is generated by simulation, the density of the data for training can be very large, given enough computing power. Thus the lack of efficiency (in both time and memory), a main disadvantage of k-NN, is not of major concern.

For our experiment, each observation was obtained by setting the type of object to be placed in the room, and randomly assigning a location within the room. Three types of objects were considered: small circle of radius 0.1, small rectangle of size 0.1×0.2, and large rectangle of size 0.3×0.6. An equal number of data for Object 1 and Object 2, and a smaller amount for Object 3 were collected. Symmetries in the data were also used; the locations of the objects were initialized to be in the top half of the room, then the simulations run, and data for an object in the same location on the bottom half of the room were inferred by switching the readings of the receivers appropriately. In all, over $10,000$ observations were generated, taking up about 16GB of storage.

Example 1. For this experiment, we placed 6 receivers from behind left wall, taking data at 100 time steps. This yielded 1164 observations with $6 \times 100 = 600$ predictors. Using $k = 1$ nearest neighbor, the average L2-norm distance between predicted and actual location of a circular object with radius 0.1 was only 0.1049, and the variance was 0.0501. It took 0.044528 seconds for each run. See Figure 2

Example II. Here we use only partial data for the reconstruction and compare the results between those of ML, k-NN in this case, and of the linear sampling method (LSM). The LSM is a well known mathematical method for solving inverse scattering problems, see [**?**]. In this experiment, both the sources and receivers are placed on one side of the room only. This is perhaps more applicable given that it may only be possible to access one external wall of the room.

For circle objects of radius 0.1, k-NN returned prediction error of the same order as the radius when 24 receivers were used, and only double that with a total of just 3 receivers placed on one side of the external wall. See Figure 3.

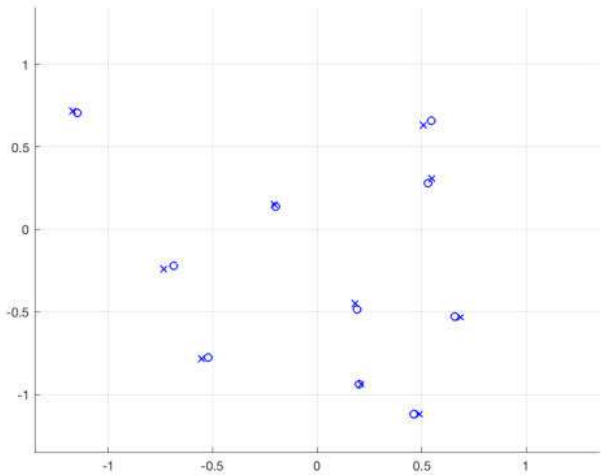

Figure 2: Illustrations k-NN prediction of center of circle.

Number of receivers	24	12	6	3
Average error	0.1523	0.1386	0.2440	0.2764
Variance of error	0.1202	0.1565	0.2518	0.2921

Figure 3: Sources & receivers on one side of room by K-NN

4. Conclusion

Through-the-wall object detection is an important area of research that has a wide range of physical and engineering applications. Using both traditional inverse methods and machine learning, we have reconstructed unknown targets behind walls using simulated data. In addition, our machine learning algorithms are capable of classifying different types of objects and determining material properties of the targets that the other reconstruction methods did not attempt. Moving forward, we would be interested in exploring more complex models including multiple objects, multiple reflections, and moving targets, to name a few.

Acknowledgement

The first author is supported in part by AFOSR grant F4FGA08305J005.

References

[1] S.R. Keith, Discrimination between Child and Adult Forms Using Radar Frequency Signature Analysis, *AFIT-ENP-13-M-20.*

[2] M. Charnley, A. Wood, Through-the-Wall Radar Detection Analysis via Numerical Modeling of Maxwell's Equations, *Journal of Computational Physics*, Vol. 313, 532-548 (2016).

[3] M. Charnley, A. Wood, A Linear Sampling Method for Through-the-Wall Radar Detection, *Journal of Computational Physics*, Vol. 347, 147-159 (2017).

Small target detection from a drone-based phased-array radar

Zaynab Guerraou[1], Ali Khenchaf[1], Fabrice Comblet[1],
Phillipe Morgand[2], Phillipe Pouliguen[3], Florent Jangal[3]

[1]Lab-STICC UMR CNRS 6285 ENSTA Bretagne
{zaynab.guerraou, Ali.khenchaf, Fabrice.comblet}@ensta-bretagne.fr
[2]Centre d'Ingénierie des Systèmes en Télécommunications en ElectroMagnétisme et Electronique
Email: morgand@cisteme.net
[3]Agence de l'Innovation de Défense (AID), 60, boulevard du Général Martial Valin, 75015 Paris, France
{Philippe.Pouliguen, florent.jangal}@intradef.gouv.fr

Abstract

In the recent years, small UAVs have become accessible for military, commercial and leisure activities. This comes with an increasing apprehension concerning their hazardous and illicit misuses. Radar systems have proved good capabilities for UAV surveillance, but small target detection still remains challenging and subject to active research. In this perspective, the present work deals with clutter mitigation and small target detection using phased-array radar and adaptive processing. The main contribution is the simulation of realistic small target and clutter data, and then the application of adaptive clutter mitigation and detection techniques, the goal being to improve the detection performance for small targets in adverse clutter environments.

1. Introduction

Small UAVs have become broadly used and their detection in complex environments is still a challenging task. The present work is conducted within the framework of the DOREDO project, aiming at detecting and localizing small obstacles such as light aircrafts and drones. The antenna system is a cylindrical array consisting of two sub-systems: The bearing system composed of a 24-column circular antenna allowing acquisitions in 360°, and the elevation system consisting of four columns, each one composed of 6 antenna patches. The system is under elaboration and the aim of the present paper is the simulation of realistic signals following the system characteristics for small target detection scenarios, and then performing signal processing and evaluating detection algorithms on the generated signals. This work is of paramount importance for applications such as radar system design. Its aim is twofold: on the one hand improving the simulation of realistic small target and ground-clutter signals, and on the other hand assessing the performance of adaptive array processing for clutter suppression as well as target detection. The paper is organized into four main parts: first the simulation of transmitted and received target signals is presented. Subsequently, CFAR target detection is assessed. Then the integration of realistic clutter statistics is addressed. The last section deals with adaptive array processing for clutter mitigation.

2. Transmitted and received target signals

Simulation of the main transmission and reception blocks for an X band airborne pulsed radar is performed. The emphasis is laid on the elevation system composed of a 6-element vertical Uniform Linear Array (ULA). Acquisitions are performed during a coherent processing interval (CPI) of 125 pulses and the generated waveform corresponds to the linear frequency modulated signal called chirp [1]. Raw I/Q complex data are then generated by considering the spatial delay between the array elements, phase and amplitude distortions, platform motion as well as thermal noise. In order to simulate realistic radar returns from targets of interest, the Radar Cross Section (RCS) from UAVs such as the DJI 3 drone have been measured in the anechoic chamber at ENSTA Bretagne. Assuming these RCS measurements, the received power is computed using the radar range equation.

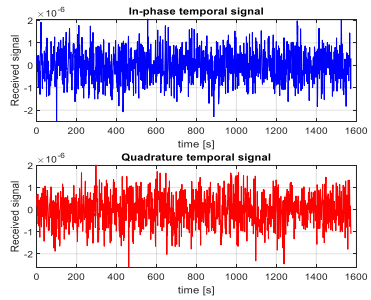

Figure 1: Generated IQ signals on array element for a target with RCS= -10 dBm², embedded in thermal noise. The SNR on each antenna element is equal to -31.5 dB

Figure 1 illustrates an example of IQ signals generation for a single array element. The simulated scenario consists in a small target ($RCS = -10\ dBm^2$), with a transmitted power of $P_t = 46\ dBm$, embedded in thermal noise. The SNR at the output of one antenna element is equal to SNR= -31.5 dB, which is very low for target detection. In order to improve the SNR, beamforming is first performed by summation of the temporal signals from the 6 channels. Then integration of the 125 pulses and range compression are performed. This processing yields to an improved SNR of the order of 16 dB.

3. CFAR detection

CFAR (Constant False Alarm Rate) detection methods consist in computing an adaptive threshold using a sliding

window while maintaining a constant false-alarm rate (CFAR) [2]. In addition to the original CA-CFAR (Cell Averaging CFAR) method, other CFAR variants have been implemented and tested against the generated signals. An example of the interest brought by the SO-CFAR (Smallest of CFAR) compared to the CA-CFAR algorithm is illustrated in figure 2. Three targets are present and two of them are closely spaced. The further target is accurately detected by both CA-CFAR and SO-CFAR. However, for the two closely spaced targets, CA-CFAR (top figure) fails at detecting the lower SNR one, as the threshold is artificially increased by the interfering target present in its reference window. SO-CFAR algorithm (bottom figure) overcomes this limitation and correctly detects both targets.

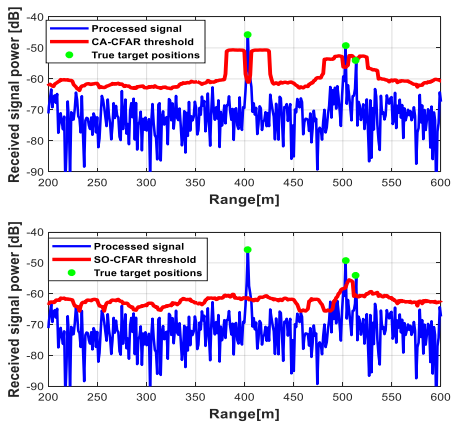

Figure 3: CFAR detection for the three targets. CA-CFAR (top figure), SO-CFAR (bottom figure)

4. Clutter signals

In the previous sections, only thermal noise was considered. For an airborne radar looking downward, terrain scattering is usually the major source of clutter that can cause important degradation in probability of detection. Terrain clutter encompasses several categories that vary in characteristics such as spatial homogeneity, nature of the overlying media (vegetation, snow…), nature of the substrate (water, soil, …) etc. Our work emphasizes on rural areas and thus considers clutter originating from trees, grasses, short vegetation and road surfaces. From a radar detection standpoint, ground clutter can be perceived as a distributed target that consists in a large number of randomly distributed scatterers. Due to its fluctuating nature, we resort to statistical analysis of the backscattering cross section per unit area, commonly called the backscattering coefficient and denoted σ^0, for which several statistical models have been proposed in the literature, such as the Rayleigh, Log-normal, Weibull and Gamma models. Note that the statistical parameters of the underlying distributions vary with sensor parameters (frequency band, polarization, acquisition geometry…), as well as the terrain nature, namely its geometrical and dielectric properties. In order to incorporate realistic clutter estimations, our simulations integrate distributions based on real clutter measurements reported in [3,4]. The authors document one of the most extensive series of measurements using different sensors covering various types of land surfaces over a large range of operating frequencies and incidence angles. Several experiments were performed following a variety of specifications including the radar platform (Airborne, Spaceborne, arch Mounted, truck, ground-based), frequency bands (L/S/C/X/Ku/Ka bands) and ranging methods (FMCW/Doppler/Pulse radars). In our work the emphasis is laid on X band pulse radar airborne data from vegetation. For illustration, figure 3 shows the frequency of occurrence of different σ^0 values for a terrain composed of grasses at a moderate incidence angle of 40°, in comparison with a Weibull distribution fit.

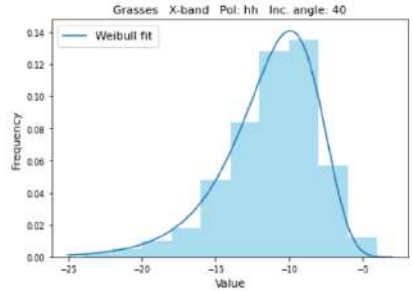

Figure 3: Example of σ^0histograms for a terrain composed of grasses at a moderate incidence angle of 40°, in comparison with a Weibull distribution fit.

5. Adaptive array processing for clutter rejection

In airborne radar, platform motion induces a shift in ground returns in both range and angle, as well as a spreading in the Doppler domain, potentially leading to a masking of targets of interest that can be perceived at slow speeds comparable to clutter measurements. Space Time Adaptive Processing (STAP) [5] is a processing technique that exploits both the spatial and temporal dimensions of the signals received by an antenna array. This processing allows to take advantage of the two-dimensional space-time properties (and thus of the angle-frequency coupling) of the received signals, which significantly improves the performance by providing coherent gain on the target signal-to-clutter ratio. Typically, the data from several range gates near the range gate of interest are used and a training strategy is defined to provide an estimate of the clutter statistics. Afterwards, an adaptive weight vector is computed based on this estimate and applied to radar data to perform clutter suppression.

References

[1] Richards, Mark A.; Scheer, James A.; Holm, William A.: "Principles of Modern Radar: Basic principles" (Radar, Sonar & Navigation, 2010) IET Digital Library

[2] Minkler, G., and Minkler, J., CFAR, The Principles of Automatic Radar Detection in Clutter, Magellan Book Co., Baltimore, MD, 1990.

[3] Cosgriff, Robert L. "Terrain Scattering Properties for Sensor System Design: (terrain Handbook I) ". Columbus: Engineering Experiment Station, College of Engineering, Ohio State University, 1960.

[4] T. Bush and F. Ulaby, "Variability in the measurement of radar backscatter," in IEEE Transactions on Antennas and Propagation, vol. 24, no. 6, pp. 896-898, November 1976, doi: 10.1109/TAP.1976.1141431.

[5] W. L. Melvin, "A STAP overview," in IEEE Aerospace and Electronic Systems Magazine, vol. 19, no. 1, pp. 19-35, Jan. 2004, doi: 10.1109/MAES.2004.1263229

Antenna and propagation measurement techniques

THz Corrugated Horn Antennas as TEM Mode-Convertor for Power Measurement and Material Characterization in Free-Space

Alireza Kazemipour, Johannes Hoffmann, Michael Wollensack, Daniel Stalder, Juerg Ruefenacht and Markus Zeier

Federal Institute of Metrology (METAS), Bern, Switzerland
*corresponding author, E-mail: alireza.kazemipour@metas.ch

Abstract

In-waveguide measurements are usually challenging at THz frequencies because of dimensional restrictions. Corrugated horn antenna is studied to show its capabilities (and limits) as WG to free-space mode convertor. Results are presented in terms of energy transfer to an open-surface detector and TEM propagation-mode on-and-near the antenna aperture. This paper shows the feasibility of using such antennas in 75-110GHz and 500-750GHz bands for power measurement and material characterization with the estimation of systematic and random errors.

1. Introduction

In recent years, the utilisation of the mm-Wave/THz range has significantly increased in a wide range of applications. Environmental studies, space technology, remote sensing, spectroscopy, wireless communications, automotive radar, security scanners and biomedical applications are among many other examples. The development and approval of high quality and safe products and systems depends on the availability of reliable measurements.

For material characterization, Vector Network Analyzer (VNA) can be used with quasi-optical associated devices to set the free-space non-contact measurements up [1]. The setup should be adequately calibrated and S-parameters derived on the material-under-test (MUT). Based on the measured S-parameters and the MUT thickness and positioning, permittivity and permeability can be extracted. A well-designed corrugated horn antenna can replace classic quasi-optical devices (pyramid horn plus lenses or parabolic mirrors) [2, 3]. However, probable systematic errors relevant to non-perfect TEM/free-space mode on the antenna aperture should be known and quantified, in advance.

For power measurement, open-surface classic optical detectors like pyroelectric and photo-acoustic devices can be characterized and used in THz domain, as well [4]. The main challenge is to suit a waveguide THz source to the open surface of the detector. Here again, a corrugated horn antenna is an appropriate choice if the scattering parameters of the antenna WG-input, aperture and the air-gap between the antenna and detector are characterized adequately.

2. Discussion and results

A long-body aperture-matched corrugated horn antenna can convert waveguide TE and TM modes to the hybrid HE_{11} mode with "quasi"-TEM electromagnetic fields on the antenna aperture (Fig.1)

A set of two corrugated horn antennas, head-to-head, with high surface aperture quality can be used as a compact material characterization device [3].

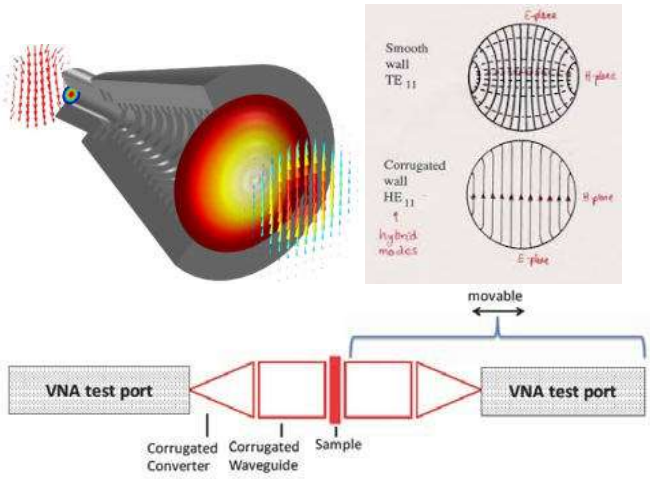

Figure 1: Schematic of mode conversion in corrugated horn antenna, and a set of two (aligned) antennas connected to the VNA test-ports for material characterization.

As the MUT is placed and measured in the air-gap between two apertures, this small space should be characterized and compared with the "real" free-space conditions. The method we use here is to assume an arbitrary air-gap as MUT and measure its permittivity. Deviations from $\varepsilon_r = 1+j0$ can demonstrate propagation mode conditions in the air-gap. Measurement results are presented (Fig.2) for the frequency-ranges 75-110GHz (3mm air-gap) and 500-750GHz (1mm air-gap). As shown, a slight rising slope (~ 0.5%) is observed around "ε_r (Re) = 1" for both frequency ranges. This should be taken into account for further assessment of errors and uncertainties. Measurements are based on transmission-only method [5] and have been performed for different air-gap distances, the tendency seems consistent for all cases.

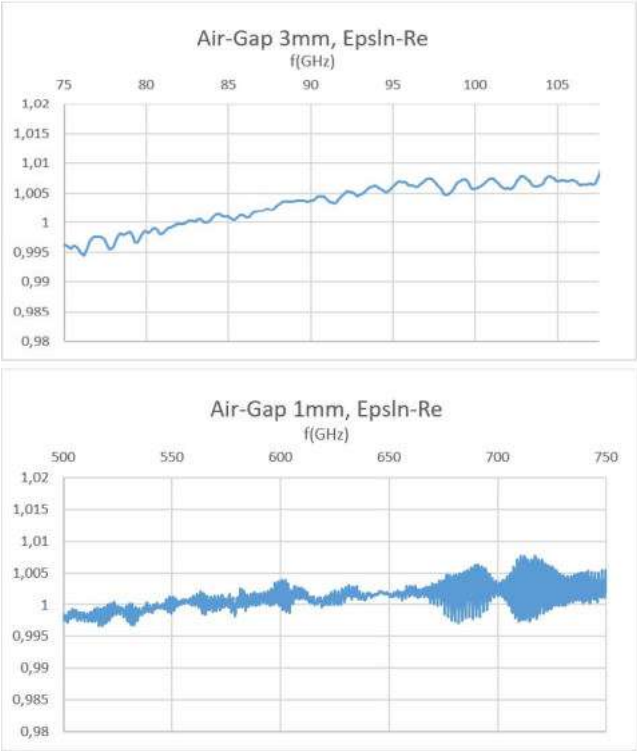

Figure 2: Propagation-mode characterization of the air-gap for 75-110GHz (top) and 500-750GHz (bottom) bands. Raw results are presented without time-gating or smoothening.

In terms of energy leakage, the air-gap can be characterized by S_{21} parameter normalized to the closed-gap case (Fig.3). This parameter is very important for the RF/THz power measurement in free-space. As shown, for the gaps up to 5mm, power transfer is well performed with losses less than 0.4dB in the 75-110GHz range.

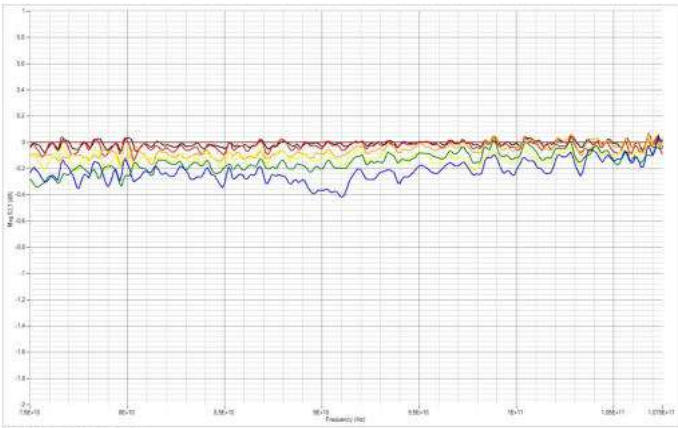

Figure 3: Power transfer via the air-gap (0.5, 1, 2, 3, 4 and 5mm) for 75-110GHz band. Raw results are presented without time-gating or smoothening.

Very low (and precisely measurable) energy leakage of the air-gap may make the corrugated horn antenna suitable for power measurement in free-space (Fig.4). The whole system should be characterized in terms of: antenna to WG-source matching, antenna input-to-aperture losses, air-gap and detector scattering, and standing-wave phenomena.

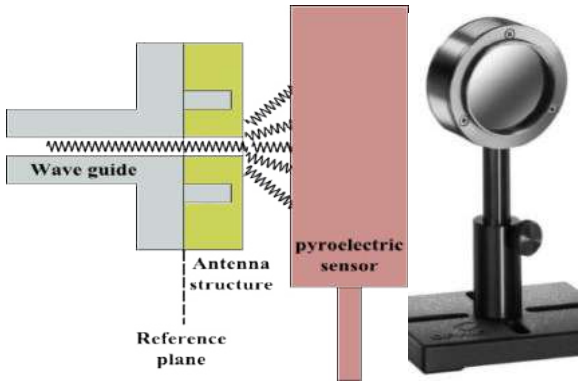

Figure 4: Schematic of THz waveguide source, antenna structure and power transfer to the open-surface sensor.

However, even the air-gap radiation and small losses make it necessary to reconsider the measurement conditions of low-refractive & low-loss materials like TPX, Teflon etc.

3. Conclusions

It is shown that the corrugated horn antenna can be characterized as TEM-mode convertor for various free-space measurements. Results are presented at 75-110GHz and 500-750GHz frequency ranges to show the propagation conditions and power transfer capability. Further works are in progress to improve the measurement system in terms of matching and multiple-reflection phenomena controlling.

Acknowledgements

This work was supported by the European Metrology Programme for Innovation and Research (EMPIR), under 18SIB09-TEMMT project. EMPIR programme is co-financed by the Participating States and from the European Union's Horizon 2020 Research and Innovation Programme.

References

[1] L. Oberto et al., "Measurement comparison among time-domain, FTIR and VNA-based spectrometers in the THz frequency range," *Metrologia* Vol. 54 (1), pp. 77-84, 2017.

[2] Y. Wang et al., "Characterization of Dielectric Materials at WR-15 band (50-75 GHz) using VNA-based Technique," *IEEE Trans. on IM,* Vol. 69, Nov. 2019.

[3] F. Cahill, *Design and Analysis of Corrugated Conical Horn Antennas with terahertz Applications,* Thesis, Maynooth University, Ireland, Sep. 2015.

[4] A. Kazemipour et al., "THz Detector Calibration Based on Microwave Power Standards," *IEEE-ICEAA Conf., Granada*, Sep. 2019.

[5] M. Hudlicka et al., "A Reliable Simple Method to Extract Material Properties in Millimeter/sub-Millimeter Wave Domain," *CPEM 2014 Conf. Digest*, pp. 576-77, 2014.

EMi/EMC/PiM chambers, instrumentation, and measurements

Assessment of Electromagnetic Field Threats to a Military Airport

D. V. Giri(1) and F. M. Tesche(2)
(1) Pro-Tech, 410 Washington Street, # 1, Wellesley, MA 02481, USA
(2) EMConsultant, USA

*Corresponding author, E-mail: Giri@DVGiri.com

Abstract

A recent area of concern is how to insure the continued functioning of critical elements of societal infrastructure amid increasing forms of terrorist activities. One new threat is the use of an HPEM source to create intentional electromagnetic interference (IEMI). This threat involves deliberately illuminating a facility or sub-system with a sufficiently intense EM field, to cause an interruption in the normal operation of the facility's electrical equipment. This effect is similar to electronic jamming, which has been used for years, but technological advances in high-power radio frequency (RF) sources and antennas now makes it possible to not only jam (or interrupt) equipment, but also to permanently damage (burn-out) equipment [1].

1. Introduction

This presentation, based on [2] describes the results of an assessment of the possible effects of an attack on a military airfield in Switzerland, using a high-power electromagnetic (HPEM) source. While such electromagnetic (EM) weapons systems are not commonplace today, there have been documented cases in the past of their being used for criminal activity. Moreover, with the rapid increase of EM source technology, it is possible that such EM weapons could pose more of a threat to critical elements society's infrastructure in the future. A general overview of the EM assessment methodology process is provided. Assessments can be performed at several levels of detail. Starting with a description of the airport, the type of assessment conducted at the airport is discussed. Important EM systems are identified. We also describe EM vulnerability estimates for various types of airport equipment, which are needed for performing an assessment. The characteristics of EM fields that could be used to target, are discussed. The nature of the EM environment is summarized, together with the details of the antennas and various source generators that might be used to produce these fields. Several EM attack scenarios that are envisioned at the airport are presented. This analysis provides an indication of the possible EM environments that could be used in such attacks, and it discusses the possible effects on the airport operations.

Civil aviation has become an integral component of present-day societies. It promotes an economic base for a community, assists and encourages trade, and is vital for the health, safety and welfare of the general public. Yet, we all know some of its vulnerabilities even from very low-level electromagnetic emitters. For example, cell phone use is prohibited in at least the takeoff and landing phases of a flight, due to its potential adverse effects on navigational electronics on-board the aircraft. Other passenger electronic devices (PED) such as lap-top computers, DVD players etc., have been known to cause interference and are prohibited during the take-off and landing phase of a commercial flight. In addition to these low-level emitters, both military and civilian aircrafts are routinely required to operate under adverse electromagnetic environments (EME), such as

- Natural- lightning electromagnetic pulse (N-LEMP)
- Electrostatic discharge (ESD)
- Electromagnetic environment in and around airports
- Intra-system electromagnetic interference (EMI)
- Inter-system EMI.

2. High Intensity Radiated Fields (HIRF) Fields

These HIRF certification levels are plotted in Figures 3 and 4 are important because if an intentional RF weapon system produces a HIRF level that exceeds the above levels by an order of magnitude, serious consequences may become possible.

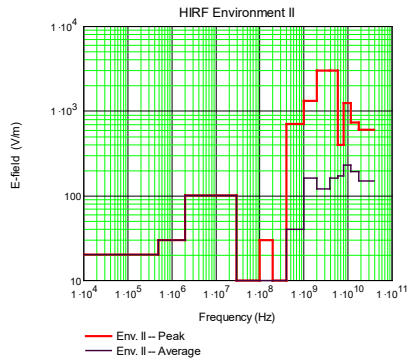

Figure 1 HIRF Type II Environments (effective September 2007).

From the examples cited above and the FAA / JAA standards it is safe to conclude that unintentional electromagnetic signals can pose a threat to aviation. It is entirely possible that RF terrorism [3 and 4] can bring such threats with intentional electromagnetic signals.
Furthermore, airports cannot run without networked computers operating in unison. Ground components such as, passenger terminals, air-traffic management (ATM) and airport vehicles are also subject to potential RF threats. There may not be a loss of life as in the case of loss of aircraft, but severe disruption of aviation services can be the price to pay. A coordinated RF attack on several passenger terminals aimed at disrupting networked computers [5, 6 and 7] can have serious psychological and economic consequences.

3. A Topological View of an Airport

A civilian airport is a facility where three components of air transportation system come together [8], as illustrated in Figure 2.

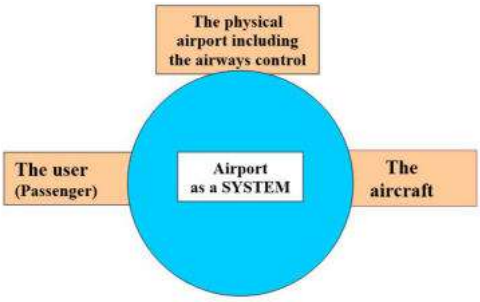

Figure 2. A system theoretic view of an airport

A typical airport operation includes, but not limited to, the following:

• Air Traffic Control • Telecommunications • Meteorology • Approach and Landing Aids • Runway Lighting • Air Field Inspections • Air Operations in Bad Weather Conditions • Power System Management • Passenger Service • Baggage Operations • Ground Handling • Airport Security	• Baggage Operations • Emergency Management • Personnel Requirements • Fire-Fighting Equipment and Readiness • Access Control • Authorized Ground Vehicles • Foaming the Runway when Needed • De-icing the aircraft when Needed • Airport Terminal Operations • Noise Control Strategies, etc • Licensing and Certification issues • Noise Control Systems

From an electromagnetic viewpoint, the following systems are of present interest to us.

- RF interfaces
- Power
- Telecommunication including navigational aids
- Air Traffic Management/Equipment(ATM/ Equipment)

4. Summary

The site survey that has been performed has resulted in a set of key places of the airport, where it would be desirable to measure the operating RF environment. This task has involved going to these parts of the airport and measure the EM environments that typically exist at different times of a typical day at the airport without involving the use of any kind of transmitters, but consists of only passive sensors, network analyzers / oscilloscopes. The passive sensor acts like a broad band receiving antenna over a frequency range of (1MHz to 4 GHz) and measures the RF environment. We have also made a determination of RF threat scenarios including electromagnetic coupling to selected systems such as aircraft in glide slope, control tower etc.The results of the measured data will feed into a determination of what it takes to disrupt the airport operation. Given the public access and proximity to the glide path of the aircraft, control tower, etc., we can then go on to determine what type (frequency, power levels, antenna aperture, directivity etc.,) of an RF weapon that can be potentially disrupt airport operations. Are such mobile RF weapons feasible, given the state-of-the-art in source technology? What are the consequences for aircraft and airport operations?

We can analyze several attack methods and several scenarios have been quantified. (Weapon type and characteristics, propagation losses, field on target)

References

[1] R. L. Gardner, “Electromagnetic Terrorism. A Real Danger” Proceedings of the XI th Symposium on Electromagnetic Compatibility, Wroclaw, Poland, June 1998,

[2] D, V, Giri, F. M. Tesche, P. F. Bertholet and M. Nyffeler, “A Preliminary Assessment of Radio Frequency Threats to Airports”, Interaction Note 634, 28 January 2020.

[3] W. A. Radasky, M. A. Messier and M. W. Wik, “Intentional Electromagnetic Interference (IEMI) - Test and data implications,” in Proceedings Zurich Symposium, Switzerland, February 2001.

[4] The URSI “Resolution of Criminal Activities using Electromagnetic Tools”, International Radio Scientific Union, General Assembly, 1999.

[5] R. Hoad, et al, 'Trends in EM susceptibility of IT Equipment', IEEE Transactions on EMC, Vol. 46, No. 3, August 2004.

[6] R. Hoad, et al, 'An Investigation into the radiated susceptibility of IT Networks', Conference Proceedings of EMC Europe, September 2004, Eindhoven, The Netherlands.

[7] R. Hoad, A. Lambourne and A. Wraight, 'HPEM and HEMP susceptibility assessments of computer equipment', EMC Zurich in Singapore, Singapore, Asia, February 2006.

[8] N. Ashford, H. P. Martin Stanton and C. A. Moore, Airport Operations, second edition, McGraw Hill, 1997.

Material Characterization and non-destructive testing

High Sensitivity SSR Based Sensor Used for Permittivity Measurement

Youness Zaarour[1], Mohammed Ali Ennasar [3], Otman El Mrabet[3], Hafid Griguer [1], Rafiq el alami[1], M'Hamed Drissi [1-2]

[1]Mohammed VI Polytechnic University, ILO, Benguerir, Morocco
[2]Univ Rennes, INSA Rennes, IETR, UMR CNRS 6164, F-35000 Rennes, France
[3]Information and Telecommunication Systems Lab, Faculty of Sciences, University of Abdelmalek Essaadi, Tetouan, Morocco
*Corresponding author, E-mail: youness.zaarour@um6p.ma

Abstract

The proposed sensor is based on a Split Square Resonator (SRR), placed in the center of the transmission line above the SSR (most sensitive region) to improve the detection. The dimensions of the SRR have been chosen so that the resonance frequency of the filter will be close to 7.85 GHz in free space. The functional principle of the designed sensor is based on placing over the sensitive position the material under test (MUT). It is based on detecting changes in dielectric properties (permittivity) of MUT present in the near-field region of the sensor, along the changes of the resonance transmission frequency (S12), caused by perturbation of resonator's electric field through MUT. To validate this conjecture, three cubic MUTs were tested (PLA, FR4 and Rogers TMM10i). This proposed design exhibits a high sensitivity close to 56% as the relative permittivity of MUT's changes from 1 to 10.

1. Introduction

In recent years, robust, miniature, inexpensive, selective, and highly sensitive technologies used for agile sensing devices in various applications have placed high demands. Sensing technology based on microwave resonance is a recently developed technology, and many researchers have been studying it in the past ten years, including microwave sensors that are employed in material characterization, precision agriculture, biomolecule detection, and concentration research. Detecting material characteristics is based on acquire knowledge about its permittivity, since it is most crucial than the permeability to distinguish different dielectrics. The use of planar transmission lines with metamaterial for material characterization is one of the technologies that become used. This technique relies on the direct interaction between the material under test (MUT) and the evanescent field of the transmission line to achieve high measurement accuracy and excellent imaging capabilities. The most popular methods for material characterization utilize dielectric measurement technology based on microwave resonators are measuring the change of magnitude/ frequency of reflection/transmission coefficient, phase, and quality factor (Q-factor). Many researchers have proposed planar metamaterials with different topologies for several application, among them, dielectric constant measurement [1-5]

In this paper, we introduce a simple shape consist of a split ring resonator (SSR) based on MTL (Microwave Transmission line) feeding, used as a sensor for dielectric material characterization.

The concept is given in Fig.1. The simplicity of the sensor permits to measure the transmission coefficient, by placing a small cubic in direct contact to the sensitive region. The structure will be as follow: Section II describes the design and an analysis of sensitivity where we discussed, the effect of MUT size. Section III includes simulation results and discussion. Finally, a conclusion of the presented work in section IV.

2. Design and Simulations

The designed device shown in Fig.2 is simulated on Rogers 5880 substrate with a dielectric constant of 2.2, TanD of 0.009 and a thickness of 0.787mm. The choice of such substrate allows to produce a relevant fringe electro-magnetic field in the sensing area, in order that the characteristics of the MUT can be well detected, thereby improving the sensitivity. In this present paper, the design is based on a single split square resonator (SSR), placed in the center of a transmission line, designed to be suitable for a resonance at 7.76GHz, with a side length of 8 mm. The path of the SSR is c=0.4mm and the SSR split length is g=0.6 mm. The transmission line is designed with 16mm strip length both sides and a=2.34 mm strip width connected to a 50Ω coaxial SMA connector to ensure the impedance matching. The substrate length and width are both 40mm

(about half the length of the long edge of a credit card), with a copper layer of 35um.

Generally, a part of the guided EM waves propagating in the transmission line, will polarize the adjacent dielectric substrate, and a part of the loaded MUT. The polarized dielectric substrate could be presented by an equivalent capacitance. In case of using a CSRR etched in the ground plane, decreasing the polarized portion of the dielectric substrate (thickness) enhances the resonating electric field to interact with MUT, thus increasing the sensitivity. While in this work, using a SRR centered in the transmission line in direct contact with MUT, increasing the polarized substrate part, guarantee an effective propagation and radiation of the electric field with the MUT, hence, increases the dependence of the minimum transmission frequency, and ensure an efficient interaction of the electric field with the MUT, and increase the sensitivity.

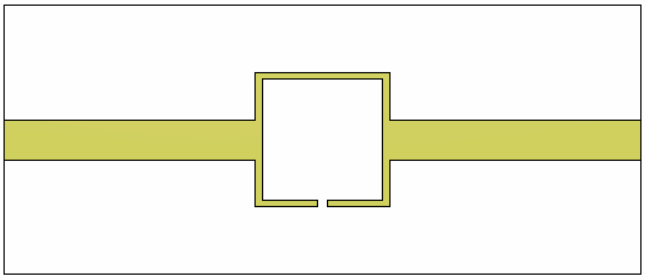

(a)

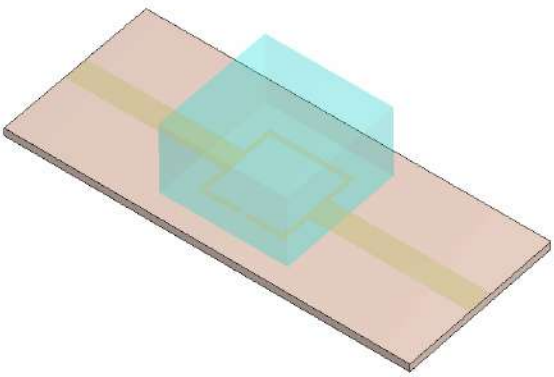

(b)

Figure 1: (a) Top view of the sensor (b) Side view of the sensor.

The sensor's sensitivity will be determined by the percentage of change in the minimum transmission frequency. It is calculated for each study and determined by (1).

$$\Delta f^{t_{min}}\,\% = \left(\frac{f_{MUT0}^{t_{min}} - f_{f_{free}}^{t_{min}}}{f_{f_{free}}^{t_{min}}}\right) * \ 100 \qquad (1)$$

where, $f_{MUT0}^{t_{min}}$ is the minimum transmission frequency with the presence of MUT, and $f_{f_{free}}^{t_{min}}$ is the free space minimum transmission frequency. Various simulations were done to choose the most sensitive sensor depending on substrate thickness. Seven cases were examined with different transmission line width to have a matching with the feeding network 50ohm impedance. All simulations were done with a variation of loaded MUT permittivity from 1 to 10 with a 1-step and Tan = 0.0012 is kept constant.

2.1. MUT size effect:

As mentioned in the previous section, the portion polarized by the EM waves changes the minimum transmission frequency by changing its size. Reducing the MUT polarized portion by the electric field will directly decrease the equivalent capacity value of MUT, therefore, affects and reduces the correlation with the minimum transmission frequency, thus decreases the sensitivity of the sensor.

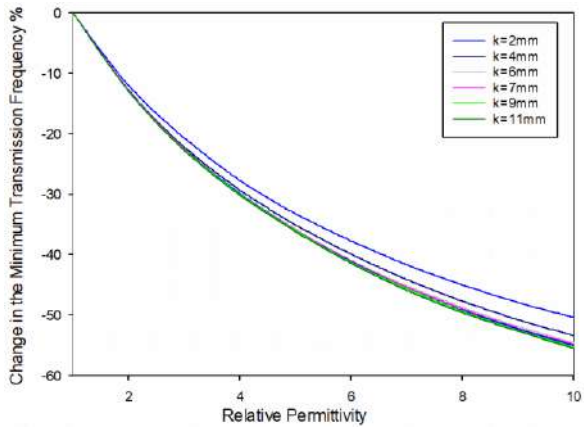

Figure 2: Change in the minimum transmission frequency versus MUT's relative permittivity with different thickness.

In this studied case, the MUT cover the SSR and a simulation of both width and thickness were done to define the accurate size that result saturation of the electric field. At a certain MUT size (thickness K), the MUT portion get polarized, and any added size will add up extra dielectric layers which will not be affected by the resonant electric field, and this is because of the achievement of saturation interaction among the resonator's field and the MUT.

The achieved results (Fig.2) proves that the sensor arrives to a specifics level of saturation, with an optimum value of K=7mm in thickness. However, same study has been done, and conclude with W=13mm.

any extra material above these values has no effect on the transmission frequency response, hence, the sensor's sensitivity will be unaffected by MUT size.

3. Simulation Results and discussion

The suggested sensor design is simulated using a commercial CST Microwave studio with the goal of examining the influence of MUT and gap size, demonstrating the reaction of different materials, and concluding with the function of permittivity versus change in minimum transmission frequency.

To perform the simulation with the setup shown in Fig.7, we are using PNA-L Network analyzer N5234B. PLA, FR-4, and ROTMM10i were used to creat three cubic MUTs. These samples have been fabricated nominal relative permittivity's of 2.3, 4.3, and 9.8, respectively. Over the split ring resonator, the MUT is charged. The transmission frequency resonances produced by various samples are shown in Fig.4. Understanding the Cavity Perturbation Theory, MUTs with a bigger relative permittivity result in a lower transmission frequency. The first simulation was done at 7.85 GHz, which is the open space transmission frequency. The three other transmission frequency corresponding to PLA, FR-4, and RO TMM10i are 6.78 GHz, 5.59 GHz, and 3.86 GHz, respectively, for The MUT the results reveal a remarkable performance of the sensing method used in this paper.

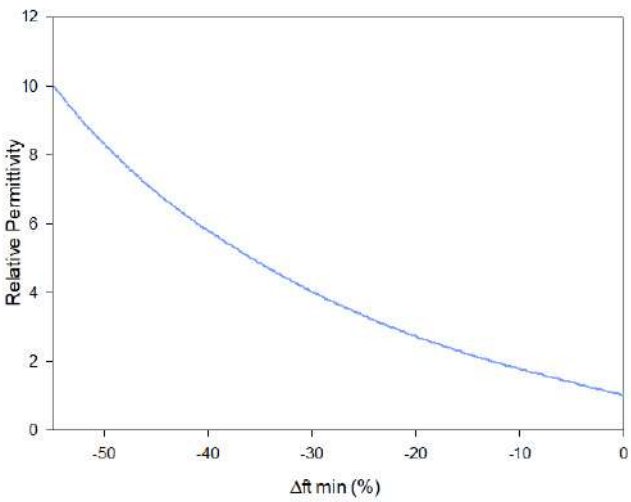

Figure 3: results obtained by model (2).

Relation 2 shows a link between the relative permittivity of the MUT and the change in the minimum transmission frequency for the sensor evaluated in the experiment.
The simulations results presented in Fig.4 are extracted using a 0.757 mm substrate load with different MUT.

$$\varepsilon_{MUT} = -4 * 10^{-5} * \left(\Delta f^{tmin}\%\right)^3 - 0.001 * \left(\Delta f^{tmin}\%\right)^2 - 0.0742 * \Delta f^{tmin}\% + 1 \qquad (2)$$

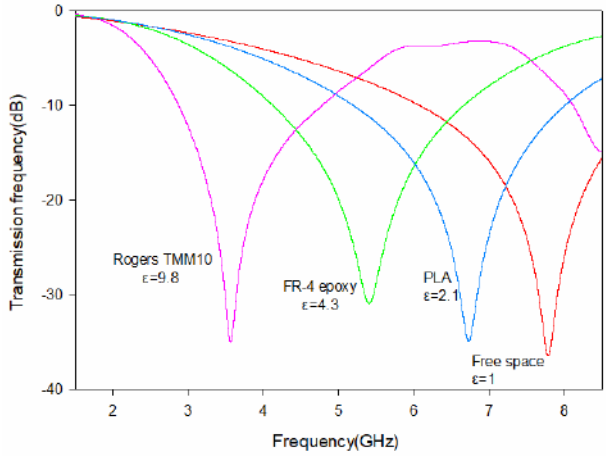

Figure 4: Comparison between numerical (solid lines) and experimental (dashed lines).

4. Conclusion

The design and testing of a sensitive sensor based on SSR, centered in a transmission line is reported in this paper. The sensor's major monitored characteristics is the change in the minimum transmission frequency of the microwave device. the design is configured to be suitable to small size of different MUT. It demonstrates a high sensitivity close to 56% while changing the MUT permittivity from 1 to 10.
The use of such a sensor to detect glucose levels with large and high sensitivity might be the subject of future research.

5. References

[1] Alotaibi, Salem A., Yepu Cui, and Manos M. Tentzeris. "CSRR Based Sensors for Relative Permittivity Measurement with Improved and Uniform Sensitivity throughout [0.9–10.9] GHz Band." IEEE Sensors Journal 20.9 (2019): 4667-4678.

[2] Haq, Tanveerul, et al. "Dual notch microwave sensors based on complementary metamaterial resonators." IEEE Access 7 (2019): 153489-153498.

[3] Ebrahimi, Amir, et al. "High-sensitivity metamaterial-inspired sensor for microfluidic dielectric characterization." IEEE Sensors Journal 14.5 (2013): 1345-1351.

[4] Zhao, Wen-Sheng, et al. "Microwave Planar Sensors for Fully Characterizing Magneto-Dielectric Materials." IEEE Access 8 (2020): 41985-41999.

[5] KT, Muhammed Shafi, et al. "Design of SRR-based microwave sensor for characterization of magnetodielectric substrates." IEEE Microwave and Wireless Components Letters 27.5 (2017): 524-526.

Giant Magnetoimpedance Microwires for Sensor Applications

Arcady Zhukov[1,2,3]*, Paula Corte-León[1,2], Lorena González-Legarreta[1], Mihail Ipatov[1,2], Juan M. Blanco[2] and Valentina Zhukova[1,2]

[1]Dpto. Fisica de Materiales, Fac. Quimicas, UPV/EHU, Paseo Manuel Lardizabal, 3, San Sebastian, 20018, Spain
[2]Dpto. de Física Aplicada, EIG, UPV/EHU, San Sebastian, Europa Plaza, 1,20018, Spain
[3]IKERBASQUE, Basque Foundation for Science, Bilbao, 48011, Spain
*corresponding author, E-mail: arkadi.joukov@ehu.es

Abstract

The influence of post-processing (annealing and stress-annealing) on the Giant magnetoimpedance (GMI) effect in thin magnetic microwires is reviewed. High GMI effect has been observed in Co-rich magnetic microwires with vanishing magnetostriction coefficient. Post-processing including annealing or stress-annealing at adequate conditions allows further improvement of GMI effect in Co-rich magnetic microwires.

1. Introduction

Magnetic and magnetoelastic sensors and smart composites utilizing soft magnetic wires with Giant Magneto-impedance present excellent features including extremely high sensitivity to external stimuli: i.e. magnetic field, stress or temperature making them suitable for many applications [1]-[3]. Most of the emerging applications require materials with reduced dimensionality and excellent soft magnetic properties, superior mechanical properties, enhanced corrosion resistance and biocompatibility [1],[4].

Generally, amorphous magnetic wires present the best combination of soft magnetic properties and superior mechanical characteristics [4],[5]. The other functional properties, like reduced dimensionality, improved corrosion resistance and biocompatibility can be achieved in amorphous microwires coated by flexible and insulating glass-coating [4], [5]. Therefore, studies of GMI effect in amorphous glass-coated microwires gained considerable attention since the 90-s [5].

The magnetoelastic anisotropy is one of the most important parameters that determine the magnetic properties [4],[5]. The most common way to tune the magnetoelastic anisotropy is the selection of proper chemical composition with nearly-zero magnetostriction coefficient, λs. Indeed, vanishing λs-value in amorphous alloys can be achieved choosing Co_xFe_{1-x} ($0 \leq x \leq 1$) alloys with x about 0.03-0.08 [5]. However, theoretical maximum GMI effect is above 3000% (i.e few times larger than GMI ratio values reported experimentally) [4,5]

Consequently, we present our recent experimental results on post- processing of magnetic microwires with aim to achieve better magnetic softness and GMI effect.

2. Materials and methods

We selected typical $Fe_{3.6}Co_{69.2}Ni_1B_{12.5}Si_{11}Mo_{1.5}C_{1.2}$ alloys with vanishing λs-value. We used micro-strip sample holder placed inside a sufficiently long solenoid that creates a homogeneous magnetic field, H. The sample impedance, Z, was measured using vector network analyzer from the reflection coefficient S_{11} using expression:

$$Z = Z_0 \frac{(1+S_{11})}{(1-S_{11})} \quad (1)$$

where Z_0=50 Ohm is the characteristic impedance of the coaxial line [6]. Described technique allows measuring of the GMI effect in extended frequency, *f*, range up to GHz frequencies. For GMI characterization we used GMI ratio, *ΔZ/Z*, defined as:

$$\Delta Z/Z = [Z(H) - Z(H_{max})]/Z(H_{max}) \quad (2)$$

where H_{max} is the maximum axial *DC* magnetic field (usually up to few kA/m).

Hysteresis loops have been measured using fluxmetric method [9]. We represent the normalized magnetization, M/M_0 versus magnetic field, *H*, where *M* is the magnetic moment at given magnetic field and M_0 is the magnetic moment of the sample at the maximum magnetic field amplitude, H_m.

3. Results and discussion

As-prepared microwires present linear hysteresis loops with low H_c (see Fig. 1a). Similarly to other Co-rich

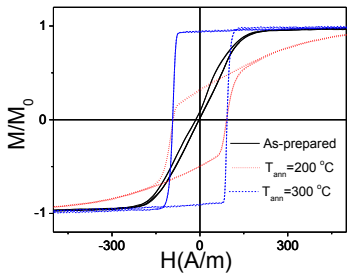

Figure 1. Hysteresis loops of as-prepared (a) and annealed at 200°C, (b), and 300 °C (c) $Fe_{3.6}Co_{69.2}Ni_1B_{12.5}Si_{11}Mo_{1.5}C_1$ microwires.

microwires with vanishing λs –values $Fe_{3.6}Co_{69.2}Ni_1B_{12.5}Si_{11}Mo_{1.5}C_{1.2}$ microwire presents drastic magnetic hardening upon annealing: an order of magnitude coercivity, H_c, rising from 5 A/m up to 90 A/m (see Fig. 1b,c). However, GMI ratio of $Fe_{3.6}Co_{69.2}Ni_1B_{12.5}Si_{11}Mo_{1.5}C_1$ microwires annealed at 300 °C is considerably higher (see Fig. 2).

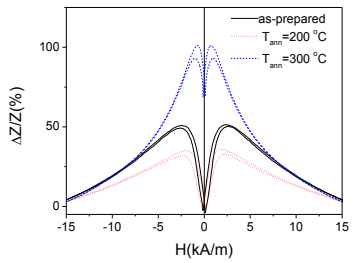

Figure 2. *ΔZ/Z (H)* dependences of as-prepared and annealed $Fe_{3.6}Co_{69.2}Ni_1B_{12.5}Si_{11}Mo_{1.5}C_{1.2}$ microwires measured at 500 MHz.

Stress-annealing allows to reduce considerably the H_c-value (see Fig.3). However, at selected annealing conditions

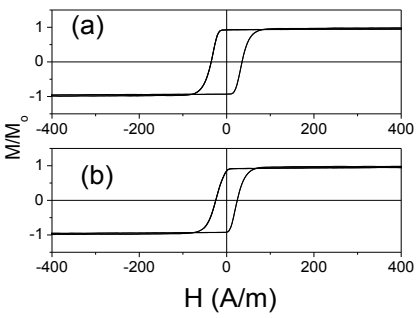

Figure 3. Hysteresis loops of $Fe_{3.6}Co_{69.2}Ni_1B_{12.5}Si_{11}Mo_{1.5}C_{1.2}$ microwires annealed at T_{ann}=300 °C for t_{ann}=1 h under 118 (a) and 236 (b) MPa.

(Tann=300 °C, tann= 1 h) the hysteresis loops shape remains rectangular. As regarding the GMI effect, all stress-annealed Co-rich microwires present a remarkable GMI ratio improvement (see comparison in Fig. 4 (a)): for f=200 MHz more than double GMI ratio improvement is observed almost for all stress-annealed samples. As can be appreciated from the frequency dependence of maximum GMI ratio, $\Delta Z/Z_m(f)$, dependencies shown in Fig. 4 (b) this $\Delta Z/Z_m$ improvement is observed for all frequency range (up to 1 GHz). It is interesting that the optimum frequency for as-prepared sample is about 100 MHz, however, for stress-annealed samples the optimal frequency shifts to about 150 MHz.

Accordingly, stress annealing of Co-rich microwires allowed considerable GMI effect improvement

4. Conclusions

We observed that the stress-annealing allows remarkable improvement of GMI effect in Co-rich microwires: about 100% GMI ratio improvement is demonstrated.

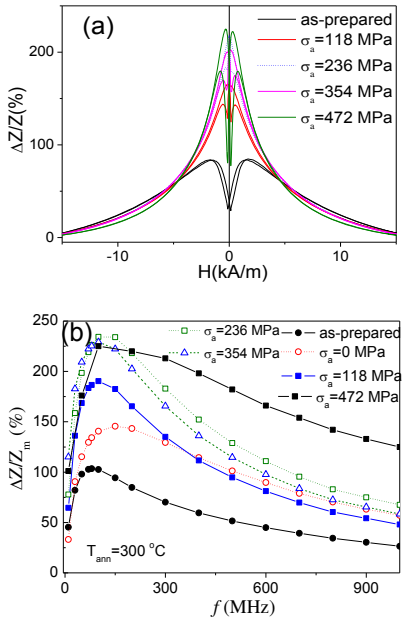

Figure 4. *ΔZ/Z(H)* dependences of as-prepared and stress-annealed at T_{ann} = 300 ºC samples at different σ_a measured at 200 MHz (a) and $\Delta Z/Z_m(f)$ dependencies for the same samples (b).

The future scope of our research will be focused on magnetic wires miniaturization and further development of appropriate post-processing.

References

[1] S. Gudoshnikov, et.al., Highly sensitive magnetometer based on the off-diagonal GMI effect in Co-rich glass-coated microwire, *Phys. Stat. Sol. (a)* 211 (5): 980–985, 2014.

[2] M. Ipatov, et.al, Tunable effective permittivity of composites based on ferromagnetic microwires with high magneto-impedance effect, Appl. Phys. A: Mater. Sci. Proc. 103 (3): 693-697, 2011

[3] T. Uchiyama, K. Mohri and Sh. Nakayama, Measurement of Spontaneous Oscillatory Magnetic Field of Guinea-Pig Smooth Muscle Preparation Using Pico-Tesla Resolution Amorphous Wire Magneto-Impedance Sensor, *IEEE Trans. Magn*. 47: 3070-3073, 2011.

[4] A. Zhukov, M. Ipatov and V. Zhukova, Advances in Giant Magnetoimpedance of Materials, Handbook of Magnetic Materials, ed. K. H. J. Buschow, vol. 24 ch. 2, (2015) 139-236.

[5] A. Zhukov, et.al., Trends in optimization of giant magnetoimpedance effect in amorphous and nanocrystalline materials, *J. Alloys Compound*. 727: 887-901, 2017.

[6] A.Zhukov, et.al., Tailoring the high-frequency giant magnetoimpedance effect of amorphous Co-rich microwires, *IEEE Magn. Lett.*, 6: 2500104, 2015

Real-time measurement system using multi-wavelength THz-wave parametric generation and detection

Kosuke Murate*, Kodo Kawase

Department of Electronics, Graduate school of Engineering, Nagoya University,
Furocho, Chikusa, Nagoya, 4648603, Japan
*corresponding author, E-mail: murate@nuee.nagoya-u.ac.jp

Abstract

In this study, we achieved real-time identification of reagents using combination of machine learning and simultaneous generation and detection of multiwavelength terahertz (THz) waves by injection seeded terahertz wave parametric generator (is-TPG).

1. Introduction

We have spent many years developing an injection-seeded terahertz (THz) wave parametric generator (is-TPG) as a high-power THz-wave source with a $LiNbO_3$ crystal. Recently, we achieved a peak power of 50 kW and frequency tunability of 0.4–5 THz[1], [2]. is-TPG is a narrow linewidth and high brightness THz wave source; therefore, it can generate one wavelength per pulse, and the wavelength was tuned for each spectroscopy. On the other hand, in this study, we aimed at simultaneous generation of multiwavelength THz waves from is-TPG. In multiwavelength generation, the wavelength does not need to be changed, which would shorten the measurement time. Averaging would also not be required because spectroscopy is done by one pulse. Moreover, we introduced machine learning for identification of samples. This would enable real-time identification system with a repetition rate equal to that of the excitation laser.

2. Principle of multi-wavelength generation and detection using is-TPG

When a high-power pump beam and seed beam are input to a $LiNbO_3$ crystal, narrow line width and high brightness THz wave is generated by parametric wavelength conversion. At that time, wide tunability of THz wave can be achieved by controlling the wavelength of the seed beam and its angle to satisfy the non-collinear phase-matching condition of the $LiNbO_3$ crystal. We call this THz wave source is-TPG[1], [2]. On the other hand, when the multi-wavelength seed beams are injected to the crystal, the energy was distributed to each wavelength and multi-wavelength THz wave is generated[3]. Although the principle of multi-wavelength generation is simple, multi-wavelength seed beam source (i.e. multiwavelength continuous-wave laser) was not easily accessible. Therefore, we prepared it by combination of multiple external cavity laser diode (ECLD).

The detection of THz wave is also possible using same principle of is-TPG[1], [2]. It is the reverse of generation; in other words, a THz wave is used as the seed beam, and a near-infrared detection beam is generated. In this method, the generation angle of the near-infrared detection beam changes based on the wavelength of the input THz wave, according to the non-collinear phase-matching condition. Therefore, one-pulse spectroscopy is achieved by inputting multi-wavelength THz waves and converting the generation angles of the resulting multi-wavelength near-infrared detection beam to THz-wave frequencies.

3. Experiment and results

A schematic diagram of the experimental system is shown in fig. 1. A pump beam emitted by a micro-chip Nd:YAG laser and a five-wavelength seed beams emitted by five ECLDs irradiate a $LiNbO_3$ crystal under non-collinear phase matching conditions, resulting in the emission of five wavelength THz waves. The emitted THz waves are focused

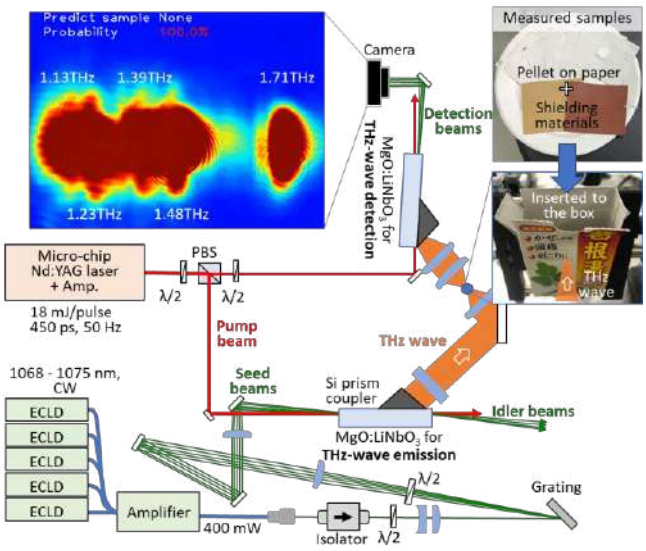

Figure 1: Real-time measurement system with combination of deep learning and multi-wavelength THz-wave parametric generation and detection. Right upper side inset shows the measured samples.

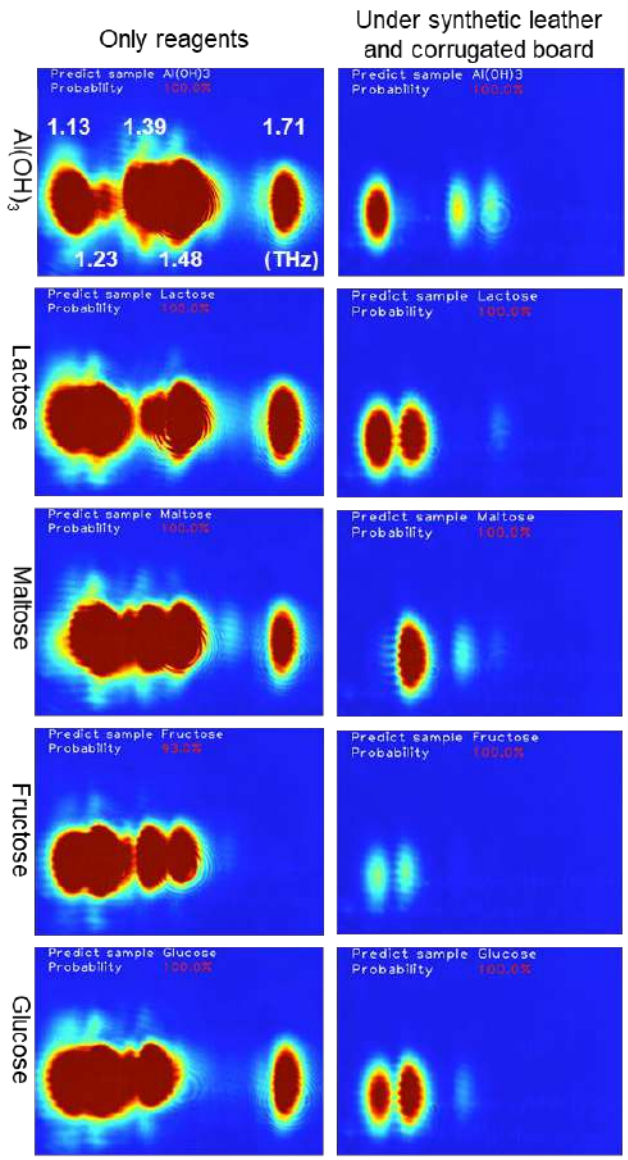

Figure 2: Screenshots of detection beams measured with camera when each sample was inserted to the THz path. The "predict sample" and "probability" shown in the upper part of each screenshot shows the identified result at that time via the CNN.

onto the sample and then it is up-converted to a near-infrared (NIR) detection beams at another crystal. Here we used camera to detect the multiple detection beams.

We measured five pellet samples of Aluminium hydroxide, Lactose, Maltose, Fructose and Glucose on the paper. Those samples were placed under some shielding materials which were and combination of those two shielding materials. The emitted THz frequencies were chosen as 1.13, 1.23, 1.39, 1.48 and 1.71 THz that matched to the absorption peak of samples.

The real-time identification was performed on images of the detection beams obtained with the camera. We input those data for the convolutional neural network (CNN)[4], [5], which is one of the deep neural network specialized for image data, and classified seven classes which were five reagents, Shielding (includes three kinds of shielding materials), and None. As training data for CNN, we used 30 images of each class, for a total of 270 images.

Upper left side inset of fig. 1 shows an image of the detection beams without any sample (i.e. None class). At that time, intensities of detection beams were saturated because it was optimized when samples with shielding materials were inserted to the THz path and attenuated THz wave. Fig. 2 shows the results of real-time measurement. We took screenshots, showing the timing when each sample was inserted to the THz path. An absorption profile corresponding to the transmitted spectrum of each sample was obtained using the multi-wavelength is-TPG in real-time. The "predict sample" shown in the upper part of each screenshot shows the sample name predicted in that instant via the CNN; "probability" corresponds to the sample prediction probability. By applying the CNN to the images of the detection beams, all samples were identified with almost 100% accuracy. This shows that, by combining multi-wavelength is-TPG with a CNN, samples can be identified through shielding material in real-time.

4. Conclusions

In this work, we achieved real-time measurement of reagents using multi-wavelength is-TPG. Sample was identified in real-time with almost 100 % prediction rate using CNN. The results of this study are expected to advance THz nondestructive testing technology.

Acknowledgements

Authors appreciate with Dr. S. Hayashi of NICT; Dr. H. Minamide, Dr. K. Nawata, and Dr. Y. Takida of Riken; and Prof. T. Taira of IMS for the fruitful discussions and Mr. R. Mitsuhashi, Ms. R. Kawaguchi and Mr. Y. Torii from Nagoya University for assistance in the experiments.

This work was partially supported by Japan Society for the Promotion of Science KAKENHI (18H03887, 19H02627); and Research Foundation for Opto-Science and Technology.

References

[1] S. Hayashi, et al., Ultrabright continuously tunable terahertz-wave generation at room temperature, *Sci. Rep.*, vol. 4, p. 5045, 2014.

[2] K. Murate and K. Kawase, Perspective: Terahertz wave parametric generator and its applications, *J. Appl. Phys.*, vol. 124, no. 16, p. 160901, 2018.

[3] K. Murate, S. Hayashi, and K. Kawase, Multiwavelength terahertz-wave parametric generator for one-pulse spectroscopy, *Appl. Phys. Express*, vol. 10, no. 3, p. 032401, 2017.

[4] A. Krizhevsky, I. Sutskever, and G. E. Hinton, ImageNet Classification with Deep Convolutional Neural Networks, in *Advances in Neural Information Processing Systems 25*, Eds. Curran Associates, Inc., pp. 1097–1105, 2012.

[5] R. Mitsuhashi, et al., Terahertz tag identifiable through shielding materials using machine learning, *Opt. Express*, vol. 28, no. 3, pp. 3517–3527, 2020.

Backward Terahertz-wave parametric oscillator and its application in nondestructive testing

Hiroaki Minamide[1]

[1]RIKEN center for Advanced Photonics, RIKEN, Sendai, Japan
*corresponding author, E-mail: minamide@riken.jp

Abstract

We demonstrated backward terahertz-wave parametric oscillation and generated terahertz-wave pulses with a high peak intensity of about 200 W at 0.3 THz. And Terahertz-wave imaging was performed using the source for nondestructive testing applications. Due to the long-time stability of terahertz-wave oscillation, transmission images with good visibility and inside information were obtained by point scanning imaging. As a result of measuring various materials, we found that the system is applicable to versatile nondestructive inspection applications.

With the maturity of modern society, various new materials and structures have been invented and developed. In production, new and old materials are efficiently utilized and provided to us as familiar manufactured products. On the other hand, quality inspections of manufactured and ready-made products are extremely important in a social environment that demands safety and security and the demand for inspection targets is expanding in accordance with the times. Until now, nondestructive testing has solved many problems using conventional technologies such as X-rays and ultrasonic waves. However, in the evolving environment of material development and inspection, there are many demands for multimodal measurement and the introduction of new technologies.

Terahertz waves (THz waves) are electromagnetic waves that exist between radio waves and light waves, and have the property of penetrating plastics, ceramics, clothing, paper, wood, and mortar. Since various materials have unique fingerprint spectra in the THz wave region, THz wave technology has attracted much attention as a non-destructive inspection tool, and researchers around the world have been vigorously engaged in research and development for about 30 years. Currently, development of equipment has progressed, and some of it has been introduced to the market. Meanwhile, light-wave technologies such as LiDAR and hyperspectral cameras are also advancing, and expectations for nondestructive inspection using THz waves are growing more sophisticated. Very recently, THz-wave imaging research has evolved from conventional two-dimensional transmission imaging to three-dimensional measurement, and artificial intelligence (AI) technology has been introduced to improve the degree of object determination and inspection accuracy, among other technological developments.

Thus, the performance requirements for THz-wave light sources are increasing more than ever in response to increasingly sophisticated THz-wave technology. We have been studying the generation of high-power THz waves from light waves by wavelength conversion using nonlinear optical effects. Recently, optical injection-type terahertz-wave parametric generation using bulk lithium niobate crystals has achieved peak intensities of up to approximately 100 kW. On the other hand, there has been insufficient development of light sources that simultaneously satisfy the requirements of miniaturization, wide wavelength tunability necessary for 3D measurement, and high-power generation of sub-THz waves with high transparency into materials.

In this paper, we describe a new backward THz-wave parametric oscillator discovered using periodically polarized inverted lithium niobate crystals as a light source that satisfies all of the above requirements and discuss its attractiveness and application to nondestructive inspection applications.

References

1. S. Hayashi, K. Nawata, T. Taira, J. Shikata, K. Kawase, and H. Minamide, Sci. Rep. 4 (2014) 5045.
2. H. Minamide, S. Hayashi, K. Nawata, T. Taira, J. Shikata, and K. Kawase, J. Infrared, Millimeter, Terahertz Waves 35, 25–37 (2014).
3. S. E. Harris, Appl. Phys. Lett. 9 (1966) 114.
4. Y. J. Ding and J. B. Khurgin, IEEE Journal of Quantum Electronics 32 (1996) 1574.

5. K. Nawata, Y. Tokizane, Y. Takida, and H. Minamide, Sci. Rep. 9 (2019) 726.
6. K. Nawata, S. Hayashi, H. Ishizuki, K. Murate, K. Imayama, Y. Takida, V. Yahia, T. Taira, K. Kawase, and H. Minamide, IEEE Trans. Terahertz Sci. Technol. 7, 617–620 (2017).
7. Y. Takida, K. Nawata, and H. Minamide, APL Photonics 5 (2020) 061301.

Acknowledgements
This work was supported (in part) by JSPS KAKENHI Grant Number JP19K05286, JP21H03747, JP21H01018, JST ACCEL Grant Number JPMJMI17F2, Japan-China Scientific Cooperation Program between JSPS and NSFC Grant Number JPJSBP120207407, Innovative Science and Technology Initiative for Security Grant Number JPJ004596, ATLA, Japan.
The author would like to thank present and previous researchers in our team of RIKEN for contributing much results and also to thank Prof. H. Ito of RIKEN/Tohoku University and Prof. M. Kumano of Tohoku University for fruitful discussions.

Mm-wave, THz, and quasi-optical antenna measurements

Ultrabroadband terahertz pulses from a Ge:Au photoconductive emitter

Abhishek Singh[1], Alexej Pashkin[*,1], Stephan Winnerl[1], Malte Welsch[1,2], Cornelius Beckh[3], Philipp Sulzer[3], Alfred Leitenstorfer[3], Manfred Helm[1,2], Harald Schneider[1]

[1]Institute of Ion Beam Physics and Materials Research, Helmholtz-Zentrum Dresden-Rossendorf, Germany
[2]Cfaed and Institute of Applied Physics, TU Dresden, Germany
[3]Department of Physics and Center for Applied Photonics, University of Konstanz, Germany

*corresponding author, E-mail: a.pashkin@hzdr.de

Abstract

Using gold-implantated germanium, where the carrier lifetime is shortened by more than three orders of magnitude, we have demonstrated a broadband photoconductive THz emitter compatible with modelocked fiber lasers operating at wavelengths of 1.1 and 1.55 μm and pulse repetition rates up to 20 MHz. The emitted THz spectrum spans up to 70 THz. This approach opens up a prospect for manufacturing of compact, high-bandwidth THz photonic devices compatible with Si CMOS technology.

1. Introduction

Germanium is a nonpolar semiconductor with missing one-phonon absorption. The absence of a Reststrahlen band enables the generation of a gapless THz spectrum spreading up to 13 THz [1], limited only by the duration of the excitation and detection laser pulses. However, in spite of other promising properties including low bandgap and small effective mass, the long, μs-scale recombination time arising from the indirect bandgap of intrinsic germanium has been prohibitive for practical application as photoconductive THz emitters. Although not essential for broadband THz emission, shorter recombination times are necessary to ensure complete carrier recombination between subsequent laser pulses and to make these emitters compatible with standard modelocked laser systems operating at pulse repetition rates up to hundreds of MHz.

2. Results

In order to make Ge a suitable photoconductive material at MHz repetition rates, we have reduced the carrier lifetime by introducing deep traps via Au implantation. Although a shorter carrier lifetime is not an essential requirement for the broadband THz emission, sub-ns lifetime ensures reliable operation of Ge:Au THz emitters at repetition rates up to few 100 MHz covering specifications of most contemporary femtosecond oscillators. Ge substrates were implanted with Au ions with energy of 330 keV and doses of $\approx 2\times10^{13}$ ions/cm^2 followed by annealing at 900℃ for several hours in order to ensure a low homogeneous concentration of gold impurities near the surface of the Ge wafer. The achieved doping density is approximately 10^{15} cm^{-3}.

The carrier lifetime in implanted Ge:Au wafers were measured using optical pump / THz probe spectroscopy. We observe a strong photoconductivity decay within 1 ns after photoexcitation and a negligible offset at negative delay times. The longest measured recombination time of 1.7 ns is more than 1000 times shorter than in an undoped Ge, where it reaches several μs.

Bowtie electrode structure was fabricated using the same fabrication process and the bowtie electrode geometry as our previous work [1]. The near-infrared pump beam is focused onto the 10-μm-gap between the electrodes. Photoexcited charge carriers are accelerated by the applied bias field (d.c. bias voltage of 10 V) producing a transient current burst. The THz beam emitted by this current in forward direction is collimated and refocused on an electro-optic crystal for field-resolved detection.

THz emission was induced by 11 fs pulses with a central wavelength around 1.1 μm (spectrum spanning from 0.9 to 1.25 μm) and an energy of 7 nJ. The generated THz transient is detected by electro-optic sampling using 8.42-fs-short probe pulses in a (110) ZnTe crystal with a thickness of 14.3 μm. Fig. 1(a) shows the recorded THz electric field in the time domain. The pulse duration comprises about 1.5 optical cycles and the estimated peak electric field in the focus reaches 0.8 kV/cm [2]. Fig. 1(b) depicts the Fourier spectrum of the THz transient spanning from the lowest detectable frequency up to 70 THz. The small dip in the spectrum at around 5 THz is caused by the response function of the ZnTe detector and the true THz emission spectrum is gapless as it has been confirmed in previous work [1].

Furthermore, we demonstrated the compatibility of the Ge:Au photoconductive antenna with the conventional telecom wavelength of 1.55 μm covered by ubiquitous Er-doped femtosecond fiber lasers. The absorption edge of Ge

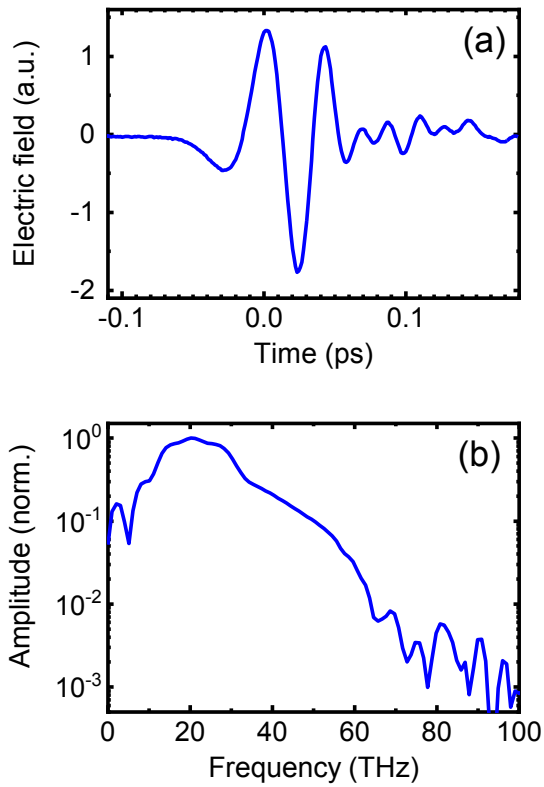

Figure 1: (a) Recorded THz pulse for pumping with 11 fs pulses centered at 1.1 µm wavelength. (b) Fourier transform of the recorded THz pulse.

at 1.87 µm is well below the telecom band. However, due to the indirect bandgap the absorption is rather weak and increases abruptly only for wavelengths shorter than 1.55 µm, for which the direct interband transitions are allowed. The photoconductive antenna was pumped with 12 fs pulses with a central wavelength around 1.55 µm and the energy of 3.5 nJ at the repetition rate of 20 MHz. The resulting THz spectrum (not shown) spans up to 50 THz demonstrating that the Ge-based photoconductive antenna is capable for broadband THz emission when pumped at telecom wavelength [2].

3. Conclusions

We have demonstrated a photoconductive THz emitter based on ion implanted germanium that generates THz transients with a gapless spectral coverage up to 70 THz – a full order of magnitude larger than existing GaAs or InGaAs-based devices. Implantation of gold ions enables us to reduce the carrier lifetime down to the nanosecond level, rendering the new device compatible with high repetition rates of femtosecond fiber lasers. Owing to the relatively low bandgap energy of germanium, it can be photoexcited using the conventional telecom band wavelengths. In our experiments we demonstrate broadband THz emission under excitation by few-cycle pulses at central wavelengths of 1.1 and 1.55 µm, produced by state-of-the-art amplified Er:fiber laser systems. Potentially, Ge-based THz devices can revolutionize THz technology due to its ultrabroad spectral bandwidth coverage and its compatibility with Si CMOS technology.

Acknowledgements

Support by R. Böttger and the Ion Beam Center (IBC) at HZDR is gratefully acknowledged. The authors would like to thank W. Skorupa for his valuable suggestions as well as I. Skorupa and U. Lucchesi for technical assistance.

References

[1] A. Singh, A. Pashkin, S. Winnerl, M. Helm, H. Schneider, Gapless Broadband Terahertz Emission from a Germanium Photoconductive Emitter, *ACS Photonics* 5: 2718−2723, 2018.

[2] A. Singh, A. Pashkin, S. Winnerl, M. Welsch, C. Beckh, P. Sulzer, A. Leitenstorfer, M. Helm, H. Schneider, Up to 70 THz bandwidth from an implanted Ge photoconductive antenna excited by a femtosecond Er:fibre laser, *Light: Science and Applications* 9:30, 2020.

Advanced numerical and theoretical tools as applied to domains ranging from modern nanophotonics

An Asynchronous Co-Simulation Method for Time-Dependent Simulations: Application to a Transmission Line Network

Imane Massaoudi[1], **Pierre Bonnet**[1]

[1]Université Clermont Auvergne, Clermont Auvergne INP, CNRS, Institut Pascal, F-63000 Clermont-Ferrand, France
*corresponding author, E-mail: imane.massaoudi@uca.fr

Abstract

Numerical co-simulation methods are increasingly used to solve complex electromagnetic compatibility problems. For the time-dependent Maxwell-Equations, these approaches may exchange information and simulation results for each temporal iteration. In this paper, we propose an asynchronous temporal co-simulation method. The approach is illustrated on a transmission lines network. The results obtained are validated with the global simulation.

1. Introduction

Co-simulation allows solving a complex problem by breaking it into simpler sub-problems [1]. Generally, the most suitable numerical method is applied to each sub-domain. However, most existing methods are synchronous and share numerical models. For time-domain co-simulation methods, an exchange of results for each temporal iteration is required [2]. We propose in this paper an asynchronous co-simulation method based only on the impulse responses of the sub-domains. The simulations are time-independent and don't require any exchange of numerical models.

2. Formulation

We aim to find the solution to a global linear system after splitting it into sub-problems via one or more exchange interfaces. To demonstrate the principle of the proposed co-simulation method, we consider the transmission line network consisting of 5 uniform lossless lines and two junctions (Fig. 1).

V_s is a Gaussian pulse of amplitude 1V, and we want to evaluate the voltage V_3 across impedance Z_{L3}.

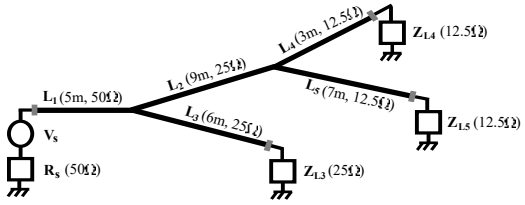

Figure 1: Lengths and characteristic impedances of the network's transmission lines

Based on the FDTD (Finite Difference Time Domain) method [3], the currents and voltages are obtained by solving the telegrapher's equations. In the following, we consider the same method (FDTD) in both sub-domains. However, the proposed approach is independent of the choice of the numerical model for sub-domains.

Let's suppose the global network is split at line L_2 into two sub-networks Y^k, each consisting of three tranmission lines $L_i^k \in \{1, 2, 3\}$ as shown in Fig.2.

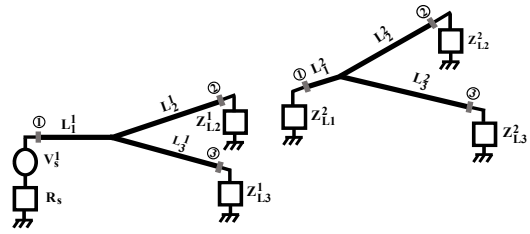

Figure 2: Sub-networks Y^1 and Y^2 after spliting the global network

For a given system, caracterised by its impulse reponse h, the product of convolution in equation (1) allows linking the output V_{out} to the input V_{in} .

$$V_{out} = h \otimes V_{in} \tag{1}$$

In the following, we consider the voltage V_{out} a (m+1)-dimensionnal discret vector evaluated for each discret time $t \in [0, m\Delta t]$, $(m \in \mathbb{N}^*)$, with Δt a discret time step which satisfies the CFL criteria.

The product of convolution in equation (1) is a matrix product, and the impulse reponse h is considered in its matrix form.

Let's define h_{ij}^k the impulse responses h_{ij}^k, for a sub-network Y^k, between the terminal points i and j.

For a sub-network k with p voltage sources V_{si}^k, q exchange interfaces and n terminations, the voltage at a measuring point j, V_j^k, is given by the following equation.

$$V_j^k = \sum_{\{i\}} h_{ij}^k \otimes V_{si}^k + \sum_{\{l\}} h_{lj}^k \otimes V_{\sim l}^k \tag{2}$$

With :

$\{i\} \subseteq \{1, ..., n\}$ a sub-set of p voltage indexes, $p \leqslant n$.

$\{l\} \subseteq \{1, ..., n\}$ a sub-set of q exchange interface indexes, $l \leqslant n$.

By applying the equation (2) to the example of Fig. 2 considering $k = 1$, $j = 3$, $i = 1$ and $l = 2$, we obtain the explicit equation (3).

$$\begin{aligned} V_3^1 &= h_{13}^1 \otimes V_{s1}^1 + h_{23}^1 \otimes V_{\sim 2}^1 \\ &= h_{13}^1 \otimes V_{s1}^1 + h_{23}^1 \otimes (h_{11}^2 \otimes (h_{12}^1 \otimes V_{s1}^1)) \end{aligned} \tag{3}$$

The equation (3) is composed of two terms, the first one translates the contribution of the real source V_{s1}^1 to the measured voltage V_3^1. While the second term, represents the contribution of the equivalent source at the exchange interface.

The term $h_{12}^1 \otimes V_{s1}^1$ represents the incoming voltage at the interface. The product of convolution of this term with h_{11}^2 is the response of the sub-network Y^2.

We compare in Fig. 3 the results obtained considering a unique simulation of the global network and the co-simulation method.

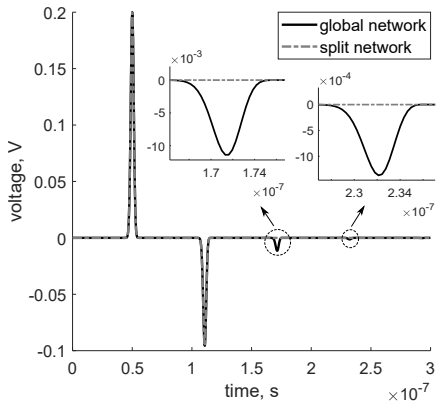

Figure 3: Voltage V_3^1 for a matched network

The first peak corresponds to the direct propagation of the Gaussian signal within lines L_1^1 and L_3^1. The second peak corresponds to the first reflection of the signal in the circuit due to the mismatch at the network's nodes.

For the first two peaks, both results overlapp and validate the equation (3).

However, the multiple Gaussian-pulse reflections along the network are not considered in the equation (3), hence the differences between the results shown in Fig. 3.

By adding an additionnal term to equation (3), we consider these multiple retro-actions between the two sub-networks. Equation (4) allows finding both contributions from each sub-network and their multiple round-trips to the q-th order.

$$V_3^1 = h_{13}^1 \otimes V_s^1 + h_{23}^1 \otimes V_{\sim 2}^1 + \sum_{i=2}^{q} h_{23}^1 \otimes (h_{11}^2 \otimes (h_{22}^1 \otimes V_{\sim 2,i}^1)) \tag{4}$$

$V_{\sim 2,i}^1$ is definied as the i-th order of the equivalent source, and is given by the equation (5).

$$V_{\sim 2,i}^1 = h_{11}^2 \otimes (h_{22}^1 \otimes V_{\sim 2,i-1}^1) \tag{5}$$

Let's consider a mismatched network at line L_2^2 loaded with $Z_{L2}^2 = 10^{10}\Omega$ (open circuit). By applying equation (5) for the order $q = 3$, the results obtained by the co-simulation method and the global simulation superpose, as shown in Fig. 4.

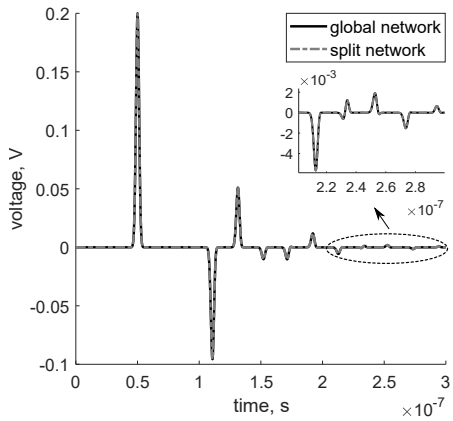

Figure 4: Voltage V_3^1 for a mismatched network

3. Conclusions

This paper presents a temporal co-simulation method applied to a transmission line network. The approach is based on evaluating impulse responses of each sub-domain and therefore preserves the confidentiality of the associated numerical models. Furthermore, the simulations are independent of time (asynchronous) and the choice of the temporal numerical method. The methodology's principle can be generalized for complex systems with multiple exchange interfaces. The proposed approach is general and can be applied for various applications: from low to high frequency, for 1D and 3D computational electromagnetics problems.

References

[1] P. Hillenbrand, M.Beltle, S. Tenbohlen, J. Hansen, Transient co-simulation of electromagnetic emissions caused by a SiC traction inverter, *2017 International Symposium on Electromagnetic Compatibility - EMC EUROPE*, pp.1-6, 2017.

[2] J.-P. Parmantier, X. Ferrieres, P. Schickele, A Hybrid Time-Domain Maxwell/MTLN-Equations Method to Simulate EM-induced-Currents on Electric Cable-Bundles Inside Cavities, *Advanced Electromagnetics* 9: 31–41, 2020.

[3] K. Yee, Numerical solution of initial boundary value problems involving Maxwell's equations in isotropic media, *IEEE Transactions on Antennas and Propagation* 14: 302–307, 1966.

Efficient computation of EM scattering from a dielectric cylinder covered with graphene strips

Brahim Guizal[1], Youssef Jeyar[1] and Mauro Antezza[1,2]

[1]Laboratoire Charles Coulomb (L2C), UMR 5221 CNRS-Universit de Montpellier, F-34095 Montpellier, France
[2]Institut Universitaire de France, 1 rue Descartes, Paris Cedex 05 F-75231, France
*corresponding author, E-mail: brahim.guizal@umontpellier.fr

Abstract

We present a numerical approach for the solution of EM scattering from a dielectric cylinder partially covered with graphene. It is based on a classical Fourier-Bessel expansion of the fields inside and outside the cylinder to which we apply the ad-hoc boundary conditions in the presence of graphene. Due to the singular nature of the electric field at the ends of the graphene sheet, we introduce auxiliary boundary conditions to better take this reality into account. The result is a very simple and very efficient method allowing the study of diffraction from such structures.

1. Introduction

Diffraction of electromagnetic waves from circular cylinders is rather a simple and classical problem [1]. In this situation, the incoming and outgoing fields can be represented in terms of circular waves expressed through Fourier-Bessel expansions. All the channels are independent because of the circular symmetry and homogeneity of the cylinder. However when this cylinder is partially covered with a sheet of graphene, this breaks the symmetry and homogeneity at the level of the surface and then all the channels can be mixed up, thus leading to interesting physical phenomena. Under this situation, the boundary conditions lead to an algebraic system linking the outgoing amplitudes of the fields to the incoming ones. This system may be singular in the case of transverse magnetic polarization (TM : the magnetic field is parallel to the direction of invariance of the cylinder). This is due to the singularities of the tangential component of the electric field at the ends of the graphene sheet. One way of solving this issue is to use a supplementary expression of this field right at the level of the circumference of the cylinder in terms of Local Basis Functions (LBFs) able to reproduce the singularities [2].

2. Results

Figure 1 shows the geometry of the diffraction problem where a plane wave (wavelength λ) is impinging on a circular cylinder (radius R and dielectric permittivity ε_r) partially covered by a graphene (conductivity σ). As already said in the introduction, this problem of diffraction can be solved through the expansion of the fields in terms of Fourier-Bessel modes. This will be called the classical method. It turns out that under TM polarization there are some singularities of the tangential electric field that cause slow convergence of the computations. This problem is handled through the introduction of LBFs that possess the same singularities of the field.

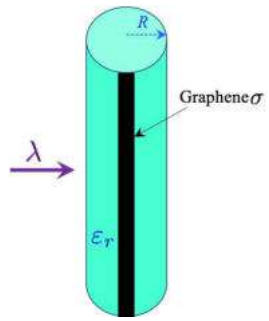

Figure 1: Sketch of the diffraction problem under consideration: an electromagnetic plane wave hits the covered dielectric cylinder under classical diffraction..

Figure 2 shows the scattering efficiency versus the wavelength, obtained with the classical method for different truncation orders M of the Fourier-Bessel series (the total

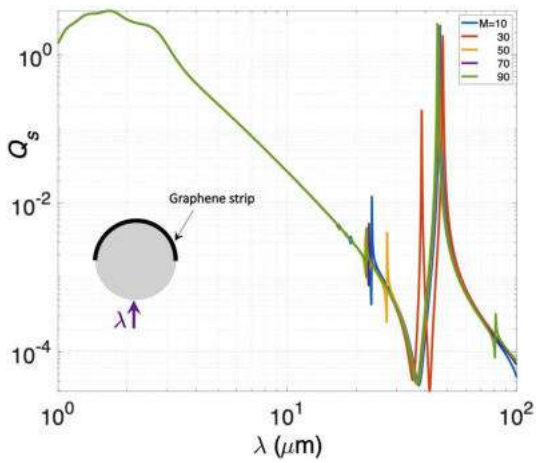

Figure 2: Scattering efficiency Q_s of a cylinder of radius $R = 0.5\mu m$ and permittivity $\varepsilon_r = 3.9$ immersed in air, with a graphene sheet of chemical potential $\mu = 0.5$ eV and T = 300 K.

number of retained coefficients in the numerical computation is $2M + 1$). It can be clearly seen that the method is instable with the appearance of many spoof resonances that change locations as M varies. In figure 3 we display the results for the LBF method which proves to be very stable and converges rapidly as compared to the classical one (the different curves are almost superimposed). For the LBFs method the number of modes necessary to achieve convergence (stabilization of the fourth digit for example) is very low about : 40 modes contrarily to the classical method where even more than 150 modes do not give the same results.

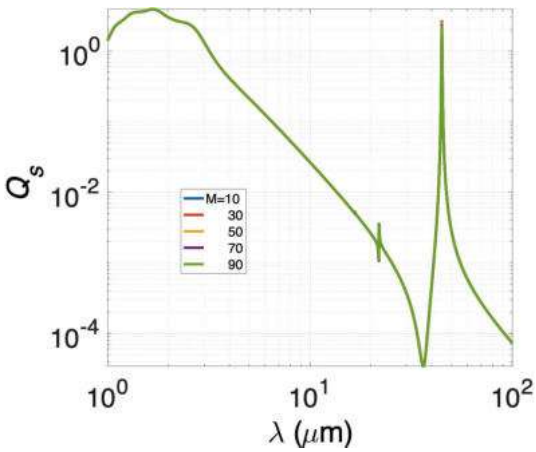

Figure 3: Same as in figure 2 but computed with the LBF method.

3. Conclusions

An efficient method to compute the scattering of an EM under TM polarization is been introduced and shown to be very efficient for treating such a problem.

References

[1] Kong, J.A., *Electromagnetic Wave Theory,* Wiley, 1986.

[2] Hwang Ruey-Bing, The numerical investigation on the turbulent heat transfer, *Scientific Reports* 10: 128551, 2020.

The polariton laser ridge: an exception to the rule

C. Brimont[1*], H. Souissi[1], M. Gromovyi[2] T. Gueye[1], L. Doyennette[1], D.D Solnyshkov [3], G. Malpuech [3], E. Cambril [2], S. Bouchoule [2] B. Alloing[4], S. Rennesson[4], F. Semond[4], J. Zúñiga-Pérez[4], T. Guillet [1]

[1]Laboratoire Charles Coulomb (L2C), UMR 5221 CNRS-Université de Montpellier, F-34095 Montpellier, France
[2]Centre de Nanosciences et de Nanotechnologies, CNRS, Université Paris-Saclay, France
[3]Université Clermont Auvergne, CNRS, SIGMA Clermont, Institut Pascal, Clermont-Ferrand, France
[4]UCA, CRHEA-CNRS, Rue Bernard Gregory, 06560 Valbonne, France
*corresponding author, E-mail: christelle.brimont@umontpellier.fr

Abstract

To highlight the specific character of polariton lasers, namely the absence of reciprocity between the processes leading to gain and loss, we present here the operation of a CW polariton laser in a ridge geometry with distributed Bragg reflectors (DBRs) forming the cavities. We explore the laser threshold under optical pumping, and we investigate the effect of varying the optical pumping length. In strinking contrast with conventional ridge lasers, the lasing effect is reached even for a pump length of just 15% of the cavity length with only a threefold increase of the overall threshold. The experimental results are compared to numerical simulations of the dynamics of the exciton reservoir and the polariton population.

1. Introduction

The achievement of a laser effect in a conventional ridge structure, requies to excite at least half of the cavity due to the reciprocity between absorption and stimulated emission. In other words, the part of the standard electrically or optically pumped laser ridge must be longer than the unpumped part where the absorption takes place. In the world of polariton lasers, physics is changed. The low waveguide losses lead to propagation distances of the order of a hundred microns. It has allowed the recent observation of phenomena with waveguide polaritons such as the formation of bright temporal solitons in GaAs heterostructures, in-plane polariton amplification and polariton lasing in a bulk ZnO waveguide. In order to illustrate the difference between a polariton and a conventional ridge laser, in a waveguide geometry, we study the effect of the pump length versus the cavity length. A model of the gain versus pump length will be discussed.

2. Results

From a GaN/(AL,Ga)N planar waveguide grown by MOVPE on sapphire, ridge waveguides structures with DBRs have been etched. Therefor, two types of confinement are present : a longitudinal brought by the presence of GaN / air reflectors and a lateral brought by deep-etched 1μm-wide ridges. The length of the cavities varying from 20 to 50μm. The cavity is optically pumped with a line-shaped spot with a controlled variable length resonantly exciting the exciton reservoir at 355nm. We perform spatially- and spectrally-resolved power-dependent microphotoluminescence experiments.

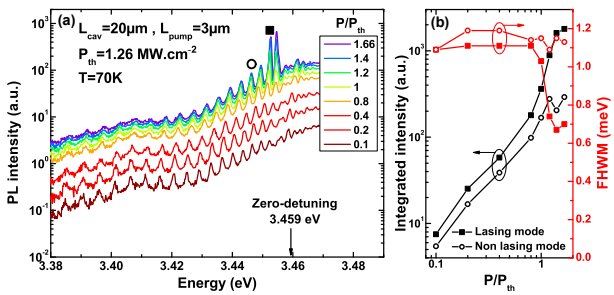

FIGURE 1 – Power-dependent (a) PL spectra across the lasing threshold, for a 20μm-long ridge ;(b) of the intensity and linewidth of the lasing and the non-lasing modes.

Figure 1(a) shows spectra evidencing the laser operation. For the mode at 3.456 eV, the intensity rapidly increases by about two orders of magnitude as well as a spectral narrowing vs the pump power, demonstrating the laser operation of the device. We can note the presence of many Fabry-Perot modes over a wide energy band. Below threshold, to assess the strong coupling regime between excitons and photons, an important step consists in qualifying the Fabry-Perot cavity. We further show that the cavity free spectral range (FSR) is determined by the LPB dispersion. We deduce that the exciton-photon coupling strength (Rabi splitting) amounts to $\Omega_{Rabi} = 66 \pm 10\ meV$.

Beyond the demonstration of the polaritonic

nature of the lasinf mode, we experimentally demonstrate how a ridge polariton laser is different from a conventional laser.

The figure 2 presents the comparison of our experimental results with a kinetic model. The agreement between theory and experience shows that the laser effect is surprisingly possible for an exciton reservoir size of less than 50% of the total length of the cavity. The relaxation of polaritons in a similar structure was simulated using the semiclassical Boltzmann equations for exciton-polaritons [1, 2] combining real and reciprocal space resolution [3, 4].

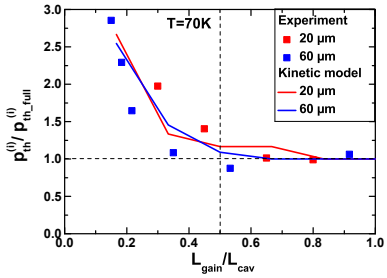

FIGURE 2 – Laser power at threshold $p_{th}^{(i)}$, integrated along the whole excitation length, vs gain length, normalized to its value $p_{th,full}^{(i)}$ for $L_{pump} = L_{cav}$.

For the conventional ridges lasers, only the cavity losses are considered. The threshold condition allows to write the modal gain $\gamma_{e-h,th}$ in the $T = 0$ limit. In this case, a laser effect is obtained if more than half of the cavity is excited (Fig 3 dash dotted line).

$$\gamma_{e-h,th} = \frac{\alpha_{cavity}.L_{cav}}{2L_{gain} - L_{cav}} \tag{1}$$

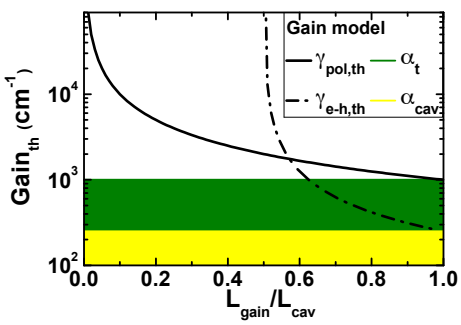

FIGURE 3 – Modal gain at threshold calculated vs gain length for the two type of laser

Contrary to the conventional laser, the polariton losses and the losses of the bare photon mode are expected in the gain region and in the unpumped section of the cavity. The polariton gain and losses are not correlated. This leads to the expression of the polariton gain at threshold :

$$\gamma_{pol,th} = \frac{(\alpha_{cavity} + \alpha_{noX} + \alpha_{pol}).L_{cav}}{L_{gain}} = \frac{\alpha_t.L_{cav}}{L_{gain}} \tag{2}$$

Here, there is no need to pump more than half of the cavity in order to observe the laser effect (Fig 3 plain line). This is a striking specificity of polariton lasers.

3. Conclusions

We have presented an experimental study of a laser with a ridge waveguide geometry, allowing to show that the polariton laser effect can be observed only by imposing a pumping section of only 15% of the total length of the cavity. A good quantitative agreement between experimental results and simulations was obtained. We explained how a ridge polariton laser is different from a conventional laser.

4. Acknowledgements

The authors acknowledge fundings from the French National Research Agency (ANR-24-CE24-0021-03, ANR-11-LABX-0014), the French Renatech network and the Region Occitanie (ALDOCT-001065).

References

[1] A.Kavokin and G.Malpuech, *Cavity polaritons*. Elsevier, Amsterdam, The Netherlands, 2003.

[2] D. Solnyshkov, H. Ouerdane, and G. Malpuech, "Kinetic phase diagrams of gan-based polariton lasers," *Journal of Applied Physics*, vol. 103, no. 1, p. 016101, 2008. [Online]. Available : https://doi.org/10.1063/1.2822148

[3] D. D. Solnyshkov, H. Terças, and G. Malpuech, "Optical amplifier based on guided polaritons in GaN and ZnO," *Applied Physics Letters*, vol. 105, no. 23, p. 231102, 2014. [Online]. Available : http://scitation.aip.org/content/aip/journal/apl/105/23/10.1063/1.4903497

[4] J. Ciers, D. D. Solnyshkov, G. Callsen, Y. Kuang, J.-F. Carlin, G. Malpuech, R. Butté, and N. Grandjean, "Polariton relaxation and polariton nonlinearities in nonresonantly cw-pumped iii-nitride slab waveguides," *Phys. Rev. B*, vol. 102, p. 155304, Oct 2020. [Online]. Available : https://link.aps.org/doi/10.1103/PhysRevB.102.155304

Casimir interaction on gratings

Brahim Guizal[1] **and Mauro Antezza**[1,2]

[1]Laboratoire Charles Coulomb (L2C), UMR 5221 CNRS-Universit de Montpellier, F-34095 Montpellier, France
[2]Institut Universitaire de France, 1 rue Descartes, Paris Cedex 05 F-75231, France
*corresponding author, E-mail: mauro.antezza@umontpellier.fr

Abstract

We will discuss some recent numerical results on the Casimir interaction between metallic gratings [1, 2, 3] . These findings pave the way to the design of a contactless quantum vacuum torsional spring, and sensors with possible relevance to micro and nanomechanical devices.

References

[1] Mingkang Wang, L. Tang, C.Y. Ng, Riccardo Messina, Brahim Guizal, J. A. Crosse, Mauro Antezza, C.T. Chan, H.B. Chan Nature Communication **12**, 600 (2021)

[2] Mauro Antezza, H. B. Chan, Brahim Guizal, V.N. Marachevsky, Riccardo Messina, Mingkang Wang, *Phys. Rev. Lett.* **124**, 013903 (2020).

[3] Riccardo Messina, Paulo A. Maia Neto, Brahim Guizal, and Mauro Antezza, Phys. Rev. A **92**, 062504 (2015)

Graphene surface magneto-plasmons excited through a magnetostatic biased graphene-strip grating : Semi analytical Approach

Maha Ben Rhouma[1], **Kofi Edee** [2] **and Brahim Guizal** [3]

[1]National Institute for Nuclear Science and Technology CEA Saclay. 91191 Gif-sur-Yvette, France
[2]Université Clermont Auvergne, Institut Pascal, BP 10448, F-63000 Clermont-Ferrand, France, CNRS, UMR 6602, France
[3]Laboratoire Charles Coulomb (L2C), UMR 5221 CNRS-Université de Montpellier, F-34095 Montpellier, France
*corresponding author, E-mail: maha.benrhouma@cea.fr/ maha.benrhouma1987@gmail.com

Abstract

We present an accurate and simple semi analytical model for investigating the magneto-plasmonic response of a 1D subwavelength graphene strip grating under an external static magnetic field when the graphene is considered as an anisotropic layer with atomic thickness. It is based on an effective medium approach (EMA) and a rigorous phase correction. The proposed model is numerically validated and evaluated by comparing the results with those obtained from the PMM method and from methods published in the litterature.

1. Introduction

Graphene magneto-plasmonics , the research area that combine magnetic and plasmonic properties of graphene, has attracted considerable interest in recent years, thanks to the unique and unsual properties of the surface magneto-plasmons supported by graphene. These properties have been exploited to design many tunable plasmonic nonreciprocal devices in the microwave and terahertz regimes such as optical isolators and absorbers. Graphene surface magneto-plasmons have been widely studied in several theoretical and experimental works under various forms and configurations. Among these structures, periodic magnetically biased graphene ribbons arrays have attracted a great deal of research interest and became one of the most studied graphene based structures. Several and various numerical methods have been employed for modelling this structure. However, it has been shown that due to the ultra-thin nature of graphene, these numerical methods suffer from slow convergence rates and require too much computational effort. In our work, we propose to model in a simple way the magnetoplasmonic response of a 1D graphene strip grating in the presence of an external magnetic field when the graphene is considered as a bulk material through a simple semi analytical approach. This Model is useful to better understand graphene surface magnetoplasmons GSMPs and may facilitate the design of various tunable devices based on graphene magnetoplasmonics.

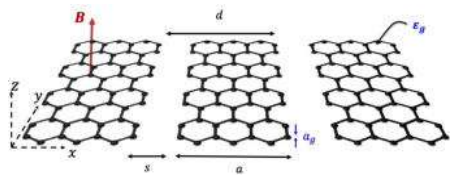

Figure 1: Sketch of the studied structure: a magnetically-biased subwavelengh graphene strip grating with width a and period $d = a + s$. The grating is surrounded by air and the magnetic field B is applied perpendicularly to the structure along the z direction.

2. Method and Results

Figure 1 depicts the structure under study which consists of a periodic array of 1D graphene ribbons under a magnetostatic bias. The width of the ribbons is a and the periodicity of the array is $d = a + s$ in the x-direction. The graphene ribbons array is suspended in free space and occupies the xy plane. It is enlightened from the lower medium $(z < 0)$ by a plane wave under normal incidence. Here, we consider the Faraday geometry where the external static magnetic field B is perpendicular to the array. Under the influence of such a magnetostatic bias, graphene will exhibit an induced anisotropy leading to asymetric surface magneto-optical conductivity and permittivity tensors.

Since, we work in the subwavelengh regime *i.e* the period d of the grating is small compared to the wavelength of the incident wave ($d \ll \lambda$), the electromagnetic response of the studied structure can be simply obtained through an effective meduim approach which consists in approximating the grating by a homogeneous anisotropic effective layer with an equivalent effective permittivity tensor. By applying this approach to the graphene permittivity tensor, we found that the latter can not reproduce the optical properties of the structure. To take into account the magnetoplasmonic resonances phenomena resulting from the coupling between the different modes living in the structure, we introduce the scattering matrix formalism. The resonance modes of the structure appear then as the zeros of the determinant of the scattring matrix applied to a cavity formed by the effective medium and graphene. A phase correction

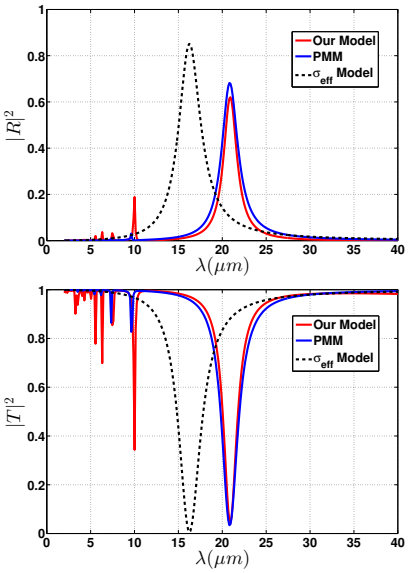

Figure 2: Comparison between the reflection and transmission spectra obtained from our Model (red solid lines) and those obtained from the PMM (blue solid lines) and from the effective medium approach [1] (dashed black lines). The results are calculated for a magnetically biased graphene strip grating with ribbon width $a = 0.9\mu$m, gap $s = 0.45\mu$m and $B = 3T$. Graphene parameters are $\mu_c = 0.6$eV, $T = 300$K and $\tau = 0.6$ps

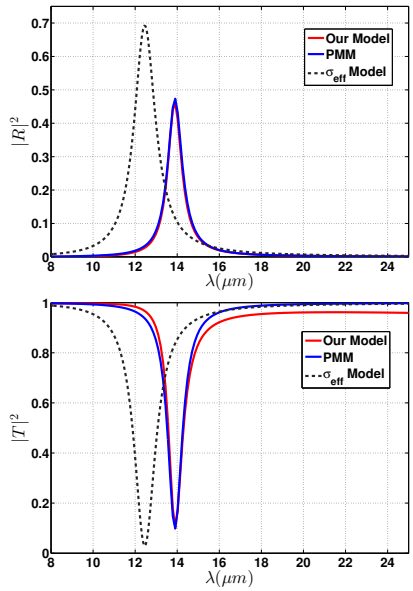

Figure 3: Comparaison between the reflection and transmission spectra obtained from our proposed Model (red solid lines) and those obtained from the PMM (blue solid lines) and from the the effective medium approach [1] (dashed black lines). The results are calculated for a graphene strip grating with ribbon width $a = 0.25\mu m$ and gap $s = 0.1\mu m$, when the magnetic bias is absent. Graphene parameters are $\mu_c = 0.4$eV, $T = 300$K and $\tau = 0. = 4$ps

is also required to take into account the periodicity effect, this term may be estimated thanks to a rigorous simulation. Finally, once the resonnance modes are obtained and using phenomenological approach, we can straightforwardly write the total transmission and reflection coefficients as the sum of two terms, the first term resulting from the resonnance phenomena and the second one introduces the contribution of a single strip of graphene.

Figure 2 shows the reflection and transmission spectra of a graphene strip grating when the applied magnetic field is taken to be $B = 3T$. The strip width is $a = 0.9\mu$m and the periodicity is assumed to be $d = 1.35\mu$m. The chemical potential of the graphene strips is set to $\mu_c = 0.6e$V and the relaxation time τ is 0.4ps These results are compared with the effective medium approach given in reference [1] and the PMM method. The computed spectra show several resonance peaks which correspond to the excitation of GSMP through the structure.

Figure 3 shows the reflection and transmission spectra computed through the proposed semi-analytical model, the PMM model and the effective conductivity approach proposed in [1] in the case of a graphene strip grating without an external magnetic field for: $a = 0.25\mu$m, $d = 0.35\mu$m, $\mu_c = 0.4$eV, $\tau = 0.4$p. In Both cases, we can see a good agreement between the PMM results and those obtained with our proposed model. By contrast, the comparison with the effective conductivity model shows that the latter cannot reproduce the magneto-optical properties of the studied graphene grating. We can also conclude that our semi-analytical model is a general approach that can efficiently and successfully treat both the case of a graphene strip grating biased with an external magnetic field as well as the particular case where no magnetic field is applied.

3. Conclusions

We have developped a simple and efficient semi analytical model based on an effective medium approach (EMA) and a rigorous phase correction, to decribe graphene surface magneto-plasmons excited in a magnetically-biased subwavelength graphene strip grating.

References

[1] J. S. Gomez-Diaz and A. Alù, Magnetically-biased graphene-based hyperbolic metasurfaces, *2016 IEEE International Symposium on Antennas and Propagation (APSURSI)* (IEEE, 2016): 359–360, 2016.

A direct and an inverse domain decomposition method applied to Fourier modal method: simulation of large scale device response

Kofi Edee*[1], Gerard Granet[1], Françoise Paladian[1], Pierre Bonnet[1]

[1]Université Clermont Auvergne, Institut Pascal, BP 10448, F-63000 Clermont-Ferrand, France, CNRS, Institut Pascal, F-63177 Aubière, France
*corresponding author, E-mail: kofi.edee@uca.fr

Abstract

A parallel spectral modal method is introduced for the frequency-domain Maxwell's equations. The method is applied to compute electromagnetic field through a large-scale surface, using the Aperiodic Fourier Modal Method (AFMM). In the proposed domain decomposition methods, a large-size surface is squared onto sub-cells. And a projector, the link between the large problem and the sequence of the small one, is defined, from the sequence of eigenfunctions of both large and small problems. This projector allows associating univocally the spectrum of any electromagnetic field component of an electromagnetic problem stated on a large-size domain with its footprint on the small-scale problem eigenfunctions, in the spectral domain. And the spectrum of the electromagnetic field component on each sub-cell may be simulated, locally with a coast that is not dependent on the number of the sub-cells, making it suitable for parallel computing. 2D validation cases are demonstrated by first, computing the electromagnetic field radiated by an electric dipole. Second, a 2D dielectric monochromatic metalens topology optimization is successfully proposed.

1. Introduction

In most electromagnetic problems, the number of unknowns required to simulate the electromagnetic components grows with respect to the size of the device geometry compared to the operating wavelength. In this context, for any rigorous full-wave methods, tackling such problems beyond limits fixed by computation time and memory, may become an infeasible task. To ensure fast and reliable numerical solutions, special care must be focused on, firstly the way the code is implemented, and, secondly, on the numerical method used to solve equations at hand.

To address the first point raised above, for a given electromagnetism problem stated on a large-scale domain, one of the intuitive methods consists in sub-structuring this computational domain. This technique consists in squaring the whole domain into a sequence of sub-domains, leading to a construction of sub-domains and interfaces matrices. The solution on each sub-domains can be performed using a parallel strategy or an iterative one. In the iterative process, the solution of the equation is only performed after solving interfaces or boundaries equations. This approach can be fruitfully considered within the context of iterative domain decomposition techniques such as the Schwarz method. However, this technique may require excessive memory and time consuming, when the number of interfaces increases. In the second strategy, suitable for parallel programming, one stitches the grid of the subdomains without applying any boundary condition. To minimize the stitching error, in this case, the size of each sub-domain may be kept relatively large compared to the wavelength, or they can also be geometrically separated each from other by a few gaps empirically determined.

Now let us focus on the second point raised earlier *i.e.* the numerical method itself. In photonics, a large class of electromagnetic field simulation is often required to solve partial differential equations (PDE) obtained from Maxwell's equations and a set of *ad-hoc* boundary conditions. *A priori*, there is no unique and universal method that allows to efficiently solve PDEs obtained from Maxwell's equations in the general case. Among all these methods, certain clearly appears to be the most commonly used, either by their simplicity of implementation, or by their ability to take into account complex geometry problems, and finally either because they are the most efficient in terms of numerical accuracy. These are: finite difference methods, finite element methods, or spectral methods [1]. These methods can be categorized into a direct-space method and spectral method. All these numerical methods involve different amounts of theoretical effort yielding different computational efficiencies. It is easy to understand that improving the efficiency of the numerical implementation and process will be often paid for with more pre-computational analytical effort and electromagnetic theory use. Spectral methods aim to approximate an unknown function, solution of differential or integral equation, by a finite sum of so-called basis functions. This method appears as an alternative to a direct-space method as finite-difference and finite element methods for numerical solving of partial differential equations. Studying diffraction by a one-dimensional dielectric and metallic lamellar grating, Lalanne in [2] compares the Fourier modal method equipped with the adaptative spatial resolution to the finite difference method. It appeared clearly in their study that the Fourier spectral modal method

performs better than the frequency domain finite difference method. In spite of previous developments, and contrary to spatial-method as finite difference method stated in time [3, 4] or frequency domain, speedup of research of numerical solutions to large scale problems thanks to a spectral method in electromagnetism poses some major challenges. And implementation of the sub-structuring technique seems to be a way to overcome this drawback. In [5] authors introduce a strategy for optimizing large area metasurface using aperiodic Fourier modal method and by stitching together individually optimized sections of the metasurface. The proposed approach is successfully applied to design a 1D large-scale dielectric metalens using the topology optimization method. Each element of the metalens is designed as a deflector with a specific additional phase condition.
In this paper, we propose a mathematical formalism based on a projector enabling us to project any eigenvectors defined on a domain Ω into a sequence of eigenfunctions of smaller boundary value problems defined on subdomains Ω_{ij}. In the proposed domain decomposition methods, a large-scale surface is, obviously, squared onto sub-cells. Hence, a projector, a link between a large problem and a small one, is introduced. This projector, defined from the sequence of eigenfunctions of both large and small problems enables to associate univocally the spectrum of any electromagnetic field component related to the large-size problem, with its restriction on the small-size problem. The spectrum of the electromagnetic field component on each sub-cell may then be simulated independently, making the proposed approach to be, optimally and simply integrated into a parallel computing scheme, for the research of solutions of larger size systems. First, we successfully demonstrate the ability of the proposed method to describe accurately a field radiated by an electric dipole in free space. We show that the solver can perform simulations of the field on each sub-cell then on a large area of metalenses in a record time. Second, we make use of this capability to yield high-performance improvement over a high-refractive-index-deeply-etched Fresnel plate zone design through optimization.

References

[1] J. Boyd, "Chebyshev and Fourier Spectral Methods," Second Revised Edition. Dover Books on Mathematics; Dover Publications; 2013. ISBN 9780486141923 (2013).

[2] P. Lalanne, ?Numerical performance of finite-difference modal methods for the electromagnetic analysis of one- dimensional lamellar gratings,? J. Opt. Soc. Am. A 17, 1033?1042 (2000).

[3] Z. Lin, V. Liu, R. Pestourie, and S. G. Johnson, ?Topology optimization of free- form large-area metasurfaces,? Opt. Express 27, 15765?15775 (2019).

[4] Lin and S. G. Johnson, ?Overlapping domains for topology optimization of large-area metasurfaces,? Opt. Express 27, 32445?32453 (2019).

[5] T. Phan, and al. "High-efficiency, large-area, topology-optimized metasurfaces," Light. Sci. Appl. **8**, 48 (2019).

Other EM topics

Microstrip Antenna Array Design for UAV Detection

Pedro Mendes Ruiz[1*], Xavier Begaud[2], François Magne[3], Etienne Leder[1]

[1]Bowen ERTE-ETSA, Les Ulis, France

[2]LTCI, Télécom Paris, Institut Polytechnique de Paris, Palaiseau, France

[3]When-AB, Paris, France

*corresponding author, E-mail: pedro.mendes@bowenfr.com

Abstract

This work presents the design and realization of four linear arrays of microstrip rectangular patch antennas. This linear array is one of the elements of a passive radar using signals from 4G base stations for UAV detection. The arrays have been validated and operate from 2.62 GHz to 2.69 GHz, with a HPBW of 82° in H-plane and a maximal gain going from 11.1 dB to 12.2 dB in the required bandwidth, with a cosecant squared pattern in the E-plane.

1. Introduction

The threat of easy-to-deploy low-cost drones requires an advanced detection for the protection of sensible sites (e.g. airport runways, stadiums, industrial sites). The goal of the DIOD project (Detection & Identification Of Drones) is to develop a passive radar that uses 4G base stations to detect small targets. This work presents the design of the receiving antenna developed in the framework of the FUI (Fond Unique Interministériel) DIOD project.

Many solutions exist to detect the presence of drones with mechanical, optical, or antenna array based solutions [1]. Passive detection of UAV can be obtained by using multiple antennas and DOA estimation [2],[3]. Another solution presented in this article is to use an antenna composed of several linear arrays that will cover an angular sector by beam steering. Each linear array is designed to produce a cosecant squared beam [4] in a plane (E-plane for this work) to receive a power independent of the radar range for a constant height target. It is also required to have a rapid decrease of the radiation pattern just before the cosecant squared shape in order to not radiate toward the ground. In the orthogonal plane (H-plane), the beam is required to be large to have a nice field of view. Each linear array must operate from 2.62 GHz to 2.69 GHz.

In section 2, we present the design of the patch antenna. In section 3, we detail the design of the feeding network. In section 4, we present simulations of the full linear array, as well as simulations using periodic boundaries to characterize the coupling of the 2D array and simulations of the 4-column array. Finally, in section 5 we present the prototype and its measurements.

2. Patch Antenna Design

The first step in our design is to optimize the patch antenna. This optimization includes the rectangular patch with an inset feed [5], the microstrip line arriving at the patch, a mitered bend and a couple of quarter wavelength transformers. The design with the optimized values is presented in Fig. 1.

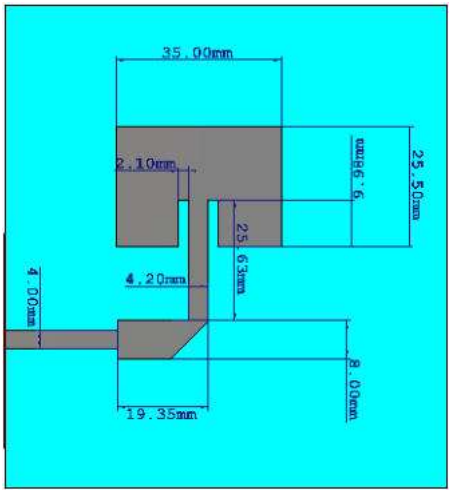

Figure 1: Front view of the optimized rectangular patch antenna with an inset feed, the feeding line arriving at the patch, a mitered bend and two quarter wavelength transformers.

Those elements were optimized using CST Studio Suite to maximize the bandwidth of the element around 2.655 GHz, the central frequency of our targeted bandwidth [6].

The substrate used for this design is AD430 from Rogers Corp., with a permittivity equal to 4.3 and a thickness of 3.175 mm. This substrate allows the rectangular patch to have good matching properties over the desired bandwidth

[5]. Moreover, using this substrate allows for an element spacing of approximately 0.56 free space wavelength when using the feeding network architecture presented in the next section.

In Fig. 2, we present the reflection coefficient of the designed patch antenna, which is below -10 dB from 2.61 GHz to 2.69 GHz. The patch antenna presented a gain of 6.5 dB and an efficiency of 80% inside the 2.62 GHz– 2.69 GHz bandwidth.

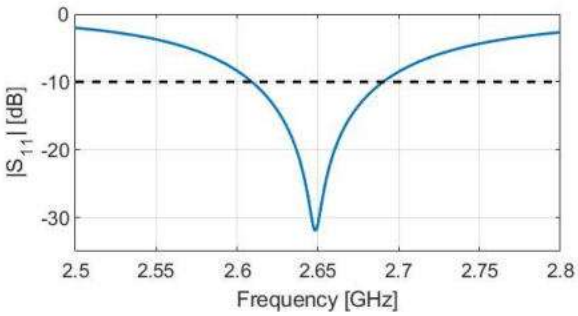

Figure 2: Reflection coefficient of the microstrip antenna presented on Fig. 1.

3. Feeding Network Design

In this section, we will first present the feeding network architecture used for this antenna array. We will then present the method used to synthesize the parameters of this feeding network, which includes:

- A multi objective genetic algorithm to obtain the currents magnitudes and phases of the array that generate the desired cosecant squared pattern;
- A transmission line model to calculate the lengths and widths of the microstrip lines to obtain those currents magnitudes and phases with the feeding network;
- An iterative procedure using CST Microwave Studio to correct the radiating pattern accounting for the different couplings and model imperfections.

3.1. Proposed Architecture

The proposed feeding network architecture consists of two series of quarter wavelength transformers with T-junctions in between them to feed each of the patch elements and with a bend at the last quarter wavelength transformer to feed the last patch antenna [7].

In between these branches, we have two microstrip lines of unequal electrical lengths, to enforce a phase difference between the two branches, and impedances, to balance the power sent to each of the branches [7].

Both of those microstrip lines arrive at a T-junction that leads to a coaxial feed.

The full architecture with the patch antennas included can be observed in Fig. 3.

3.2. Multi Objective Genetic Algorithm

In order to obtain the desired cosecant squared we used a multi objective genetic algorithm optimization [8]. For this optimization, we considered the set of four consecutive quarter wavelength transformers as equivalent to an amplitude ponderation of the currents on the ith patch in comparison to the $(i-1)^{th}$ patch, with the first patch of each branch normalized to one. As a first approach we consider that the amplitudes on the patches are decreasing the farther we go from the center feed and the maximal reduction is bounded to a third.

Table 1: Feeding Network Optimization Parameters

Left Branch			Right Branch			Phase
$\frac{I_{1left}}{I_{2left}}$	$\frac{I_{2left}}{I_{3left}}$	$\frac{I_{3left}}{I_{4left}}$	$\frac{I_{1right}}{I_{2right}}$	$\frac{I_{2right}}{I_{3right}}$	$\frac{I_{3right}}{I_{4right}}$	$X_{left} - X_{right}$
1.82	1.74	1.09	1.94	1.93	1.09	60°

Moreover, the lines with unequal electrical length on the central feed are equivalent to a phase difference between the currents on left patches and the right patches. Those parameters are summed up in Table I. The indexes of the current magnitudes go from one for the patches closer to the center to four for the outer patches.

The design variables are then optimized to minimize three cost functions:

- one to optimize the formed radiation pattern (Eq. 1);

$$cost_1 = \max\{20*\log_{10}[E_{model}(\theta)/\csc^2\theta]\}, \quad (1)$$

$$0° < \theta < 40°$$

- one for the sidelobe level (Eq. 2);

$$cost_2 = \max\{20*\log_{10}[E_{model}(\theta)/\max(E_{model}(\theta))]\}, \quad (2)$$

$$\theta < 0° \ \& \ \theta > 40°$$

- one for the decrease rate of the main beam of the radiation pattern towards the ground (Eq. 3).

$$cost_3 = \theta_{AFpeak} - \theta_{null}, \quad (3)$$

with θ_{AFpeak} corresponding to the maximum of the array factor for θ between 0° and 40° and $\theta_{null} < \theta_{AFpeak}$ the closest angle to θ_{AFpeak} which satisfies Eq. 4.

$$20*\log_{10}(E_{model}(\theta_{AFpeak}) / E_{model}(\theta_{null})) = 17dB, \quad (4)$$

The radiation pattern of the array was modeled as an Array Factor multiplied by a $\cos\theta^q$ model of the element pattern (Eq. 5) for the calculation of the cost functions [9].

$$E_{model}(\theta) = AF(\theta) \cos^q\theta, \ q=3.5, \quad (5)$$

with the value of q chosen to approximate the element pattern of the patch from Section 2.

We used the Matlab multi objective genetic algorithms from the Global Optimization Toolbox [10] to optimize this

design. The multi objective genetic algorithm gives us 70 dominant solutions for the optimization problem. We restricted these solutions by selection only those which respect the inequalities in Eq. 6.

$$\text{cost1} < 3\text{dB}, \text{cost2} < -10\text{dB}, \text{cost 3} < 15°, \quad (6)$$

We manually selected a solution with a good trade-off between the three cost functions from this reduced set of dominant solutions and the design currents obtained from this solution are presented in Table 1.

3.3. Feeding Network Parameters

Once we calculated the design currents, we moved on to calculating the physical dimensions of the feeding network capable of realizing them. First, we will calculate the impedances of the quarter wavelength transformers needed for this design. Then we will use LineCalc, a Keysight ADS microstrip design tool [11], in order to calculate the physical widths and lengths of each microstrip quarter wavelength transformer.

In order to calculate the impedances we will use (1), which gives the magnitude of the current on the ith element in function of the magnitude of the currents on the $(i-1)^{th}$ element and the impedances of four consecutive quarter wavelength transformers [7].

$$\frac{I_{i-1}}{I_i} = \frac{Z_{c1}Z_{c3}}{Z_{c2}Z_{c4}}, \quad (7)$$

The indexes of the quarter wavelength transformers in each group of four goes from 1 for the transformers closer to the center of the array to 4 for the ones farther from the center.

We have chosen the impedances of the first and fourth transformer in each group of four quarter wavelength transformers to be equal to, respectively, 70 Ω and 50 Ω. The other two transformers are then calculated to obtain the desired current magnitudes. The impedances of the quarter wavelength transformers are summed up in Table 2.

Concerning the center feed lines we calculated their electrical length in order to realize the phase difference between the patches to the left and to the right of the coaxial feed. As for their impedance, we simulated the full feeding network using ADS and tuned the values in order to balance the power sent to the patches to the left and to the right of the coaxial feed [11].

Table 2: Quarter Wavelength Transformer Impedances

Left Branch 1st		Left Branch 2nd		Left Branch 3rd	
Zc2_1L	Zc3_1L	Zc2_2L	Zc3_2L	Zc2_3L	Zc3_3L
50 Ω	65 Ω	52 Ω	65 Ω	65 Ω	51 Ω
Right Branch 1st		Right Branch 2nd		Right Branch 3rd	
Zc2_1R	Zc3_1R	Zc2_2R	Zc3_2R	Zc2_3R	Zc3_3R
50 Ω	69 Ω	50 Ω	69 Ω	65 Ω	51 Ω

3.4. Iterative Correction

Using the patch antenna from Fig. 1 and the feeding network parameters calculated as in the last section we simulated the full array using CST Microwave Studio [6].

However, because of coupling effects not taken into account during the design, the amplitude of the currents arriving at the patches does not follow the designed values.

Moreover, the phase difference between the patches to the left and to the right of the coaxial feed is more dependent on frequency then expected from the ADS simulations.

Finally, the resonance frequency of the reflection coefficient is no longer placed at the center of the target bandwidth.

Table 3: Feeding Network Physical Dimensions

All values in mm	Zc2		Zc3	
	Length	Width	Length	Width
Transformer 1 Left	14.81	11.90	16.44	0.92
Transformer 2 Left	16.03	2.26	15.12	8.09
Transformer 3 Left	15.34	6.11	15.92	2.71
Transformer 1 Right	14.99	9.47	15.98	2.48
Transformer 2 Right	15.67	3.96	15.82	3.16

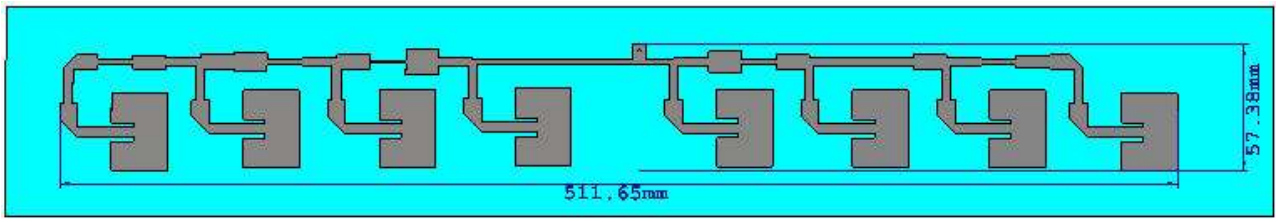

Figure 3: Front view of the optimized linear array of microstrip rectangular patches with inset feeds (Fig. 1). The array is fed from the center via a coaxial cable. Two microstrip lines of different lengths realize the phase difference between the four patches to the left and the four patches to the right.

Transformer 3 Right	15.88	2.88	15.51	4.94
	Zc1		Zc4	
	Length	Width	Length	Width
All Transformers	15.80	3.36	15.34	6.25
	Left of coaxial feed		Right of coaxial feed	
	Length	Width	Length	Width
Center feed	76.25	1.80	15.88	2.91

In order to correct the resonance frequency, it is sufficient to slightly change the length of the patches, while proportionally changing the length of the inset feed.

As for the feeding currents, we followed an iterative correction based on the observation of surface currents obtained from the CST simulation:

- We simulate the array using CST with a surface current monitor at the lower, upper and central frequencies (2.62GHz, 2.655GHz and 2.69GHz);
- If the S11 resonance is not centered we fine tune the length of the patches (keeping the inset feed length at the same proportional length);
- We check the radiating pattern at the lower, upper and central frequencies (2.62GHz, 2.655GHz and 2.69GHz). If they are as designed, we stop.
- When look at the surface current RMS value at each of the patches radiating edges at the side further from the feeding network (which is less disturbed by it). We calculate the ratios from one patch to the next and, if the value is different from the prescribed value from Table 1 we change the transformer impedances to compensate this variation. We also check if both central patches have the same RMS current, and if not we change the impedance of one of the lines in the center of the array to compensate.
- We check the phases of the surface currents at the patches radiating edges to assure the phase difference is as prescribed. If it is not the case, we compensate by varying the length of the transmission lines at the center of the array.

The parameters of the optimized design are shown in Table 3, and the array front view is presented in Fig. 3.

4. Antenna Array Simulations

In this section we will present the simulation results of the antenna array design following the procedure described in Section 3 (Table 3, Fig. 3). We will first present the results for one isolated column. Then we will include the coupling effects when using several columns side by side in a 2D array by means of periodic boundaries conditions.

4.1. Single Column Simulation

In Fig. 4, we show, for the array in Fig. 3, the reflection coefficient and the realized gain in E and H-planes at 2.62 GHz, 2.65 GHz and 2.69 GHz.

As we can see on the E-plane plane, the array presents a slow decrease rate in the realized gain inside of the formed zone, while presenting lobes at least 10 dB than the main beam. The array presents a HPBW of 76° in the H-plane cut. The array has a reflection coefficient bandwidth going from 2.62 GHz to 2.70 GHz. The maximal realized gain of the array goes from 12.3 dB to 13.2 dB in the design bandwidth.

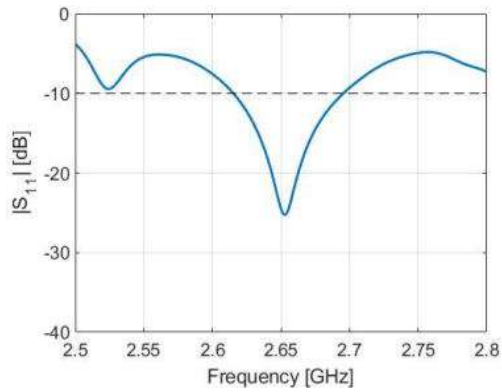

(a)

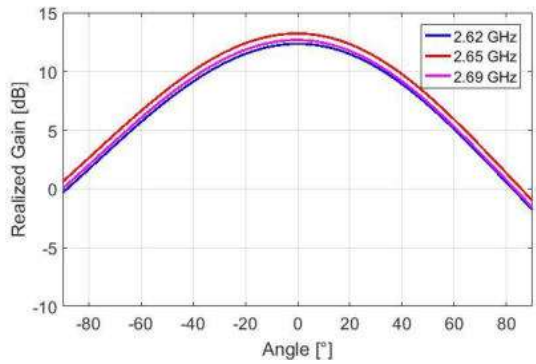

(b)

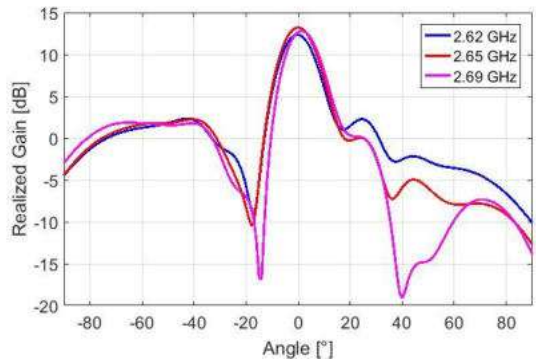

(c)

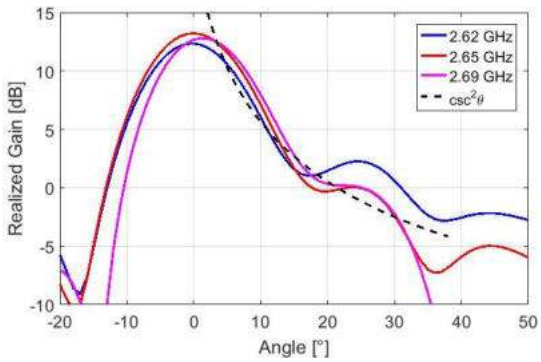

(d)

Figure 4: Results from the simulation of the array in Fig. 3. In (a) we have the reflection coefficient, in (b) the realized gain in the H-plane, in (c) the realized gain in the E-plane and in (d) a zoom on Fig. 4 (c) with the $csc^2\theta$ pattern superposed for reference.

4.2. Coupling effects

In Fig. 5, we show, for the array in Fig. 3 calculated with periodic boundaries conditions to obtain an infinite array with a spacing of 65 mm, the reflection coefficient and the realized gain in E and H planes at 2.62 GHz, 2.65 GHz and 2.69 GHz.

As we can see on the E-plane, the array presents a slow decrease rate in the realized gain inside of the formed zone as expected from the results in Fig.4. However, at 2.69 GHz the coupling between the arrays causes a 1.7 dB rise of the sidelobe level.

The array presents a HPBW of 90° in the H-plane cut, 14° larger than the isolated array. The main beam direction is however skewed by 20°.

The array presents a reflection coefficient bandwidth going from 2.62 GHz to 2.71 GHz, slightly larger than that of the isolated array. There is a small drop in the realized gain, which goes from 11.1 dB to 12 dB in the design bandwidth. The coupling between arrays causes this drop.

The performances of the array are not substantially degraded by the presence of neighboring linear arrays, thus this linear array is suitable for use in a 2D array.

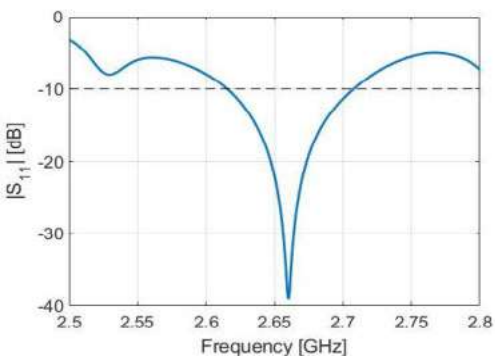

(a)

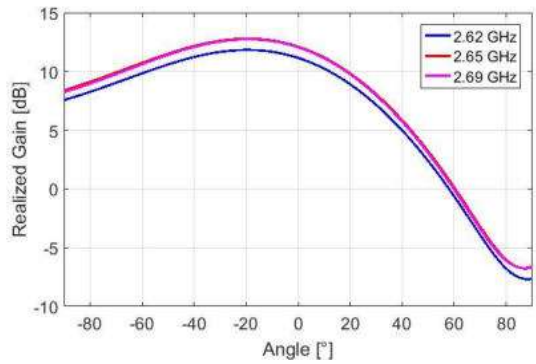

(b)

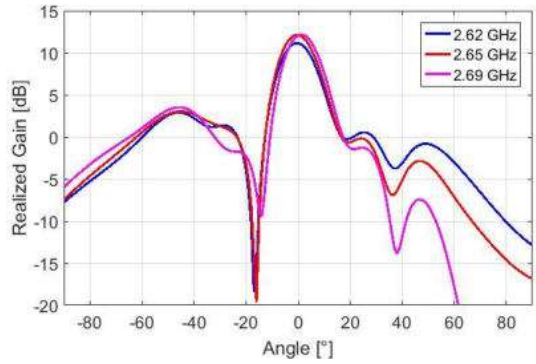

(c)

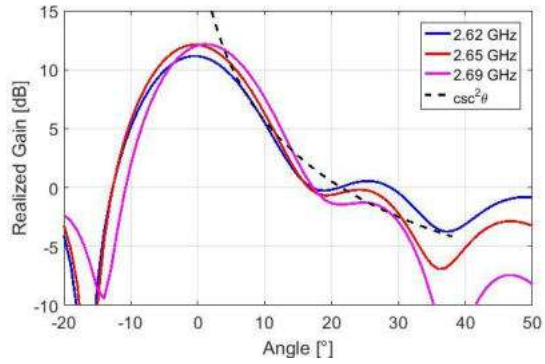

(d)

Figure 5: Results from the simulation of the array in Fig. 3 with periodic boundaries (spacing between columns equal to 65 mm). In (a) we have the reflection coefficient, in (b) the realized gain in the H-plane, in (c) the realized gain in the E-plane and in (d) a zoom on Fig. 5 (c) with the $csc^2\theta$ pattern superposed for reference.

4.3. Four Column Simulation

In Fig. 6, we show the four columns finite array, consisting of four copies of the array in Fig. 3 spaced by 65mm. In Fig. 7, we present the reflection coefficient and the realized gain in E and H planes at 2.62 GHz, 2.65 GHz and 2.69 GHz for this array.

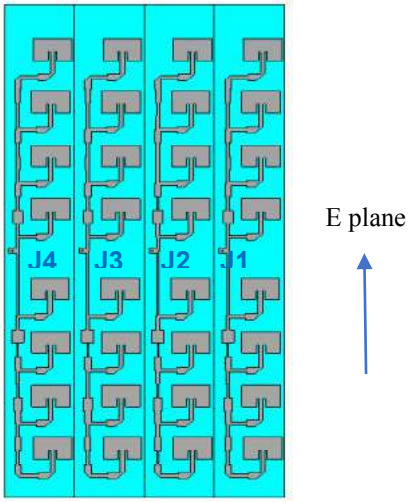

Figure 6: Front view of the 4-column array of microstrip rectangular patches with inset feeds. The array is fed from the center of each column via coaxial cables.

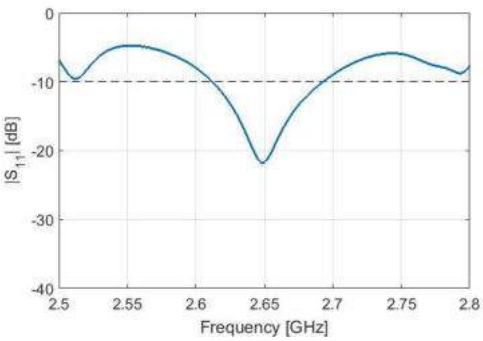

(a)

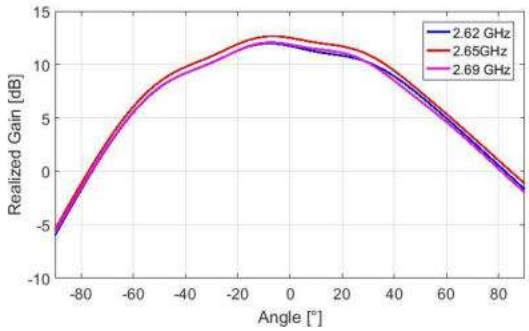

(b)

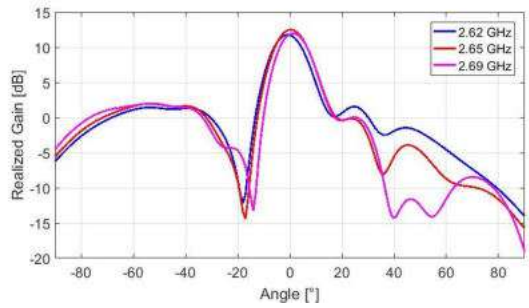

(c)

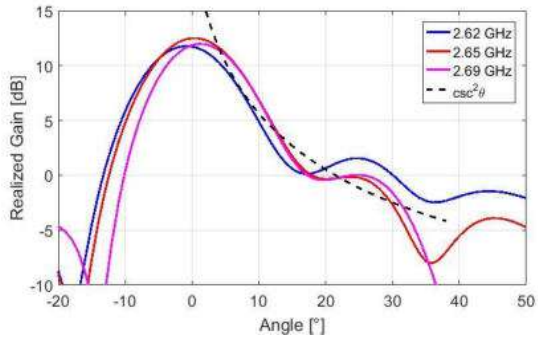

(d)

Figure 7: Results from the simulation of the array in Fig. 6 (4 times the array in Fig. 3 with spacing between columns equal to 65 mm). In (a) we have the reflection coefficient, in (b) the realized gain in the H-plane, in (c) the realized gain in the E-plane and in (d) a zoom on Fig. 5 (c) with the $csc^2\theta$ pattern superposed for reference.

As we can see on the E-plane, the array presents a slow decrease rate in the realized gain inside of the formed zone as expected from the results in Fig.4 and Fig. 5.The worst case sidelobe level is below -10 dB.

The array presents a HPBW of 78° in the H-plane cut, closer to that predicted by the isolated array. The main beam direction is however skewed by 8°, less than predicted by the infinite array simulation.

The array presents a reflection coefficient bandwidth going from 2.61 GHz to 2.69 GHz. The realized gain goes from 11.6 dB to 12.5 dB in the design bandwidth, in between the values for the single column and the infinite array.

5. Antenna Array Prototype

The array was designed originally using the AD430 substrate. However, the material became obsolete so we choose to build it using the Kappa438 substrate, which has very similar characteristics to the AD430. The datasheet value for the relative permittivity for this material is 4.38 and the thickness for our prototype is 3.048mm

As the thickness used for our antenna is not a standard value for this substrate, we built a first prototype of the single column array so that we could obtain the material properties by retrofitting simulations. By closely analyzing the Kappa438 properties, we noticed that it presents a certain level of anisotropy [12]. For our retrofit simulations (Fig. 8), we considered this anisotropy and converged at the value:

$$(\varepsilon_{rx}, \varepsilon_{ry}, \varepsilon_{rz}) = (4.55, 4.55, 4.16), \qquad (8)$$

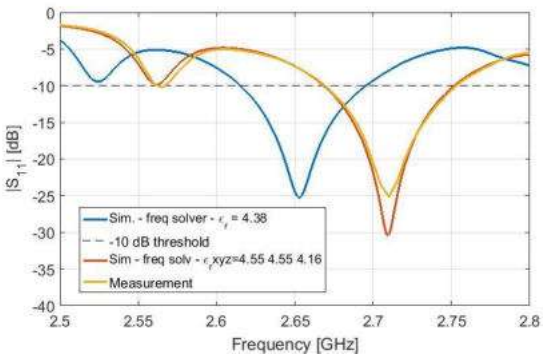

Figure 8: Reflection coefficient of the array in Fig. 3 simulated with CST using a $\varepsilon_r = 4.38$ substrate in blue, using a (ε_{rx}, ε_{ry}, ε_{rz}) = (4.55, 4.55, 4.16) substrate in red and the measured prototype first run in yellow.

The first prototype had the bandwidth slightly shifted up from the desired bandwidth and, to correct that, we scaled the entire array by 1.02 (verifying that it did bring the bandwidth to the desired range, 2.62GHz - 2.69GHz, by simulating the array using the retrofitted values of the Kappa438).

The antenna compose with four linear arrays was realized and measured in an anechoic chamber. The measurement of the reflection coefficient is given in Fig. 9. Each linear array is measured when 50 Ohms load the others.

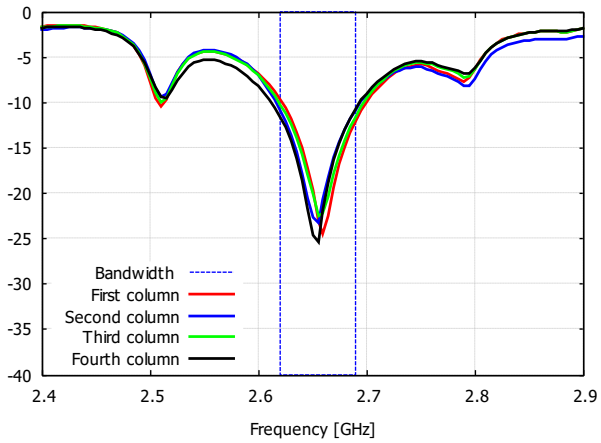

Figure 9: Reflection coefficient of one linear array among the three others.

The levels are below -10 dB in the required bandwidth between 2.62 GHz and 2.69 GHz. We can also note a good similarity between the four measurements. The coupling terms were also measured and are less than -20 dB throughout the bandwidth.

The measured radiation pattern in the E plane is plotted in Fig. 10 and compared to the simulations. Only the J3 array is fed (the other arrays being loaded by 50 Ohms).

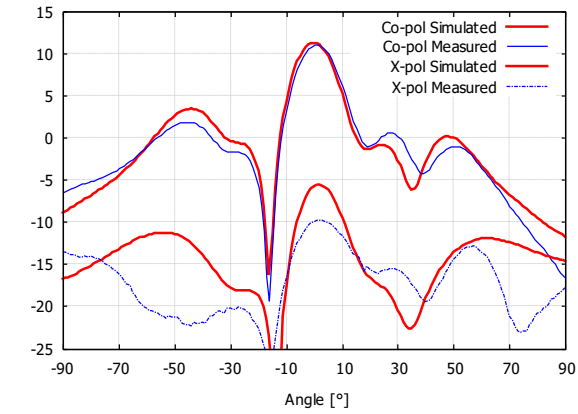

a)

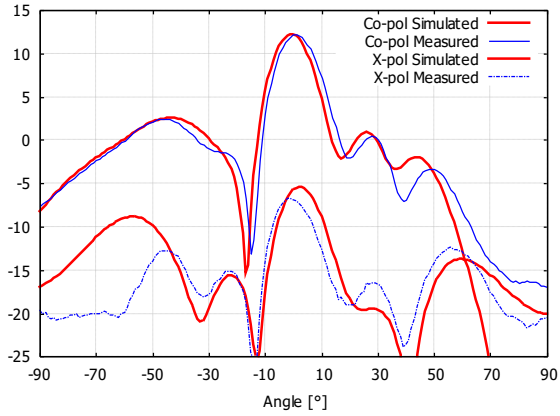

b)

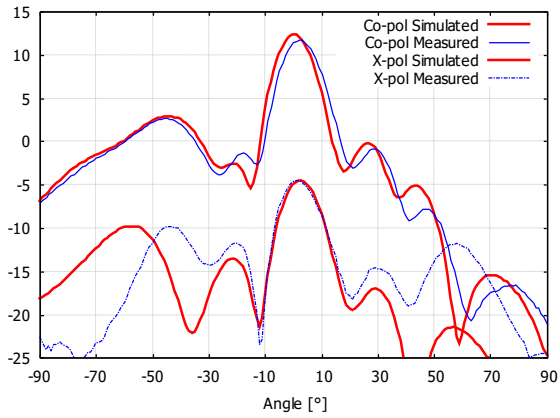

c)

Figure 10: Comparison between the measured and simulated E-plane radiation patterns when the J3 array is fed at 2.62 GHz (a), 2.655GHz (b) and 2.69 GHz (c).

The measured radiation pattern in the H plane is plotted in Fig. 11 and compared to the simulations. Only the J3 array is fed (the other arrays being loaded by 50 Ohms).

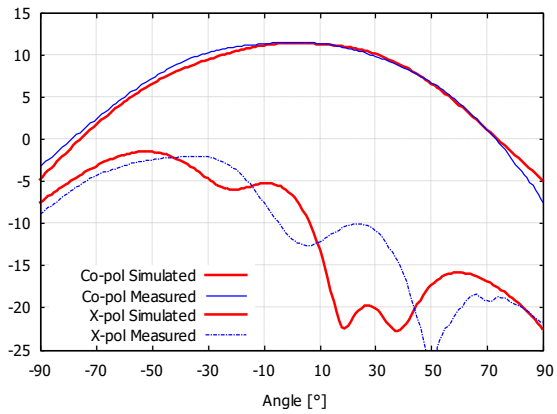

a)

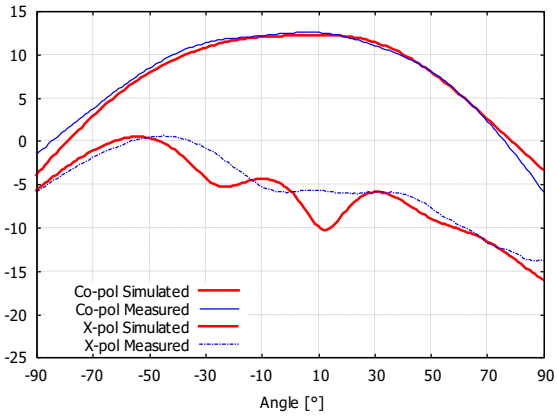

b)

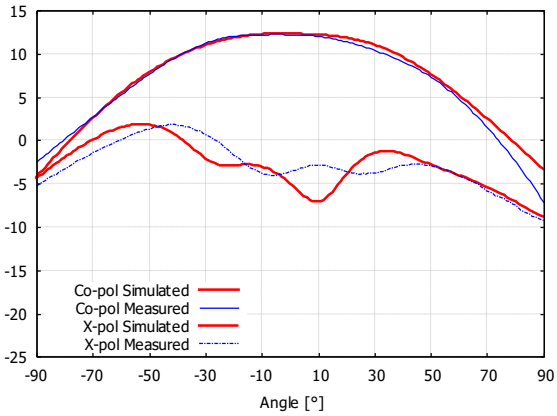

c)

Figure 11: Comparison between the measured and simulated H-plane radiation patterns when the J3 array is fed at 2.62 GHz (a), 2.655GHz (b) and 2.69 GHz (c).

For all the measurements, there is good agreement with the simulated results. In E-plane, the shape of the radiation pattern follows the cosecant squared law (towards the sky, positive angles) and the decrease of the radiation pattern is obtained around 15° (towards the ground, negative angles). In H-plane, the radiation patterns have HPBW equal to 84° at 2.62 GHz, 88° at 2.655 GHz and 82° at 2.69 GHz. The gain levels vary between 11 dB and 12.9 dB. The cross polarization components remains 17 dB below the main component on-axis.

6. Conclusions

Four linear arrays of microstrip rectangular patches has been developed and simulated using different simulators. Each linear array has been designed to have a cosecant squared radiation pattern in the E-plane and to presents a 90° HPBW in the H-plane. The design steps procedure has been detailed and a first realization made it possible to take into account the deviations of the materials used. Then four linear arrays has been realized and measured. Each array bandwidth goes from 2.62 GHz to 2.69 GHz with a reflection coefficient below -10 dB and the realized gain that goes from 11.1 dB to 12.2 dB in the required bandwidth. These measurement results, in agreement with the simulation, demonstrate that the arrays have the required specifications in terms of matching and shape of radiation patterns. All of these results validate the design of the four linear arrays.

Acknowledgements

This project has received funding from the Banque Publique d'Investissement and the Conseil Régional d'Ile-de-France (Paris Region) in the framework of the FUI program DIOD.

References

[1] S. Park, H. T. Kim, S. Lee, H. Joo and H. Kim, Survey on Anti-Drone Systems: Components, Designs, and Challenges, *IEEE Access*, vol. 9, pp. 42635-42659, 2021.

[2] R. K. Miranda, D. A. Ando, J. P. da Costa, and M. T. de Oliveira, Enhanced direction of arrival estimation via received signal strength of directional antennas, *Proceedings of the 2018 IEEE International Symposium on Signal Processing and Information Technology (ISSPIT)*, pp. 162–167, 2018.

[3] D. A. Ando, R. K. Miranda, J. P. da Costa, and M. T. de Oliveira, A novel direction of arrival estimation algorithm via received signal strength of directional antennas, *Proceedings of the 2018 Workshop on Communication Networks and Power Systems (WCNPS)*, pp. 1–5, 2018.

[4] R. C. Hansen, Array pattern control and synthesis, *Proc. IEEE*, vol. 80, pp. 141-151, Jan. 1992.

[5] J. L. Volakis, *Antenna Engineering Handbook*, 4th Edition, McGraw-Hill Education, 2014.

[6] CST Studio Suite 2016.

[7] D. M. Pozar, *Microwave Engineering*, 4th Edition, John Wiley & Sons, 2012.

[8] R. L. Haupt, D. H. Werner, *Genetic Algorithms in Electromagnetics*, John Wiley & Sons, 2006.

[9] R. L. Haupt, *Antenna Arrays, a Computational Approach,* John Wiley & Sons, 2010.

[10] Matlab 2018 Global Optimization Toolbox.

[11] ADS 2018 Keysight.

[12] MWI Microwave Impedance Calculator, Rogers Corporation, 2019.

MMW 60 GHz Tunable Periodic Filter

Abdolreza Divsalar, Shahin Salarian, Dariush Mirshekar-Syahkal,

RF & Microwave Research Lab, School of Computer Science and Electronic Engineering
University of Essex, Colchester, United Kingdom
E-mail: adivsa@essex.ac.uk

Abstract

A novel mm-wave periodic filter structure has been proposed based on a new design approach. The filter performs at 60 GHz with 3.5 GHz bandwidth. The structure composed of periodic Microstrip stubs on BL037 Liquid Crystal substrate. Changing the bias voltage of LC provides a tunability from 58.5 to 62 GHz, while maintains the fractional bandwidth around 5%. The return loss of passband is better than 10dB with insertion loss variation from 3.8 to 5 dB. In addition, the effect of a different LC substrate (i.e. GT3-23001) has been investigated which provides similar behavior with a wider tuning distance.

1. Introduction

Broadband MMW 60 GHz transmission systems are the most promising technology to respond to the demanding requirements of increased data rate and wide bandwidth of future indoor fast data/audio/video distributions and communication systems [1].

However, due to the different allocated free licensed frequency bands around the world regions and because of required set-ups and internal functions, tunable filters and adaptive components would be required for future 60 GHz wireless systems. A filter with periodic structure at equal intervals, is a filter with a series of deep notches in its frequency response. Each notch acts as narrow band-stop filter, with a high-quality factor. These filters will be used to remove periodic noises and undesired frequencies. In microwave micro-strip filters, operation frequency and filter characteristics would be a function of both physical (i.e. dimensions and thickness of conducting strip and substrate layer) and electrical characteristics of the microstrip structure which consists of a conducting strip separated from a copper ground plane by a dielectric layer known as the substrate. For a tunable filter the physical characteristics cannot be changed for a built component, therefore the possible control would be on the electrical characteristic. The electrical characteristic can be controlled by changing the effective permittivity (i.e. ε_{eff}) of the dielectric layer(s). Filter tuning in microwave components is possible using ferroelectric, piezoelectric and Liquid Crystal (LC) materials. The basics of these approaches are varying electrical properties of the above-mentioned materials with a bias voltage to tune the RF component. Among these materials, LCs have the advantages of lower cost, lower operating voltage, virtually no power consumption and benefits from having stable and continuous electrical tuning. Several reports of tunable filter experimental & simulation designs in frequencies up to 33 GHz band have been published in the recent years [2].

2. Theory of Periodic Structure

A Periodic Filter is a structure formed by cells of similar repeated components to provide filtering characteristics. Cascade structure of capacitive stubs periodically loaded to a transmission line can form a periodic filter. Each capacitive stub can be presented as a Susceptance *jb* to form the following structure of Fig.1:

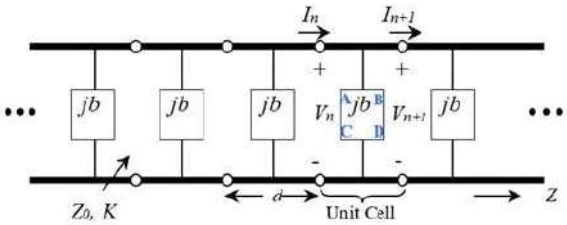

Fig. 1. Periodic Structure

3. Design Method

Traditional method of microstrip filter design starts determining the values of the lumped inductive and capacitive components from the available tables for the allowed ripples and the order of the filter, and then the dimensions of distributed elements of microstrip would be obtained step by step using Richard Transformation and Kuruda identities. Periodic Structures consist of cascade of a number of identical "Unit Cells" providing distributed inductance/capacitance to obtain the required filter performance. Therefore, design of periodic structure starts with the design of the Unit Cell.

The proposed design method for determining of the "unit cell" parameters and then periodic filter is shown in the

flowchart of Fig 2. This novel method is obtained from the theoretical analysis of periodical structures.

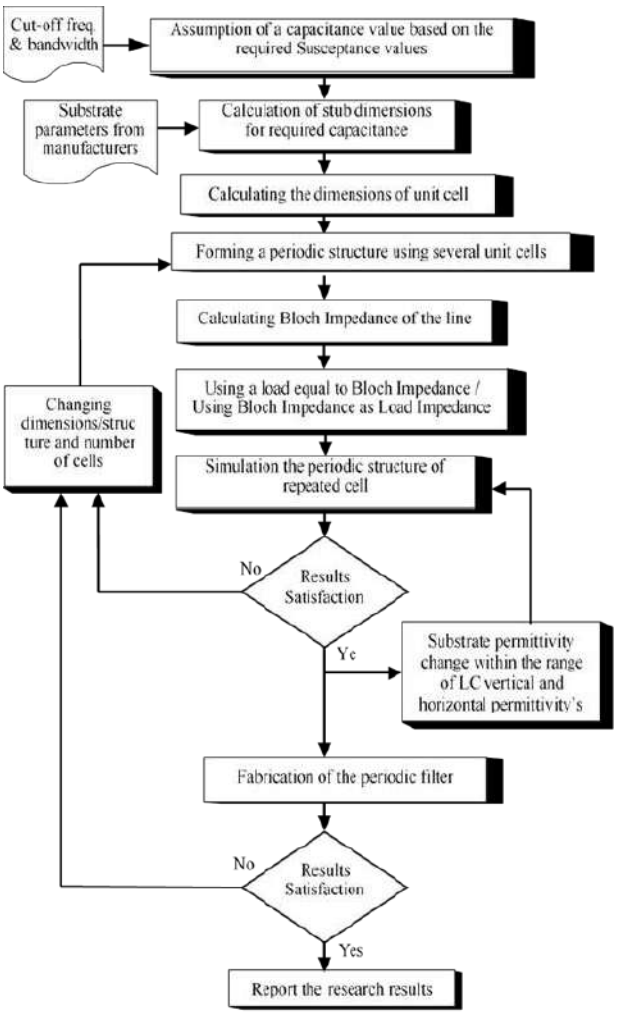

Fig. 2. Proposed design procedure for periodic filter

Unlike traditional filter design method, we do not have sets of formulas and tables for different filter models (i.e. Butterworth, Chebyshev, Elliptical). The proposed method for filter design is based on initial estimations for the key elements to meet the requirements of periodic structure kd-βd diagram and required operating frequency region. The required bandwidth and other filter specifications, would be the design parameters which defines the number of "unit cells".

4. Liquid Crystal Substrate

Different methods have been reported to provide tunebility in microwave components using Liquid Crystal (LC) materials. The basics of these approaches are varying electrical properties of the LC with a bias voltage to tune the RF component. LCs have the advantages of lower cost, lower operating voltage, virtually no power consumption and also benefits from having stable and continuous electrical tuning. LCs can flow like liquids, but still its molecules are oriented in a crystal-like way. Nematic LCs are anisotropic materials, and their physical properties change with the alignment and direction of rod-shaped molecules. The relative permittivity of a nematic LC varies between two values of $\varepsilon_{r-\parallel}$ and $\varepsilon_{r\perp}$ for when the molecular orientations are aligned (parallel) or perpendicular with the surface of LC. An external voltage that changes the LC director field can control the molecular orientation of LC. The difference between $\varepsilon_{r-\parallel}$ and $\varepsilon_{r\perp}$ is known as liquid crystal anisotropy. Because of the fluid nature of liquid crystal material, it should be confined in a cavity inside the device and then sealed. For this reason, the topology of inverted-microstrip in that the line substrate covers liquid crystal cavity, seems to be the most adequate to implement the filter [3].

Below table lists some of the most common nematic liquid crystals which are already used at microwave frequencies [4]. We have used two different types of BL037 and GT3-23001liquid crystal substrates for our design and simulations.

Table 1. The most common liquid crystal specifications at room temperature 20°C

Liquid Crystal	Permittivity		Dielectric anisotropy
	$\varepsilon_{r\perp}$	$\varepsilon_{r-\parallel}$	$\Delta\varepsilon$
K15(5CB)	2.72	2.90	0.18
BL037	2.35	2.61	0.26
BL006	2.62–2.69	3.11–3.12	0.49–0.43
E7	2.72	3.17	0.45
GT3-23001	2.46–2.50	3.28–3.30	0.82–0.80
GT3-24002	2.50	3.30	0.80

5. Results and Discussion

Different periodic structures are designed and simulated with 3, 5, and 7 unit cells with the calculated parameters based on the proposed method, using the ADS software. The band-pass/band-stop behavior of the structure has been maintained in different number of cells, however, the frequency response and number of notches and width of pass-band (i.e. filter bandwidth) has changed for different number of unit cells. Fig. 3 shows the results for a filter with 5 stubs.

In another simulation, the permittivity of the substrate of the 5-cell periodic structure has been changed to demonstrate the changes in the electrical characteristic of Liquid Crystal substrate as the bias voltage changes. As shown in Fig. 4(a), for BL037 LC, the pass band shifts from 60.5-64 GHz to 57-60.5 GHz. This is an ideal tuning performance as there is no overlap between the pass-bands for such a small liquid crystal anisotropy.

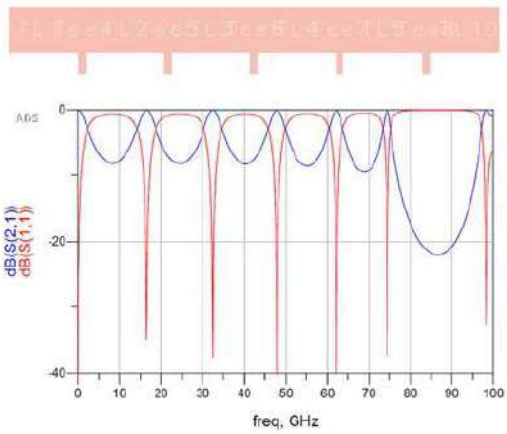

Fig. 3. Simulation results of 5-unit cells in a periodic structure

In simulation of Fig. 4(b), the substrate is GT3-23001 liquid crystal, the pass-band of a 5 sell periodic structure moves between band 58-61.5 GHz to 53-54.5 GHz, also the adjacent band 62-64 GHz which is narrower would be available if the bias voltage change the permittivity of the liquid crystal. For GT3-23001 the anisotropy is much more than BL037 and provides a much better isolation between pass-bands, therefore this LC can be used for the applications when a large separation is needed.

6. Conclusions

Various Periodic Filters based on LC have been designed modelled and investigated using capacitive open circuit stubs in 60GHs. A novel design method and procedure using kd-βd curve has been proposed for periodic structures. Different numbers of repeating cells for periodic structures have been simulated to analyses the effect of the number of repeating cells on filter performance.

References

[1] Aydin Babakhani, Xiang Guan, Abbas Komijani, Arun Natarajan and Ali Hajimiri, "A 77-GHz Phased-Array Transceiver With On-Chip Antennas in Silicon: Receiver and Antennas", IEEE Journal of Solid-State Circuits, Vol. 41, NO. 12, Dec. 2006.

[2] S. Missaoui and M. Kaddour, "Liquid-Crystal Based Reconfigurable Tuneable Filter with DBR Topology", International Scholarly Research Network, Volume 2011, Article ID 784615

[3] V. Urruchi, C. Marcos, J. Tottcilla, J. M. Sanchez-Pena and K Garbat, "Tuneable notch filter based on liquid crystal technology for microwave applications," Review of Scientific Instruments 84, 2013

[4] Pouria Yaghmae, Onur Hamza karabey, Bevan Bates, Christophe Fumeaux, and Rolf Jakoby," Electrically Tuned Microwave Devices Using Liquid Crystal Technology," International Journal of Antennas and propagation, Volume 2013

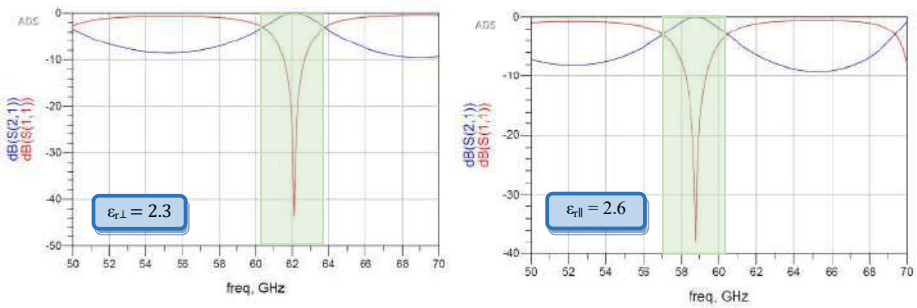

(a) Liquid Crystal BL037: $\varepsilon_{r\perp} = 2.3$, $\varepsilon_{r\parallel} = 2.61$

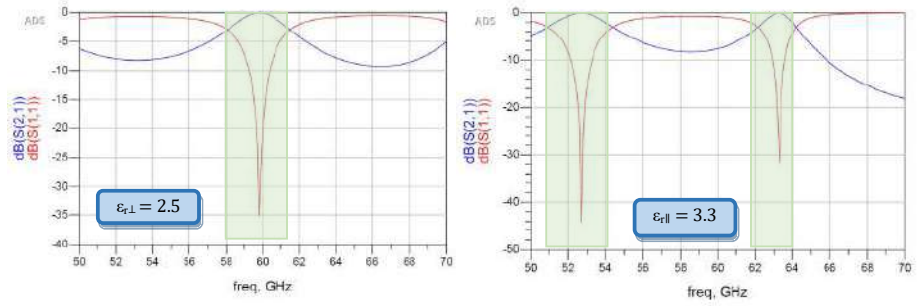

(b) Liquid Crystal GT3-23001: $\varepsilon_{r\perp} = 2.5$, $\varepsilon_{r\parallel} = 3.3$

Fig. 4. Frequency tuning with liquid crystal